# UC San Diego

## UC San Diego Electronic Theses and Dissertations

### Title

Finite element response sensitivity and reliability analysis of Soil-Foundation-Structure-Interaction (SFSI) systems

### Permalink

https://escholarship.org/uc/item/1jv9c7xb

### Author

Gu, Quan

### Publication Date

2008

Peer reviewed|Thesis/dissertation

eScholarship.org Powered by the California Digital Library
University of California

UNIVERSITY OF CALIFORNIA, SAN DIEGO

# FINITE ELEMENT RESPONSE SENSITIVITY AND RELIABILITY ANALYSIS OF SOIL-FOUNDATION-STRUCTURE-INTERACTION (SFSI) SYSTEMS

A dissertation submitted in partial satisfaction of the requirements for the degree

Doctor of Philosophy

in

Structural Engineering

by

Quan Gu

Committee in charge:

Professor Joel P. Conte, Chair
Professor Ahmed Elgamal
Professor Philip E. Gill
Professor J. Enrique Luco
Professor Hidenori Murakami

2008

Copyright

Quan Gu, 2008

All rights reserved.

The dissertation of Quan Gu is approved, and it is acceptable in quality and form for publication on microfilm:

_____

_____

_____

_____

_____
Chair

University of California, San Diego

2008

To my son Eric Gu and my wife Surong Huang.

## TABLE OF CONTENTS

Signature Page . . . . . iii

Dedication . . . . . iv

Table of Contents . . . . . v

List of Tables . . . . . xiii

List of Figures . . . . . xvii

Acknowledgements . . . . . xxxiv

Vita . . . . . xxxvi

Abstract of the dissertation . . . . . xxxvii

**CHAPTER 1: INTRODUCTION . . . . . 1**

1.1 Background . . . . . 1

1.2 Objectives . . . . . 5

1.3 Literature Review . . . . . 8

1.4 Software Platforms . . . . . 9

1.4.1 FEAP . . . . . 9

1.4.2 FEDEASLab-FERUM . . . . . 10

1.4.3 OpenSees . . . . . 11

1.5 Organization of the Dissertation . . . . . 12

**CHAPTER 2: FRAMEWORK OF RELIABILITY ANALYSIS AND PROBABILISTIC CHARACTERIZATION OF SSI SYSTEMS . . . . . 14**

2.1 Computational Framework for Reliability Analysis of SSI Systems . . . . . 14

2.2 SSI System and its Finite Element Model . . . . . 18

2.2.1 Nonlinear Dynamic Models of SSI Systems . . . . . 18

2.2.2 Stochastic Modeling of Earthquake Loading . . . . . 20

2.2.3 Representation of Uncertainty in Structural and Geotechnical Material Properties . . . . . 22

2.2.4 Limit-State Surface Design, Topology and Visualization . . . . . 23

2.2.5 Development of Limit-State Functions for Structures and SSI Systems . . . . . 25

2.3 Design Point Search and Failure Probability Computation . . . . . 26

2.3.1 Design Point(s) Search . . . . . 26

2.3.2 Approximate Evaluation of the Probability Content of the Failure Domain . . . . . 28

**CHAPTER 3: FINITE ELEMENT RESPONSE SENSITIVITY ANALYSIS FRAMEWORK FOR STRUCTURAL AND GEOTECHNICAL SYSTEMS . . . . . 30**

3.1 General Displacement Based FE Response Sensitivities by Direct Differentiation Method (DDM) . . . . . 30

3.2 Response Sensitivity Computation at the Structural Level . . . . . 32

3.2.1 Response Sensitivity with respect to Nodal Coordinates . . . . . 38

3.2.2 Response Sensitivity with respect to Material Parameters . . . . . 41

3.2.3 Response Sensitivity with respect to Load Parameters . . . . . 43

3.3 Response Sensitivity Computation at the Element Level . . . . . 45

3.4 Response Sensitivity Computation at Section and Material Level . . . . . 46

3.4.1 Sensitivity computatoin for 1D $J_2$ (Von Mises) Plasticity model . . . 47

3.5 Issues regarding the Sensitivity Algorithm Based on DDM . . . . . 57

3.5.1 Sensitivity Convergence Studies . . . . . 61

3.5.2 Discontinuities of Response Sensitivities, and Propagation of Discontinuities from Local material properties to Global Response Sensitivities . . . . . 128

3.5.3 Effect of Damping . . . . . 143

3.5.4 Post Stiffness Studies . . . . . 159

3.6 Conclusions for the Issues of the Sensitivity Analysis . . . . . 175

**CHAPTER 4: FINITE ELEMENT RESPONSE SENSITIVITY ANALYSIS FRAMEWORK FOR STRUCTURAL AND GEOTECHNICAL SYSTEMS . . . . . 177**

4.1 Introduction . . . . . 177

4.2 Multi-Yield-Surface $J_2$ Plasticity Clay Model . . . . . 177

4.2.1 Multi-Yield Surface . . . . . 178

4.2.2 Flow Rule (Continuum Form) . . . . . 182

4.2.3 Discretized Form of Flow Rule . . . . . 183

4.2.4 Hardening Law . . . . . 187

4.3 Consistent Tangent Operator . . . . . 192

4.3.1 Continuum Tangent Operator . . . . . 193

4.3.2 Consistent Tangent Moduli . . . . . 195

4.3.3 Three-Dimensional Block Subjected to Quasi-Static Cyclic Loading . . . . . 200

4.3.3.1 Comparison of Convergence Rate and Computational Time . . 203

4.3.3.2 Comparison of Convergence Rate for Smaller Convergence Tolerance . . . . . 207

4.3.3.3 Convergence Rate Comparison for Varying Number of Yield Surfaces . . . . . 211

4.3.4 Layered Soil Column Subjected to Earthquake Base Excitation . . 215

4.3.4.1 Comparison of the Convergence Rate and Computational Time between the Use of Consistent and Continuum Tangent Moduli . . . . . 219

4.3.4.2 Comparison of Convergence Rates with Smaller Convergence Tolerance . . . . . 223

4.3.4.3 Comparison of the Convergence Rates with Varying Time Step Size . . . . . 227

4.3.4.4 Comparison of the Convergence Rate using Different Number of Yield Surfaces . . . . . 230

4.3.5 Conclusions . . . . . 233

4.3.6 Appendix A. Derivation of Stress Correction . . . . . 235

4.3.7 Sensitivity Computation . . . . . 242

4.3.7.1 Initial Surface Sensitivity . . . . . 242

4.3.7.2 Stress Sensitivity . . . . . 244

4.3.7.3 Active Surface Update . . . . . 246

4.3.7.4 Update Inner Surface Sensitivities . . . . . 247

4.3.7.5 Numerical Examples . . . . . 248

4.3.7.6 Summary . . . . . 271

4.4 Extention of Sensitivity Framework to Multiple Point Constraint Handlers . . . . . 271

4.4.1 Sensitivity Computation . . . . . 272

4.4.1.1 Transformation Equations Method. . . . . 273

4.4.1.2 Lagrange Multipliers Method. . . . . 275

4.4.1.3 Penalty Functions Method . . . . . 275

4.5 Extention of Sensitivity Framework to Variable Transient Integration Analysis . . . . . 276

4.6 Examples of Response Sensitivity Analysis of SFSI Systems . . . . . 276

4.6.1 2D SFSI System. . . . . 276

4.6.2 3D Pile Soil System. . . . . 304

4.6.3 3D SFSI System. . . . . 314

4.7 Conclusion. . . . . 342

**CHAPTER 5: PROBABILISTIC PUSHOVER ANALYSIS OF STRUCTURAL AND GEOTECHNICAL SYSTEMS . . . . . 344**

5.1 First-Order Second-Moment Probabilistic Response Analysis. . . . . 347

5.2 Probabilistic Response Analysis Using Monte Carlo Simulation . . . . . 349

5.3 Estimation of Response probability distributions . . . . . 351

5.4 Application Examples . . . . . 352

5.4.1 Three-Dimensional R/C Frame Building . . . . . 352

5.4.2 Two-Dimensional SFSI System. . . . . 375

5.4.3 Conclusions . . . . . 393

5.5 APPENDIX A . . . . . 394

**CHAPTER 6: RELIABILITY ANALYSIS FOR STRUCTURAL AND GEOTECHNICAL SYSTEMS . . . . . 396**

6.1 Introduction and Background . . . . . 396

6.1.1 Classical Time Invariant Reliability Analysis in Performance Based Engineering . . . . . 396

6.2 SNOPT Based Design Point Search Algorithm . . . . . 407

6.2.1 Integration of SNOPT into OpenSees as Reliability Tool . . . . . 409

6.3 Sampling Analysis. . . . . 413

6.3.1 Zero-One Indicator-Based Monte Carlo Simulation, or Crude Monte Carlo Method . . . . . 413

6.3.2 Importance Sampling Method (IS) . . . . . 414

6.3.3 Orthogonal Plane Sampling Method (OPS) . . . . . 418

6.4 Application Examples of Time Invariant Reliability Analysis of SFSI System . . . . . 423

6.4.1 2D SFSI Example . . . . . 423

6.5 Time Variant Reliability Analysis . . . . . 435

6.5.1 Background . . . . . 435

6.5.2 Rice's Formula . . . . . 437

6.5.3 Estimation of Mean Out Crossing Rate . . . . . 440

6.5.4 FORM Approximation of the Mean Upcrossing Rate and Failure Probability . . . . . 442

6.5.5 Discrete Representation of Stochastic Excitation . . . . . 446

6.6 Application Examples of Time variant Reliability Analysis of SFSI System . . . . . 449

6.6.1 2D SFSI System . . . . . 449

6.7 Multi-Dimentional Visualization in Principle Planes (MVPP) . . . . . 457

6.8 Design Point-Response Surface Method-Simulation (DP-RS-Sim) Technique . . . . . 460

6.8.1 Response Surface Method . . . . . 461

6.8.2 Nonlinear Surface Fitting . . . . . 463

6.8.3 Linear Part Estimate . . . . . 465

6.8.4 Estimation of Values on the Second LSF . . . . . 467

6.8.5 The Fitting Process in OpenSees . . . . . 467

6.8.6 FE Divergence Case . . . . . 469

6.8.7 Application Example . . . . . 469

6.8.8 Conclusions of DP-RS-Sim Method . . . . . 481

6.9 Conclusions . . . . . 482

**CHAPTER 7: NONLINEAR MODEL UPDATING AND PARAMETER CALIBRATION FOR STRUCTURAL AND GEOTECHNICAL SYSTEMS . . . . . 485**

7.1 Overview of Finite Element Model Updating . . . . . 485

7.2 SNOPT as a General Optimization Tool Box for Structural and Geotechnical Model Updating . . . . . 487

7.3 Integration of SNOPT into OpenSees as a General Optimization Tool . . . 488

7.4 Nonlinear Model Updating for Soil Column . . . . . 493

7.4.1 Numerical Example 1. Nonlinear Model Updating of a Soil Column Subjected to Weak Ground Motions. . . . . 493

7.4.2 Numerical Example 2. Nonlinear Model Updating for a Soil Column Subjected to Strong Ground Motions . . . . . 507

7.4.3 Real Example 1, Linear Model Updating . . . . . 516

7.4.4 Real Example 2, Nonlinear Model Updating . . . . . 524

7.5 Conclusions . . . . . 534

**CHAPTER 8: USER'S GUIDE TO RESPONSE SENSITIVITY AND RELIABILILTY ANALYSES OF SSI SYSTEM IN OPENSEES. . . . . 536**

8.1 SSI Model Development . . . . . 536

8.1.1 Basic Requirements . . . . . 537

8.1.2 Structure Model . . . . . 541

8.1.3 Soil Model . . . . . 541

8.1.4 Connection between Structure and Soil . . . . . 541
8.1.5 Load Pattern . . . . . 542
8.1.6 Adaptive Integration Time Step . . . . . 542
8.1.7 Response Sensitivity Recorder . . . . . 543
8.2 Response Sensitivity Analysis . . . . . 544
8.2.1 Two Stage Analysis . . . . . 544
8.2.2 Random Variable Updating . . . . . 545
8.3 Reliability Analysis . . . . . 546
8.3.1 Design Point Search . . . . . 546
8.3.2 FORM, SORM and Mean Upcrossing Rate Analyses . . . . . 547
8.3.3 Sampling Analysis . . . . . 550
8.3.4 Response Surface Method . . . . . 552
8.4 General SNOPT Based Optimization . . . . . 555

**CHAPTER 9: CONCLUSIONS . . . . . 559**

9.1 Summary of Contributions and Findings . . . . . 559
9.2 Recommendations for Future Work . . . . . 566

**REFERENCE . . . . . 566**

# LIST OF TABLES


Table 3.1: FEM differentiation results . . . . . 66

Table 3.2: Minimum number of elements per beam/column required for convergence of global response and its sensitivities . . . . . 81

Table 3.3: Minimum number of elements per beam/column required for convergence of local response and its sensitivities . . . . . 81

Table 3.4: FE differentiation results . . . . . 88

Table 3.5: Element number per beam/column required in global convergence case . . 107

Table 3.6: Element number per beam/column required in local convergence case . . . 107

Table 3.7: Largest time interval (sec.) required for global convergence . . . . . 127

Table 3.8: Largest time interval (sec.) required for local convergence . . . . . 127

Table 4.1: Unbalanced force versus iteration number in load step # 20 (tol = 1E-4 [kN]) . . . . . 206

Table 4.2: Last incremental displacement versus iteration number in load step # 20 (tol = 1E-8 [m]) . . . . . 206

Table 4.3: Last incremental energy versus iteration number in load step # 20 (tol = 1E-12 $[kN \cdot m]$). . . . . 206

Table 4.4: Unbalanced force versus iteration number in load step # 15 (tol = 1E-8 [kN]) . . . . . 210

Table 4.5: Last incremental displacement versus iteration number in load step # 15 (tol = 1E-12 [m]) . . . . . 210

Table 4.6: Last incremental energy versus iteration number in load step # 15 (tol = 1E-20 $[kN \cdot m]$ ) . . . . . 210

Table 4.7: Unbalanced force versus iteration number in load step # 10 (tol = 1E-4 [kN]) . . . . . 214

Table 4.8: Last incremental displacement versus iteration number in load step # 10 (tol = 1E-8 [m]) . . . . . 215

Table 4.9: Last incremental energy versus iteration number in load step # 10 (tol = 1E-12 $[kN \cdot m]$ ) . . . . . 215

Table 4.10: Material properties of various layers of soil column . . . . . 216

Table 4.11: Unbalanced force versus iteration number in load step # 30 (tol = 1E-4 $[kN \cdot m]$ ) . . . . . 222

Table 4.12: Last incremental displacement versus iteration number in load step # 30 (tol = 1E-8 [m]) . . . . . 222

Table 4.13: Last incremental energy versus iteration number in load step # 30 (tol = 1E-12 $[kN \cdot m]$ ) . . . . . 222

Table 4.14: Unbalanced force versus iteration number in load step # 40 (tol = 1E-8 [kN]) . . . . . 226

Table 4.15: Last incremental displacement versus iteration number in load step # 40 (tol = 1E-12 [m]) . . . . . 226

Table 4.16: Last incremental energy versus iteration number in load step # 40 (tol = 1E-20 $[kN \cdot m]$ ) . . . . . 226

Table 4.17: Unbalanced force versus iteration number in load step # 60 (tol = 1E-4 [kN]) . . . . . 229

Table 4.18: Last incremental displacement versus iteration number in load step # 60 (tol = 1E-8 [m]) . . . . . 229

Table 4.19: Last incremental energy versus iteration number in load step # 60 (tol = 1E-12 $[kN \cdot m]$ ) . . . . . 229

Table 4.20: Unbalanced force versus iteration number in load step # 30 (tol = 1E-4 [kN]) . . . . . 232

Table 4.21: Last incremental displacement versus iteration number in load step # 30 (tol = 1E-8 [m]) . . . . . 232

Table 4.22: Last incremental energy versus iteration number in load step # 30 (tol = 1E-12 $[kN \cdot m]$ ) . . . . . 233

Table 4.23: Material parameters . . . . . 278

Table 4.24: Material parameters . . . . . 305

Table 4.25: Material parameters (unit:kPa) . . . . . 316

Table 5.1: Marginal PDFs of material parameters for the three-story building (distribution parameters for lognormal distribution: (1) $\lambda = \mu_{\log(X)}$, (2) $\zeta = \sigma_{\log(X)}$; for beta distribution: (1) $x_{min}$, (2) $x_{max}$, (3) $\alpha_1$, (4) $\alpha_2$). . . 355

Table 5.2: Normalized sensitivities computed by DDM of $u_{x3}$ to material parameters and their relative contribution to variance of $u_{x3}$ at different load levels (three-story building) . . . . . 363

Table 5.3: Contribution (%) of the cross-correlation terms to the variance of the response quantity $u_{3x}$ (three-story building) . . . . . 366

Table 5.4: Material parameters (with lognormal distributions) for the two-dimensional SFSI system . . . . . 378

Table 5.5: Normalized sensitivities computed by DDM of $u_1$ to material parameters and their relative contribution to variance of $u_1$ at different load levels (two-dimensional SFSI system) . . . . . 384

Table 5.6: Contribution (%) of the cross-correlation terms to the variance of the response quantity $u_1$ (two-dimensional SFSI system). . . . . 386

Table 6.1: Probabilistic properties of structure material (all has lognormal distribution except for the ones without c.o.v., unit: kPa) . . . . . 427

Table 6.2: Probabilistic properties of soil material (all have lognormal distributions, unit: kPa ) . . . . . 427

Table 6.3: Probabilistic properties of load pattern ( lognormal distribution, unit: kN ) . . . . . 427

Table 6.4: Correlation between RVs . . . . . 428

Table 6.5: Comparison of various methods for computing the $P_f$ ( LSF:$g_1 = \Delta_{limit} - \Delta_1$ ) . . . . . 433

Table 6.6: Comparison of various methods for computing the $P_f$ ( LSF :$g_2 = u_{limit} - (u_1 - u_3)$ ) . . . . . 434

Table 6.7: Comparison of mean upcrossing rate and mean upcrossing events obtained by using FORM, OPS and MCS . . . . . 453

Table 6.8: Material properties. . . . . 471

Table 6.9: Principal curvatuers . . . . . 471

Table 6.10: Comparison of various methods for computing the $P_f$ . . . . . 480

Table 7.1: Real parameters and initial parameters used in model updating . . . . . 496

Table 7.2: Parameters obtained by updating procedure when using DDM and FFD . . 500

Table 7.3: Comparison of objective function values when using DDM or FFD . . . . . 501

Table 7.4: Parameters obtained by updating procedure when using DDM and FFD . . 504

Table 7.5: Comparison of objective function values by using DDM or FFD . . . . . 504

Table 7.6: Parameters obtained by updating procedure when using DDM and FFD . . 505

Table 7.7: Parameters obtained by updating procedure when using DDM and FFD . . 506

Table 7.8: Parameters obtained by updating procedure when using DDM and FFD . . 511

Table 7.9: Objective function values comparison between using DDM and FFD . . . . 511

Table 7.10: Parameters obtained by updating procedure when using DDM and FFD . . 514

Table 7.11: Objective function values comparison between using DDM and FFD . . . . 514

Table 7.12: SNOPT optimization results . . . . . 519

Table 7.13: Parameters obtained by SNOPT . . . . . 528

Table 8.1: Sensitivity parameters available in uniaxial materials. . . . . 539

# LIST OF FIGURES


Figure 3.1: Typical newton raphson iteration algorithm . . . . . 35

Figure 3.2: Return map algorithm in the uniaxial case with pure kinematicic hardening ($H_{iso}$= 0). . . . . 47

Figure 3.3: Finite element model of five-story single-bay moment-resisting frame . . 57

Figure 3.4: Load cases: static push-over and earthquake base excitation . . . . . 58

Figure 3.5: Section constitutive model (moment-curvature) . . . . . 60

Figure 3.6: Record of 1940 El Centro earthquake N-S comp. . . . . 60

Figure 3.7: Responses of the 5 story building to static push-over force . . . . . 61

Figure 3.8: Sensitivity of roof displacement to I . . . . . 62

Figure 3.9: Sensitivity of roof displacement to $M_{y0}$ . . . . . 63

Figure 3.10: Sensitivity of roof displacement to $H_{kin}$ . . . . . 64

Figure 3.11: Sensitivity of roof displacement to $H_{iso}$ . . . . . 65

Figure 3.12: Roof displacement with increasing number of elements per beam/column . . . . . 67

Figure 3.13: Sensitivity of roof displacement to I with increasing number of elements per beam/column . . . . . 68

Figure 3.14: Sensitivity of roof displacement to $M_{y0}$ with increasing number of elements per beam/column . . . . . 69

Figure 3.15: Sensitivity of roof displacement to $H_{kin}$ with increasing number of elements per beam/column . . . . . 70

Figure 3.16: Sensitivity of roof displacement to Hiso with increasing number of elements per beam/column . . . . . 71

Figure 3.17: Plastic curvature at 1st Gauss point with with increasing number of elements per beam/column . . . . . 72

Figure 3.18: Accumulated plastic curvature at 1st Gauss point with increasing number of elements per beam/column . . . . . 73

Figure 3.19: Sensitivity of plastic curvature to I with increasing number of elements per beam/column . . . . . 74

Figure 3.20: Sensitivity of plastic curvature to $M_{y0}$ with increasing number of elements per beam/column . . . . . 75

Figure 3.21: Sensitivity of plastic curvature to $H_{kin}$ with increasing number of elements per beam/column . . . . . 76

Figure 3.22: Sensitivity of plastic curvature to $H_{iso}$ with increasing number of elements per beam/column . . . . . 77

Figure 3.23: Sensitivity of accumulated plastic curvature to I with increasing number of elements per beam/column . . . . . 78

Figure 3.24: Sensitivity of accumulated plastic curvature to $M_{y0}$ with increasing number of elements per beam/column . . . . . 79

Figure 3.25: Sensitivity of accumulated plastic curvature to $H_{kin}$ with increasing number of elements per beam/column . . . . . 80

Figure 3.26: Sensitivity of accumulated plastic curvature to $H_{iso}$ with increasing number of elements per beam/column . . . . . 81

Figure 3.27: Responses of the 5 story building to earthquake input . . . . . 83

Figure 3.28: Sensitivity of roof displacement to I . . . . . 84

Figure 3.29: Sensitivity of roof displacement to $M_{y0}$ . . . . . 85

Figure 3.30: Sensitivity of roof displacement to $H_{kin}$ . . . . . 86

Figure 3.31: Sensitivity of roof displacement to $H_{iso}$ . . . . . 87

Figure 3.32: Sensitivity of roof displacement to earthquake input $\ddot{\mathbf{u}}_g(t = 4.22s)$ . . . . 88

Figure 3.33: Displacement of floors with increasing number of elements per beam/column . . . . . 89

Figure 3.34: Sensitivity of roof displacement to I with increasing number of elements per beam/column . . . . . 90

Figure 3.35: Sensitivity of roof displacement to $M_{y0}$ with increasing number of elements per beam/column . . . . . 91

Figure 3.36: Sensitivity of roof displacement to $H_{kin}$ with increasing number of elements per beam/columner . . . . . 92

Figure 3.37: Sensitivity of roof displacement to $H_{iso}$ with increasing number of elements per beam/column . . . . . 93

Figure 3.38: Sensitivity of roof displacement to $\ddot{\mathbf{u}}_g(t = 7.60s)$ with increasing number of elements per beam/column . . . . . 94

Figure 3.39: Moment curvature responses with increasing number of elements per beam/column . . . . . 95

Figure 3.40: Plastic curvature with increasing number of elements per beam/column . . 96

Figure 3.41: Accumulated plastic curvature with increasing number of elements per beam/column . . . . . 97

Figure 3.42: Sensitivity of plastic curvature to I with increasing number of elements per beam/column . . . . . 98

Figure 3.43: Sensitivity of plastic curvature to My0 with increasing number of elements per beam/column . . . . . 99

Figure 3.44: Sensitivity of plastic curvature to $H_{kin}$ with increasing number of elements per beam/column . . . . . 100

Figure 3.45: Sensitivity of plastic curvature to $H_{iso}$ with increasing number of elements per beam/column . . . . . 101

Figure 3.46: Sensitivity of plastic curvature to $\ddot{\mathbf{u}}_g(t = 7.60s)$ with increasing number of elements per beam/column . . . . . 102

Figure 3.47: Sensitivity of accumulated plastic curvature to I increasing number of elements per beam/column . . . . . 103

Figure 3.48: Sensitivity of accumulated plastic curvature to $M_{y0}$ with increasing number of elements per beam/column . . . . . 104

Figure 3.49: Sensitivity of accumulated plastic curvature to $H_{kin}$ with increasing number of elements per beam/column . . . . . 105

Figure 3.50: Sensitivity of accumulated plastic curvature to $H_{iso}$ with increasing

number of elements per beam/column . . . . . 106

Figure 3.51: Sensitivity of accumulated plastic curvature to $\ddot{\mathbf{u}}_g(t= 7.60s)$ with increasing number of elements per beam/column . . . . . 107

Figure 3.52: Convergence of roof displacement with respect to time step size . . . . . 109

Figure 3.53: Convergence of roof displacement sensitivity to I with respect to time step size . . . . . 110

Figure 3.54: Convergence of roof displacement sensitivity to $M_{y0}$ with respect to time step size . . . . . 111

Figure 3.55: Convergence of roof displacement sensitivity to $H_{kin}$ with respect to time step size . . . . . 112

Figure 3.56: Convergence of roof displacement sensitivity to $H_{iso}$ with respect to time step size . . . . . 113

Figure 3.57: Convergence of roof displacement sensitivity to $\ddot{\mathbf{u}}_g(t= 7.60s)$ with respect to time step size . . . . . 114

Figure 3.58: Convergence of moment curvature relationship with respect to time step size . . . . . 115

Figure 3.59: Convergence of plastic curvature with respect to time step size. . . . . 116

Figure 3.60: Convergence of accumulated plastic curvature with respect to time step size . . . . . 117

Figure 3.61: Sensitivity of plastic curvature to I with respect to time step size . . . . . 118

Figure 3.62: Sensitivity of plastic curvature to $M_{y0}$ with respect to time step size . . . 119

Figure 3.63: Sensitivity of plastic curvature to $H_{kin}$ with respect to time step size . . . 120

Figure 3.64: Sensitivity of plastic curvature to $H_{iso}$ with respect to time step size. . . . 121

Figure 3.65: Sensitivity of plastic curvature to $\ddot{\mathbf{u}}_g(t= 7.60s)$ with respect to time step size . . . . . 122

Figure 3.66: Sensitivity of accumulated plastic curvature to I with respect to time step size . . . . . 123

Figure 3.67: Sensitivity of accumulated plastic curvature to $M_{y0}$ with respect to

time step size . . . . . 124

Figure 3.68: Sensitivity of accumulated plastic curvature to $H_{kin}$ with respect to time step size . . . . . 125

Figure 3.69: Sensitivity of accumulated plastic curvature to $H_{iso}$ with respect to time step size . . . . . 126

Figure 3.70: Sensitivity of accumulated plastic curvature to $\ddot{\mathbf{u}}_g(t = 7.60s)$ with respect to time step size . . . . . 127

Figure 3.71: The maximun distributed force on the frame . . . . . 129

Figure 3.72: The numbers of yielded Gauss points . . . . . 130

Figure 3.73: Sensitivity of roof displacement to material parameter I . . . . . 131

Figure 3.74: Sensitivity of roof displacement to $M_{y0}$ . . . . . 132

Figure 3.75: Sensitivity of roof displacement to Hkin . . . . . 133

Figure 3.76: Sensitivity of roof displacement to $H_{iso}$ . . . . . 134

Figure 3.77: Sensitivity of plastic curvature to I . . . . . 135

Figure 3.78: Sensitivity of plastic curvature to $M_{y0}$ . . . . . 136

Figure 3.79: Sensitivity of plastic curvature to $H_{kin}$ . . . . . 137

Figure 3.80: Sensitivity of plastic curvature to $H_{iso}$ . . . . . 138

Figure 3.81: Sensitivity of accumulated plastic curvature to I . . . . . 139

Figure 3.82: Sensitivity of accumulated plastic curvature to $M_{y0}$. . . . . 140

Figure 3.83: Sensitivity of accumulated plastic curvature to $H_{kin}$ . . . . . 141

Figure 3.84: Sensitivity of accumulated plastic curvature to $H_{iso}$ . . . . . 142

Figure 3.85: Sensitivity of roof displacement to $H_{iso}$ . . . . . 143

Figure 3.86: Sensitivity of roof displacement to $H_{kin}$ . . . . . 144

Figure 3.87: Sensitivity of roof displacement to I . . . . . 145

Figure 3.88: Sensitivity of roof displacement to $M_{y0}$ . . . . . 146

Figure 3.89: Accumulated plastic curvature . . . . . 147

Figure 3.90: Plastic curvature . . . . . 148

Figure 3.91: Sensitivity of plastic curvature to $H_{iso}$ . . . . . 149

Figure 3.92: Sensitivity of plastic curvature to $H_{kin}$ . . . . . 150

Figure 3.93: Sensitivity of plastic curvature to I . . . . . 151

Figure 3.94: Sensitivity of plastic curvature to $M_{y0}$ . . . . . 152

Figure 3.95: Sensitivity of plastic curvature to $\ddot{\mathbf{u}}_g(t= 7.60s)$ . . . . . 153

Figure 3.96: Moment curvature responses . . . . . 154

Figure 3.97: Sensitivity of accumulated plastic curvature to $H_{iso}$. . . . . 155

Figure 3.98: Sensitivity of accumulated plastic curvature to $H_{kin}$ . . . . . 156

Figure 3.99: Sensitivity of accumulated plastic curvature to I . . . . . 157

Figure 3.100:Sensitivity of accumulated plastic curvature to $M_{y0}$ . . . . . 158

Figure 3.101:Sensitivity of $\bar{\chi}^p$ to $\ddot{\mathbf{u}}_g(t= 7.60s)$ . . . . . 159

Figure 3.102:Response sensitivity of roof displacement to $H_{iso}$ . . . . . 160

Figure 3.103:Response sensitivity of roof displacement to $H_{kin}$ . . . . . 161

Figure 3.104:Response sensitivity of roof displacement to I . . . . . 162

Figure 3.105:Response sensitivity of roof displacement to $M_{y0}$ . . . . . 163

Figure 3.106:Accumulated plastic curvature . . . . . 164

Figure 3.107:Plastic curvature . . . . . 165

Figure 3.108:Sensitivity of accumulated plastic curvature to $H_{iso}$ . . . . . 166

Figure 3.109:Sensitivity of accumulated plastic curvature to $H_{kin}$ . . . . . 167

Figure 3.110:Sensitivity of accumulated plastic curvature to I . . . . . 168

Figure 3.111:Sensitivity of accumulated plastic curvature to $M_{y0}$. . . . . 169

Figure 3.112:Sensitivity of $\bar{\chi}^p$ to $\ddot{\mathbf{u}}_g(t= 7.60s)$ . . . . . 170

Figure 3.113:Sensitivity of plastic curvature to $H_{iso}$ . . . . . 171

Figure 3.114:Sensitivity of plastic curvature to $H_{kin}$ . . . . . 172

Figure 3.115:Sensitivity of plastic curvature to I . . . . . 173

Figure 3.116:Sensitivity of plastic curvature to $M_{y0}$ . . . . . 174

Figure 3.117:Sensitivity of $\chi^p$ to $\ddot{\mathbf{u}}_g(t= 7.60s)$ . . . . . 175

Figure 4.1: Yield surfaces of multi-yield-surface $J_2$ plasticity model in principal deviatoric stress space . . . . . 180

Figure 4.2: Flow rule of multi-yield-surface $J_2$ plasticity model . . . . . 184

Figure 4.3: Hardening rule of multi-yield-surface $J_2$ plasticity model . . . . . 188

Figure 4.4: Updates of inner yield surfaces . . . . . 191

Figure 4.5: Solid block of clay subjected to horizontal quasi-static cyclic loads . . . . 200

Figure 4.6: Time variation of quasi-static cyclic loads . . . . . 201

Figure 4.7: Force vs. displacement response of node A . . . . . 202

Figure 4.8: Shear stress - strain response at Gauss point G (see Figure 4.1). . . . . 203

Figure 4.9: Convergence rate comparison using unbalanced force as test for convergence (tol = 1E-4 [kN]) . . . . . 204

Figure 4.10: Convergence rate comparison using displacement increment as test for convergence (tol = 1E-8 [m]) . . . . . 205

Figure 4.11: Convergence rate comparison using energy increment as test for convergence (tol = 1E-12 $[kN \cdot m]$) . . . . . 205

Figure 4.12: Convergence rate comparison using unbalanced force as test for convergence with smaller tolerance (tol = 1E-8 [kN]) . . . . . 208

Figure 4.13: Convergence rate comparison using displacement increment as test for convergence with smaller tolerance (tol = 1E-12 [m]) . . . . . 209

Figure 4.14: Convergence rate comparison using energy increment as test for convergence with smaller tolerance (tol = 1E-20 [kN · m]) . . . . . 209

Figure 4.15: Convergence rate comparison using unbalanced force as test for convergence with varying number of yield surfaces (tol = 1E-4 [kN]) 212

Figure 4.16: Convergence rate comparison using displacement increment as test for convergence with varying number of yield surfaces (tol = 1E-8 [m]) . . . . . 213

Figure 4.17: Convergence rate comparison using energy increment as test for convergence with varying number of yield surfaces (tol = 1E-12 [kN · m]) . . . . . 214

Figure 4.18: Layered soil column subjected to total base acceleration (unit: [m]) . . . . 217

Figure 4.19: Total acceleration at the base of the soil column . . . . . 218

Figure 4.20: Response of different soil layers . . . . . 218

Figure 4.21: Shear stress vs shear strain at the point C, D, E, and F . . . . . 219

Figure 4.22: Convergence rate comparison using unbalanced force as test for convergence (tol = 1E-4 [kN]) 220

Figure 4.23: Convergence rate comparison using displacement increment as test for convergence (tol = 1E-8 [m]) 221

Figure 4.24: Convergence rate comparison using energy increment as test for convergence (tol = 1E-12 [kN · m]) . . . . . 221

Figure 4.25: Convergence rate comparison using unbalanced force as test for convergence with smaller tolerance (tol = 1E-8 [kN]) . . . . . 224

Figure 4.26: Convergence rate comparison using displacement increment as test for convergence with smaller tolerance (tol = 1E-12 [m]) . . . . . 225

Figure 4.27: Convergence rate comparison using energy increment as test for convergence with smaller tolerance (tol = 1E-20 [kN · m]) . . . . . 225

Figure 4.28: Convergence rate comparison using unbalanced force as test for convergence for longer time step (tol = 1E-4 [kN]) . . . . . 227

Figure 4.29: Convergence rate comparison using displacement increment as test for convergence for longer time step (tol = 1E-8 [m]) . . . . . 228

Figure 4.30: Convergence rate comparison using energy increment as test for convergence for longer time step (tol = 1E-12 [kN · m]) . . . . . 228

Figure 4.31: Convergence rate comparison using unbalanced force as test for convergence with 40 yield surfaces (tol = 1E-4 [kN]) . . . . . 231

Figure 4.32: Convergence rate comparison using displacement increment as test for convergence with 40 yield surfaces (tol = 1E-8 [m]) . . . . . 231

Figure 4.33: Convergence rate comparison using energy increment as test for convergence with 40 yield surfaces (tol = 1E-12 [kN · m]) 232

Figure 4.34: Schematic of plastic stress correction for the second yield surface in the multi-yield surface $J_2$ plasticity model . . . . . 239

Figure 4.35: Response sensitivities with respect to G . . . . . 249

Figure 4.36: Response sensitivities respect to G (zoomed) . . . . . 250

Figure 4.37: Response sensitivities respect to $\tau_{max}$ . . . . . 251

Figure 4.38: Response sensitivities with respect to bulk moduli . . . . . 252

Figure 4.39: Sensitivity of response $u_6$ with respect to $G_1$ . . . . . 253

Figure 4.40: Sensitivity of response $u_6$ with respect to $G_1$, detailed view . . . . . 254

Figure 4.41: Sensitivity of response $u_1$ with respect to $G_4$ . . . . . 255

Figure 4.42: Sensitivity of response $u_1$ with respect to $G_4$, detailed view . . . . . 256

Figure 4.43: Sensitivity of response $u_5$ with respect to $\tau_{max,2}$ . . . . . 257

Figure 4.44: Sensitivity of response $u_5$ with respect to $\tau_{max,2}$, detailed view . . . . . 258

Figure 4.45: Sensitivity of response $u_2$ with respect to $\tau_{max,6}$ . . . . . 259

Figure 4.46: Sensitivity of response $u_2$ with respect to $\tau_{max,6}$, detailed view . . . . . 260

Figure 4.47: Sensitivity of response $u_6$ with respect to bulk moduli $k_6$ . . . . . 261

Figure 4.48: Sensitivity of response $u_6$ with respect to bulk moduli $k_6$, detailed view 262

Figure 4.49: Relative importance of shear modulis $G_i$'s on top horizontal displacement . . . . . 263

Figure 4.50: Relative influence of shear modulis $G_6$ on the displacements . . . . . 264

Figure 4.51: Relative importance of shear modulis $\tau_{max,i}$ on second top horizontal displacement $u_5$ . . . . . 265

Figure 4.52: Relative influence of shear strength $\tau_{max,5}$ on the displacements . . . . . 266

Figure 4.53: Relative importance of bulk modulus $K_i$'s on top horizontal displacement . . . . . 267

Figure 4.54: Relative importance of $\theta$'s on top horizontal displacement . . . . . 268

Figure 4.55: Relative importance of $\theta$'s on top horizontal displacement . . . . . 269

Figure 4.56: Relative importance of q's on top horizontal displacement . . . . . 270

Figure 4.57: 2-D model of SFSI system: geometry, section properties and soil model 277

Figure 4.58: Boundary conditions and multipoint constraints. . . . . 279

Figure 4.59: Response histories at different floors and layers . . . . . 280

Figure 4.60: Local response histories . . . . . 281

Figure 4.61: Sensitivity of response $u_1$ with respect to steel $\sigma_Y$ . . . . . 282

Figure 4.62: Sensitivity of response $u_1$ with respect to the shear modulus $G_4$ . . . . . 283

Figure 4.63: Relative importance of $\theta$'s on the first floor drift . . . . . 285

Figure 4.64: Relative importance of $\theta$'s on the first floor drift . . . . . 286

Figure 4.65: Relative importance of $\theta$'s on the first floor drift . . . . . 287

Figure 4.66: Response histories at different floors and layers . . . . . 288

Figure 4.67: Local response histories . . . . . 289

Figure 4.68: Sensitivity of response $u_1$ with respect to steel elastic moduli E . . . . . 290

Figure 4.69: Sensitivity of response $u_1$ with respect to the third layer low strain shear modulus $G_3$ . . . . . 291

Figure 4.70: Sensitivity of response $u_1$ with respect to the third layer maximum shear strength $\tau_3$ . . . . . 292

Figure 4.71: Sensitivity of stress at point B with respect to the third layer maximum shear strength $\tau_3$ . . . . . 293

Figure 4.72: Sensitivity of stress at point B with respect to the third layer maximum shear strength $\tau_3$ (zoomed) . . . . . 294

Figure 4.73: Relative importance of θ's on the first floor drift . . . . . 295

Figure 4.74: Relative importance of θ's on the first floor drift . . . . . 296

Figure 4.75: Relative importance of θ's on the first floor drift . . . . . 297

Figure 4.76: Relative importance of θ's on the first floor drift . . . . . 298

Figure 4.77: Relative importance of θ's on the shear stress at Gauss point B . . . . . 300

Figure 4.78: Relative importance of θ's on the shear stress at Gauss point B . . . . . 301

Figure 4.79: Relative importance of θ's on the shear stress at Gauss point B . . . . . 302

Figure 4.80: Relative importance of θ's on the shear stress at Gauss point B . . . . . 303

Figure 4.81: Example of 3D pile soil system . . . . . 306

Figure 4.82: Response of the 3D pile soil system . . . . . 307

Figure 4.83: Local responses . . . . . 308

Figure 4.84: Sensitivity of nodal displacement at top of beam with respect to core concrete $\varepsilon_{co}$ . . . . . 309

Figure 4.85: Relative importance of θ's to the first floor drift . . . . . 310

Figure 4.86: Relative importance of θ's on the first floor drift . . . . . 311

Figure 4.87: Relative importance of θ's on the first floor drift . . . . . 312

Figure 4.88: Relative importance of θ's on the first floor drift . . . . . 313

Figure 4.89: Example of 3D SFSI system . . . . . 315

Figure 4.90: Section properties of the column of 3D SFSI system . . . . . 317

Figure 4.91: Base excitation taken as the earthquake record of Tabas 1978 . . . . . 318

Figure 4.92: Response in x direction of the 3D pile soil system . . . . . 319

Figure 4.93: Response in y direction of the 3D pile soil system . . . . . 320

Figure 4.94: Local responses . . . . . 321

Figure 4.95: Sensitivity of nodal displacement at the second floor with respect to the low strain shear modulus of the first layer soil $G_1$ . . . . . 322

Figure 4.96: Relative importance of θ's on the first floor drift in x direction . . . . . 324

Figure 4.97: Relative importance of θ's on the first floor drift in x direction . . . . . 325

Figure 4.98: Relative importance of θ's on the first floor drift in x direction . . . . . 326

Figure 4.99: Relative importance of θ's on the first floor drift in x direction . . . . . 327

Figure 4.100: Relative importance of θ's on the first floor drift in x direction . . . . . 328

Figure 4.101: Relative importance of θ's on the first floor drift in y direction . . . . . 329

Figure 4.102: Relative importance of θ's on the first floor drift in y direction . . . . . 330

Figure 4.103: Relative importance of θ's on the first floor drift in y direction . . . . . 331

Figure 4.104: Relative importance of θ's on the first floor drift in y direction . . . . . 332

Figure 4.105: Relative importance of θ's on the first floor drift in y direction . . . . . 333

Figure 4.106: Relative importance of θ's on the second floor drift in x direction . . . . . 335

Figure 4.107: Relative importance of θ's on the second floor drift in x directions . . . . 336

Figure 4.108: Relative importance of θ's on the second floor drift in y direction . . . . . 337

Figure 4.109: Relative importance of θ's on the second floor drift in y direction . . . . . 338

Figure 4.110: Relative importance of θ's on the strain at point B . . . . . 339

Figure 4.111: Relative importance of θ's on the strain at point B . . . . . 340

Figure 4.112: Relative importance of θ's on the moment at point A . . . . . 341

Figure 4.113: Relative importance of θ's on the moment at point A . . . . . 342

Figure 5.1: Geometry, cross-sectional properties, applied horizontal loads and material constitutive models for the three-story R/C building ..... 353

Figure 5.2: Probabilistic response of the three-story R/C building ..... 357

Figure 5.3: ProStandard deviation of the three-story R/C building ..... 358

Figure 5.4: Coefficient of variation of the mean response at different load levels computed using MCS for the three-story R/C building ..... 361

Figure 5.5: CDFs of $u_{x3}$ for different load levels estimated using MCS for the three-story R/C building ..... 362

Figure 5.6: Tornado diagrams for the three-story R/C building ..... 367

Figure 5.7: Correlation of response quantity $u_{3x}$ with material parameter $f_{c,cover}$ for the three-story R/C building ..... 370

Figure 5.8: Correlation of response quantities $u_{3x}$ and $u_{1x}$ for the three-story R/C building ..... 371

Figure 5.9: CDF, PDF and relation of the response $u_{3x}$ of the three-story R/C building as function of fc,cover for $P_{tot}$ = 300kN ..... 372

Figure 5.10: CDF, PDF and relation of the response $u_{3x}$ of the three-story R/C building as function of fc,cover for $P_{tot}$ = 450kN ..... 373

Figure 5.11: CDF, PDF and relation of the response $u_{3x}$ of the three-story R/C building as function of $f_y$ for $P_{tot}$ = 450kN ..... 374

Figure 5.12: 2-D model of SFSI system: geometry, section properties and soil model 376

Figure 5.13: Probabilistic response of the two-dimensional SFSI system ..... 380

Figure 5.14: Standard deviation of the two-dimensional SFSI system ..... 382

Figure 5.15: Coefficient of variation of the mean response at different load levels computed using MCS for the two-dimensional SFSI system ..... 383

Figure 5.16: Tornado diagrams for the two-dimensional SFSI system ..... 389

Figure 5.17: CDF, PDF and relation of the response $u_1$ of the three-story R/C building as function of $f_{c,cover}$ for $P_{tot}$ = 630kN ..... 391

Figure 5.18: CDF, PDF and relation of the response $u_1$ of the three-story R/C building as function of $\tau_3$ for $P_{tot}$ = 630kN ..... 392

Figure 6.1: Failure probability in 2 random variable case . . . . . 400

Figure 6.2: FORM and SORM methods . . . . . 401

Figure 6.3: Probability transformation . . . . . 403

Figure 6.4: Design point search algorithm . . . . . 407

Figure 6.5: Linking of SNOPT with OpenSees as Reliability Analysis Tool . . . . . 410

Figure 6.6: Wrap of SNOPT tool box as a design point searching tool . . . . . 411

Figure 6.7: The importance sampling distribution h(x) is such that it emphasises a sub-part of the failure region in which f($\boldsymbol{\theta}$) is relatively small . . . . . 415

Figure 6.8: Importance sampling combined with the design point in standard normal space . . . . . 417

Figure 6.9: Sampling in the orthogonal plane . . . . . 418

Figure 6.10 2-D model of SFSI system: geometry, section properties and soil model 424

Figure 6.11: Boundary conditions and multipoint constraints. . . . . 426

Figure 6.12: Design points of $g_2 = u_{limit} - (u_1 - u_3)$ corresponding to different criterion levels. . . . . 429

Figure 6.13: Design points of $g_1 = \Delta_{limit} - \Delta_1$ corresponding to different criterion levels 430

Figure 6.14: Design points of $g_1 = \Delta_{limit} - \Delta_1$ corresponding to various criteria . . . 431

Figure 6.15: Design points of $g_2 = u_{limit} - (u_1 - u_3)$ corresponding to various criteria . . . . . 432

Figure 6.16: Mean upcrossing rate analysis. . . . . 436

Figure 6.17: The first excursion failure event . . . . . 437

Figure 6.18: The contour of $f_{y\dot{y}}(y, \dot{y}, t)$ . . . . . 438

Figure 6.19: Failure domain of the parallel system for computing the mean out-crossing rate . . . . . 442

Figure 6.20: Discrete representation of a white noise . . . . . 448

Figure 6.21: Comparison of the FORM approximation of the mean upcrossing rate and OPS results . . . . . 451

Figure 6.22: Mean upcrossing events and failure probability estimates. . . . . 452

Figure 6.23: Design points . . . . . 454

Figure 6.24: First floor response histories at design points . . . . . 455

Figure 6.25: Points where the local responses are recorded . . . . . 456

Figure 6.26: Stress strain responses at point B of the third soil layer. . . . . 456

Figure 6.27: Moment curvature responses at point A. . . . . 457

Figure 6.28: Response surface fitting method . . . . . 466

Figure 6.29: 2-D model of frame: geometry, section properties and material model . . 470

Figure 6.30: Response surface at DP on the first principal plane . . . . . 472

Figure 6.31: Contour of response surface at DP on the first principal plane . . . . . 473

Figure 6.32: Response surface at DP on the second principal plane . . . . . 474

Figure 6.33: Contour of response surface at DP on the second principal plane . . . . . 475

Figure 6.34: Response surface at DP on the third principal plane . . . . . 476

Figure 6.35: Contour of response surface at DP on the third principal plane . . . . . 477

Figure 6.36: Response surface at DP on the fourth principal plane . . . . . 478

Figure 6.37: Contour of response surface at DP on the fourth principal plane . . . . . 479

Figure 7.1: Interface of SNOPT tool box as a general optimization tool . . . . . 488

Figure 7.2: Integration of SNOPT tool box into OpenSees as a general optimization tool box . . . . . 490

Figure 7.3: Communication between C++ class and user defined funciton in TCL . 491

Figure 7.4: Soil column subject to base excitation . . . . . 495

Figure 7.5: FFT of the acceleration . . . . . 496

Figure 7.6: Experimental' soil responses at different height of the soil . . . . . 497

Figure 7.7: Comparison of 'experimental' soil responses with those obtained by using 'initial' parameter values . . . . . 498

Figure 7.8: Comparison of objective function values resulting from the use of DDM and FFD . . . . . 502

Figure 7.9: Experimental' responses with 2% noise . . . . . 503

Figure 7.10: Soil column subjected to strong base excitation . . . . . 508

Figure 7.11: Experimental' soil responses at different heights of the soil column . . . . 509

Figure 7.12: Comparison of 'Experimental' soil responses with responses obtained by using initial values of parameters . . . . . 510

Figure 7.13: Comparison of objective function values resulting from the use of DDM and FFD . . . . . 512

Figure 7.14: Experimental' responses with 2% noise . . . . . 513

Figure 7.15: Comparison of objective function values resulting from the use of DDM and FFD . . . . . 515

Figure 7.16: Soil column subject to base excitation . . . . . 517

Figure 7.17: Recorded soil responses at different depths . . . . . 518

Figure 7.18: Comparison of real soil responses with responses obtained by using initial values of parameters . . . . . 520

Figure 7.19: Comparison of actual soil responses with FE simulated responses after model updating . . . . . 521

Figure 7.20: Comparison of actual soil responses with FE simulated responses after model updating (zoomed) . . . . . 522

Figure 7.21: Comparison of actual soil responses with FE simulated responses in the frequency domain . . . . . 523

Figure 7.22: Comparison of actual soil responses with FE responses computed with parameters in Table 7.13 for May 20 1986 earthquake . . . . . 524

Figure 7.23: Recorded soil responses at different depths . . . . . 525

Figure 7.24: Comparison of actual soil responses with responses obtained by using SNOPT results in Table 7.12 as initial parameter values . . . . . 526

Figure 7.25: Comparison of actual soil responses with responses obtained by using SNOPT results in Table 7.12 as initial parameter values in the frequency domain . . . . . 527

Figure 7.26: Comparison of actual soil responses with FE simulation responses . . . . 529

Figure 7.27: Comparison of actual soil responses with FE simulation responses during time interval 15-25 sec. . . . . 530

Figure 7.28: Comparison of actual soil responses with FE simulation responses in the frequency domain . . . . . 531

Figure 7.29: Shear stress-strain responses at point A in Figure 7.16 . . . . . 532

Figure 7.30: Comparison of actual soil responses with FE simulated responses . . . . . 533

Figure 7.31: Shear stress-strain responses at point A in Figure 7.16 . . . . . 534

Figure 8.1: SNOPT based design point search algorithm . . . . . 547

Figure 8.2: Mean upcrossing rate analysis command . . . . . 548

# ACKNOWLEDGEMENTS

I would like to express my most sincere and deepest gratitude to my advisor, Professor Joel P. Conte. Without his support in both my academic research and personal life, I would not have obtained my Ph.D. at UCSD. During the past six years, Prof. Conte has provided me with great help in solving academic problems. He has helped me shape my character with his rigorous and inspiring guidance. He encouraged me to develop the habit of deeper understanding and independent thinking.

I wish to give my special thanks to the members of my doctoral committee. Professor Philip E. Gill who has aided me greatly with his expertise in the field of computational optimization. Professor Ahmed Elgamal who has cooperated with me and shared documentation and derivation of the clay soil model used in this dissertation. Professor J. Enrique Luco who has given me advice about research directions and in solving difficult technical problems encountered during this research. Professor Hidenori Murakami, in whose class I have learned the fundamental concepts of and programming techniques in nonlinear finite element analysis. I would like to thank them all for the time they have dedicated to help me with my research.

I would like to thank my collaborators. My research on reliability analysis methods has strongly benefited from my collaboration with Professor Michele Barbato. And my research on nonlinear soil-structure-interaction has greatly benefited from my interaction with Dr. Zhaohui Yang.

I also would like to thank the members of the development team of OpenSees at U.C. Berkeley: Dr. Frank Mckenna who always offered his help when I encountered problems in OpenSees, Professor Michael H. Scott who helped me to combine the SNOPT-OpenSees framework presented herein with his newly developed advanced FE model parameterization framework, Professor Terje Hawkaas who gave me great help in developing the framework for response sensitivity and reliability analysis in OpenSees, Professor Gregory L. Fenves who kindly provided office space and asked his students to help me when I was working together with Frank McKenna at U.C. Berkeley, Professor Armen Der Kiureghian who gave me valuable advice in solving problems in reliability analysis of SFSI systems.

I want to give my thanks to my colleagues and friends at UCSD: Ozgur Ozcelik, Linjun Yan, Hong Guan, Maurizio Gobbato, Babak Moaveni, Gabriel Acero, Yuyi Zhang, Xianfei He, Andre Barbosa, Marco Faggella, Jinchi Lu, Liangcai He, Linjun Yan, Zhiqiang Chen, Barbara Chang, and many other dear friends who helped me and shared with me the highs and the lows of my life at San Diego. I owe a big thanks to my friend and colleague Jiddu Bezares-Chavez, who has helped me to improve my writing ability. I also would like to thank my friend Marc Robinson, who helped me to clean my thesis and papers.

Partial support of this research by the National Science Foundation under Grant No. CMS-0010112 and by the Pacific Earthquake Engineering Research (PEER) Center through the Earthquake Engineering Research Centers Program of the National Science Foundation under Award No. EEC-9701568 are gratefully acknowledged.

# VITA

| | |
|---|---|
| 1997 | Bachelor of Engineering, Tsinghua University, China |
| 2001 | Master of Science, Tsinghua University, China |
| 2001-2007 | Research Assistant, University of California, San Diego |
| 2008 | Doctor of Philosophy, University of California, San Diego |

# PUBLICATIONS

Gu, Q., Conte J.P., (2003) Convergence Studies in Nonlinear Finite Element Response Sensitivity Analysis. *The 9th International Conference on Applications of Statistics and Probability in Civil Engineering*, Berkeley, California, USA.

Barbato, M., Gu, Q., and Conte, J.P., 2006. Response Sensitivity and Probabilistic Response Analyses of Reinforced Concrete Frame Structures, *Proceeding* of 8$^{th}$ National Conference on Earthquake Engineering, San Francisco, CA, USA.

Barbato, M., Gu, Q., and Conte, J.P., September 2006. Framework for Finite Element Response Sensitivity and Reliability analyses of Structural and Geotechnical Systems, *First European Conference on Earthquake Engineering and Seismology (a joint event of the 13th ECEE & 30th General Assembly of the ESC)*, Geneva, Switzerland.

Gu, Q., and Conte, J.P., May 2008. Response Sensitivity Analysis of Soil-Structure Interaction (SSI) Systems, *Fourth Decennial Geotechnical Earthquake Engineering and Soil Dynamics Conference*, Sacramento, California.

Gu, Q., Conte, J. P., Yang, Z., and Elgamal A., 2008. Consistent Tangent Operator for Multi-Yield-Surface $J_2$ Plasticity Material Model, submitted to *International Journal for Numerical Methods in Engineering.*

Gu, Q., Conte, J. P., Yang, Z., and Elgamal A., 2008. Response Sensitivity Analysis of A Multi-Yield-Surface $J_2$ Plasticity Model by Direct Differentiation Method, submitted to *International Journal for Numerical Methods in Engineering.*

Gu, Q., Barbato, M., and Conte, J.P., 2008. Handling of Constraints in Finite Element Response Sensitivity Analysis, submitted to *Journal of Engineering Mechanics*, ASCE.

# ABSTRACT OF THE DISSERTATION

**Fininte Element Response Sensitivity and Reliability Analysis of Soil-Foundation-Structure-Interaction (SFSI) Systems**

by

Quan Gu

Doctor of Philosophy in Structural Engineering

University of California, San Diego, 2008

Professor Joel P. Conte, Chair

Performance-based earthquake engineering (PBEE) has emerged as a powerful method of analysis and design philosophy in earthquake engineering and is leading the way to a new generation of seismic design guidelines. PBEE requires a comprehensive understanding of the earthquake response of Soil-Foundation-Structure-Interaction (SFSI) systems when damage occurs in the structural system during the earthquake. In the context of PBEE, this research combines finite element (FE) modeling and seismic response analysis of SFSI

systems with state-of-the-art methods in response sensitivity and reliability analysis. New analytical and numerical methods are developed and existing algorithms adopted for studying the propagation of uncertainties in nonlinear static and dynamic analyses of SFSI systems and for probabilistic performance assessment of these systems.

This research makes several contributions to reliability analysis of structural and SFSI systems. For the purpose of accurately and efficiently computing the response gradients, an ‘exact’ FE response sensitivity computation algorithm based on the Direct Differentiation Method (DDM) and available in the widely used FE analysis software framework OpenSees is further extended to various types of material models, finite elements and multi-point constraint equations used in modeling large-scale realistic SFSI systems. As a main contribution to this research, this sensitivity algorithm is extended to a multi-yield surface $J_2$ plasticity model used extensively to model clay soil materials in seismic response analysis. Related to response sensitivity analysis of SFSI systems, several issues are studied, such as discontinuities in response sensitivities, the relative importance of various soil and structural material parameters in regards to a specified aspect of the system response (i.e., response parameters).

As contributions to the reliability analysis of structural and SFSI systems, several existing solution tools such as first-order reliability method (FORM), second-order reliability method (SORM), and various sampling techniques, such as importance sampling (IS) and orthogonal plane sampling (OPS), are implemented in OpenSees and/or further improved to solving reliability analysis problems of structural and SFSI systems. A powerful general-purpose optimization toolbox SNOPT, developed by Professor Philip

Gill at UCSD, is integrated into the reliability analysis framework in OpenSees and customized for efficiently finding the design point(s) of structural and SFSI systems. For time variant reliability analysis, an existing mean upcrossing rate analysis algorithm is implemented in OpenSees and improved. It is found that the FORM approximation for mean upcrossing rate is significantly inaccurate, especially in cases of highly nonlinear response behavior of the system analyzed. In such case, the OPS method based on the design point(s) of the reliability problem significantly improves the FORM approximation of the mean upcrossing rate and therefore of the upper bound of the failure probability.

In order to study the topology of limit-state surfaces (LSS) for reliability problems, a new visualization method called Multi-dimensional Visualization in Principal Plane (MVPP) is developed and implemented in OpenSees. The geometrical insight gained from the MVPP has led to the development of a new hybrid computational reliability method, called the DP-RS-Sim method, which combines the design point (DP) search, the response surface methodology (RS), and simulation techniques (Sim). This method is applied for the time invariant reliability analysis of a realistic nonlinear structural system.

Several other closely related topics are studied. A simplified probabilistic response analysis method is developed taking advantage of DDM-based response sensitivity analysis. This method is then applied to a nonlinear structural and SFSI system. It is much more efficient than the crude Monte Carlo Simulation method and provides, at low computational cost, good estimates of the mean and standard deviation of the response for low to moderate level of material nonlinearity in the response. A general-purpose OpenSees-SNOPT based optimization framework was developed and applied to soil

model updating problems using numerically simulated data. It is found that the optimization process is significantly more efficient when using the DDM-based over the FDM-based sensitivities. Additionally, nonlinear FE model updating is performed for an actual site, the Lotung downhole array in Taiwan, and based on data recorded during a 1986 earthquake.

# CHAPTER 1

# INTRODUCTION

## 1.1 Background

Earthquakes cause damage to buildings, bridges, dams, and people. There can be a great loss of lives. It can also create landslides, floods and tsunamis. In the last decade earthquakes around the world killed almost 100,000 people, affected 14 million people, and produced losses estimated at more than $215 billion. In 1999 alone, two strong earthquakes in western Turkey caused the deaths of over 16,000 people, the destruction of more than 60,000 homes and economic losses of about $40 billion (over one quarter of the country's GDP). Between 2004 and 2005, the Sumatra-Andaman and Sumatra earthquakes in the Indian Ocean caused a worldwide death toll of nearly 280,000 with thousands of others missing. The economic losses were estimated at over $10 Billion.

During the past quarter century, fewer than 200 lives have been lost in the United States as a result of earthquakes. In 1994, the Northridge earthquake in the Los Angeles area resulted in 61 fatalities, over 8,000 injuries, and direct capital losses of nearly $50 billion. There is an awareness that similar if not larger events are likely. Fortunately, over the past 40 years considerable progress has been made in understanding the nature of earthquakes and how they damage structures, and in improving the seismic performance of the

built environment. However, much remains unknown regarding the prevention or mitigation of earthquake damage in the US and worldwide, leaving room for further studies.

During an earthquake, the soil-structure interaction (SSI) effects play an important role in determining the behavior of structures like buildings, bridges, etc. The seismic excitation experienced can be considered a function of the fault rupture mechanism, travel path effects, local site effects, and SSI effects (Stewart et al. 1999a; Stewart et al. 1999b). Irrespective of the structure, the local soil conditions can dramatically influence the earthquake motion from the bedrock level to the ground surface, through their dynamic filtering effects. One example is the 1985 Mexico City earthquake where deep soft soils amplified the ground motion and modified the frequency of ground shaking. Similar behavior was observed during the 1989 Loma Prieta earthquake, in which the sections of the Cypress freeway in Oakland collapsed due to the soil-related motion amplification.

Past research has shown that for a specific structure, the responses during an earthquake may be totally different when the structure is founded on deformable soil when compared to a rigid foundation. This difference is due to the fact that the SSI may increase the natural periods of the systems, change the system damping due to wave radiation, or modify the effective seismic excitation (Jennings et al. 1973; Luco 1980; Luco et al. 1988; Merritt et al. 1954; Stewart et al. 1999a; Stewart et al. 1999b; Trifunac 2000; Veletsos et al. 1974; Wong et al. 1988). For large and extended structures such as long bridges, the spatial variation of the ground motion (also referred to as asynchronous multi-support seismic excitations), may have significant effects on the bridge response (Deodatis et al. 2000; Der Kiureghian et al. 1992; Harichandran et al. 1996; Nazmy et al. 1992; Saxena et

al. 2000; Shrikhande et al. 1999; Zerva 1990). The spatial variation of earthquake ground motion includes both incoherence (loss of coherence with separation distance) due to reflection and scattering of seismic waves and wave propagation/passage effects (Harichandran et al. 1986; Harichandran 1991).

Analytical formulations for SSI are numerous, ranging from complex, two- and three-dimensional finite-element analysis procedures capable of incorporating fully nonlinear dynamic soil and structural modeling (Borja et al. 1992; Borja et al. 2000; Conte et al. 2002; Koutsourelakis et al. 2002; Zhang et al. 2003) to simplified nonlinear substructure approaches (Makris et al. 1994; Zhang et al. 2002; Zhang et al. 2004) to simplified linear substructure techniques suitable for implementation in Building Codes (Stewart et al. 2003). The majority of past research on SSI is based on the substructure approach with linear substructures and is formulated in the frequency domain. The most advanced nonlinear SFSI models are formulated using the direct approach in which an integrated model incorporating the structure, its foundations, and the surrounding soil is analyzed as a whole.

However, the complex nature of the SSI during the passage of seismic waves has made it difficult to predict or determine the conditions under which the SSI can be beneficial or detrimental to structural performance during a strong earthquake (Bielak 1978; Celebi 1998; Mylonakis et al. 2000; Priestley et al. 1987; Resendiz et al. 1985; Veletsos et al. 1973).

Due to the complex and still poorly understood nature of SSI effects, the prediction of structural performance can be done only in a probabilistic sense. Uncertainties are not avoidable and should be presented in any model of SSI systems. Uncertainties can be for-

mally grouped into inherent or aleatory and epistemic uncertainty. Inherent/aleatory uncertainty is defined as the intrinsic variability (or natural randomness) of engineering/ physical quantities such as material (soil, concrete, steel, …) properties, geometric properties, seismological variables (earthquake magnitude M and site-to-source distance S), ground motion time history at a specific point, and spatial variation of ground motion. Inherent uncertainties can be viewed as a property of nature. They are irreducible and can be estimated from observations using the frequentist interpretation of probability. In contrast, epistemic uncertainty results from a lack of knowledge or information and shortcomings in measurement or calculation. It arises due to (a) the use of structural, load, and probabilistic models that are idealized, simplified, incorrectly calibrated, and/or of questionable applicability (i.e., modeling uncertainty), and (b) imperfect model parameter estimation due to limited data, measurement errors, etc. (i.e., small sampling uncertainty). The predictions made on the basis of these models are inaccurate to some unknown degree. Epistemic uncertainty can usually be reduced by using more accurate/sophisticated models, acquiring additional data, and improving measurement procedures. Thus, inherent and epistemic uncertainties are very different in nature. This difference should be recognized and accounted for by the next generation of seismic design methodologies.

Foundation soil materials may be characterized by uncertain material properties and stochastic (random) spatial variability (Lacasse et al. 1996; Lumb 1966). Random field models (Vanmarcke 1977; Vanmarcke 1983) to represent the spatial variability of soil properties have been used in a number of studies to investigate the influence of uncertain and spatially variable soil properties/parameters on performance (e.g., underground water

seepage; foundation settlement) of geotechnical/foundation systems (Fenton 2002; Griffiths et al. 1997; Rackwitz 2000; Vanmarcke 1977). These random field soil models are typically defined by their mean, variance, and spatial correlation structure (e.g., spatial correlation length or scale of fluctuation), which are usually calibrated with in-situ soil data (Davis 1986; DeGroot 1996; Fenton 1999). The scale of fluctuation describes how rapidly a soil property changes with position. In a recent report, Jones et al. (Jones et al. 2002) provide background information, available data, and numerous references on the uncertainty and spatial variability of soil properties. The intrinsic variability of structural material properties (e.g., Young's modulus of steel/concrete, yield strength of steel, compressive/tensile strength of concrete) has been documented and characterized extensively in the literature (Lu et al. 1994; Mirza et al. 1979b, Mirza et al. 1979c). Uncertainty in reinforced concrete member geometry has also been studied and documented in the literature (Mirza et al. 1979a).

## 1.2 Objectives

Performance-based earthquake engineering (PBEE) has emerged as a new analysis and design philosophy in earthquake engineering (Cornell et al. 2000; Moehle et al. 2004; Porter 2003) and is leading the way to a new generation of seismic design guidelines (AASHTO 1998; ATC-55 2005; ATC-58 2005; BSSC 2003; ICC 2003; SEAOC 1995). The performance-based seismic design approach prescribes performance objectives to be achieved by a structure during earthquakes for various hazard levels. PBEE requires a comprehensive understanding of the earthquake response of a structure (SFSI system) when damage occurs in the structural system over the course of an earthquake (cracking,

yielding, crashing, fracture, and so forth). In the long term, using PBEE, structures will be rated for a given performance level at a given hazard level. However, due to the inherent and epistemic uncertainties characterizing material and geometric properties of the structure (or SFSI system) and the earthquake excitation, the satisfaction of structural performance objectives can only be defined in probabilistic terms (e.g., acceptable annual probability of limit-state exceedance).

In the context of PBEE, the objective of this research is to combine finite element modeling and seismic response analysis of Soil-Structure-Interaction (SSI) systems with state-of-the-art methods in sensitivity and reliability analysis. The research is trying to adopt existing algorithms or develop new analytical methodologies for studying the propagation of uncertainties and failure probabilities of the structure or SSI systems. This study is applied to both static push over and stochastic earthquake loading cases.

Several contributions are made to reliability analysis of structural and SFSI systems. For the purpose of accurately and efficiently computing the response gradients, an ‘exact’ FE response sensitivity computation algorithm based on the Direct Differentiation Method (DDM) and available in the widely used FE analysis software framework OpenSees is further extended to various types of material models, finite elements and multi-point constraint equations used in modeling large-scale realistic SFSI systems. As a main contribution to this research, this sensitivity algorithm is extended to a multi-yield surface $J_2$ plasticity model used extensively to model clay soil materials in seismic response analysis. Related to response sensitivity analysis of SFSI systems, several issues are studied, such as discontinuities in response sensitivities, the relative importance of various soil and

structural material parameters in regards to a specified aspect of the system response (i.e., response parameters).

As contributions to the reliability analysis of structural and SFSI systems, several existing solution tools such as first-order reliability method (FORM), second-order reliability method (SORM), and various sampling techniques, such as importance sampling (IS) and orthogonal plane sampling (OPS), are implemented in OpenSees and/or further improved to solving reliability analysis problems of structural and SFSI systems. A powerful general-purpose optimization toolbox SNOPT, developed by Professor Philip Gill at UCSD, is integrated into the reliability analysis framework in OpenSees and customized for efficiently finding the design point(s) of structural and SFSI systems. For time variant reliability analysis, an existing mean upcrossing rate analysis algorithm is implemented in OpenSees and improved. It is found that the FORM approximation for mean upcrossing rate is significantly inaccurate, especially in cases of highly nonlinear response behavior of the system analyzed. In such case, the OPS method based on the design point(s) of the reliability problem significantly improves the FORM approximation of the mean upcrossing rate and therefore of the upper bound of the failure probability.

In order to study the topology of limit-state surfaces (LSS) for reliability problems, a new visualization method called Multi-dimensional Visualization in Principal Plane (MVPP) is developed and implemented in OpenSees. The geometrical insight gained from the MVPP has led to the development of a new hybrid computational reliability method, called the DP-RS-Sim method, which combines the design point (DP) search, the response

surface methodology (RS), and simulation techniques (Sim). This method is applied for the time invariant reliability analysis of a realistic nonlinear structural system.

Several other closely related topics are studied. A simplified probabilistic response analysis method is developed taking advantage of DDM-based response sensitivity analysis. This method is then applied to a nonlinear structural and SFSI system. It is much more efficient than the crude Monte Carlo Simulation method and provides, at low computational cost, good estimates of the mean and standard deviation of the response for low to moderate level of material nonlinearity in the response. A general-purpose OpenSees-SNOPT based optimization framework was developed and applied to soil model updating problems using numerically simulated data. It is found that the optimization process is significantly more efficient when using the DDM-based over the FDM-based sensitivities. Additionally, nonlinear FE model updating is performed for an actual site, the Lotung downhole array in Taiwan, and based on data recorded during a 1986 earthquake.

Two main sources of inherent/intrinsic uncertainty are being considered in this study: (i) soil and structural material properties, (ii) earthquake excitation time histories. Part of the results can be readily used in the engineering practice leading to a more rational treatment of uncertainties and safer and more economic design of structural systems.

## 1.3 Literature Review

Lutes et al. (Jin et al. 2000; Lutes et al. 2000) have conducted pioneering analytical studies to investigate the effect of uncertain soil-foundation and superstructure properties on structural response in seismically excited soil-structure interacting systems. Their work

focuses on simple linear elastic SSI systems subjected to stochastic earthquake excitation and shows that for non-negligible system parameter uncertainty, there may be significant uncertainty about the spectral density of structural response. Toubalem et al. (Toubalem et al. 1999) studied the effects of the random horizontal and vertical spatial variability of stiffness of the soil medium on transfer functions and resonant frequencies of some simple linear soil-structure interaction systems. Few other researchers (Koutsourelakis et al. 2002; Tantalla et al. 2001) have analyzed nonlinear soil and soil-structure interacting systems (with simple structure) with uncertain material properties, subjected to stochastic earthquake loading. Their methodology included random field modeling of soil properties, random process modeling of earthquake loading, nonlinear finite element analysis based on elastoplastic soil models, and Monte Carlo simulation.

## 1.4 Software Platform for the Study

### 1.4.1 FEAP

The Finite Element Analysis Program (FEAP),(O. C. Zienkiewicz et al. 2000) written by Prof. Robert L. Taylor at UC Berkeley, is a general purpose finite element package for the analysis of structure system. The program includes the ability to construct arbitrarily complex finite element models using a library of one-, two-, and three dimensional elements for linear and non-linear deformations. In addition, a number of material models (isotropic, orthotropic, plasticity, etc.) are available to model the constitutive properties of the materials used. A number of solution procedures are available for linear, non-linear, and time-accurate problems. A part of the work in this dissertation is based on FEAP.

### 1.4.2 FEDEASLab-FERUM

FEDEASLab (Finite Elements in Design, Evaluation and Analysis of Structures using Matlab) was originally developed by Prof. Filippou at the University of California, Berkeley (Filippou et al. 2004). It is a Matlab (Matlab User's Guide 1997) toolbox suitable for linear and nonlinear, static and dynamic structural analysis, which has the advantage of providing a general framework for physical parameterization of finite element models and response sensitivity computation using the DDM (Franchin 2004). One of the key features of FEDEASLab is its strict modularity that keeps separate the different hierarchical levels encountered in structural analysis (i.e., structure, element, section and material levels). It is an integral simulation component of NEESgrid <http://www.neesgrid.org> that is particularly suitable for concept development, for education, and for simulations of small structures.

FERUM (Finite Element Reliability Using Matlab) is a Matlab toolbox to perform finite element reliability analysis originally developed by Prof. Der Kiureghian and his students at the University of California, Berkeley (http://www.ce.berkeley.edu/~haukaas/FERUM/ferum.html). The coupling between FEDEASLab and FERUM was first established by Franchin (Franchin 2004). Over the last few years, Joel Conte at the University of California in San Diego, has significantly enhanced the original capabilities of FEDEASLab-FERUM (Barbato et al. 2005; Barbato et al. 2008; Conte et al. 2004; Zona et al. 2005). FEDEASLab-FERUM has proven to be an excellent and versatile research tool for algorithm developments in nonlinear finite element reliability analysis. However, Matlab has proven to be slow when solving large scale problems. As a result, in

this dissertation, many new algorithms are developed and tested first in FEDEASLab-FERUM, then reimplemented into C++ based OpenSees (http://opensees.berkeley.edu).

### 1.4.3 OpenSees

OpenSees (Open System for Earthquake Engineering Simulation), is an open source software framework used to model structural and geotechnical systems and simulate their earthquake response. This framework has been under development by the Pacific Earthquake Engineering Research Center (PEER) since 1997 through the National Science Foundation (NSF) engineering and education centers program (McKenna et al. 2000; McKenna et al. 2004). OpenSees supports a wide range of simulation models, solution procedures, and distributed computing models. It also has very attractive capabilities for physical parameterization of SSI models, probabilistic modeling, response sensitivity analysis (Gu et al. 2008a; Gu et al. 2008b) and reliability analysis (Haukaas et al. 2003; Haukaas et al. 2004).

OpenSees has been recently adopted as a NEESgrid simulation component. Over the last years OpenSees has been extensively used for large-scale modeling and simulation of an actual bridge-ground system (Conte et al. 2002; Zhang et al. 2003; Zhang et al. 2004). In this dissertation, the sensitivity and reliability framework in OpenSees has been greatly enhanced for structural and geotechnical systems. The combination of FEDEASLab-FERUM as research prototyping as well as an educational tool with OpenSees as a framework for large-scale seismic response simulation and reliability analysis, is an ideal research platform.

All algorithms mentioned in this dissertation are developed in OpenSees for the purpose of performing the reliability analysis on real large scale structures or SSI problems.

## 1.5 Organization of the Dissertation

In this dissertation, several closely related topics are presented. The first research topic is FE response sensitivity analysis of the structural and geotechnical systems, which is covered in Chapters 3 through 4. Chapter 3 presented the complete theory of the FE response sensitivity analysis based on the Direct Differentiation Method (DDM). Some issues like the convergence rate of DDM, the damping effect, and the poststiffness, are studied. In Chapter 4 the DDM based sensitivity algorithm is extended to a multi-yield surface $J_2$ plasticity soil model, as well as other necessary elements, materials, constraints, and various analyses. Thus, the sensitivity and reliability algorithms are extended to geotechnical systems and are capable of solving Soil Structure Interaction (SSI) problems. Concerning applications, several SSI systems are studied for the response and response sensitivities. As a by-product, the normalized sensitivities are employed to measure the relative importance of the material parameters in determining the response under consideration. In Chapter 5, a simplified probabilistic response analysis is performed for the SSI system, based on the DDM based response sensitivity analysis. Chapter 6 presents a last review of the structural reliability analysis methods based on the design point (DP) concept, including the time invariant and time variant reliability analysis. These methods include the classical FORM, SORM, Monte Carlo Simulation (MCS), as well as various newly developed or newly adopted methods. These “new” methods include mean upcrossing rate analysis, Orthogonal Plane Sampling (OPS), Importance Sampling (IS) methods.

A hybrid method combining DP and OPS is used to solve time variant reliability problems of SSI systems and greatly improve the classical FORM approximation of the mean upcrossing rate. In order to study the limit state function (LSF) or limit state surface (LSS), a new methodology for visualization of hyper-surfaces defined in high-dimensional spaces is developed and implemented. A new reliability method that combines the knowledge of the design point, response surface method, and simulation technique (DP-RS-Sim) are developed and implemented. These methods are used for a 2D SFSI system for both time invariant and time variant reliability analyses. Chapter 7 develops a general framework for nonlinear FE model updating based on a general purpose optimization tool box SNOPT. The convergence rate of SNOPT is compared between using DDM and the finite difference method (FDM) as gradients. A real example of nonlinear soil FE model updating in Lotung Taiwan, China is presented. Chapter 8 is the user's manual for the newly developed sensitivity and reliability analysis framework in OpenSees. Chapter 9 summarizes the work in this dissertation, highlights the research findings, and provides suggestions for future research.

# CHAPTER 2

# FRAMEWORK OF RELIABILITY ANALYSIS AND PROBABILISTIC CHARACTERIZATION OF SSI SYSTEMS

## 2.1 Computational Framework for Reliability Analysis of SSI Systems

The structural reliability problem consists of computing the probability of failure, $P_f$, of a structure or SSI system under consideration given the probabilistic characterization of the system. These characterizations which include loading, the geometric and material properties of the system, and other performance parameters, are all modeled as random variables (Ditlevsen et al. 1996). In structural reliability analysis, failure is usually defined as the exceedance/violation of some limit-state or performance function(s).

Let the vector $\boldsymbol{\Theta}$ denote the basic random variables defining the external loads, geometric and material properties of a given system, while the vector **S** represents the resulting response quantities of interest. The response quantities **S** are also known as *Engineering Demand Parameters* (EDPs). Deterministic realizations of $\boldsymbol{\Theta}$ and **S** will be denoted by $\boldsymbol{\theta}$ and **s**, respectively. The EDPs **S** are implicit functions of the basic random variables $\boldsymbol{\Theta}$, i.e., $\mathbf{s} = \mathbf{f}(\boldsymbol{\theta})$, where the vector function **f** is not known analytically, but can only be evaluated numerically through a finite element (FE) algorithm. In performance-based design, nodal displacement quantities **U** or deformation quantities (e.g., interstory

drifts for building structures) are common choices for **S**, and are obtained directly from numerical integration of the equations of motion. After spacial discretization using the FE method, the response can be obtained by the following nonlinear differential equation:

$$\boldsymbol{M}(\theta)\ddot{\boldsymbol{u}}(t,\theta) + \boldsymbol{C}(\theta)\dot{\boldsymbol{u}}(t,\theta) + \boldsymbol{R}(\boldsymbol{u}(t,\theta),\theta) = \boldsymbol{F}(t,\theta) \tag{2.1}$$

where t = time, θ = scalar sensitivity parameter (material or loading variable), $\mathbf{u}(t)$, $\dot{\mathbf{u}}(t)$, $\ddot{\mathbf{u}}(t)$ = nodal displacement, velocity and acceleration vectors, **M** = mass matrix, **C** = damping matrix, **R**(**u**, t) = history dependent internal (inelastic) resisting force vector, **F**(t) = applied dynamic load vector (Conte 2001; Conte et al. 2003).

Let g(**Θ**, **S**) denote a scalar limit-state function (LSF) for the system considered, such that $g(\boldsymbol{\Theta}, \mathbf{S}) \le 0$ defines the failure domain/region. The hyper-surface defined by $g(\boldsymbol{\Theta}, \mathbf{S}) = 0$ is called the limit-state surface (LSS). The probability of failure for a time-invariant reliability problem can be expressed as

$$P_f = P[g(\boldsymbol{\theta}) \le 0] = \int_{g(\boldsymbol{\theta}) \le 0} f_{\boldsymbol{\Theta}}(\boldsymbol{\theta}) d\boldsymbol{\theta} \tag{2.2}$$

where $f_{\boldsymbol{\Theta}}(\boldsymbol{\theta})$ denotes the joint probability density function (PDF) of random vector **Θ**. The close form solution of the integral in Eq. (2) is not possible to compute for real-world problems and can be evaluated only approximately. There are well established procedures consisting of introducing a one-to-one mapping/transformation between the physical space of the variables **Θ** and the standard normal space of variables **Y,** and then computing the probability of failure $P_f$ as,

$$P_f = P[g(Y) \le 0] = \int_{G(Y) \le 0} \varphi_Y(y) dy \tag{2.3}$$

where $\varphi_Y(y)$ denotes the standard normal joint PDF and $G(\boldsymbol{Y}) = g(\boldsymbol{\Theta}(\boldsymbol{Y}), S(\boldsymbol{\Theta}(\boldsymbol{Y})))$ is the limit-state function in the standard normal space. There are methods by which the random variable vector may be transformed from the physical space into the standard normal space. In this dissertation, Nataf model for joint distributions is the chosen method for the aforementioned probability transformation. This model is completely defined by specifying the marginal distributions and the correlation structures of the random variables. Nataf model allows a relative wide range of correlation values compared with other joint distribution models, e.g., the Morgenstern model(Liu et al. 1986) .

Solving the integral in Equation (2.3) is a formidable task as well, however this new form of the integral is suitable for approximate solutions taking advantage of the rotational symmetry of the standard normal joint PDF and its exponential decay in both the radial and tangential directions. An optimum point at which to approximate the limit-state surface is the “design point”, defined as the most likely failure point in the standard normal space. In the standard normal space, the design point on the limit-state surface is the closest point to the origin. Finding the design point is a crucial step for many approximate methods, such as FORM, SORM and importance sampling, to evaluate the integral in Equation (2.3)(AASHTO 1998; Breitung 1984; Der Kiureghian et al. 1987). Moreover, the integral in Equation (2.3) is an essential building block in approximate solution methods for time-variant reliability problems (i.e., computation of mean rate of out-crossing the limit-state surface for stochastic dynamic problems) by using time-invariant reliability methods (Hagen et al. 1991; Li et al. 1995; Vijalapura et al. 1999).

The design point **y*** is obtained as a solution to the constrained optimization problem (Liu et al. 1991)

$$\boldsymbol{y}^* = \begin{array}{c} min \ \frac{1}{2}\boldsymbol{y}^T\boldsymbol{y} \\ \text{s.t. } G(\boldsymbol{y}) = 0 \end{array} \tag{2.4}$$

Where **y** is the random variable vector in the standard normal space. In view of the generality of a limit-state surface defined for a nonlinear mechanics-based system (such as a SSI system), there can be multiple points that satisfy Equation (2.4) referred to as multiple design points in the literature. Special algorithms need to be developed for problems characterized by multiple design points (AASHTO 1998; Der Kiureghian et al. 1996; Kuschel 1998; Zhang et al.1994).

The most effective techniques for solving the constrained optimization problem in Equation (2.4) are gradient-based optimization algorithms (Gill et al. 1981; Liu et al. 1991) when coupled with accurate and efficient computation of the gradient of the constraint function G(**Y**), requiring computation of the sensitivities of the EDPs **S** to parameters **Θ**. Using the chain rule of differentiation, we have

$$\nabla_{\boldsymbol{Y}} G = (\nabla_{\boldsymbol{S}} g\big|_{\boldsymbol{\theta}} \cdot \nabla_{\boldsymbol{\theta}} \boldsymbol{S} + \nabla_{\boldsymbol{\theta}} g\big|_{\boldsymbol{S}}) \cdot \nabla_{\boldsymbol{Y}} \boldsymbol{\theta} \tag{2.5}$$

where $\nabla_{\boldsymbol{S}} g\big|_{\boldsymbol{\theta}}$ and $\nabla_{\boldsymbol{\theta}} g\big|_{\boldsymbol{S}}$ are the gradients of limit-state function g with respect to its explicit dependency on quantities **S** and **Θ**, respectively, and can usually be computed analytically. The term $\nabla_{\boldsymbol{\theta}} \boldsymbol{S}$ denotes the response sensitivities of response parameters **S** to parameters **Θ**, while $\nabla_Y \boldsymbol{\theta}$ is the gradient of the physical space parameters with respect to the standard normal space parameters. Thus, finite element response sensitivities are key

components in propagating uncertainties from basic loading, geometric, and material parameters to the response parameters of nonlinear finite element models.

For real-world problems, response simulation of a SSI system (computation of **s** for given **θ**) is performed using advanced mechanics-based nonlinear computational models founded on the finite element method. The constrained optimization problem in Equation (2.4) usually takes place in a high-dimensional space. Finite element reliability analysis requires the calculations of responses and their sensitivities to parameters $\boldsymbol{\Theta}$, $\nabla_{\boldsymbol{\theta}} \boldsymbol{S}$ . An accurate and efficient way to perform finite element response sensitivity analysis is through the Direct Differentiation Method (DDM) (Zhang et al. 1993; Kleiber et al. 1997) (Barbato et al. 2005; Barbato et al. 2008; Conte 2001; Conte et al. 2003; Conte et al. 2004; Zona et al. 2005). In order to perform the Reliability analysis on real SSI problems, the DDM based sensitivity analysis is extended to several elements, materials, constraints and the integratorAnalysis. This will be discussed in greater detail in chapter 3.

## 2.2 SSI System and its Finite Element Model

### 2.2.1 Nonlinear Dynamic Models of SSI Systems

In principle, powerful tools of finite element methods have rendered possible the solution of any properly posed boundary value problem in soil mechanics (Prevost 1995). Since the 1960's numerical formulations have been proposed throughout the soil mechanics literature. Extensive reviews on constitutive soil models are given by Scott (1985), Dafalias and co-workers (AASHTO 1998; Dafalias 1986a; Dafalias et al. 1986b), and Prevost and Popescu (1996).

Among these soil constitutive models, the "Multi-yield surface $J_2$ plasticity model" is selected to model the soil (clay) behavior. This plasticity model was first developed by Iwan (1967) and Mroz (1967), and was later applied by Prevost (1977; 1978a; 1978b) to soil mechanics. The advantage of this model is that in contrast to the classical $J_2$ (or Von Mises) plasticity model with a single yield surface, the multi-yield-surface $J_2$ plasticity model employs the concept of a field of plastic moduli to achieve a very flexible representation of the material plastic behavior under cyclic loading conditions. Another advantage of the model is that the material properties are defined by a very limited number of parameters: low strain shear moduli, maximum shear strength $\tau_{max}$, and bulk moduli, all of which may be obtained easily by the experiments. (program DYNAFLOW, Prevost 1995; program CYCLIC, Elgamal et al. 2002).

Recent years have seen great advances in nonlinear analysis of frame structures. In this dissertation, structural elements (e.g., beam, columns/piers, foundation piles, pile caps) are modeled using state-of-the-art displacement based, fiber-section, spread plasticity, nonlinear frame elements, with realistic constitutive laws for the structural materials (steel, concrete). Using material-nonlinear frame elements, the behavior of frame structures can be simulated accurately far into their actual nonlinear range and near their failure range.

The SSI model is developed in OpenSees, a powerful simulation platform for SSI systems with broad capabilities for modeling structural and geotechnical materials. Furthermore a wide range of nonlinear solution strategies for integrating the equations of motion of large-scale nonlinear systems are available (McKenna and Fenves, 2000; 2004). The

program provides an appropriate platform for conducting fully nonlinear soil studies (e.g., seismic soil studies) and soil-foundation-structure studies, which are able to reproduce complex soil behaviors observed in the laboratory or in the field (Elgamal et al. 2003; Yang et al. 2003).

### 2.2.2 Stochastic Modeling of Earthquake Loading

For SSI systems, the seismic input must be defined along the boundary of the computational soil domain. Under the assumptions of (i) vertically incident shear waves, (ii) a linear elastic, homogeneous, undamped semi-infinite half-space underlying the nonlinear computational soil domain, and (iii) the horizontal lower boundary of the soil domain, it can be shown that the wave propagation in the computational soil domain can be driven by equivalent seismic forces applied along the bottom boundary of the soil domain equipped with Lysmer-Kuhlemeyer absorbing/transmitting boundaries (Lysmer and Kuhlemeyer 1969; Zhang et al. 2003). The equivalent seismic forces are proportional to the soil mass density, shear wave velocity, and velocity of incident wave motion.

The incident earthquake motion at a point on the boundary of the computational soil domain should be defined as a random process able to represent the temporal variations in both the intensity (amplitude nonstationarity) and the frequency content (frequency non-stationarity) typical of actual earthquake ground motions.

In practice, in order to solve random vibration problems by the methods of structural reliability, the input processes must be represented in terms of a finite number of random variables along time axis.

There are several methods available for discrete representation of random processes. One method is used in conjunction with sampling techniques to generate realizations of a random process based on a pre-defined power spectral density (PSD) function.

The spectrum is discretized into a number of frequency intervals of width $\Delta\omega$, with $\omega_i$ (i = 1,2..N) denoting the center frequency points. For a two-sided PSD function S(ω) the variance of a frequency interval is $\sigma^2 = 2S(\omega)\Delta\omega$. One method of creating a realization is to create two vectors of randomly selected numbers $A_i$ = Normal(0, 1) and $\theta_i$ = Uniform(0, 2π) and evaluate the following sum at each time instant t:

$$x(t) = \mu(t) + \sum_{i=1}^{N} \sqrt{2S(\omega_i)\Delta\omega} A_i \cos(\omega_i t + \theta_i) \tag{2.6}$$

where μ(t) is a time-varying mean function.

Another simple but widely used method to form this stochastic input x(t) is: (Haukaas dissertation 2003, p153; Der Kiureghian 2000; Li and Der Kiureghian 1995; Koo and Der Kiureghian 2003)

$$x(t) = \mu(t) + c_2 \sum_{k=1}^{K} q_k(t) \sum_{i=1}^{N} Y_{ik} h_k(t - t_k) \tag{2.7}$$

where μ(t) is a time-varying mean function. $Y_{ik}$'s are standard normal random variables representing a train of pulses. These pulses are equally spaced along the time axis with the total number of impulses denoted by N. This train of impulse may represent Gaussian white noise when the number of pulses over a finite time interval is large enough. (Haukaas dissertation 2003). This basic process Y is modified by multiplying by a unit impulse

response function $h_k(t-t_k)$ of a filter at each time point $t_k$, for each pulse $y_k$. The pulses may represent intermittent ruptures at the fault, whereas the filter may represent the (soil) medium through which the waves travel. One option for the filter is the linear single-degree-of-freedom (SDOF) oscillator characterized by its natural frequency and damping ratio (Koo dissertation 2003). $q_k(t)$ is a modulating function used to further control the variance of process along the time axis. The number of the modulating functions is designated as K, while $c_2$ is a constant used to control the overall intensity of the process. Equation (2.7) represents a general non-stationary stochastic random process.

In this dissertation, the simplest white noise input is used as earthquake input. In Equation (2.7), let the modulating function $q_k(t)$ =1, K=1, $c_2$=1. $Y_k h(t-t_k)$ is the linear interpolation between impulses $Y_{k-1}$ and $Y_k$. Then Equation (2.7) is simplified to represent a stationary Gaussian white noise with zero mean and constant standard deviation. The details are discuss in Chapter 6.

### 2.2.3 Representation of Uncertainty in Structural and Geotechnical Material Properties

SSI systems present large uncertainties both in the material and geometric parameters characterizing structures, foundations and soils. The material uncertainties in the ground medium as well as in the structure are mathematically described by random fields. Finite element reliability analysis methods require discretization of the continuous-parameter random fields into a finite number of random variables. Discretization methods need to accurately represent random fields with as few random variables as possible, given that

reliability analysis computational cost increases strongly with the number of random variables considered. Several methods for discretization of random fields have been proposed in the past, e.g., Midpoint Method (MP) (Li et al. 1993), the Spatial Averaging (SA) method (Vanmarcke et al. 1983), the Shape Function method (SF) (Liu et al. 1986), the Series Expansion (SE) method (Lawrence 1987), and the Optimal Linear Estimation method (Li et al. 1993). In our research, the MP method is used, due to its simplicity and mathematical convenience.

Physically meaningful parameters will be considered for describing uncertainties of the materials, (e.g., initial modulus $E_c$ and the compressive strength $f'_c$ of the concrete; Elastic modulus $E_s$ and the yield strength $f_y$ of the reinforcing steel; the low-strain shear modulus G and the maximum shear strength $\tau_{max}$ of the soil model, etc.).

### 2.2.4 Limit-State Surface Design, Topology and Visualization

Seismic reliability analysis of large-scale SSI systems is a very complex problem due to the implicit nature of the limit-state surface (LSS), the high computational cost of each limit-state function (LSF) evaluation, and therefore the unknown or at best very partially known topology of the limit-state surface(s) in the high-dimensional standard normal space. Due to the generality of the problem at hand, the limit-state surface(s) in general does (do) not necessarily have the usual desirable properties of continuity, smoothness, convexity, single-connectedness, boundedness, etc.

The reliability methods of interest in this dissertation require transformation of the physical random variables $\boldsymbol{\Theta}$ into the standard normal space $\mathbf{Y}$ through Nataf transforma-

tion. In general, the limit-state surface in the physical space, $g(\boldsymbol{\Theta}, \mathbf{S}) = 0$, is a nonlinear hypersurface, the topology of which is further modified by the nonlinear mapping between the physical and standard normal spaces. The geometric and analytical properties of the limit-state surface in the standard normal space, $G(\boldsymbol{Y}) = g(\boldsymbol{\Theta}(\boldsymbol{Y}), S(\boldsymbol{\Theta}(\boldsymbol{Y}))) = 0$, are of much interest in reliability analysis.

Few researchers have studied the topology of the limit-state surface(s) for nonlinear stochastic finite element models of structural systems (Barbato et al. 2005c; Kiureghian 2000), particularly in the study of SSI systems. In spite of this lack of understanding, methods (such as FORM/SORM) and algorithms have been developed to find design point(s) and evaluate the probability of failure (i.e., limit-state exceedance). It is clear that such methods could produce grossly erroneous results when the unknown topology of the limit-state surface does not meet the assumptions made about its geometric properties. The high-dimensionality of the geometric interpretation of the finite element reliability analysis problem causes additional difficulties in graphically representing the LSS using traditional methods (e.g., 2-D plots, contour lines, perspective of 3-D objects on 2-D supports).

Knowledge about the topology of limit-state surface(s) for structural and SSI systems would not only foster the development of new, more efficient and more robust algorithms for the design point(s) search, but also more accurate methods for evaluating the probability content of the failure domain. It is of uttermost importance to investigate and classify general geometric and analytical properties of limit-state surfaces and their dependence on the stochastic characterization of loading and material parameters.

In this dissertation, a new visualization technique called the Multidimensional Visualization in the Principal Planes (MVPP) is developed and applied to structures and SSI systems. The topology study of the LSS is performed near the design point and along each of the principal directions of the hessian matrix at that point. The principal directions are the directions along which the LSS has the largest curvature. In structural reliability problems, these directions are most interesting since they explain the difference between FORM results and the real failure probability. In practice, the LSS is visualized in each principal plane as a curve. The principal plane is defined by the design point direction and a principal direction.

According to the visualization of the LSS of some structural and SSI problems, at the design point only a few (no more than 10) curvatures are far from zero. These directions represent directions along which the LSF is far from linear and needs to be considered as a nonlinear function. From this fact, a new methodology called “Design-Point Response-Surface-Method Simulation” (DP-RS-Sim) is developed in which only along the first few principal directions the LSF is considered as nonlinear and represented accurately by the response surface method, while along all other directions it is treated as linear. The new methodology will be explained in detail later.

### 2.2.5 Development of Limit-State Functions for Structures and SSI Systems

Several limit-state functions related to physical damage states of SSI systems will be developed considering a set of global and local nonlinear response parameters that are used as performance indicators in assessing structure-foundation systems at the service-

ability and the collapse performance levels. A variety of such candidate damage indices have been defined in the literature (DiPasquale et al. 1987; Park et al. 1985; Powell et al. 1988) and others can be introduced considering common failure mechanisms of SSI systems. In these indices, Maximum value type indices and cumulative damage type indices are two commonly used indices. In this dissertation, maximum value type indices are used to study the damage directly inflicted to the structure. These indices include maximum interstory drift for building structures, maximum top drift, etc.

## 2.3 Design Point Search and Failure Probability Computation

Several methods exist for finding an approximate solution to the structural reliability problem in Equation (2.2), such as FORM, SORM, importance sampling, etc. Two crucial steps can be recognized as common to these methodologies: (i) search for the design point(s), and (ii) approximate evaluation of the probability content of the failure domain.

### 2.3.1 Design Point(s) Search

As shown in 2.1, the first problem is formulated as a constrained optimization problem cast in the standard normal space (Liu et al. 1991). This problem is very challenging for real-world structural and SSI systems due to the following facts:

- the random parameter space presents high dimensionality, because of the discretization in terms of random variables of the stochastic seismic input and the random fields of soil properties;
- the strong (material and geometric) nonlinear behavior reached by the structure or SSI systems near the failure domain and thus near the design point(s);

- distortions induced by the transformation between the standard normal space and the physical space;
- evaluation of the constraint function and its first-order derivatives is very expensive, while second-order derivatives are extremely expensive.

In order to effectively deal with these difficulties, the following methods were implemented or introduced:

1. Solve the design point search problem, in its classical form given in Equation (2.4), by using the state-of-the-art in computational optimization. In the present dissertation, a general purpose optimization tool box sparse nonlinear optimization (SNOPT) has been integrated into OpenSees for solving the design point searching problem. It is observed that, already in this preliminary stage, consistent research progress has been achieved for obtaining insight into the physical and numerical nature of the problem. In fact, it is necessary to clarify if and under what circumstances recent optimization algorithms are more efficient and robust in the design point search problem than the widely used classical or improved Hasofer-Lind-Rackwitz-Fiessler (HL-RF) algorithms (Kiureghian et al. 1986; Hasofer et al. 1992; Rackwitz et al. 1978). The optimization algorithms and software are customized so that the physics and the geometry of the problem are exploited.

2. For the design point(s) search for the time variant problems with a stochastic modeling of uncertain properties, the design point at the inital time point are shifted along the time axis to form a new “warm“ starting point at a later time point. This method is observed to be very efficient, and at times crucial for solving design point(s) search for real structure or SSI reliability problems.

### 2.3.2 Approximate Evaluation of the Probability Content of the Failure Domain

After finding the design point(s), accurate methods for computation of the probability of failure of a structure or SSI system are required. As previously noted, asymptotic techniques such as FORM and SORM sometimes lead to very inaccurate results even if the computation of the design point(s) is very accurate, especially when the limit state surface is far from a plane. In this research, particular attention was given to hybrid methodologies combining the use of the design point(s) with reduced-variance simulation techniques, such as importance sampling using distributions peaked at the design point(s) (Au et al. 2003), Orthogonal Plane sampling (OPS) which take advantage of the design point and the design point direction. These methods gives very close failure probability by using an acceptable number of simulations.

Based on the information of Design point(s), the hessian Matrix at the design point was computed using the finite difference of the LSS Gradients. After the hessian matrix was known, the principal directions the LSS at the design point(s) were computed by eigen analysis of the hessian matrix. These directions represent the largest gradients on the Limit State Surface. It was observed that only the first several principal curvatures are far from zero and the LSF along these directions need to be considered nonlinear, while other principal curvatures are so close to zero that in these direction the LSF may be considered linear.

Based on this knowledge, the DP-RS-Sim method is developed. In this method, the LSF is represented nonlinearly in the first several principal directions and linearly in other directions.A grid plane is defined by two directions, selected from either the design point

direction or the first several principal directions. Several grid planes are employed, on which the response surface is fit nonlinearly. The total number of grid plane is N(N+1)/2, where N is the number of principal directions considered.

In each grid plane, a mesh is created according to the user's requirements (how refined is the mesh, what is the boundary, etc.). The values of the LSF at mesh points are evaluated by finite element computation, and the LSF was represented approximately by using the response surface methods and surface fitting techniques. After the surface is approximated, the failure probability may be easily computed using IS methods. This method was developed, implemented and applied to structures and SSI systems.

It is noteworthy that structural reliability problems often present multiple design points, each contributing in a non-negligible way to the probability of failure of the structure. Thus, it is necessary to be able to find all the important design points and accurately describe the failure domain in their neighborhoods for meaningful calculations. The multiple design points problems is not studied in this dissertation.

# CHAPTER 3

# FINITE ELEMENT RESPONSE SENSITIVITY ANALYSIS FRAMEWORK FOR STRUCTURAL AND GEOTECHNICAL SYSTEMS

## 3.1 General Displacement Based FE Response Sensitivities by Direct Differentiation Method (DDM)

As mentioned in Chapter 2, in seismic reliability analysis of civil structures, the inherent random variability or uncertainty associated with both the structure or SSI system and earthquake dynamic loading must be taken into consideration. Furthermore, in order to evaluate the probability of structural failure that occurs usually in the domain of nonlinear response behavior both materially and geometrically, these sensitivity and reliability analysis are necessarily based on the nonlinear finite element models of structures able to capture the salient features of the actual ultimate structural behavior under strong earthquakes. Besides their use in structural reliability analysis, finite element response sensitivity analysis represents an essential ingredient for gradient-based optimization methods needed in structural optimization, structural identification, finite element model updating, structural health monitoring, and even structural control (in the context of semi-active control systems based on real-time modification of structural system parameters).

Several methodologies are available for response sensitivity computation, such as the Finite Difference Method (FDM), the Adjunct Method (AM), the Perturbation Method (PM), and the Direct Differentiation Method (DDM). These methods are described by Zhang and Der Kiureghian(1993), Kleiber et al.(1992, 1997), Conte et al.(2001, 2003,2004), Gu and Conte(2003). FDM is the simplest method for response sensitivity computation, but is computationally prohibitive and can be negatively affected by numerical noise. The AM is extremely efficient for linear and non-linear elastic structural models, but is not competitive with other methods for path-dependent problems. The PM is computationally efficient but generally not very accurate. The DDM, on the other hand, is very general, efficient and accurate and is applicable to any material constitutive model. This paper focuses on the sensitivity analysis based on DDM for SSI systems.

This chapter focuses on the derivation of the material sensitivity computation algorithm based on the direct differentiation method (DDM). This algorithm is based on the spatial discretization of the governing response equations (in space and time) using the finite element method. In the context of nonlinear FE analysis, the DDM based response sensitivities are computed at each time step, after convergence is achieved for the response computation. This requires differentiation of the FE algorithm for the response computation with respect to each sensitivity parameter $\theta$. Consequently, the response sensitivity computation algorithm involves the various hierarchical layers of FE response analysis, namely: (1) structure level, (2) element level, (3) Gauss point level (or section level), and (4) material level. Details on the derivation of the DDM-based sensitivity equations for classical displacement-based, force-based and mixed finite elements can be found in a

number of references (Zhang and Der Kiureghian 1993, Kleiber et al. 1997, Conte et al. 2001, 2003, Gu and Conte 2003).

## 3.2 Response Sensitivity Computation at the Structural Level

After spatial discretization using the finite element method, the equation of motion of a materially-nonlinear-only structural system is given by the following nonlinear matrix differential equation:

$$\boldsymbol{M}(\theta)\ddot{\boldsymbol{u}}(t,\theta) + \boldsymbol{C}(\theta)\dot{\boldsymbol{u}}(t,\theta) + \boldsymbol{R}(\boldsymbol{u}(t,\theta),\theta) = \boldsymbol{F}(t,\theta) \tag{3.1}$$

where t = time, θ = scalar sensitivity parameter (material or loading variable), **u**(t) = vector of nodal displacements, **C** = damping matrix, **M** = mass matrix, **R**(**u**, t) = history dependent internal (inelastic) resisting force vector, which is not considered as a function of velocity $\dot{\boldsymbol{u}}(t,\theta)$ in this dissertation, **F**(t) = dynamic load vector, and a superposed dot denotes differentiation with respect to time. The potential dependence of each term of the equation of motion on the sensitivity parameter θ is shown explicitly in (3.1).

We assume without loss of generality that the equation of motion (3.1) is integrated numerically in time using the Newmark-β method of structural dynamics (Chopra 2001), i.e.,

$$\begin{aligned}
\ddot{\boldsymbol{u}}_{n+1} &= \left(1-\frac{1}{2\beta}\right)\ddot{\boldsymbol{u}}_n - \frac{1}{\beta(\Delta t)}\dot{\boldsymbol{u}}_n + \frac{1}{\beta(\Delta t)^2}(\boldsymbol{u}_{n+1}-\boldsymbol{u}_n) \\
\dot{\boldsymbol{u}}_{n+1} &= (\Delta t)\left(1-\frac{\alpha}{2\beta}\right)\ddot{\boldsymbol{u}}_n + \left(1-\frac{\alpha}{\beta}\right)\dot{\boldsymbol{u}}_n + \frac{\alpha}{\beta(\Delta t)}(\boldsymbol{u}_{n+1}-\boldsymbol{u}_n)
\end{aligned} \tag{3.2}$$

where we select $\alpha = 1/2$, $\beta = 1/4$. Substitution of Eqs. (3.2) into equation of motion (3.1) expressed at discrete time $t = t_{n+1} = (n+1)\,\Delta t$, in which Δt denotes the constant time

increment, yields the nonlinear equation in the unknowns $\mathbf{u}_{n+1} = \mathbf{u}(t_{n+1})$, the residual $\psi(\mathbf{u}_{n+1})$ is,

$$\psi(\mathbf{u}_{n+1}) = \tilde{\boldsymbol{F}}_{n+1} - \left[\frac{1}{\beta(\Delta t)^2}\boldsymbol{M}\boldsymbol{u}_{n+1} + \frac{\alpha}{\beta(\Delta t)}\boldsymbol{C}\boldsymbol{u}_{n+1} + \boldsymbol{R}(\boldsymbol{u}_{n+1})\right] = \mathbf{0} \tag{3.3}$$

where

$$\tilde{\boldsymbol{F}}_{n+1} = \boldsymbol{F}_{n+1} + \boldsymbol{M}\left[\frac{1}{\beta(\Delta t)^2}\boldsymbol{u}_n + \frac{1}{\beta(\Delta t)}\dot{\boldsymbol{u}}_n - \left(1 - \frac{1}{2\beta}\right)\ddot{\boldsymbol{u}}_n\right] + \boldsymbol{C}\left[\frac{\alpha}{\beta(\Delta t)}\boldsymbol{u}_n - \left(1 - \frac{\alpha}{\beta}\right)\dot{\boldsymbol{u}}_n - (\Delta t)\left(1 - \frac{\alpha}{2\beta}\right)\ddot{\boldsymbol{u}}_n\right]$$

We solve Equation (3.3) using an incremental Newton-Raphson iterative method. (Simo and Hughes 1998) as shown in Figure 3.1. Assuming that a Newton-Raphson iterative procedure is used to solve Equation (3.3) over time step $[t_n, t_{n+1}]$ by solving a sequence of linearized problems of the form

$$(\boldsymbol{K}_T^{dyn})_{n+1}^{i}\,\delta\boldsymbol{u}_n^{i+1} = \Psi_{n+1}^{i} \quad i = 0, 1, 2, \ldots \tag{3.4}$$

where

$$(\boldsymbol{K}_T^{dyn})_{n+1}^{i} = \left[\frac{1}{\beta(\Delta t)^2}\boldsymbol{M} + \frac{\alpha}{\beta(\Delta t)}\boldsymbol{C} + (\boldsymbol{K}_T^{stat})_{n+1}^{i}\right] \tag{3.5}$$

and

$$\Psi_{n+1}^{i} = \tilde{\boldsymbol{F}}_{n+1} - \left[\frac{1}{\beta(\Delta t)^2}\boldsymbol{M}\boldsymbol{u}_{n+1}^{i} + \frac{\alpha}{\beta(\Delta t)}\boldsymbol{C}\boldsymbol{u}_{n+1}^{i} + \boldsymbol{R}(\boldsymbol{u}_{n+1}^{i})\right] \tag{3.6}$$

As shown in Figure 3.1, the updated nodal displacement vector $\boldsymbol{u}_{n+1}^{i+1}$, or displacement vector at the end of iteration # (i+1) of time step $[t_n, t_{n+1}]$, is obtained as

$$\boldsymbol{u}_{n+1}^{i+1} = \boldsymbol{u}_n + \Delta\boldsymbol{u}_n^{i+1} = \boldsymbol{u}_{n+1}^{i} + \delta\boldsymbol{u}_n^{i+1} \tag{3.7}$$

where $\Delta \boldsymbol{u}_n^{i+1}$ and $\delta \boldsymbol{u}_n^{i+1}$ denote the total incremental displacement vector from the last converged step and the last incremental displacement vector, respectively. In (3.5), $\boldsymbol{K}_T^{dyn}$ denotes the tangent dynamic stiffness matrix and the *consistent tangent stiffness matrix* $(\boldsymbol{K}_T^{stat})_{n+1}^{i}$ in Equation (3.5) is obtained as $(\boldsymbol{K}_T^{stat})_{n+1} = \dfrac{\partial \boldsymbol{R}_{n+1}}{\partial \boldsymbol{u}_{n+1}}$. The 'consistent' here emphasizes that the tangent operator is 'consistent' with the constitutive law integration scheme, which guarantees the quadratic rate of asymptotic convergence of iterative solution strategies based on Newton's method, as will be discussed in detail in Chapter 4.

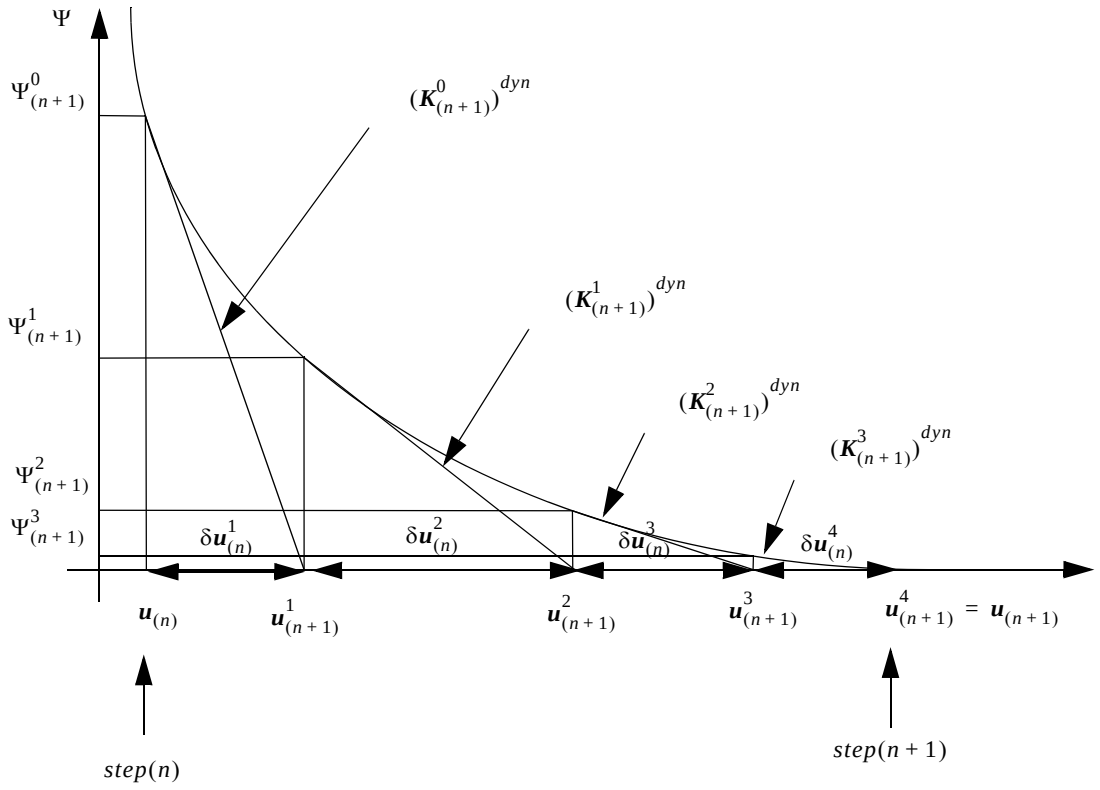


**Figure 3.1 Typical newton raphson iteration algorithm**

After the $u_{n+1}$ is obtained which satisfies Equation (3.3), the sensitivity computation is performed before the histories variables (stresses, strains, etc.) are updated with new state variables corresponding to the $u_{n+1}$ (often by a 'commit' operation). The sensitivity computation includes two sequential steps, i.e computation of the conditional and unconditional derivatives.

Differentiating Eq. (3.3) with respect to θ using the chain rule, recognizing that $\boldsymbol{\sigma} = \boldsymbol{\sigma}(\boldsymbol{\epsilon}(t, \theta), \theta)$ where $\boldsymbol{\sigma}$ and $\boldsymbol{\epsilon}$ denote the stress and strain tensors, respectively, we obtain:

$$\left[\frac{1}{\beta(\Delta t)^2}\boldsymbol{M} + \frac{\alpha}{\beta(\Delta t)}\boldsymbol{C} + (\boldsymbol{K}_T^{stat})_{n+1}\right]\frac{\partial \boldsymbol{u}_{n+1}}{\partial \theta} = -\left(\frac{1}{\beta(\Delta t)^2}\frac{\partial \boldsymbol{M}}{\partial \theta} + \frac{\alpha}{\beta(\Delta t)}\frac{\partial \boldsymbol{C}}{\partial \theta}\right)\boldsymbol{u}_{n+1} - \frac{\partial \boldsymbol{R}(\boldsymbol{u}_{n+1}(\theta), \theta)}{\partial \theta}\bigg|_{u_{n+1}} + \frac{\partial \tilde{\boldsymbol{F}}_{n+1}}{\partial \theta} \tag{3.8}$$

In Equation (3.8),

$$\frac{\partial \tilde{\boldsymbol{F}}_{n+1}}{\partial \theta} = \frac{\partial \boldsymbol{F}_{n+1}}{\partial \theta} + \frac{\partial \boldsymbol{M}}{\partial \theta}\left(\frac{1}{\beta(\Delta t)^2}\boldsymbol{u}_n + \frac{1}{\beta(\Delta t)}\dot{\boldsymbol{u}}_n - \left(1 - \frac{1}{2\beta}\right)\ddot{\boldsymbol{u}}_n\right) +$$

$$\boldsymbol{M}\left[\frac{1}{\beta(\Delta t)^2}\frac{\partial \boldsymbol{u}_n}{\partial \theta} + \frac{1}{\beta(\Delta t)}\frac{\partial \dot{\boldsymbol{u}}_n}{\partial \theta} - \left(1 - \frac{1}{2\beta}\right)\frac{\partial \ddot{\boldsymbol{u}}_n}{\partial \theta}\right] +$$

$$\frac{\partial \boldsymbol{C}}{\partial \theta}\left[\frac{\alpha}{\beta(\Delta t)}\boldsymbol{u}_n - \left(1 - \frac{\alpha}{\beta}\right)\dot{\boldsymbol{u}}_n - (\Delta t)\left(1 - \frac{\alpha}{2\beta}\right)\ddot{\boldsymbol{u}}_n\right] +$$

$$\boldsymbol{C}\left[\frac{\alpha}{\beta(\Delta t)}\frac{\partial \boldsymbol{u}_n}{\partial \theta} - \left(1 - \frac{\alpha}{\beta}\right)\frac{\partial \dot{\boldsymbol{u}}_n}{\partial \theta} - (\Delta t)\left(1 - \frac{\alpha}{2\beta}\right)\frac{\partial \ddot{\boldsymbol{u}}_n}{\partial \theta}\right]$$

In Equation (3.8), the computation of all items on the right hand side (RHS) are not difficult except for $\left.\frac{\partial \boldsymbol{R}(\boldsymbol{u}_{n+1}(\theta), \theta)}{\partial \theta}\right|_{u_{n+1}}$. This term represents the partial derivative of the internal resisting force vector $\mathbf{R}(\mathbf{u}_{n+1})$ with respect to sensitivity parameter θ under the condition that the displacement vector $\mathbf{u}_{n+1}$ remains fixed. From Equation (3.8), this conditional derivative term can be expressed as an assembly of contributions from all elements:

$$\left.\frac{\partial \boldsymbol{R}(\boldsymbol{u}_{n+1}(\theta),\theta)}{\partial\theta}\right|_{\boldsymbol{u}_{n+1}} = \left.\frac{\partial}{\partial\theta}\left[\sum_{n=1}^{Nel}\int_{\Omega_e}\boldsymbol{B}^T(\boldsymbol{x})\cdot\boldsymbol{\sigma}(\boldsymbol{x})\cdot d\Omega_e\right]\right|_{\boldsymbol{u}_{n+1}} \tag{3.9}$$

where $|_{\boldsymbol{u}_{n+1}}$ denotes the derivative with respect to θ for fixed displacement vector $\boldsymbol{u}_{n+1}$. And $\boldsymbol{B}$ is the strain-displacement transformation matrix.

This sensitivity with fixed displacement $\left.\frac{\partial \boldsymbol{R}(\boldsymbol{u}_{n+1}(\theta),\theta)}{\partial\theta}\right|_{\boldsymbol{u}_{n+1}}$ is also referred as the conditional derivative of the internal resisting force vector $\mathbf{R}(\mathbf{u}_{n+1})$. To solve the sensitivity equation (3.8) at the n+1 step, only the conditional derivative is necessary, while the unconditional derivative is required for solving the sensitivity equation at the subsequent step. This is due to the fact that at the material point, the computation of the conditional derivative of the stress/strain at time step n+2 depends on the unconditional derivative of stress/strain at time step n+1. In the sensitivity framework, there are two sequential steps to call the assembly of the sensitivity from all elements: one is for the conditional derivative $\left.\frac{\partial \boldsymbol{R}(\boldsymbol{u}_{n+1}(\theta),\theta)}{\partial\theta}\right|_{\boldsymbol{u}_{n+1}}$ and the other is for the unconditional derivative $\frac{\partial \boldsymbol{R}(\boldsymbol{u}_{n+1}(\theta),\theta)}{\partial\theta}$.

Analytical expressions for this history dependent conditional derivative of the stress vector have been derived by Zhang and Der Kiureghian (1993) and Conte et. al. (1995a, 1998) for the constitutive Von Mises $J_2$ plasticity model, and by Conte et. al (1995a,

1995b) for the constitutive cap plasticity model in the case of a return map constitutive integration algorithm (Simo and Hughes 1998).

Numerous random variables may be considered to represent the uncertainties of the FE model. Three main classes are considered: material parameters, external loading, and nodal coordinates. This dissertation considers the first two cases.

### 3.2.1 Response Sensitivity with respect to Nodal Coordinates

In the finite element method, a special case of the integration in Equation (3.9) is that the element force can be obtained directly and does not need to be integrated from the material points. This is the case for elastic beam or truss,

$$\boldsymbol{R} = \boldsymbol{K}\boldsymbol{u} \tag{3.10}$$

where **K** is the tangent modulus.

Then Equation (3.9) is simplified as,

$$\left.\frac{\partial \boldsymbol{R}(\boldsymbol{u}_{n+1}(\theta),\theta)}{\partial\theta}\right|_{\boldsymbol{u}_{n+1}} = \left.\frac{\partial \boldsymbol{K}(\boldsymbol{u}_{n+1}(\theta),\theta)}{\partial\theta}\right|_{\boldsymbol{u}_{n+1}} \cdot \boldsymbol{u}_{n+1} \tag{3.11}$$

In the general case, the conditional derivative of the internal force in Equation (3.9) may be obtained by numerical integration, e.g., Gauss quadrature, For each element, the integration may be evaluated by,

$$\begin{aligned} \boldsymbol{R}(\boldsymbol{u}_{n+1}(\theta),\theta) &= \sum_{n=1}^{Nel} \int_{\Omega_e} \boldsymbol{B}^T(\boldsymbol{x}) \cdot \boldsymbol{\sigma}(\boldsymbol{x}) \cdot d\Omega_e \\ &= \sum_{m=1}^{NumPoints} \omega_m \boldsymbol{B}^T(\zeta^m) \cdot \boldsymbol{\sigma}(\zeta^m) \cdot \left|\boldsymbol{J}^m_{x,\zeta}\right| \end{aligned} \tag{3.12}$$

where $\omega_m$ is weight, $\zeta^m$ is the local coordinate at Gauss point m, $\boldsymbol{B}(\zeta^m)$ is the first order differentiation of the shape function with respect to coordinate and evaluated at Gauss point m, $\left|\boldsymbol{J}_{x,\zeta}^m\right|$ is the determinant of the Jacobian evaluated at Gauss point m.

Take advantage of the following relation (Gurtin 1981 ):

$\frac{\partial\left|\boldsymbol{J}_{x,\zeta}\right|}{\partial\theta} = \frac{\partial\left|\boldsymbol{J}_{x,\zeta}\right|}{\partial\boldsymbol{J}_{x,\zeta}} \cdot \frac{\partial\boldsymbol{J}_{x,\zeta}}{\partial\theta} = \left|\boldsymbol{J}_{x,\zeta}\right| \cdot (\boldsymbol{J}_{x,\zeta})^{-T} \cdot \frac{\partial}{\partial\zeta}\left(\frac{\partial x}{\partial\theta}\right)$, which is nonzero only if the sensitivity variable is a nodal coordinate.

Differentiating Equation (3.12) with parameter θ with displacement fixed, it can be shown that:

$$\begin{aligned}
\frac{\partial}{\partial\theta}\left[\sum_{n=1}^{Nel}\int_{\Omega_e}\boldsymbol{B}^T(\boldsymbol{x})\cdot\boldsymbol{\sigma}(\boldsymbol{x})\cdot d\Omega_e\right]\Bigg|_{\boldsymbol{u}_{n+1}} &= \sum_{m=1}^{NumPoints}\frac{\partial}{\partial\theta}[\omega_m\boldsymbol{B}^T(\zeta^m)\cdot\boldsymbol{\sigma}(\zeta^m)\cdot\left|\boldsymbol{J}_{x,\zeta}^m\right|]\Big|_{\boldsymbol{u}_{n+1}} \\
&= \sum_{m=1}^{NumPoints}\omega_m\left|\boldsymbol{J}_{x,\zeta}^m\right|\Bigg[\boldsymbol{B}^T(\zeta^m)\cdot\frac{\partial\boldsymbol{\sigma}(\zeta^m)}{\partial\boldsymbol{\epsilon}}\cdot\frac{\partial\boldsymbol{B}}{\partial\theta}\Big|_{\boldsymbol{u}_{n+1}}\cdot\boldsymbol{u}_{n+1} \\
&\quad + \boldsymbol{B}^T(\zeta^m)\cdot\frac{\partial\boldsymbol{\sigma}(\zeta^m)}{\partial\theta}\Big|_{\substack{\boldsymbol{u}_{n+1}\\ \boldsymbol{\epsilon}_{n+1}}} \\
&\quad + \frac{\partial\boldsymbol{B}^T(\zeta^m)}{\partial\theta}\Big|_{\boldsymbol{u}_{n+1}}\cdot\boldsymbol{\sigma}(\zeta^m) \\
&\quad + \boldsymbol{B}^T(\zeta^m)\cdot\boldsymbol{\sigma}(\zeta^m)\cdot(\boldsymbol{J}_{x,\zeta}^m)^{-T}\cdot\frac{\partial}{\partial\zeta}\left(\frac{\partial x}{\partial\theta}\right)\Bigg]
\end{aligned} \tag{3.13}$$

where N is the shape function.

In Equation (3.13), the $\boldsymbol{B}^T(\zeta^m) \cdot \frac{\partial \boldsymbol{\sigma}(\zeta^m)}{\partial \boldsymbol{\epsilon}} \cdot \left.\frac{\partial \boldsymbol{B}^T}{\partial \theta}\right|_{\boldsymbol{u}_{n+1}} \cdot \boldsymbol{u}_{n+1}$ , $\left.\frac{\partial \boldsymbol{B}^T(\zeta^m)}{\partial \theta}\right|_{\boldsymbol{u}_{n+1}} \cdot \boldsymbol{\sigma}(\zeta^m)$ and $\boldsymbol{B}^T(\zeta^m) \cdot \boldsymbol{\sigma}(\zeta^m) \cdot (\boldsymbol{J}^m_{x,\zeta})^{-T} \cdot \frac{\partial}{\partial \zeta}\left(\frac{\partial x}{\partial \theta}\right)$ are nonzero if the sensitivity variable θ is a nodal coordinate. These represent parts of the contributions from uncertainties of the nodal coordinates.

Another place where the uncertainties of nodal coordinate have contribution is in the the distributed mass matrix, whose contribution is shown in $\frac{\partial \boldsymbol{M}}{\partial \theta}$ in Equation (3.8). In FEM, the distributed mass is computed as:

$$\boldsymbol{M} = \sum_{m=1}^{NumPoints} \omega_m N(\zeta^m) \cdot N^T(\zeta^m) \cdot \rho \cdot \left|\boldsymbol{J}^m_{x,\zeta}\right| \tag{3.14}$$

and so the sensitivity of the Mass matrix to the nodal coordinate is,

$$\begin{aligned} \frac{\partial \boldsymbol{M}}{\partial \theta} = \sum_{m=1}^{NumPoints} \omega_m \left|\boldsymbol{J}^m_{x,\zeta}\right| \Big[ & N(\zeta^m) \cdot N^T(\zeta^m) \cdot \frac{\partial \rho}{\partial \theta} \\ & + \frac{\partial N(\zeta^m)}{\partial \theta} \cdot N^T(\zeta^m) \cdot \rho \\ & + N(\zeta^m) \cdot \frac{\partial N^T(\zeta^m)}{\partial \theta} \rho \\ & + N(\zeta^m) \cdot N^T(\zeta^m) \cdot \rho \cdot (\boldsymbol{J}_{x,\zeta})^{-T} \cdot \frac{\partial}{\partial \zeta}\left(\frac{\partial x}{\partial \theta}\right) \Big] \end{aligned} \tag{3.15}$$

In this Equation (3.15), item $\frac{\partial N(\zeta^m)}{\partial \theta} \cdot N^T(\zeta^m) \cdot \rho \quad N(\zeta^m) \cdot \frac{\partial N^T(\zeta^m)}{\partial \theta} \rho$ and $N(\zeta^m) \cdot N^T(\zeta^m) \cdot \rho \cdot (\boldsymbol{J}_{x,\zeta})^{-T} \cdot \frac{\partial}{\partial \zeta}\left(\frac{\partial x}{\partial \theta}\right)$ will be nonzero if the sensitivity variable is a nodal coordinate.

If Rayleigh Damping is used:

$$\boldsymbol{C} = \alpha \boldsymbol{M} + \beta \boldsymbol{K}_{init} \tag{3.16}$$

then

$$\frac{\partial \boldsymbol{C}}{\partial \theta} = \frac{\partial \alpha}{\partial \theta}\boldsymbol{M} + \alpha \frac{\partial \boldsymbol{M}}{\partial \theta} + \frac{\partial \beta}{\partial \theta}\boldsymbol{K}_{init} + \beta \frac{\partial \boldsymbol{K}_{init}}{\partial \theta} \tag{3.17}$$

The item $\frac{\partial \boldsymbol{M}}{\partial \theta}$ is the same as in Equation (3.15).

The third place where nodal uncertainties contribute to the sensitivity Equation (3.8) is the term $\frac{\partial \boldsymbol{F}_{n+1}}{\partial \theta}$. Since the forces are added either as nodal or body forces, which in both cases depend on the nodal coordinates. (Haukass T. 2001).

In this dissertation, nodal coordinate uncertainties are not considered in the system uncertainties. Instead, much emphasis is placed on the uncertainties of the material and loading parameters.

### 3.2.2 Response Sensitivity with respect to Material Parameters

The material uncertainties are represented by

(1) the parameters defining the material constitutive law, such as elastic moduli E in elastic materials. The contribution of these uncertainties are shown in Equation (3.13) by the item $\left.\frac{\partial \boldsymbol{\sigma}(\zeta^m)}{\partial \theta}\right|_{\substack{\boldsymbol{u}_{n+1} \\ \boldsymbol{\epsilon}_{n+1}}}$.

(2) the mass density ρ, whose contribution is shown in $\frac{\partial \boldsymbol{M}}{\partial \theta}$ in Equation (3.15). The item $N(\zeta^m) \cdot N^T(\zeta^m) \cdot \frac{\partial \rho}{\partial \theta}$ is nonzero if $\theta = \rho$.

If Rayleigh damping is used, the items $\frac{\partial \boldsymbol{M}}{\partial \theta}$ and $\frac{\partial \boldsymbol{K}_{init}}{\partial \theta}$ in Equation (3.17) are nonzero for material parameter uncertainty cases. The term $\frac{\partial \boldsymbol{K}_{init}}{\partial \theta}$ is computed by assembling the contribution from all elements,

$$\frac{\partial \boldsymbol{K}_{init}}{\partial \theta} = \sum_{n=1}^{Nel} \int_{\Omega_\backslash} \boldsymbol{B}^T(\boldsymbol{x}) \cdot \frac{\partial \boldsymbol{D}(\boldsymbol{x})^{init}}{\partial \theta} \cdot \boldsymbol{B}(\boldsymbol{x}) d\Omega \tag{3.18}$$

where $\boldsymbol{D}(\boldsymbol{x})^{init}$ is the material initial tangent stiffness matrix.

The material mass density is also found to contribute in the cases of distributed elements and volume loads in the form of:

$$\boldsymbol{F}^{ext,\,surf} = \int_{\Omega_e} \boldsymbol{t} \cdot \hat{\boldsymbol{e}} d\Omega_e + \int_{\Omega} \rho \boldsymbol{b} \cdot \hat{\boldsymbol{e}} d\Omega \tag{3.19}$$

where **t** is surface force, **b** is body force, $\hat{\boldsymbol{e}}$ is the unit tensor. Differentiating Equation (3.19) with respect to θ,

$$\frac{\partial \boldsymbol{F}^{ext,\,surf}}{\partial \theta} = \int_{\Omega_e} \frac{\partial \boldsymbol{t}}{\partial \theta} \cdot \hat{\boldsymbol{e}} d\Omega_e + \int_{\Omega} \rho \frac{\partial \boldsymbol{b}}{\partial \theta} \cdot \hat{\boldsymbol{e}} d\Omega + \int_{\Omega} \frac{\partial \rho}{\partial \theta} \boldsymbol{b} \cdot \hat{\boldsymbol{e}} d\Omega \tag{3.20}$$

The last item $\int_{\Omega} \frac{\partial \rho}{\partial \theta} \boldsymbol{b} \cdot \hat{\boldsymbol{e}} d\Omega$ is nonzero if the random variable is material mass density ρ.

(3) The lumped mass uncertainties are also considered in the item $\frac{\partial \boldsymbol{M}}{\partial \theta}$, which may be obtained by direct assembly of the contributions from all nodes that have the specified random variable m.

(4) The contributions due to other random variables such as the cross sectional area in beam and truss elements are considered in $\frac{\partial \boldsymbol{K}}{\partial \theta}$ and $\frac{\partial \boldsymbol{K}_{init}}{\partial \theta}$.

### 3.2.3 Response Sensitivity with respect to Load Parameters

The load sensitivities are considered in the item $\frac{\partial \boldsymbol{F}_{n+1}}{\partial \theta}$ in Equation (3.8). Three kinds of loads are identified:

(1) Distributed element loads

Distributed element loads include the surface load and volume load as shown in Equation (3.20). The sensitivity part $\int_{\Omega_e} \frac{\partial \boldsymbol{t}}{\partial \theta} \cdot \hat{\boldsymbol{e}} d\Omega_e$, $\int_{\Omega} \rho \frac{\partial \boldsymbol{b}}{\partial \theta} \cdot \hat{\boldsymbol{e}} d\Omega$ may be nonzero in Equation (3.15) if the random variables are surface or volume loads.

(2) Nodal loads

The nodal load vector is obtained by assembling the nodal forces from all nodes.

$$P = \overset{numDOF}{\underset{i=1}{A}} p_i(\theta) \tag{3.21}$$

Where $\overset{numDOF}{\underset{i=1}{A}}$ denotes assembly through the degrees of freedom from 1 to numDOF. The sensitivity is:

$$\frac{\partial P}{\partial \theta} = \overset{numDOF}{\underset{i=1}{A}} \left( \frac{\partial p_i(\theta)}{\partial \theta} \right) \tag{3.22}$$

(3) Base excitation load

As mentioned in chapter 2, the earthquake input is,

$$x(t) = \mu(t) + c_2 \sum_{k=1}^{K} q_k(t) \sum_{i=1}^{N} Y_{ik} h_k(t - t_k) \tag{3.23}$$

differentiating with respect to $\theta$,

$$\frac{\partial x(t)}{\partial \theta} = \mu(t) + c_2 \sum_{k=1}^{K} q_k(t) \sum_{i=1}^{N} \frac{\partial Y_{ik}}{\partial \theta} h_k(t - t_k) \tag{3.24}$$

## 3.3 Response Sensitivity Computation at the Element Level

The sensitivity framework as developed in OpenSees by Haukaas and Derkiureghian (ref) considers 1D truss and 2D Beam-Column elements with fiber sections consisting of 1D uniaxial materials: elastic material, Kent-Scott-Park concrete material, and bilinear steel material. In order to solve complicated SSI problems, this framework has been greatly extended for various elements, including four-node quadrilateral bilinear isoparametric element, zero-length element, DispBeamColumn3d element, and 3D bbarbrick element. (refer Cook, OpenSees manual).

In Equation (3.8), the conditional derivative of the internal force vector $\left.\frac{\partial \boldsymbol{R}(\boldsymbol{u}_{n+1}(\theta), \theta)}{\partial \theta}\right|_{u_{n+1}}$ is assembled from all elements. Only for the computation of material sensitivity,

$$\begin{aligned} \frac{\partial}{\partial \theta}\left[\sum_{n=1}^{Nel} \int_{\Omega_e} \boldsymbol{B}^T(\boldsymbol{x}) \cdot \boldsymbol{\sigma}(\boldsymbol{x}) \cdot d\Omega_e\right]\Bigg|_{\boldsymbol{u}_{n+1}} &= \sum_{n=1}^{Nel} \int_{\Omega_e} \boldsymbol{B}^T(\boldsymbol{x}) \cdot \left.\frac{\partial \boldsymbol{\sigma}(\boldsymbol{x})}{\partial \theta}\right|_{\boldsymbol{u}_{n+1}} \cdot d\Omega_e \\ &= \sum_{m=1}^{NumPoints} \omega_m \left|\boldsymbol{J}^m_{x,\zeta}\right| \boldsymbol{B}^T(\zeta^m) \cdot \left.\frac{\partial \boldsymbol{\sigma}(\zeta^m)}{\partial \theta}\right|_{\substack{\boldsymbol{u}_{n+1} \\ \boldsymbol{\epsilon}_{n+1}}} \end{aligned} \tag{3.25}$$

It is noticed that the conditional derivative of the stress vector $\left.\frac{\partial \boldsymbol{\sigma}(\zeta^m)}{\partial \theta}\right|_{\substack{\boldsymbol{u}_{n+1} \\ \boldsymbol{\epsilon}_{n+1}}}$, is obtained from the section or material level. Thus, here the function of Equation (3.25) is to assemble all contributions from sections or materials. It is worth mentioning that the

assembly will loop all elements even if some do not explicitly include the sensitivity parameter $\theta$, since their conditional stress derivatives are nonzero.

Other implementations include sensitivity computations with respect to element parameters such as mass density $\rho$ and area A, etc.

## 3.4 Response Sensitivity Computation at Section and Material Level

Several sections and materials are implemented in order to perform the sensitivity analysis for the SSI system including 2D and 3D fiber sections, section aggregation, uniaxial Bouc-wen material, smoothed Popovics-Saenz model (Balan et al. 1997, 2001; Kwon and Spacone 2002, Zona et al. 2005) , smooth steel Menegotto-Pinto (MP) materials, and 3D pressure independent multi yield surface $J_2$ plasticity soil material.

In this section the sensitivity analysis for a 1D von Mises $J_2$ plasticity material model is explained in detail in order to show the complete computational framework of the sensitivity analysis. This sensitivity analysis is implemented in FEAP by the author as well as OpenSees and FedeasLab by others, based on which some sensitivity analysis aspects ( e.g., discontinuities, convergence rate, etc.) are studied. While the sensitivity derivative for the smoothed Popovics-Saenz model (Balan et al. 1997, 2001; Kwon and Spacone 2002, Zona et al. 2005) , and smooth steel Menegotto-Pinto (MP) materials and 3D pressure independent multi yield surface $J_2$ plasticity soil model are shown in the $4^{th}$ Chapter in detail.

### 3.4.1 Sensitivity computation for 1D $J_2$ (von Mises) Plasticity model

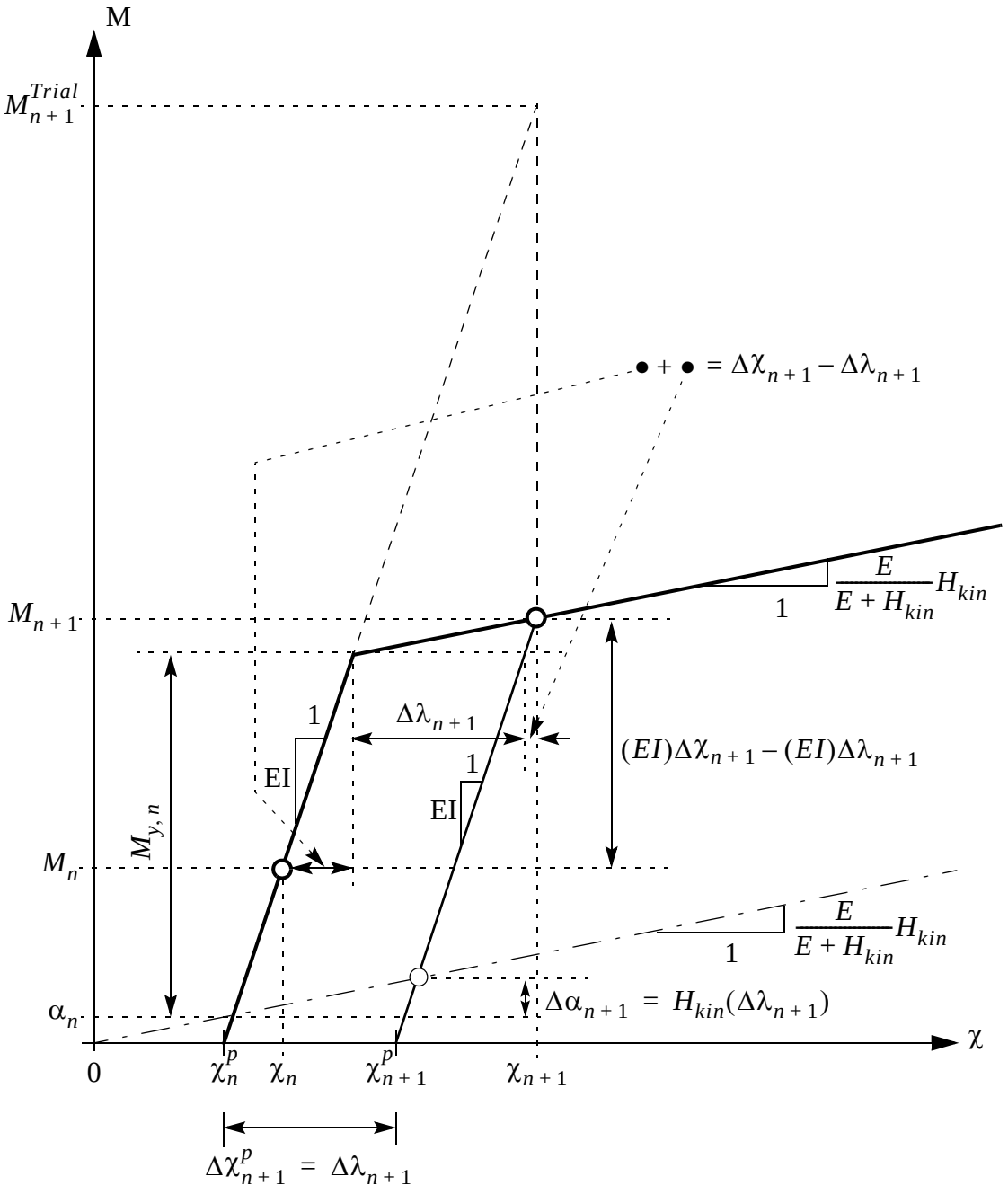


**Figure 3.2 Return map algorithm in the uniaxial case with pure kinematici hardening ($H_{iso}$= 0)**

This section shows the steps required to compute the response and response sensitivi-

ties in both conditional and unconditional cases for a 1D $J_2$ Plasticity model with the von Mises yield criterion. As shown in Figure 3.2, the plasticity model assumes the following relations:

1. Additive decomposition of the total strain, i.e, the total strain $\varepsilon$ can be additively split into an elastic part $\varepsilon^e$ and a plastic part $\varepsilon^p$:

$$\varepsilon = \varepsilon^e + \varepsilon^p \tag{3.26}$$

2. Elastic stress-strain relations:

$$\sigma = E \cdot \varepsilon^e \tag{3.27}$$

where E is the elastic Young's modulus of the material.

3. Flow rule:

$$\dot{\varepsilon}^p = \dot{\lambda} \cdot \operatorname{sgn}(\sigma - \alpha) \tag{3.28}$$

where $\dot{\lambda}$ is the consistency parameter and $\operatorname{sgn}(\ldots)$ denotes the sign function.

4. Hardening laws (linear kinematic and linear isotropic hardening):

$$\begin{aligned} \dot{\alpha} &= H_{kin} \cdot \dot{\varepsilon}^p \\ \dot{\bar{\varepsilon}}^p &= \dot{\lambda} \\ \sigma_y &= \sigma_{y0} + H_{iso} \cdot \bar{\varepsilon}^p \end{aligned} \tag{3.29}$$

where $\dot{\bar{\varepsilon}}^p = \sqrt{\dot{\varepsilon}^p} = \left|\dot{\varepsilon}^p\right|$ denotes the rate of effective plastic strain, $\bar{\varepsilon}^p = \int_0^t \dot{\bar{\varepsilon}}^p \cdot dt$ is the effective or cumulative plastic strain, $\sigma_{y0}$ is the initial yield stress, $\sigma_y$ is the current yield stress and $H_{kin}$ and $H_{iso}$ are the kinematic and isotropic hardening moduli, respectively.

5. Kuhn-Tucker conditions for loading/unloading:

$$\dot{\lambda} \geq 0, \quad f(\sigma, \alpha, \bar{\varepsilon}^p) \leq 0 \quad \text{and} \quad \dot{\lambda} \cdot f = 0 \tag{3.30}$$

6. Plastic consistency condition:

$$\dot{\lambda} \geq 0, \quad \dot{f}(\sigma, \alpha, \bar{\varepsilon}^p) \leq 0 \quad \text{and} \quad \dot{\lambda} \cdot \dot{f} = 0 \tag{3.31}$$

The yield function is of the form

$$f(\sigma, \alpha, \bar{\varepsilon}^p) = |\sigma - \alpha| - (\sigma_{y0} + H_{iso}\bar{\varepsilon}^p) \tag{3.32}$$

The 1D $J_2$ plasticity model with pure linear kinematic hardening ($H_{iso} = 0$) corresponds to the bilinear inelastic model shown in Figure 3.2. The rate constitutive equations above have to be integrated numerically in order to obtain the stress history for a given strain history. Using the implicit backward Euler scheme to time-discretize the rate equations over the time step $[t_n, t_{n+1}]$, the following discretized material constitutive equations are obtained:

1. Additive split of the total strain:

$$\varepsilon_{n+1} = \varepsilon^e_{n+1} + \varepsilon^p_{n+1} \tag{3.33}$$

2. Elastic stress-strain relation:

$$\sigma_{n+1} = E \cdot \varepsilon^e_{n+1} \tag{3.34}$$

3. Flow rule:

$$\varepsilon^p_{n+1} = \varepsilon^p_n + \Delta\lambda \cdot \operatorname{sgn}(\sigma_{n+1} - \alpha_{n+1}) \tag{3.35}$$

where $\Delta\lambda = \int_{t_n}^{t_{n+1}} \dot{\lambda} \cdot dt \cong \dot{\lambda}_{n+1} \cdot \Delta t$ is the discrete consistency parameter.

4. Hardening laws (linear kinematic and linear isotropic hardening):

$$\begin{aligned} \alpha_{n+1} &= \alpha_n + H_{kin} \cdot \Delta\lambda \cdot \operatorname{sgn}(\sigma_{n+1} - \alpha_{n+1}) \\ \bar{\varepsilon}^p_{n+1} &= \bar{\varepsilon}^p_n + \Delta\lambda \\ \sigma_{y,\,n+1} &= \sigma_{y,\,n} + H_{iso} \cdot \Delta\lambda \end{aligned} \tag{3.36}$$

5. Kuhn-Tucker loading/unloading and plastic consistency conditions:

$$\Delta\lambda \geq 0, \quad f(\sigma_{n+1}, \alpha_{n+1}, \bar{\varepsilon}^p_{n+1}) \leq 0 \quad \text{and} \quad \Delta\lambda \cdot f(\sigma_{n+1}, \alpha_{n+1}, \bar{\varepsilon}^p_{n+1}) = 0 \tag{3.37}$$

The subscript $(\ldots)_{n+1}$ denotes that the quantity is evaluated at time $t_{n+1}$. The above discretized constitutive equations are solved by using the effective elasto-plastic operator split method with the return map concept. This is based on the notion of the closest-point-projection in the stress space (Simo and Hughes 1998). The stress $\sigma_{n+1}$ is solved in two steps, namely (1) a elastic trial step and (2) a plastic corrector step.

Elastic Trial:

$$\begin{aligned} \Delta\lambda^{Trial} &= 0 \\ (\varepsilon^p_{n+1})^{Trial} &= \varepsilon^p_n \\ \alpha^{Trial}_{n+1} &= \alpha_n \\ (\bar{\varepsilon}^p_{n+1})^{Trial} &= \bar{\varepsilon}^p_n \\ \sigma^{Trial}_{n+1} &= E(\varepsilon_{n+1} - \varepsilon^p_n) \\ \sigma^{Trial}_{y,\,n+1} &= \sigma_{y,\,n} \end{aligned} \tag{3.38}$$

IF $\{f(\sigma^{Trial}_{n+1}, \alpha^{Trial}_{n+1}, (\bar{\varepsilon}^p_{n+1})^{Trial}) \leq 0\}$ THEN

Update all the state/history variables at time $t_{n+1}$ by assigning the corresponding trial values to them, i.e., $(\ldots)_{n+1} = (\ldots)_{n+1}^{Trial}$ and EXIT.

ELSE

Plastic Corrector Step Using the Return Map Algorithm:

The plastic corrector step is based upon satisfying the consistency condition in discrete form:

$$f_{n+1} = \left|\sigma_{n+1} - \alpha_{n+1}\right| - \sigma_{y,\,n+1} = 0 \tag{3.39}$$

where

$$\begin{aligned} \sigma_{n+1} &= E(\varepsilon_{n+1} - \varepsilon_{n+1}^{p}) \\ &= E(\varepsilon_{n+1} - \varepsilon_{n}^{p} - (\Delta\lambda \cdot \operatorname{sgn}(\sigma_{n+1} - \alpha_{n+1}))) \\ &= \sigma_{n+1}^{Trial} - E \cdot \Delta\lambda \cdot \operatorname{sgn}(\sigma_{n+1} - \alpha_{n+1}) \end{aligned} \tag{3.40}$$

$$\begin{aligned} \alpha_{n+1} &= \alpha_{n} + H_{kin} \cdot \Delta\lambda \cdot \operatorname{sgn}(\sigma_{n+1} - \alpha_{n+1}) \\ &= \alpha_{n+1}^{Trial} + H_{kin} \cdot \Delta\lambda \cdot \operatorname{sgn}(\sigma_{n+1} - \alpha_{n+1}) \end{aligned} \tag{3.41}$$

$$\sigma_{y,\,n+1} = \sigma_{y,\,n} + H_{iso} \cdot \Delta\lambda \tag{3.42}$$

Using the expressions for $\sigma_{n+1}$ and $\alpha_{n+1}$ in Eqs. (3.41) and (3.42) and defining

$$n_{n+1} = \frac{\sigma_{n+1} - \alpha_{n+1}}{\left|\sigma_{n+1} - \alpha_{n+1}\right|} = \operatorname{sgn}(\sigma_{n+1} - \alpha_{n+1}), \tag{3.43}$$

we obtain

$$\sigma_{n+1} - \alpha_{n+1} = \left|\sigma_{n+1} - \alpha_{n+1}\right| \cdot n_{n+1} = (\sigma_{n+1}^{Trial} - \alpha_{n+1}^{Trial}) - (E + H_{kin}) \cdot \Delta\lambda \cdot n_{n+1} \tag{3.44}$$

By analyzing the signs of the three terms of the equation formed by the second equal sign in (3.44), it follows that

$$\mathrm{sgn}(\sigma_{n+1} - \alpha_{n+1}) \;=\; \mathrm{sgn}(\sigma^{Trial}_{n+1} - \alpha^{Trial}_{n+1}) \;=\; n_{n+1} \tag{3.45}$$

and

$$\left|\sigma_{n+1} - \alpha_{n+1}\right| \;=\; \left|\sigma^{Trial}_{n+1} - \alpha^{Trial}_{n+1}\right| - (E + H_{kin})\Delta\lambda\,. \tag{3.46}$$

Therefore, using (3.42), the discrete consistency condition in (3.39) is written as

$$\left|\sigma^{Trial}_{n+1} - \alpha^{Trial}_{n+1}\right| - (E + H_{kin}) \cdot \Delta\lambda - \sigma_{y,\,n} - H_{iso} \cdot \Delta\lambda \;=\; 0 \tag{3.47}$$

The discrete consistency parameter $\Delta\lambda$ can be obtained from the above equation as

$$\Delta\lambda \;=\; \frac{\left|\sigma^{Trial}_{n+1} - \alpha^{Trial}_{n+1}\right| - \sigma_{y,\,n}}{E + H_{iso} + H_{kin}} \tag{3.48}$$

Given $\varepsilon_{n+1}$, once $\Delta\lambda$ is known, the state/history variables at $t_{n+1}$ (i.e., $\varepsilon^{p}_{n+1}$, $\sigma_{n+1}$, $\alpha_{n+1}$, $\bar{\varepsilon}^{p}_{n+1}$, $\sigma_{y,\,n+1}$) are obtained from Eqs. (3.35), (3.36), (3.40) and (3.45). The above discrete constitutive integration scheme for 1D $J_2$ plasticity is represented graphically in Figure 3.2 for a plastic step.

Response Sensitivity Calculations

It was shown earlier that the formation of the response sensitivity equation, (3.8), requires computation of the derivative $d\sigma_{n+1}/d\varepsilon_{n+1}$ in order to get the consistent tangent stiffness matrix $\boldsymbol{K}^{stat}_{T} \;=\; \dfrac{\partial \boldsymbol{R}}{\partial \boldsymbol{u}}$. Also, the conditional derivative term $\partial\sigma_{n+1}/\partial\theta\big|_{\varepsilon_{n+1}}$ needs to be computed to evaluate the term $\partial \boldsymbol{R}/\partial\theta\big|_{\boldsymbol{u}}$ in the right-hand-side of the response sensitivity

equation (3.8). The derivative $d\sigma_{n+1}/d\varepsilon_{n+1}$ may be obtained by differentiating the discrete constitutive integration algorithm.

For the elastic case,

$$\varepsilon^{p}_{n+1} = (\varepsilon^{p}_{n+1})^{Trial} = \varepsilon^{p}_{n}, \text{ and } d\sigma_{n+1} = E \cdot d\varepsilon_{n+1}. \tag{3.49}$$

When the current step is plastic,

$$d\sigma_{n+1} = E \cdot (d\varepsilon_{n+1} - d\varepsilon^{p}_{n+1}) \tag{3.50}$$

$$\text{and} \qquad d\varepsilon^{p}_{n+1} = d(\Delta\lambda) \cdot n_{n+1} \tag{3.51}$$

The discrete consistency parameter $\Delta\lambda$ is obtained from the discrete consistency condition in (3.39). Thus, taking differentials on both sides of the discrete consistency condition, using Equations (3.40), (3.41), (3.42), one may get

$$\begin{aligned} df_{n+1} &= d\left|\sigma_{n+1} - \alpha_{n+1}\right| - d\sigma_{y,\,n+1} = 0 \\ &= d(\sigma_{n+1} - \alpha_{n+1})n_{n+1} - d\sigma_{y,\,n+1} = 0 \\ &= E(d\varepsilon_{n+1} - d\varepsilon^{p}_{n+1})n_{n+1} - H_{kin} \cdot d(\Delta\lambda) - H_{iso} \cdot d(\Delta\lambda) \end{aligned} \tag{3.52}$$

Multiplying last equation by $n_{n+1}$ and using the expression in Equation (3.51) for $d\varepsilon^{p}_{n+1}$, we obtain

$$d(\Delta\lambda) = \left(\frac{E}{E + H_{kin} + H_{iso}}\right) \cdot d\varepsilon_{n+1} \cdot n_{n+1} \tag{3.53}$$

Substituting Equations. (3.51) and (3.53) into (3.50) yields

$$d\sigma_{n+1} = E \cdot \left(1 - \frac{E}{E + H_{kin} + H_{iso}}\right) \cdot d\varepsilon_{n+1} \tag{3.54}$$

Therefore, in the case of the 1-D $J_2$ plasticity model, the consistent elastoplastic material tangent modulus is given by

$$D_T = E \cdot \left(1 - \frac{E}{E + H_{kin} + H_{iso}}\right) = \frac{H_{kin} + H_{iso}}{E + H_{kin} + H_{iso}} \cdot E \tag{3.55}$$

which is shown in Figure 3.2 in the case of pure kinematic hardening ($H_{iso} = 0$) and corresponds to the post-yield stiffness of the bilinear inelastic model. In the present case, the consistent material tangent modulus is identical to the continuum tangent modulus.

Consider the conditional derivative of a generic state/history variable, $\partial(\dots)/\partial\theta\big|_{\boldsymbol{u}}$. In the current case, the random variables considered are only material and load parameters, thus fixing the displacement $\mathbf{u}(t_{n+1}) = \mathbf{u}_{n+1}$ is equivalent to fixing the strain $\boldsymbol{\epsilon}_{n+1}$. Therefore, the conditional derivatives of the state/history variables are simply obtained by setting all the occurrences of the derivative $\partial\boldsymbol{\epsilon}_{n+1}/\partial\theta$ in the expressions for the (unconditional) derivatives of the state/history variables, $\partial(\dots)/\partial\theta$ equal to zero.

During the current time step $[t_n, t_{n+1}]$, if no plastic deformation occurs, the trial solutions for the state variables given by the elastic predictor step are the correct solutions. Differentiating Equation (3.38) with respect to the sensitivity parameter $\theta$, we obtain

$$\frac{\partial}{\partial\theta}(\Delta\lambda) = 0 \tag{3.56}$$

$$\frac{\partial\varepsilon^p_{n+1}}{\partial\theta} = \frac{\partial\varepsilon^p_n}{\partial\theta} \tag{3.57}$$

$$\frac{\partial\alpha_{n+1}}{\partial\theta} = \frac{\partial\alpha_n}{\partial\theta} \tag{3.58}$$

$$\frac{\partial \bar{\varepsilon}^{p}_{n+1}}{\partial \theta} = \frac{\partial \bar{\varepsilon}^{p}_{n}}{\partial \theta} \tag{3.59}$$

$$\frac{\partial \sigma_{n+1}}{\partial \theta} = E\left(\frac{\partial \varepsilon_{n+1}}{\partial \theta} - \frac{\partial \varepsilon^{p}_{n}}{\partial \theta}\right) + \frac{\partial E}{\partial \theta}(\varepsilon_{n+1} - \varepsilon^{p}_{n}) \tag{3.60}$$

$$\frac{\partial \sigma_{y,\,n+1}}{\partial \theta} = \frac{\partial \sigma_{y,\,n}}{\partial \theta} \tag{3.61}$$

However, if plastic deformation takes place during the current step $[t_n, t_{n+1}]$, the elastoplastic constitutive relations in the discrete form are differentiated with respect to the sensitivity parameter $\theta$ in order to compute the derivatives of the state/history variables at $t_{n+1}$. Differentiating (3.40) with respect to $\theta$ produces

$$\frac{\partial \sigma_{n+1}}{\partial \theta} = E \cdot \left(\frac{\partial \varepsilon_{n+1}}{\partial \theta} - \frac{\partial \varepsilon^{p}_{n+1}}{\partial \theta}\right) + \frac{\partial E}{\partial \theta} \cdot (\varepsilon_{n+1} - \varepsilon^{p}_{n+1}) \tag{3.62}$$

The derivative $\frac{\partial \varepsilon^{p}_{n+1}}{\partial \theta}$ is obtained by differentiating (3.35) with respect to $\theta$, using (3.43), as

$$\frac{\partial \varepsilon^{p}_{n+1}}{\partial \theta} = \frac{\partial \varepsilon^{p}_{n}}{\partial \theta} + \frac{\partial (\Delta\lambda)}{\partial \theta} \cdot n_{n+1} \tag{3.63}$$

where the derivative of $n_{n+1}$ with respect to sensitivity parameter $\theta$ is zero. Using (3.45), (3.48) takes the form

$$\begin{aligned} \Delta\lambda &= \frac{\left|\sigma^{Trial}_{n+1} - \alpha^{Trial}_{n+1}\right| - \sigma_{y,\,n}}{E + H_{iso} + H_{kin}} \\ &= \frac{(\sigma^{Trial}_{n+1} - \alpha^{Trial}_{n+1}) \cdot n_{n+1} - \sigma_{y,\,n}}{E + H_{iso} + H_{kin}} \end{aligned} \tag{3.64}$$

Differentiating (3.64) with respect to θ yields

$$\frac{\partial(\Delta\lambda)}{\partial\theta} = \frac{(E + H_{iso} + H_{kin}) \cdot \left(\left(\frac{\partial\sigma_{n+1}^{Trial}}{\partial\theta} - \frac{\partial\alpha_n}{\partial\theta}\right) \cdot n_{n+1} - \frac{\partial\sigma_{y,n}}{\partial\theta}\right)}{(E + H_{iso} + H_{kin})^2} - \frac{\left(\frac{\partial E}{\partial\theta} + \frac{\partial H_{iso}}{\partial\theta} + \frac{\partial H_{kin}}{\partial\theta}\right) \cdot ((\sigma_{n+1}^{Trial} - \alpha_n) \cdot n_{n+1} - \sigma_{y,n})}{(E + H_{iso} + H_{kin})^2} \tag{3.65}$$

where the derivative of $\sigma_{n+1}^{Trial}$ with respect to θ can be obtained as

$$\frac{\partial\sigma_{n+1}^{Trial}}{\partial\theta} = E \cdot \left(\frac{\partial\varepsilon_{n+1}}{\partial\theta} - \frac{\partial\varepsilon_n^p}{\partial\theta}\right) + \frac{\partial E}{\partial\theta} \cdot (\varepsilon_{n+1} - \varepsilon_n^p) \tag{3.66}$$

The derivatives of the remaining state/history variables, $\bar{\varepsilon}_{n+1}^p$, $\sigma_{y,n+1}$, and $\alpha_{n+1}$, with respect to the sensitivity parameter θ are obtained by differentiating Eqs. (3.36) as

$$\frac{\partial\bar{\varepsilon}_{n+1}^p}{\partial\theta} = \frac{\partial\bar{\varepsilon}_n^p}{\partial\theta} + \frac{\partial(\Delta\lambda)}{\partial\theta} \tag{3.67}$$

$$\frac{\partial\sigma_{y,n+1}}{\partial\theta} = \frac{\partial\sigma_{y,n}}{\partial\theta} + \frac{\partial H_{iso}}{\partial\theta} \cdot \Delta\lambda + H_{iso} \cdot \frac{\partial(\Delta\lambda)}{\partial\theta} \tag{3.68}$$

$$\frac{\partial\alpha_{n+1}}{\partial\theta} = \frac{\partial\alpha_n}{\partial\theta} + \frac{\partial H_{kin}}{\partial\theta} \cdot (\Delta\lambda) \cdot n_{n+1} + H_{kin} \cdot \frac{\partial(\Delta\lambda)}{\partial\theta} \cdot n_{n+1} \tag{3.69}$$

The conditional derivative $\partial\boldsymbol{R}/\partial\theta\big|_{\boldsymbol{u}}$ in the response sensitivity equation (3.8) at the structure level requires computation of the conditional derivative $\left.\frac{\partial\sigma_{n+1}}{\partial\theta}\right|_{\boldsymbol{u}_{n+1}}$ at each Gauss

quadrature point of the finite element model of the structure. As mentioned earlier, this can be achieved by substituting $\frac{\partial \varepsilon_{n+1}}{\partial \theta}$ with zero in Eqs. (3.62), (3.63), (3.65), and (3.66).

## 3.5 Issues regarding the Sensitivity Algorithm Based on DDM

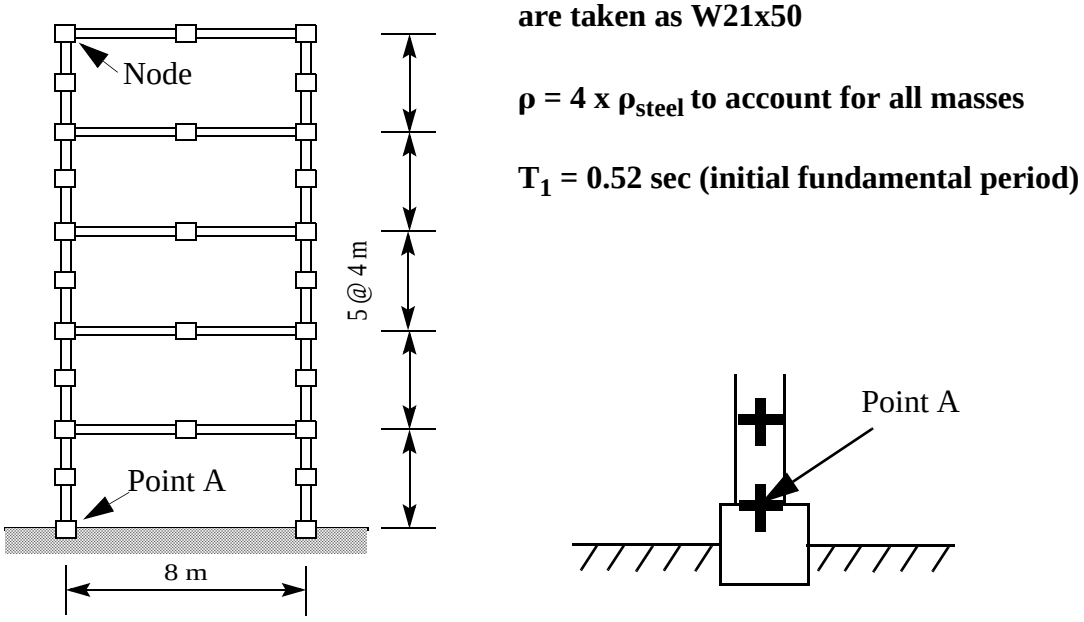


**Figure 3.3 Finite element model of five-story single-bay moment-resisting frame**

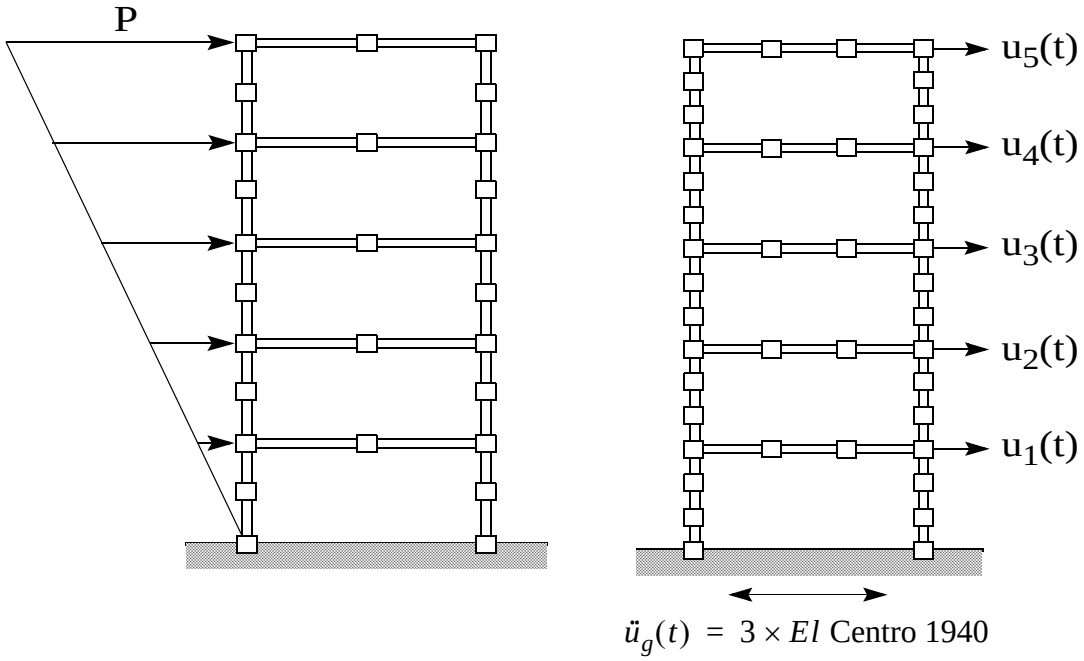


**Figure 3.4 Load cases: static push-over and earthquake base excitation**

In this section, a test structure consisting of a five-story single-bay steel moment-resisting frame is studied as shown in Figure 3.3. This frame is subjected to:

(a) a nonlinear static push-over analysis under an inverted triangular pattern of horizontal loads applied at floor levels as shown in Figure 3.4.

(b) a nonlinear response history analysis for earthquake base excitation as shown in Figure 3.4.

This frame is modeled using a displacement-based simplified distributed plasticity 2-D beam-column element implemented in FEAP (Taylor 1998). Unless stated otherwise, the frame is modeled using two and three elements per beam/column in the static and dynamic case, respectively (Figure 3.4). The source of material nonlinearity is the

moment-curvature relation, which is modeled using the 1-D J2 plasticity model with linear kinematic hardening and zero isotropic hardening as shown in Figure 3.5. The axial force-strain relation is taken as linear elastic and uncoupled from the flexural behavior. The effects of shear deformations are neglected. All columns and beams use $W21 \times 50$ steel sections with a yield moment $M_{y0} = 384.2[kN \cdot m]$. A 20 percent post-yield to initial flexural stiffness ratio is assumed. A material density 4 times that of steel, i.e., $\rho = 31600[Kg \cdot m^{-3}]$, is used to account for typical additional masses (e.g., slabs, cross-beams, floors, ceilings,...). The frame has an initial fundamental period of 0.52 sec. while the Young's modulus of steel is taken as $E = 200[GPa]$. The isotropic and kinematic hardening moduli are $H_{iso} = 0.0, H_{kin} = 20480[kN \cdot m^2]$ . The cross-sectional properties of the steel sections are $A = 0.009484[m^2]$ and $I = 0.0004096[m^4]$. There are 5 Gauss-Lobato points per beam-column element. For the static push-over, the lateral force P applied at the roof level (Figure 3.4) increases from 0 to 230.5 [kN]. In the dynamic case, no damping is included in the model until stated otherwise, and the earthquake input is taken as the balanced 1940 El Centro record (Figure 3.6) scaled up by a factor of 3. During both the static push-over and the dynamic response, the frame yields significantly.

1-D $J_2$ (von Mises) plasticity model with linear kinematic hardening and zero isotropic hardening

$$\frac{H_{kin} + H_{iso}}{EI + H_{kin} + H_{iso}} EI = 0.20 \text{ EI}$$

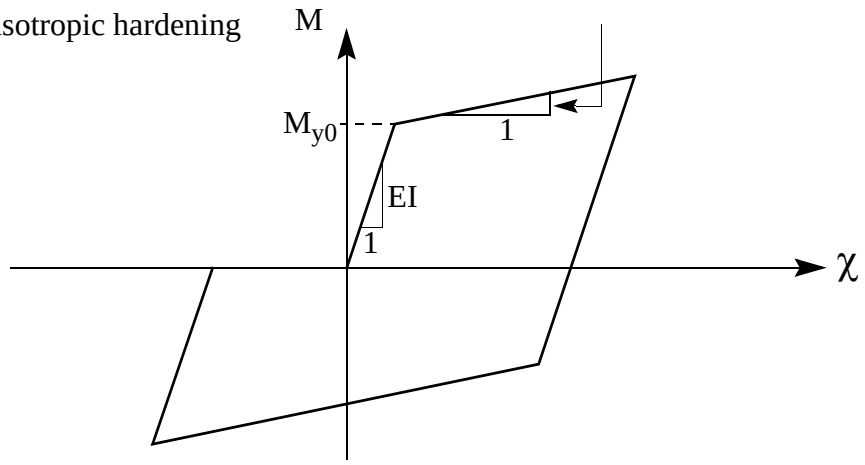


**Figure 3.5 Section constitutive model (moment-curvature)**

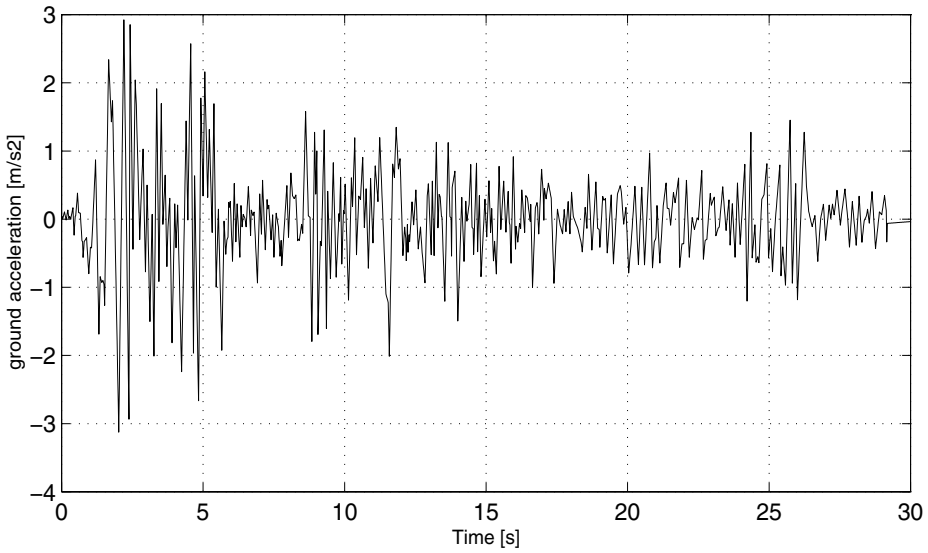


**Figure 3.6 Record of 1940 El Centro earthquake N-S comp.**

The following five sensitivity parameters are considered in the response sensitivity studies presented below: moment of inertia *I* of steel sections, initial yield moment $M_{y0}$, isotropic and kinematic hardening moduli $H_{iso}$ and $H_{kin}$, earthquake ground acceleration $\ddot{u}_g(t = 4.22\,\text{sec})$ and $\ddot{u}_g(t = 7.60\,\text{sec})$. Note that times 4.22 and 7.60 are selected randomly.

### 3.5.1 Sensitivity Convergence Studies

***Case 1: Nonlinear Static Push-Over Case***

The total displacement of the structure of the 5 floors are shown in Figure 3.7

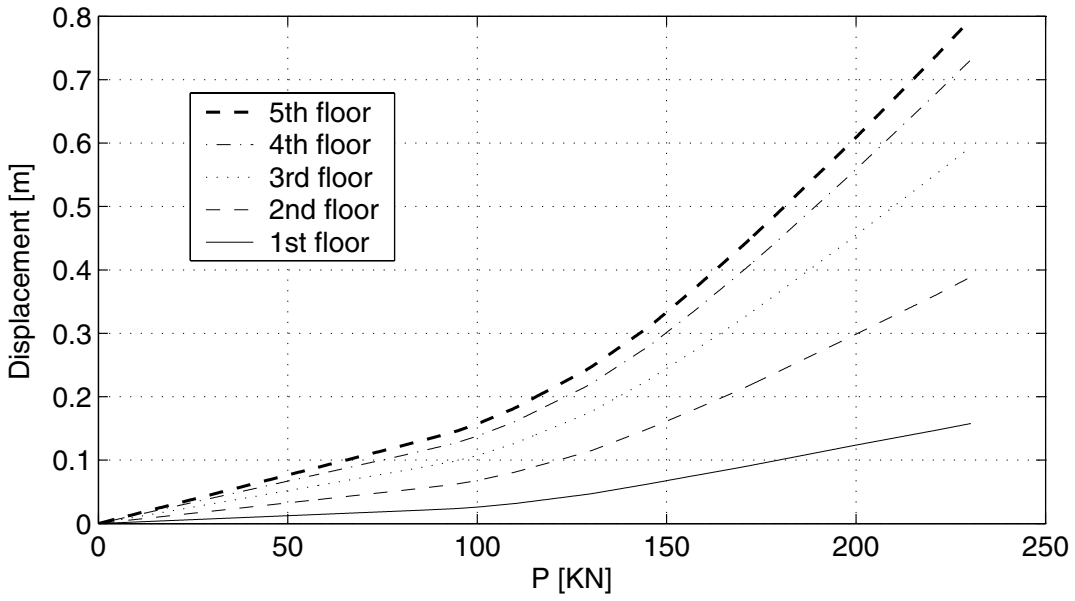


**Figure 3.7 Responses of the 5 story building to static push-over force**

***a. Sensitivity Convergence of Forward Finite Difference(FFD) towards DDM***

Here the sensitivities of the horizontal displacement response of Node B (Figure 3.3) is studied as the frame is subjected to the monotonic static push-over case. A set of different relative sensitivity parameter increments, $\frac{\Delta\theta}{\theta}$ , is used to study the convergence of response sensitivity results obtained using FFD to those obtained using DDM. FFD and DDM results expressed in normalized or semi-normalized forms are compared in Figure 3.8 through Figure 3.11.

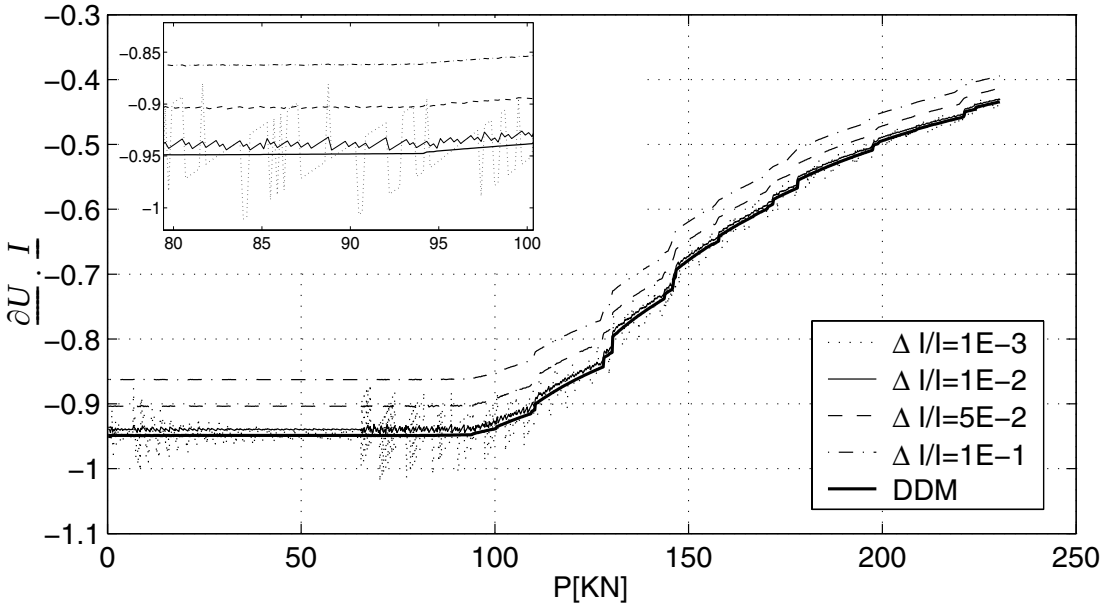


**Figure 3.8 Sensitivity of roof displacement to I**

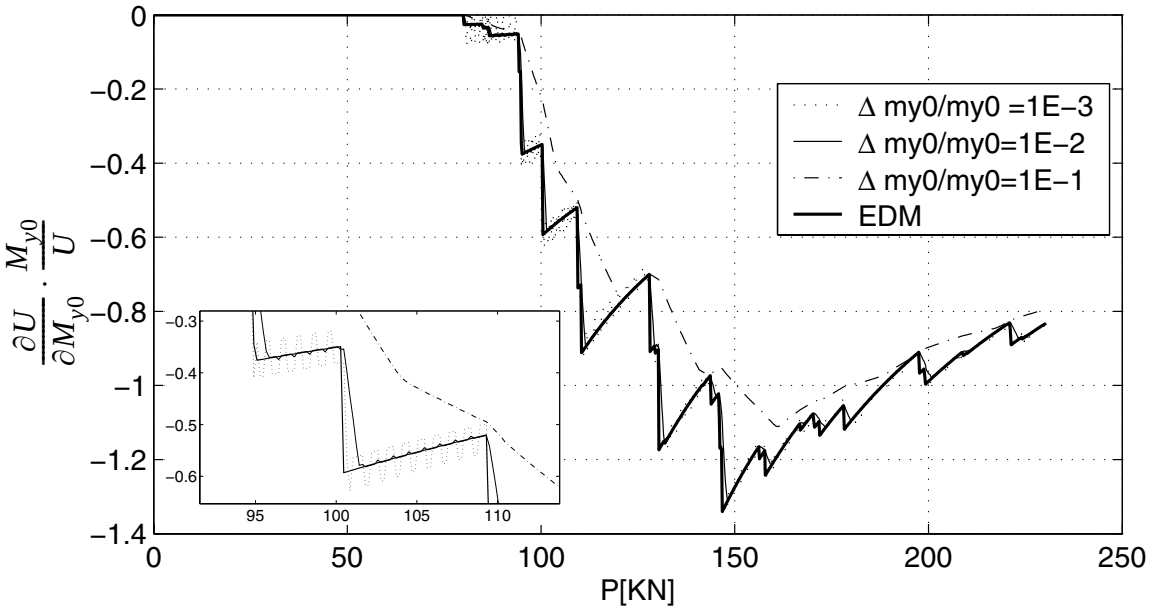


**Figure 3.9 Sensitivity of roof displacement to $M_{y0}$**

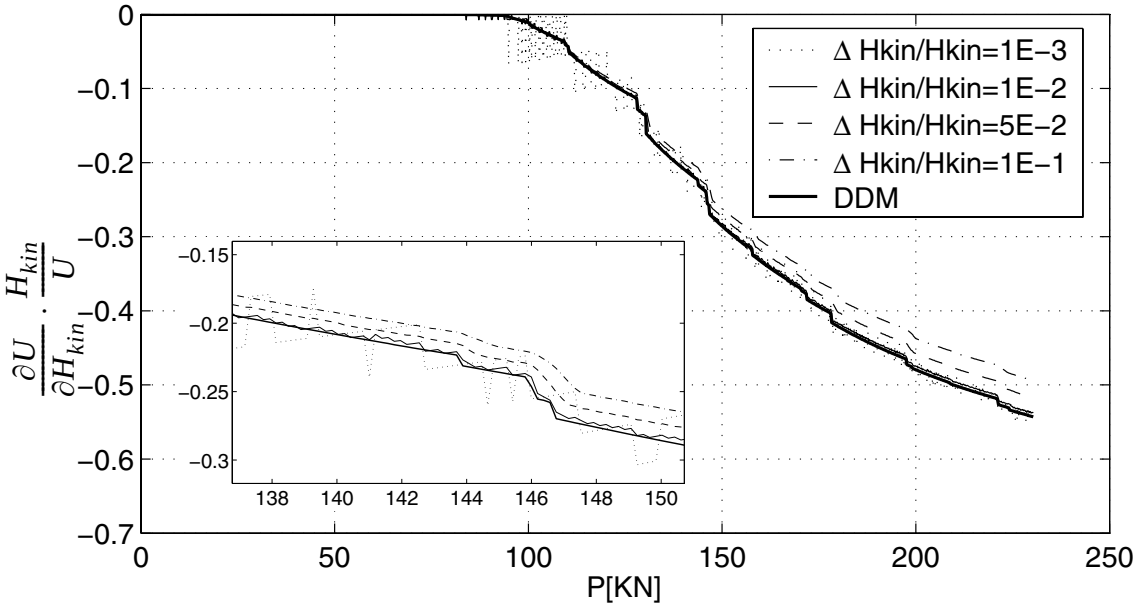


**Figure 3.10 Sensitivity of roof displacement to Hkin**

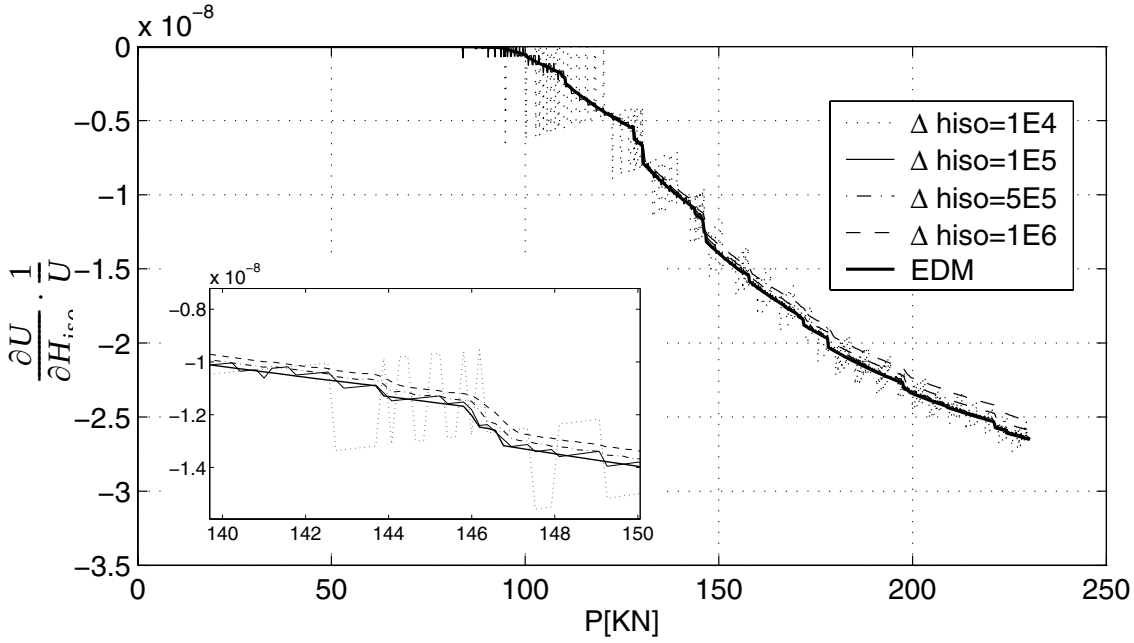


**Figure 3.11 Sensitivity of roof displacement to $H_{iso}$**

It is observed that for each sensitivity parameter $\theta$, as the perturbation $\frac{\Delta\theta}{\theta}$ is decreased, the FFD results approach those of the DDM. Furthermore there is an optimum value of $\frac{\Delta\theta}{\theta}$ that leads the FFD results to best approximate the DDM results. When the relative sensitivity parameter increment surpasses this optimum value, the finite difference results worsen due to truncation error (i.e., effects of higher order terms in Taylor series expansion of response parameter). If we decrease the relative sensitivity parameter increment below this optimum value, so as to reduce the truncation error, we have an excessive condition error due to round-off errors. In some cases, there may not be any sensitivity parameter increment which yields an acceptable error. This is the so-called “stepsize

dilemma." It is noteworthy that for a given structural system, the optimum value of $\frac{\Delta\theta}{\theta}$ depends on the parameter and the load case.

For the response analyses considered here, the optimum value and acceptable range of the sensitivity parameters are summarized in Table 3.1. Notice that in Table 3.1, $\Delta H_{iso}$ is not normalized because the nominal value of $\theta$ is zero (i.e., no isotropic hardening).

**Table 3.1 FEM differentiation results**

| $\theta$ | Material sensitivity variables | | | |
|---|---|---|---|---|
| | $\frac{\Delta I}{I}$ | $\frac{\Delta M_{y0}}{M_{y0}}$ | $\frac{\Delta H_{kin}}{H_{kin}}$ | $\Delta H_{iso}$ |
| Best $\frac{\Delta\theta}{\theta}$ | $1\times10^{-2}$ | $1\times10^{-2}$ | $1\times10^{-2}$ | $1\times10^{5}$ |
| Range of $\frac{\Delta\theta}{\theta}$ | $10^{-3}\sim10^{-1}$ | $10^{-3}\sim10^{-1}$ | $10^{-3}\sim10^{-1}$ | $10^{4}\sim10^{6}$ |

***b. Convergence of Response and Response Sensitivities with respect to Spatial Discretization***

This section examines the convergence of global and local response parameters, as well as their sensitivities, with respect to the spatial discretization (i.e., number of finite elements per beam/column). Here, a global response parameter is taken as the horizontal displacement at node B, (i.e., roof displacement), while the local response parameters are chosen as the moment-curvature, $M-\chi$, plastic curvature, $\chi_p$, and accumulated plastic curvature, $\bar{\chi}_p$, at Gauss-Lobato point A at the bottom of the left column of the frame (Figure

3.3). The spatial discretization was varied from 1 to 8 finite elements per beam/column. Some computational results are shown in Figures 3.12 through 3.26. Furthermore, for each response parameter and load case, the minimum number of elements per beam/column required to achieve convergence of response and response sensitivities is reported in Table 3.2 for the global response parameter and in Table 3.3 for local response parameters.

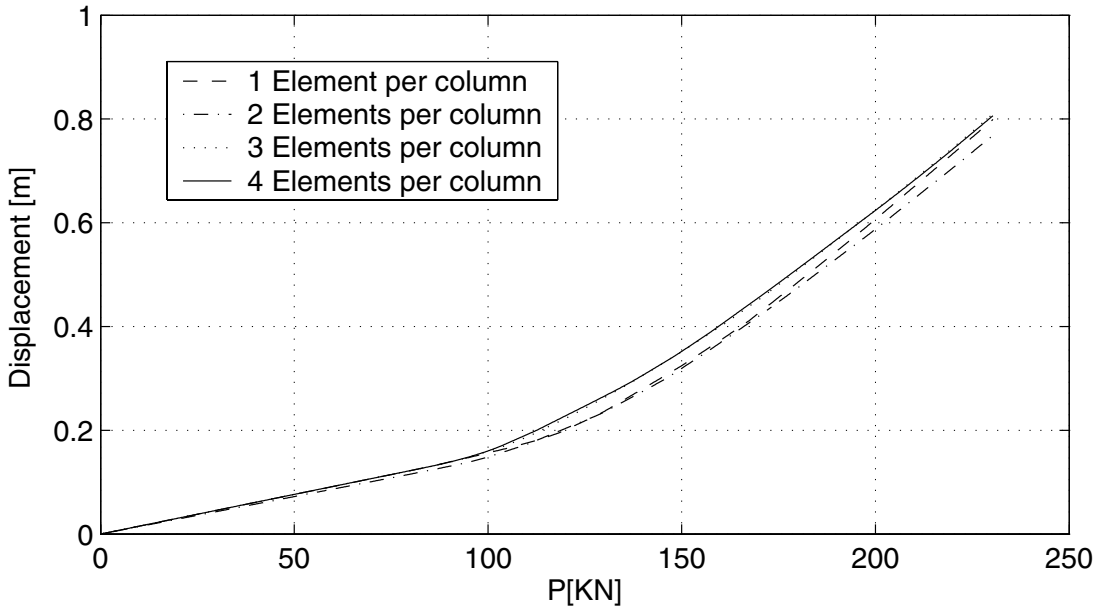


**Figure 3.12 Roof displacement with increasing number of elements per beam/column**

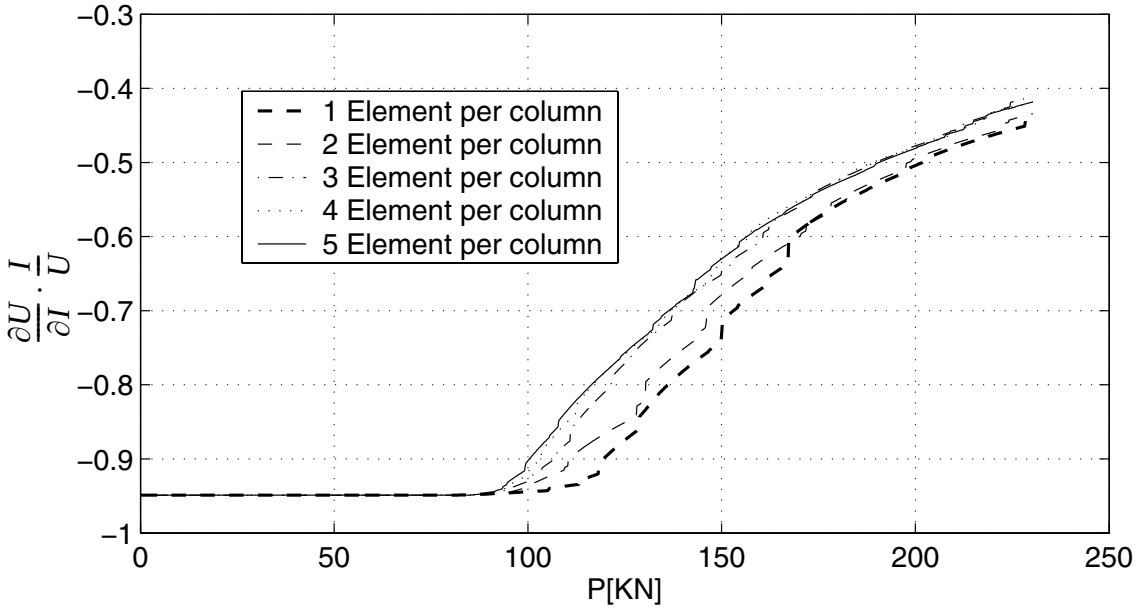


**Figure 3.13 Sensitivity of roof displacement to I with increasing number of elements per beam/column**

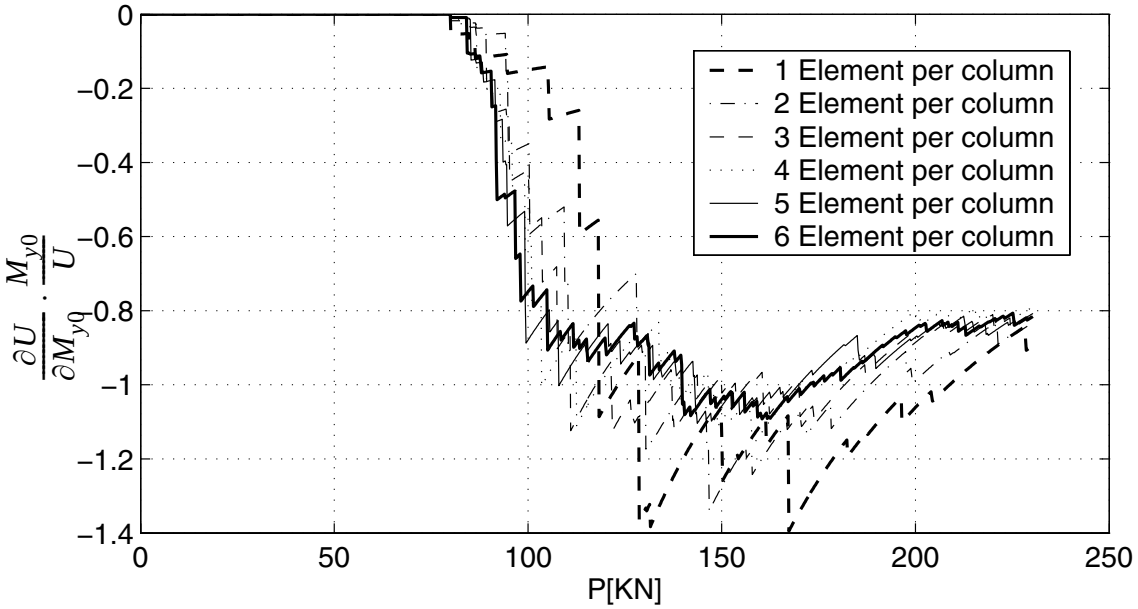


**Figure 3.14 Sensitivity of roof displacement to $M_{y0}$ with increasing number of elements per beam/column**

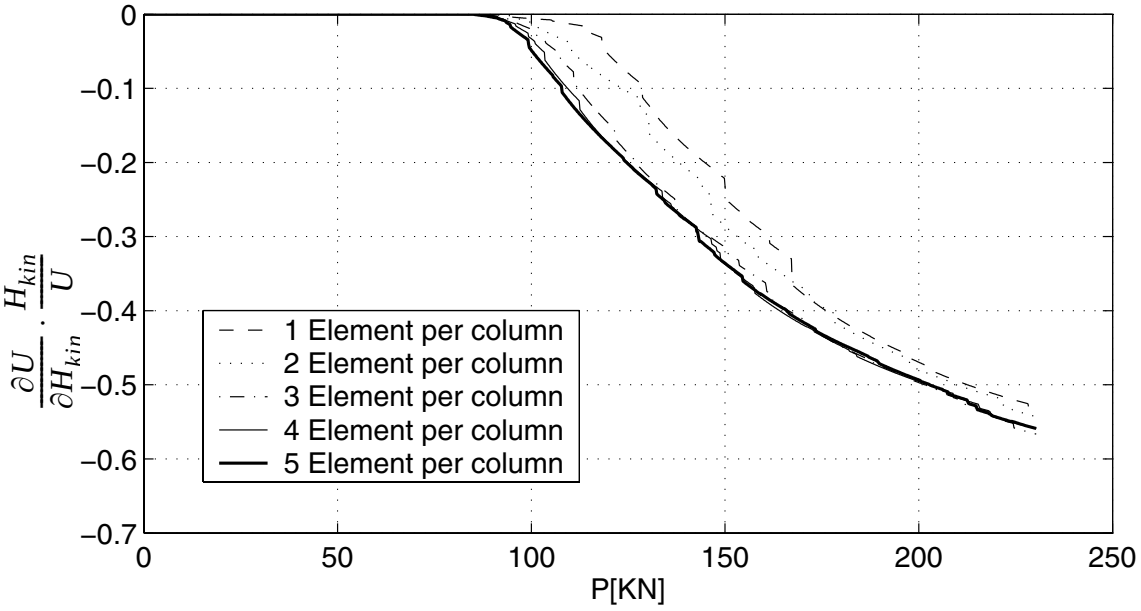


**Figure 3.15 Sensitivity of roof displacement to $H_{kin}$ with increasing number of elements per beam/column**

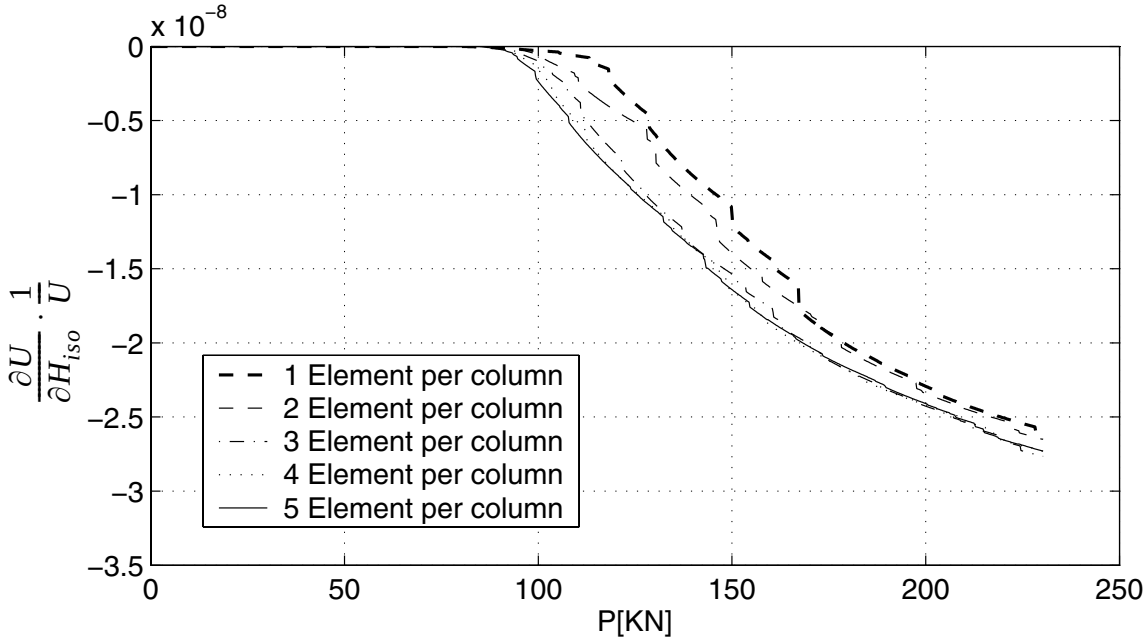


**Figure 3.16 Sensitivity of roof displacement to Hiso with increasing number of elements per beam/column**

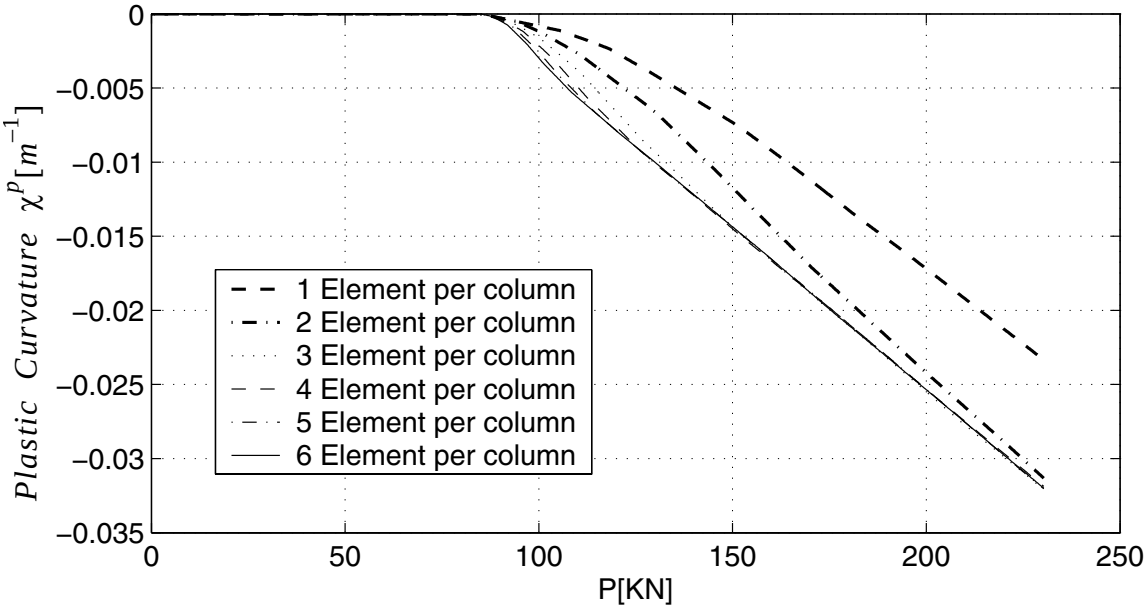


**Figure 3.17 Plastic curvature at 1st Gauss point with increasing number of elements per beam/column**

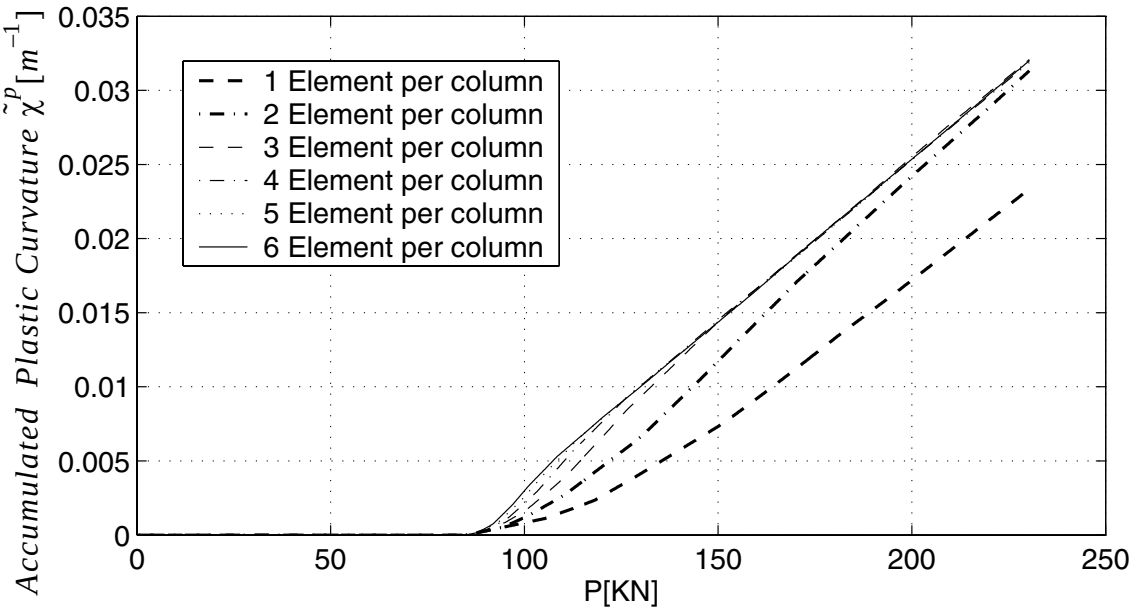


**Figure 3.18 Accumulated plastic curvature at 1st Gauss point with increasing number of elements per beam/column**

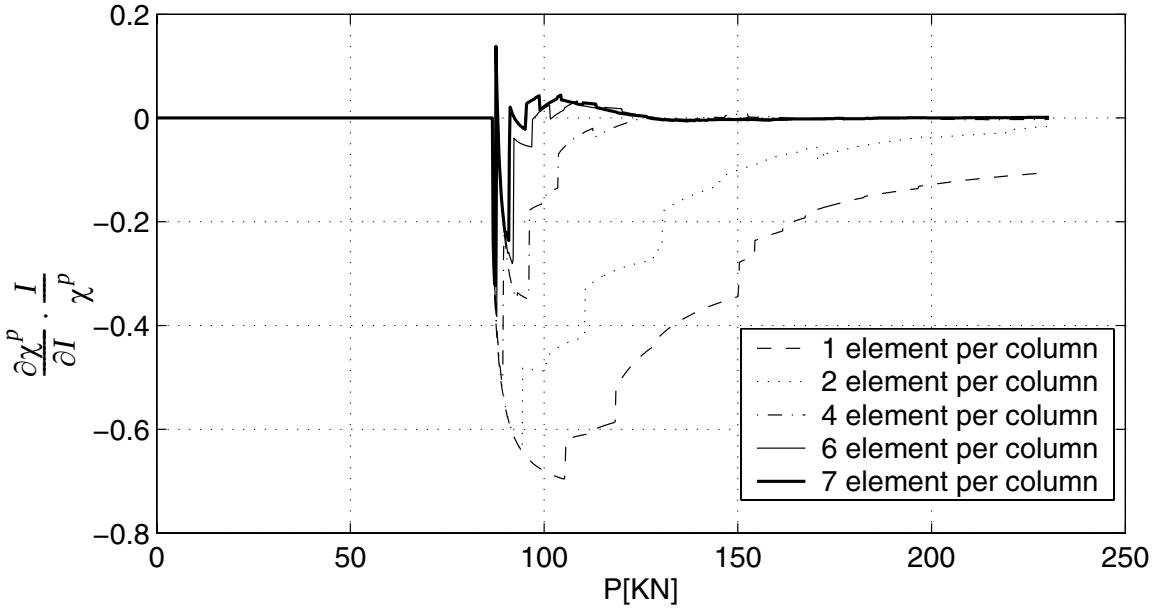


**Figure 3.19 Sensitivity of plastic curvature to I with increasing number of elements per beam/column**

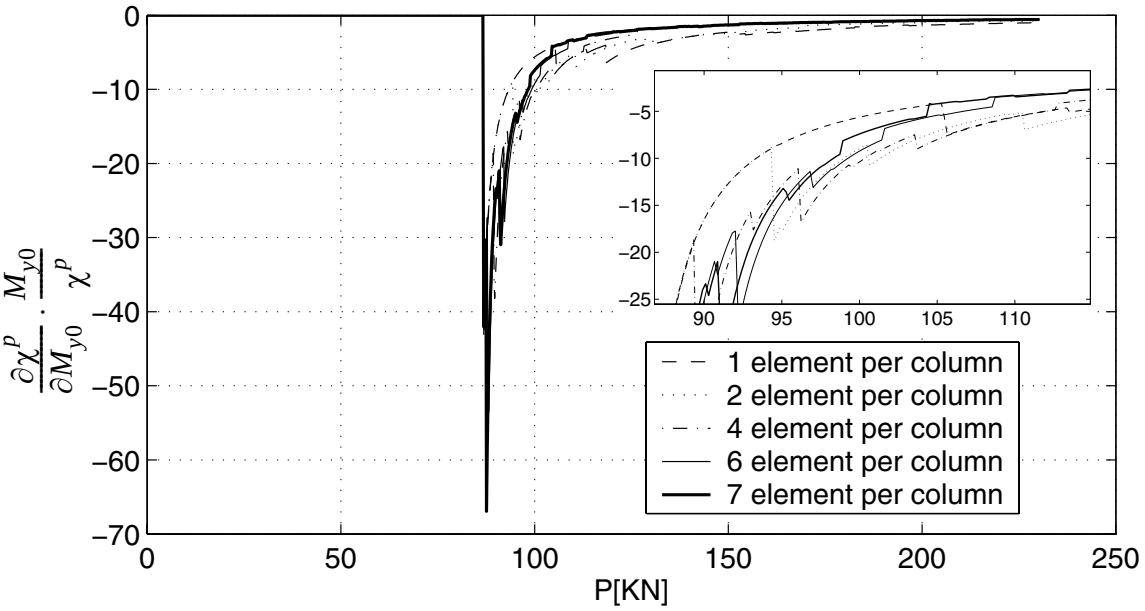


**Figure 3.20 Sensitivity of plastic curvature to $M_{y0}$ with increasing number of elements per beam/column**

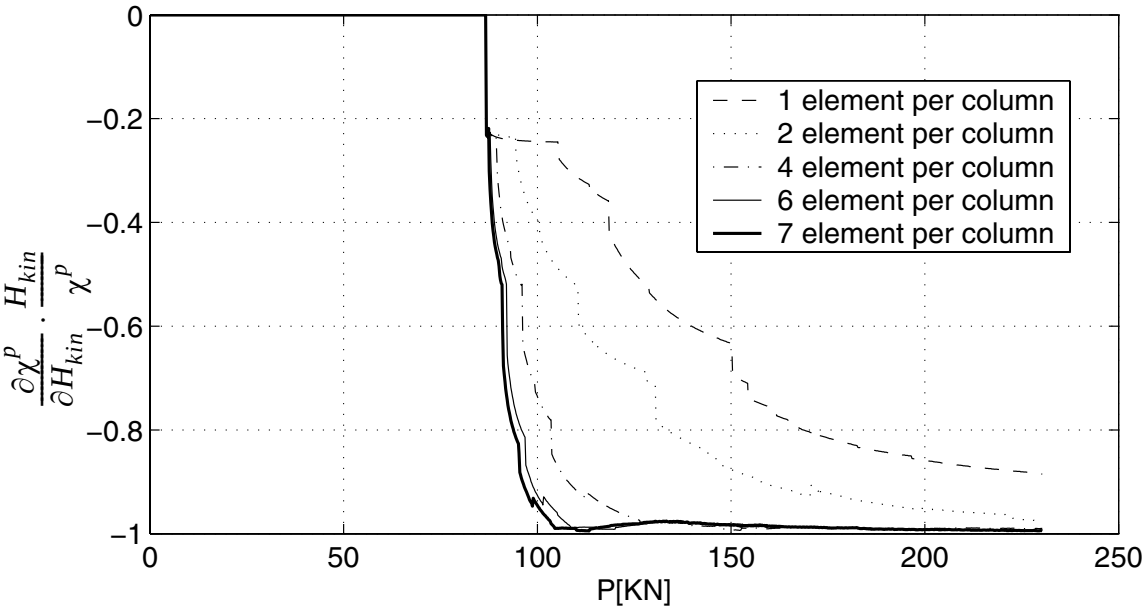


**Figure 3.21 Sensitivity of plastic curvature to $H_{kin}$ with increasing number of elements per beam/column**

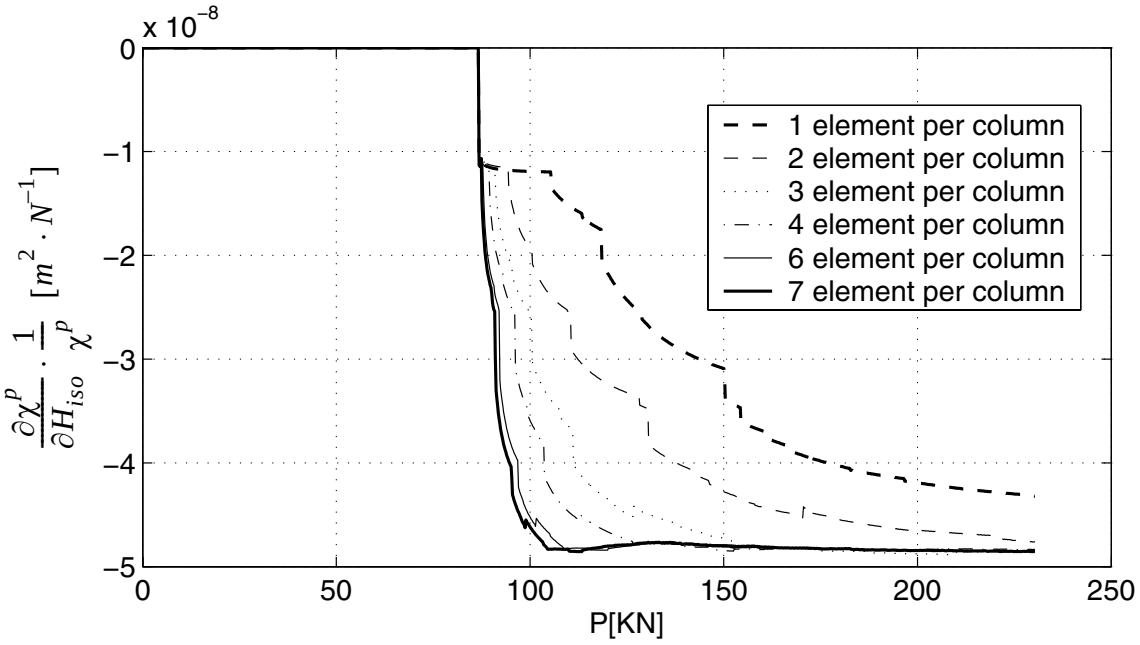


**Figure 3.22 Sensitivity of plastic curvature to $H_{iso}$ with increasing number of elements per beam/column**

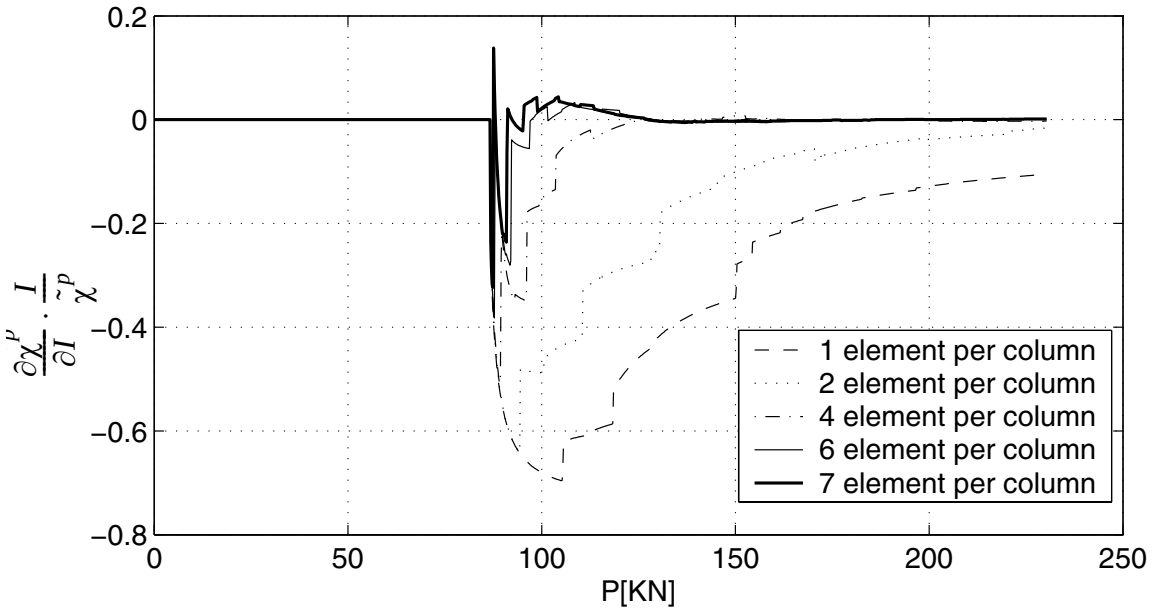


**Figure 3.23 Sensitivity of accumulated plastic curvature to I with increasing number of elements per beam/column**

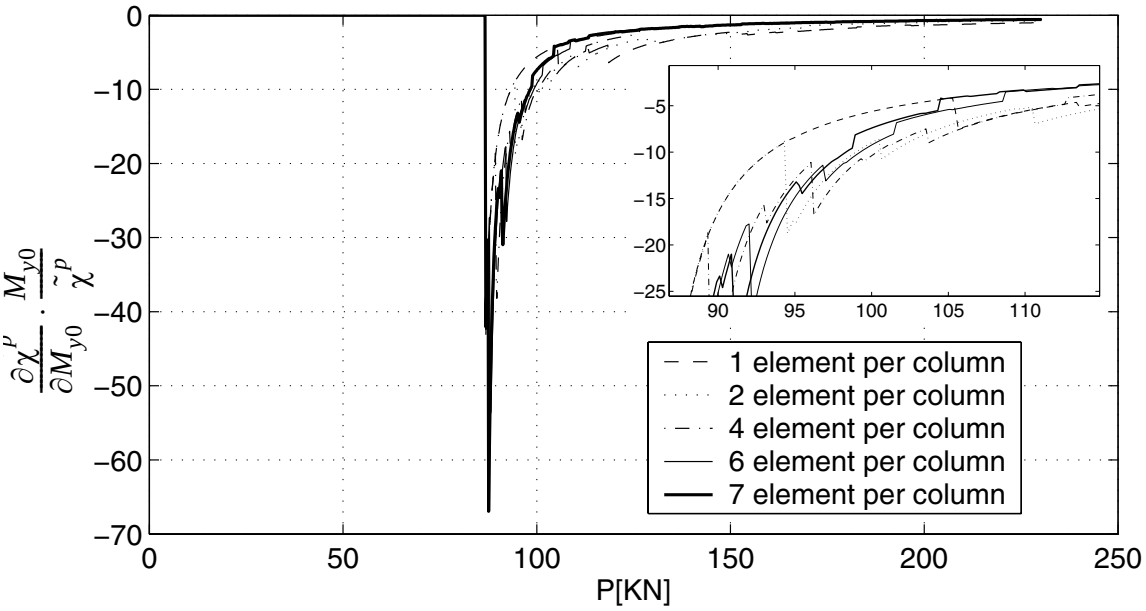


**Figure 3.24 Sensitivity of accumulated plastic curvature to $M_{y0}$ with increasing number of elements per beam/column**

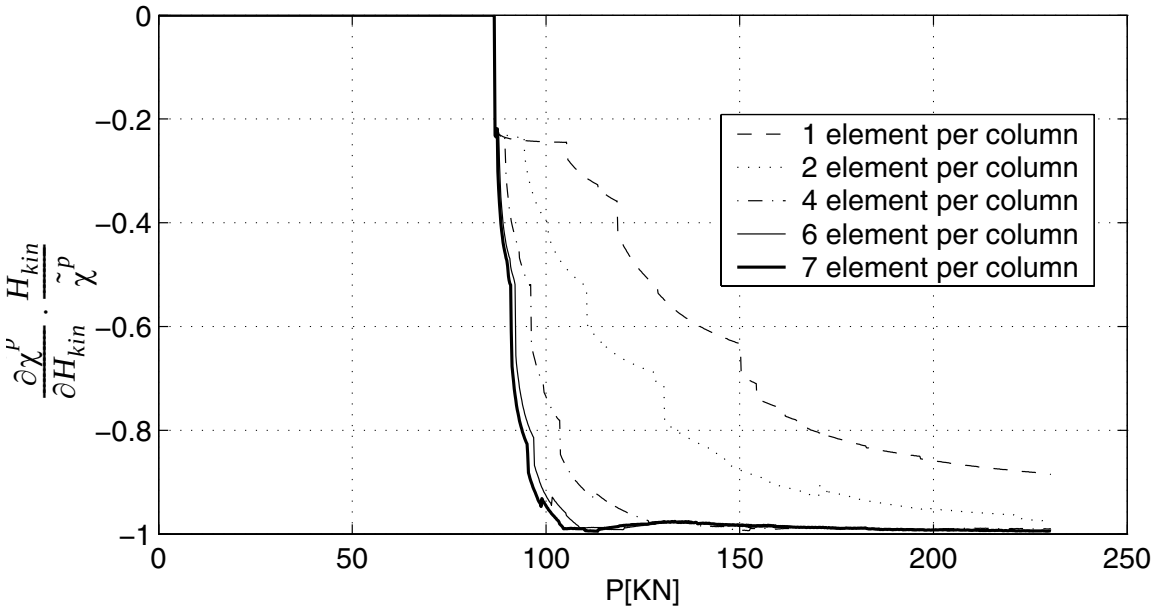


**Figure 3.25 Sensitivity of accumulated plastic curvature to $H_{kin}$ with increasing number of elements per beam/column**

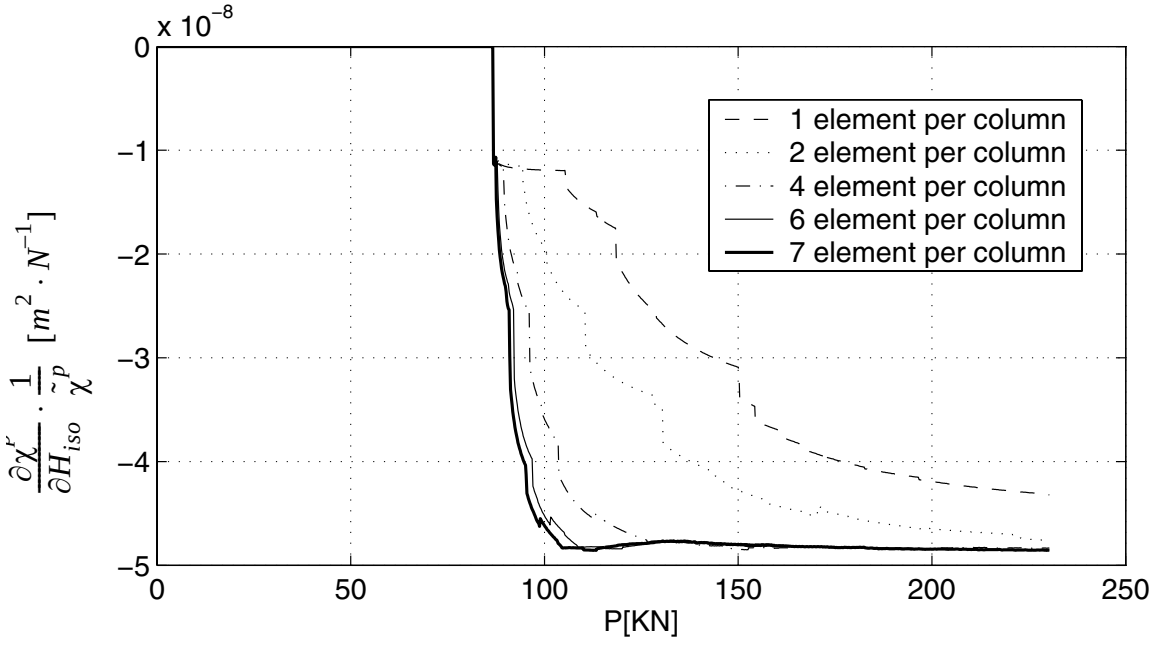


**Figure 3.26 Sensitivity of accumulated plastic curvature to $H_{iso}$ with increasing number of elements per beam/column**

**Table 3.2 Minimum number of elements per beam/column required for convergence of global response and its sensitivities**

| $\frac{\partial u}{\partial I}$ | $\frac{\partial u}{\partial M_{y0}}$ | $\frac{\partial u}{\partial H_{kin}}$ | $\frac{\partial u}{\partial H_{iso}}$ | Response u |
|---|---|---|---|---|
| 4 | 5 | 4 | 4 | 3 |

**Table 3.3 Minimum number of elements per beam/column required for convergence of local response and its sensitivities**

| $\chi_p$ | $\frac{\partial \chi_p}{\partial I}$ | $\frac{\partial \chi_p}{\partial M_{y0}}$ | $\frac{\partial \chi_p}{\partial H_{kin}}$ | $\frac{\partial \chi_p}{\partial H_{iso}}$ | $\tilde{\chi}_p$ | $\frac{\partial \tilde{\chi}_p}{\partial I}$ | $\frac{\partial \tilde{\chi}_p}{\partial M_{y0}}$ | $\frac{\partial \tilde{\chi}_p}{\partial H_{kin}}$ | $\frac{\partial \tilde{\chi}_p}{\partial H_{iso}}$ |
|---|---|---|---|---|---|---|---|---|---|
| 5 | 6 | 6 | 6 | 6 | 5 | 6 | 6 | 6 | 6 |

From the results obtained, we observe that:

(1) Global response parameters converge with fewer finite elements per beam/column than local response parameters (compare results in Tables 3.2 and 3.3).

(2) A given response parameter, global or local, converges with fewer elements per beam/column than its sensitivities. This is due to the fact that the response sensitivities are less smooth than the responses themselves; in fact, the response sensitivities are only piecewise continuous, with discontinuities due to material state transitions between elastic and plastic states at Gauss points (Conte et al. 2002).

(3) Sensitivities of global response parameters converge with slightly fewer elements per beam/column than sensitivities of local response parameters in the static push-over case. However, this is not always true in the dynamic case as will be explained later.

***Case 2, Dynamic case***

In this section, the frame mentioned before is restudied for dynamic case. The displacement of the 5 floors is shown in Figure 3.27. The convergence of global and local response parameters, as well as their sensitivities, with different perturbation size, number of elements per beam/column and time step size is investigated.

***a. Sensitivity Convergence of FFD towards DDM***

The sensitivities of the horizontal displacement response of Node B (Figure 3.3) are studied as the frame is subjected to the earthquake base excitation. A set of different relative sensitivity parameter increments, $\frac{\Delta\theta}{\theta}$ , is used to study the convergence of response sensitivity results obtained using forward finite difference analysis to those obtained using

the DDM. Finite difference and DDM results expressed in normalized or semi-normalized forms are compared in Figure 3.28 to Figure 3.32 and the best value, the lower and upper bound of the perturbation $\frac{\Delta\theta}{\theta}$ are listed in Table 3.4.

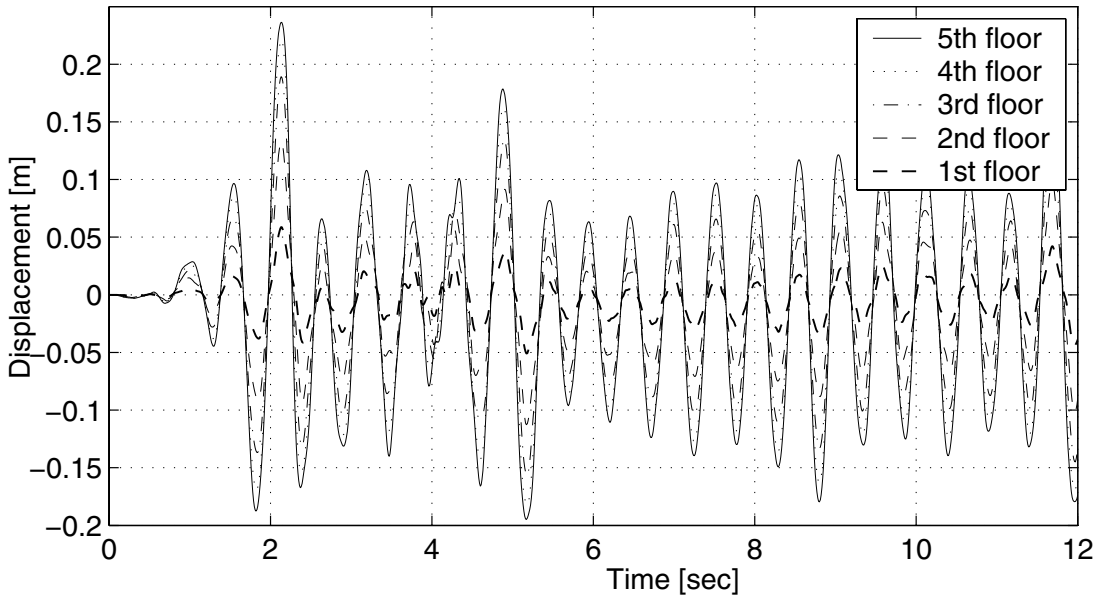


**Figure 3.27 Responses of the 5 story building to earthquake input**

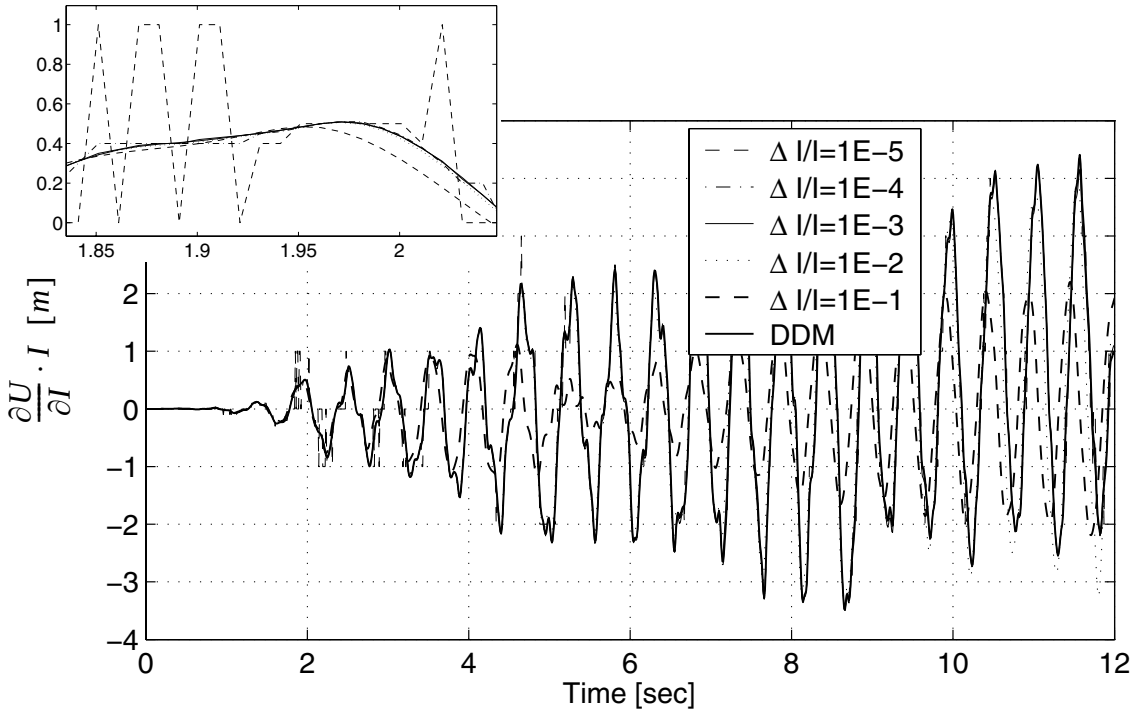


**Figure 3.28 Sensitivity of roof displacement to I**

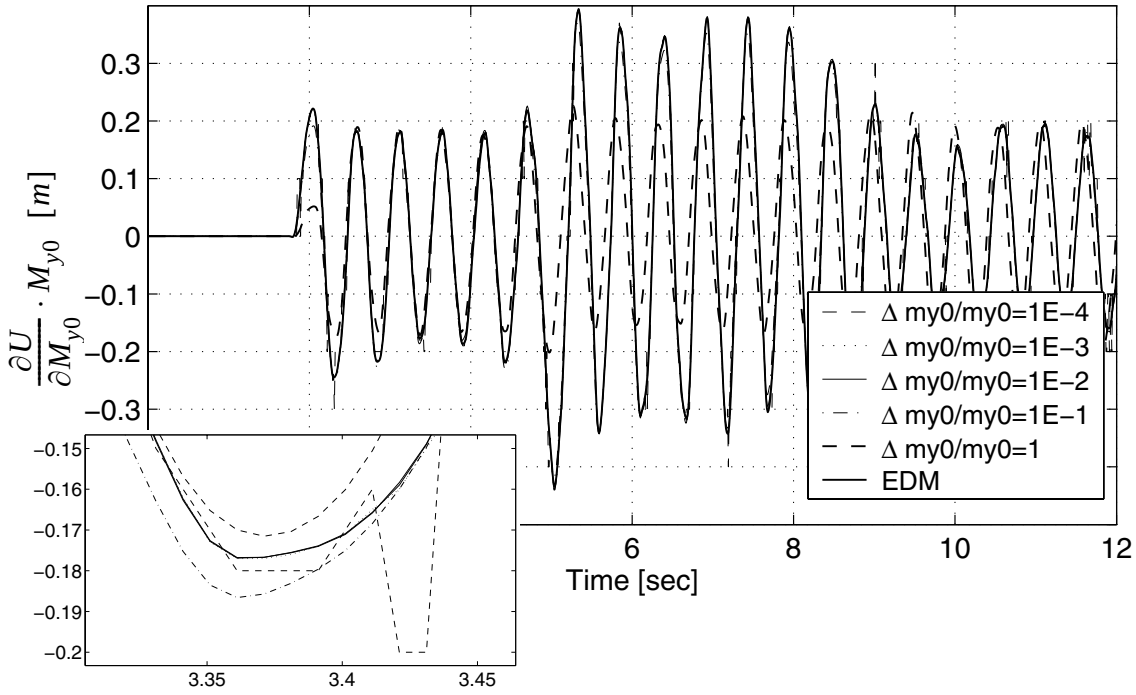


**Figure 3.29 Sensitivity of roof displacement to $M_{y0}$**

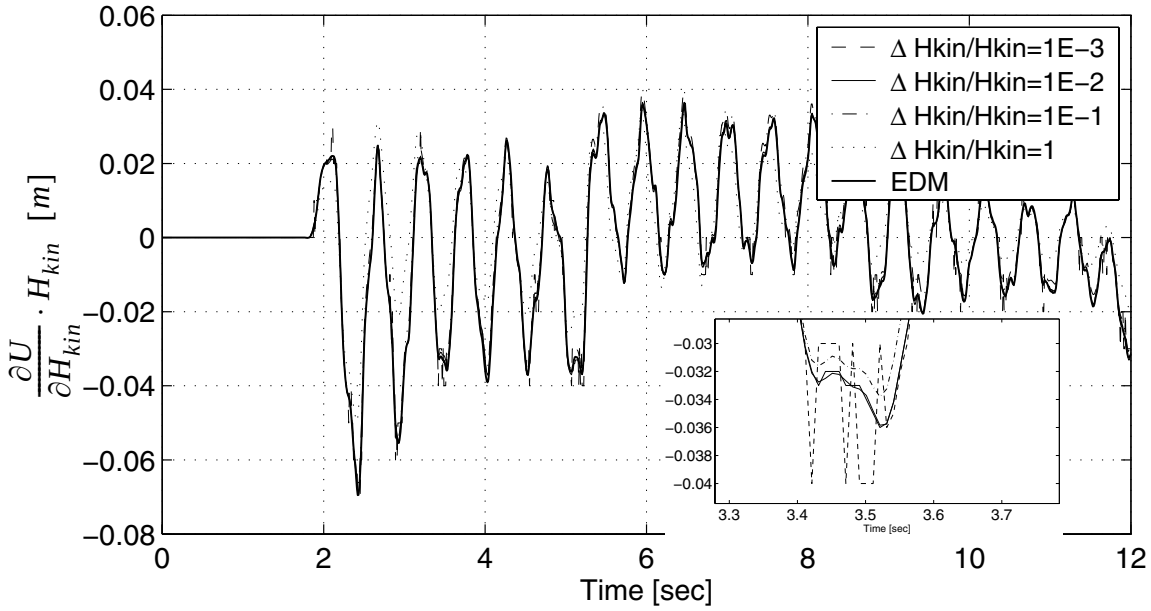


**Figure 3.30 Sensitivity of roof displacement to Hkin**

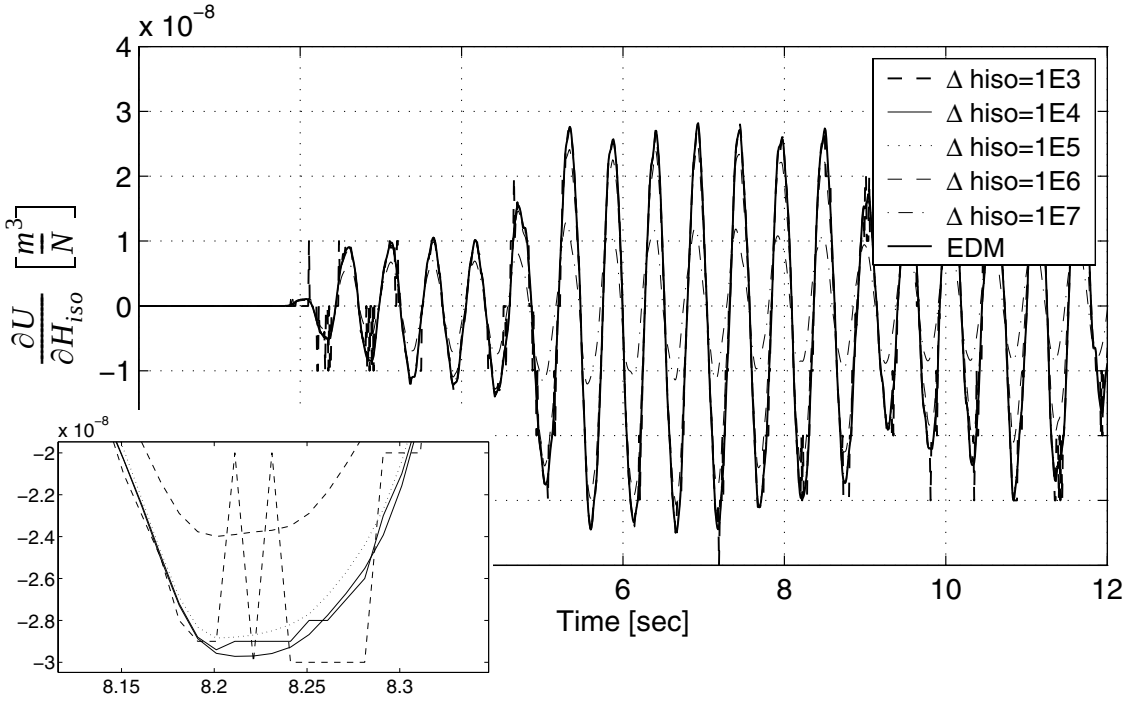


**Figure 3.31 Sensitivity of roof displacement to $H_{iso}$**

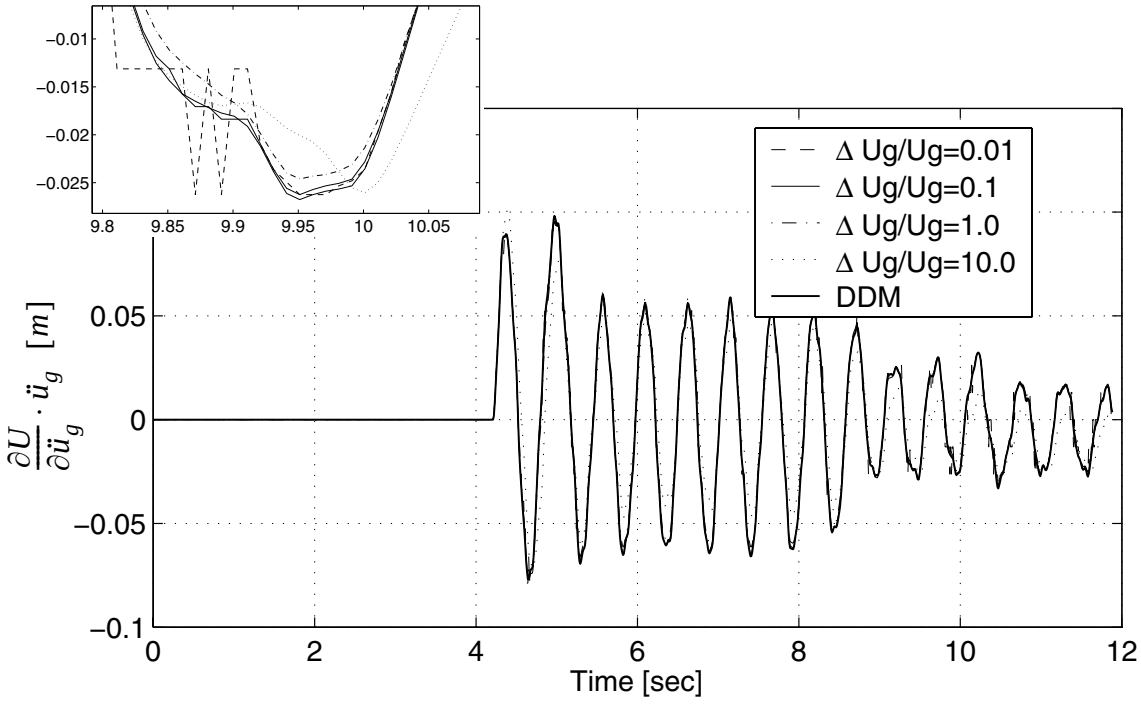


**Figure 3.32 Sensitivity of roof displacement to earthquake input $\ddot{\boldsymbol{u}}_g(t = 4.22s)$**

**Table 3.4 FE differentiation results**

| θ | Material sensitivity variables | | | | Earthquake input variable |
|---|---|---|---|---|---|
| | $\frac{\Delta I}{I}$ | $\frac{\Delta M_{y0}}{M_{y0}}$ | $\frac{\Delta H_{kin}}{H_{kin}}$ | $\Delta H_{iso}$ | $\frac{\nabla \ddot{\boldsymbol{u}}_g}{\ddot{\boldsymbol{u}}_g}(t = 4.22s)$ |
| Best $\frac{\Delta\theta}{\theta}$ | $1 \times 10^{-3}$ | $1 \times 10^{-2}$ | $1 \times 10^{-2}$ | $1 \times 10^{4}$ | $1 \times 10^{-1}$ |
| Range of $\frac{\Delta\theta}{\theta}$ | $10^{5} \sim 10^{-1}$ | $10^{-4} \sim 1$ | $10^{-3} \sim 1$ | $10^{3} \sim 10^{7}$ | $10^{-2} \sim 10^{1}$ |

For the response analyses considered here, the optimum value and acceptable range of the sensitivity parameters are summarized in Table 3.4. It is observed that in the dynamic

case, the optimum value of $\frac{\Delta\theta}{\theta}$ is at least one order of magnitude larger for the discrete load parameter than for the material parameters.

***b. Convergence of Response and Response Sensitivities with respect to Spatial Discretization***

This section examines the convergence of global response parameters, as well as the sensitivities of the global and local variables taken the same as static load case, with respect to the spatial discretization. The spatial discretization was varied from 1 to 8 finite elements per beam/column. Some computational results are shown in Figures 3.33 through 3.51. The minimum number of elements per beam/column required to achieve convergence of response and their sensitivities are tabulated in Tables 3.5 and 3.6.

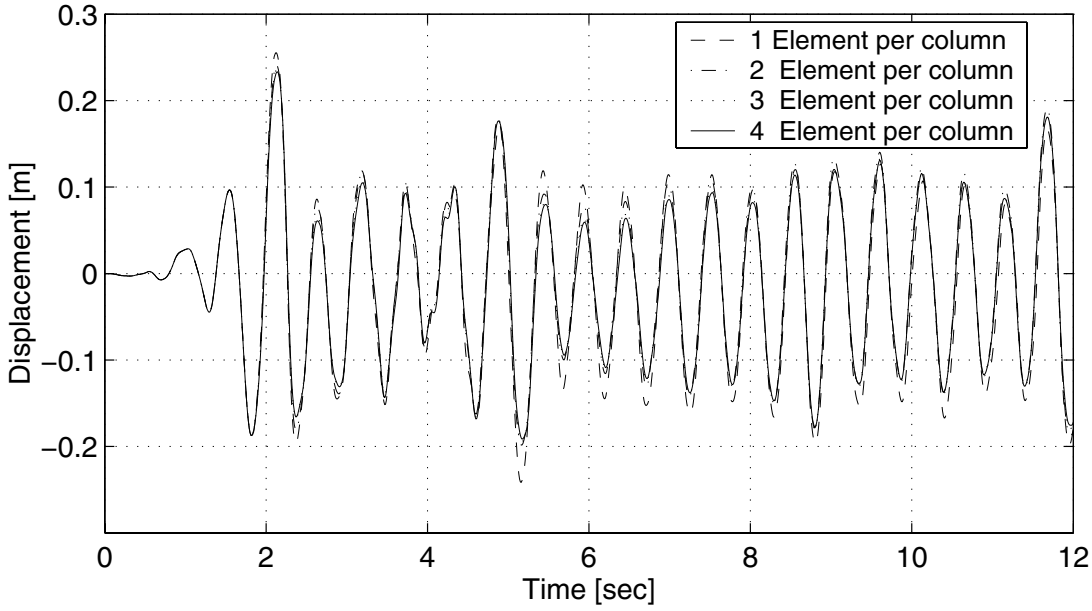


**Figure 3.33 Displacement of floors with increasing number of elements per beam/column**

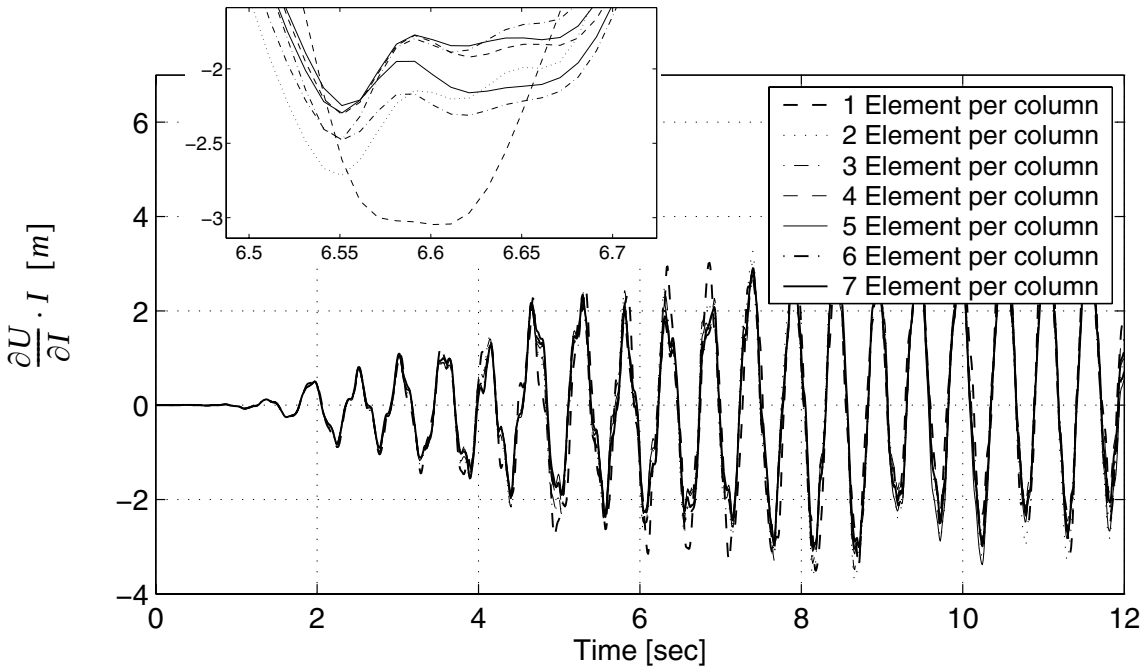


**Figure 3.34 Sensitivity of roof displacement to I with increasing number of elements per beam/column**

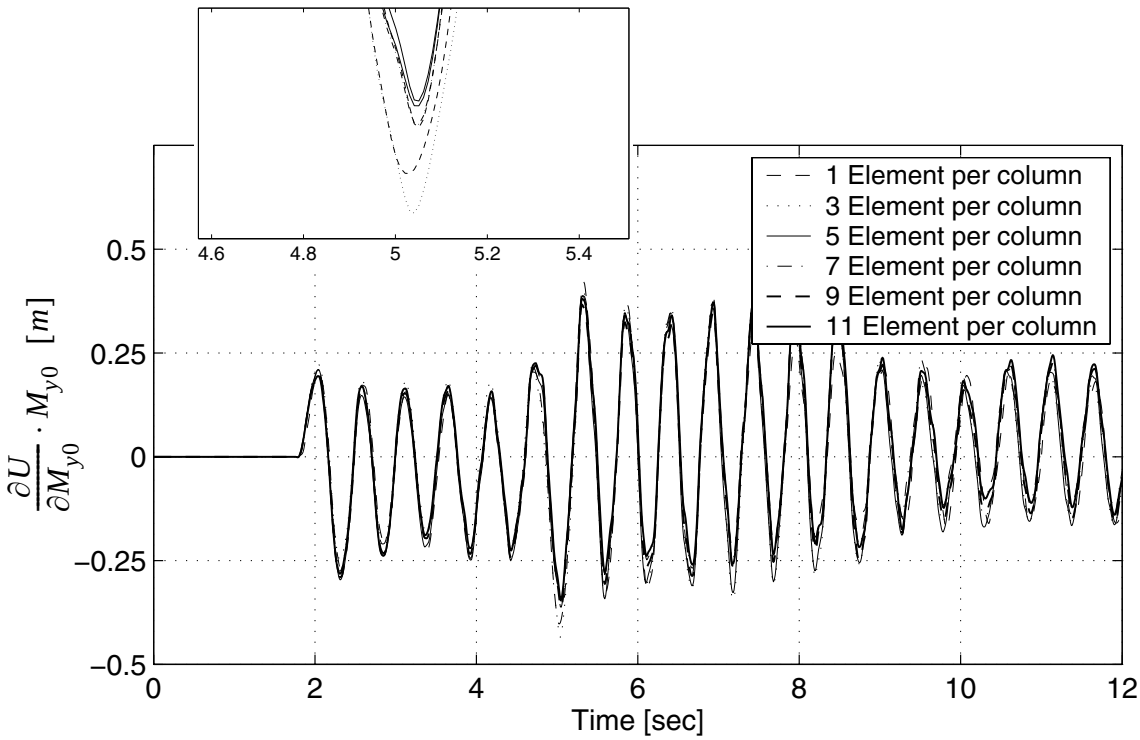


**Figure 3.35 Sensitivity of roof displacement to $M_{y0}$ with increasing number of elements per beam/column**

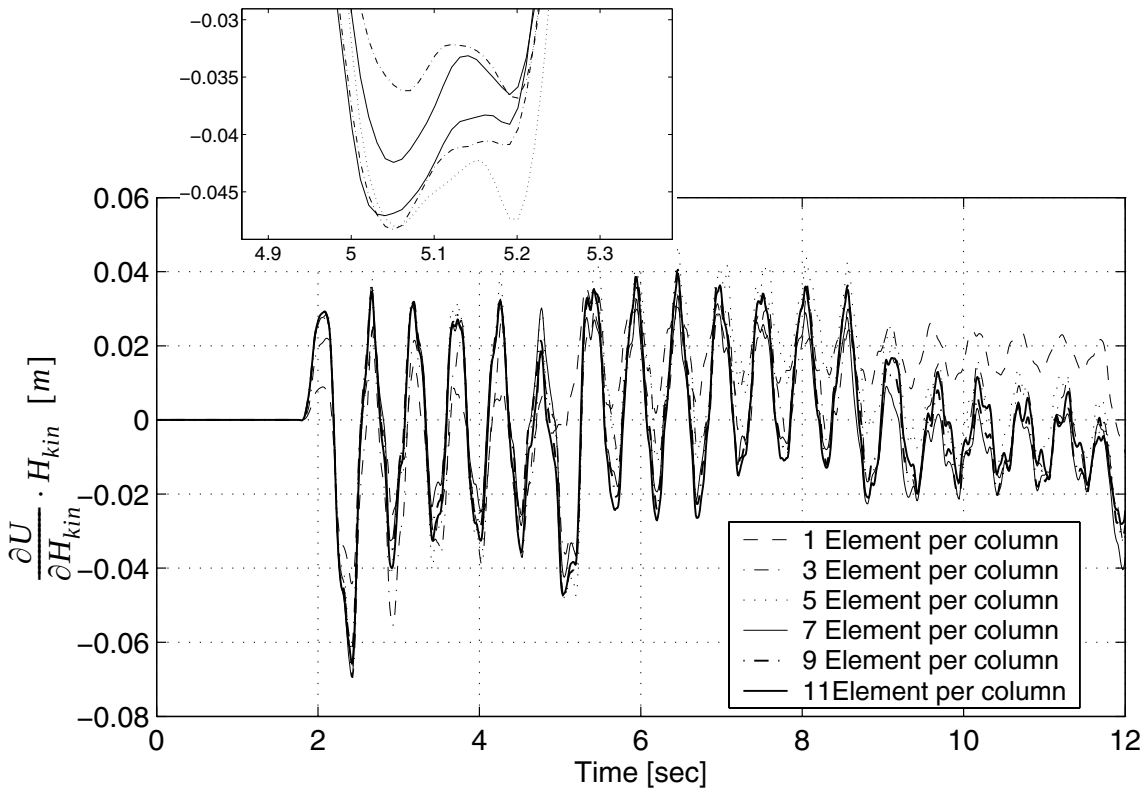


**Figure 3.36 Sensitivity of roof displacement to $H_{kin}$ with increasing number of elements per beam/column**

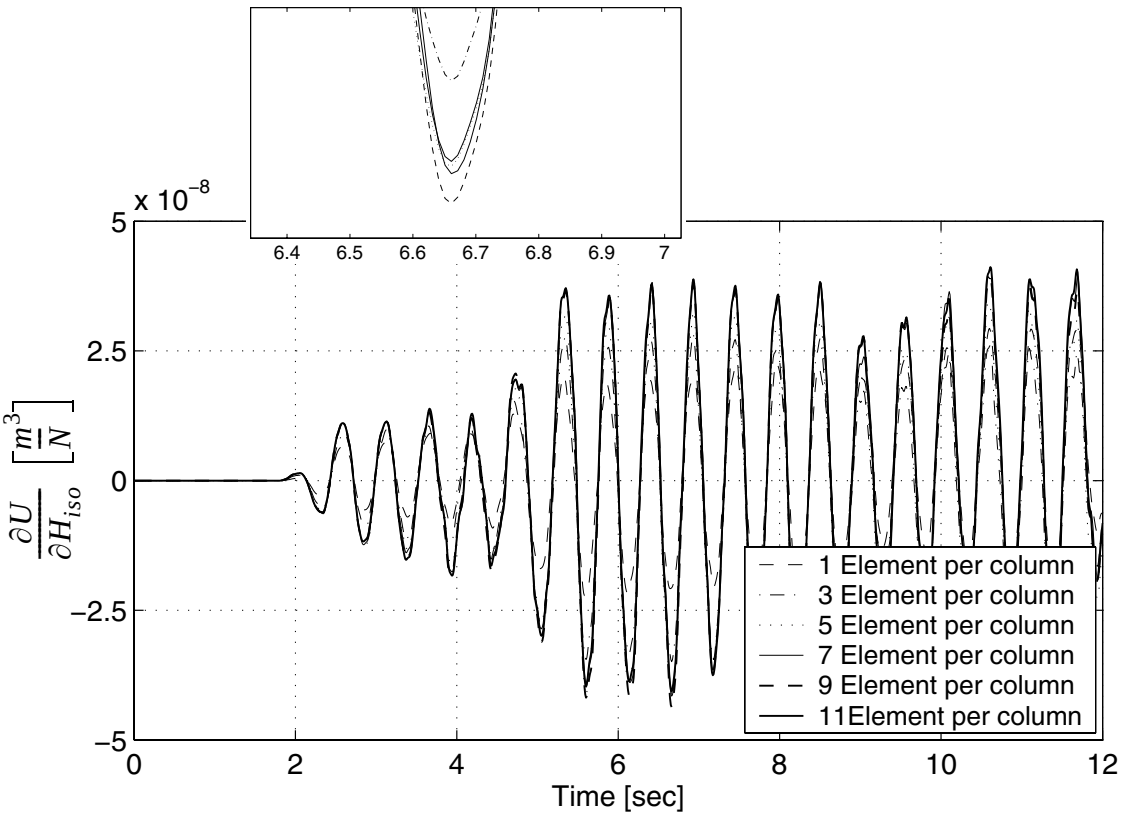


**Figure 3.37 Sensitivity of roof displacement to $H_{iso}$ with increasing number of elements per beam/column**

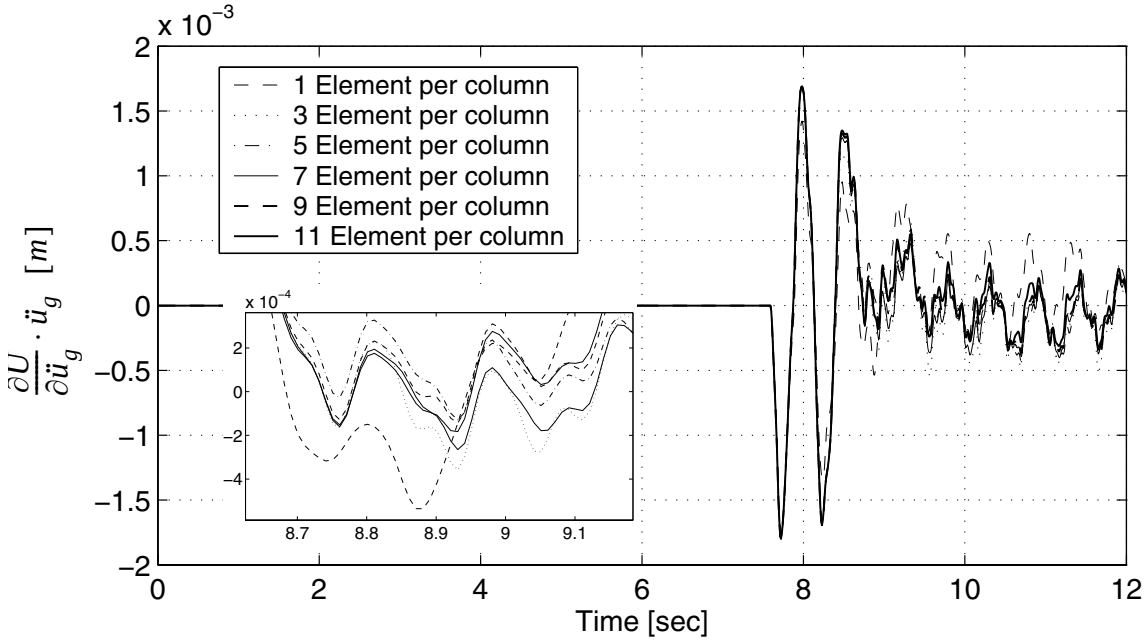


**Figure 3.38 Sensitivity of roof displacement to $\ddot{u}_g(t = 7.60s)$ with increasing number of elements per beam/column**

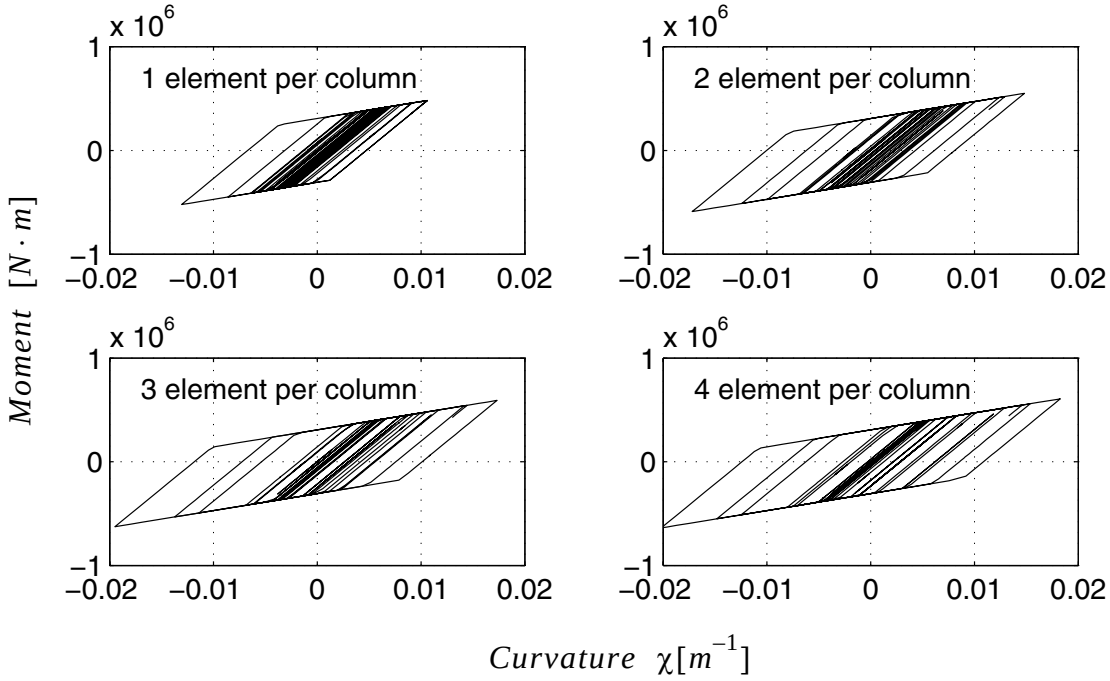


**Figure 3.39 Moment curvature responses with increasing number of elements per beam/column**

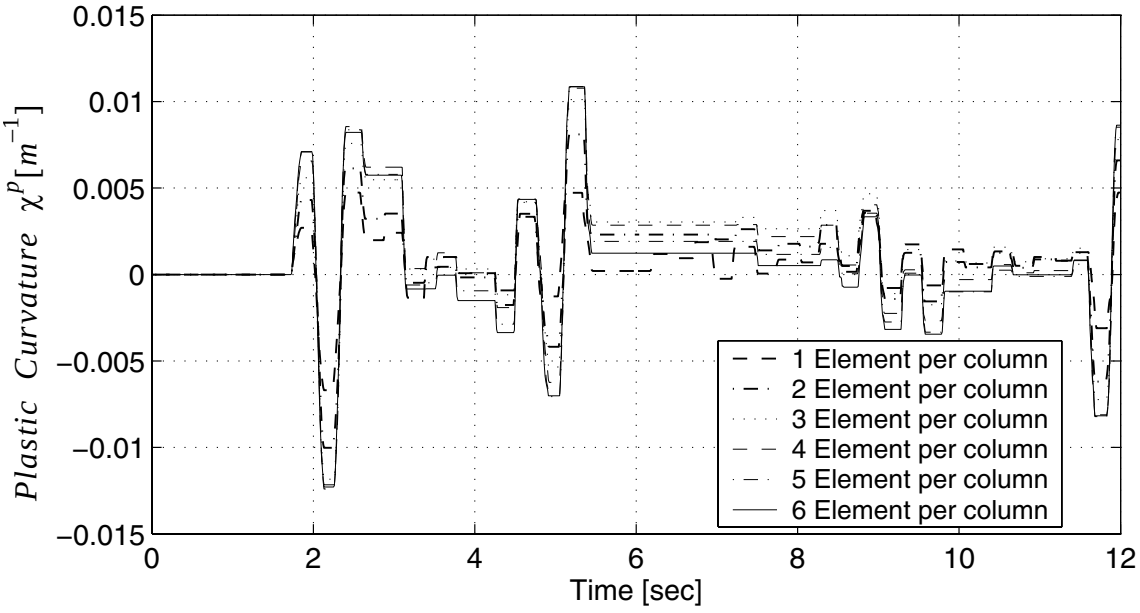


**Figure 3.40 Plastic curvature with increasing number of elements per beam/column**

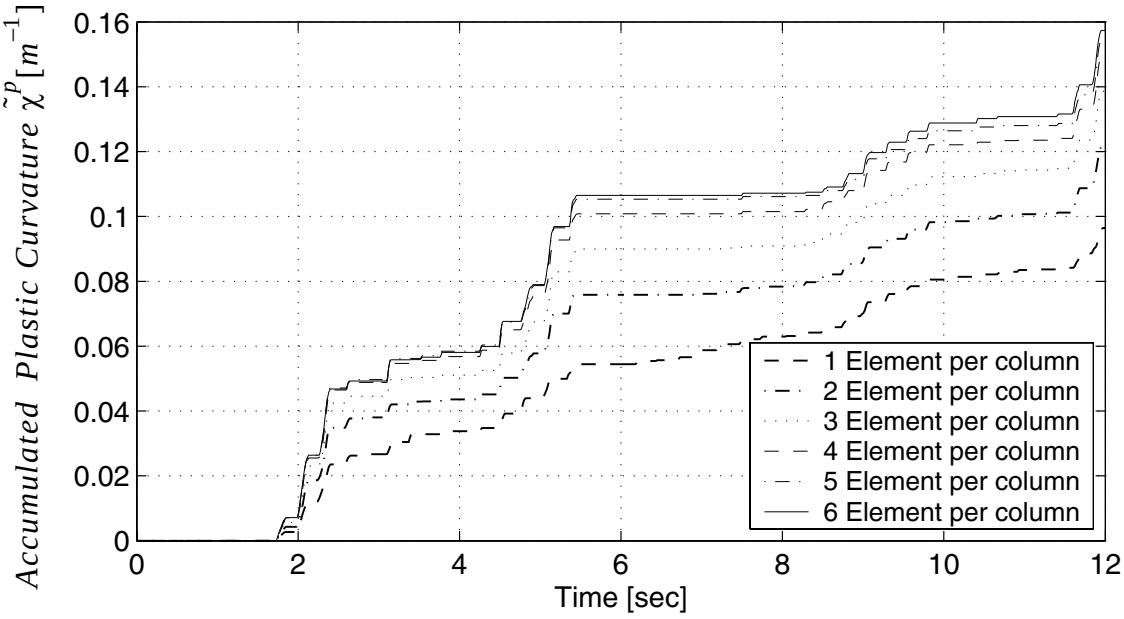


**Figure 3.41 Accumulated plastic curvature with increasing number of elements per beam/column**

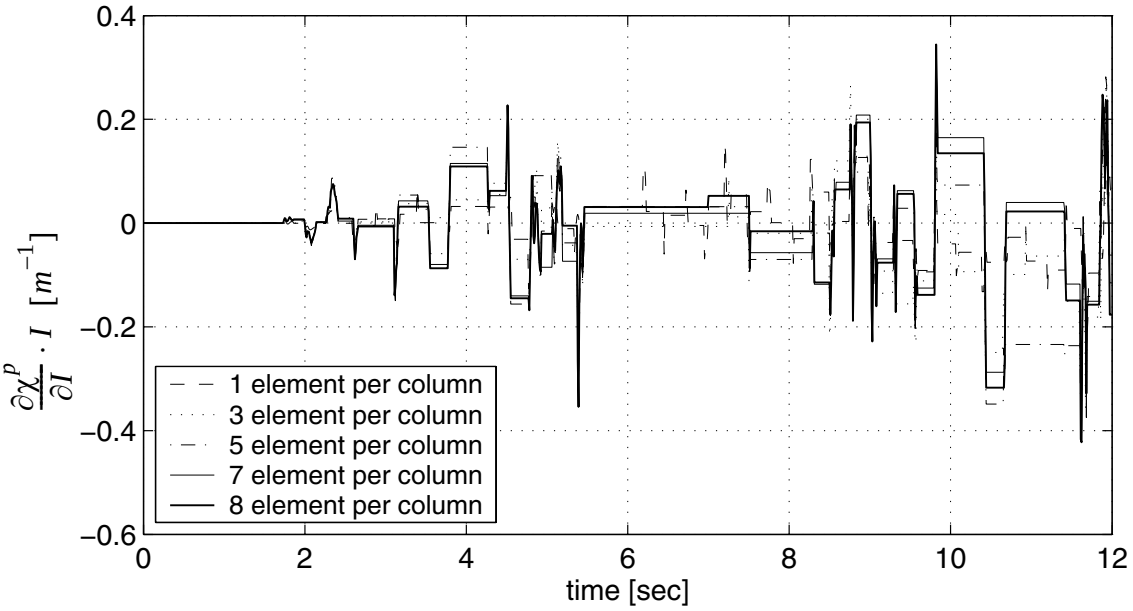


**Figure 3.42 Sensitivity of plastic curvature to I with increasing number of elements per beam/column**

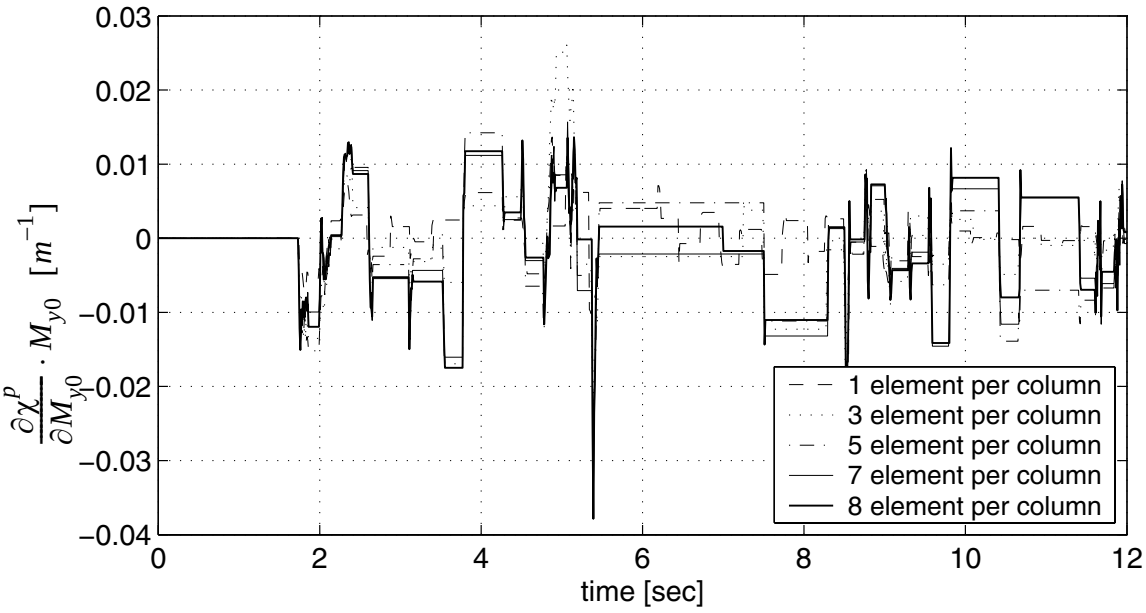


**Figure 3.43 Sensitivity of plastic curvature to My0 with increasing number of elements per beam/column**

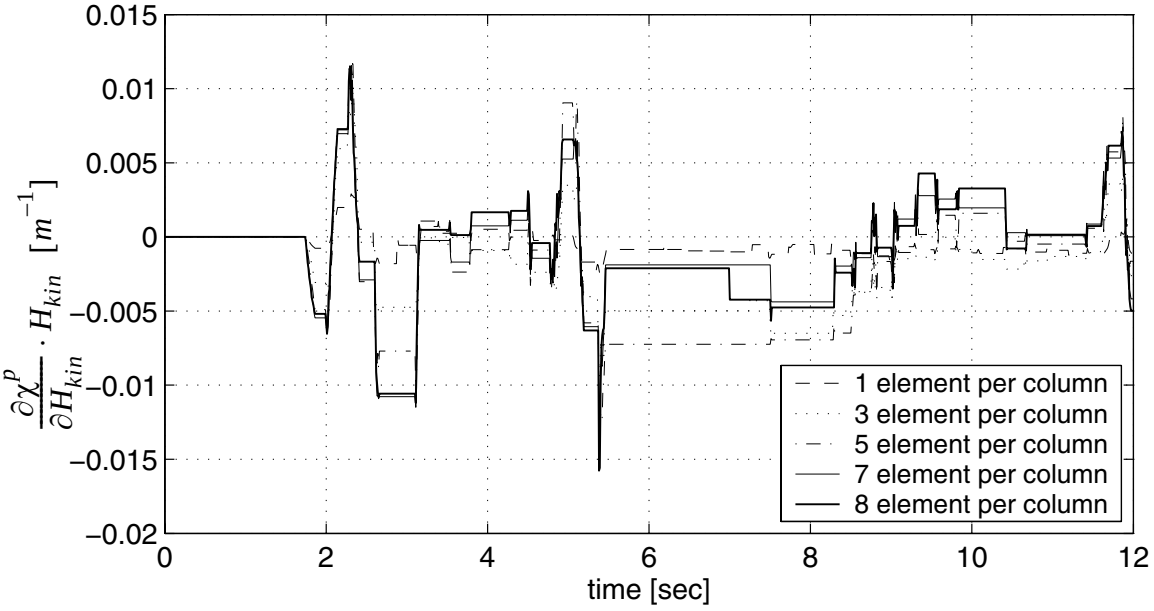


**Figure 3.44 Sensitivity of plastic curvature to $H_{kin}$ with increasing number of elements per beam/column**

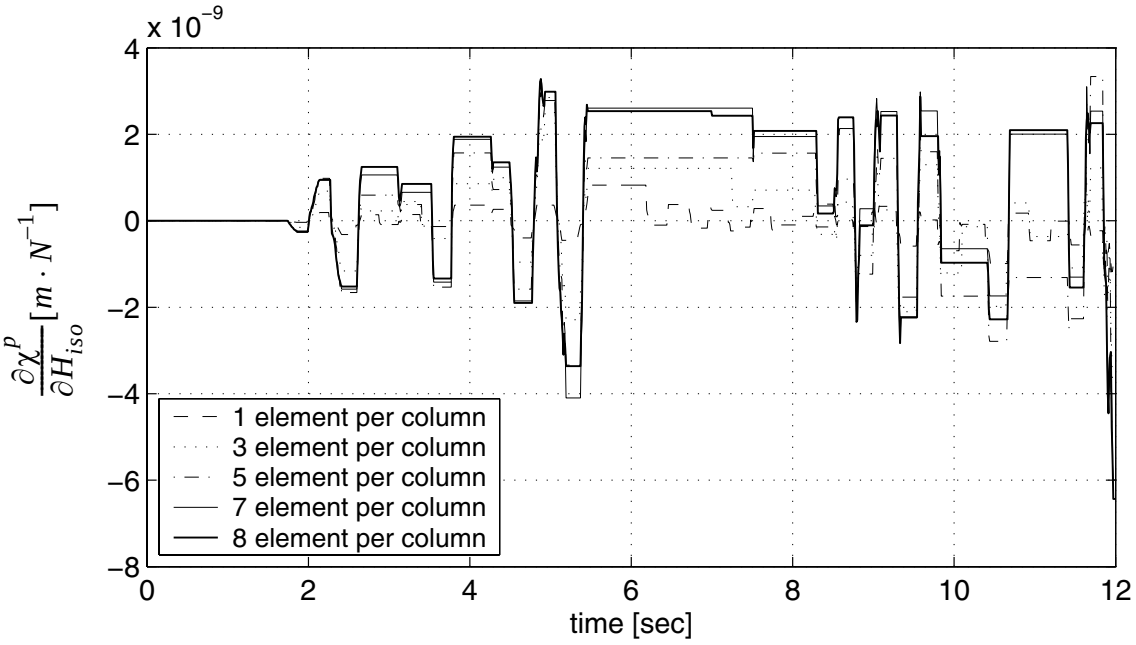


**Figure 3.45 Sensitivity of plastic curvature to $H_{iso}$ with increasing number of elements per beam/column**

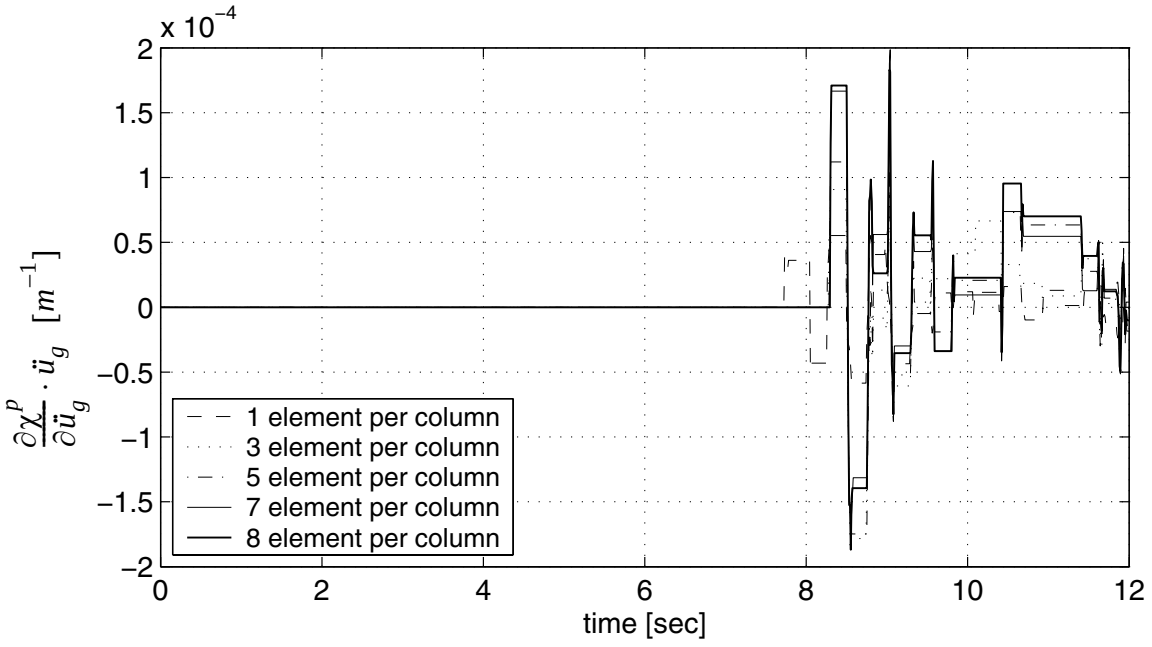


**Figure 3.46 Sensitivity of plastic curvature to $\ddot{u}_g(t = 7.60s)$ with increasing number of elements per beam/column**

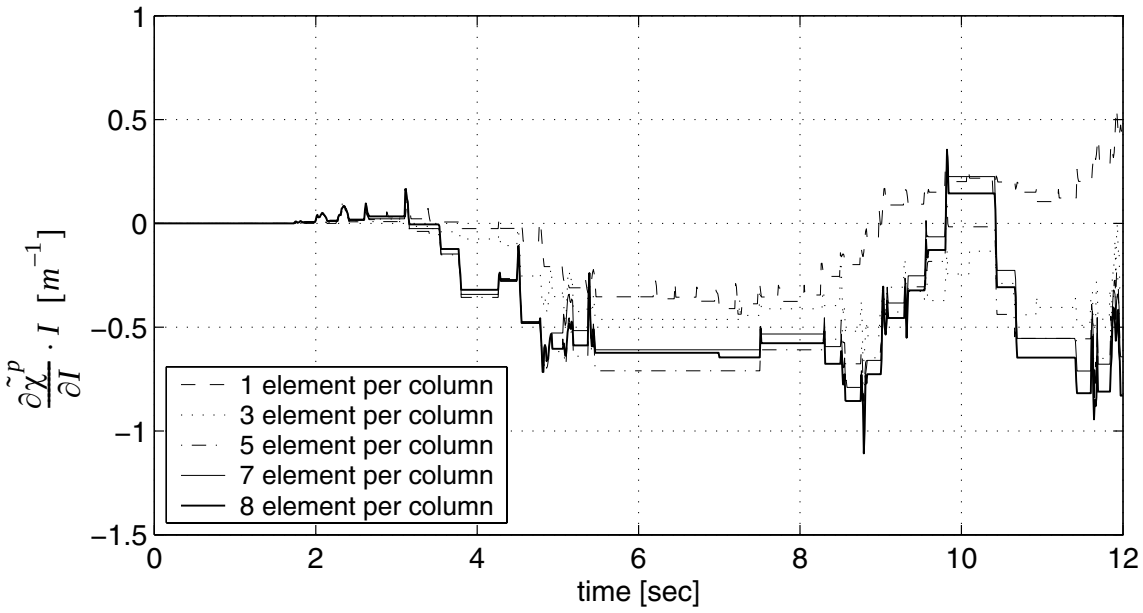


**Figure 3.47 Sensitivity of accumulated plastic curvature to I increasing number of elements per beam/column**

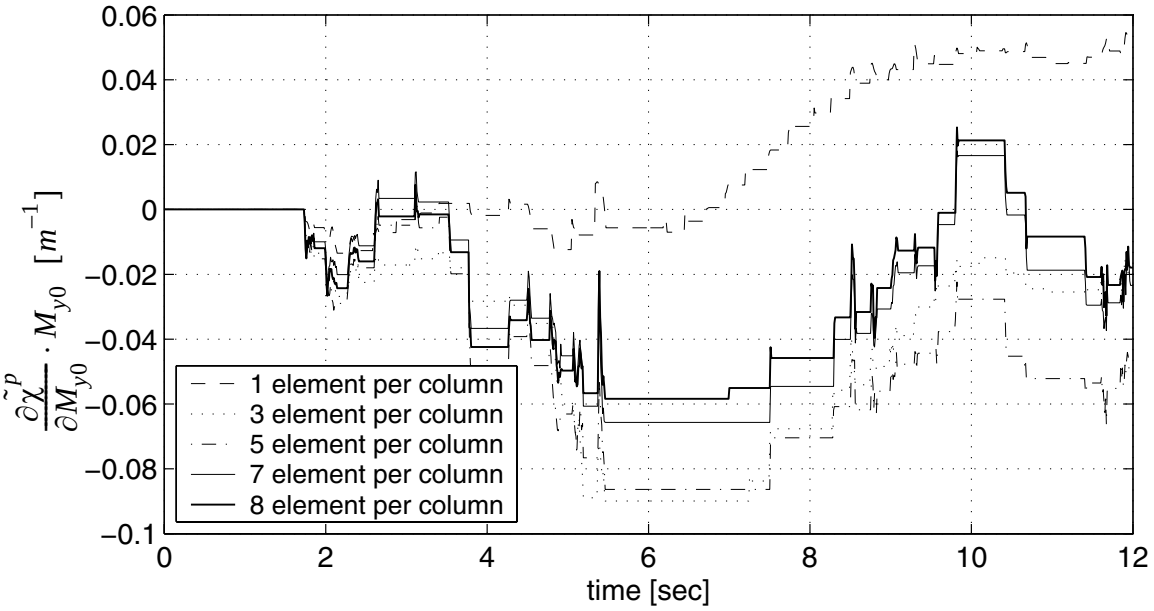


**Figure 3.48 Sensitivity of accumulated plastic curvature to $M_{y0}$ with increasing number of elements per beam/column**

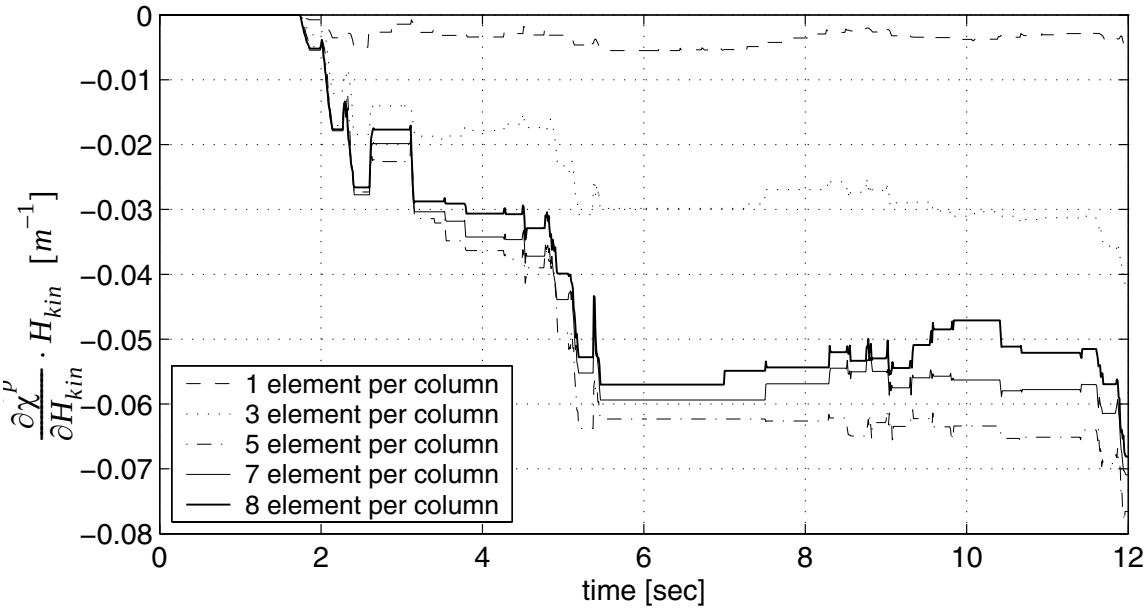


**Figure 3.49 Sensitivity of accumulated plastic curvature to $H_{kin}$ with increasing number of elements per beam/column**

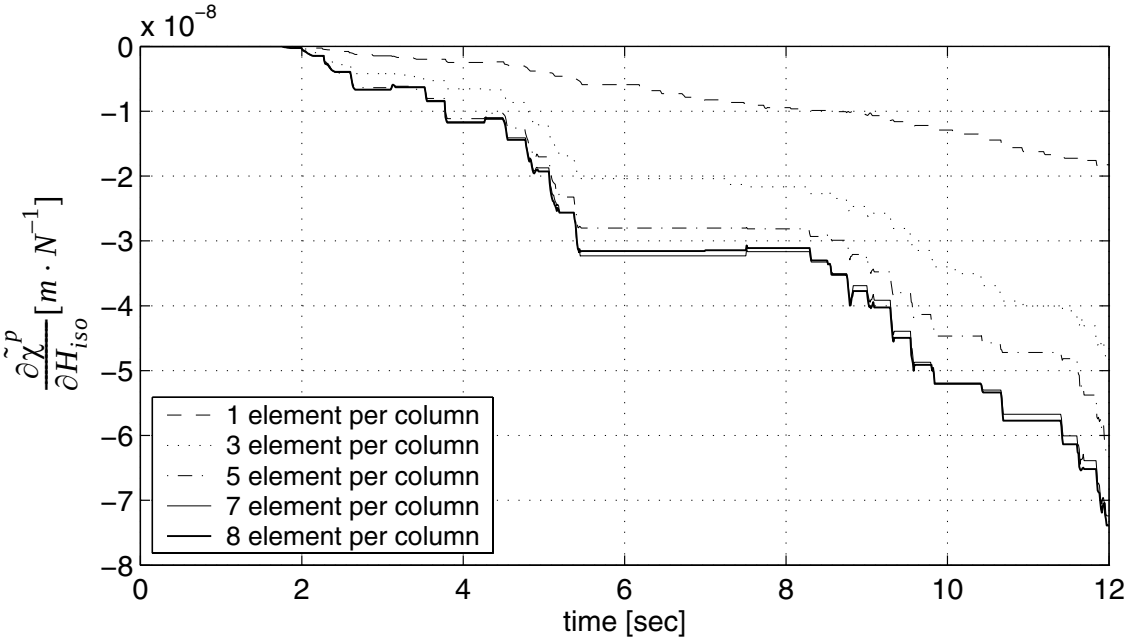


**Figure 3.50 Sensitivity of accumulated plastic curvature to $H_{iso}$ with increasing number of elements per beam/column**

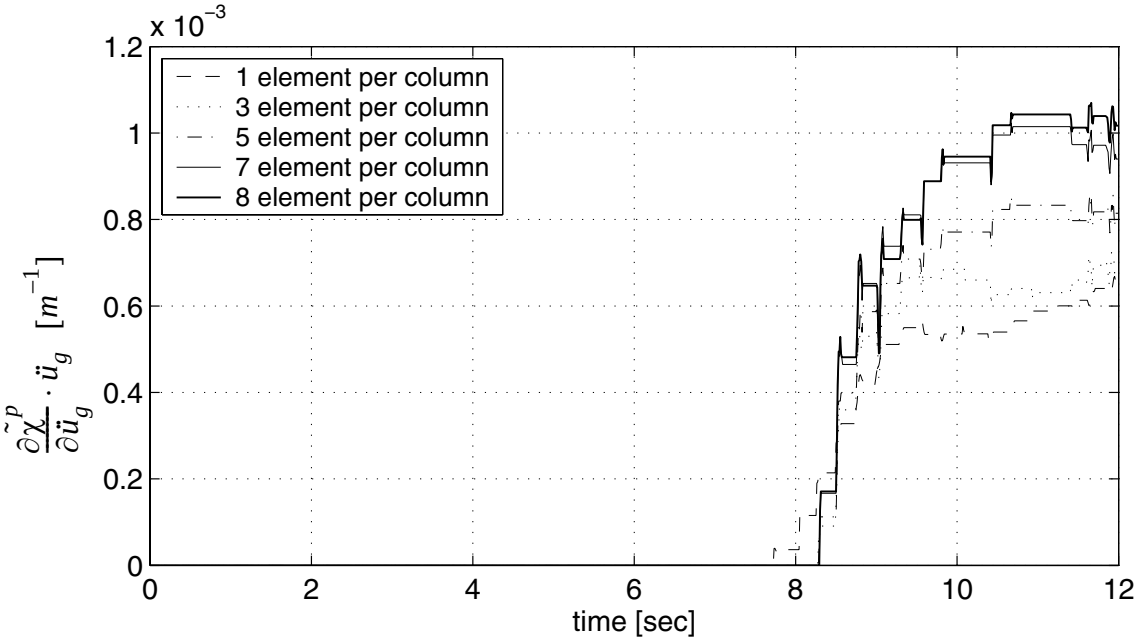


**Figure 3.51 Sensitivity of accumulated plastic curvature to $\ddot{\boldsymbol{u}}_g(t = 7.60s)$ with increasing number of elements per beam/column**

**Table 3.5 Element number per beam/column required in global convergence case**

| $\frac{\partial u}{\partial I}$ | $\frac{\partial u}{\partial M_{y0}}$ | $\frac{\partial u}{\partial H_{kin}}$ | $\frac{\partial u}{\partial H_{iso}}$ | $\frac{\partial u}{\partial \ddot{\boldsymbol{u}}_g}(7.60s)$ | Response u |
|---|---|---|---|---|---|
| 6 | 9 | 9 | 7 | 7 | 3 |

**Table 3.6 Element number per beam/column required in local convergence case**

| $M \sim \chi$ | $\chi_p$ | $\frac{\partial \chi_p}{\partial I}$ | $\frac{\partial \chi_p}{\partial M_{y0}}$ | $\frac{\partial \chi_p}{\partial H_{kin}}$ | $\frac{\partial \chi_p}{\partial H_{iso}}$ | $\frac{\partial \chi_p}{\partial \ddot{u}_g}$ | $\tilde{\chi}_p$ | $\frac{\partial \tilde{\chi}_p}{\partial I}$ | $\frac{\partial \tilde{\chi}_p}{\partial M_{y0}}$ | $\frac{\partial \tilde{\chi}_p}{\partial H_{kin}}$ | $\frac{\partial \tilde{\chi}_p}{\partial H_{iso}}$ | $\frac{\partial \tilde{\chi}_p}{\partial \ddot{u}_g}$ |
|---|---|---|---|---|---|---|---|---|---|---|---|---|
| 3 | 5 | 7 | 7 | 7 | 7 | 7 | 5 | 7 | 7 | 7 | 7 | 7 |

From the results obtained, it is observe that:

(1) Global response parameters converge with fewer finite elements per beam/column than local response parameters.

(2) A given response parameter, global or local, converges with fewer elements per beam/ column than its sensitivities.

(3) Sensitivities of global response parameters converge with slightly more elements per beam/column than sensitivities of local response parameters. This is in contrast to results in static push-over cases.

***c. Convergence of Response and Response Sensitivities with respect to Temporal Discretization***

The convergence is studied for both responses and their sensitivities with time steps varying from 20 ms to 0.5 ms. Some computational results are shown in Figures 3.52 through 3.70. Furthermore, for each response parameter and load case, the maximum time step size required to achieve convergence of the response and its response sensitivities is reported in Table 3.7 for the global response parameter and in Table 3.8 for the local response parameters respectively.

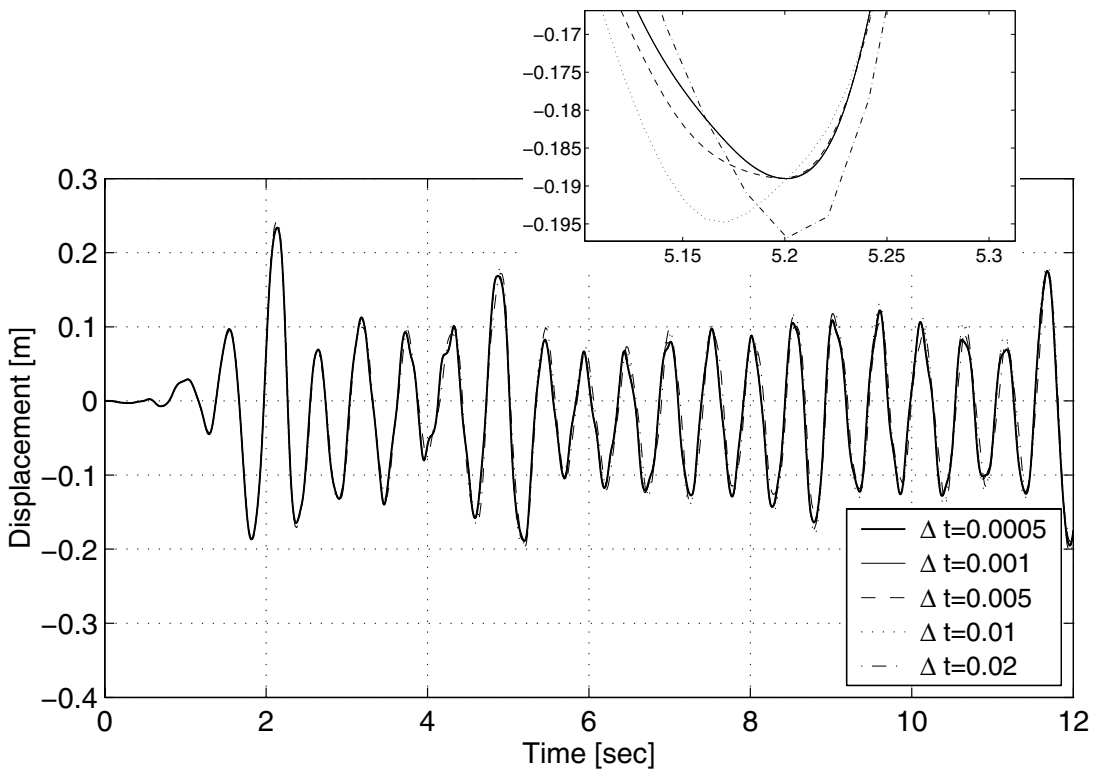


**Figure 3.52 Convergence of roof displacement with respect to time step size**

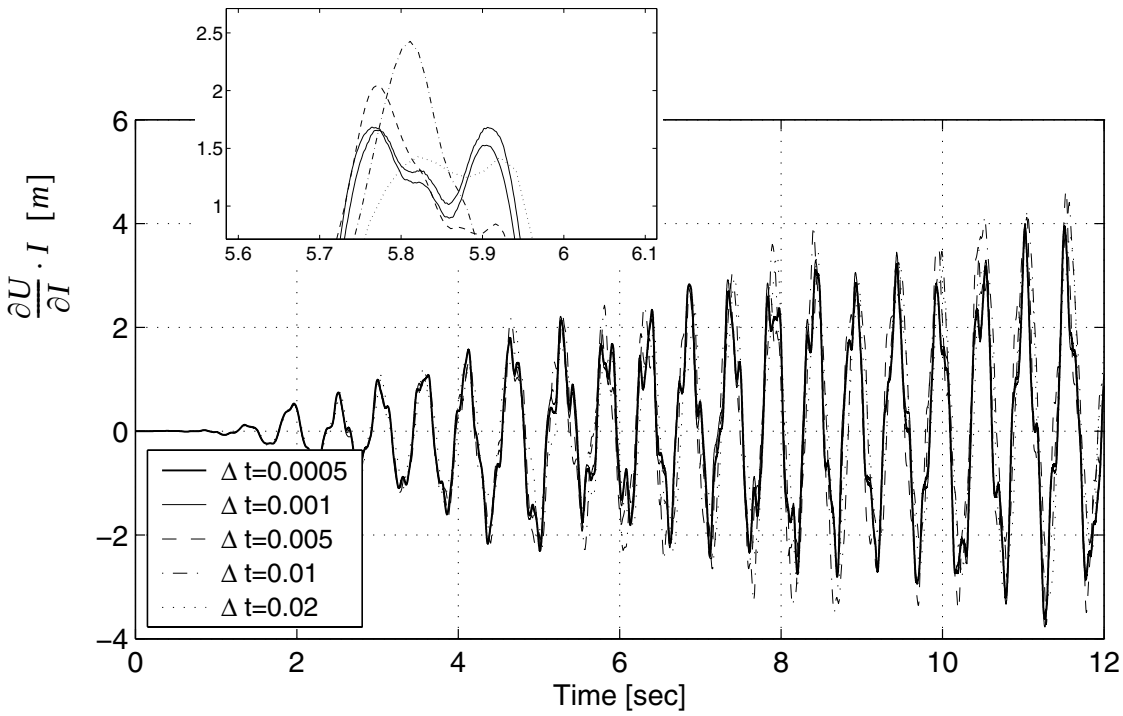


**Figure 3.53 Convergence of roof displacement sensitivity to I with respect to time step size**

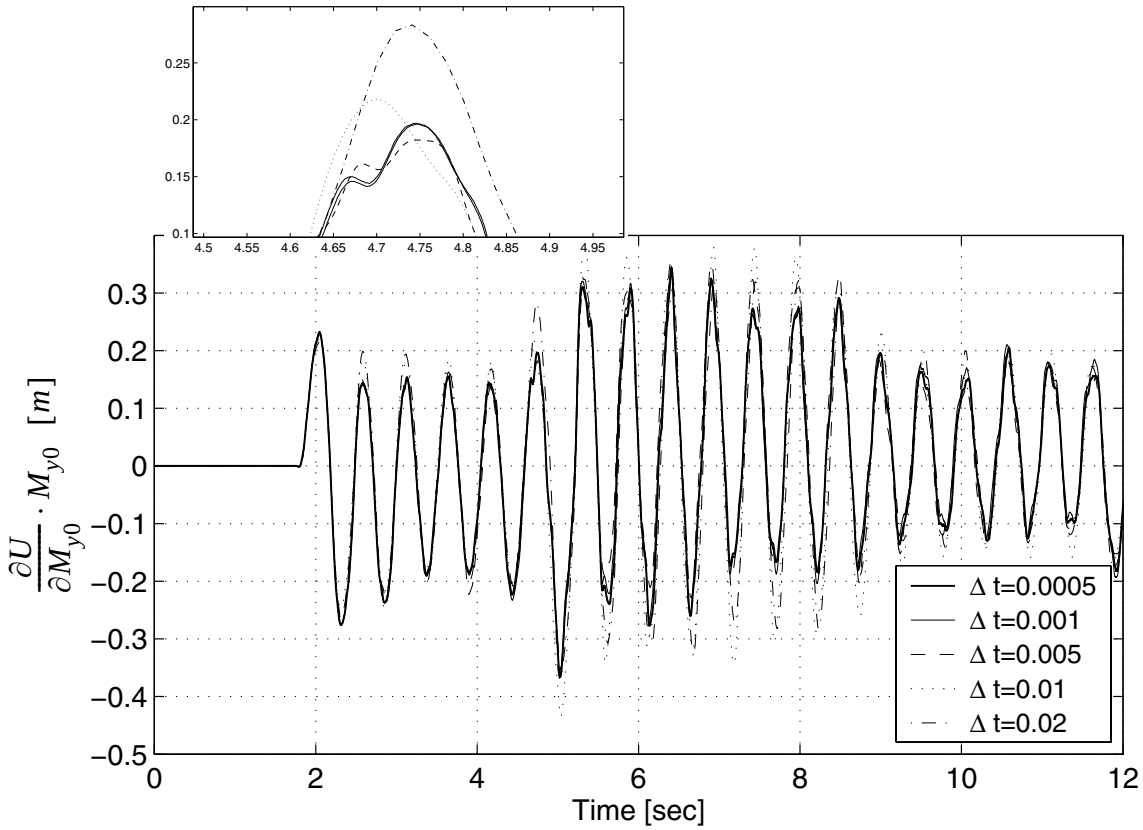


**Figure 3.54 Convergence of roof displacement sensitivity to $M_{y0}$ with respect to time step size**

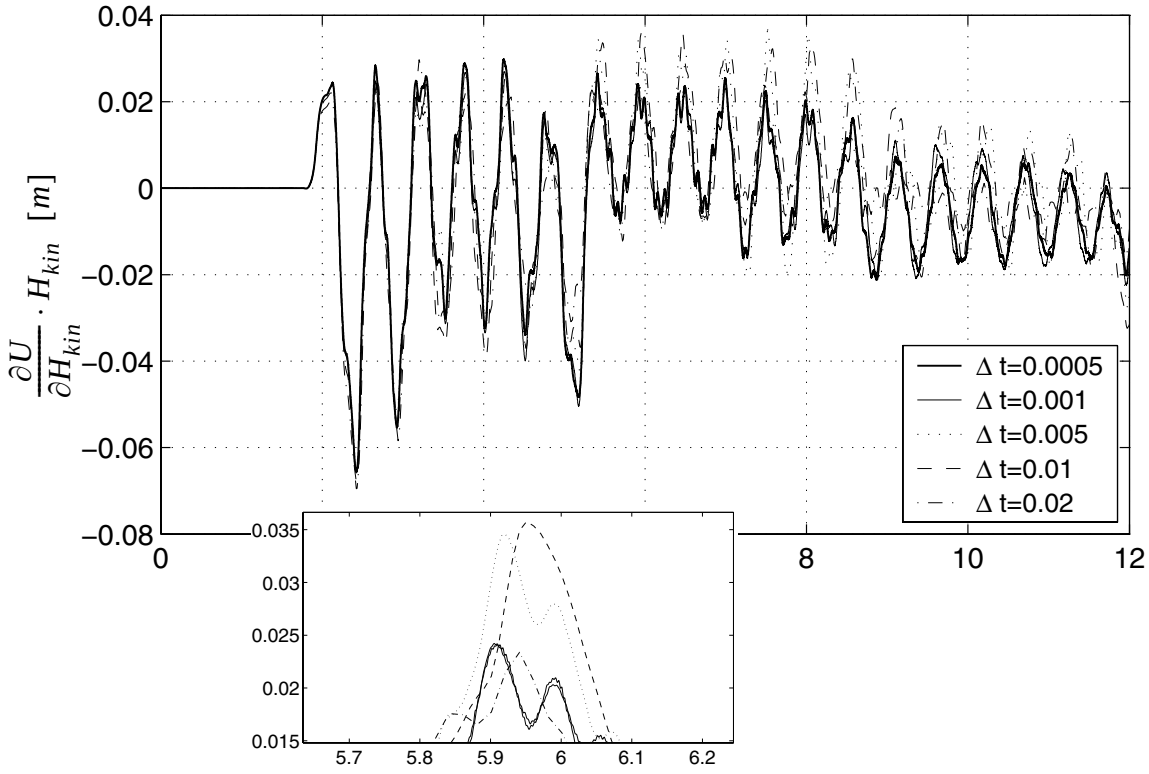


**Figure 3.55 Convergence of roof displacement sensitivity to $H_{kin}$ with respect to time step size**

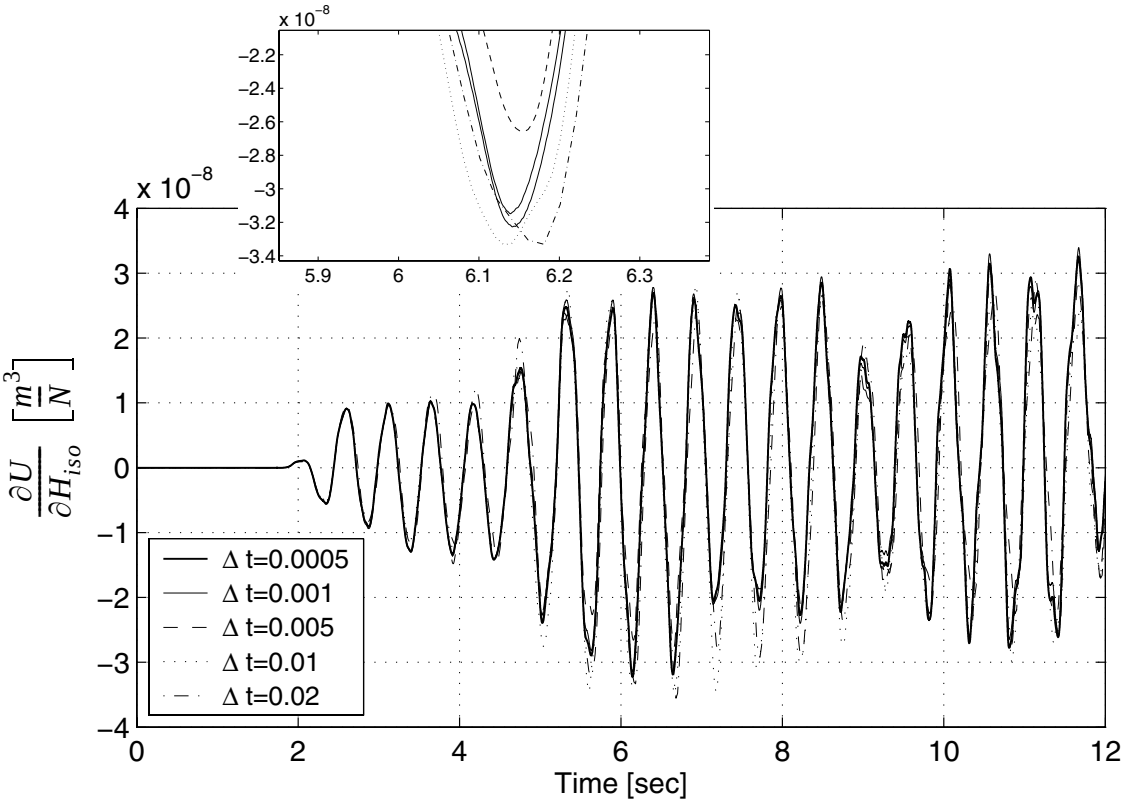


**Figure 3.56 Convergence of roof displacement sensitivity to $H_{iso}$ with respect to time step size**

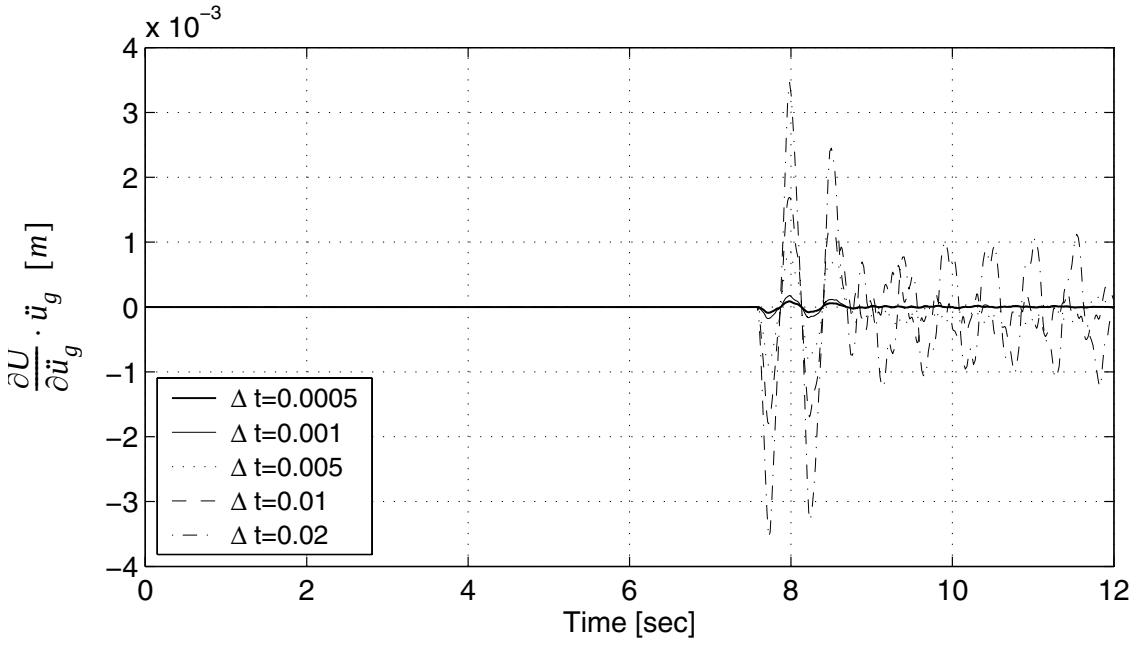


**Figure 3.57 Convergence of roof displacement sensitivity to $\ddot{u}_g(t = 7.60s)$ with respect to time step size**

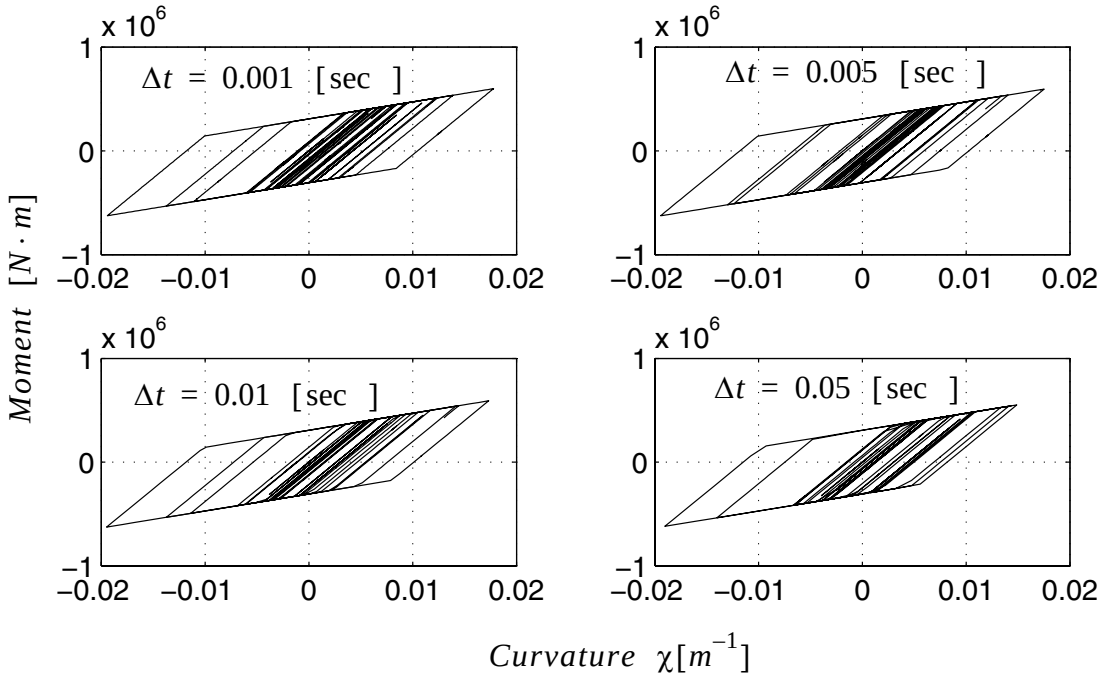


**Figure 3.58 Convergence of moment curvature relationship with respect to time step size**

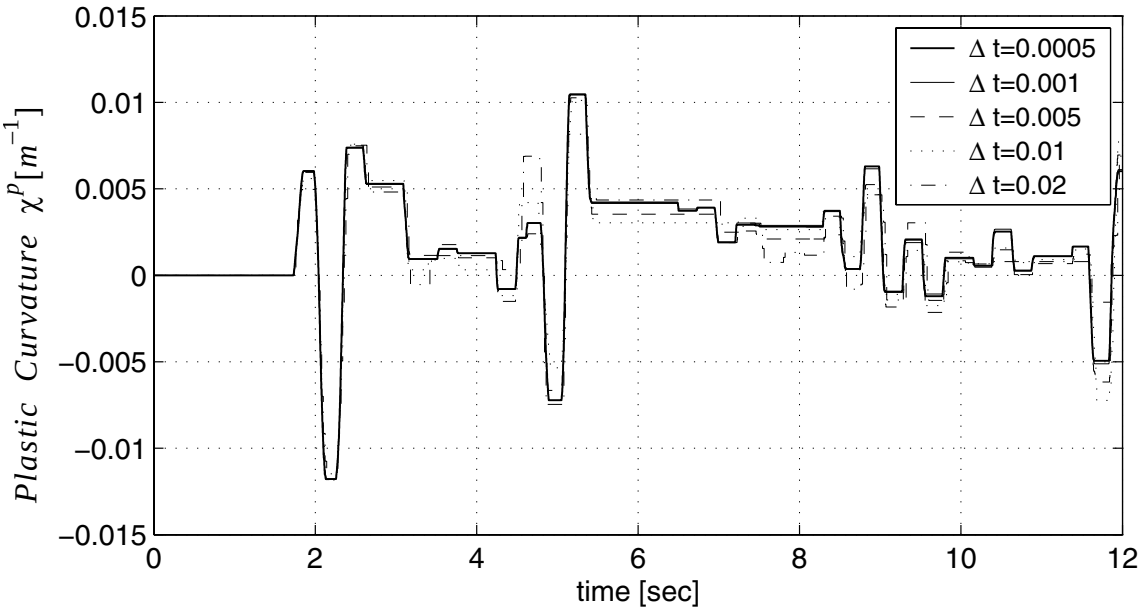


**Figure 3.59 Convergence of plastic curvature with respect to time step size**

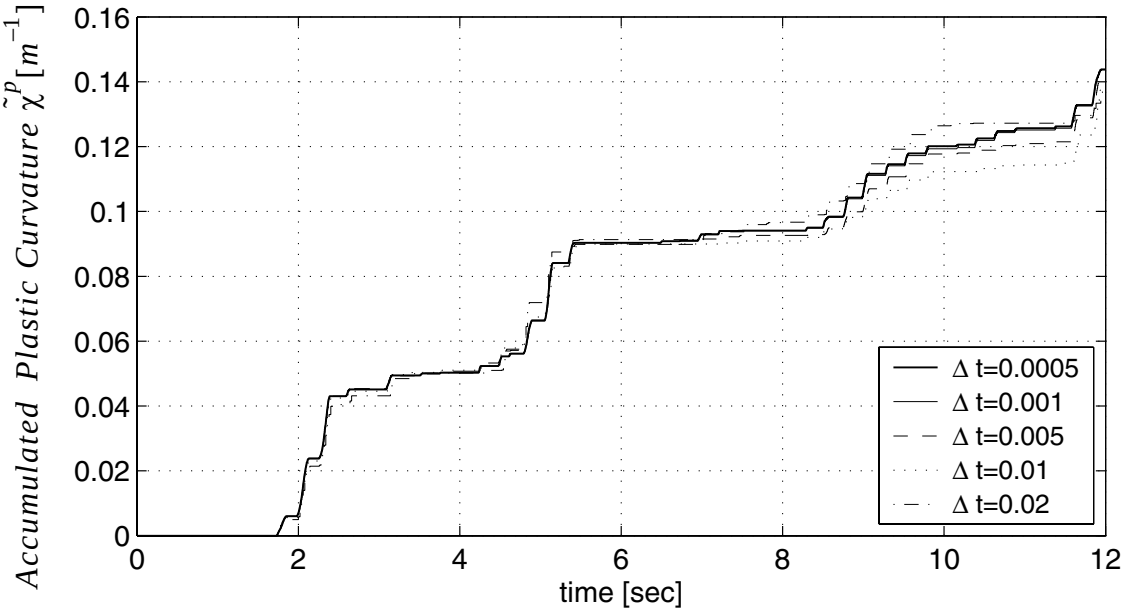


**Figure 3.60 Convergence of accumulated plastic curvature with respect to time step size**

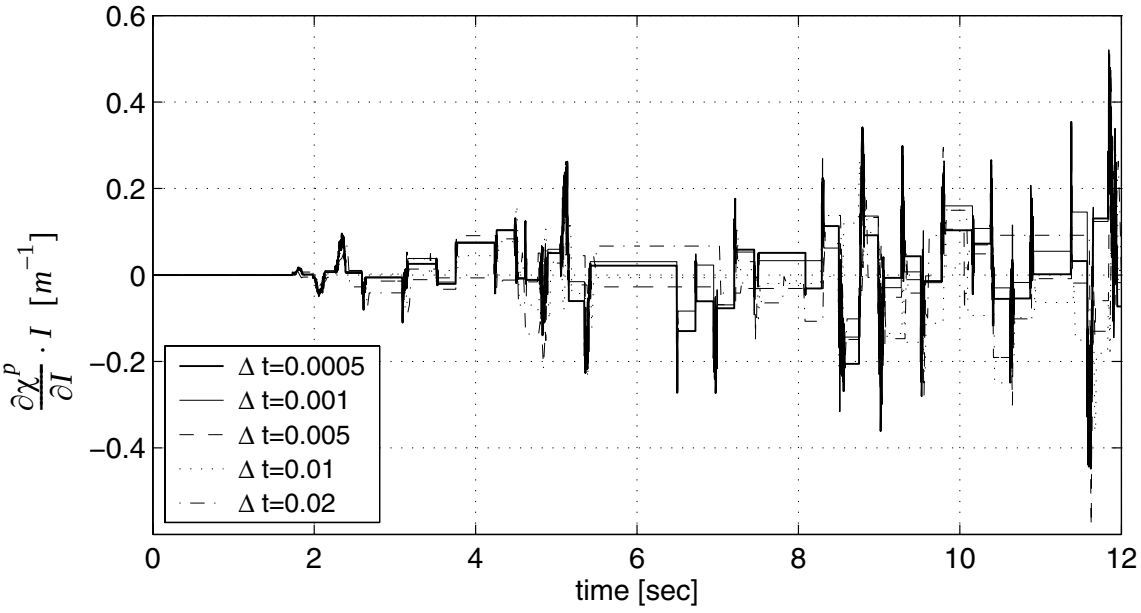


**Figure 3.61 Sensitivity of plastic curvature to I with respect to time step size**

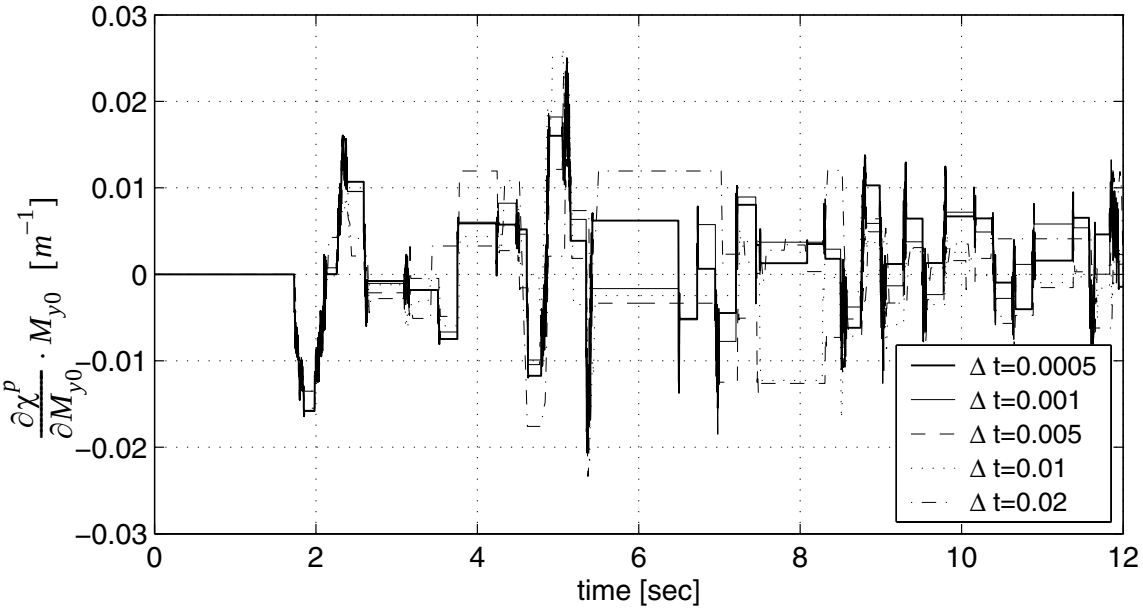


**Figure 3.62 Sensitivity of plastic curvature to $M_{y0}$ with respect to time step size**

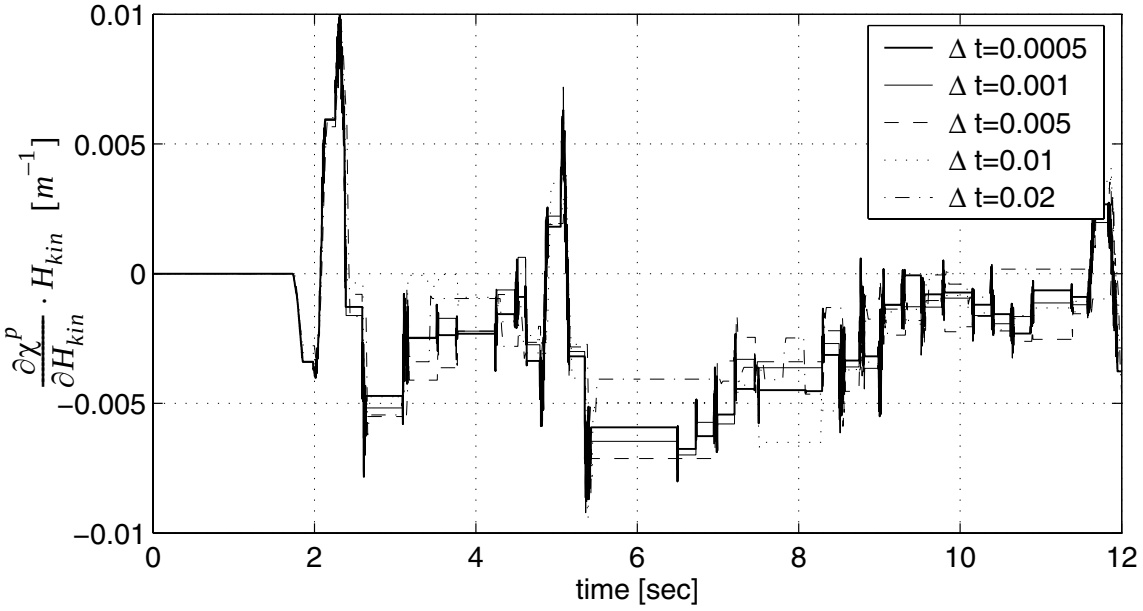


**Figure 3.63 Sensitivity of plastic curvature to $H_{kin}$ with respect to time step size**

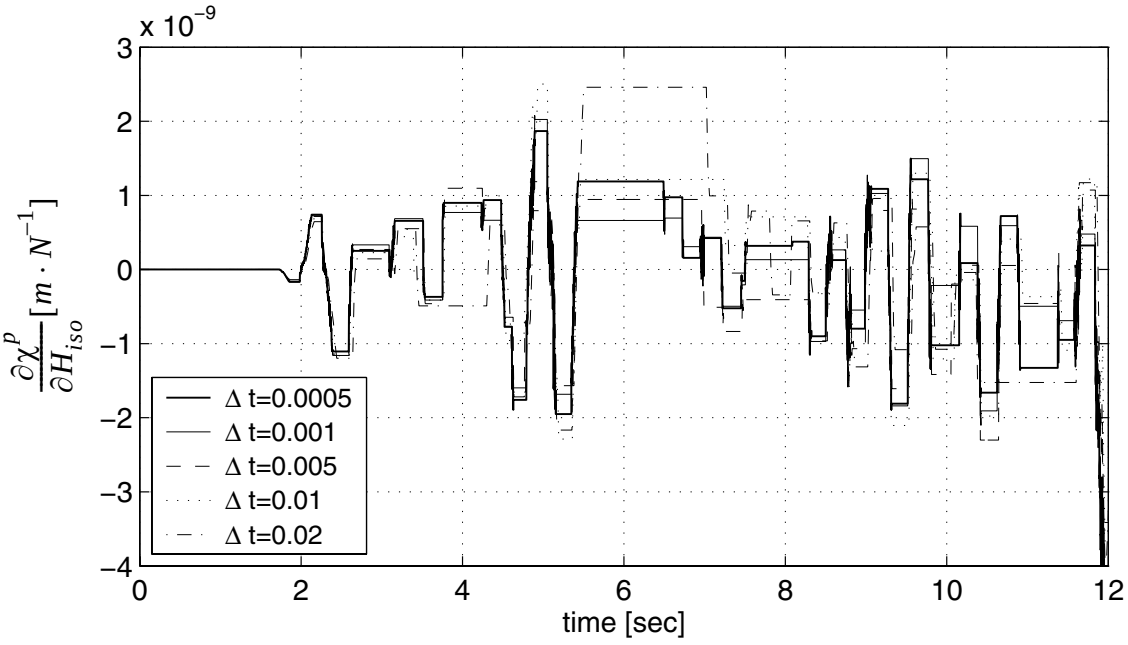


**Figure 3.64 Sensitivity of plastic curvature to $H_{iso}$ with respect to time step size**

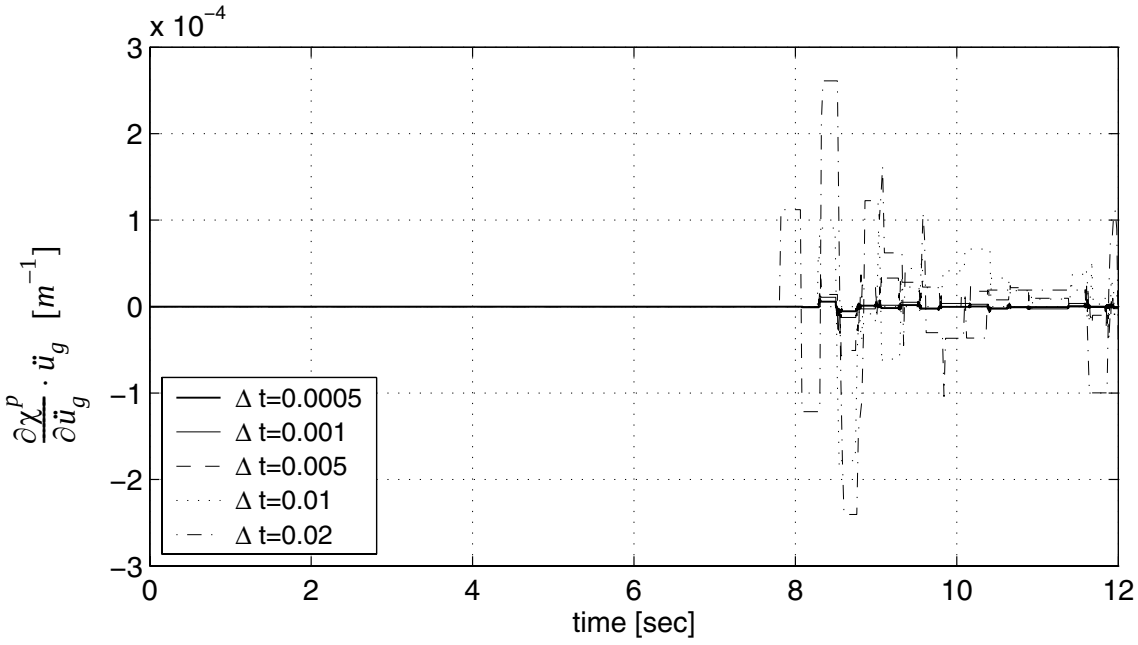


**Figure 3.65 Sensitivity of plastic curvature to $\ddot{u}_g(t= 7.60s)$ with respect to time step size**

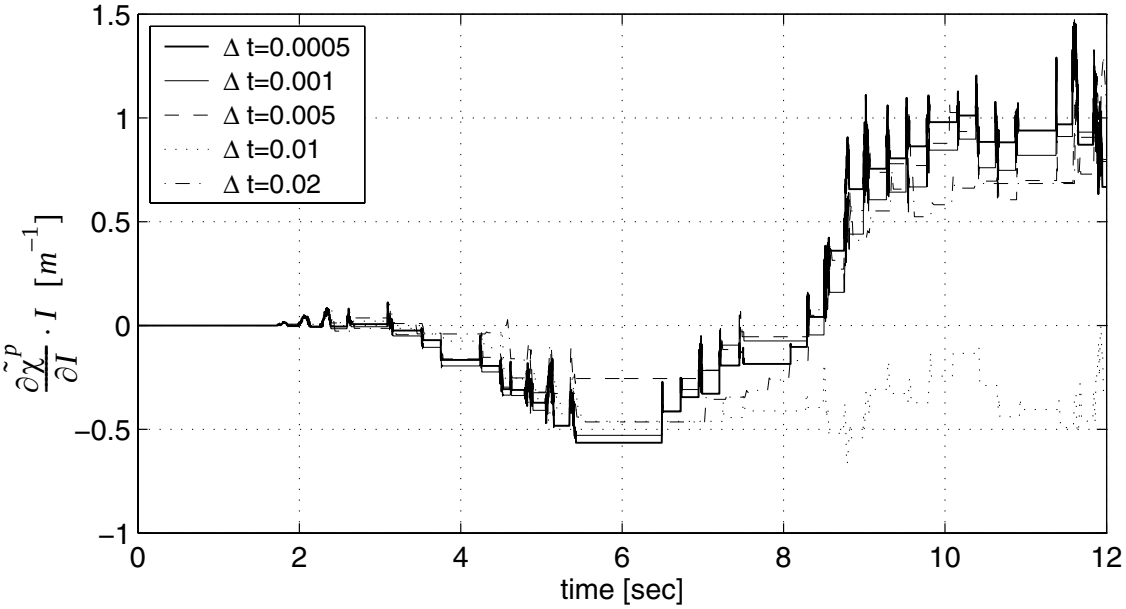


**Figure 3.66 Sensitivity of accumulated plastic curvature to I with respect to time step size**

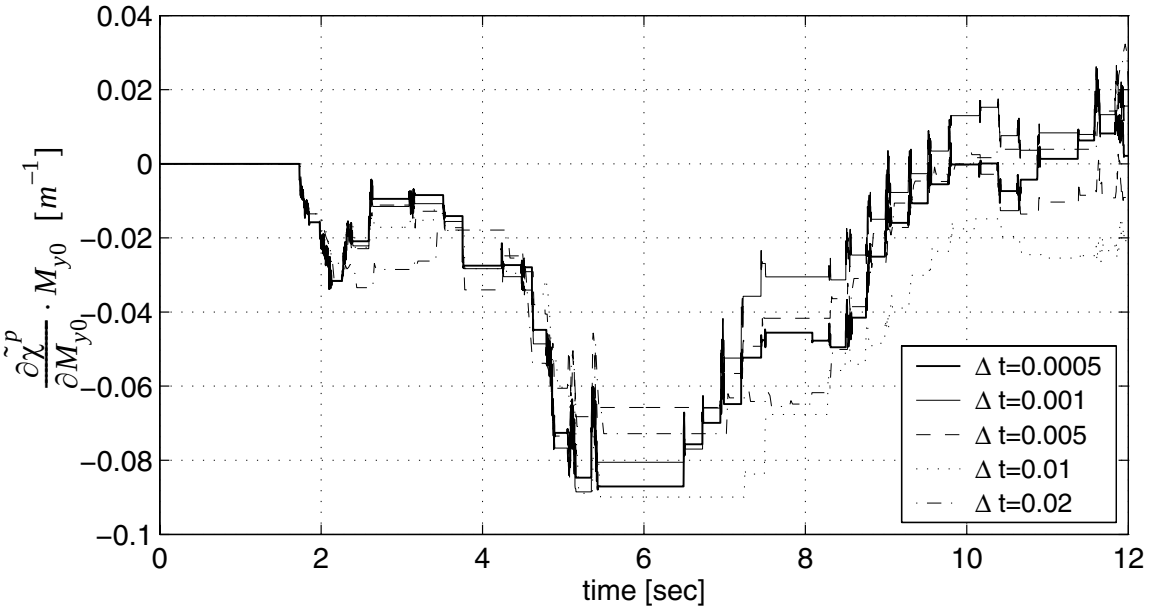


**Figure 3.67 Sensitivity of accumulated plastic curvature to $M_{y0}$ with respect to time step size**

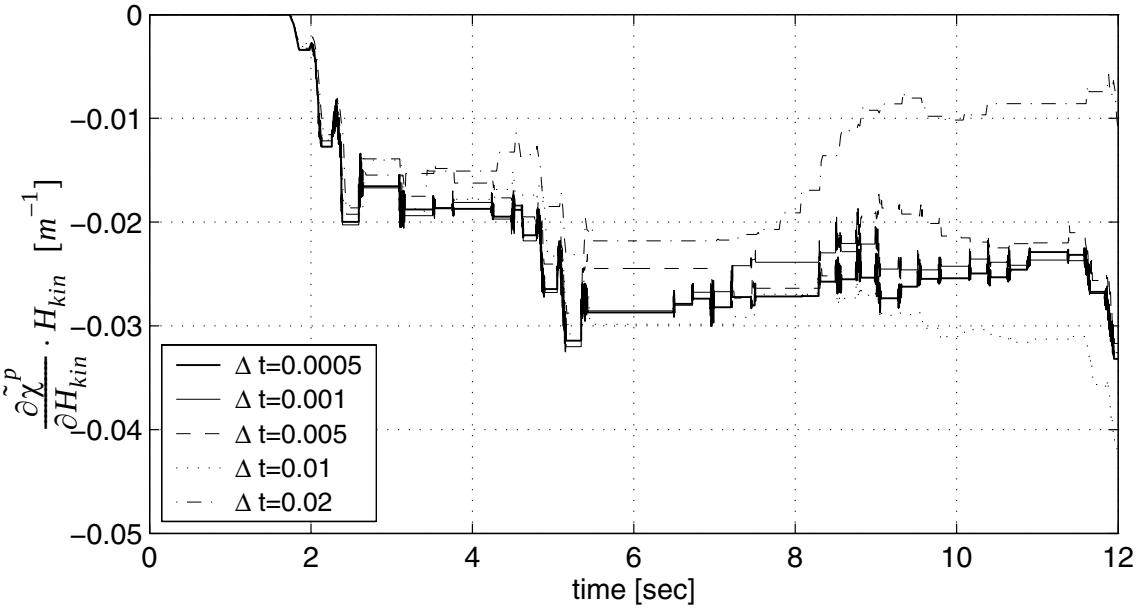


**Figure 3.68 Sensitivity of accumulated plastic curvature to $H_{kin}$ with respect to time step size**

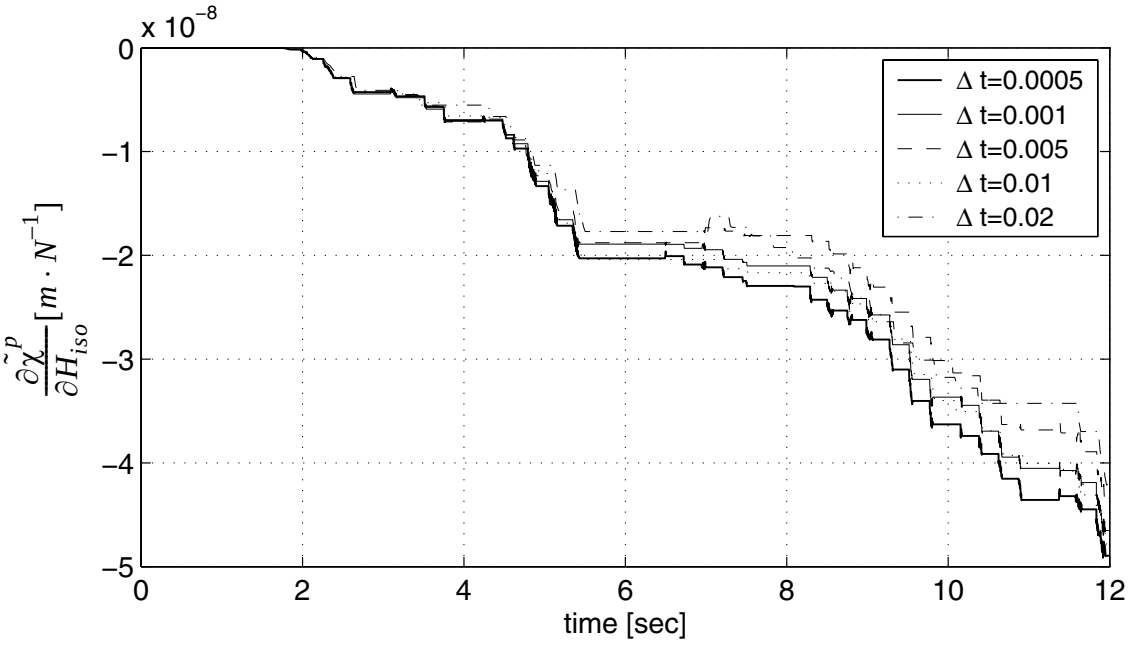


**Figure 3.69 Sensitivity of accumulated plastic curvature to $H_{iso}$ with respect to time step size**

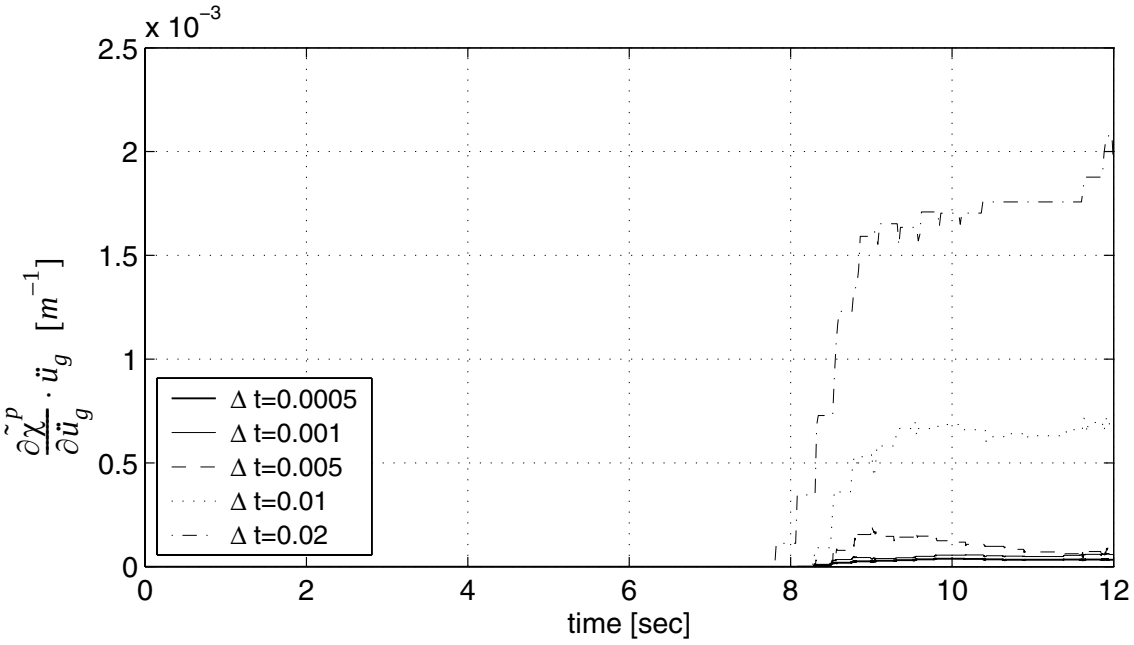


**Figure 3.70 Sensitivity of accumulated plastic curvature to $\ddot{u}_g(t= 7.60s)$ with respect to time step size**

**Table 3.7 Largest time interval (sec.) required for global convergence**

| $\frac{\partial u}{\partial I}$ | $\frac{\partial u}{\partial M_{y0}}$ | $\frac{\partial u}{\partial H_{kin}}$ | $\frac{\partial u}{\partial H_{iso}}$ | $\frac{\partial u}{\partial \ddot{u}g}$ $(t= 7.60s)$ | Resp. (u) |
|---|---|---|---|---|---|
| $10^{-3}$ | $10^{-3}$ | $10^{-3}$ | $10^{-3}$ | $10^{-3}$ | $5 \times 10^{-3}$ |

**Table 3.8 Largest time interval (sec.) required for local convergence**

| $M \sim \chi$ | $\chi_p$ | $\frac{\partial \chi_p}{\partial I}$ | $\frac{\partial \chi_p}{\partial M_{y0}}$ | $\frac{\partial \chi_p}{\partial H_{kin}}$ | $\frac{\partial \chi_p}{\partial H_{iso}}$ | $\frac{\partial \chi_p}{\partial \ddot{u}_g}$ | $\tilde{\chi}_p$ | $\frac{\partial \tilde{\chi}_p}{\partial I}$ | $\frac{\partial \tilde{\chi}_p}{\partial M_{y0}}$ | $\frac{\partial \tilde{\chi}_p}{\partial H_{kin}}$ | $\frac{\partial \tilde{\chi}_p}{\partial H_{iso}}$ | $\frac{\partial \tilde{\chi}_p}{\partial \ddot{u}_g}$ |
|---|---|---|---|---|---|---|---|---|---|---|---|---|
| $10^{-2}$ | $5 \times 10^{-3}$ | $10^{-3}$ | $10^{-3}$ | $10^{-3}$ | $10^{-3}$ | $10^{-3}$ | $10^{-3}$ | $10^{-3}$ | $10^{-3}$ | $10^{-3}$ | $10^{-3}$ | $10^{-3}$ |

Based on the results obtained, it is observed that:

(1) Both global and local response parameters converge at a larger time step size than their respective sensitivities.

(2) Sensitivities of global and local response parameters tend to converge at the same time step size.

(3) The global response parameter converges at a time step size larger than or equal to that required for local response parameters.

### 3.5.2 Discontinuities of Response Sensitivities, and Propagation of Discontinuities from Local material properties to Global Response Sensitivities

This section studies the discontinuities in the response sensitivities for the model mentioned above while subjected to the cyclic push-over force as shown in Figure 3.71.

During each time step of the response computation, at one Gauss point, the step is either an elastic step or a plastic step depending on whether there is plastic flow. The derivative $\frac{\partial(\Delta\lambda)}{\partial\theta}$ is zero for elastic steps and finite for plastic steps even if $\Delta\lambda \to 0$. If a point is in an elastic state in a previous step but enters a plastic state in the current step, there is a 'sudden' jump in $\frac{\partial(\Delta\lambda)}{\partial\theta}$ during the transition from the elastic to plastic material states, causing discontinuities in the sensitivity of local variables at this point, such as $\frac{\partial\chi_p}{\partial\theta}$ and $\frac{\partial\tilde{\chi}_p}{\partial\theta}$. This local discontinuities will propagate mathematically and physically into the global level via FEM assembly. It is worth mentioning that if the point changes transitions from the plastic to elastic state, there will be no discontinuity in the sensitivity computa-

tion at the Gauss point, and thus will not cause discontinuity at the global level (Haukaas 2001).

The propagation of discontinuities from local to global response sensitivities is illustrated with the frame in Figure 3.3 subjected to a static push-over force as shown in Figure 3.71. The relationship between the number of yield Gauss points, and the response and their sensitivities are shown in Figures 3.72 through 3.84.

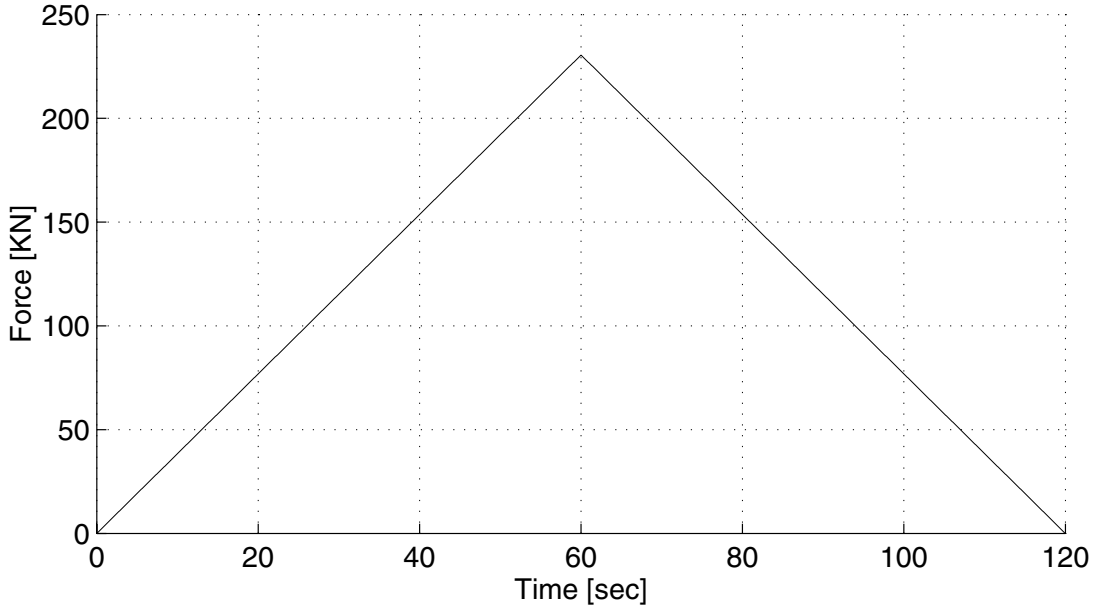


**Figure 3.71 The maximum distributed force on the frame**

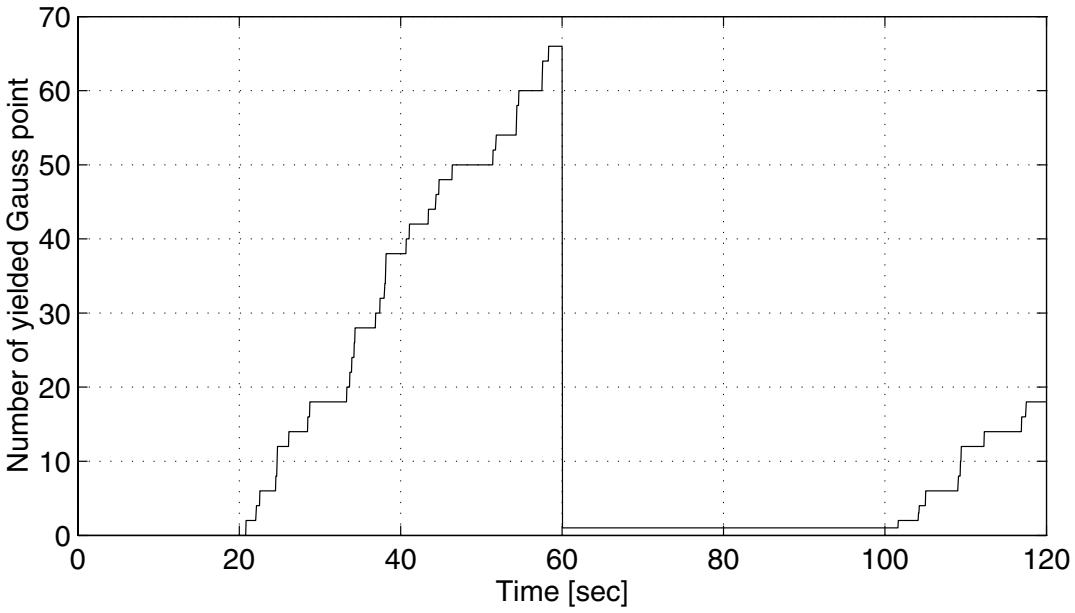


**Figure 3.72 The numbers of yielded Gauss points**

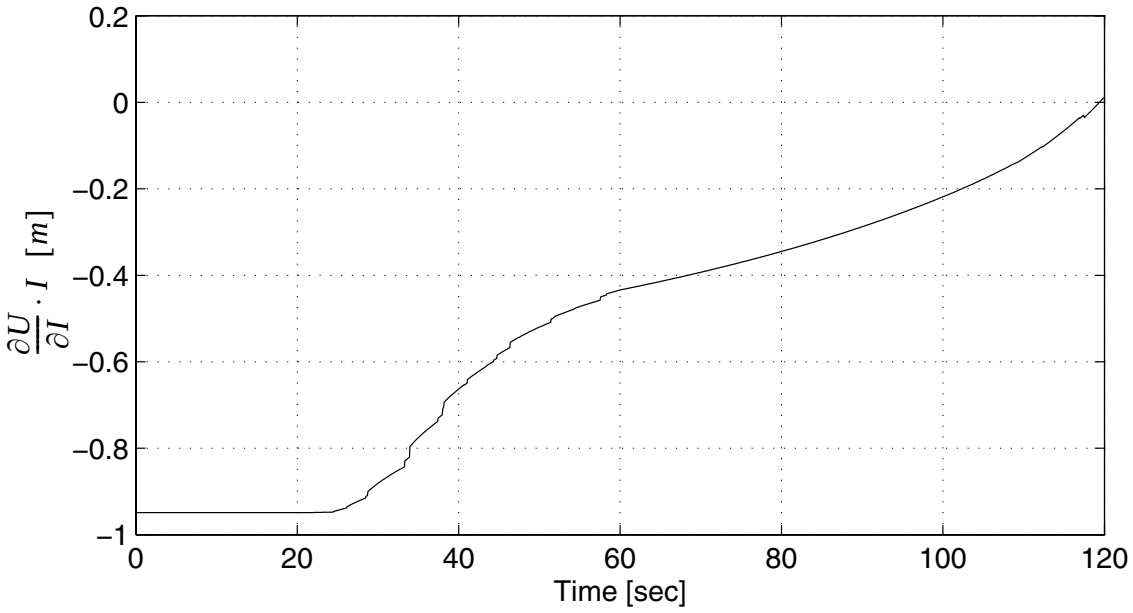


**Figure 3.73 Sensitivity of roof displacement to material parameter I**

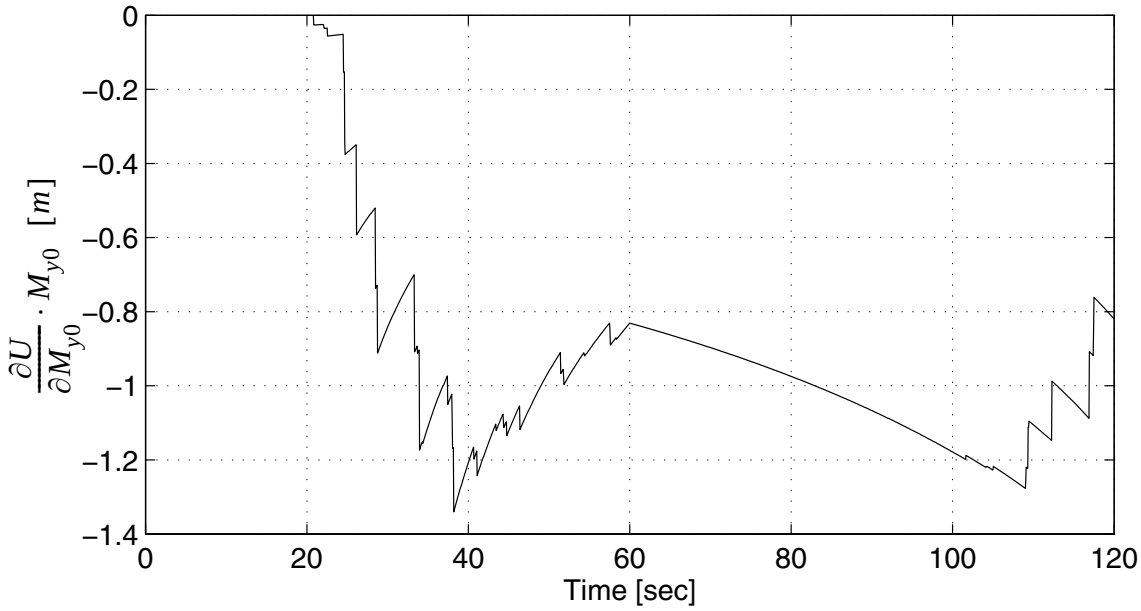


**Figure 3.74 Sensitivity of roof displacement to $M_{y0}$**

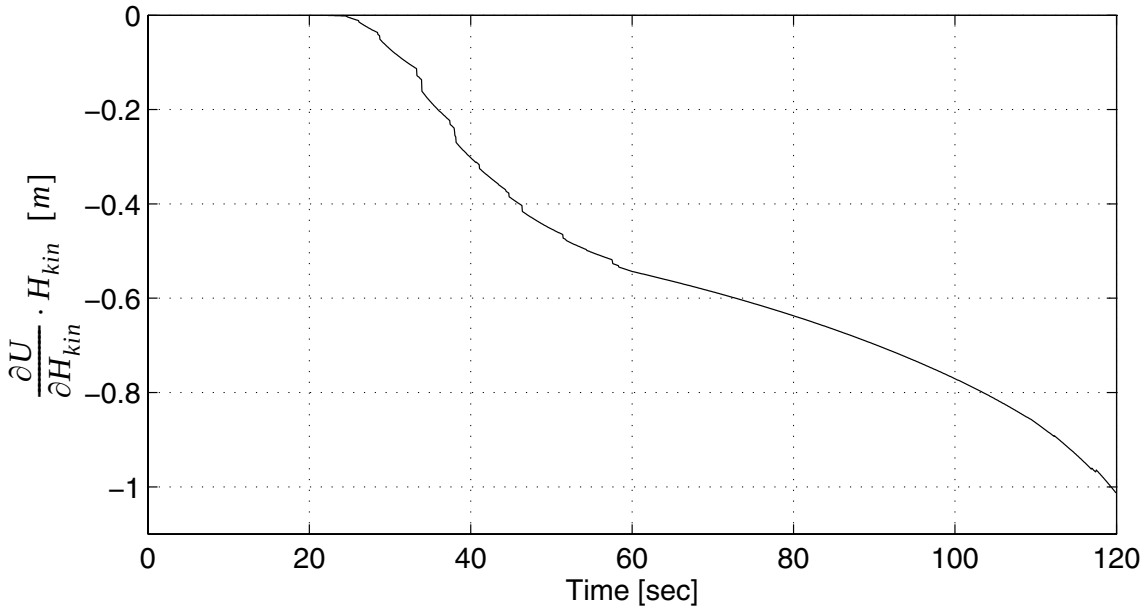


**Figure 3.75 Sensitivity of roof displacement to Hkin**

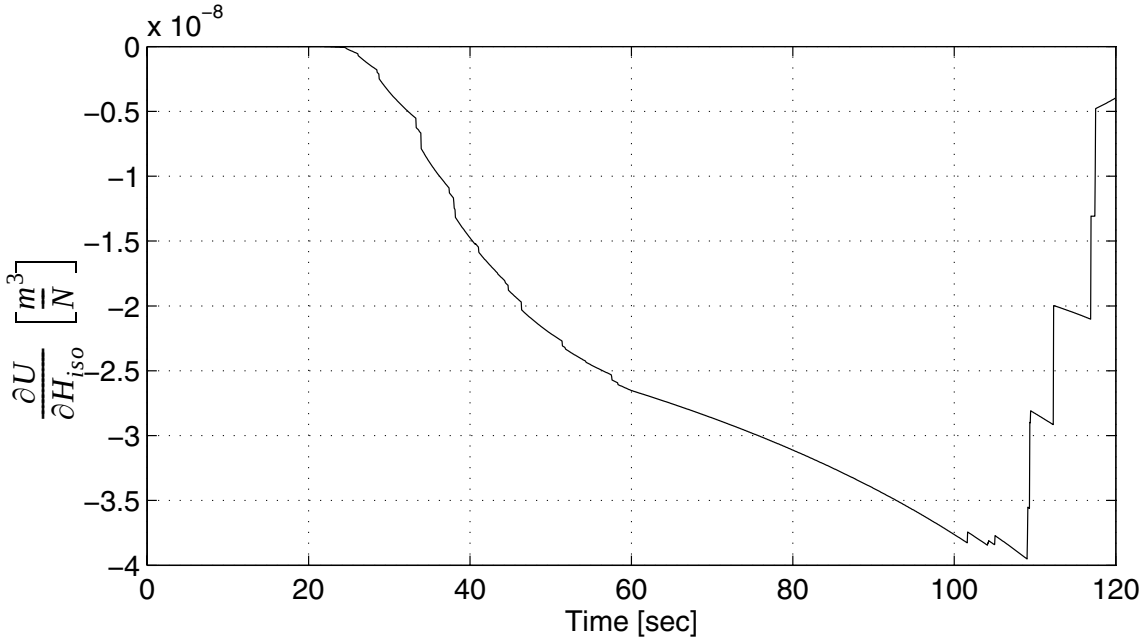


**Figure 3.76 Sensitivity of roof displacement to $H_{iso}$**

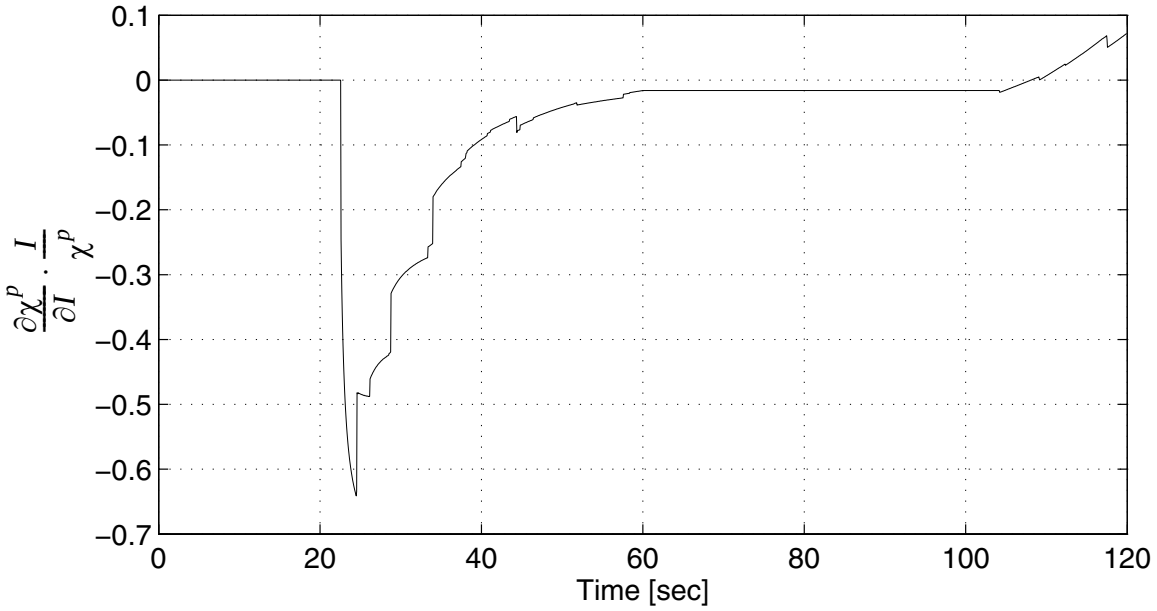


**Figure 3.77 Sensitivity of plastic curvature to I**

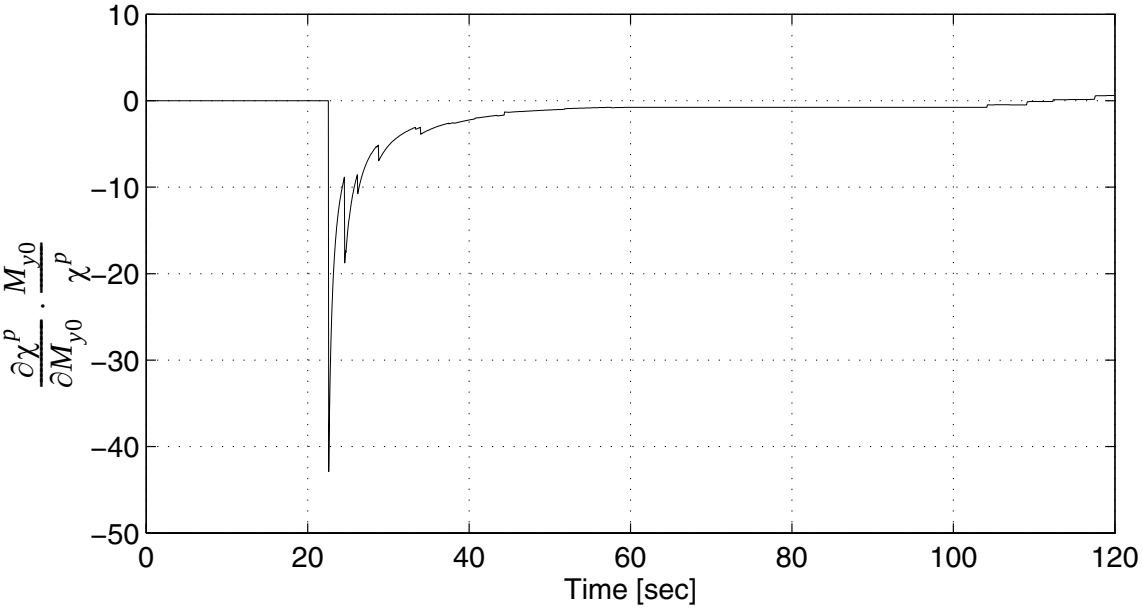


**Figure 3.78 Sensitivity of plastic curvature to $M_{y0}$**

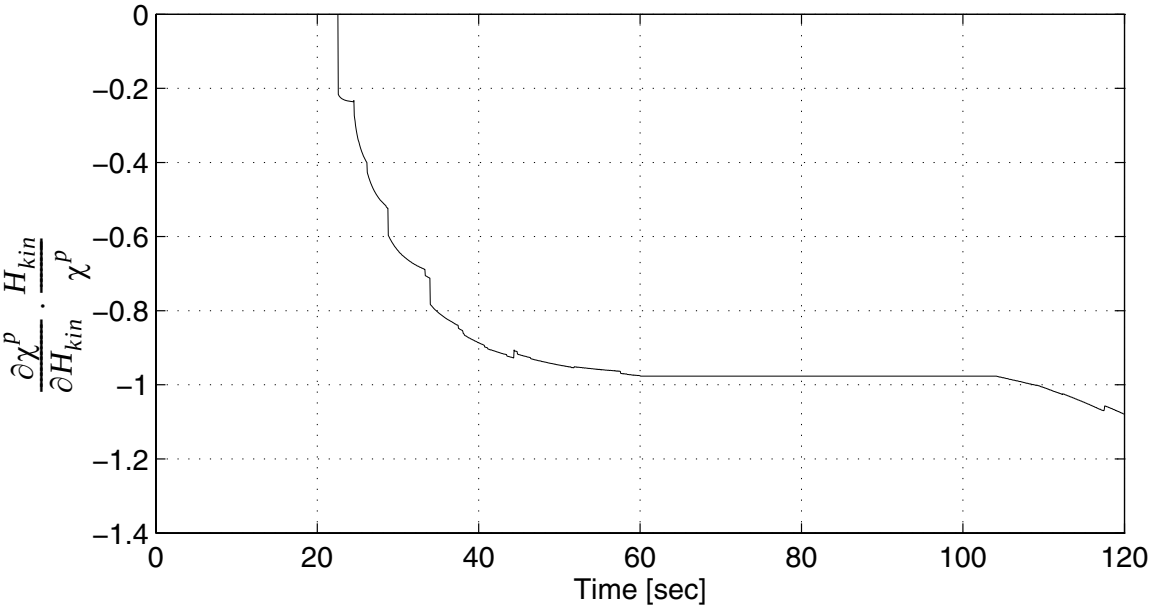


**Figure 3.79 Sensitivity of plastic curvature to $H_{kin}$**

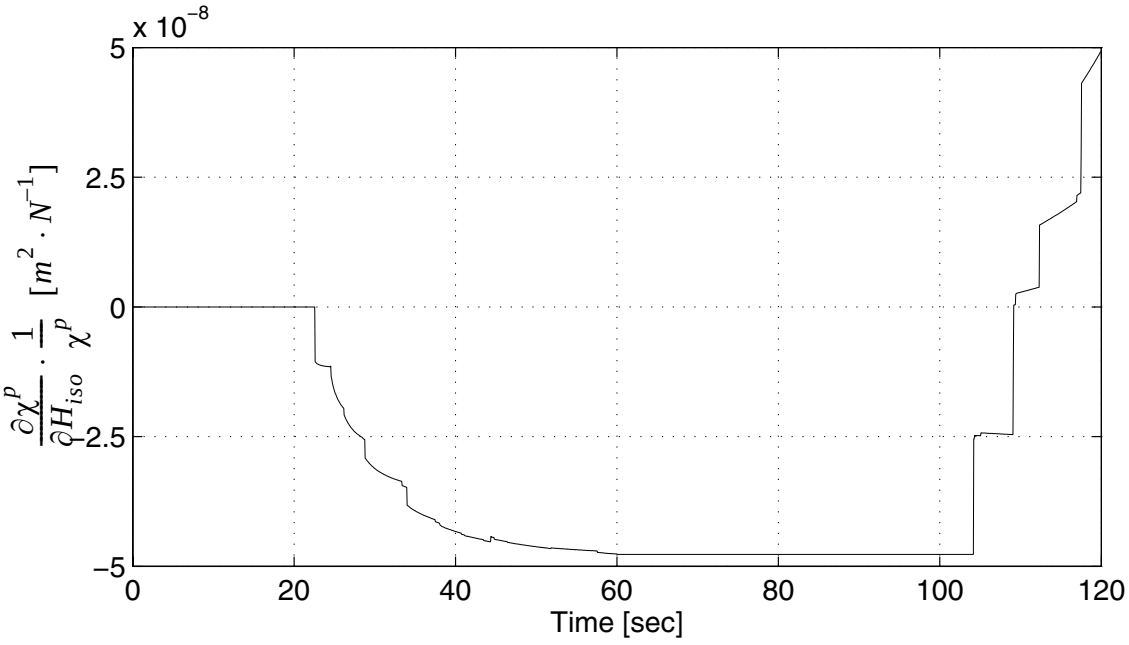


**Figure 3.80 Sensitivity of plastic curvature to $H_{iso}$**

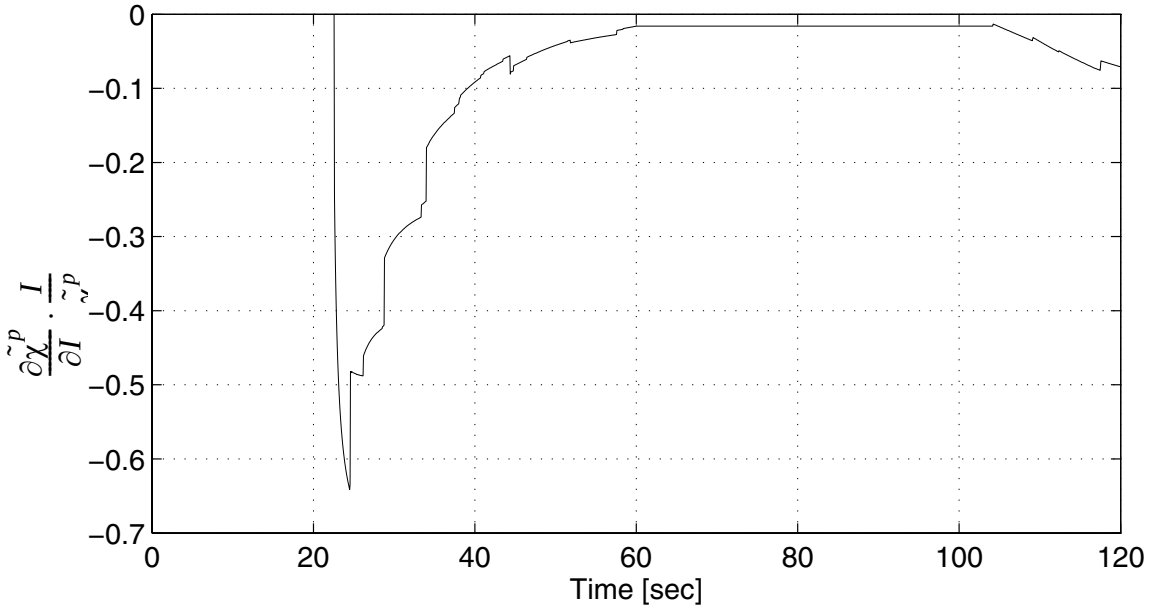


**Figure 3.81 Sensitivity of accumulated plastic curvature to I**

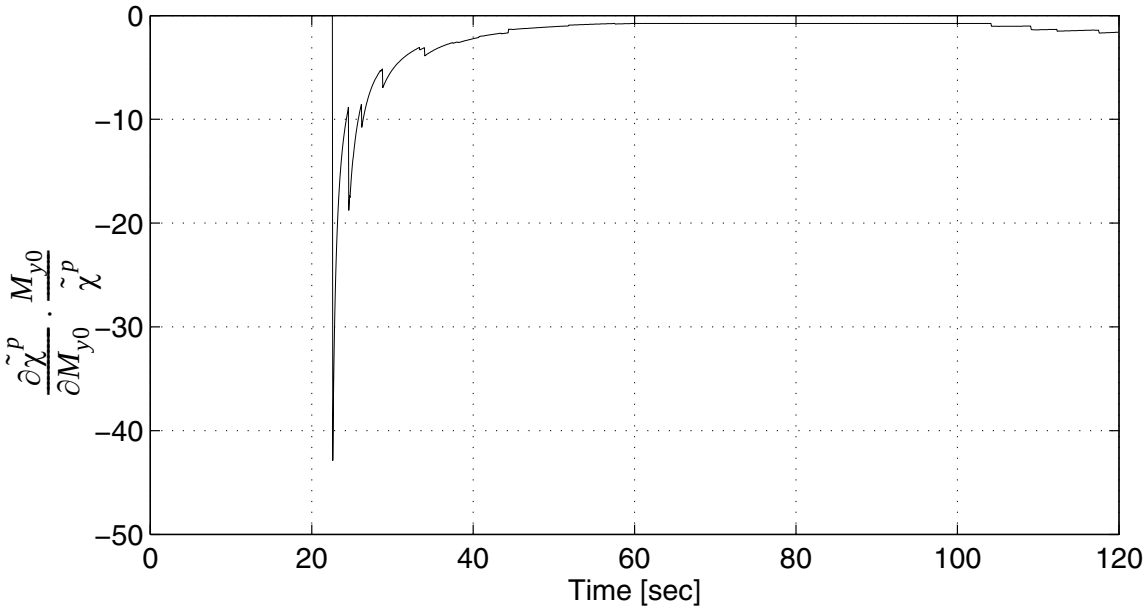


**Figure 3.82 Sensitivity of accumulated plastic curvature to $M_{y0}$**

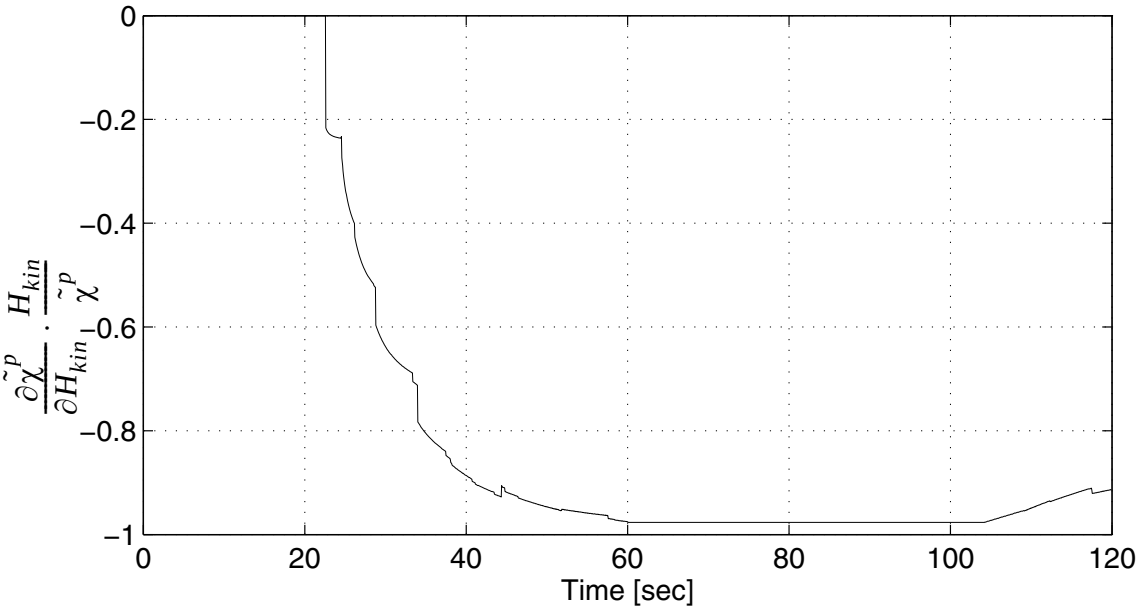


**Figure 3.83 Sensitivity of accumulated plastic curvature to $H_{kin}$**

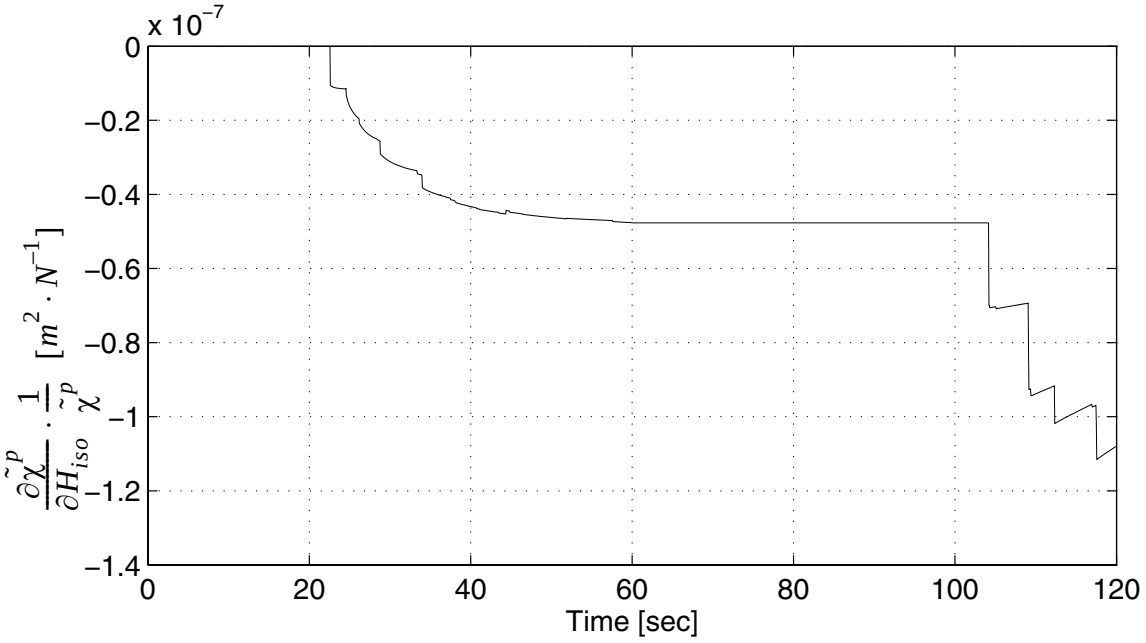


**Figure 3.84 Sensitivity of accumulated plastic curvature to $H_{iso}$**

From the figure above it is clear that:

(1) Each discontinuity in the sensitivity of global or local variables corresponds to a transition of some Gauss points from the elastic to plastic state.

(2) Local discontinuities are bigger than global discontinuities.

(3) Transitions of some Gauss points from the elastic to plastic states will not necessarily cause local or global discontinuities.

(4) Transition of Gauss points from the plastic to elastic states will not cause local or global discontinuities. This could be observed at the unloading time point (t=60 sec).

### 3.5.3 Effect of Damping

A comparison of the response sensitivity analysis between cases involving (1) Rayleigh damping with a damping ratio of 5% and (2) no damping, was performed while considering the same frame and ground excitation as in section 3.5.1. A portion of the results are shown in Figures 3.85 to 3.101. All sensitivities are normalized except the $H_{iso}$ because $H_{iso}$ =0.

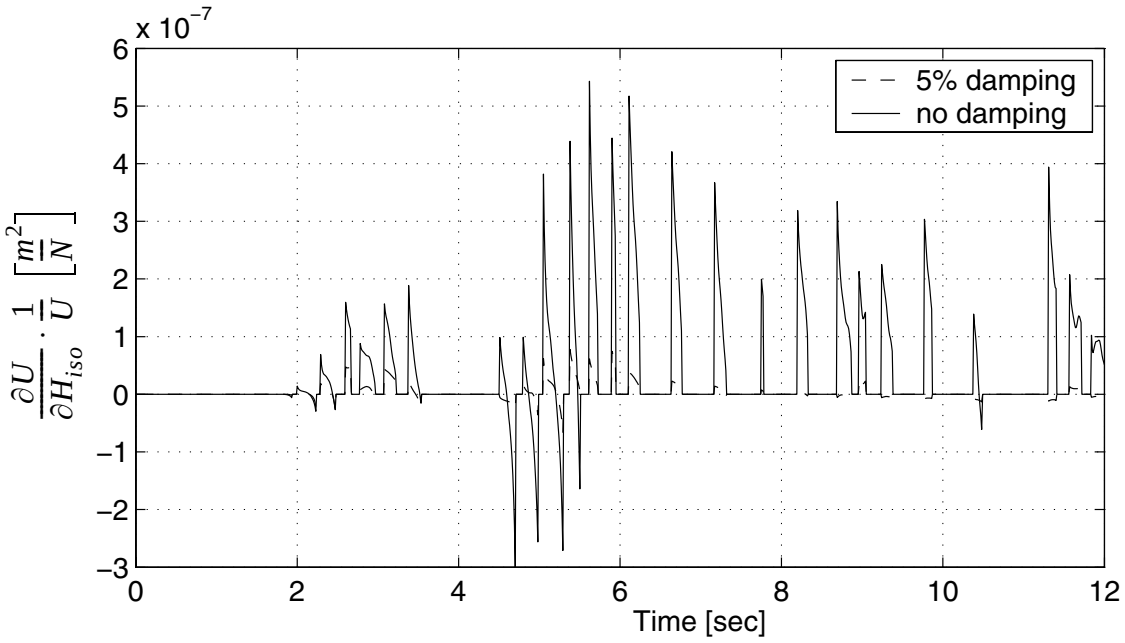


**Figure 3.85 Sensitivity of roof displacement to $H_{iso}$**

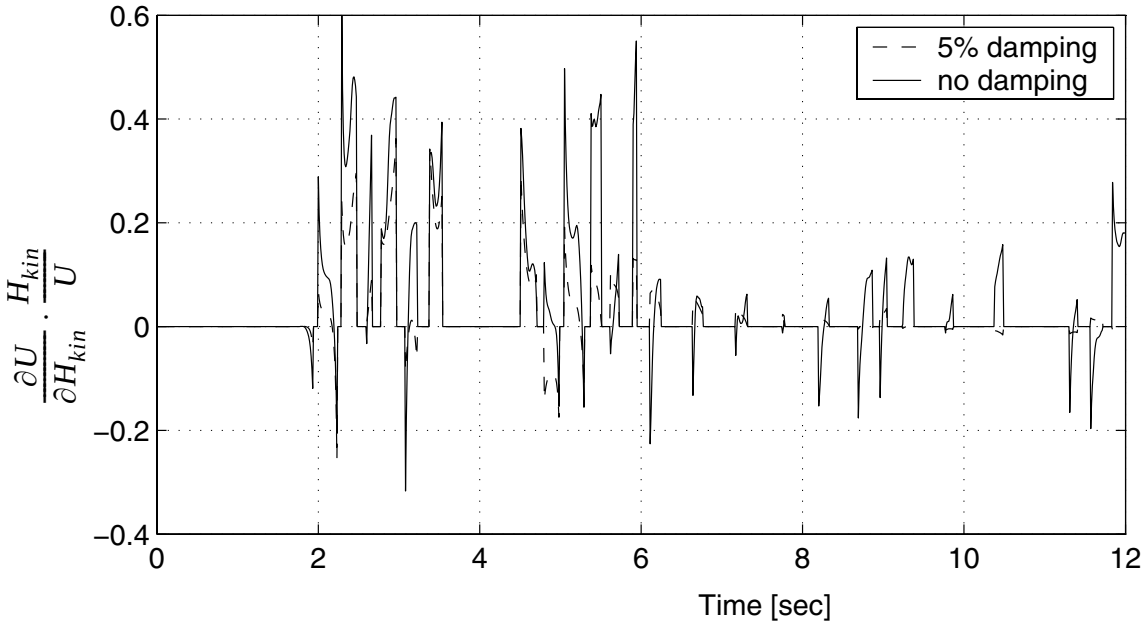


**Figure 3.86 Sensitivity of roof displacement to $H_{kin}$**

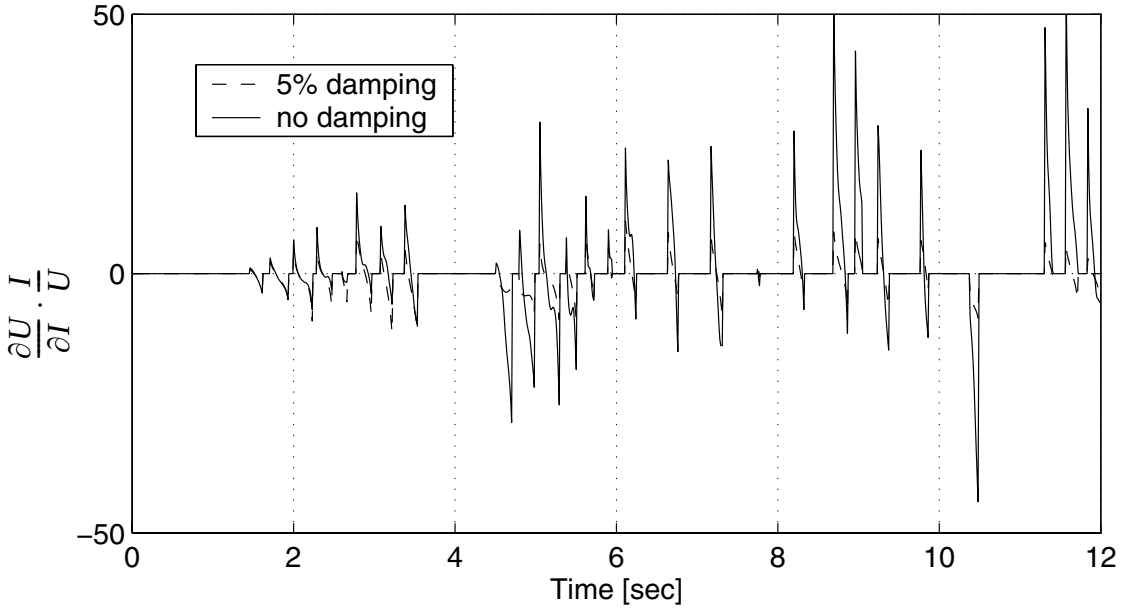


**Figure 3.87 Sensitivity of roof displacement to I**

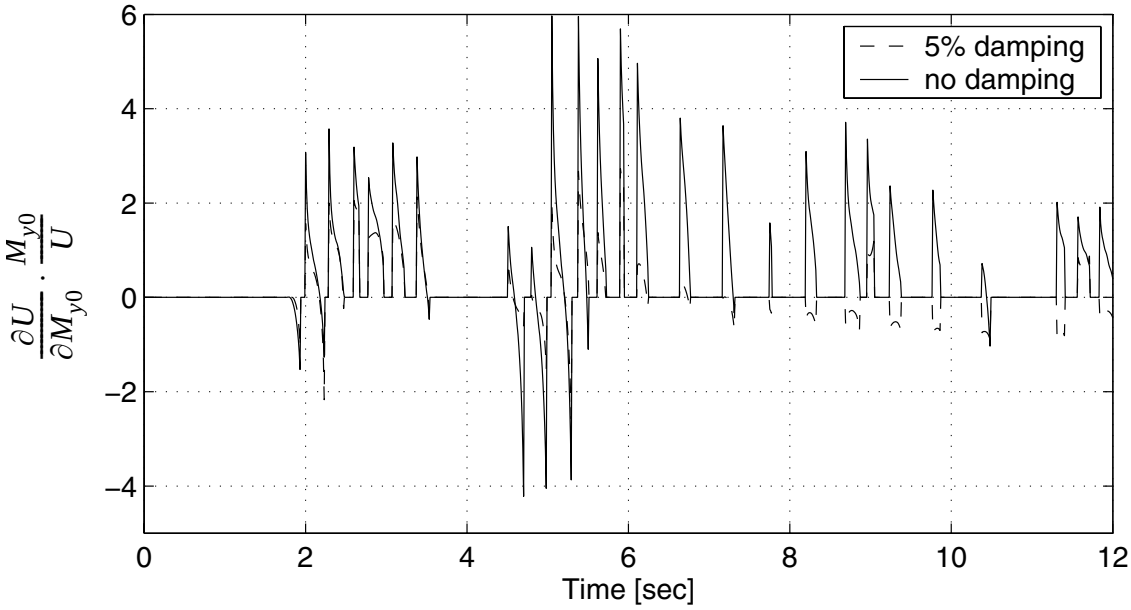


**Figure 3.88 Sensitivity of roof displacement to $M_{y0}$**

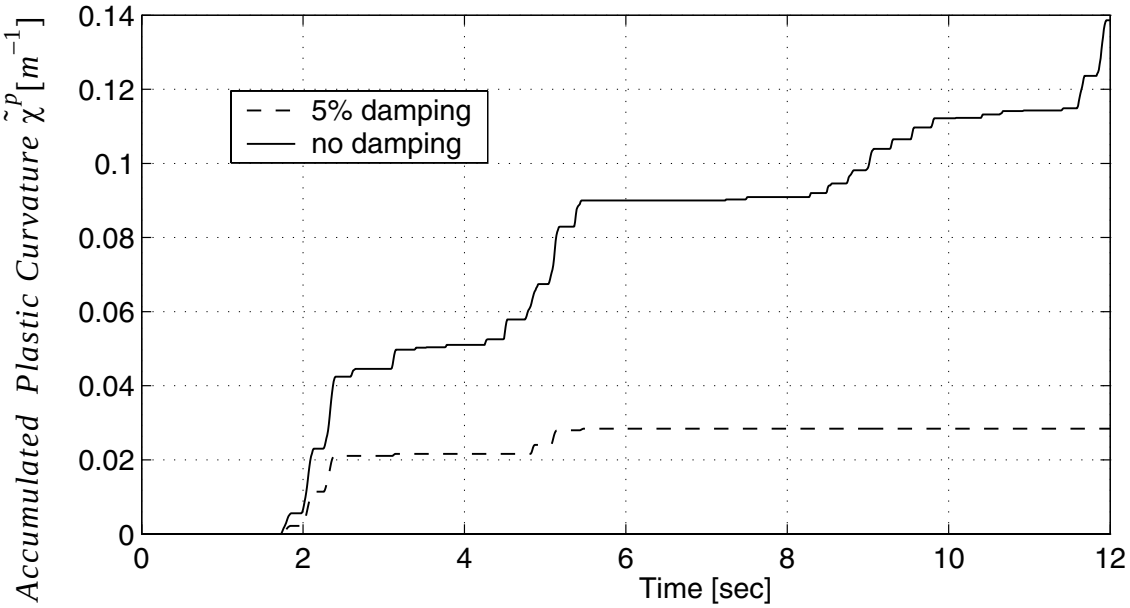


**Figure 3.89 Accumulated plastic curvature**

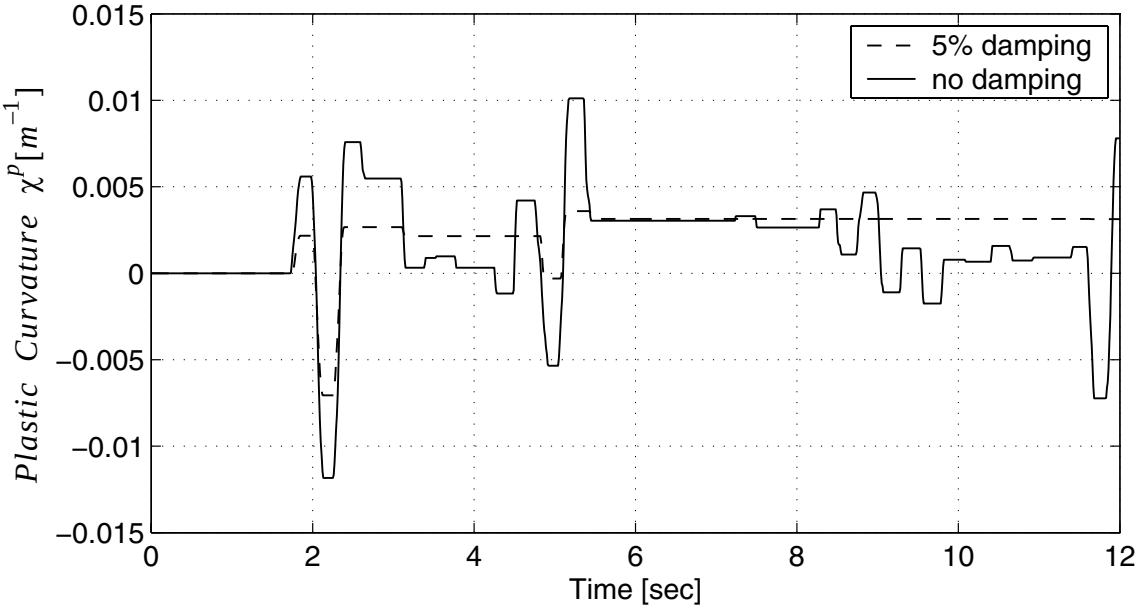


**Figure 3.90 Plastic curvature**

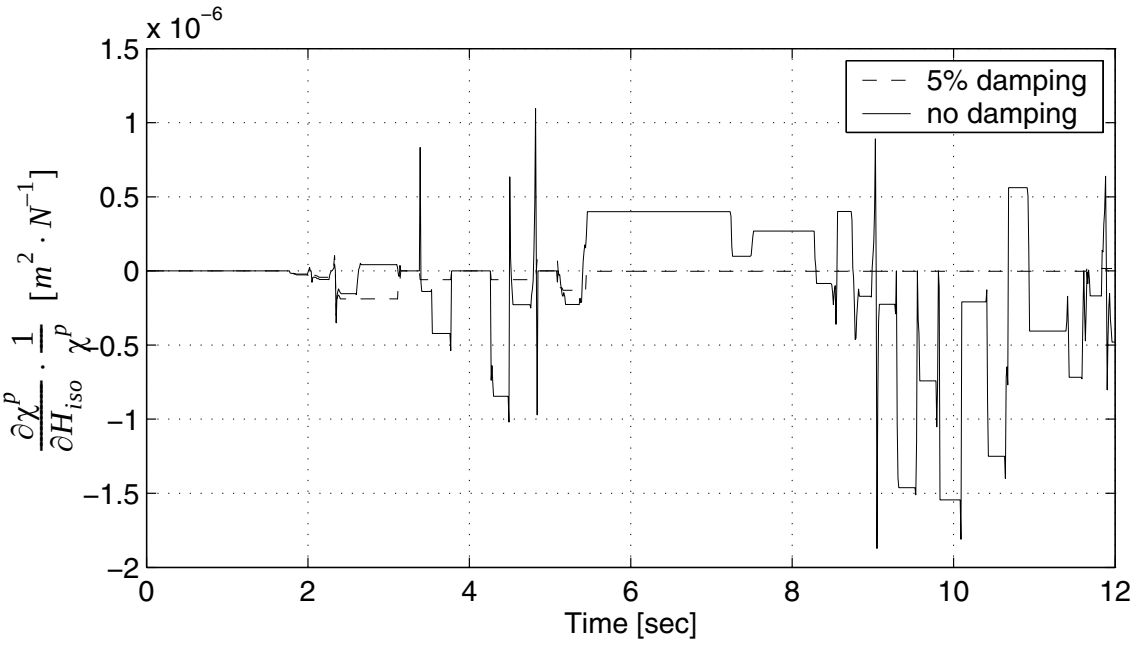


**Figure 3.91 Sensitivity of plastic curvature to $H_{iso}$**

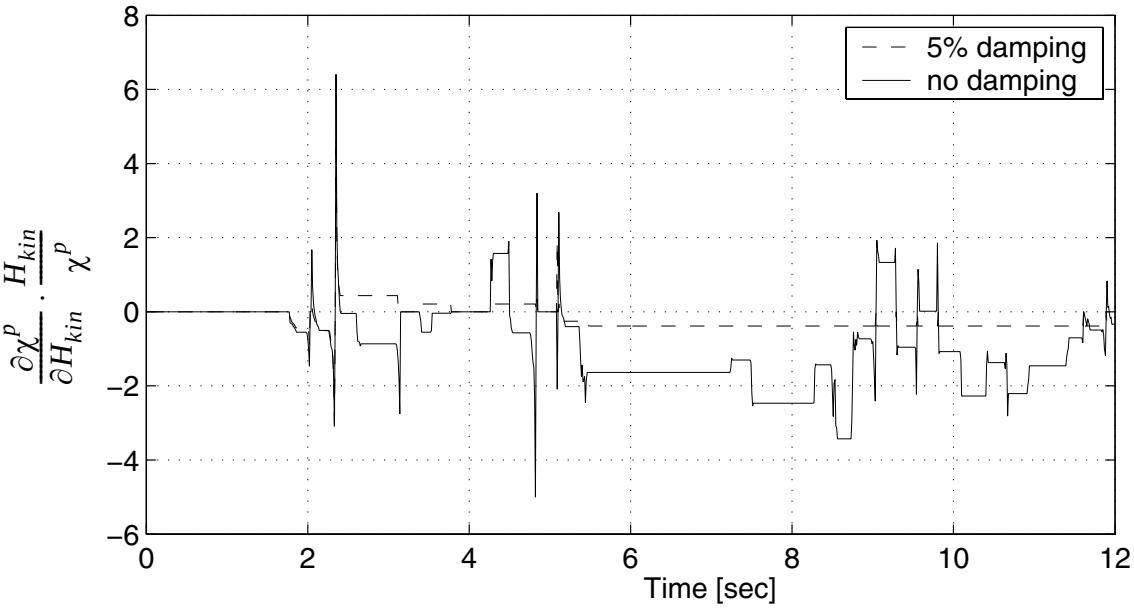


**Figure 3.92 Sensitivity of plastic curvature to $H_{kin}$**

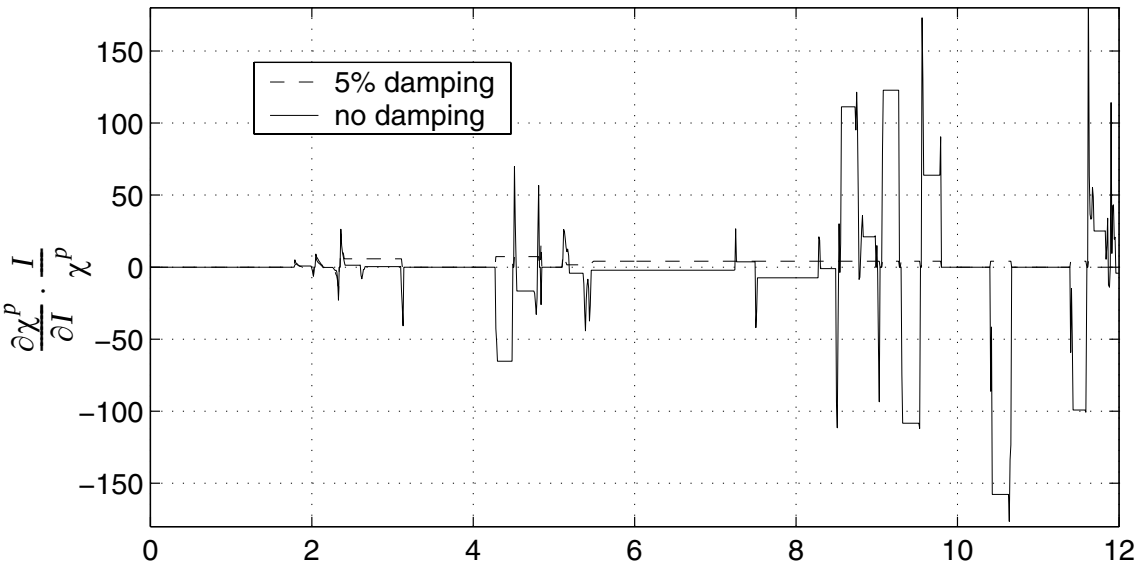


**Figure 3.93 Sensitivity of plastic curvature to I**

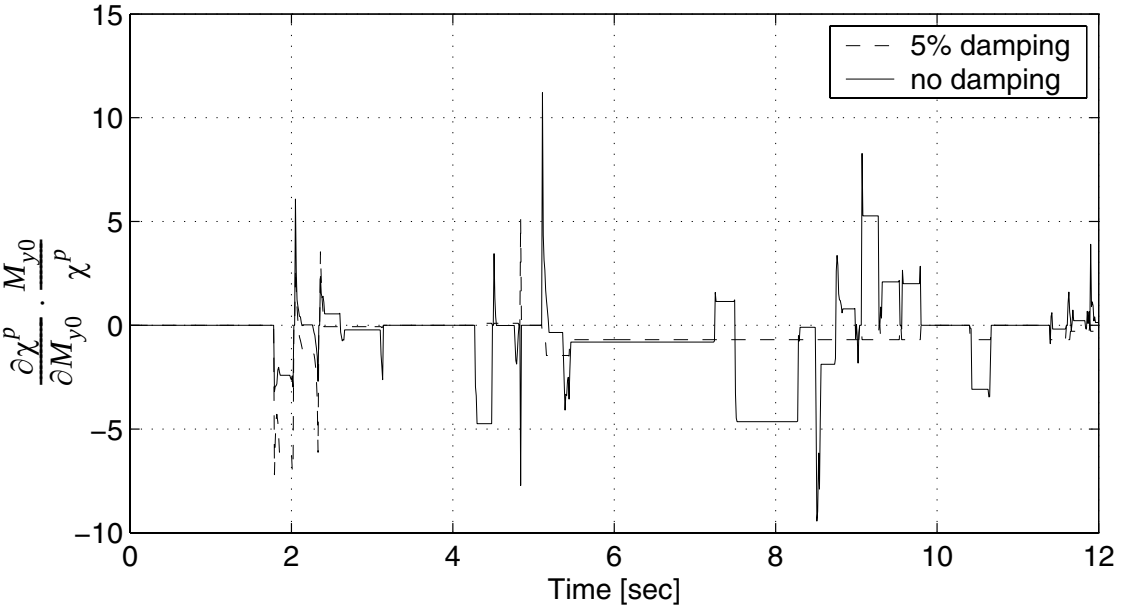


**Figure 3.94 Sensitivity of plastic curvature to $M_{y0}$**

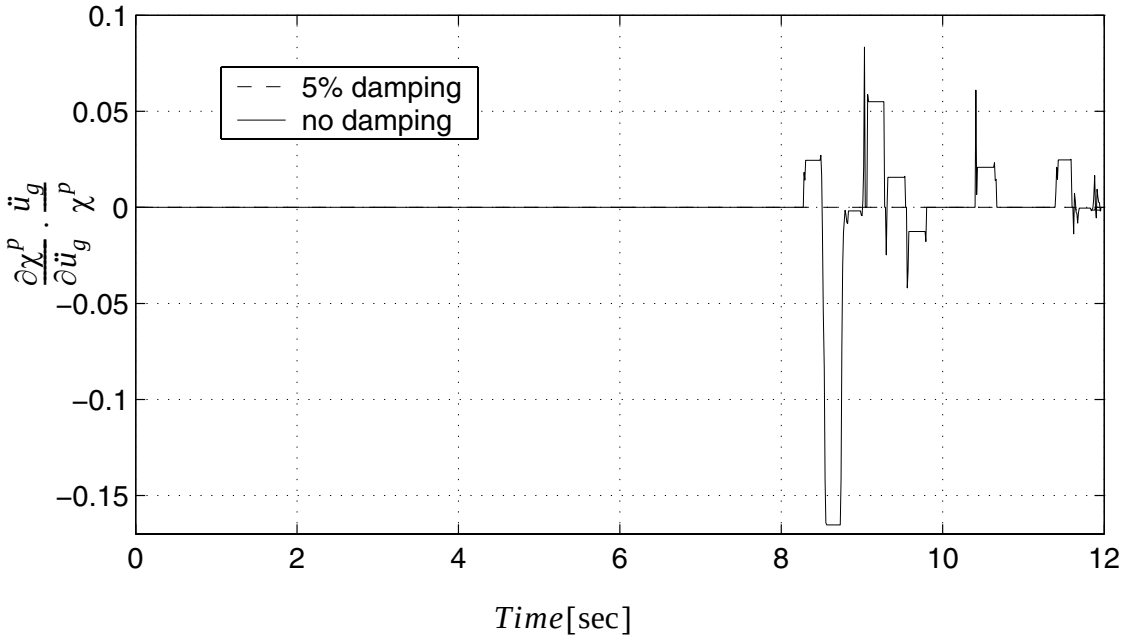


**Figure 3.95 Sensitivity of plastic curvature to $\ddot{u}_g(t = 7.60s)$**

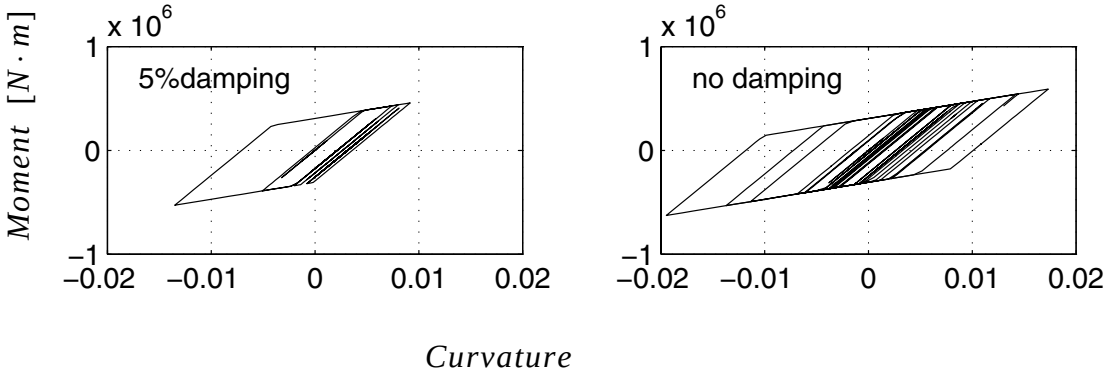


**Figure 3.96 Moment curvature responses**

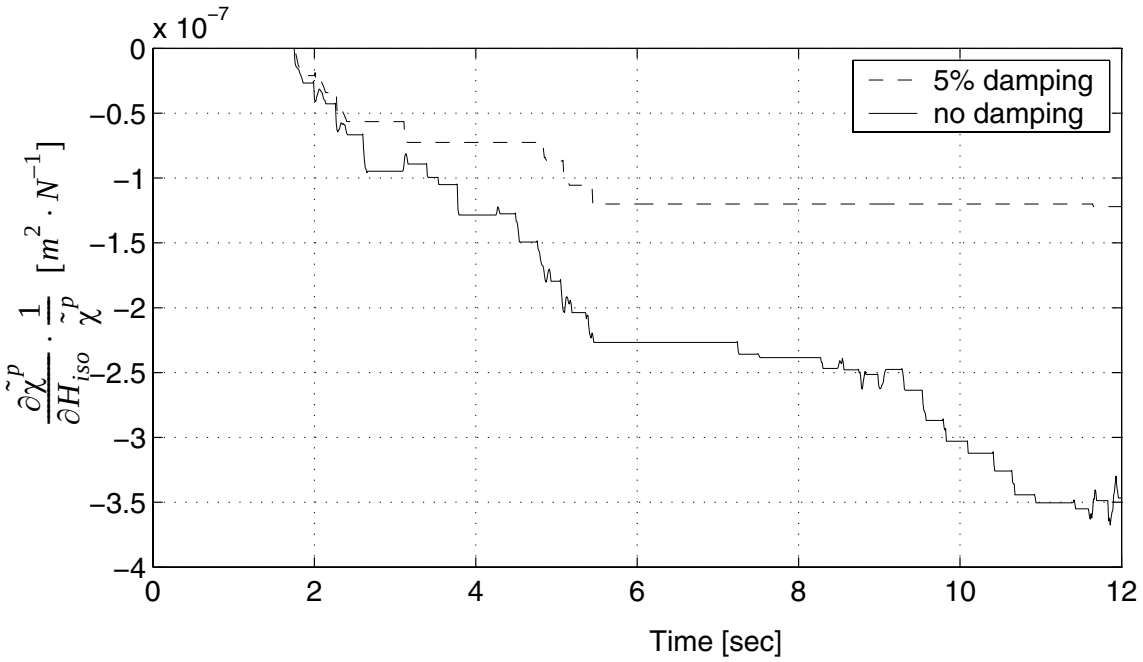


**Figure 3.97 Sensitivity of accumulated plastic curvature to $H_{iso}$**

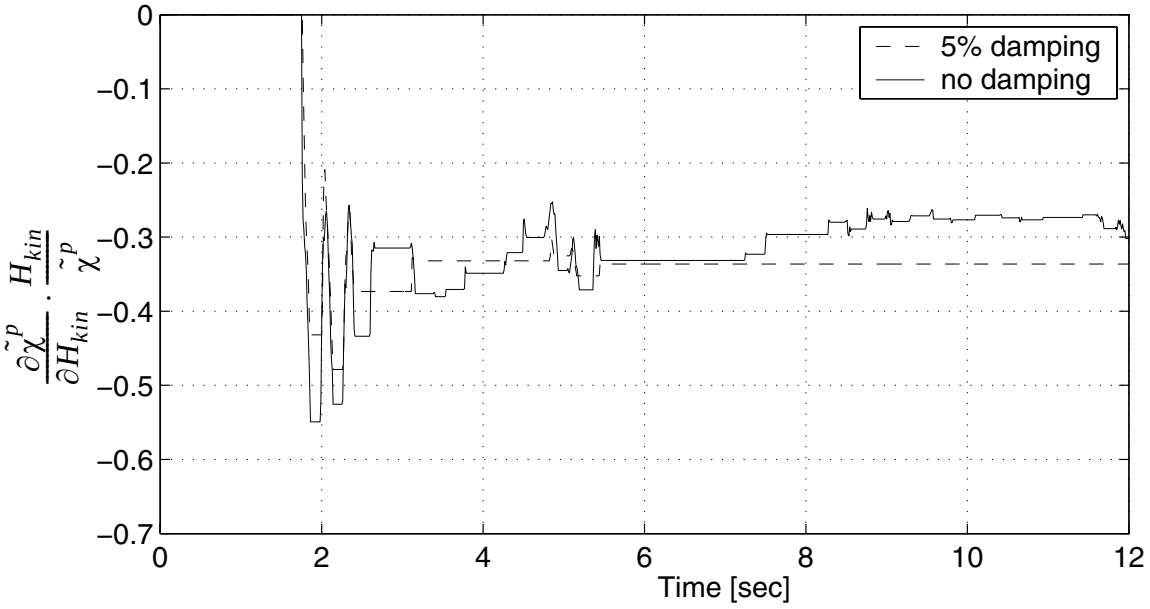


**Figure 3.98 Sensitivity of accumulated plastic curvature to $H_{kin}$**

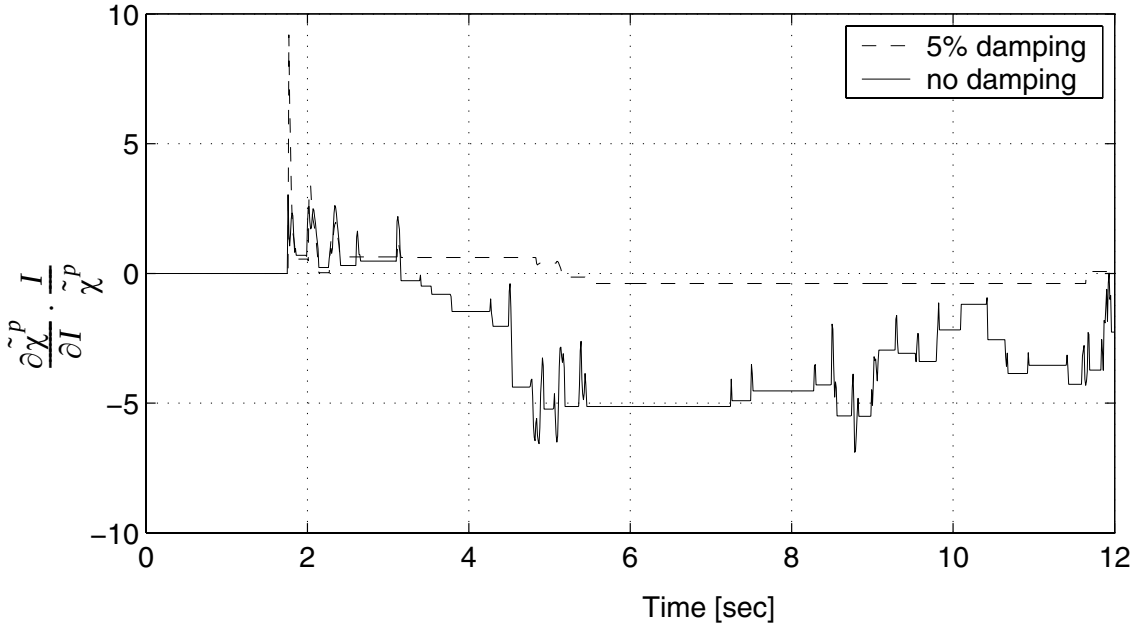


**Figure 3.99 Sensitivity of accumulated plastic curvature to I**

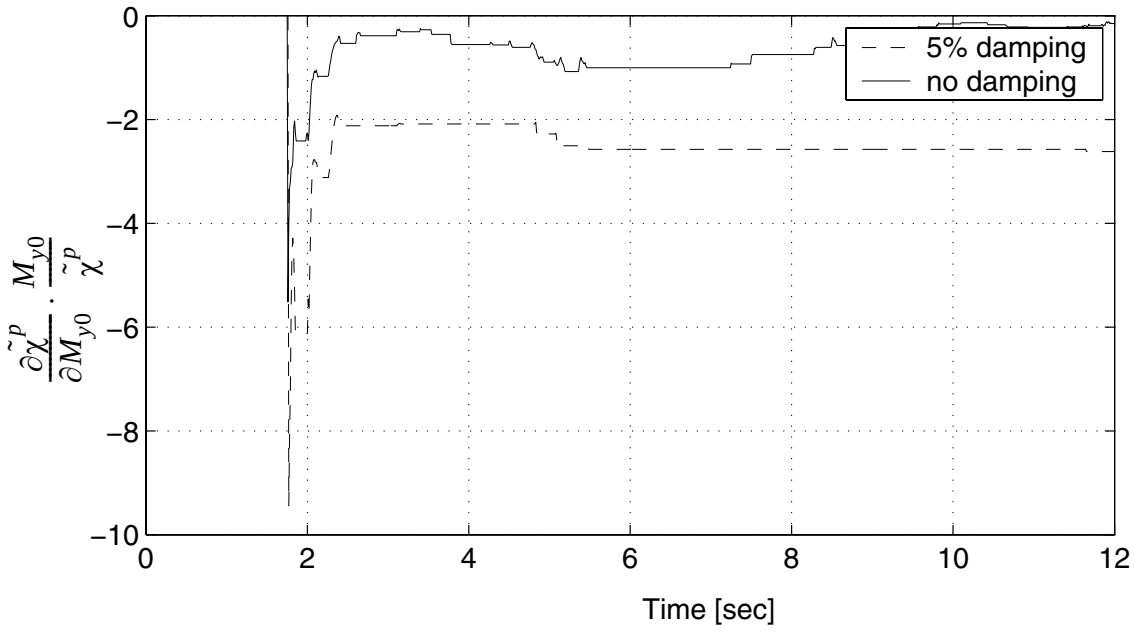


**Figure 3.100 Sensitivity of accumulated plastic curvature to $M_{y0}$**

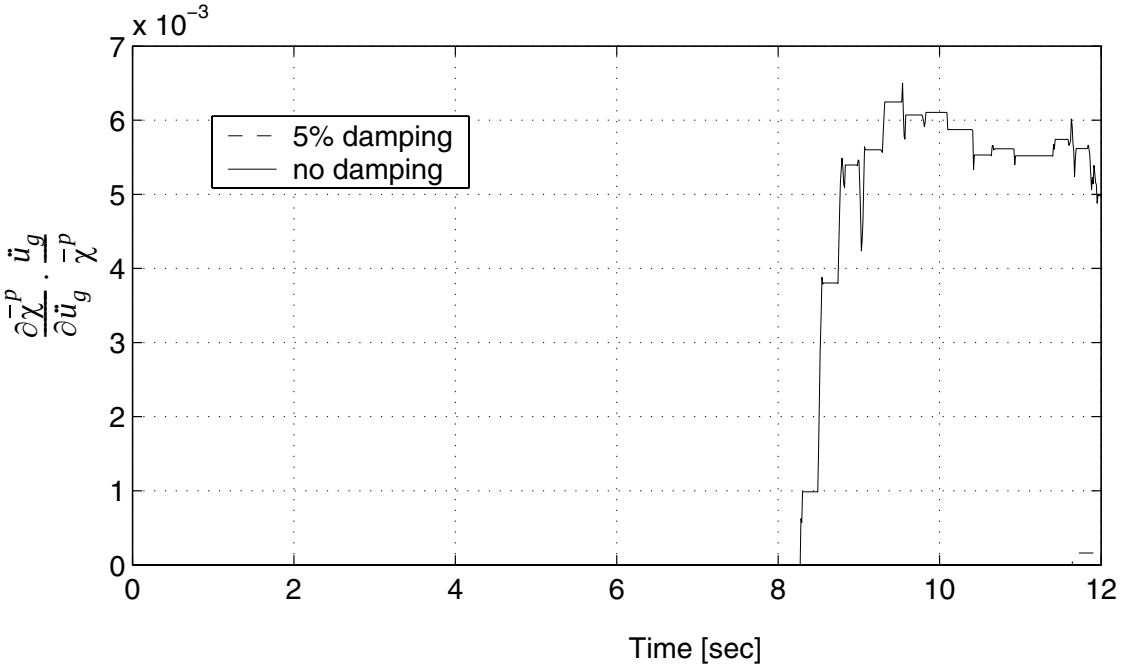


**Figure 3.101 Sensitivity of $\bar{\chi}^p$ to $\ddot{u}_g(t = 7.60s)$**

From these figures the following conclusions can be made:

(1) Both global and local response sensitivities decrease when 5% damping is considered than when it is not.

(2) When damping is considered, discontinuities of response sensitivities become smaller than for the dampingless case.

### 3.5.4 Post Stiffness Studies

Based on the same dampingless frame and earthquake scenario as in section 3.5.1, a comparison of the frame response sensitivities is made between a non-post-stiffness case

(with zero $H_{kin}$) and a 20% post-stiffness case. Part of the results are shown in Figures 3.102 through 3.117.

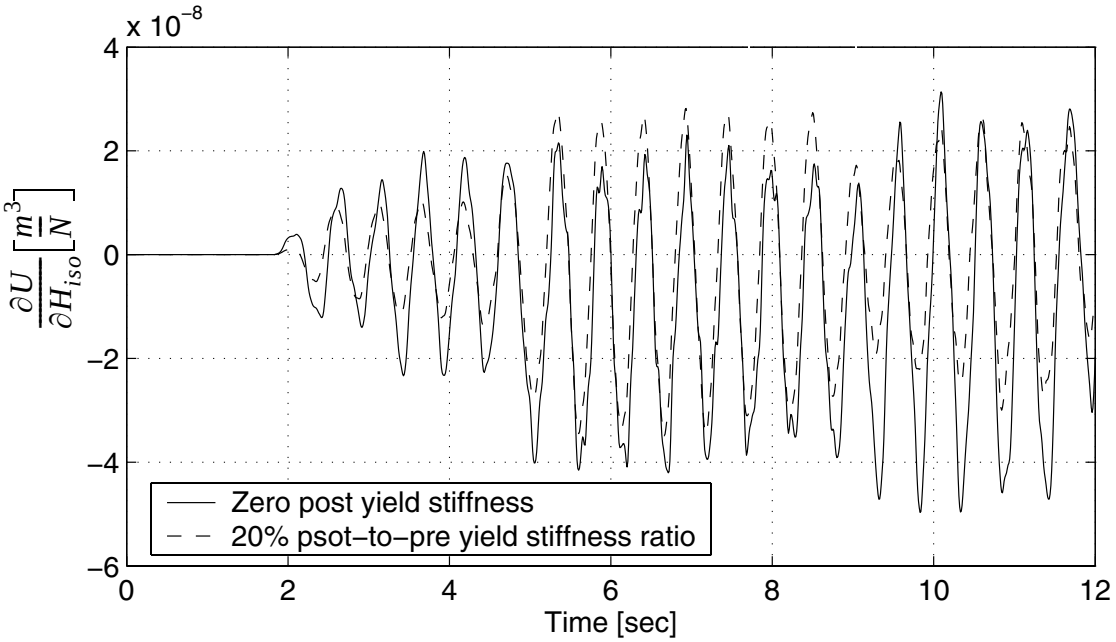


**Figure 3.102 Response sensitivity of roof displacement to $H_{iso}$**

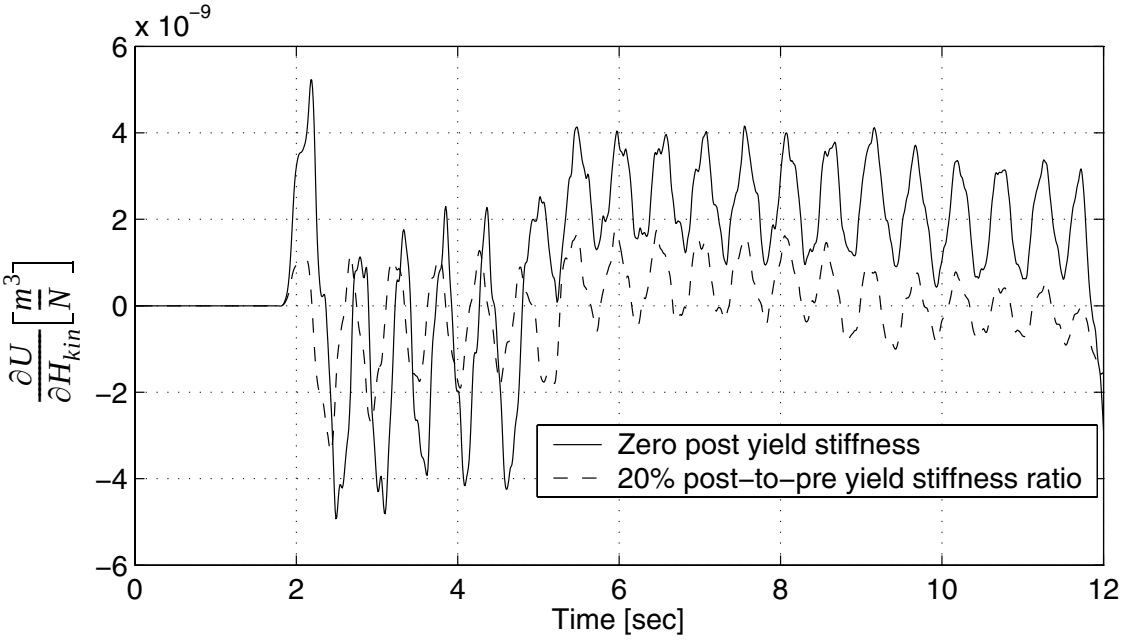


**Figure 3.103 Response sensitivity of roof displacement to $H_{kin}$**

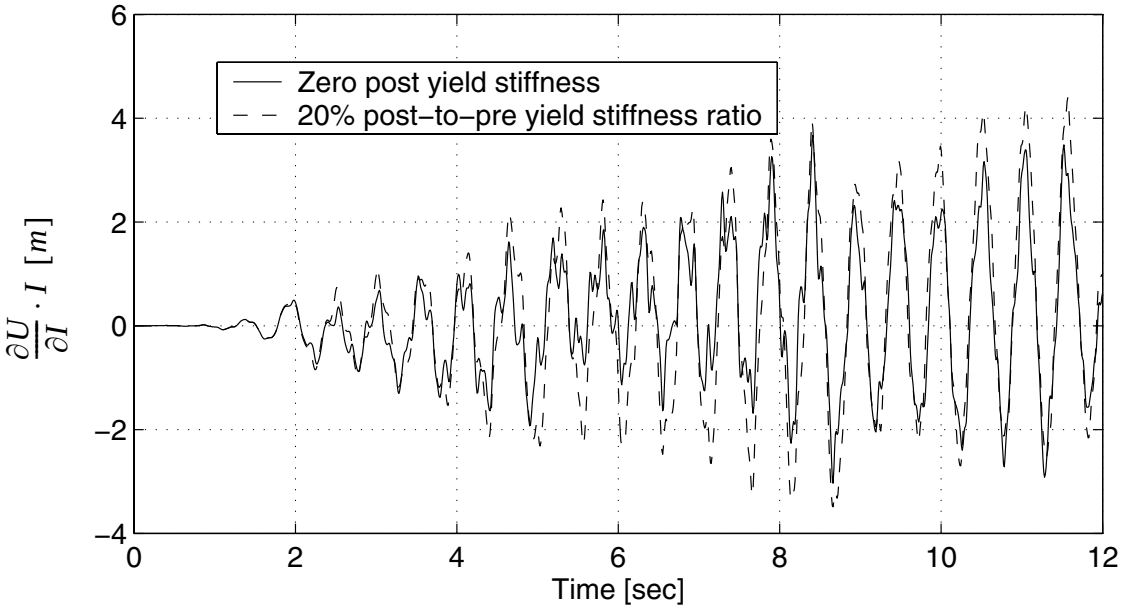


**Figure 3.104 Response sensitivity of roof displacement to I**

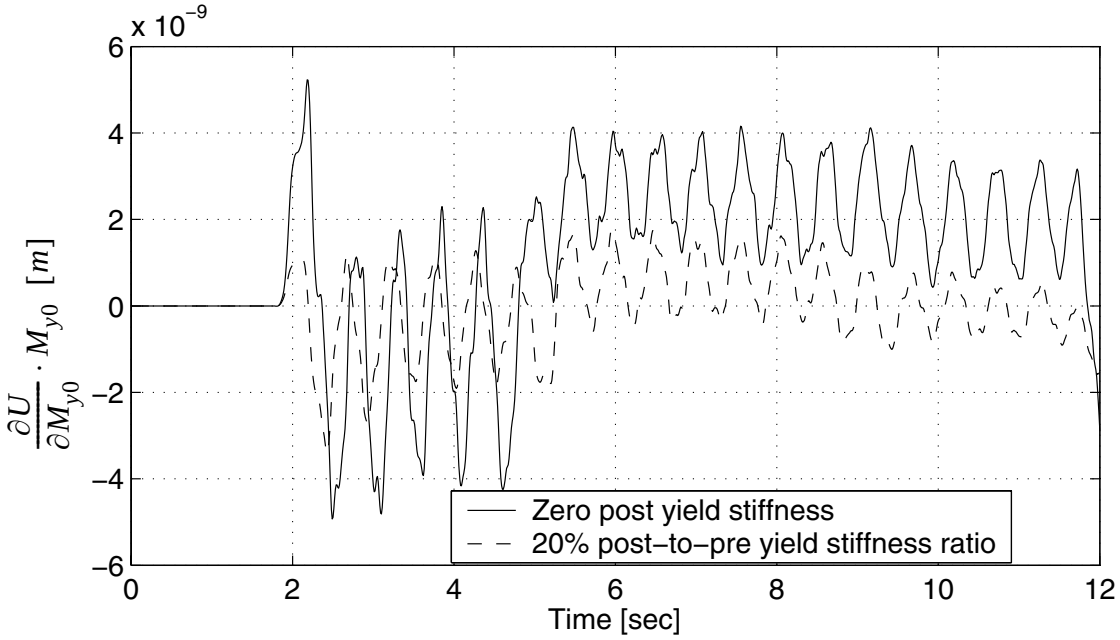


**Figure 3.105 Response sensitivity of roof displacement to $M_{y0}$**

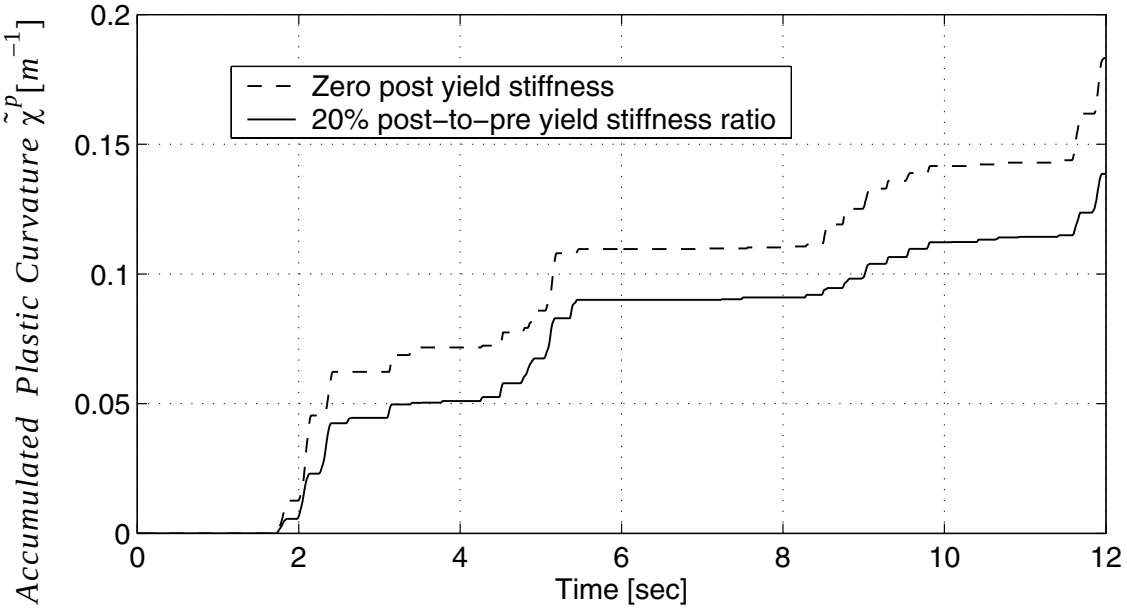


**Figure 3.106 Accumulated plastic curvature**

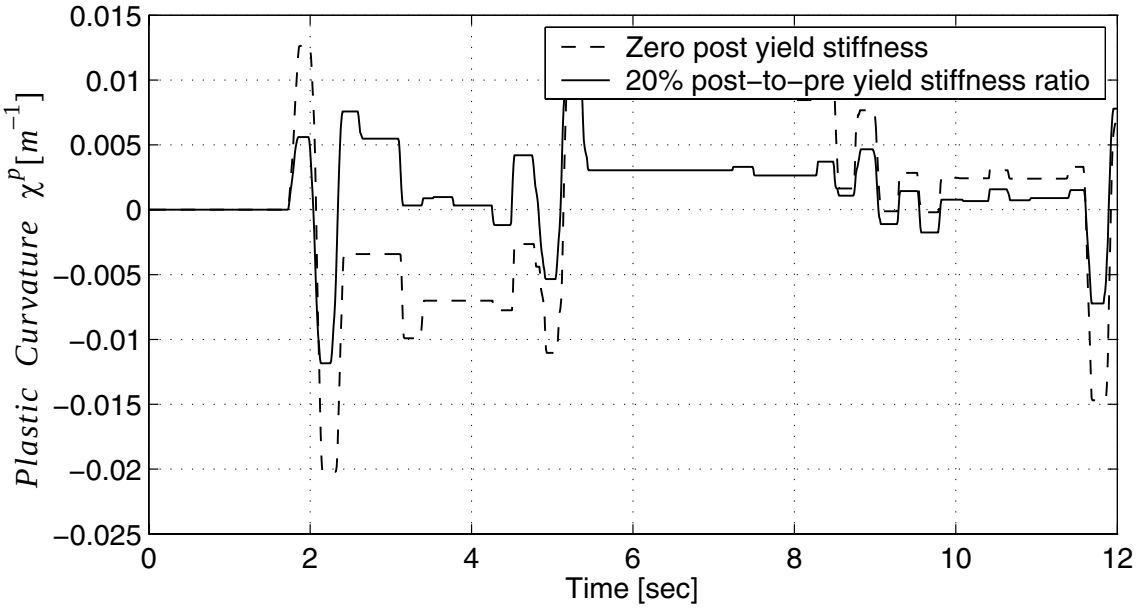


**Figure 3.107 Plastic curvature**

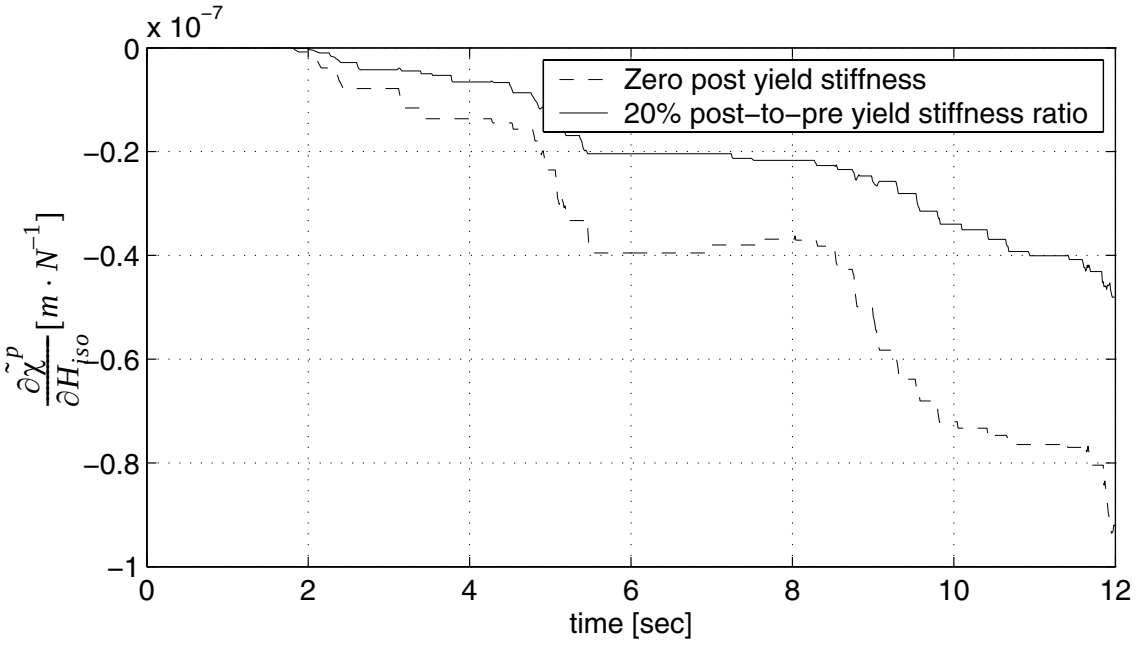


**Figure 3.108 Sensitivity of accumulated plastic curvature to $H_{iso}$**

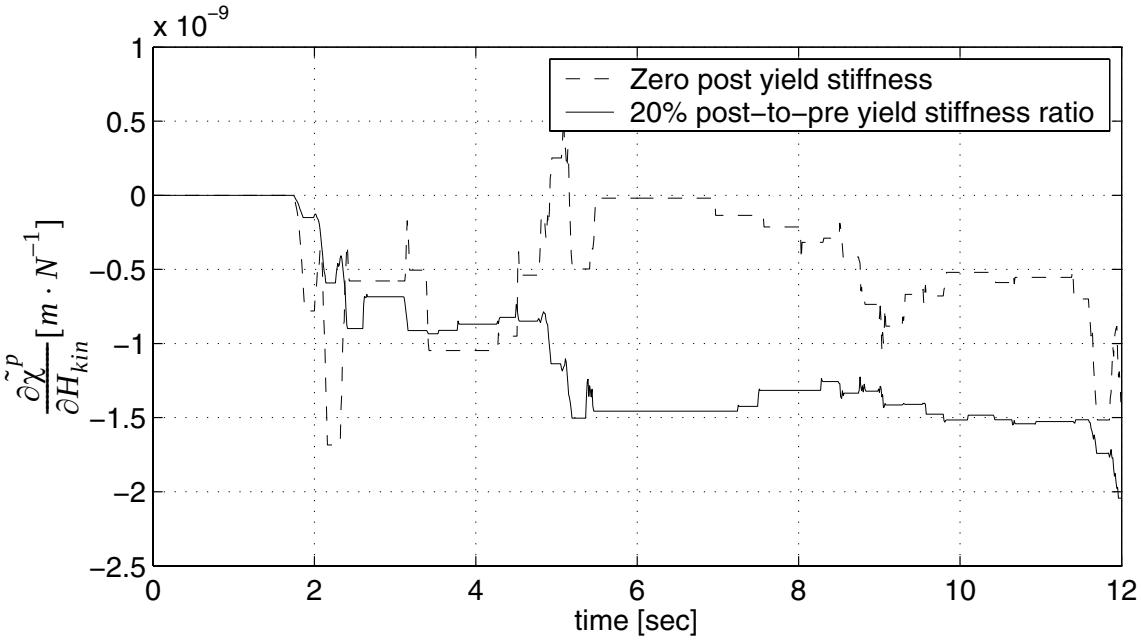


**Figure 3.109 Sensitivity of accumulated plastic curvature to $H_{kin}$**

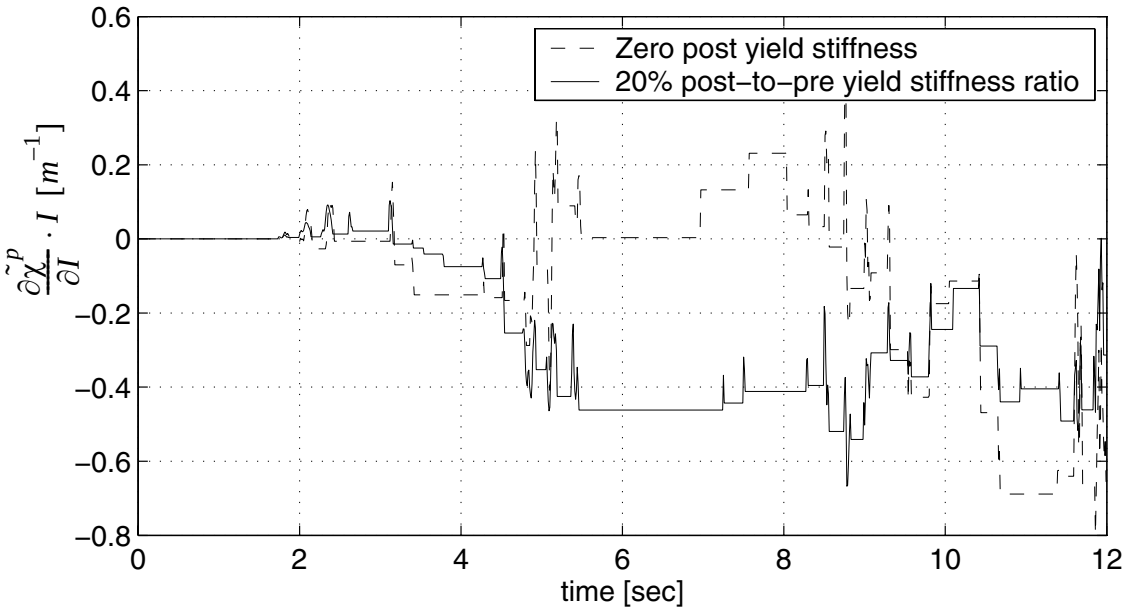


**Figure 3.110 Sensitivity of accumulated plastic curvature to I**

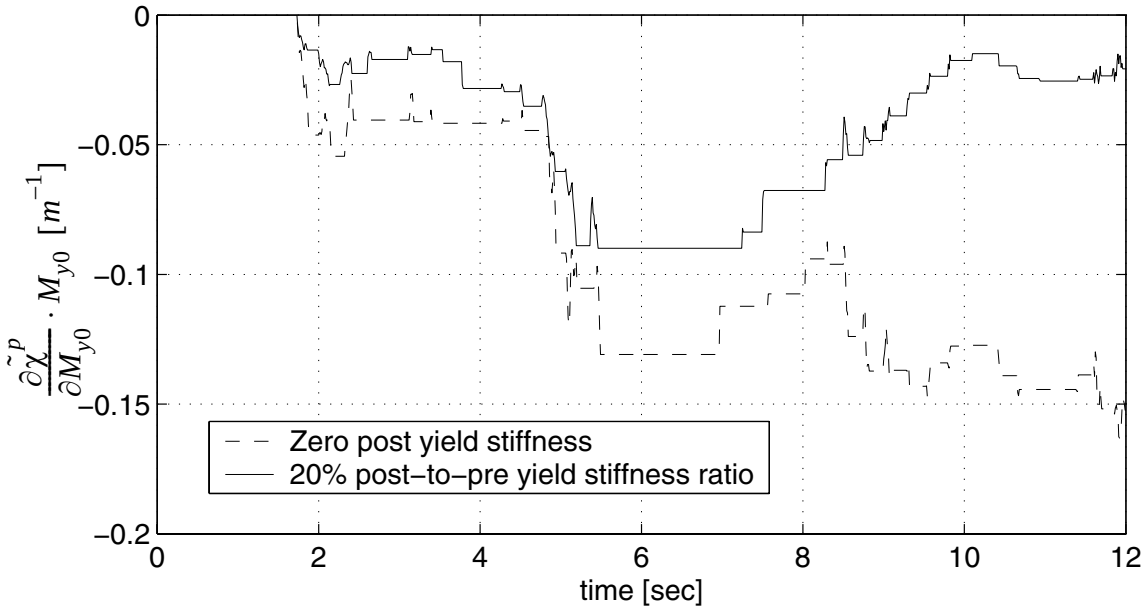


**Figure 3.111 Sensitivity of accumulated plastic curvature to $M_{y0}$**

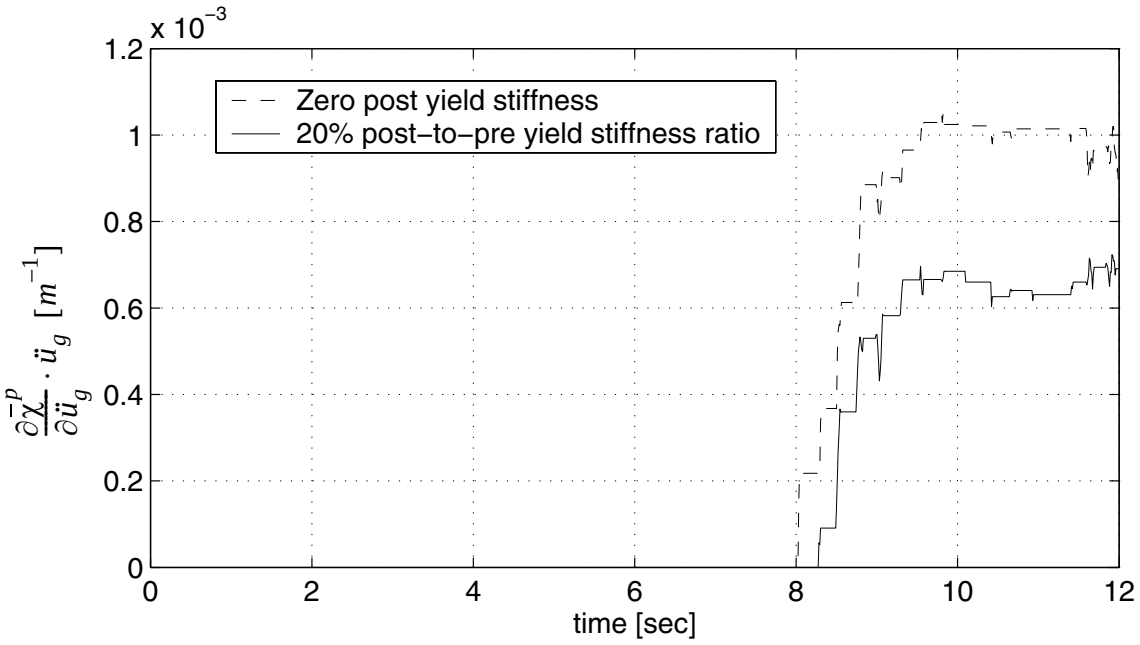


**Figure 3.112 Sensitivity of $\bar{\chi}^p$ to $\ddot{\boldsymbol{u}}_g(t = 7.60s)$**

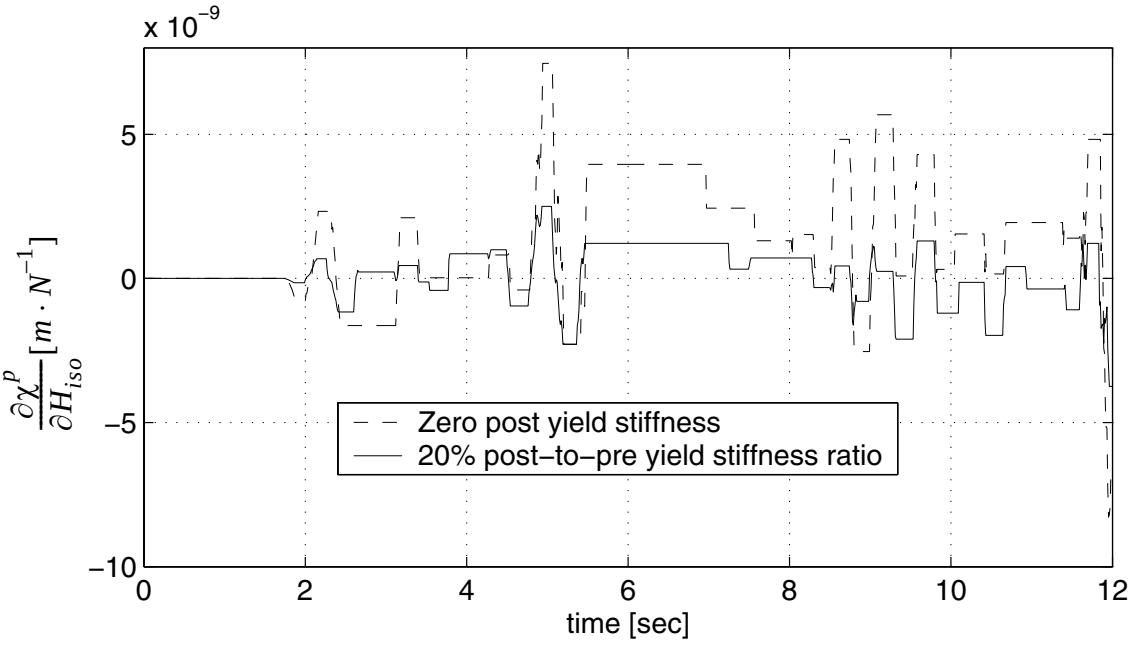


**Figure 3.113 Sensitivity of plastic curvature to $H_{iso}$**

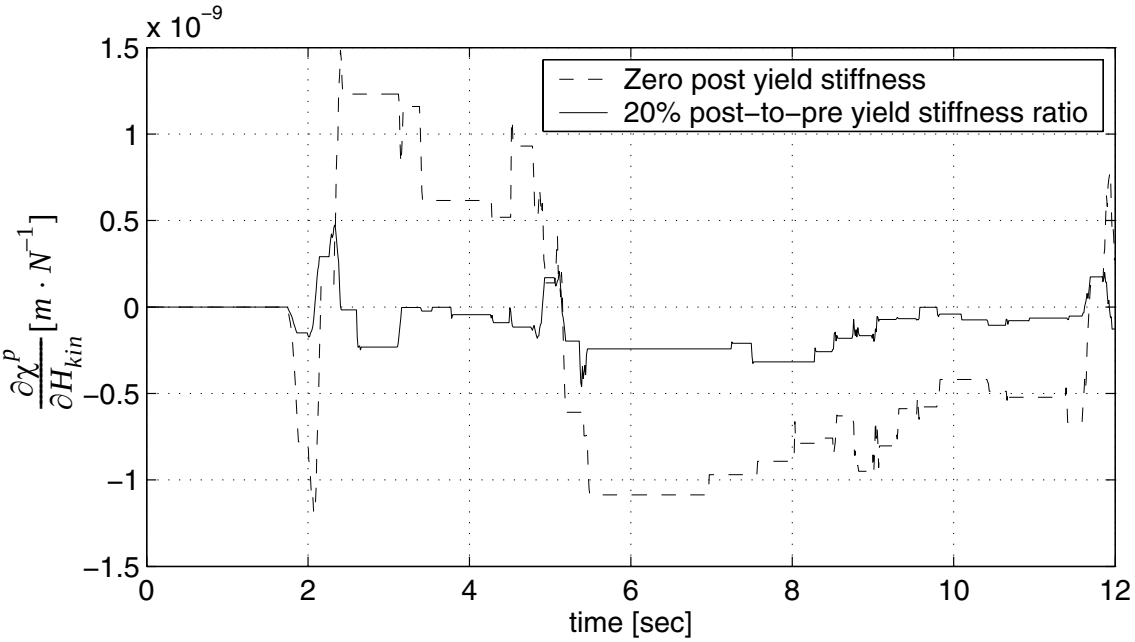


**Figure 3.114 Sensitivity of plastic curvature to $H_{kin}$**

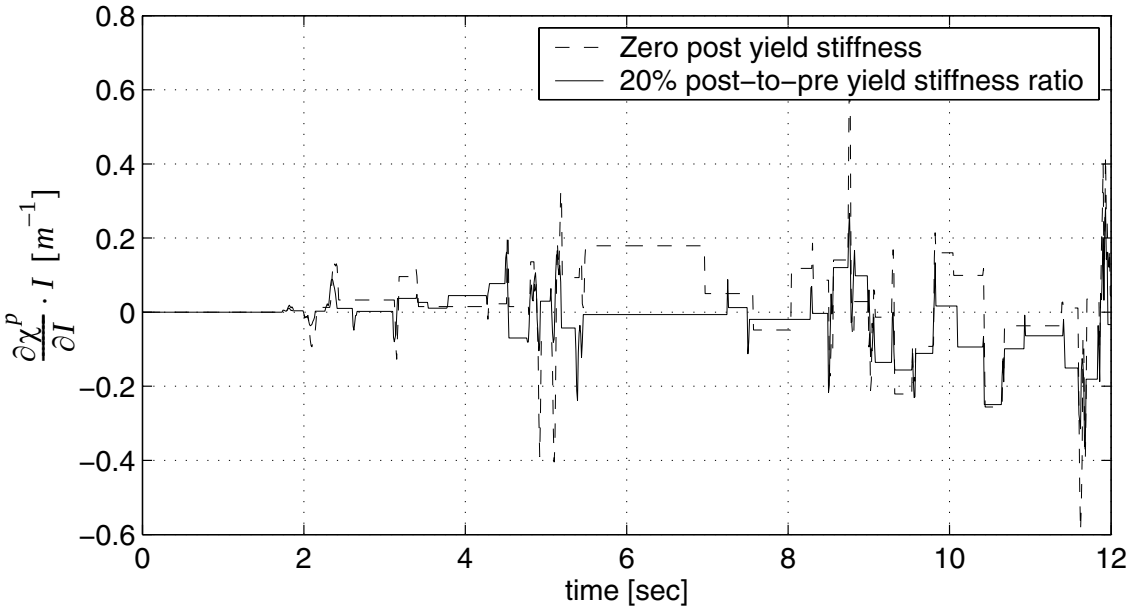


**Figure 3.115 Sensitivity of plastic curvature to I**

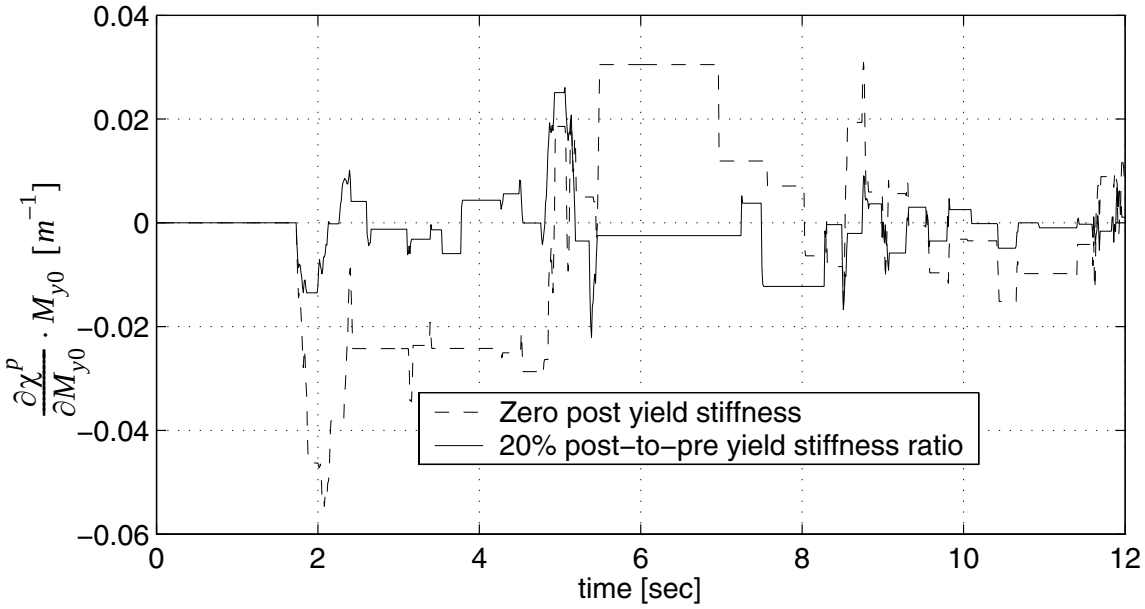


**Figure 3.116 Sensitivity of plastic curvature to $M_{y0}$**

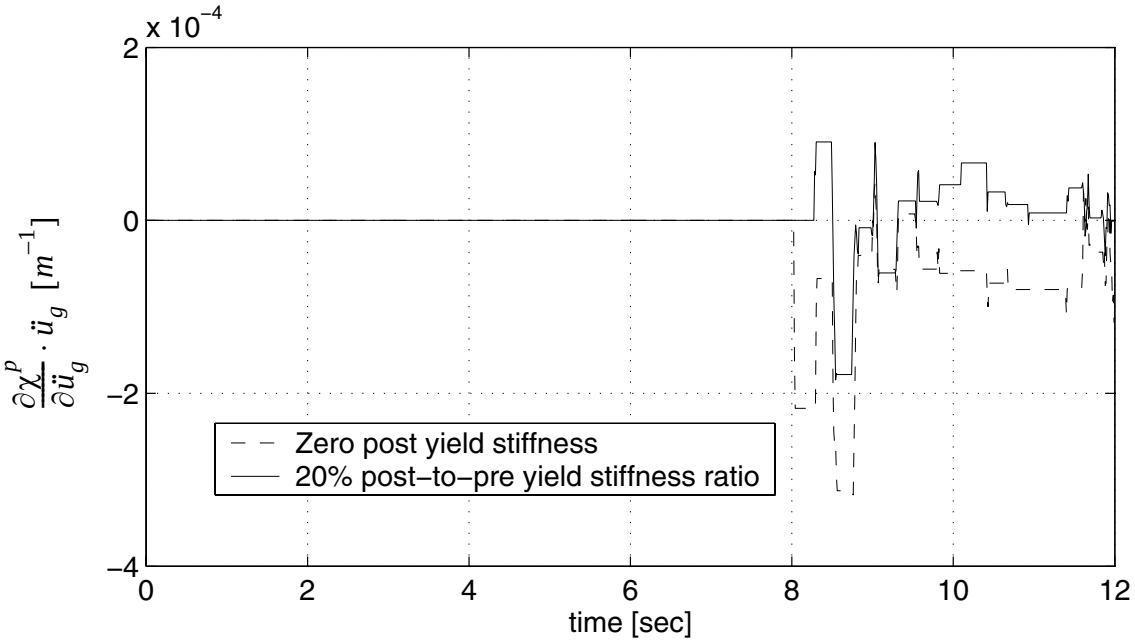


**Figure 3.117 Sensitivity of $\chi^p$ to $\ddot{\boldsymbol{u}}_g(t= 7.60s)$**

From these figures, it is observed that in most cases, in contrast to the 20% post stiffness case, zero post-stiffness leads to:

(1) greater sensitivities.

(2) further shifting of both responses and their sensitivities from zero.

(3) greater discontinuities of response sensitivities.

## 3.6 Conclusions for the Issues of the Sensitivity Analysis

In this section, the complete response sensitivity analysis derivation based on Direct Differentiation Method (DDM) is presented. This derivation considers the differentiation of the FE algorithm for the response computation with respect to the material, geometry

and load parameters. The response sensitivity computation algorithm involves the various hierarchical layers of FE response analysis, namely: (1) structure level, (2) element level, (3) Gauss point level (or section level), and (4) material level. As an illustration example, sensitivity analysis for a 1D Von Mises $J_2$ plasticity material model is performed. Based on the example, many issues of sensitivity are studied.

When using FFD to verify DDM results, the FFD results converge to the DDM results asymptotically with reduced perturbation $\frac{\Delta\theta}{\theta}$ . For each random variable there is a best value and an acceptable range of the perturbation $\frac{\Delta\theta}{\theta}$ , beyond which the FFD results diverge due to the round off error.

The convergence of variable sensitivities based on DDM is studied. It is found that the convergence of the response sensitivities, with respect to both temporal and spatial resolutions, is slower than the convergence of the responses. The sensitivity discontinuity is caused by the stress state transition at Gauss points from the elastic to plastic state. However this transition is not guaranteed to cause discontinuities.

Damping effects both the response sensitivities and their discontinuities: when damping is considered, global and local response sensitivities decrease, and the discontinuities of response sensitivities become smaller.

Post-stiffness also affects response sensitivities and their discontinuities: in contrast to the nonzero post-stiffness case, zero post-stiffness leads to greater sensitivities, further shifting of both responses and their sensitivities from zero, and greater discontinuities of response sensitivities.

# CHAPTER 4

# FINITE ELEMENT RESPONSE SENSITIVITY ANALYSIS FRAMEWORK FOR STRUCTURAL AND GEOTECHNICAL SYSTEM

## 4.1 Introduction

In this Chapter, a multi-yield-surface $J_2$ plasticity model, used to simulate clay behavior, is introduced into the sensitivity and reliability framework. The derivations of the consistent tangent modulus and response sensitivity are developed for this model. Response sensitivity analysis is performed on several SSI systems which are modeled using the aforementioned soil model and existing material models for structures.

## 4.2 Multi-Yield-Surface $J_2$ Plasticity Clay Model

This section illustrates in detail the existing multi-yield-surface $J_2$ plasticity model. This plasticity model was first developed by Iwan (1967) and Mroz (1967) , then applied by Prevost in soil mechanics (1977, 1978), and recently implemented in OpenSees by Elgamal et al. (2002, 2003) with the tangent stiffness matrix based on the continuum tangent moduli. OpenSees is an open source software framework for advanced modeling and simulation of structural and geotechnical systems developed under the auspice of the

Pacific Earthquake Engineering Research (PEER) Center. In contrast to the classical $J_2$ (or Von Mises) plasticity model with a single yield surface, the multi-yield-surface $J_2$ plasticity model employs the concept of a field of plastic moduli (Prevost 1977, 1978) to achieve a better representation of the material plastic behavior under cyclic loading conditions. This field is defined by a collection of nested yield surfaces of constant size (i.e., no isotropic hardening) in the stress space, which define the regions of constant plastic shear moduli (and constant tangent shear moduli). At each time or load step, it is not possible to know a priori which and how many yield surfaces will be reached (or activated) until convergence (or global equilibrium) is achieved at this step. Hence, the expression of the consistent tangent moduli (or operators) at the current stress point (not necessarily converged) depends on all of those yield surfaces that have contributed to the change of stress state from the last converged time or load step.

### 4.2.1 Multi-Yield Surface

Each yield surface of this multi-yield-surface $J_2$ plasticity model is defined in the deviatoric stress space as

$$f = \left\{ \frac{3}{2} ((\boldsymbol{\tau} - \boldsymbol{\alpha}) : (\boldsymbol{\tau} - \boldsymbol{\alpha})) \right\}^{\frac{1}{2}} - K = 0 \tag{4.1}$$

where $\boldsymbol{\tau}$ denotes the deviatoric stress tensor and $\boldsymbol{\alpha}$, referred to as back-stress tensor, denotes the center of the yield surface $\{f = 0\}$ in the deviatoric stress space. Parameter K represents the size (radius) of the yield surface which defines the region of constant plastic

shear moduli. The dyadic tensor product of tensors **A** and **B** is defined as $\boldsymbol{A}:\mathbf{B} = A_{ij}B_{ij}$. The back-stress $\boldsymbol{\alpha}$ is initialized to zero at the beginning of loading.

In geotechnical engineering, soil nonlinear shear behavior is described by a shear stress-strain backbone curve (Elgamal 2002) as shown in Figure 4.1.

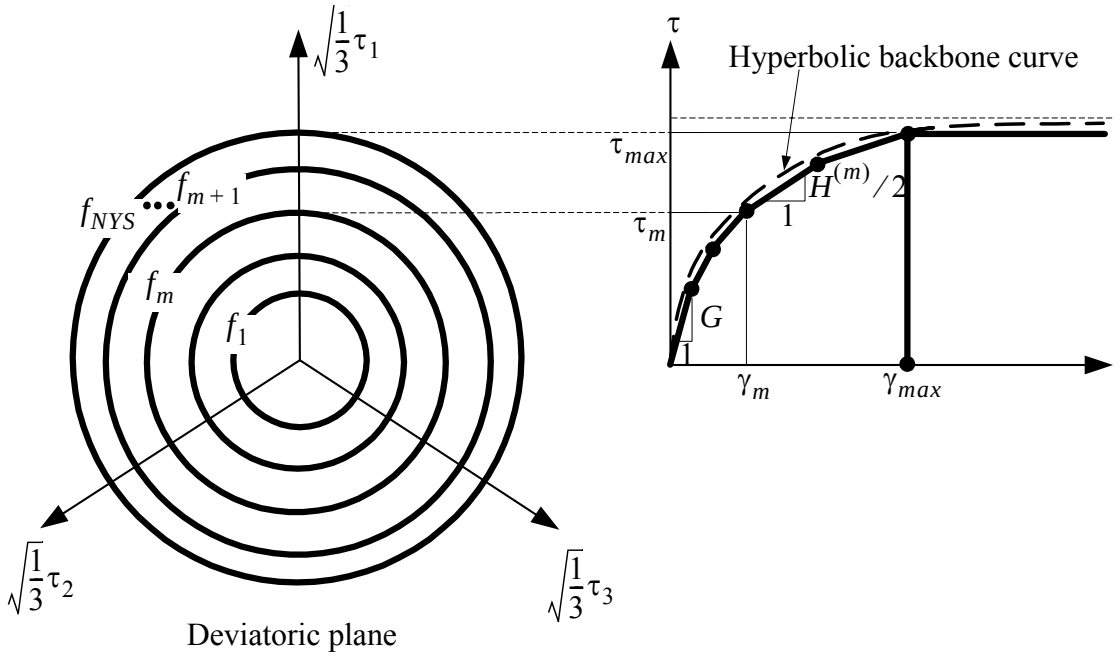


(a) Octahedral shear stress-strain

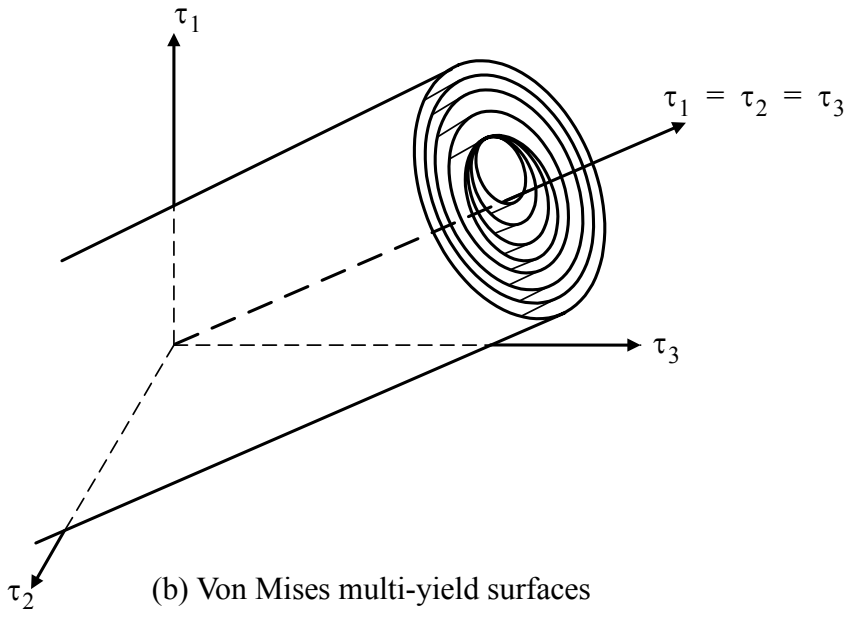


(b) Von Mises multi-yield surfaces

**Figure 4.1 Yield surfaces of multi-yield-surface $J_2$ plasticity model in principal deviatoric stress space**

The experimentally determined backbone curve can be approximated by the hyperbolic formula as

$$\tau = \frac{G\gamma}{1 + \frac{\gamma}{\gamma_r}} \tag{4.2}$$

where $\tau$ and $\gamma$ denote the octahedral shear stress and shear strain, respectively, and G is the low-strain shear modulus. Parameter $\gamma_r$ is a reference shear strain defined as

$$\gamma_r = \frac{\gamma_{max} \cdot \tau_{max}}{G \cdot \gamma_{max} - \tau_{max}} \tag{4.3}$$

where $\tau_{max}$, called shear strength, is the shear stress corresponding to the shear strain $\gamma = \gamma_{max}$ (selected sufficiently large so that $\tau_{max} \approx \tau(\gamma = \infty)$ ) (Figure 4.1).

Within the framework of multi-yield-surface plasticity, the hyperbolic backbone curve in Equation (4.2) is replaced by a piecewise linear approximation as shown in Figure 4.1. Each line segment represents the domain of a yield surface $\{f_i = 0\}$ of size $K_i$ characterized by an elasto-plastic shear modulus $H^{(i)}$ for i = 1, 2, ..., NYS, where NYS denotes the total number of yield surfaces. Parameter $H^{(i)}$ is conveniently defined as $H^{(i)} = 2\left(\frac{\tau_{i+1} - \tau_i}{\gamma_{i+1} - \gamma_i}\right)$ [15].

Then, for every point j on the $\tau \sim\gamma$ curve, the corresponding shear stress and shear strain are computed as,

$$\tau_j = \tau_{max} \cdot \frac{j}{NYS} \text{ and } \gamma_j = \frac{\tau_j \cdot \gamma_r}{G \cdot \gamma_r - \tau_j} \tag{4.4}$$

Loop for each yield surface j from 1 to NYS-1,

$$(\Delta\gamma)_j = \gamma_{j+1} - \gamma_j \tag{4.5}$$

$$(\Delta\tau)_j = \tau_{j+1} - \tau_j \tag{4.6}$$

$$K_j = \frac{3}{\sqrt{2}}\tau_j \tag{4.7}$$

$$H_j = \frac{2(\Delta\tau)_j}{(\Delta\gamma)_j} \tag{4.8}$$

$$H'_j = \frac{2G \cdot H_j}{2G - H_j} \tag{4.9}$$

For the last yield surface, set H(NYS)=H'(NYS)=0.

Therefore the initial yield surfaces are given by a set of concentric cylindrical surfaces whose axes coincide with the hydrostatic axis in the effective stress space as shown in Figure 4.1. Also, The outermost yield surface $f_p$ represents a failure surface and is a geometrical boundary in stress space.

### 4.2.2 Flow Rule (Continuum Form)

A constant plastic shear modulus $H'^{(i)}$ defined as

$$\frac{1}{H'^{(i)}} = \frac{1}{H^{(i)}} - \frac{1}{2G} \tag{4.10}$$

is associated with each yield surface $\{f_i = 0\}$. The plastic shear modulus associated with the outermost yield surface is set to zero, i.e., $H'^{(NYS)} = 0$. An associative flow rule is used to compute the plastic strain increments. In the deviatoric stress space, the plastic

strain increment vector lies along the exterior normal to the yield surface at the stress point. In tensor notation, the plastic strain increment is expressed as

$$d\boldsymbol{\epsilon}^p = \frac{1}{H'}\boldsymbol{Q} \cdot \langle L \rangle \tag{4.11}$$

where the second-order unit tensor $\boldsymbol{Q}$ defined as

$$\boldsymbol{Q} = \frac{1}{Q}\frac{\partial f}{\partial \boldsymbol{\sigma}}, \tag{4.12}$$

in which $Q = \left\{ \frac{\partial f}{\partial \boldsymbol{\sigma}} : \frac{\partial f}{\partial \boldsymbol{\sigma}} \right\}^{\frac{1}{2}}$, represents the plastic flow direction normal to the yield surface {f = 0} at the current stress point. Parameter L in Equation (4.11), referred to as the plastic loading function, is defined as the projection of the stress increment vector $d\boldsymbol{\tau}$ onto the direction normal to the yield surface, i.e.,

$$L = \boldsymbol{Q} : d\boldsymbol{\tau} \tag{4.13}$$

The symbol $\langle\ \rangle$ in (4.11) denotes the MacCauley's brackets defined such that $\langle L \rangle = max(L, 0)$.

### 4.2.3 Discretized Form of Flow Rule

The flow rule defined above in differential (continuum) form is integrated numerically over a trial time step (or load step) using an elastic predictor-plastic corrector procedure illustrated in Figure 4.2

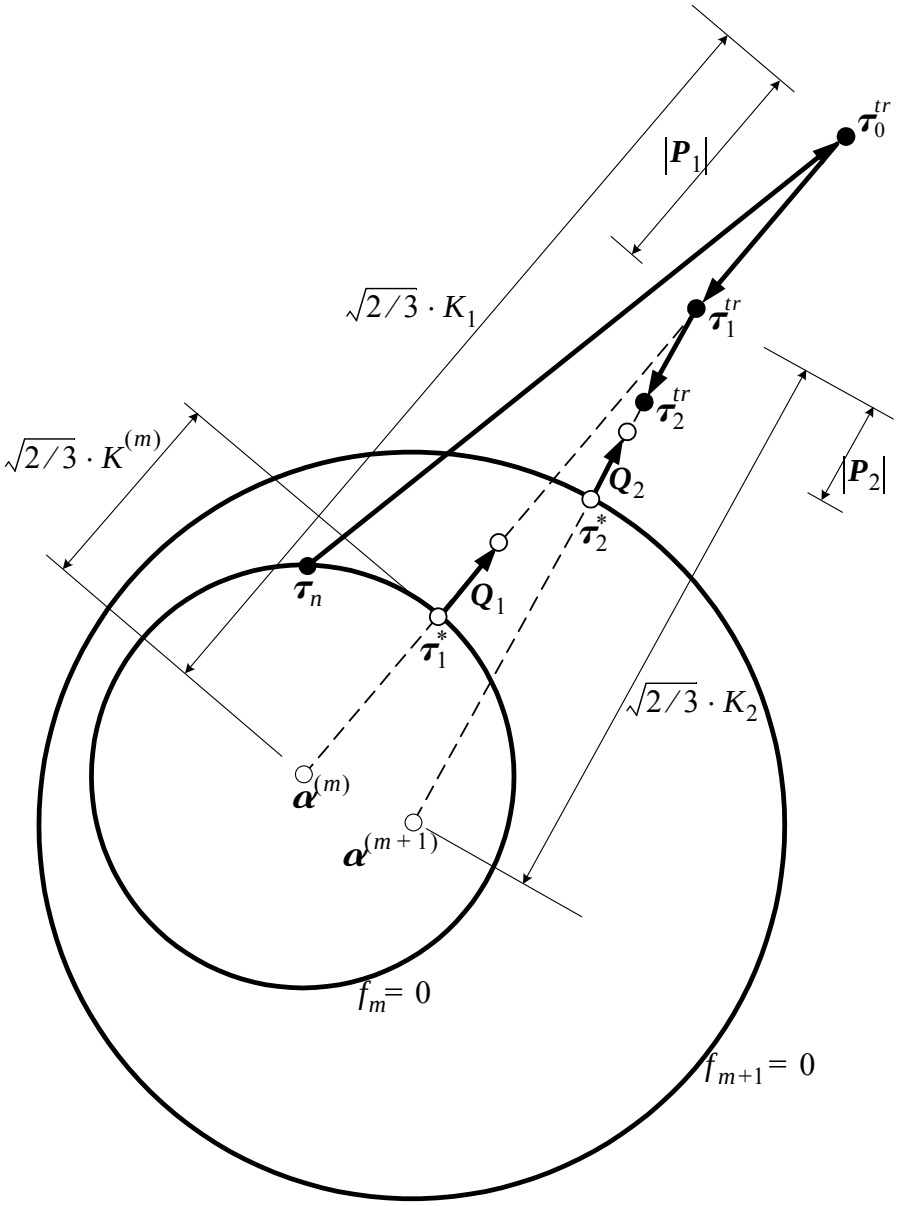


**Figure 4.2 Flow rule of multi-yield-surface $J_2$ plasticity model**

In Figure 4.2, as an illustration, two corrective iterations before convergence is achieved. In this figure, subscript *i* is attached to the parameters and quantities related to

the i-th corrective iteration. Assuming that the current active yield surface is $\{f_m = 0\}$ with its center at $\boldsymbol{\alpha}^{(m)}$, the elastic trial (deviatoric) stress $\boldsymbol{\tau}_0^{tr}$ is obtained as

$$\boldsymbol{\tau}_0^{\mathrm{tr}} = \boldsymbol{\tau}_n + 2\mathrm{G} \cdot \Delta \boldsymbol{e} \tag{4.14}$$

where $\boldsymbol{\tau}_n$ is the converged deviatoric stress at the last time step (n-th time step), and $\Delta \boldsymbol{e}$ denotes the total (from last converged step) deviatoric strain increment in the current step. The contact stress $\boldsymbol{\tau}_1^*$, defined as the intersection point of vector $\boldsymbol{\tau}_0^{\mathrm{tr}} - \boldsymbol{\alpha}^{(m)}$ and the current active yield surface $f_m$, can be computed as (see Figure 4.2)

$$\boldsymbol{\tau}_1^* = \frac{K^{(m)}}{K_1}(\boldsymbol{\tau}_0^{\mathrm{tr}} - \boldsymbol{\alpha}^{(m)}) + \boldsymbol{\alpha}^{(m)} \tag{4.15}$$

where $K_1$ is defined as

$$K_1 = \sqrt{\frac{3}{2}(\boldsymbol{\tau}_0^{\mathrm{tr}} - \boldsymbol{\alpha}^{(m)}) : (\boldsymbol{\tau}_0^{\mathrm{tr}} - \boldsymbol{\alpha}^{(m)})} \tag{4.16}$$

which is proportional to the distance from $\boldsymbol{\tau}_0^{\mathrm{tr}}$ to $\boldsymbol{\alpha}^{(m)}$.

The vector normal to the yield surface at $\boldsymbol{\tau}_1^*$ is derived from (4.12) or Figure 4.2 as

$$\boldsymbol{Q}_1 = \frac{(\boldsymbol{\tau}_1^* - \boldsymbol{\alpha}^{(m)})}{((\boldsymbol{\tau}_1^* - \boldsymbol{\alpha}^{(m)}) : (\boldsymbol{\tau}_1^* - \boldsymbol{\alpha}^{(m)}))^{\frac{1}{2}}} \tag{4.17}$$

Define the plastic stress correction tensor as

$$\boldsymbol{P}_i = \boldsymbol{\tau}_i^{\mathrm{tr}} - \boldsymbol{\tau}_{i-1}^{\mathrm{tr}} \quad (\mathrm{i} = 1, 2, \ldots). \tag{4.18}$$

The plastic stress correction tensor at the first iteration in (4.18) can be expressed as (see Appendix A),

$$\boldsymbol{P}_1 = 2G \cdot \frac{\boldsymbol{Q}_1 : (\boldsymbol{\tau}_0^{\mathrm{tr}} - \boldsymbol{\tau}_1^*)}{(H'^{(m)} + 2 \cdot G)} \boldsymbol{Q}_1 \tag{4.19}$$

The plastic loading function L is then obtained from (4.13) as

$$L_1 = \boldsymbol{P}_1 : \boldsymbol{Q}_1 = 2G \cdot \frac{\boldsymbol{Q}_1 : (\boldsymbol{\tau}_0^{\mathrm{tr}} - \boldsymbol{\tau}_1^*)}{(H'^{(m)} + 2 \cdot G)} \tag{4.20}$$

Then

$$\boldsymbol{P}_1 = L_1 \boldsymbol{Q}_1 , \tag{4.21}$$

The trial stress after the plastic correction for the current active yield surface ($f_m = 0$) is given by

$$\boldsymbol{\tau}_1^{\mathrm{tr}} = \boldsymbol{\tau}_0^{tr} - \boldsymbol{P}_1 \tag{4.22}$$

If the trial stress $\boldsymbol{\tau}_1^{tr}$ is out of the next yield surface $f_{m+1}$, the active yield surface index is set to m = m+1, the subscript (for the iteration number) is set to i = i+1, and the above plastic correction process, Equations (4.15) through (4.22), is repeated until the trial stress $\boldsymbol{\tau}_i^{tr}$ does not cross anymore yield surfaces, except for the plastic stress correction tensor and the plastic loading function (Equations 4.19 and 4.20) that are replaced by Equations 4.23 and 4.24 below.

The plastic stress correction tensor is,

$$\boldsymbol{P}_i = 2G \cdot \frac{\boldsymbol{Q}_i : (\boldsymbol{\tau}_{i-1}^{\mathrm{tr}} - \boldsymbol{\tau}_i^*)}{(H'^{(m)} + 2 \cdot G)} \cdot \frac{(H'^{(m-1)} - H'^{(m)})}{H'^{(m-1)}} \cdot \boldsymbol{Q}_i \; (\mathrm{i} = 2, 3, \ldots .) \tag{4.23}$$

While the plastic loading function is,

$$L_i = 2G \cdot \frac{\boldsymbol{Q}_i : (\boldsymbol{\tau}_{i-1}^{\mathrm{tr}} - \boldsymbol{\tau}_i^*)}{(H'^{(m)} + 2 \cdot G)} \cdot \frac{(H'^{(m-1)} - H'^{(m)})}{H'^{(m-1)}} \; (\mathrm{i} = 2, 3, \ldots .) \tag{4.24}$$

After "convergence" of the deviatoric trial stress $\boldsymbol{\tau}_i^{tr}$ to $\boldsymbol{\tau}$ (referred to as the current stress herein), the volumetric stress $\sigma^{vol}$ is updated to

$$\sigma^{vol} = \sigma_n^{vol} + B(\Delta\boldsymbol{\epsilon} : \boldsymbol{I}) \tag{4.25}$$

where B = elastic bulk modulus, $\Delta\boldsymbol{\epsilon}$ = total strain increment, and **I** = second order unit tensor. Then, the new total stress (at the end of the integration of the material constitutive law over a trial time/load step) referred to as the current stress point is given by

$$\boldsymbol{\sigma} = \boldsymbol{\tau} + \sigma^{vol}\boldsymbol{I} \tag{4.26}$$

### 4.2.4 Hardening Law

A pure deviatoric kinematic hardening rule is employed to conveniently generate hysteretic cyclic response. All yield surfaces may translate in the stress space by the stress point without changing in form and orientation. In the context of multi-surface plasticity, translation of the active yield surface $f_m$ is generally governed by the consideration that no overlapping is allowed between yield surfaces. The translation direction $\boldsymbol{\mu}$ as shown in Figure 4.3 is defined as (Elgamal et al [14]) :

$$\boldsymbol{\mu} = [\boldsymbol{\tau}_T - \boldsymbol{\alpha}^{(m)}] - \frac{K^{(m)}}{K^{(m+1)}}[\boldsymbol{\tau}_T - \boldsymbol{\alpha}^{(m+1)}] \tag{4.27}$$

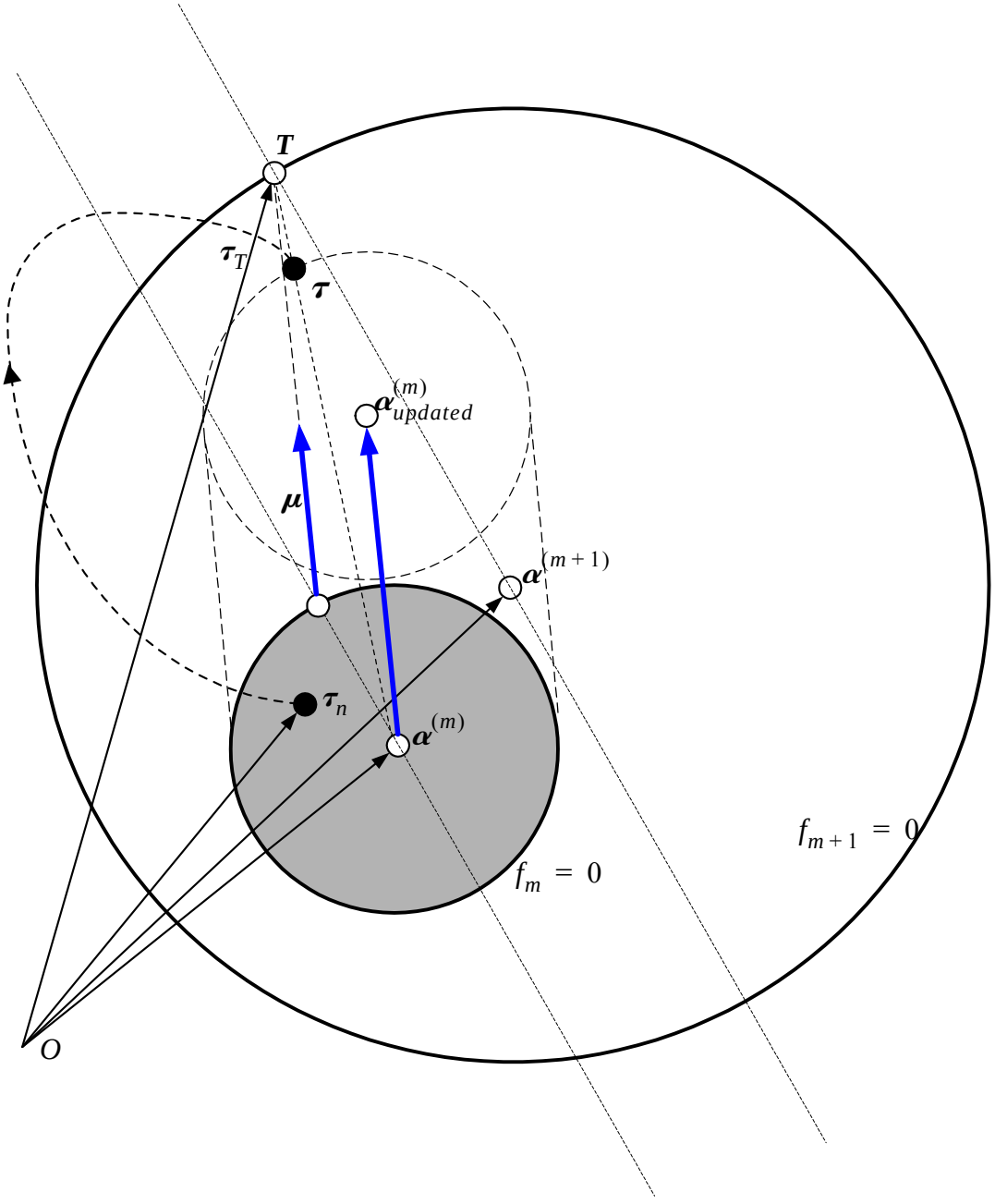


**Figure 4.3 Hardening rule of multi-yield-surface $J_2$ plasticity model**

where $\boldsymbol{\tau}_T$ is the deviatoric stress tensor defining the position of point T ( Figure 4.3) as the intersection of $f_{m+1}$ with the vector connecting the inner surface center $\boldsymbol{\alpha}^{(m)}$ and the updated stress state ($\boldsymbol{\tau}$+d$\boldsymbol{\tau}$). This rule (Eq. (4.27)) is also based on the Mroz [6] conjugate-points concept, and allows no overlapping of yield surfaces(Elgamal et al [14]).

After "convergence" of the deviatoric trial stress $\boldsymbol{\tau}_i^{tr}$ to the current stress $\boldsymbol{\tau}$, the multi-yield surfaces need to be updated.

1. active surface update.

Compute the deviatoric stress $\boldsymbol{\tau}_T$ (refer Figure 4.3).

$$\boldsymbol{\tau}_T = \boldsymbol{\alpha}^{(m)} + x(\boldsymbol{\tau} - \boldsymbol{\alpha}^{(m)}) \tag{4.28}$$

where x is obtained from the condition that $\boldsymbol{\tau}_T$ is on the surface m+1. Thus $\boldsymbol{\tau}_T$ must satisfy,

$$f_{m+1} = (\boldsymbol{\tau} - \boldsymbol{\alpha}^{(m+1)}):(\boldsymbol{\tau} - \boldsymbol{\alpha}^{(m+\bar{1})}) - \frac{2}{3}(K^{(m+1)})^2 = 0 \tag{4.29}$$

From (4.29) x could be solved for as a solution to

$$Ax^2 + Bx + C = 0 \tag{4.30}$$

where A,B,C are defined as,

$$A = (\boldsymbol{\tau} - \boldsymbol{\alpha}^{(m)}):(\boldsymbol{\tau} - \boldsymbol{\alpha}^{(m)}) \tag{4.31}$$

$$B = 2 \cdot (\boldsymbol{\alpha}^{(m)} - \boldsymbol{\alpha}^{(m+1)}):(\boldsymbol{\tau} - \boldsymbol{\alpha}^{(m)}) \tag{4.32}$$

$$C = (\boldsymbol{\alpha}^{(m)} - \boldsymbol{\alpha}^{(m+1)}):(\boldsymbol{\alpha}^{(m)} - \boldsymbol{\alpha}^{(m+1)}) - \frac{2}{3}(K^{(m+1)})^2 \tag{4.33}$$

Once $\boldsymbol{\tau}_T$ is known, the direction of surface center translation $\boldsymbol{\mu}$ can be computed from (4.27).

After obtaining $\boldsymbol{\mu}$, the translation quantity 'a' is computed such that the current stress $\boldsymbol{\tau}$ is on the surface m after translation of the m$^{th}$ surface. Hence,

$$f_m = [\boldsymbol{\tau} - (\boldsymbol{\alpha}^{(m)} + a\boldsymbol{\mu})] : [\boldsymbol{\tau} - (\boldsymbol{\alpha}^{(m)} + a\boldsymbol{\mu})] - \frac{2}{3}(K^{(m)})^2 = 0 \tag{4.34}$$

which is equivalent to solving for 'a' from the following equation

$$Aa^2 + Ba + C = 0 \tag{4.35}$$

where A,B,C are defined as,

$$A = \boldsymbol{\mu} : \boldsymbol{\mu} \tag{4.36}$$

$$B = -2 \cdot \boldsymbol{\mu} : (\boldsymbol{\tau} - \boldsymbol{\alpha}^{(m)}) \tag{4.37}$$

$$C = (\boldsymbol{\tau} - \boldsymbol{\alpha}^{(m)}) : (\boldsymbol{\tau} - \boldsymbol{\alpha}^{(m)}) - \frac{2}{3}(K^{(m)})^2 \tag{4.38}$$

Then the active surface center is update as,

$$\boldsymbol{\alpha}^{(m)} = \boldsymbol{\alpha}^{(m)} + a\boldsymbol{\mu} \tag{4.39}$$

2. inner surface update.

After the active surface $f_m$ is updated, all the inner yield surfaces $f_0$, $f_1$, ..., $f_{m-1}$ needed to be updated such that all the inner surfaces and the active surface $f_m$ are tangent to each other at the current stress point $\boldsymbol{\tau}$ as shown in Figure 4.4.

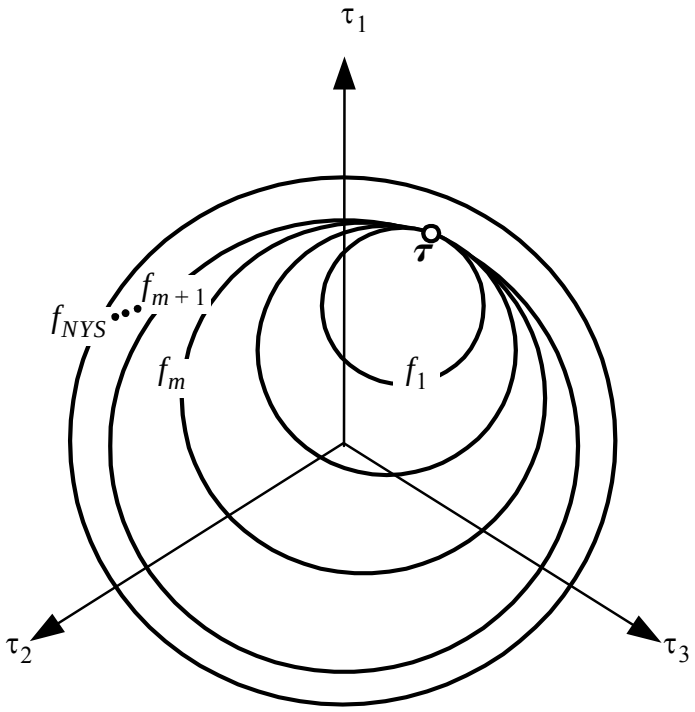


**Figure 4.4 Updates of inner yield surfaces**

From similarity

$$\frac{\boldsymbol{\tau}-\boldsymbol{\alpha}^{(m)}}{K^{(m)}} = \frac{\boldsymbol{\tau}-\boldsymbol{\alpha}^{(m-1)}}{K^{(m-1)}} = \ \ldots \ = \frac{\boldsymbol{\tau}-\boldsymbol{\alpha}^{(0)}}{K^{(0)}} \tag{4.40}$$

The above hardening law determines the movement of the inner yield surfaces.

From (4.40), the center of each inner surfaces is determined by,

$$\boldsymbol{\alpha}^{(i)} = \boldsymbol{\tau} - \frac{K^{(i)}(\boldsymbol{\tau}-\boldsymbol{\alpha}^{(m)})}{K^{(m)}} \quad 1 \le i \le m-1 \tag{4.41}$$

where $a^{(i)}$ and $K^{(i)}$, are the center and radius of the $i^{th}$ surface respectively, and m is the number of the current or active surface.

## 4.3 Consistent Tangent Operator

As a general class of nonlinear problems in continuum mechanics, rate-independent elasto-plasticity problems are typically solved through the Finite Element Method (FEM) and using Newton's method. Newton's method is used in conjunction with an incremental-iterative solution procedure which, at each time or load step, reduces the nonlinear problem to a sequence of linearized problems called iterations. Thus, at every iteration, a linearized incremental problem is solved, which requires the tangent stiffness matrix of the structure. In general, this tangent stiffness matrix can be computed from the material tangent moduli (operators) at the material (or integration point) level. In rate-independent plasticity, the material constitutive behavior is described by rate constitutive equations ($\dot{\boldsymbol{\sigma}} = \dot{\boldsymbol{\sigma}}(\dot{\boldsymbol{\epsilon}})$). The above incremental-iterative process requires these rate constitutive equations to be integrated numerically over a sequence of discrete time or load steps, i.e., $\Delta\boldsymbol{\sigma} = \Delta\boldsymbol{\sigma}(\Delta\boldsymbol{\epsilon})$. Two types of material tangent moduli can be selected to form the structure stiffness matrix: continuum tangent moduli and consistent tangent moduli. Consistent tangent moduli (also called algorithmic tangent moduli) are obtained through differentiation of the incremental constitutive equations ($\Delta\boldsymbol{\sigma} = \Delta\boldsymbol{\sigma}(\Delta\boldsymbol{\epsilon})$) with respect to the total incremental strains $\Delta\boldsymbol{\epsilon}$, while the continuum tangent moduli are defined as the differentiation of the rate constitutive equations ($\dot{\boldsymbol{\sigma}} = \dot{\boldsymbol{\sigma}}(\dot{\boldsymbol{\epsilon}})$) with respect to the strain rate $\dot{\boldsymbol{\epsilon}}$ [1]. Previous studies (1977,1978) show that use of the consistent tangent moduli guarantees

the quadratic rate of asymptotic convergence of Newton's iterative process. Furthermore, for parameter sensitivity analysis in nonlinear mechanics using the Direct Differentiation Method (DDM), the consistent tangent moduli are also required when differentiating the discretized response equations (i.e., static or dynamic equilibrium equations) with respect to material, geometric or loading parameters in order to obtain the governing response sensitivity equations.

In this section, a general methodology is presented to compute the consistent tangent moduli by accumulating the contributions from all yield surfaces affecting the stress change from the last converged time/load step. The algorithm derived herein to compute the consistent tangent moduli of the multi-yield-surface $J_2$ soil plasticity model is then implemented in OpenSees. Application examples are presented to verify the quadratic rate of asymptotic convergence of Newton's iterative process obtained when using the derived consistent tangent moduli. Based on these examples, the convergence rate and computational time obtained when using consistent and continuum tangent moduli are compared.

As an alternative and classical method for computing the tangent modulus, the continuum tangent modulus method is presented and is later compared with the consistent tangent modulus method.

### 4.3.1 Continuum Tangent Operator

The continuum elastoplastic tangent moduli are obtained through differentiation with respect to $d\boldsymbol{\epsilon}$ of the rate constitutive equation $d\boldsymbol{\sigma} = d\boldsymbol{\sigma}(d\boldsymbol{\epsilon})$, where $d\boldsymbol{\sigma}$ and $d\boldsymbol{\epsilon}$ denote infinitesimal increments in total stress and strain, respectively. In small strain plasticity,

the decomposition of the total strain into the elastic and plastic parts can be expressed in infinitesimal form as

$$d\boldsymbol{\epsilon} = d\boldsymbol{\epsilon}^e + d\boldsymbol{\epsilon}^p \tag{4.42}$$

where $d\boldsymbol{\epsilon}^e$ and $d\boldsymbol{\epsilon}^p$ denote infinitesimal increments of elastic and plastic (irreversible) strains, respectively. The constitutive equation is based on the relationship between the elastic strain and the stress, which is the same as in linear elasticity, i.e.,

$$d\boldsymbol{\sigma} = \boldsymbol{C}:d\boldsymbol{\epsilon}^e = \boldsymbol{C}:(d\boldsymbol{\epsilon}-d\boldsymbol{\epsilon}^p) = \boldsymbol{C}^{ep}:d\boldsymbol{\epsilon} \tag{4.43}$$

where **C** denotes the tensor of elastic moduli, which in the case of isotropic elasticity can be expressed as $C_{ijkl} = \lambda\delta_{ij}\delta_{kl} + \mu(\delta_{ik}\delta_{jl} + \delta_{il}\delta_{jk})$ where $\lambda$ and $\mu$ are Lamé constants, and $\mathbf{C}^{ep}$ represents the tensor of continuum elastoplastic tangent moduli. Note that Lamé constant $\mu$ is identical to the low-strain shear modulus G.

In multi-yield-surface $J_2$ plasticity, the continuum elastoplastic material tangent moduli tensor can be obtained as

$$\boldsymbol{C}^{ep} = \boldsymbol{C} - \frac{1}{H}(\boldsymbol{H} \otimes \boldsymbol{H}) \tag{4.44}$$

where the tensor product of two tensors **A** and **B** is defined as $[\boldsymbol{A} \otimes \boldsymbol{B}]_{ijkl} = A_{ij} \cdot B_{kl}$ and

$H = (12G + 6H'^{(m)})(K^{(m)})^2$, $\boldsymbol{H} = 6G(\boldsymbol{\tau} - \boldsymbol{\alpha})$

### 4.3.2 Consistent Tangent Moduli

Consistent tangent moduli were first introduced by Taylor and Simo. These moduli are obtained by differentiating directly the discretized constitutive equation $\Delta\boldsymbol{\sigma} = \Delta\boldsymbol{\sigma}(\Delta\boldsymbol{\epsilon})$ with respect to the strain increment $\Delta\boldsymbol{\epsilon}$. This ensures that the tangent operator is 'consistent' with the constitutive law integration scheme, which guarantees the quadratic rate of asymptotic convergence of iterative solution strategies (at the structure level) based on Newton's method. The consistent tangent moduli (also called algorithmic tangent moduli in the literature) are defined at a material point as

$$\boldsymbol{C}^{ep}_{n+1} = \left.\frac{\partial\boldsymbol{\sigma}(\boldsymbol{\sigma}_n, \boldsymbol{\epsilon}_n, \boldsymbol{\epsilon}^p_n \ldots, \boldsymbol{\epsilon} - \boldsymbol{\epsilon}_n)}{\partial\boldsymbol{\epsilon}}\right|_{\boldsymbol{\epsilon} = \boldsymbol{\epsilon}_{n+1}} \tag{4.45}$$

where $\boldsymbol{\sigma}(\boldsymbol{\sigma}_n, \boldsymbol{\epsilon}_n, \boldsymbol{\epsilon}^p_n \ldots, \boldsymbol{\epsilon} - \boldsymbol{\epsilon}_n)$ denotes the incremental material response function, and the notation $f|_{\boldsymbol{\epsilon} = \boldsymbol{\epsilon}_{n+1}}$ indicates that function f is evaluated at $\boldsymbol{\epsilon} = \boldsymbol{\epsilon}_{n+1}$. It is worth mentioning that the stress $\boldsymbol{\sigma}$ is not necessarily the converged one at the structure level at the end of the current time step, i.e., it could be the stress at the end of a non-converged iteration at the structure level. The material consistent tangent moduli give raise to the consistent tangent stiffness matrix at both the element and structural levels.

In the following part, the consistent tangent operator is derived for the multi-yield-surface $J_2$ plasticity material model based on the stress updating process defined in Equations (4.14) through (4.26).

1. *Differentiation of the elastic trial deviatoric stress with respect to the current deviatoric strain.* From (4.14), it follows that

$$\frac{\partial \boldsymbol{\tau}_0^{\mathrm{tr}}}{\partial \boldsymbol{e}_{n+1}} = 2\mathrm{G} \cdot \boldsymbol{I}_4 \tag{4.46}$$

where the derivative of tensor **A** with respect to tensor **B** is defined as $\frac{\partial \boldsymbol{A}}{\partial \boldsymbol{B}} = \frac{\partial A_{ij}}{\partial B_{kl}} \hat{\boldsymbol{e}}_i \otimes \hat{\boldsymbol{e}}_j \otimes \hat{\boldsymbol{e}}_k \otimes \hat{\boldsymbol{e}}_l$ in which $\hat{\boldsymbol{e}}_i$ is the base vector defined as the unit vector along the $i^{th}$ axis, and the 4th order symmetric unit tensor $\mathbf{I}_4$ is defined as $\boldsymbol{I}_4 = \frac{1}{2}(\delta_{il}\delta_{jk} + \delta_{ik}\delta_{jl})\, \hat{\boldsymbol{e}}_i \otimes \hat{\boldsymbol{e}}_j \otimes \hat{\boldsymbol{e}}_k \otimes \hat{\boldsymbol{e}}_l$.

*2. Differentiation of the contact stress with respect to the current deviatoric strain.* Differentiating (4.15) and (4.16) for the $i^{th}$ iteration with respect to $\boldsymbol{e}_{n+1}$ yields

$$\frac{\partial K_i}{\partial \boldsymbol{e}_{n+1}} = \frac{3}{2K_i}(\boldsymbol{\tau}_{i-1}^{\mathrm{tr}} - \boldsymbol{\alpha}^{(m)}) : \frac{\partial \boldsymbol{\tau}_{i-1}^{\mathrm{tr}}}{\partial \boldsymbol{e}_{n+1}} \qquad (\mathrm{i} = 1, 2, \ldots) \tag{4.47}$$

$$\frac{\partial \boldsymbol{\tau}_i^*}{\partial \boldsymbol{e}_{n+1}} = \frac{K^{(m)}}{K_i} \cdot \left(\frac{\partial \boldsymbol{\tau}_{i-1}^{\mathrm{tr}}}{\partial \boldsymbol{e}_{n+1}}\right) - \frac{K^{(m)}}{K_i^2}(\boldsymbol{\tau}_{i-1}^{\mathrm{tr}} - \boldsymbol{\alpha}^{(m)}) \otimes \left(\frac{\partial K_i}{\partial \boldsymbol{e}_{n+1}}\right) \qquad (\mathrm{i} = 1, 2, \ldots) \tag{4.48}$$

*3. Differentiation of the unit vector normal to the yield surface with respect to the current deviatoric strain.* Differentiating (4.17) for the $i^{th}$ iteration with respect to $\boldsymbol{e}_{n+1}$ gives

$$\begin{aligned}\frac{\partial \boldsymbol{Q}_i}{\partial \boldsymbol{e}_{n+1}} &= \frac{1}{((\boldsymbol{\tau}_i^* - \boldsymbol{\alpha}^{(m)}) : (\boldsymbol{\tau}_i^* - \boldsymbol{\alpha}^{(m)}))^{\frac{1}{2}}} \cdot \frac{\partial \boldsymbol{\tau}_i^*}{\partial \boldsymbol{e}_{n+1}} \\ &- \frac{1}{((\boldsymbol{\tau}_i^* - \boldsymbol{\alpha}^{(m)}) : (\boldsymbol{\tau}_i^* - \boldsymbol{\alpha}^{(m)}))^{\frac{3}{2}}} \cdot (\boldsymbol{\tau}_i^* - \boldsymbol{\alpha}^{(m)}) \otimes (\boldsymbol{\tau}_i^* - \boldsymbol{\alpha}^{(m)}) : \frac{\partial \boldsymbol{\tau}_i^*}{\partial \boldsymbol{e}_{n+1}}\end{aligned} \qquad (\mathrm{i} = 1, 2, \ldots) \tag{4.49}$$

*4. Differentiation of the plastic stress correction tensor with respect to the current deviatoric strain.* From (4.19) and (4.23), it follows that

$$\frac{\partial \boldsymbol{P}_1}{\partial \boldsymbol{e}_{n+1}} = \frac{2G}{(H'^{(m)} + 2G)} \boldsymbol{Q}_1 \otimes \left( (\boldsymbol{\tau}_0^{\mathrm{tr}} - \boldsymbol{\tau}_1^*) : \frac{\partial \boldsymbol{Q}_1}{\partial \boldsymbol{e}_{n+1}} + \boldsymbol{Q}_1 : \left( \frac{\partial \boldsymbol{\tau}_0^{\mathrm{tr}}}{\partial \boldsymbol{e}_{n+1}} - \frac{\partial \boldsymbol{\tau}_1^*}{\partial \boldsymbol{e}_{n+1}} \right) \right) + 2G \cdot \frac{\boldsymbol{Q}_1 : (\boldsymbol{\tau}_0^{\mathrm{tr}} - \boldsymbol{\tau}_1^*)}{(H'^{(m)} + 2G)} \cdot \frac{\partial \boldsymbol{Q}_i}{\partial \boldsymbol{e}_{n+1}} \tag{4.50}$$

for the first iteration (i = 1) and

$$\frac{\partial \boldsymbol{P}_i}{\partial \boldsymbol{e}_{n+1}} = \frac{(H'^{(m-1)} - H'^{(m)})}{H'^{(m-1)}} \frac{2G}{(H'^{(m)} + 2G)} \boldsymbol{Q}_i \otimes \left( (\boldsymbol{\tau}_{i-1}^{\mathrm{tr}} - \boldsymbol{\tau}_i^*) : \frac{\partial \boldsymbol{Q}_i}{\partial \boldsymbol{e}_{n+1}} + \boldsymbol{Q}_i : \left( \frac{\partial \boldsymbol{\tau}_{i-1}^{\mathrm{tr}}}{\partial \boldsymbol{e}_{n+1}} - \frac{\partial \boldsymbol{\tau}_i^*}{\partial \boldsymbol{e}_{n+1}} \right) \right) + 2G \cdot \frac{\boldsymbol{Q}_i : (\boldsymbol{\tau}_{i-1}^{\mathrm{tr}} - \boldsymbol{\tau}_i^*)}{(H'^{(m)} + 2G)} \cdot \frac{(H'^{(m-1)} - H'^{(m)})}{H'^{(m-1)}} \cdot \frac{\partial \boldsymbol{Q}_i}{\partial \boldsymbol{e}_{n+1}} \tag{4.51}$$

for subsequent iterations ( i = 2, 3, 4, ... ) if the current stress $\boldsymbol{\tau}_1^{\mathrm{tr}}$ is out of the next yield surface.

*5. Differentiation of the new trial stress after plastic correction with respect to the current deviatoric strain.* Differentiating (4.22) for the i$^{\mathrm{th}}$ iteration with respect to $\boldsymbol{e}_{n+1}$ gives

$$\frac{\partial \boldsymbol{\tau}_i^{tr}}{\partial \boldsymbol{e}_{n+1}} = \frac{\partial \boldsymbol{\tau}_{i-1}^{tr}}{\partial \boldsymbol{e}_{n+1}} - \frac{\partial \boldsymbol{P}_i}{\partial \boldsymbol{e}_{n+}} \tag{4.52}$$

If the trial stress at the i$^{\mathrm{th}}$ iteration is out of the next yield surface ($f_{m+1}$), the active yield surface index is updated to m = m+1, the subscript (for the iteration number) is set to i = i+1, and the derivative computations in steps 2 to 5 above are repeated.

After "convergence" of the deviatoric stress sequence $\boldsymbol{\tau}_i^{tr}$ (i = 0, 1, 2, 3, ...) to $\boldsymbol{\tau}$ at the end of the trial time/load step, the material consistent tangent moduli are finally obtained as the differentiation of the current (total) stress $\boldsymbol{\sigma}$ with respect to the current (total) strain $\boldsymbol{\epsilon}_{n+1}$, see (4.45), as shown below. From the relation between the deviatoric strain tensor $\boldsymbol{e}_{n+1}$ and total strain tensor $\boldsymbol{\epsilon}_{n+1}$, i.e., $\boldsymbol{e}_{n+1} = \boldsymbol{\epsilon}_{n+1} - \frac{1}{3}(\boldsymbol{\epsilon}:\boldsymbol{I})\boldsymbol{I}$, it follows that

$$\frac{\partial \boldsymbol{e}_{n+1}}{\partial \boldsymbol{\epsilon}_{n+1}} = \boldsymbol{I}_4 - \frac{1}{3}\boldsymbol{I} \otimes \boldsymbol{I} \tag{4.53}$$

Then, the differentiation of the current stress $\boldsymbol{\tau}$ with respect to the total strain $\boldsymbol{\epsilon}_{n+1}$ can be expressed as, using the chain rule of differentiation and (4.53),

$$\frac{\partial \boldsymbol{\tau}}{\partial \boldsymbol{\epsilon}_{n+1}} = \left(\frac{\partial \boldsymbol{\tau}}{\partial \boldsymbol{e}_{n+1}}\right):\left(\frac{\partial \boldsymbol{e}_{n+1}}{\partial \boldsymbol{\epsilon}_{n+1}}\right) = \left(\frac{\partial \boldsymbol{\tau}}{\partial \boldsymbol{e}_{n+1}}\right):\left(\boldsymbol{I}_4 - \frac{1}{3}\boldsymbol{I} \otimes \boldsymbol{I}\right) = \frac{\partial \boldsymbol{\tau}}{\partial \boldsymbol{e}_{n+1}} - \frac{1}{3}\left(\frac{\partial \boldsymbol{\tau}}{\partial \boldsymbol{e}_{n+1}}:\boldsymbol{I}\right) \otimes \boldsymbol{I} \tag{4.54}$$

The relation between the total stress and deviatoric stress tensors given in (4.26) can be re-written as $\boldsymbol{\sigma} = \boldsymbol{\tau} + \sigma^{vol} \cdot \boldsymbol{I} = \boldsymbol{\tau} + B(\boldsymbol{\epsilon}:\boldsymbol{I}) \cdot \boldsymbol{I}$. Then,

$$\frac{\partial \boldsymbol{\sigma}}{\partial \boldsymbol{\epsilon}_{n+1}} = \frac{\partial \boldsymbol{\tau}}{\partial \boldsymbol{\epsilon}_{n+1}} + B(\boldsymbol{I} \otimes \boldsymbol{I}) \tag{4.55}$$

The material consistent tangent moduli given in (4.55) depend on the sensitivities (with respect to strains) of all trial stresses $\boldsymbol{\tau}_i^{tr}$ (i = 0, 1, 2, ...) yielding the current stress state $\boldsymbol{\sigma}$, according to the incremental process defined by Equations (4.46) through (4.52) or steps 1 through 5. Thus, in the case of multiple surface plasticity, the consistent tangent moduli cannot be evaluated directly from a single expression, but need to be computed in an incremental/additive manner.

The above results for the material consistent tangent moduli, derived in tensor notation, need to be converted into matrix and vector notation for software implementation purposes. In this section, the $2^{nd}$ order tensors and $4^{th}$-order tensors are represented as vectors and matrices, respectively, as

$$\boldsymbol{\sigma} = \begin{Bmatrix} \sigma_{11} \\ \sigma_{22} \\ \sigma_{33} \\ \sigma_{12} \\ \sigma_{23} \\ \sigma_{31} \end{Bmatrix} \tag{4.56}$$

$$\text{and } \frac{\partial \boldsymbol{\sigma}}{\partial \boldsymbol{\epsilon}} = \begin{bmatrix} \frac{\partial \sigma_{11}}{\partial \varepsilon_{11}} & \frac{\partial \sigma_{11}}{\partial \varepsilon_{22}} & \frac{\partial \sigma_{11}}{\partial \varepsilon_{33}} & \frac{\partial \sigma_{11}}{\partial \varepsilon_{12}} & \frac{\partial \sigma_{11}}{\partial \varepsilon_{23}} & \frac{\partial \sigma_{11}}{\partial \varepsilon_{31}} \\ \frac{\partial \sigma_{22}}{\partial \varepsilon_{11}} & \frac{\partial \sigma_{22}}{\partial \varepsilon_{22}} & \frac{\partial \sigma_{22}}{\partial \varepsilon_{33}} & \frac{\partial \sigma_{22}}{\partial \varepsilon_{12}} & \frac{\partial \sigma_{22}}{\partial \varepsilon_{23}} & \frac{\partial \sigma_{22}}{\partial \varepsilon_{31}} \\ \frac{\partial \sigma_{33}}{\partial \varepsilon_{11}} & \frac{\partial \sigma_{33}}{\partial \varepsilon_{22}} & \frac{\partial \sigma_{33}}{\partial \varepsilon_{33}} & \frac{\partial \sigma_{33}}{\partial \varepsilon_{12}} & \frac{\partial \sigma_{33}}{\partial \varepsilon_{23}} & \frac{\partial \sigma_{33}}{\partial \varepsilon_{31}} \\ \frac{\partial \sigma_{12}}{\partial \varepsilon_{11}} & \frac{\partial \sigma_{12}}{\partial \varepsilon_{22}} & \frac{\partial \sigma_{12}}{\partial \varepsilon_{33}} & \frac{\partial \sigma_{12}}{\partial \varepsilon_{12}} & \frac{\partial \sigma_{12}}{\partial \varepsilon_{23}} & \frac{\partial \sigma_{12}}{\partial \varepsilon_{31}} \\ \frac{\partial \sigma_{23}}{\partial \varepsilon_{11}} & \frac{\partial \sigma_{23}}{\partial \varepsilon_{22}} & \frac{\partial \sigma_{23}}{\partial \varepsilon_{33}} & \frac{\partial \sigma_{23}}{\partial \varepsilon_{12}} & \frac{\partial \sigma_{23}}{\partial \varepsilon_{23}} & \frac{\partial \sigma_{23}}{\partial \varepsilon_{31}} \\ \frac{\partial \sigma_{31}}{\partial \varepsilon_{11}} & \frac{\partial \sigma_{31}}{\partial \varepsilon_{22}} & \frac{\partial \sigma_{31}}{\partial \varepsilon_{33}} & \frac{\partial \sigma_{31}}{\partial \varepsilon_{12}} & \frac{\partial \sigma_{31}}{\partial \varepsilon_{23}} & \frac{\partial \sigma_{31}}{\partial \varepsilon_{31}} \end{bmatrix} \tag{4.57}$$

### 4.3.3 Three-Dimensional Block Subjected to Quasi-Static Cyclic Loading

In this section, a three-dimensional (3D) solid block of dimensions $1m \times 1m \times 1m$ subjected to quasi-static cyclic loads in both horizontal directions, see Figure 4.5, is used as first application and validation example.

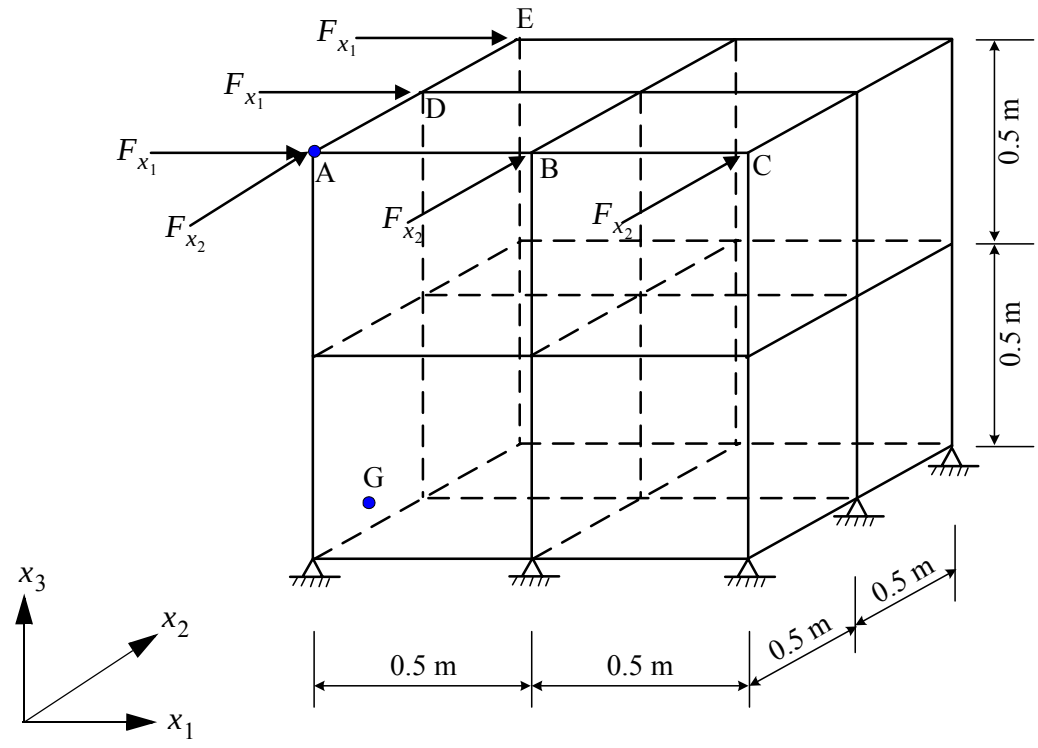


**Figure 4.5 Solid block of clay subjected to horizontal quasi-static cyclic loads**

As shown in Figure 4.5, the block is discretized into 8 brick elements consisting of displacement-based eight-noded, trilinear isoparametric finite element with eight integration points each. The material represents medium clay with the following constitutive material parameters: low-strain shear modulus G = 60000 kPa, bulk modulus B = 240000 KPa,

(Poisson's ratio = 0.38) maximum shear stress $\tau_{max}$ = 30 kPa. The points ($\tau_j$, $\gamma_j$) defining the piecewise linear approximation of the τ-γ backbone curve are defined such that their projections on the $\tau_j$ axis are uniformly spaced as shown in Figure 4.1. The bottom nodes of the model are fixed and top nodes {A, B, C} and {A, D, E} are subjected to concentrated horizontal forces $F_{x_1}(t) = 2.0\sin(0.2\pi t)\lceil kN \rceil$ and $F_{x_2}(t) = 2.0\sin(0.2\pi t + 0.5\pi)\lceil kN \rceil$, respectively, as shown in Figure 4.6. The number of yield surfaces is set to 20 unless specified otherwise.

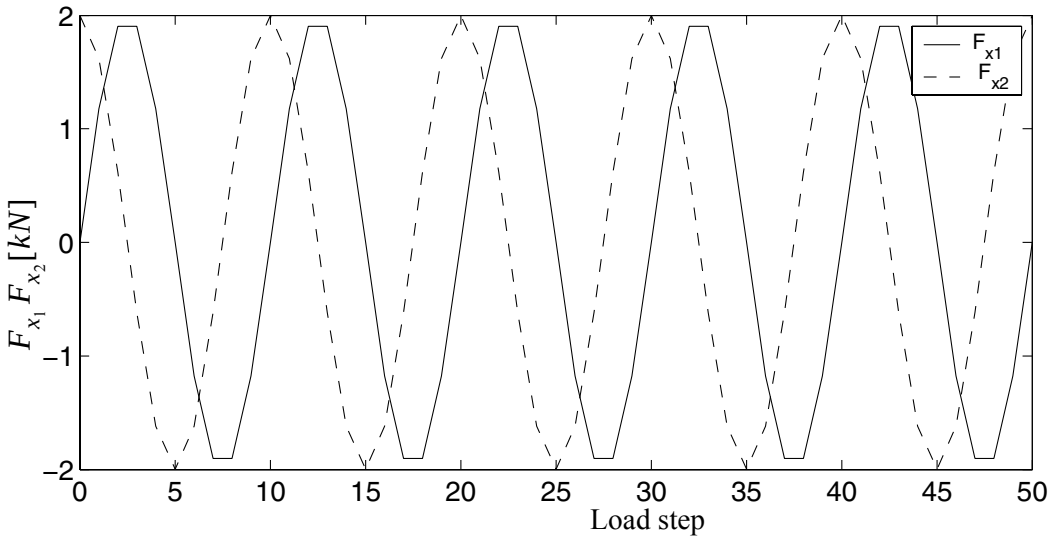


**Figure 4.6 Time variation of quasi-static cyclic loads**

The nodal displacement response of node A in the x-direction is shown in Figure 4.7 as a function of the force $F_{x_1}(t)$, while the hysteretic shear stress - strain response

$(\sigma_{31} - \varepsilon_{31})$ at Gauss point G (see Figure 4.5) is plotted in Figure 4.8. From these figures it is noted that significant yielding of the material is observed during the cyclic loading considered.

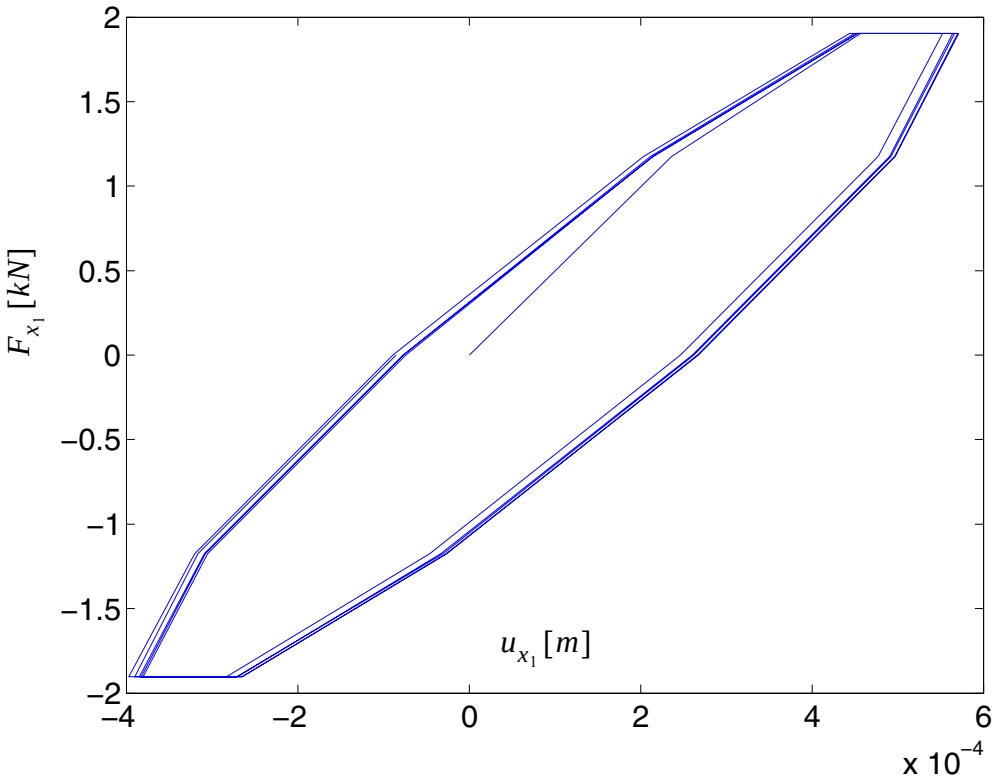


**Figure 4.7 Force vs. displacement response of node A**

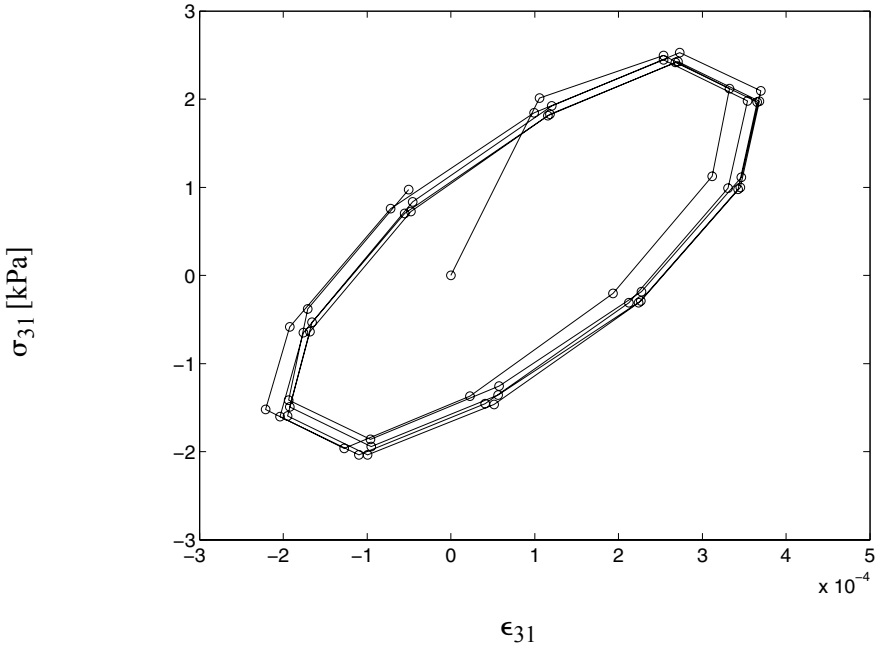


**Figure 4.8 Shear stress - strain response at Gauss point G (see Figure 4.1)**

#### 4.3.3.1 Comparison of Convergence Rate and Computational Time

In this section, the number of Newton-Raphson iterations at the "structure" level needed to reach convergence at each time or loading step using the material consistent tangent moduli is compared to the number of iterations needed when using material continuum tangent moduli (Figures 4.9 to 4.11). The convergence criteria used to produce the results in these figures are: unbalanced force (tolerance = $10^{-4}$[kN]), displacement increment (tolerance = $10^{-8}$[m]), and energy increment (tolerance = $10^{-12}[kN \cdot m]$). In each figure, the computational time is provided in the legend. The computational time (clock time and not CPU time) depends on the CPU speed, memory capability, and the background processes. For each comparison, the two problems are run consecutively on the

same machine, and the ratio of the CPU time over computational time is high (near one), comparison of the computational times can be used to compare the speed of the two algorithms. Tables 4.1 to 4.3 provide the unbalanced force, last incremental displacement, and energy, respectively, as a function of the iteration number for a representative load step (step # 20) computed using the material continuum and consistent tangent moduli.

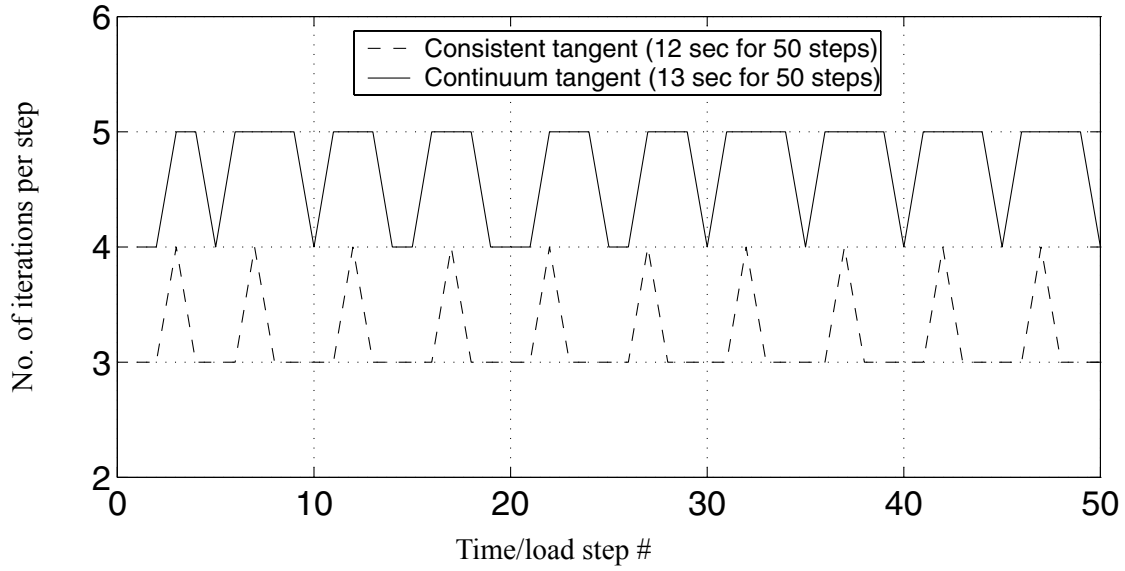


**Figure 4.9 Convergence rate comparison using unbalanced force as test for convergence (tol = 1E-4 [kN])**

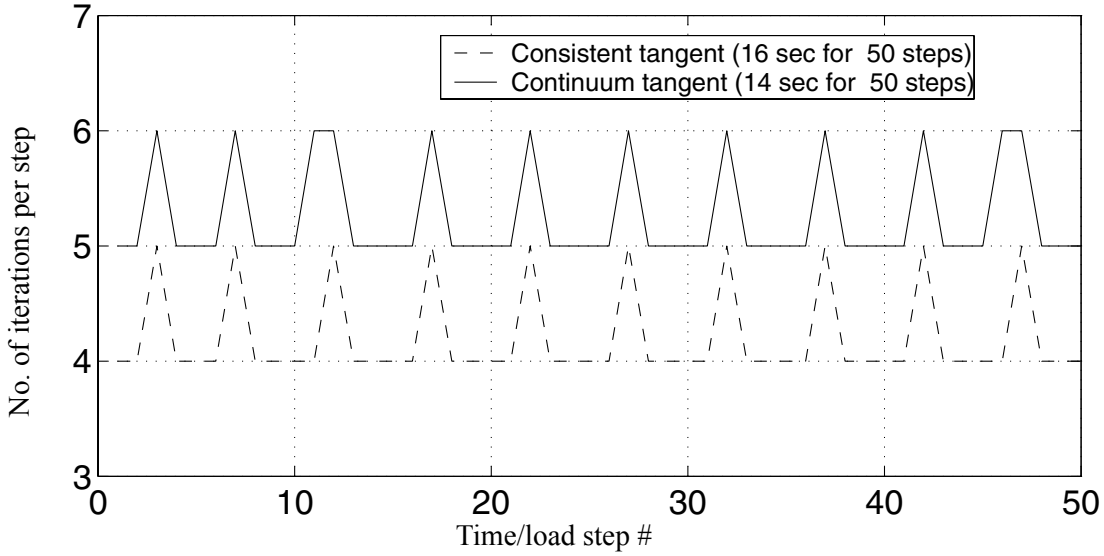


**Figure 4.10 Convergence rate comparison using displacement increment as test for convergence (tol = 1E-8 [m])**

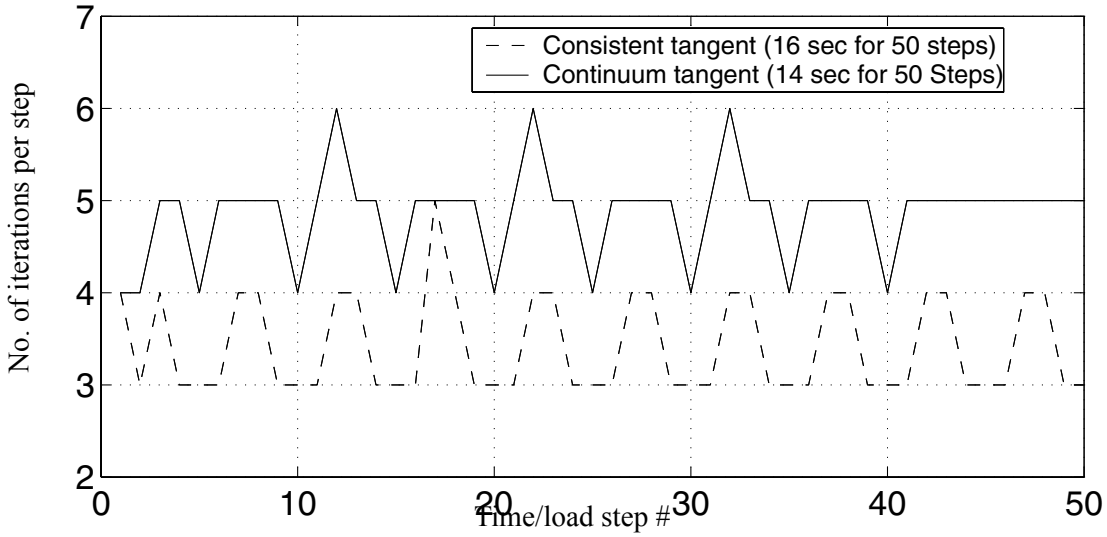


**Figure 4.11 Convergence rate comparison using energy increment as test for convergence (tol = 1E-12 $[kN \cdot m]$)**

**Table 4.1 Unbalanced force versus iteration number in load step # 20 (tol = 1E-4 [kN])**

| iteration # | 1 | 2 | 3 | 4 |
|---|---|---|---|---|
| consistent tangent | 1.00E-1 | 2.01E-3 | 3.61E-7 | – |
| continuum tangent | 1.41E-1 | 7.87E-3 | 6.82E-4 | 7.82E-5 |

**Table 4.2 Last incremental displacement versus iteration number in load step # 20 (tol = 1E-8 [m])**

| iteration # | 1 | 2 | 3 | 4 | 5 |
|---|---|---|---|---|---|
| consistent tangent | 1.87E-4 | 1.38E-5 | 1.52E-7 | 2.71E-11 | – |
| continuum tangent | 1.89E-4 | 1.69E-5 | 4.79E-7 | 3.09E-8 | 3.62E-9 |

**Table 4.3 Last incremental energy versus iteration number in load step # 20 (tol = 1E-12 $[kN \cdot m]$)**

| iteration # | 1 | 2 | 3 | 4 |
|---|---|---|---|---|
| consistent tangent | 2.05E-6 | 7.99E-9 | 1.78E-13 | – |
| continuum tangent | 2.25E-6 | 3.77E-9 | 1.24E-11 | 7.39E-14 |

From the results of this benchmark problem, the following observations can be made:

- The number of iterations per load step is consistently lower (16.7% - 25%) when using consistent tangent moduli over continuum tangent moduli.

- The computational time remains the same when using either the consistent or the continuum tangent moduli. This is due to the fact that although the number of iterations is reduced when using the consistent tangent moduli, more computational work is required to form the consistent tangent stiffness matrix than the continuum tangent stiffness matrix at each time or load step. In a later section, it will be shown that for tighter convergence criteria (smaller tolerance), the use of consistent tangent moduli will save a larger proportion of iterations which will result in a reduction in the computational time.
- From Table 4.1, it is observed that when using the consistent tangent moduli, the unbalanced forces exhibit an asymptotic rate of quadratic convergence as expected, which is not the case when using the continuum tangent moduli. It is also observed from Tables 4.2-4.3 that the rate of convergence of the last incremental displacement and energy, although not quadratic, is much higher for the consistent than for the continuum tangent moduli.

#### 4.3.3.2 Comparison of Convergence Rate for Smaller Convergence Tolerance

In this section, the model defined in Section 4.3.3 is re-evaluated with tighter convergence tolerances. The computational conditions are the same, except for the tolerances that are set to $10^{-8}$[kN], $10^{-12}$[m], and $10^{-20}$ [$kN \cdot m$ ] for the convergence criteria based on the unbalanced force, displacement increment, and energy increment, respectively. The number of Newton-Raphson iterations needed to reach convergence at each time or loading step when using the continuum and consistent material tangent moduli are compared

in Figures 4.12 through 4.14. At representative load step # 15, the unbalanced force, last incremental displacement and last incremental energy as a function of the iteration number are reported in Tables 4.4 through 4.6, respectively, when using both continuum and consistent tangent material moduli. These results demonstrate, as in Section 4.3.3.1, that the convergence rate is significantly improved when using consistent tangent moduli (asymptotic rate of quadratic convergence of unbalanced forces) over using continuum tangent moduli.

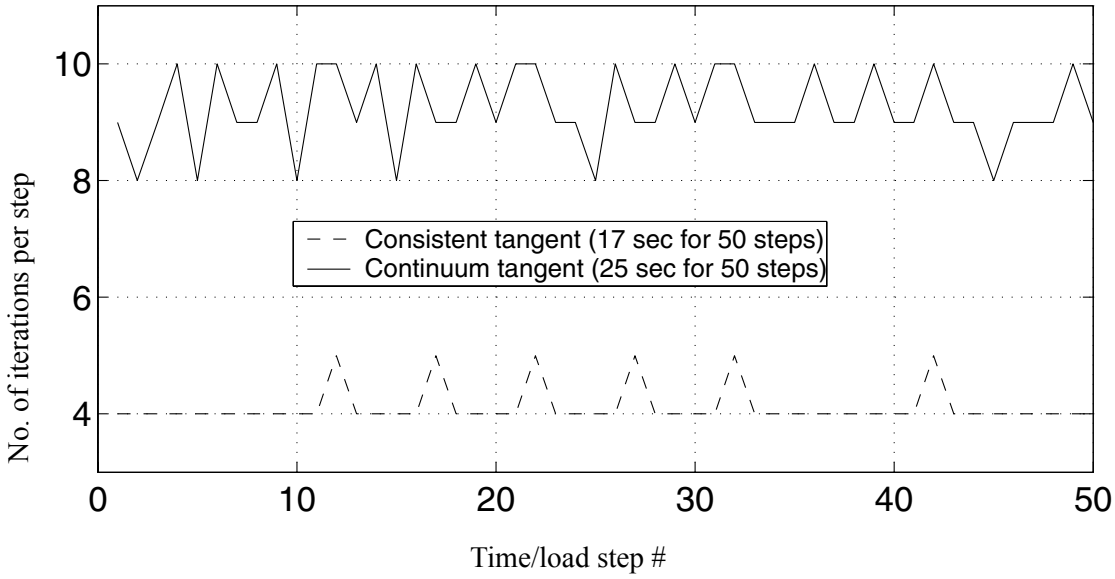


**Figure 4.12 Convergence rate comparison using unbalanced force as test for convergence with smaller tolerance (tol = 1E-8 [kN])**

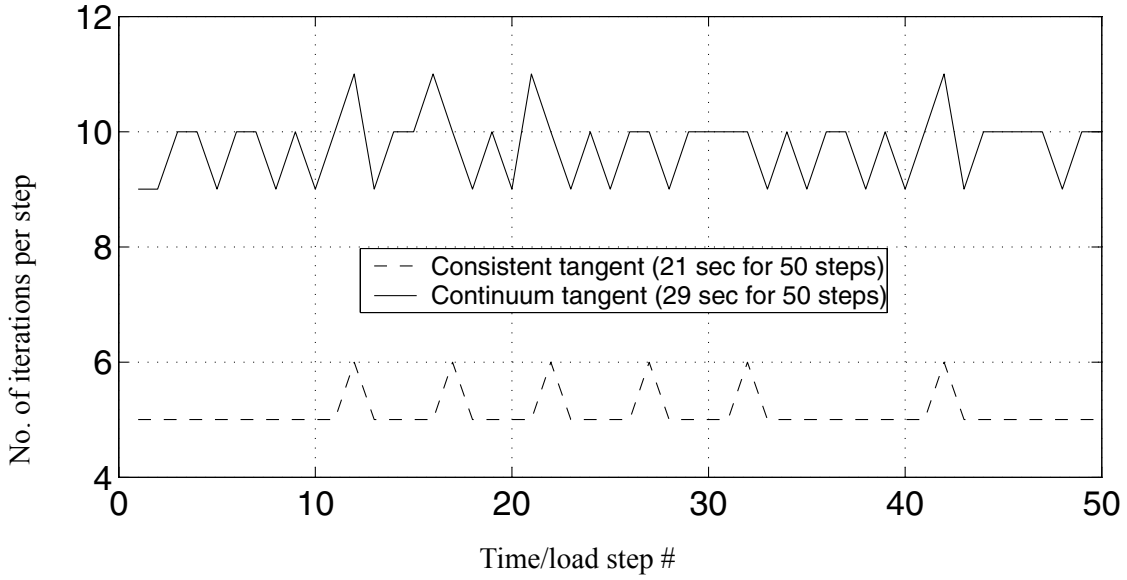


**Figure 4.13 Convergence rate comparison using displacement increment as test for convergence with smaller tolerance (tol = 1E-12 [m])**

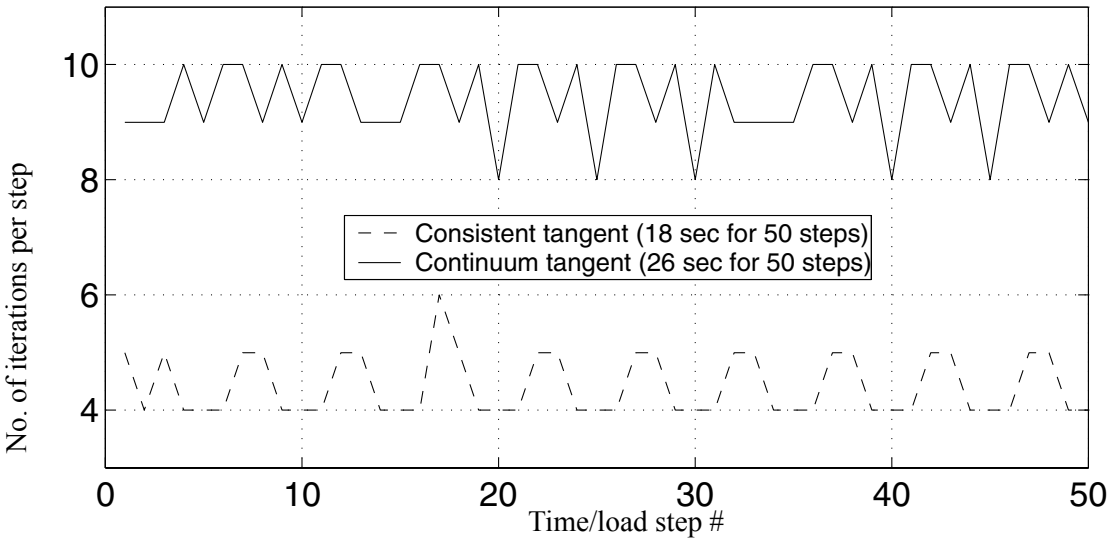


**Figure 4.14 Convergence rate comparison using energy increment as test for convergence with smaller tolerance (tol = 1E-20 $[kN \cdot m]$)**

**Table 4.4 Unbalanced force versus iteration number in load step # 15 (tol = 1E-8 [kN])**

| iteration # | 1 | 2 | 3 | 4 | 5 | 6 | 7 | 8 |
|---|---|---|---|---|---|---|---|---|
| consis-tent tan-gent | 1.14E-1 | 2.98E-3 | 1.01E-6 | 1.69E-13 | – | – | – | – |
| continu um tangent | 1.09E-1 | 4.58E-3 | 3.23E-4 | 3.08E-5 | 3.47E-6 | 4.26E-7 | 5.38E-8 | 6.88E-9 |

**Table 4.5 Last incremental displacement versus iteration number in load step # 15 (tol = 1E-12 [m])**

| iteration # | 1 | 2 | 3 | 4 | 5 | 6 | 7 | 8 | 9 | 10 |
|---|---|---|---|---|---|---|---|---|---|---|
| consis-tent tan-gent | 1.86 E-4 | 1.63 E-5 | 2.17 E-7 | 6.71 E-11 | 9.59 E-18 | – | – | – | – | – |
| continu um tangent | 1.88 E-4 | 1.76 E-5 | 4.08 E-7 | 3.35 E-8 | 4.17 E-9 | 5.33 E-10 | 6.90 E-11 | 8.90 E-12 | 1.15 E-12 | 1.47 E-13 |

**Table 4.6 Last incremental energy versus iteration number in load step # 15 (tol = 1E-20 $[kN \cdot m]$)**

| iteration # | 1 | 2 | 3 | 4 | 5 | 6 | 7 | 8 | 9 |
|---|---|---|---|---|---|---|---|---|---|
| consis-tent tan-gent | 2.60E-6 | 5.40E-9 | 5.00E-14 | 2.78E-24 | – | – | – | – | – |

**Table 4.6 Last incremental energy versus iteration number in load step # 15 (tol = 1E-20 $[kN \cdot m]$)**

| iteration # | 1 | 2 | 3 | 4 | 5 | 6 | 7 | 8 | 9 |
|---|---|---|---|---|---|---|---|---|---|
| continuum tangent | 1.81E-6 | 6.83E-9 | 4.66E-11 | 5.59E-13 | 8.40E-15 | 1.34E-16 | 2.19E-18 | 3.59E-20 | 5.91E-22 |

Comparing the results in Sections 4.3.3.2 and 4.3.3.1, it is observed that the advantage of using the consistent over the continuum tangent moduli becomes more pronounced (in terms of both the number of iterations per step and the computational time) with tighter convergence tolerance. Only when the tolerance is small enough such that the sequence of trial stresses $\boldsymbol{\tau}_i^{tr}$ approaches the solution point inside the convergence region, does the use of consistent tangent moduli ensure a quadratic convergence of the Newton process.

#### 4.3.3.3 Convergence Rate Comparison for Varying Number of Yield Surfaces

This section examines the effect of using 40 versus 20 yield surfaces in defining the backbone curve of the material constitutive model, on the convergence rate of the Newton process. The comparative results are shown in Figures 4.15 through 4.17 and Tables 4.7 through 4.9. The convergence criteria used to perform these simulations are the same as in Section 4.3.3.1, i.e., tolerance = $10^{-4}$[kN] for unbalanced force, tolerance = $10^{-8}$[m] for displacement increment, and tolerance = $10^{-12}[kN \cdot m]$ for energy increment.

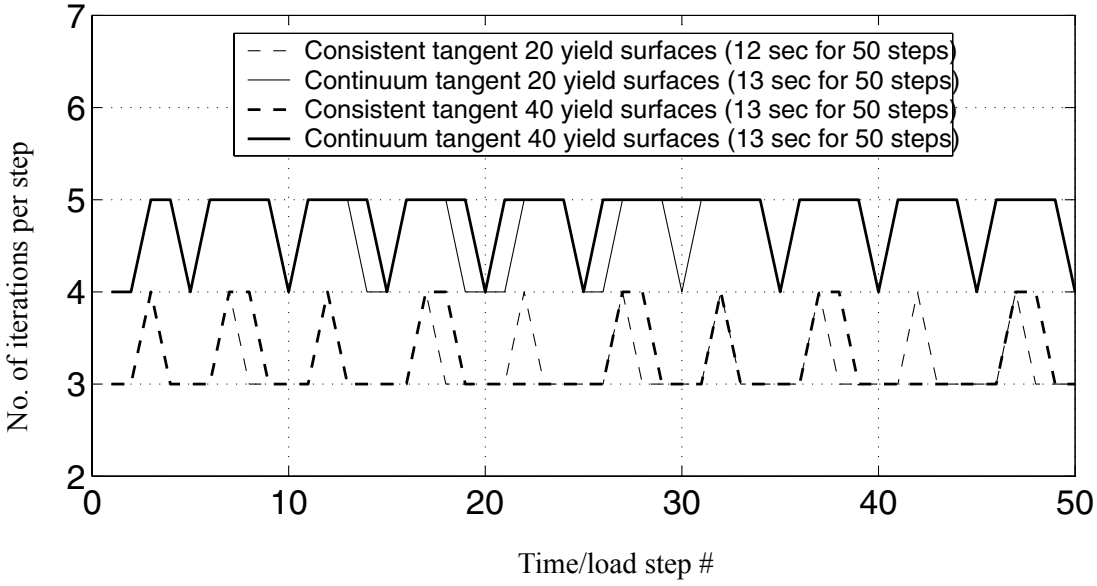


**Figure 4.15 Convergence rate comparison using unbalanced force as test for convergence with varying number of yield surfaces (tol = 1E-4 [kN])**

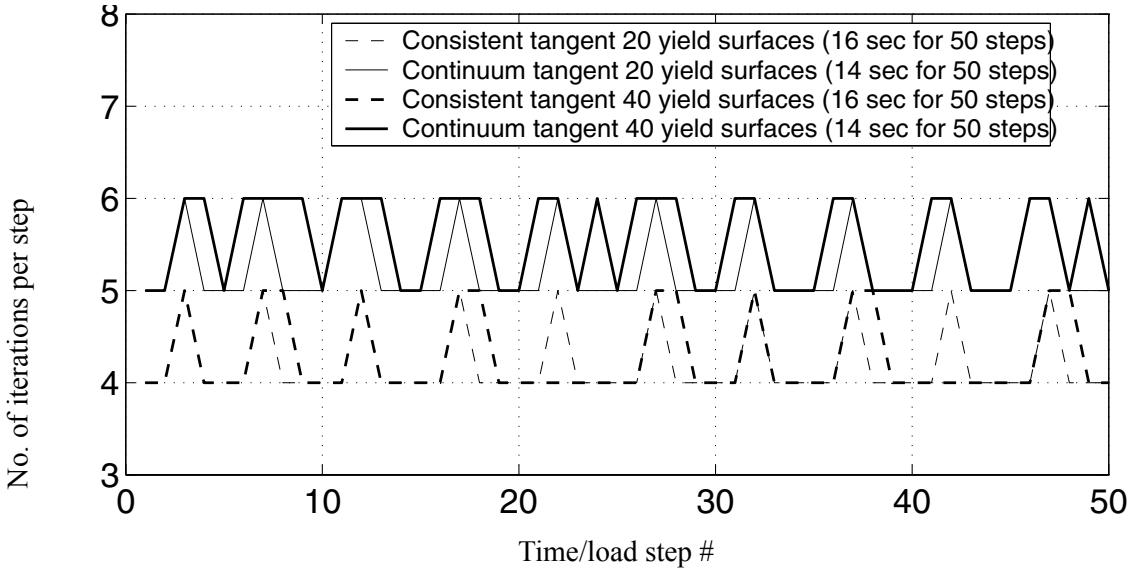


**Figure 4.16 Convergence rate comparison using displacement increment as test for convergence with varying number of yield surfaces (tol = 1E-8 [m])**

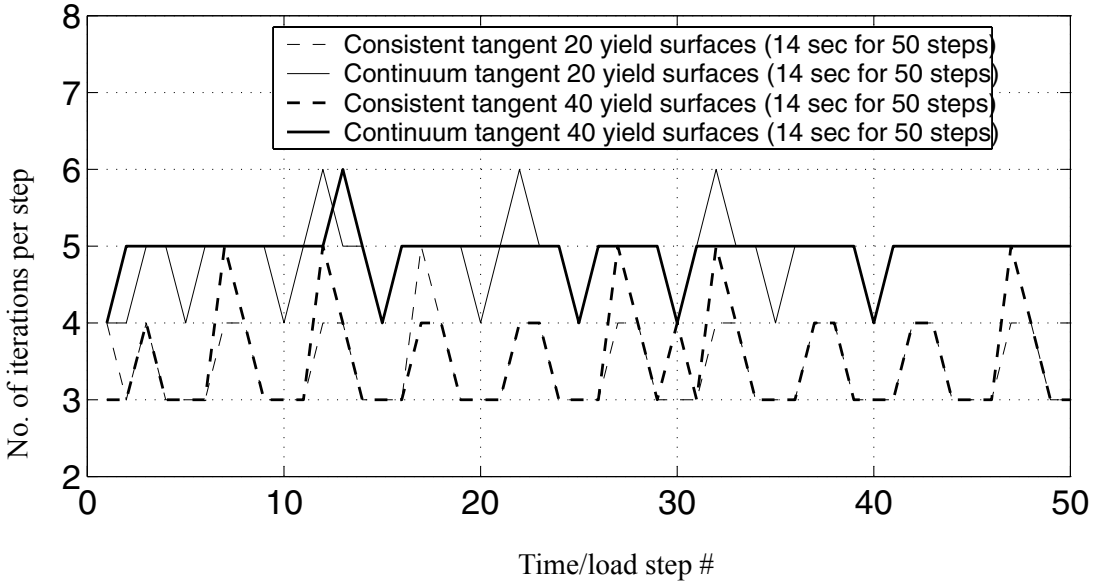


**Figure 4.17 Convergence rate comparison using energy increment as test for convergence with varying number of yield surfaces (tol = 1E-12 $[kN \cdot m]$)**

**Table 4.7 Unbalanced force versus iteration number in load step # 10 (tol = 1E-4 [kN])**

| iteration # | 1 | 2 | 3 | 4 |
|---|---|---|---|---|
| consistent tangent | 1.11E-1 | 2.11E-3 | 1.76E-5 | – |
| continuum tangent | 1.26E-1 | 7.69E-3 | 6.73E-4 | 7.79E-5 |

**Table 4.8 Last incremental displacement versus iteration number in load step # 10 (tol = 1E-8 [m])**

| iteration # | 1 | 2 | 3 | 4 | 5 |
|---|---|---|---|---|---|
| consistent tangent | 1.87E-4 | 1.45E-5 | 1.72E-7 | 5.43E-11 | – |
| continuum tangent | 1.89E-4 | 1.67E-5 | 4.59E-7 | 3.73E-8 | 4.67E-9 |

**Table 4.9 Last incremental energy versus iteration number in load step # 10 (tol = 1E-12 $[kN \cdot m]$)**

| iteration # | 1 | 2 | 3 | 4 | 5 |
|---|---|---|---|---|---|
| consistent tangent | 2.54E-6 | 3.10E-9 | 7.44E-13 | – | – |
| continuum tangent | 2.05E-6 | 6.00E-9 | 9.81E-11 | 1.11E-12 | 1.67E-14 |

Comparing the results in Sections 4.3.3.3 and 4.3.3.1, it is noticed that the convergence rate is better when using the consistent tangent moduli over the continuum tangent moduli, regardless of the number of yield surfaces used in the material constitutive model. In this comparative example, the difference in convergence rates is not very significant due to the lax convergence tolerance used in the computations.

### 4.3.4 Layered Soil Column Subjected to Earthquake Base Excitation

The second benchmark problem consists of a multi-layered soil column subjected to earthquake base excitation. This soil column is representative of the local soil condition at

the site of the Humbolt Bay Middle Channel Bridge near Eureka in northern California. A multi-yield-surface $J_2$ plasticity material model with 20 yield surfaces is employed to describe the various layers of soil as shown in Table 4.10. The soil column is discretized into a 2D finite element model consisting of 28 four-node quadratic bilinear isoparametric elements with 4 Gauss points each as shown in Figure 4.18. The soil column is assumed to be under simple shear condition and the displacements of corresponding nodes at left and right boundaries are set to be same for both horizontal and vertical directions. The total horizontal acceleration at the base of the soil column, see Figure 4.19, was obtained elsewhere (through deconvolution of a ground surface free field motion. The Newmark-beta direct step-by-step integration method with parameters $\beta = 0.2756, \gamma = 0.55$ is used with a constant time step $\Delta t = 0.01$ sec for integrating the equation of motion of the system. The horizontal displacement response of the soil column (relative to the base) at the top of each soil layer is shown in Figure 4.20. At the lowest layer, the relation of shear stress $\sigma_{xz}$ and shear strain $\varepsilon_{xz}$ at Gauss point C (Figure 4.18) is shown in Figure 4.21. From these figures that significant yielding of the material is observed during the earthquake.

**Table 4.10 Material properties of various layers of soil column**

| Mat. | G(KPa) | $\tau_{max}(KPa)$ |
|---|---|---|
| 1 | 54450 | 33 |
| 2 | 33800 | 26 |
| 3 | 96800 | 44 |
| 4 | 61250 | 35 |

**Table 4.10 Material properties of various layers of soil column**

| Mat. | G(KPa) | $\tau_{max}(KPa)$ |
|---|---|---|
| 5 | 180000 | 60 |
| 6 | 369800 | 86 |

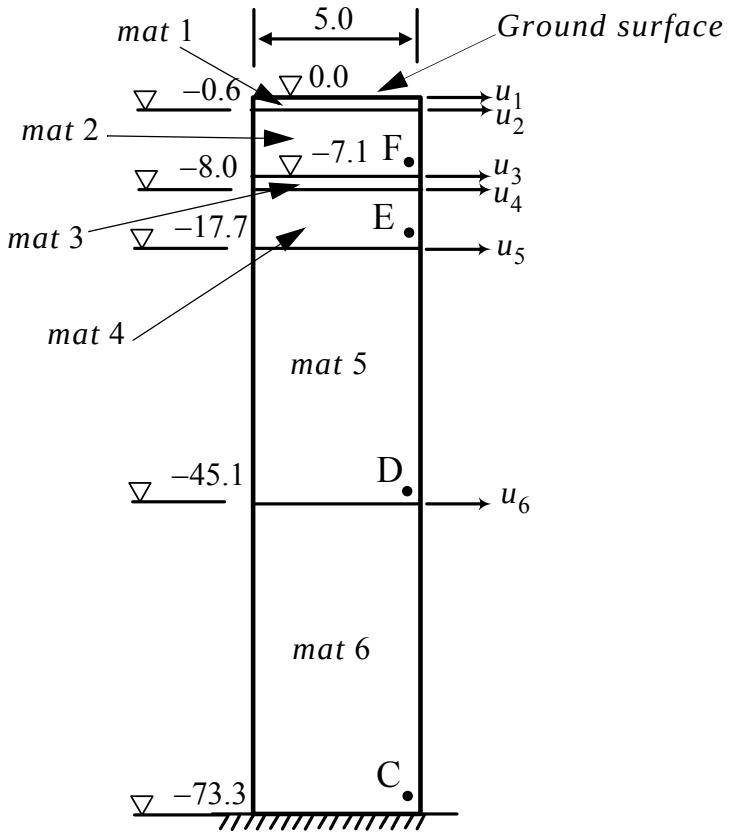


**Figure 4.18 Layered soil column subjected to total base acceleration (unit: [m])**

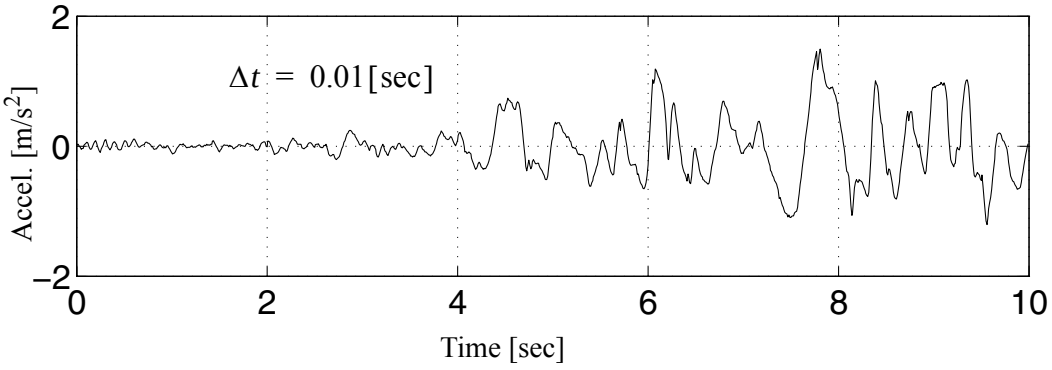


**Figure 4.19 Total acceleration at the base of the soil column**

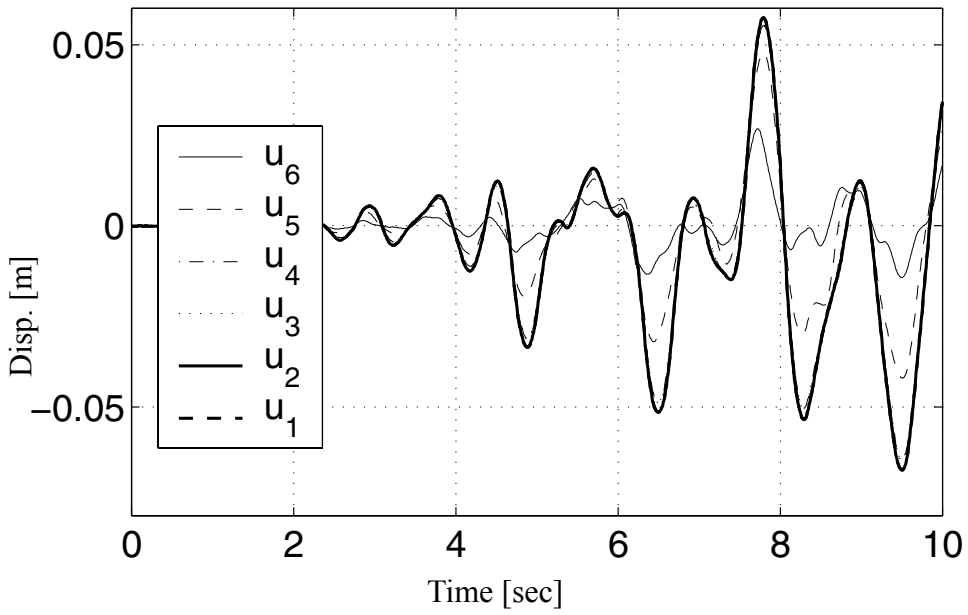


**Figure 4.20 Response of different soil layers**

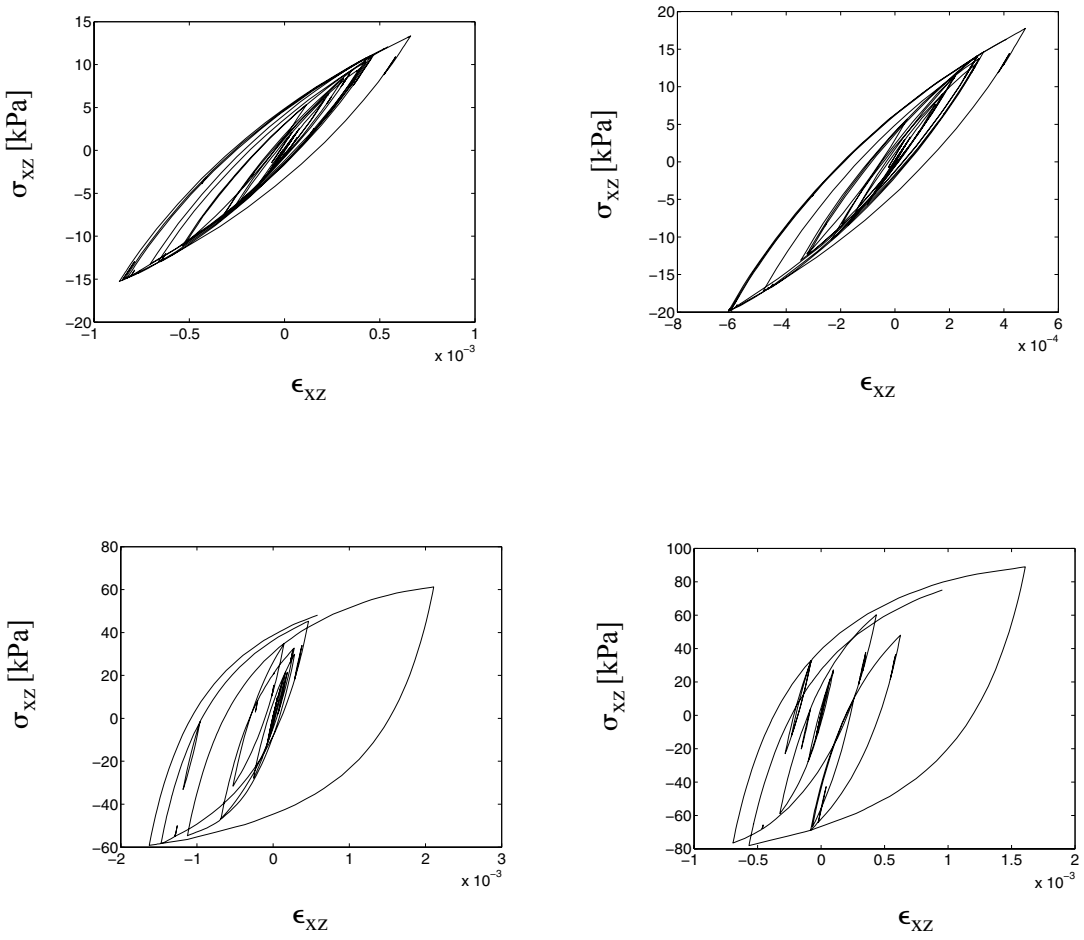


**Figure 4.21 Shear stress vs shear strain at the point C, D, E, and F**

#### 4.3.4.1 Comparison of the Convergence Rate and Computational Time between the Use of Consistent and Continuum Tangent Moduli

In this section, the number of iterations to reach convergence at every time step is investigated for both the case of using consistent tangent moduli and that of using continuous tangent moduli, as shown in Figures 4.22- 4.24. The convergence criteria is based on

the unbalanced force (tolerance = $10^{-4}$[kN]), increment of displacement(tolerance = $10^{-8}$[m]), and incremental energy (tolerance = $10^{-12}[kN \cdot m]$), respectively.

At representative load step 30, for both the case of using the continuum tangent operator and that of using the consistent tangent operator, the unbalanced force, last incremental displacement and energy as a function of iteration number are reported in Tables 4.11 - 4.13, respectively.

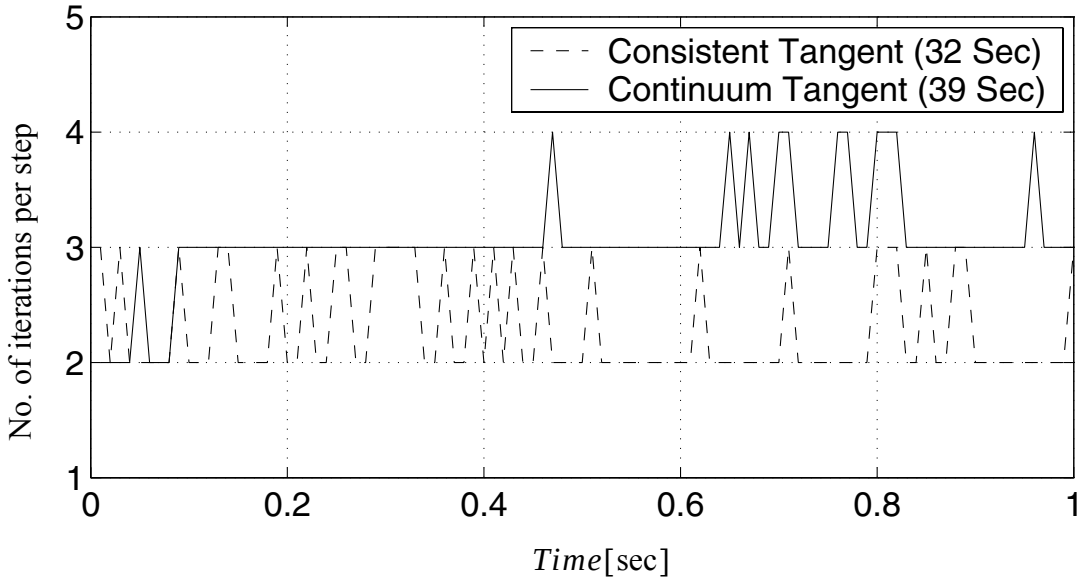


**Figure 4.22 Convergence rate comparison using unbalanced force as test for convergence (tol = 1E-4 [kN])**

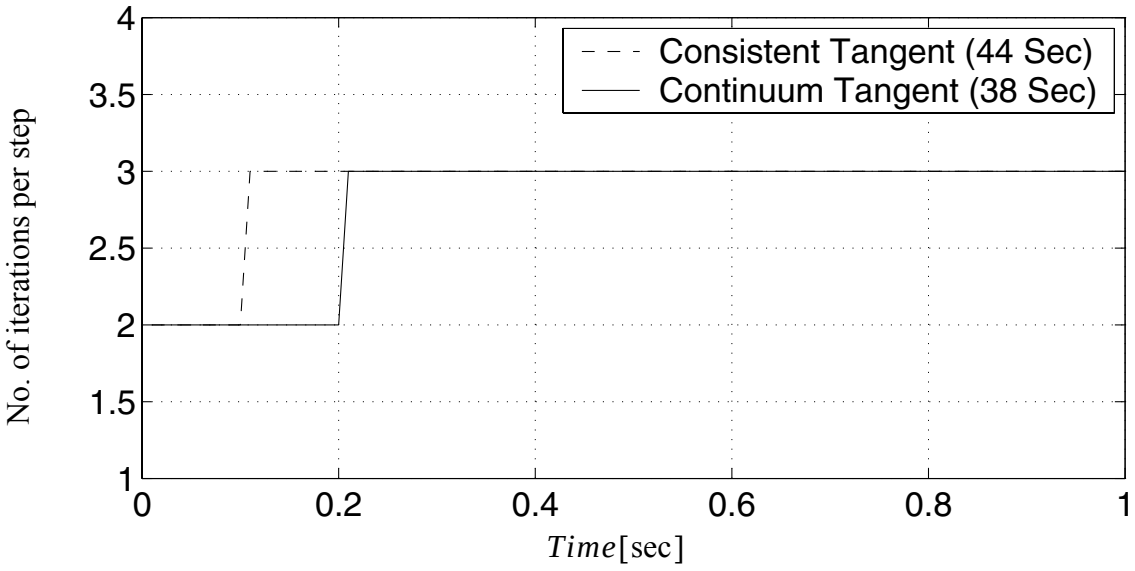


**Figure 4.23 Convergence rate comparison using displacement increment as test for convergence (tol = 1E-8 [m])**

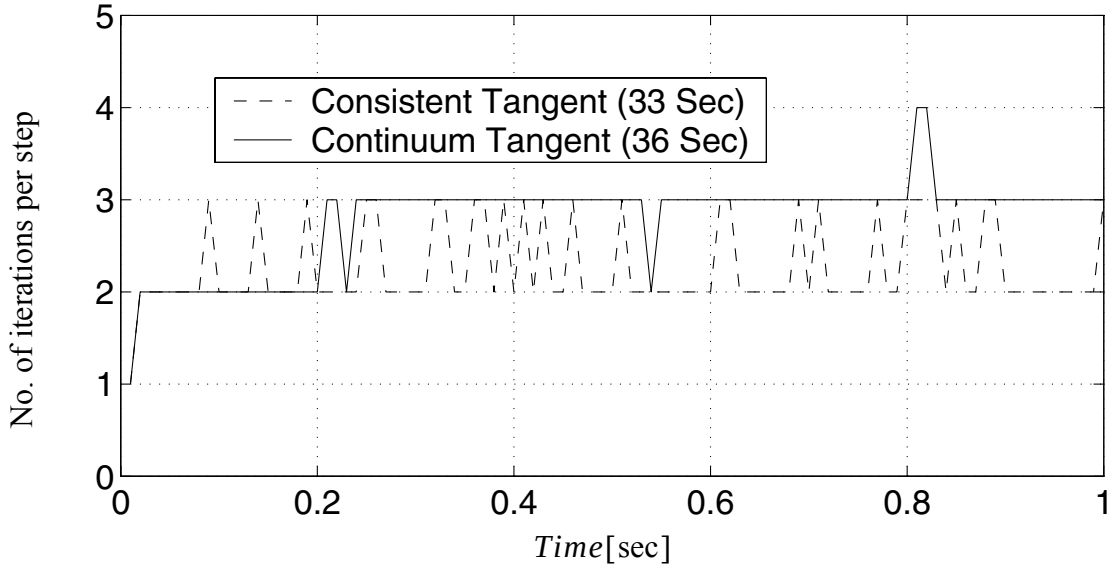


**Figure 4.24 Convergence rate comparison using energy increment as test for convergence (tol = 1E-12 $[kN \cdot m]$)**

**Table 4.11 Unbalanced force versus iteration number in load step # 30 (tol = 1E-4 $[kN \cdot m]$)**

| iteration # | 1 | 2 | 3 |
|---|---|---|---|
| consistent tangent | 1.32 | 1.16E-4 | 2.61E-10 |
| continuum tangent | 9.61E-1 | 2.29E-3 | 1.24E-5 |

**Table 4.12 Last incremental displacement versus iteration number in load step # 30 (tol = 1E-8 [m])**

| iteration # | 1 | 2 | 3 |
|---|---|---|---|
| consistent tangent | 4.39E-5 | 5.63E-8 | 1.13E-13 |
| continuum tangent | 4.39E-5 | 3.56E-8 | 1.36E-10 |

**Table 4.13 Last incremental energy versus iteration number in load step # 30 (tol = 1E-12 $[kN \cdot m]$)**

| iteration # | 1 | 2 | 3 |
|---|---|---|---|
| consistent tangent | 2.54E-6 | 7.50E-15 | – |
| continuum tangent | 2.05E-6 | 1.51E-11 | 3.88E-16 |

From these results, the following observations can be made:

- The convergence rate at every load step as measured by the number of iterations is faster by 0% - 50%, when using consistent tangent moduli instead of continuum tangent moduli. It is noteworthy to mention that occasionally convergence rate is slower when using consistent tangent moduli over continuum tangent moduli, because the convergence tolerance is bigger than convergence 'radius' such that the quadratic convergence rate is never achieved before convergence when using consistent tangent moduli .
- The computational time is almost the same when using either of the two tangent moduli. While the number of iterations is reduced when using the consistent tangent moduli, more computational work is required to form the consistent tangent moduli than the continuum tangent moduli at each time or load step.
- From Table 4.11, it is observed that when using the consistent tangent moduli, the unbalanced forces exhibit an asymptotic rate of quadratic convergence. It is also observed from Tables 4.12-4.13 that the rate of convergence of the last incremental displacement and energy is much higher for the consistent tangent moduli than for the continuum tangent moduli.

#### 4.3.4.2 Comparison of Convergence Rates with Smaller Convergence Tolerance

In this section, the model described in section 4.3.4 is reconsidered with stricter tolerance. The computational conditions are the same, however the tolerances are set to $10^{-8}$[kN], $10^{-12}$[m], and $10^{-20}$ $[kN \cdot m]$ for the convergence criteria based on the unbalanced force, displacement increment, and energy increment, respectively. The number of the

iterations versus load step number are given in 4.25-4.27. At representative load step 40, the unbalanced force, last incremental displacement and incremental energy as a function of iteration number are reported in Tables 4.14 - 4.16, respectively.

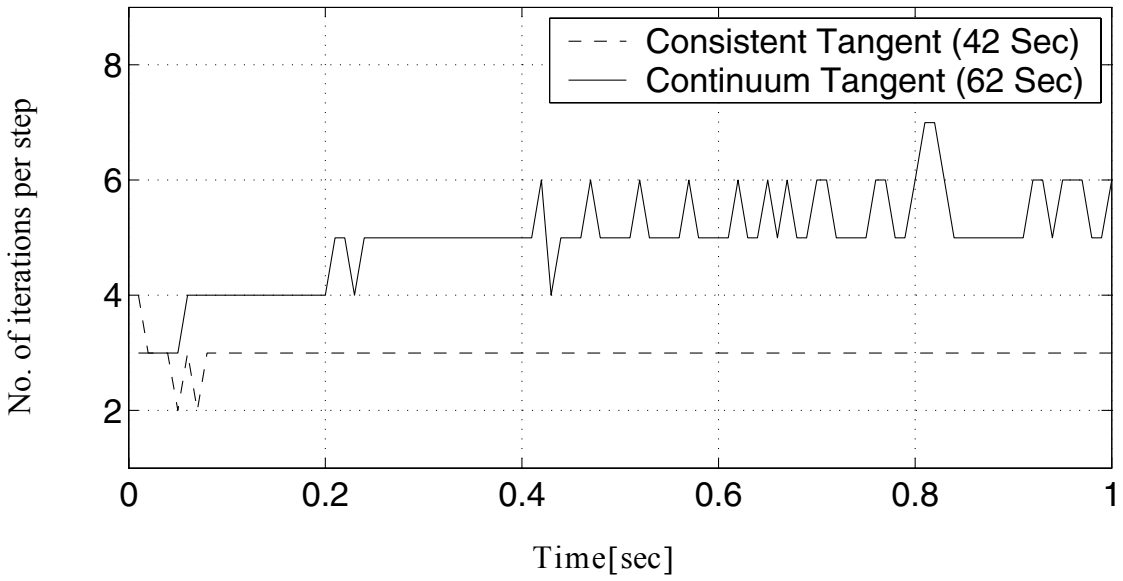


**Figure 4.25 Convergence rate comparison using unbalanced force as test for convergence with smaller tolerance (tol = 1E-8 [kN])**

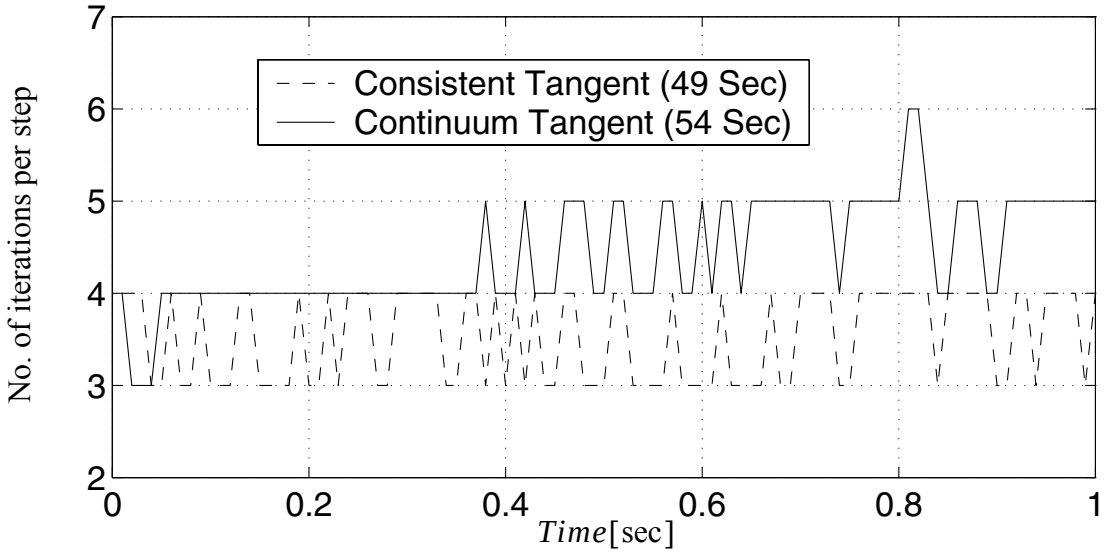


**Figure 4.26 Convergence rate comparison using displacement increment as test for convergence with smaller tolerance (tol = 1E-12 [m])**

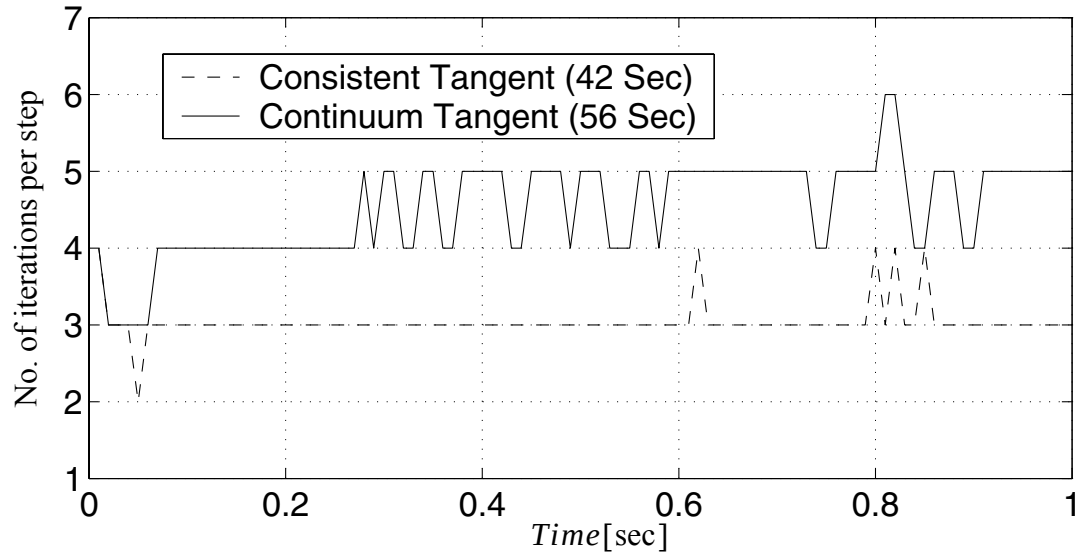


**Figure 4.27 Convergence rate comparison using energy increment as test for convergence with smaller tolerance (tol = 1E-20 $[kN \cdot m]$)**

**Table 4.14 Unbalanced force versus iteration number in load step # 40 (tol = 1E-8 [kN])**

| iteration # | 1 | 2 | 3 | 4 | 5 |
|---|---|---|---|---|---|
| consistent tangent | 1.12 | 2.50E-6 | 2.65E-10 | – | – |
| continuum tangent | 8.03E-1 | 1.98E-3 | 1.35E-5 | 7.92E-8 | 6.75E-10 |

**Table 4.15 Last incremental displacement versus iteration number in load step # 40 (tol = 1E-12 [m])**

| iteration # | 1 | 2 | 3 | 4 |
|---|---|---|---|---|
| consistent tangent | 6.51E-5 | 6.11E-8 | 1.95E-13 | – |
| continuum tangent | 6.51E-5 | 3.65E-8 | 1.58E-10 | 7.29E-13 |

**Table 4.16 Last incremental energy versus iteration number in load step # 40 (tol = 1E-20 $[kN \cdot m]$)**

| iteration # | 1 | 2 | 3 | 4 | 5 |
|---|---|---|---|---|---|
| consistent tangent | 3.06E-6 | 1.42E-14 | 2.40E-25 | – | – |
| continuum tangent | 2.27E-6 | 1.62E-11 | 6.00E-16 | 2.64E-20 | 1.26E-24 |

These results demonstrate that the use of the consistent tangent moduli reduces the number of iteration steps needed to reach convergence by about 40%, and the computational time by 10% to 25%, when compared with the use of the continuum tangent moduli.

Comparing results in 4.3.4.1 and 4.3.4.2, it is observed that the advantage of the use of the consistent tangent moduli is more evident when the tolerance is stricter.

#### 4.3.4.3 Comparison of the Convergence Rates with Varying Time Step Size

In this section, the convergence rate and computational time are compared for the use of the consistent tangent moduli and the continuous tangent moduli when time step is purposely exaggerated to $\Delta t = 0.05[\text{sec}]$ , with all other conditions remaining the same as in section 4.3.4.1. The results are shown in Figures 4.28-4.30. At representative load step 60, the unbalanced force, last incremental displacement and energy as a function of iteration number are reported in Tables 4.17 - 4.19, respectively, for both the case of using the continuum tangent operator and that of using the consistent tangent operator.

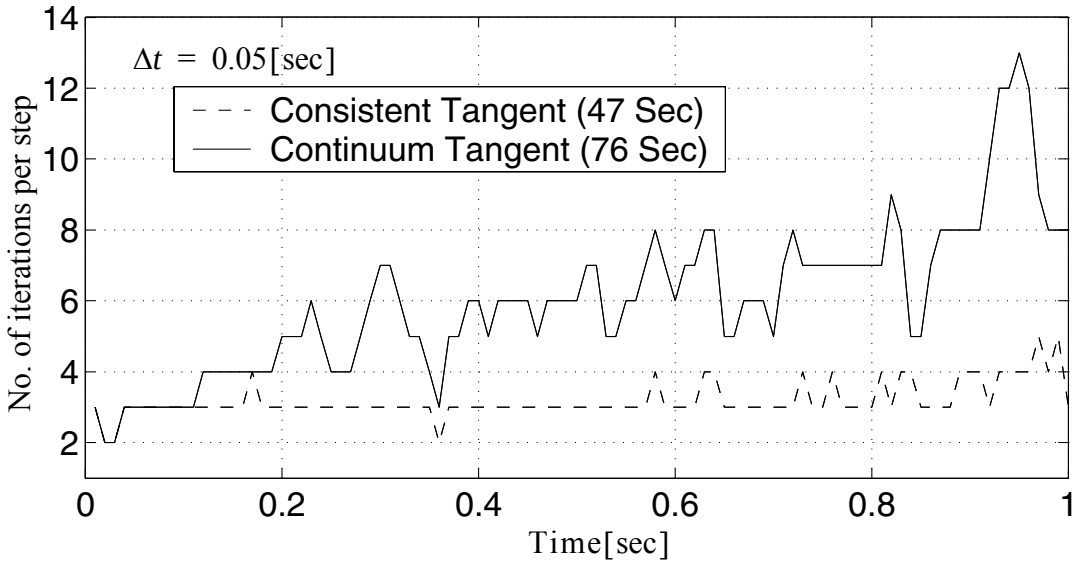


**Figure 4.28 Convergence rate comparison using unbalanced force as test for convergence for longer time step (tol = 1E-4 [kN])**

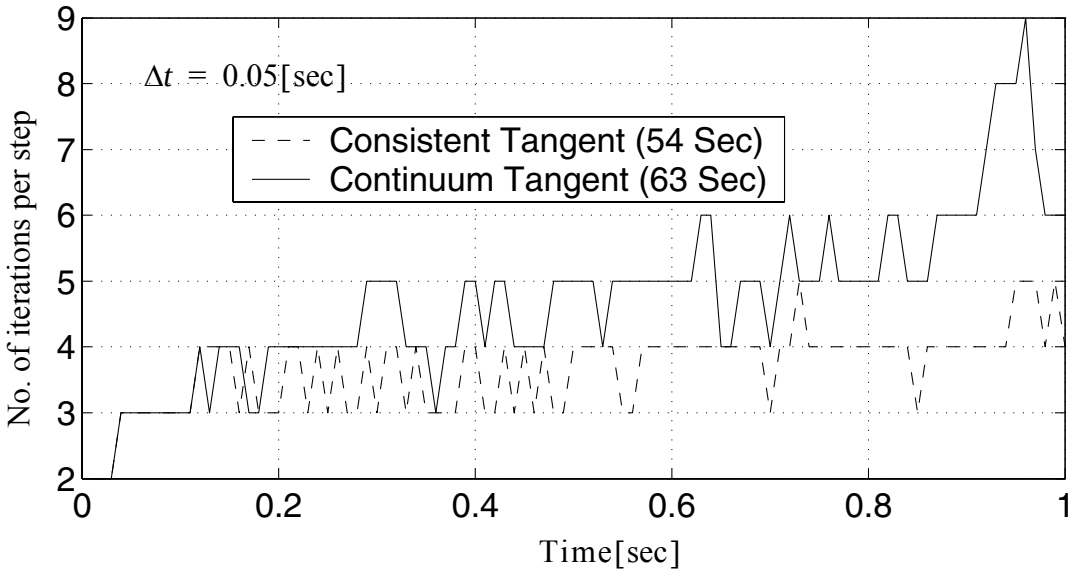


**Figure 4.29 Convergence rate comparison using displacement increment as test for convergence for longer time step (tol = 1E-8 [m])**

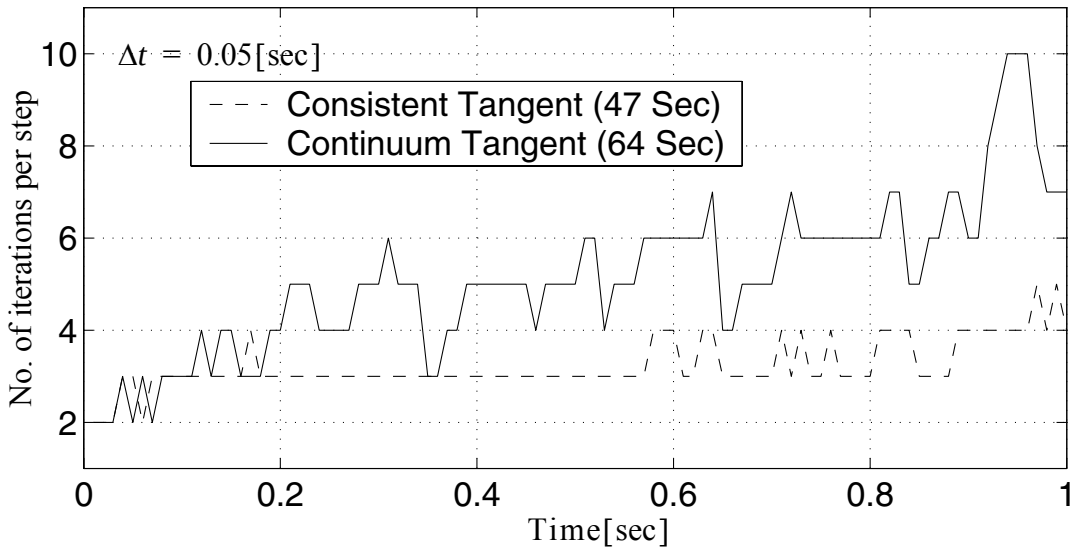


**Figure 4.30 Convergence rate comparison using energy increment as test for convergence for longer time step (tol = 1E-12 $[kN \cdot m]$)**

**Table 4.17 Unbalanced force versus iteration number in load step # 60 (tol = 1E-4 [kN])**

| iteration # | 1 | 2 | 3 | 4 | 5 | 6 |
|---|---|---|---|---|---|---|
| consis-tent tan-gent | 2.86E1 | 6.10E-1 | 3.35E-5 | – | – | – |
| continuu m tangent | 9.64E1 | 4.16 | 2.22E-1 | 1.36E-2 | 8.86E-4 | 6.37E-5 |

**Table 4.18 Last incremental displacement versus iteration number in load step # 60 (tol = 1E-8 [m])**

| iteration # | 1 | 2 | 3 | 4 | 5 |
|---|---|---|---|---|---|
| consistent tangent | 2.78E-3 | 7.55E-5 | 3.71E-7 | 3.24E-11 | – |
| continuum tangent | 2.79E-3 | 5.17E-5 | 1.19E-6 | 6.00E-8 | 3.88E-9 |

**Table 4.19 Last incremental energy versus iteration number in load step # 60 (tol = 1E-12 $[kN \cdot m]$)**

| iteration # | 1 | 2 | 3 | 4 | 5 | |
|---|---|---|---|---|---|---|
| consis-tent tan-gent | 9.74E-3 | 1.40E-6 | 2.06E-12 | 6.25E-23 | – | – |
| continuu m tangent | 6.62E-3 | 4.19E-5 | 8.19E-8 | 2.58E-10 | 1.10E-12 | 6.50E-15 |

It is observed from this data that the use of consistent tangent moduli reduced the number of iterations per time step needed to achieve convergence by 0% to 69%, and computational time by 14% to 38%.

Comparing the results in section 4.3.4.3 and section 4.3.4.1, it is observed that when the time step is increased, the advantage of consistent tangent moduli becomes more evident. When the time step is larger, the difference between the equation $\Delta\boldsymbol{\sigma} = \Delta\boldsymbol{\sigma}(\Delta\boldsymbol{\epsilon})$ and $\dot{\boldsymbol{\sigma}} = \dot{\boldsymbol{\sigma}}(\dot{\boldsymbol{\epsilon}})$ becomes more significant, as does the differentiation of stress $\boldsymbol{\sigma}$ to strain $\boldsymbol{\epsilon}$, which are defined as consistent tangent moduli and continuum tangent moduli. In this case, the continuum tangent moduli are more 'inconsistent' with the Newton process, leading to a loss of quadratic rate of asymptotic convergence which characterizes Newton's method.

#### 4.3.4.4 Comparison of the Convergence Rate using Different Number of Yield Surfaces

This section examines the effect on the convergence rate of the use of 20 and 40 yield surfaces in describing the model, as shown in Figures 4.31 - 4.33 and Tables 4.20 - 4.22. The convergence criteria used to get the results are the same as that in section 4.3.4.1: unbalanced force (tolerance = $10^{-4}$[kN]), displacement increment (tolerance = $10^{-8}$[m]), and energy increment (tolerance = $10^{-12}[kN \cdot m]$). Comparing sections 4.3.4.4 and 4.3.4.1, it is noticed that the convergence rate is better when using the consistent tangent moduli than when using the continuum tangent moduli, regardless of the number of yield surfaces in the model.

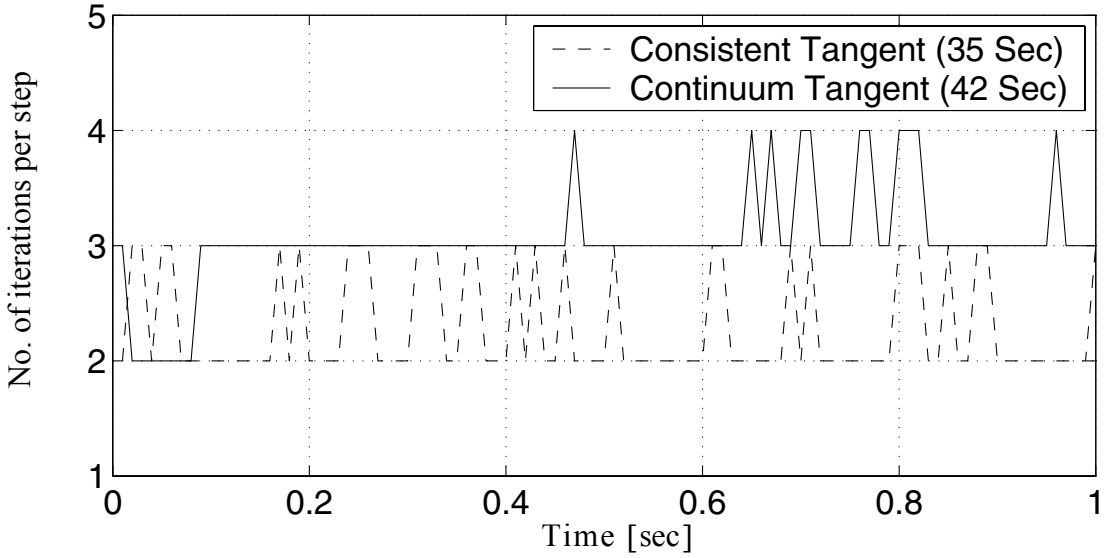


**Figure 4.31 Convergence rate comparison using unbalanced force as test for convergence with 40 yield surfaces (tol = 1E-4 [kN])**

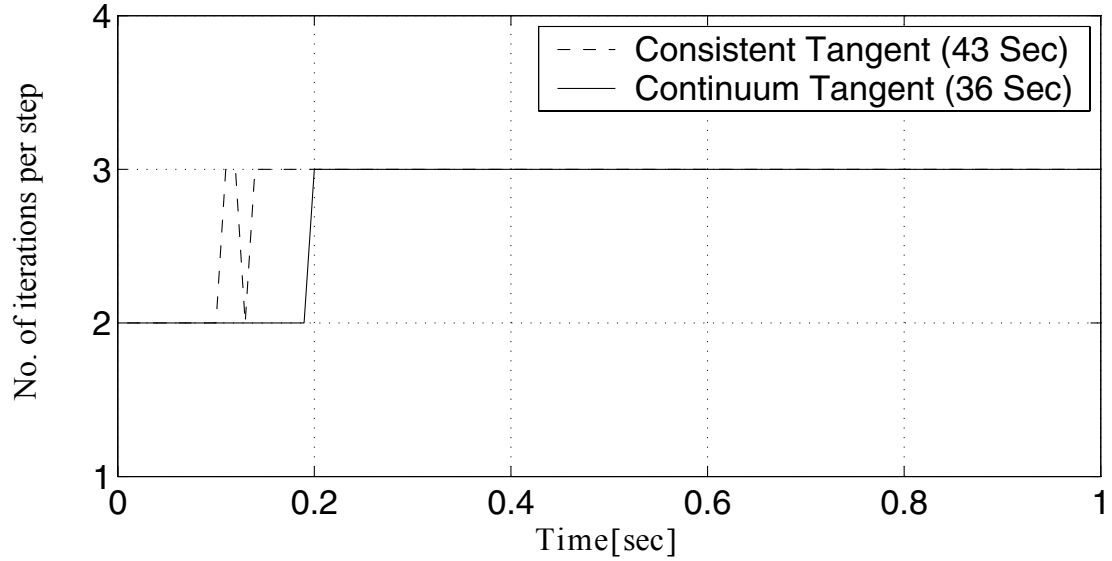


**Figure 4.32 Convergence rate comparison using displacement increment as test for convergence with 40 yield surfaces (tol = 1E-8 [m])**

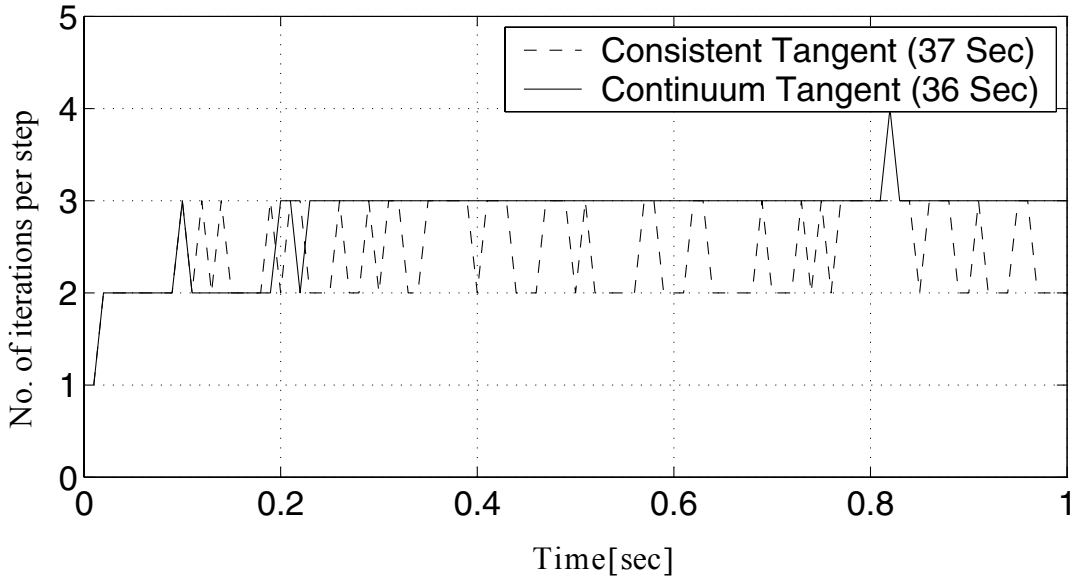


**Figure 4.33 Convergence rate comparison using energy increment as test for convergence with 40 yield surfaces (tol = 1E-12 $[kN \cdot m]$)**

**Table 4.20 Unbalanced force versus iteration number in load step # 30 (tol = 1E-4 [kN])**

| iteration # | 1 | 2 | 3 |
|---|---|---|---|
| consistent tangent | 1.31 | 2.08E-6 | – |
| continuum tangent | 9.61E-1 | 2.29E-3 | 1.23E-5 |

**Table 4.21 Last incremental displacement versus iteration number in load step # 30 (tol = 1E-8 [m])**

| iteration # | 1 | 2 | 3 |
|---|---|---|---|
| consistent tangent | 4.39E-5 | 5.58E-8 | 1.45E-11 |

**Table 4.21 Last incremental displacement versus iteration number in load step # 30 (tol = 1E-8 [m])**

| iteration # | 1 | 2 | 3 |
|---|---|---|---|
| continuum tangent | 4.39E-5 | 3.52E-8 | 1.85E-10 |

**Table 4.22 Last incremental energy versus iteration number in load step # 30 (tol = 1E-12 $[kN \cdot m]$)**

| iteration # | 1 | 2 | 3 |
|---|---|---|---|
| consistent tangent | 3.41E-6 | 2.20E-13 | – |
| continuum tangent | 2.76E-6 | 2.97E-11 | 1.45E-15 |

### 4.3.5 Conclusions

For Nonlinear problems involving rate constitutive equations, such as rate-independent elasto-plasticity, consistent tangent moduli (operator) play an important role in preserving the quadratic rate of asymptotic convergence of incremental-iterative solution schemes based on Newton's method. On the other hand, consistent tangent moduli are necessary in structural response sensitivity analysis based on the Direct Differentiation Method (DDM).

In this section, consistent tangent moduli have been derived for the Multi-yield $J_2$ plasticity model, a very versatile material model used extensively in geotechnical engineering. Derivative and software implementation have been verified through two application examples. The comparison studies are performed between continuum tangent moduli and

consistent tangent moduli in term of convergence rate and computation time of Newton's process. The results obtained indicate the followings:

- When the convergence tolerance is lax, the Newton process converges slightly faster when using the consistent tangent moduli rather than the continuum tangent moduli. However, this does not ensure a reduction in computational time when compared with the use of continuum tangent moduli, since more computational work is required to form the consistent tangent moduli than the continuum tangent moduli at each time or load step.
- When the tolerance is tightened, using consistent tangent moduli reduces both the number of iterations needed to achieve convergence per step and the computational time. The decreasing unbalanced forces show an asymptotically quadratic convergence of the Newton process when using consistent tangent moduli.
- In dynamic cases, when the time step increases, the use of the consistent tangent moduli reduces both the number of iterations needed to achieve convergence per step and computational time.
- Increasing the number of yield surfaces in the Multi-Yield $J_2$ plasticity model has a negligible effect on the comparison between using consistent tangent moduli and continuum tangent moduli when considering the convergence rate and computational time.

### 4.3.6 Appendix A. Derivation of stress correction

The following provides the derivation of Equations (4.19) and (4.23) based on the flowchart of the integration algorithm for the multi-yield surface $J_2$ plasticity model by Prevost 1978. Although not the focus of this paper, these derivations provide insight into this model.

*A.1. Derivation of stress correction for the first crossed yield surface.*

The stress correction for the first crossed yield surface is similar to that for classical $J_2$ single surface plasticity. The stress correction computation is based on the following two sets of discretized relations.

*(a) Incremental stress-strain relation:*

In small strain plasticity, the decomposition of the total strain into the elastic and plastic parts can be expressed in discretized form as $\Delta\boldsymbol{\epsilon} = \Delta\boldsymbol{\epsilon}^e + \Delta\boldsymbol{\epsilon}^p = \Delta\boldsymbol{\epsilon}^e + \Delta\boldsymbol{e}^p$. The equality $\Delta\boldsymbol{\epsilon}^p = \Delta\boldsymbol{e}^p$ stems from the pressure invariant nature of the plasticity model considered here (i.e., isochoric plastic deformations). The incremental stress-strain relation for linear elastic isotropic material can be expressed as

$$\boldsymbol{\tau} - \boldsymbol{\tau}_n = \Delta\boldsymbol{\tau} = [\boldsymbol{C}:\Delta\boldsymbol{\epsilon}^e]^{dev} = [\boldsymbol{C}:(\Delta\boldsymbol{\epsilon}-\Delta\boldsymbol{e}^p)]^{dev} = 2G([\Delta\boldsymbol{\epsilon}]^{dev} - \Delta\boldsymbol{e}^p) \qquad \text{(A1)}$$

where $\boldsymbol{\tau}_n$ represents the deviatoric stress at the last converged load/time step and the superscript $[...]^{dev}$ denotes the deviatoric part of the quantity inside the brackets. The tensor of elastic moduli $\mathbf{C}$ can be expressed as $\mathbf{C} = \lambda\boldsymbol{I}\otimes\boldsymbol{I} + 2G\boldsymbol{I}_4$. Equation (A1) can be rewritten as

$$\boldsymbol{\tau} = \boldsymbol{\tau}_n + \Delta\boldsymbol{\tau} = \boldsymbol{\tau}_n + 2G[\Delta\boldsymbol{\epsilon}]^{dev} - 2G\Delta\boldsymbol{e}^p = \boldsymbol{\tau}_0^{tr} - 2G\Delta\boldsymbol{e}^p \tag{A2}$$

Defining the plastic stress correction tensor as (see Figure 4.2)

$$\boldsymbol{P}_1 = 2G\Delta\boldsymbol{e}^p, \tag{A3}$$

the current deviatoric stress can be expressed as

$$\boldsymbol{\tau} = \boldsymbol{\tau}_0^{tr} - \boldsymbol{P}_1 = \boldsymbol{\tau}_1^{tr} \tag{A4}$$

*(b) Discretized form of flow rule:*

In incremental form, the continuum flow rule in Equations (4.11) and (4.13) becomes

$$\Delta\boldsymbol{e}^p = \frac{1}{H'^{(m)}}\boldsymbol{Q}_1\langle L\rangle = \frac{1}{H'^{(m)}}\boldsymbol{Q}_1\langle \boldsymbol{Q}_1{:}\Delta\boldsymbol{\tau}\rangle \tag{A5}$$

where $H'^{(m)}$ is the plastic shear modulus of the current (or active) yield surface. The plastic strain increment tensor in Equation (A5) must obey the Kuhn-Tucker complementarity conditions expressed as $\frac{\langle L\rangle}{H'^{(m)}} f_m(\boldsymbol{\tau}, \boldsymbol{\alpha}) = 0$ where $L = \boldsymbol{Q}_1{:}\Delta\boldsymbol{\tau}$. It can be shown that at the end of the first iterative correction, $\langle \boldsymbol{Q}_1{:}\Delta\boldsymbol{\tau}\rangle$ can be replaced by $\langle \boldsymbol{Q}_1{:}(\boldsymbol{\tau} - \boldsymbol{\tau}_A)\rangle$ where $\boldsymbol{\tau}_A$ is the intersection of $(\boldsymbol{\tau}_0^{tr} - \boldsymbol{\tau}_n)$ with the yield surface $\{f_m = 0\}$ (see Figure 4.34). In addition, for the current plastic loading case, $\langle \boldsymbol{Q}_1{:}(\boldsymbol{\tau} - \boldsymbol{\tau}_A)\rangle$ can be approximated by $\boldsymbol{Q}_1{:}(\boldsymbol{\tau} - \boldsymbol{\tau}_1^*)$. Thus, Equation (A5) becomes

$$\Delta\boldsymbol{e}^p = \frac{1}{H'^{(m)}}\boldsymbol{Q}_1 \otimes \boldsymbol{Q}_1{:}(\boldsymbol{\tau} - \boldsymbol{\tau}_1^*) \tag{A6}$$

Solving Equations (A2) and (A6) for the total plastic strain increment $\Delta\boldsymbol{e}^p$ yields

$$\Delta \boldsymbol{e}^{p} = \frac{\boldsymbol{Q}_1 : (\boldsymbol{\tau}_0^{\mathrm{tr}} - \boldsymbol{\tau}_1^{*})}{(H'^{(m)} + 2G)} \boldsymbol{Q}_1 \tag{A7}$$

Then from Equation (A3)

$$\boldsymbol{P}_1 = 2G\Delta \boldsymbol{e}^{p} = 2G \frac{\boldsymbol{Q}_1 : (\boldsymbol{\tau}_0^{\mathrm{tr}} - \boldsymbol{\tau}_1^{*})}{(H'^{(m)} + 2G)} \boldsymbol{Q}_1 \tag{A8}$$

*A.2. Derivation of stress correction for the second and successive crossed yield surfaces.*

After completion of the stress correction for the first yield surface, if the stress point lies outside the next larger yield surface, then before continuing the stress correction corresponding to the next yield surface, some small but crucial correction to the stress $\boldsymbol{\tau}_1^{tr}$ must be made to account for the fact that the plastic stress correction has actually been 'overrelaxed' at the first stress correction step (Prevost technique note).

The total deviatoric strain increment $[\Delta \boldsymbol{\epsilon}]^{dev}$ may be subdivided into three parts (E-A, A-B, and B-C, see Figure 34), where E is the stress point $\boldsymbol{\tau}_n$ at the last converged time/ load step. Stress path E-A is linear elastic, i.e, $f_m \leq 0$ and the equality holds only at point A. A-B is the path of the stress state between the first yield surface ($f_m = 0$) and the second yield surface ($f_{m+1} = 0$). Stress point B may be obtained by the 'elastic predictor A-D, plastic corrector D-B' process and by satisfying the consistency condition $f_{m+1} = 0$. The exact position of point B could be obtained iteratively.

The entire elastic predictor E-F has been relaxed plastically to stress point $\boldsymbol{\tau}_1^{tr}$ (point G in Figure 34) according to the first yield surface ($f_m = 0$) only. The portion D-F of the

elastic predictor E-F should be relaxed plastically according to the second yield surface ($f_{m+1} = 0$). Thus, the plastic stress correction F-G ($-\boldsymbol{P}_1$) must be scaled back to F-H (see Figure 35) where the deviatoric plastic strain at point H is the same as at point B (i.e., $\boldsymbol{e}^p_H = \boldsymbol{e}^p_B$). Then plastic stress correction F-H is followed by the plastic stress correction H-I according to the second yield surface ($f_{m+1} = 0$) resulting in stress state $\boldsymbol{\tau}^{tr}_2$. The plastic strain from stress point G to stress point I can be decomposed as (see Figure 35)

$$\Delta\boldsymbol{\epsilon}^p_{GI} = -\Delta\boldsymbol{\epsilon}^p_{HG} + \Delta\boldsymbol{\epsilon}^p_{HI} \tag{A9}$$

Note that both $\Delta\boldsymbol{\epsilon}^p_{HG}$ and $\Delta\boldsymbol{\epsilon}^p_{HI}$ correspond to the plastic loading case. The second stress correction ($-\boldsymbol{P}_2$) is obtained from the following two sets of discretized relations.

*(a) Incremental stress-strain relation (from G ($\boldsymbol{\tau}^{tr}_1$) to I ($\boldsymbol{\tau}^{tr}_2$)):*

Since, between stress points G and I (see Figure 35), the total strain remains unchanged, i.e., $\Delta\boldsymbol{\epsilon}_{GI} = \boldsymbol{0}$, it follows that

$$-\boldsymbol{\tau}^{tr}_1 = \boldsymbol{C}:(\Delta\boldsymbol{\epsilon}^e_{GI}) = \boldsymbol{C}:(\Delta\boldsymbol{\epsilon}_{GI} - \Delta\boldsymbol{\epsilon}^p_{GI}) = -\boldsymbol{C}:\Delta\boldsymbol{\epsilon}^p_{GI} = -2G\Delta\boldsymbol{\epsilon} \tag{A10}$$

where $\Delta\boldsymbol{\epsilon}^p_{GI} = \Delta\boldsymbol{e}^p_{GI}$.

*2, Discretized form of flow rule:*

The plastic strain increment from stress point H to stress point I is given by the plastic strain increment from stress point B to stress point I and defined as, according to (4.11),

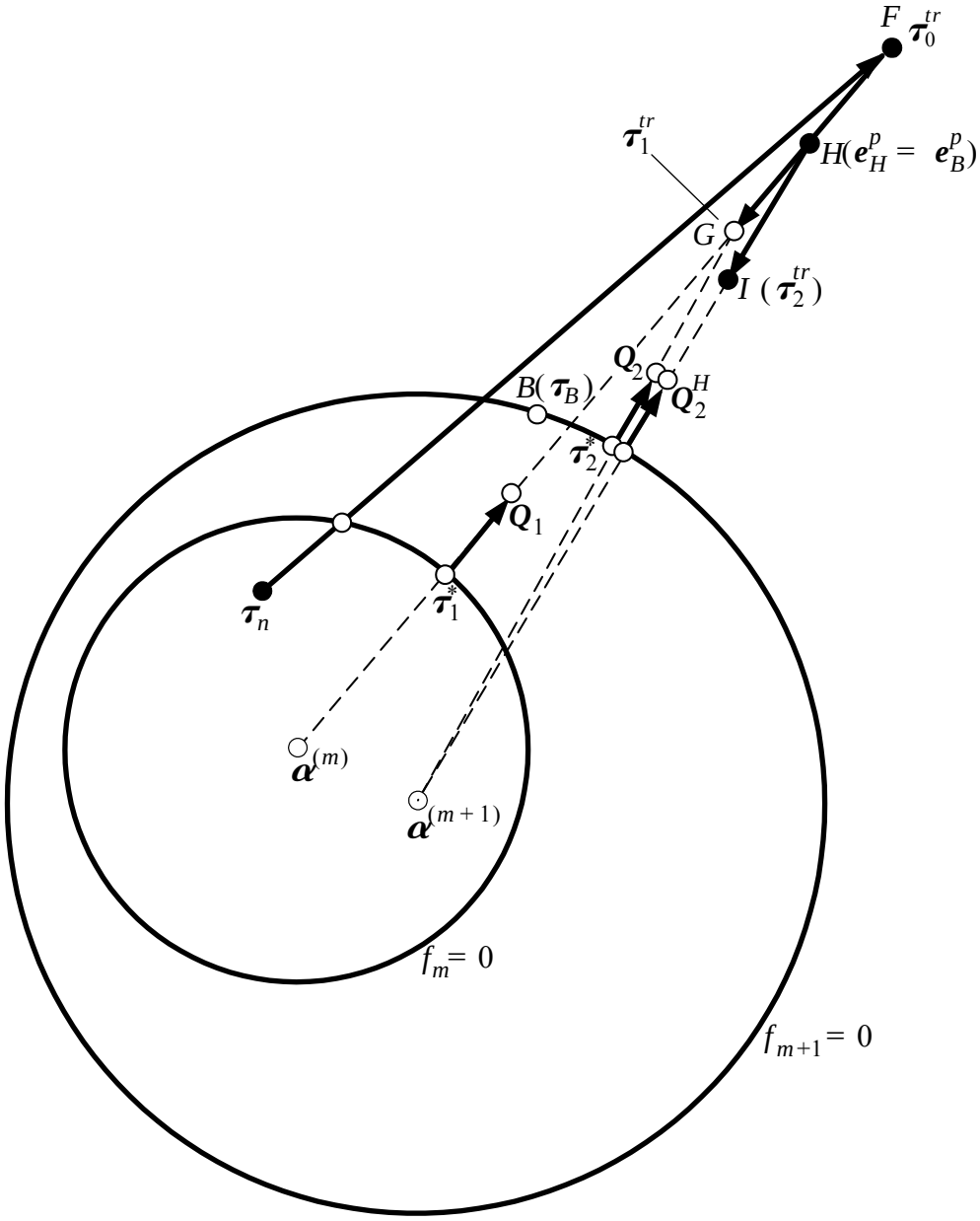


**Figure 4.34 Schematic of plastic stress correction for the second yield surface in the multi-yield surface $J_2$ plasticity model**

$$\Delta\boldsymbol{\epsilon}^{p}_{HI} = \frac{1}{H'^{(m+1)}}\boldsymbol{Q}_2^{H}\langle L_2\rangle = \frac{1}{H'^{(m+1)}}\boldsymbol{Q}_2^{H}\langle \boldsymbol{Q}_2^{H}{:}\Delta\boldsymbol{\tau}_2\rangle \tag{A11}$$

where $\Delta\boldsymbol{\tau}_2$ is defined as the stress change from B to I (see Figure 34). For the plastic loading case, $\langle \boldsymbol{Q}_2^{H}{:}\Delta\boldsymbol{\tau}_2\rangle$ can be approximated with $\boldsymbol{Q}_2{:}(\boldsymbol{\tau}_2^{tr} - \boldsymbol{\tau}_2^{*})$ (see Figure 35) in which $\boldsymbol{\tau}_2^{*}$ and $\boldsymbol{Q}_2$ are as defined in Equations (15) and (17), respectively. Substituting this approximation as well as $\boldsymbol{Q}_2^{H} \cong \boldsymbol{Q}_2$ into Equation (A11), which in turn is substituted into Equation (A9), yields

$$\Delta\boldsymbol{\epsilon}^{p}_{HI} = \Delta\boldsymbol{\epsilon}^{p}_{HG} + \Delta\boldsymbol{\epsilon}^{p}_{GI} = \frac{1}{H'^{(m+1)}}\boldsymbol{Q}_2 \cdot (\boldsymbol{Q}_2{:}(\boldsymbol{\tau}_2^{tr} - \boldsymbol{\tau}_2^{*})) \tag{A12}$$

The plastic strain increment $\Delta\boldsymbol{\epsilon}^{p}_{HG}$ corresponding to the stress increment H-G by which the stress state was over relaxed (according to the first yield surface), can be approximated as (see (4.11) and Figure 35)

$$\Delta\boldsymbol{\epsilon}^{p}_{HG} = \frac{1}{H'^{(m)}}\boldsymbol{Q}_1 \cdot (\boldsymbol{Q}_1{:}(\boldsymbol{\tau}_1^{tr} - \boldsymbol{\tau}_B)) \approx \frac{1}{H'^{(m)}}\boldsymbol{Q}_1 \cdot (\boldsymbol{Q}_1{:}(\boldsymbol{\tau}_1^{tr} - \boldsymbol{\tau}_2^{*})) \tag{A13}$$

Substituting (A13) into Equation (A12) gives

$$\Delta\boldsymbol{\epsilon}^{p}_{GI} = \frac{1}{H'^{(m+1)}}\boldsymbol{Q}_2 \cdot (\boldsymbol{Q}_2{:}(\boldsymbol{\tau}_2^{tr} - \boldsymbol{\tau}_2^{*})) - \frac{1}{H'^{(m)}}\boldsymbol{Q}_1 \cdot (\boldsymbol{Q}_1{:}(\boldsymbol{\tau}_1^{tr} - \boldsymbol{\tau}_2^{*})) \tag{A14}$$

Solving Equations (A10) and (A14) for $\boldsymbol{\tau}_2^{tr}$ and $\Delta\boldsymbol{\epsilon}^{p}_{GI}$, it is found that

$$\Delta\boldsymbol{\epsilon}^{p}_{GI} = \frac{(H'^{(m)} + 2G \cdot \boldsymbol{Q}_1{:}\boldsymbol{Q}_2)}{H'^{(m)}(H'^{(m+1)} + 2G)} \cdot \boldsymbol{Q}_2 \otimes \boldsymbol{Q}_2{:}(\boldsymbol{\tau}_1^{tr} - \boldsymbol{\tau}_2^{*}) - \frac{1}{H'^{(m)}}\boldsymbol{Q}_1 \otimes \boldsymbol{Q}_1{:}(\boldsymbol{\tau}_1^{tr} - \boldsymbol{\tau}_2^{*}) \tag{A15}$$

The second plastic stress correction $\boldsymbol{P}_2$ can then be obtained as

$$\boldsymbol{P}_2 = \boldsymbol{C}:\Delta\boldsymbol{\epsilon}^p_{GI} = 2G\frac{(H'^{(m)} + 2G\cdot\boldsymbol{Q}_1:\boldsymbol{Q}_2)}{H'^{(m)}(H'^{(m+1)} + 2G)}\cdot\boldsymbol{Q}_2\otimes\boldsymbol{Q}_2:(\boldsymbol{\tau}_1^{tr} - \boldsymbol{\tau}_2^*) - \frac{2G}{H'^{(m)}}\boldsymbol{Q}_1\otimes\boldsymbol{Q}_1:(\boldsymbol{\tau}_1^{tr} - \boldsymbol{\tau}_2^*) \tag{A16}$$

After the second plastic stress correction, if the stress lies outside the next yield surface, the correction process from Equation (A9) to Equation (A16) is repeated with the subscript for the iteration number set i = 3. More generally, the plastic stress correction for iteration i (corresponding to yield surface $f_{m+i-1} = 0$) is given by

$$\boldsymbol{P}_i = 2G\frac{(H'^{(m+i-2)} + 2G\cdot\boldsymbol{Q}_{i-1}:\boldsymbol{Q}_i)}{H'^{(m+i-2)}(H'^{(m+i-1)} + 2G)}\cdot\boldsymbol{Q}_i\otimes\boldsymbol{Q}_i:(\boldsymbol{\tau}_{i-1}^{tr} - \boldsymbol{\tau}_i^*) - \frac{2G}{H'^{(m+i-2)}}\boldsymbol{Q}_{i-1}\otimes\boldsymbol{Q}_{i-1}:(\boldsymbol{\tau}_{i-1}^{tr} - \boldsymbol{\tau}_i^*) \tag{A17}$$

If the number of yield surfaces used to represent the original shear stress-strain backbone curve (see (4.2)) is large enough (say NYS > 20) such that the unit tensors normal to the two consecutive yield surfaces $f_{m+i-2} = 0$ and $f_{m+i-1} = 0$ corresponding to stress points $\boldsymbol{\tau}_{i-2}^{tr}$ and $\boldsymbol{\tau}_{i-1}^{tr}$, respectively, are close, then

$$\boldsymbol{Q}_{i-1} \approx \boldsymbol{Q}_i \tag{A18}$$

and Equation (A17) further simplifies to

$$\boldsymbol{P}_i = 2G\frac{(H'^{(m+i-2)} - H'^{(m+i-1)})}{H'^{(m+i-2)}(H'^{(m+i-1)} + 2G)}\cdot\boldsymbol{Q}_i\otimes\boldsymbol{Q}_i:(\boldsymbol{\tau}_{i-1}^{tr} - \boldsymbol{\tau}_i^*) \tag{A19}$$

### 4.3.7 Sensitivity Computation

The derivation of the response sensitivity for the pressure independent multi-yield-surface $J_2$ plasticity material model based on DDM, is presented in this section. Application examples are provided to validate the sensitivity results.

As was mentioned in Chapter 3, the conditional derivative of the internal resisting force vector $\mathbf{R}(\mathbf{u}_{n+1})$ represents the partial derivative of the internal resisting force vector, $\mathbf{R}(\mathbf{u}_{n+1})$, with respect to sensitivity parameter θ under the condition that the displacement vector $\mathbf{u}_{n+1}$ remains fixed. The conditional derivative of the internal resisting force vector could be obtained by assemble contribution of all elements,

$$\left.\frac{\partial \boldsymbol{R}(\boldsymbol{u}_{n+1}(\theta),\theta)}{\partial\theta}\right|_{\boldsymbol{u}_{n+1}} = \sum_{i=1}^{Nel}\int_{\Omega}\boldsymbol{B}^{T}\left.\frac{\partial\boldsymbol{\sigma}(\boldsymbol{\epsilon}_{n+1}(\theta),\theta)}{\partial\theta}\right|_{\boldsymbol{\epsilon}_{n+1}} d\Omega \tag{4.58}$$

In the next sections, the stress sensitivity is derived based on the flowchart of the stress computation process. The material sensitivity parameter θ could be low-strain shear moduli G, bulk moduli K, and the Peak shear $\tau_{max}$ as shown in Figure 4.1.

#### 4.3.7.1 Initial Surface Sensitivity

First, the initial surface sensitivity is derived. Differenting (4.3) with respect to the sensitivity parameter θ results in,

$$\begin{aligned}\frac{\partial\gamma_r}{\partial\theta} = \frac{1}{(G\cdot\gamma_{max}-\tau_{max})^2}\Bigg[&\gamma_{max}\cdot\frac{\partial\tau_{max}}{\partial\theta}\cdot(G\cdot\gamma_{max}-\tau_{max})\\ &-\gamma_{max}\cdot\tau_{max}\cdot\left(\frac{\partial G}{\partial\theta}\cdot\gamma_{max}-\frac{\partial\tau_{max}}{\partial\theta}\right)\Bigg]\end{aligned} \tag{4.59}$$

From (4.4), differentiating with respect to $\theta$ for each surface with number j from 1 to NYS,

$$\frac{\partial \tau_j}{\partial \theta} = \frac{\partial \tau_{max}}{\partial \theta} \cdot \frac{j}{NYS} \tag{4.60}$$

$$\begin{aligned} \frac{\partial \gamma_j}{\partial \theta} = \frac{1}{(G \cdot \gamma_r - \tau_j)^2} \Bigg[ \left( \frac{\partial \tau_j}{\partial \theta} \cdot \gamma_r + \tau_j \cdot \frac{\partial \gamma_r}{\partial \theta} \right) \cdot (G \cdot \gamma_r - \tau_j) \\ -\tau_j \cdot \gamma_r \cdot \left( \frac{\partial G}{\partial \theta} \cdot \gamma_r + G \cdot \frac{\partial \gamma_r}{\partial \theta} - \frac{\partial \tau_j}{\partial \theta} \right) \Bigg] \end{aligned} \tag{4.61}$$

Looping from the first surface to the NYS-1 surface, from (4.4) to (4.9),

$$\frac{\partial (\Delta\gamma)_j}{\partial \theta} = \frac{\partial \gamma_{j+1}}{\partial \theta} - \frac{\partial \gamma_j}{\partial \theta} \tag{4.62}$$

$$\frac{\partial (\Delta\tau)_j}{\partial \theta} = \frac{\partial \tau_{j+1}}{\partial \theta} - \frac{\partial \tau_j}{\partial \theta} \tag{4.63}$$

$$\frac{\partial K_j}{\partial \theta} = \frac{3}{\sqrt{2}} \frac{\partial \tau_j}{\partial \theta} \tag{4.64}$$

$$\frac{\partial H_j}{\partial \theta} = \frac{2}{(\Delta\gamma)_j^2} \left[ \frac{\partial (\Delta\tau)_j}{\partial \theta} \cdot (\Delta\gamma)_j - (\Delta\tau)_j \cdot \frac{(\partial \Delta\gamma)_j}{\partial \theta} \right] \tag{4.65}$$

$$\frac{\partial H'_j}{\partial \theta} = \frac{2}{(2G - H_j)^2} \cdot \left\{ \left[ \frac{\partial G}{\partial \theta} \cdot H_j + G \cdot \frac{\partial H_j}{\partial \theta} \right] \cdot (2G - H_j) - G \cdot H_j \cdot \left( 2\frac{\partial G}{\partial \theta} - \frac{\partial H_j}{\partial \theta} \right) \right\} \tag{4.66}$$

For the last surface, $\frac{\partial H_j}{\partial \theta} = 0$, $\frac{\partial H_j'}{\partial \theta} = 0$.

#### 4.3.7.2 Stress Sensitivity

Then compute the sensitivity of the deviatoric stress, which follows the steps of Equations (4.14) to (4.41). From (4.14), it is obtained,

$$\frac{\partial \tau^{\mathrm{tr}}}{\partial \theta} = \frac{\partial \tau}{\partial \theta} + 2\frac{\partial \mathrm{G}}{\partial \theta} \cdot \Delta \boldsymbol{e} + 2\mathrm{G} \cdot \frac{\partial \Delta \boldsymbol{e}}{\partial \theta} \tag{4.67}$$

The subscript i is removed for convenience. The sensitivity of contact stress $\tau^*$ is obtained from (4.15),

$$\frac{\partial \tau^*}{\partial \theta} = \frac{1}{K^2}\left\{\left[\frac{\partial K^{(m)}}{\partial \theta}(\tau^{\mathrm{tr}} - \alpha^{(m)}) + K^{(m)}\left(\frac{\partial \tau^{\mathrm{tr}}}{\partial \theta} - \frac{\partial \alpha^{(m)}}{\partial \theta}\right)\right] \cdot K - K^{(m)}(\tau^{\mathrm{tr}} - \alpha^{(m)}) \cdot \frac{\partial K}{\partial \theta}\right\} + \alpha^{(m)} \tag{4.68}$$

where sensitivity of K is obtained from (4.16) as,

$$\frac{\partial K}{\partial \theta} = \frac{3}{2K}\left(\frac{\partial \tau^{\mathrm{tr}}}{\partial \theta} - \frac{\partial \alpha^{(m)}}{\partial \theta}\right) : (\tau^{\mathrm{tr}} - \alpha^{(m)}) \tag{4.69}$$

The sensitivity of surface normal is then derived from (4.17) as,

$$\frac{\partial \boldsymbol{Q}}{\partial \theta} = \frac{((\tau^* - \alpha^{(m)}) : (\tau^* - \alpha^{(m)}))^{\frac{1}{2}} \cdot \left(\frac{\partial \tau^*}{\partial \theta} - \frac{\partial \alpha^{(m)}}{\partial \theta}\right)}{(\tau^* - \alpha^{(m)}) : (\tau^* - \alpha^{(m)})} - \frac{\left(\frac{\partial \tau^*}{\partial \theta} - \frac{\partial \alpha^{(m)}}{\partial \theta}\right) : (\tau^* - \alpha^{(m)})}{((\tau^* - \alpha^{(m)}) : (\tau^* - \alpha^{(m)}))^{3/2}} \cdot (\tau^* - \alpha^{(m)}) \tag{4.70}$$

Then the sensitivity of the plastic loading function is obtained from (4.20) as

$$\frac{\partial L}{\partial \theta} = 2\frac{\partial G}{\partial \theta}\cdot\frac{\boldsymbol{Q}:(\boldsymbol{\tau}^{\mathrm{tr}}-\boldsymbol{\tau}^{*})}{(H^{'(m)}+2\cdot G)}+ 2G\cdot\frac{\left[\frac{\partial \boldsymbol{Q}}{\partial \theta}:(\tau^{\mathrm{tr}}-\tau^{*})+\boldsymbol{Q}:\left(\frac{\partial \tau^{\mathrm{tr}}}{\partial \theta}-\frac{\partial \tau^{*}}{\partial \theta}\right)\right]\cdot(H^{'(m)}+2\cdot G)}{(H^{'(m)}+2\cdot G)^{2}} -2G\cdot\frac{\boldsymbol{Q}:(\tau^{\mathrm{tr}}-\tau^{*})\cdot\left(\frac{\partial H^{'(m)}}{\partial \theta}+2\cdot\frac{\partial G}{\partial \theta}\right)}{(H^{'(m)}+2\cdot G)^{2}} \tag{4.71}$$

if the stress is beyond the next yield surface. Then from (4.24),

$$\frac{\partial L}{\partial \theta} = \frac{\partial L}{\partial \theta}\cdot\frac{(H^{'(m-1)}-H^{'(m)})}{H^{'(m-1)}}+L\cdot\frac{-\frac{\partial H^{'(m)}}{\partial \theta}\cdot H^{'(m-1)}+H^{'(m)}\cdot\frac{\partial H^{'(m-1)}}{\partial \theta}}{[H^{'(m-1)}]^{2}} \tag{4.72}$$

the sensitivity of the stress after the plastic correction corresponding to current surface is obtained from (4.22) as

$$\frac{\partial \tau^{tr}}{\partial \theta} = \frac{\partial \tau^{tr}}{\partial \theta}-\frac{\partial L}{\partial \theta}\cdot\boldsymbol{Q}-L\cdot\frac{\partial \boldsymbol{Q}}{\partial \theta} \tag{4.73}$$

If the trial stress is still beyond the next yield surface n+1, increment the active surface number m by 1, repeating this process (Equations (4.68)-(4.73)) until the trial stress no longer crosses any surfaces.

After obtaining the deviatoric stress, the sensitivity of the stress volume $\sigma_{n+1}^{\ vol}$ is determined using (4.25),

$$\frac{\partial \sigma_{n+1}^{\ vol}}{\partial \theta} = \frac{\partial \sigma_{n}^{\ vol}}{\partial \theta}+\frac{\partial B}{\partial \theta}\times\Delta\boldsymbol{\epsilon}_{ii}+B\times\frac{\partial \Delta\boldsymbol{\epsilon}_{ii}}{\partial \theta} \tag{4.74}$$

where B is the bulk modulus and $\boldsymbol{\epsilon}$ is the total stress.

From (4.26), the sensitivity of the total stress is,

$$\frac{\partial \boldsymbol{\sigma}}{\partial \theta} = \frac{\partial \boldsymbol{\tau}}{\partial \theta} + \frac{\partial \sigma^{vol}}{\partial \theta}\boldsymbol{I} \tag{4.75}$$

#### 4.3.7.3 Active Surface Update

The sensitivity of stress $\boldsymbol{\tau}_T$ at point T (Figure 4.3) is determined using (4.28),

$$\frac{\partial \boldsymbol{\tau}_T}{\partial \theta} = \frac{\partial \boldsymbol{\alpha}^{(m)}}{\partial \theta} + \frac{\partial x}{\partial \theta}(\boldsymbol{\tau} - \boldsymbol{\alpha}^{(m)}) + x\left(\frac{\partial \boldsymbol{\tau}}{\partial \theta} - \frac{\partial \boldsymbol{\alpha}^{(m)}}{\partial \theta}\right) \tag{4.76}$$

where $\frac{\partial x}{\partial \theta}$ is obtained from (4.30),

$$\frac{\partial x}{\partial \theta} = \frac{-\frac{\partial A}{\partial \theta}x^2 - \frac{\partial B}{\partial \theta}x - \frac{\partial c}{\partial \theta}}{2 \cdot A \cdot x + B} \tag{4.77}$$

where $\frac{\partial A}{\partial \theta}, \frac{\partial B}{\partial \theta}, \frac{\partial C}{\partial \theta}$ are obtained from Equations (4.31) to (4.33) as,

$$\frac{\partial A}{\partial \theta} = \left(\frac{\partial \boldsymbol{\tau}}{\partial \theta} - \frac{\partial \boldsymbol{\alpha}^{(m)}}{\partial \theta}\right) : (\boldsymbol{\tau} - \boldsymbol{\alpha}^{(m)}) \tag{4.78}$$

$$\frac{\partial B}{\partial \theta} = 2 \cdot \left(\frac{\partial \boldsymbol{\alpha}^{(m)}}{\partial \theta} - \frac{\partial \boldsymbol{\alpha}^{(m+1)}}{\partial \theta}\right) : (\boldsymbol{\tau} - \boldsymbol{\alpha}^{(m)}) + 2 \cdot (\boldsymbol{\alpha}^{(m)} - \boldsymbol{\alpha}^{(m+1)}) : \left(\frac{\partial \boldsymbol{\tau}}{\partial \theta} - \frac{\partial \boldsymbol{\alpha}^{(m)}}{\partial \theta}\right) \tag{4.79}$$

$$\frac{\partial C}{\partial \theta} = 2 \cdot \left(\frac{\partial \boldsymbol{\alpha}^{(m)}}{\partial \theta} - \frac{\partial \boldsymbol{\alpha}^{(m+1)}}{\partial \theta}\right) : (\boldsymbol{\alpha}^{(m)} - \boldsymbol{\alpha}^{(m+1)}) - \frac{4}{3}K^{(m+1)} \cdot \frac{\partial K^{(m+1)}}{\partial \theta} \tag{4.80}$$

The sensitivity of the direction of surface center translation $\boldsymbol{\mu}$, is obtained by differentiation of (4.27) with respect to $\theta$,

$$\frac{\partial \boldsymbol{\mu}}{\partial \theta} = \left[\frac{\partial \boldsymbol{\tau}_T}{\partial \theta} - \frac{\partial \boldsymbol{\alpha}^{(m)}}{\partial \theta}\right] - \left(\frac{\frac{\partial K^{(m)}}{\partial \theta} K^{(m+1)} - K^{(m)} \frac{\partial K^{(m+1)}}{\partial \theta}}{K^{(m+1)}}\right)\left[\boldsymbol{\tau}_T - \boldsymbol{\alpha}^{(m+1)}\right] - \frac{K^{(m)}}{K^{(m+1)}}\left[\frac{\partial \boldsymbol{\tau}_T}{\partial \theta} - \frac{\partial \boldsymbol{\alpha}^{(m+1)}}{\partial \theta}\right] \tag{4.81}$$

After $\frac{\partial \boldsymbol{\mu}}{\partial \theta}$ is obtained, the sensitivity of translation quantity 'a' is computed using (4.35) as,

$$\frac{\partial a}{\partial \theta} = \frac{-\frac{\partial A}{\partial \theta} a^2 - \frac{\partial B}{\partial \theta} a - \frac{\partial c}{\partial \theta}}{2 \cdot A \cdot a + B} \tag{4.82}$$

where $\frac{\partial A}{\partial \theta}, \frac{\partial B}{\partial \theta}, \frac{\partial C}{\partial \theta}$ are obtained from Equations (4.36) to (4.38) as,

$$\frac{\partial A}{\partial \theta} = 2\frac{\partial \boldsymbol{\mu}}{\partial \theta} : \boldsymbol{\mu} \tag{4.83}$$

$$\frac{\partial B}{\partial \theta} = -2 \cdot \frac{\partial \boldsymbol{\mu}}{\partial \theta} : (\boldsymbol{\tau} - \boldsymbol{\alpha}^{(m)}) - 2 \cdot \boldsymbol{\mu} : \left(\frac{\partial \boldsymbol{\tau}}{\partial \theta} - \frac{\partial \boldsymbol{\alpha}^{(m)}}{\partial \theta}\right) \tag{4.84}$$

$$\frac{\partial C}{\partial \theta} = 2 \cdot \left(\frac{\partial \boldsymbol{\tau}}{\partial \theta} - \frac{\partial \boldsymbol{\alpha}^{(m)}}{\partial \theta}\right) : (\boldsymbol{\tau} - \boldsymbol{\alpha}^{(m)}) - \frac{4}{3} K^{(m+1)} \cdot \frac{\partial K^{(m+1)}}{\partial \theta} \tag{4.85}$$

Then from (4.39) the sensitivity of updated active surface center is obtained as,

$$\frac{\partial \boldsymbol{\alpha}^{(m)}}{\partial \theta} = \frac{\partial \boldsymbol{\alpha}^{(m)}}{\partial \theta} + \frac{\partial a}{\partial \theta} \boldsymbol{\mu} + a \frac{\partial \boldsymbol{\mu}}{\partial \theta} \tag{4.86}$$

#### 4.3.7.4 Update Inner Surface Sensitivities

From (4.41), the sensitivity of the center of each inner surfaces is determined by,

$$\frac{\partial \boldsymbol{\alpha}^{(i)}}{\partial \theta} = \frac{\partial \boldsymbol{\tau}}{\partial \theta} - \frac{K^{(m)}\frac{\partial K^{(i)}}{\partial \theta}(\boldsymbol{\tau} - \boldsymbol{\alpha}^{(m)}) + K^{(m)}K^{(i)}\left(\frac{\partial \boldsymbol{\tau}}{\partial \theta} - \frac{\partial \boldsymbol{\alpha}^{(m)}}{\partial \theta}\right) - \frac{\partial K^{(m)}}{\partial \theta}K^{(i)}(\boldsymbol{\tau} - \partial \boldsymbol{\alpha}^{(m)})}{(K^{(m)})^2} \tag{4.87}$$

where $1 \le i \le m-1$.

#### 4.3.7.5 Numerical Examples

Example of 3D soil block subjected to quasi-static push-over loads.

In this section, response sensitivity analysis is performed for the 3D solid block used in section 4.3.3 as shown in Figure 4.5. The number of yielding surfaces is set to 20.

The sensitivities of the displacement at point A (figure 4.5) in the x direction with respect to shear moduli G, Peak Shear $\tau_{max}$, and bulk moduli B are studied and verified with the Forward Finite Difference method (FFD). Figures 4.35 to 4.38 show part of the results.

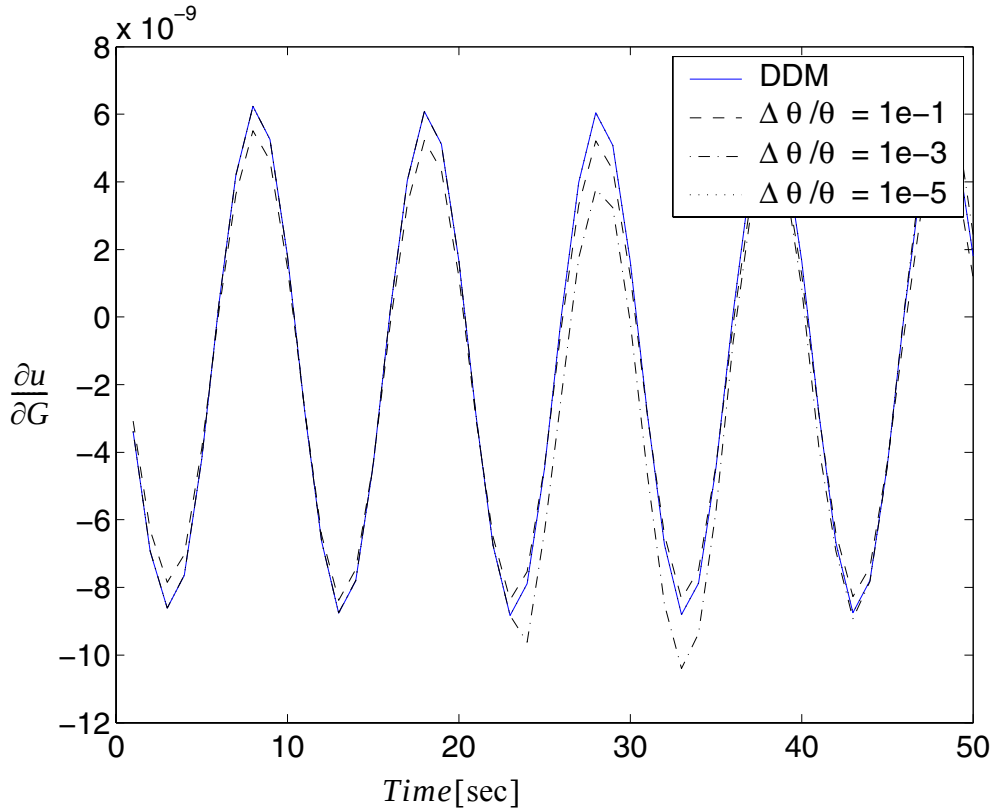


**Figure 4.35 Response sensitivities with respect to G**

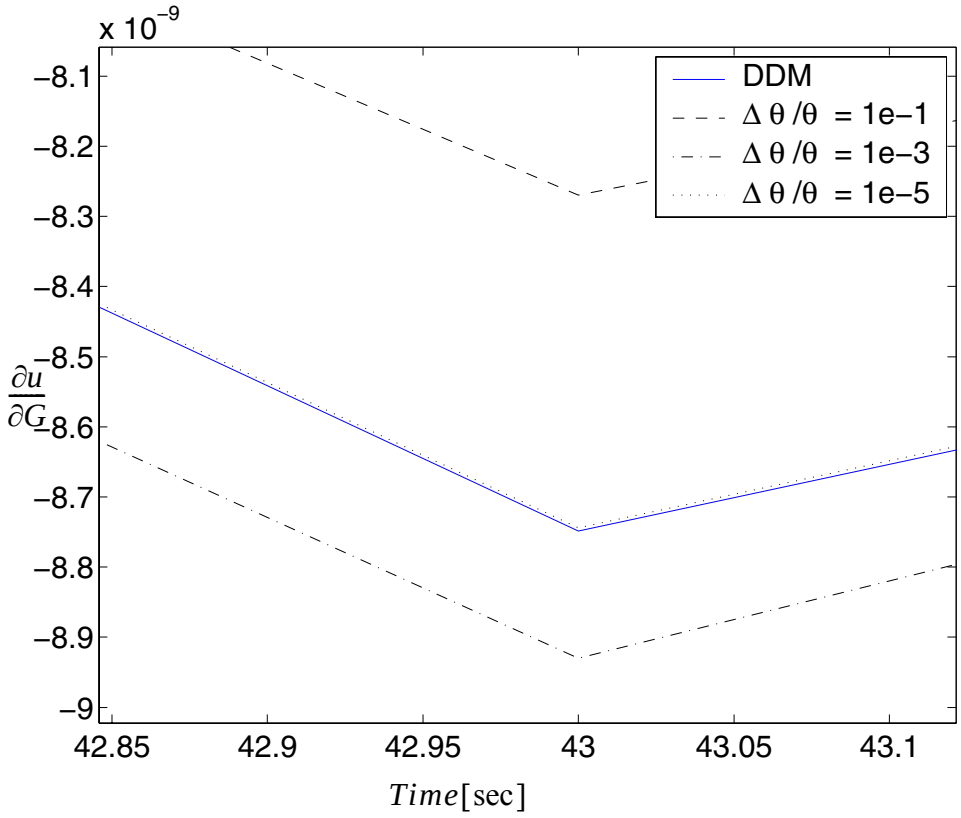


**Figure 4.36 Response sensitivities respect to G (zoomed)**

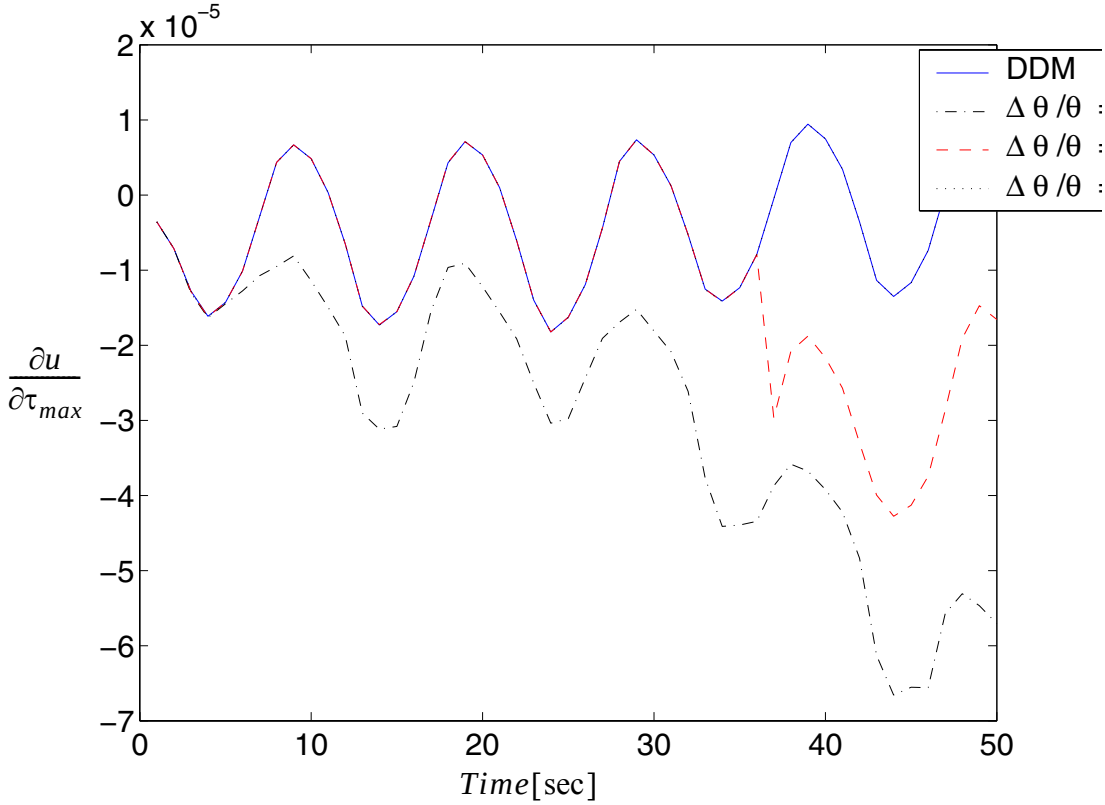


**Figure 4.37 Response sensitivities respect to $\tau_{max}$**

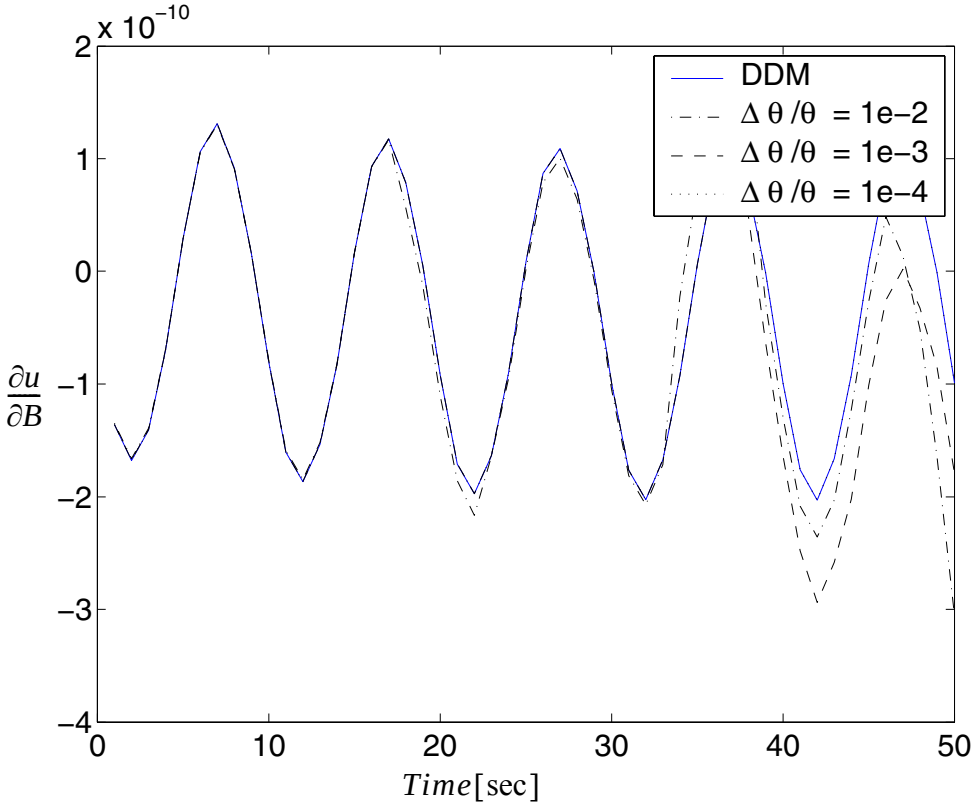


**Figure 4.38 Response sensitivities with respect to bulk moduli**

It is observed that within an acceptable range, with reduced perturbation $\frac{\Delta\theta}{\theta}$, the results of the FFD method approach those of DDM. However when the perturbation is so small that it is out of an acceptable range decided by the computational round off error, FFD results diverge suddenly.

Example of soil column modeled with 2D 4-node quadratic elements subjected to base excitation.

In this section, response sensitivity analysis is performed for the soil column mentioned in section 4.3.4 as shown in Figure 4.18. Sensitivity variables are chosen as low

strain shear modulus G and the maximum shear strength $\tau_{max}$ at each soil layer. Part of the sensitivity results are verified in Figures 4.39 through 4.46.

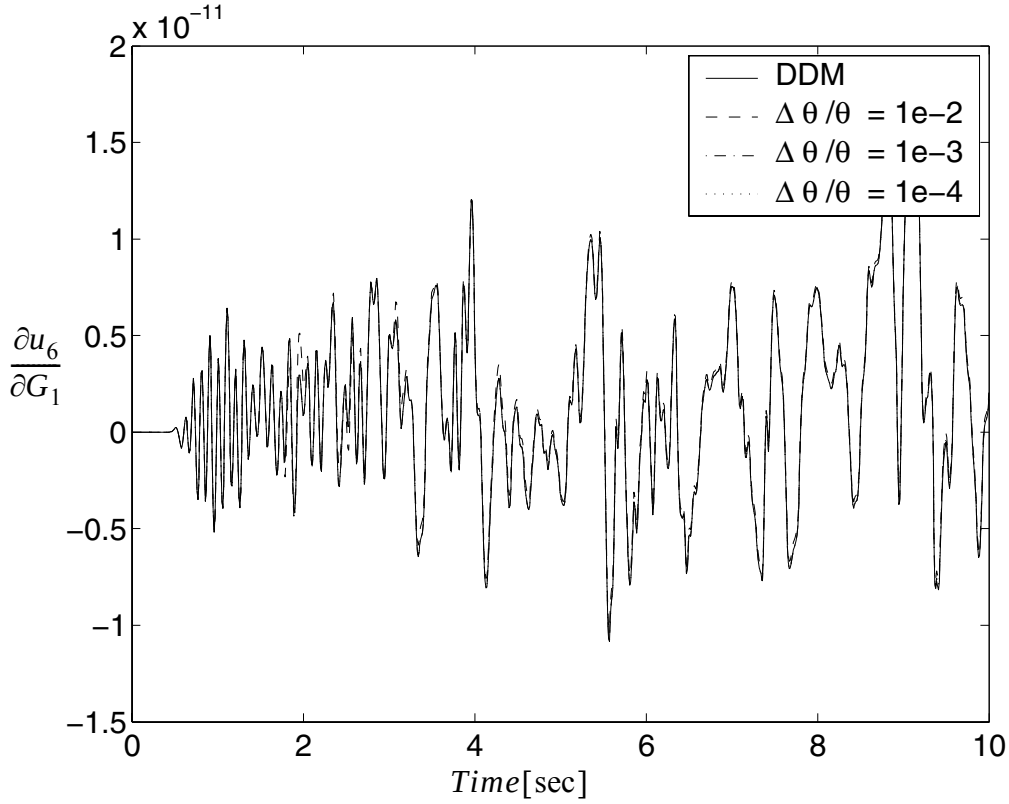


**Figure 4.39 Sensitivity of response $u_6$ with respect to $G_1$ (refer to Figure 4.18)**

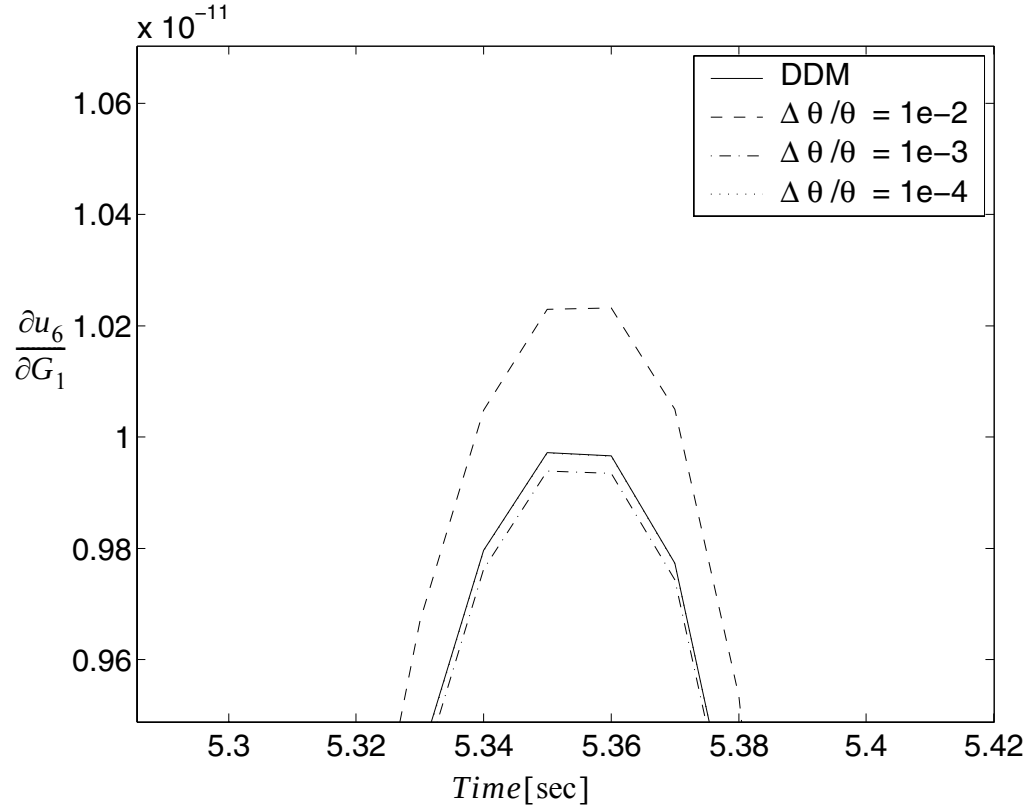


**Figure 4.40 Sensitivity of response $u_6$ with respect to $G_1$, detailed view (refer to Figure 4.18)**

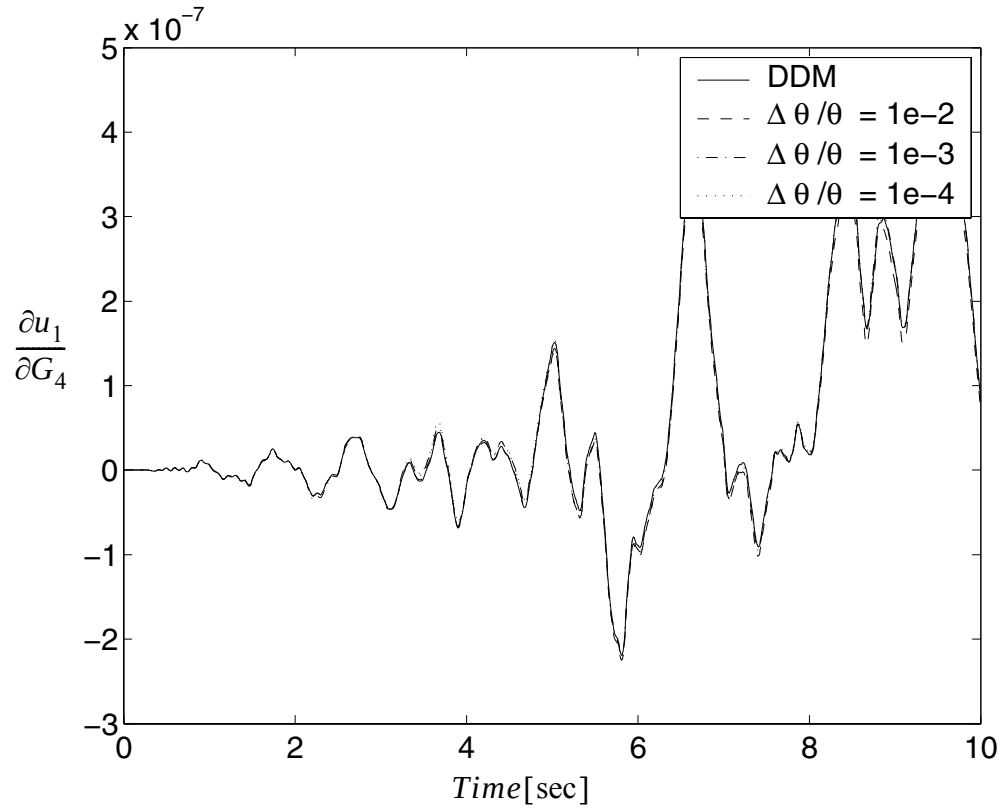


**Figure 4.41 Sensitivity of response $u_1$ with respect to $G_4$ (refer to Figure 4.18)**

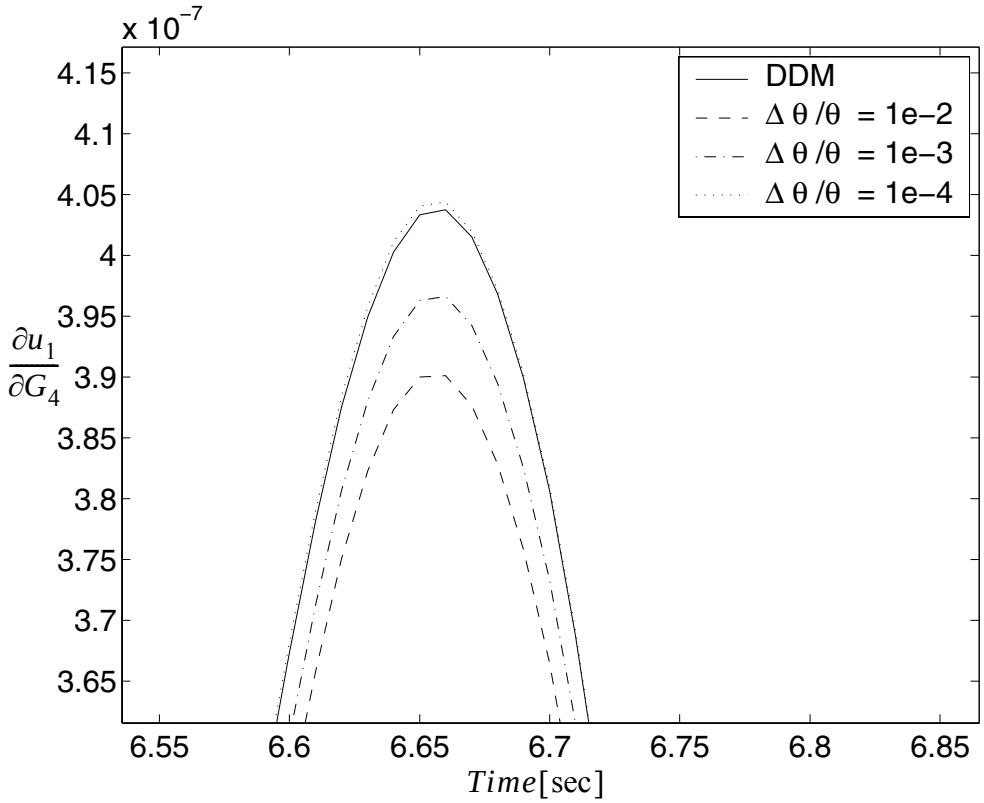


**Figure 4.42 Sensitivity of response $u_1$ with respect to $G_4$, detailed view (refer to Figure 4.18)**

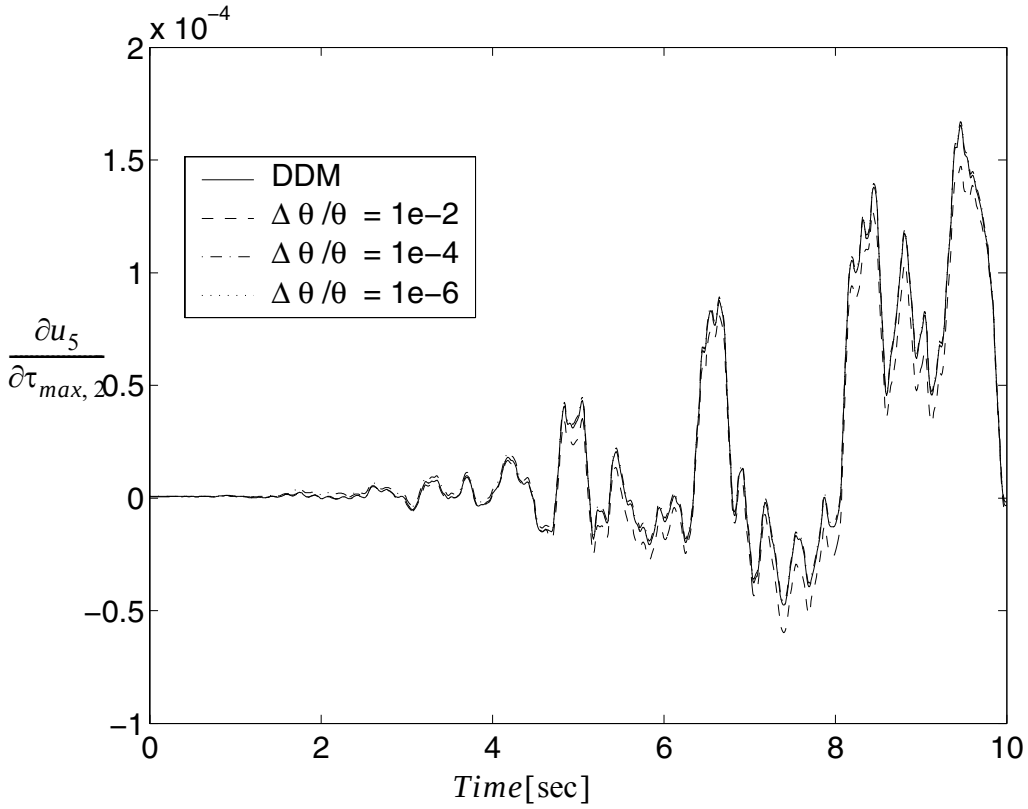


**Figure 4.43 Sensitivity of response $u_5$ with respect to $\tau_{max,2}$ (refer to Figure 4.18)**

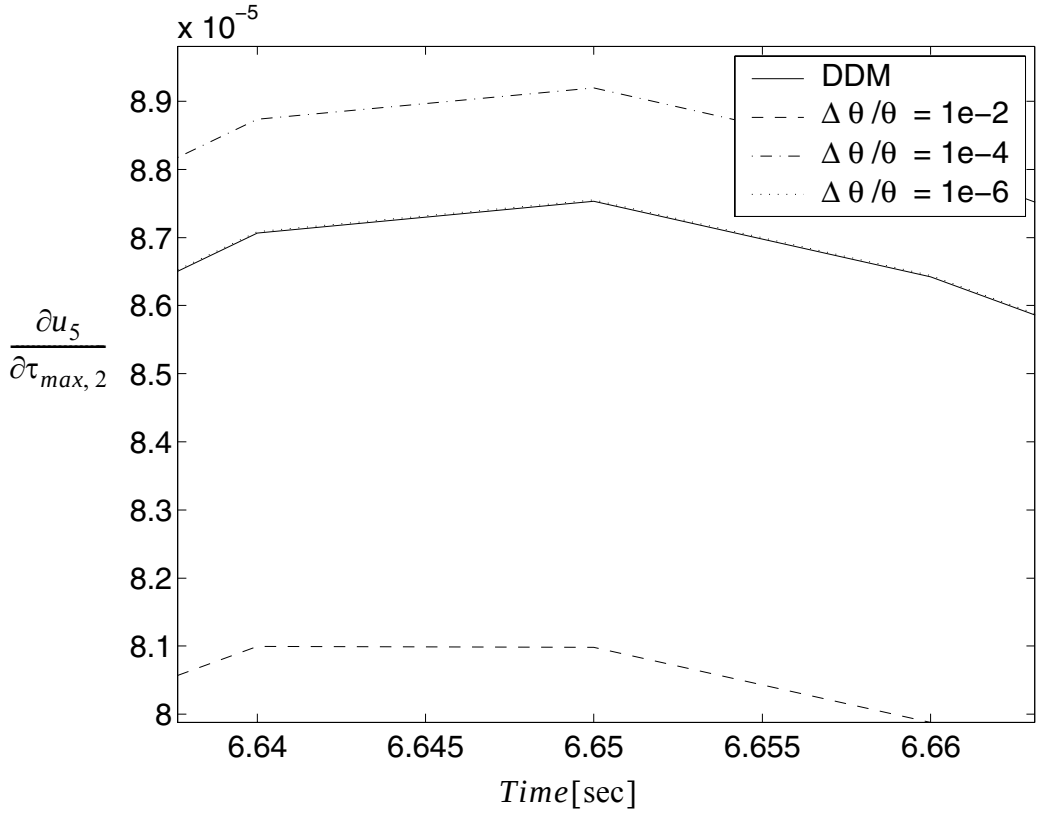


**Figure 4.44 Sensitivity of response $u_5$ with respect to $\tau_{max,2}$, detailed view (refer to Figure 4.18)**

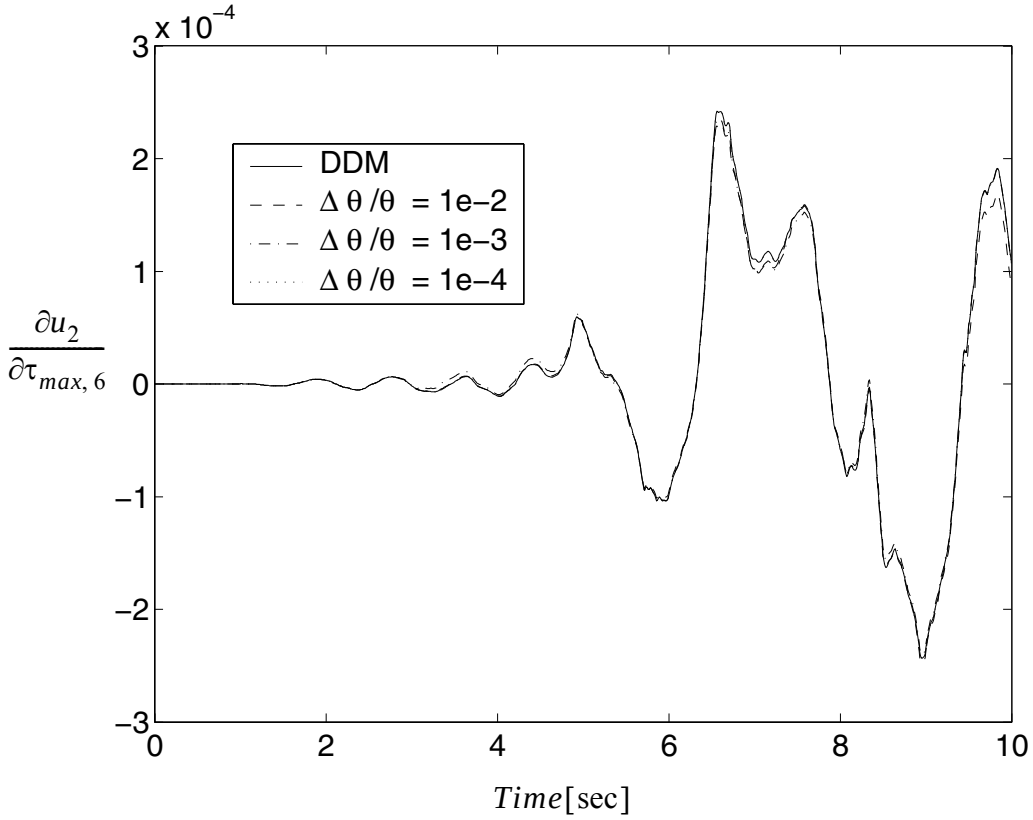


**Figure 4.45 Sensitivity of response $u_2$ with respect to $\tau_{max,6}$ (refer to Figure 4.18)**

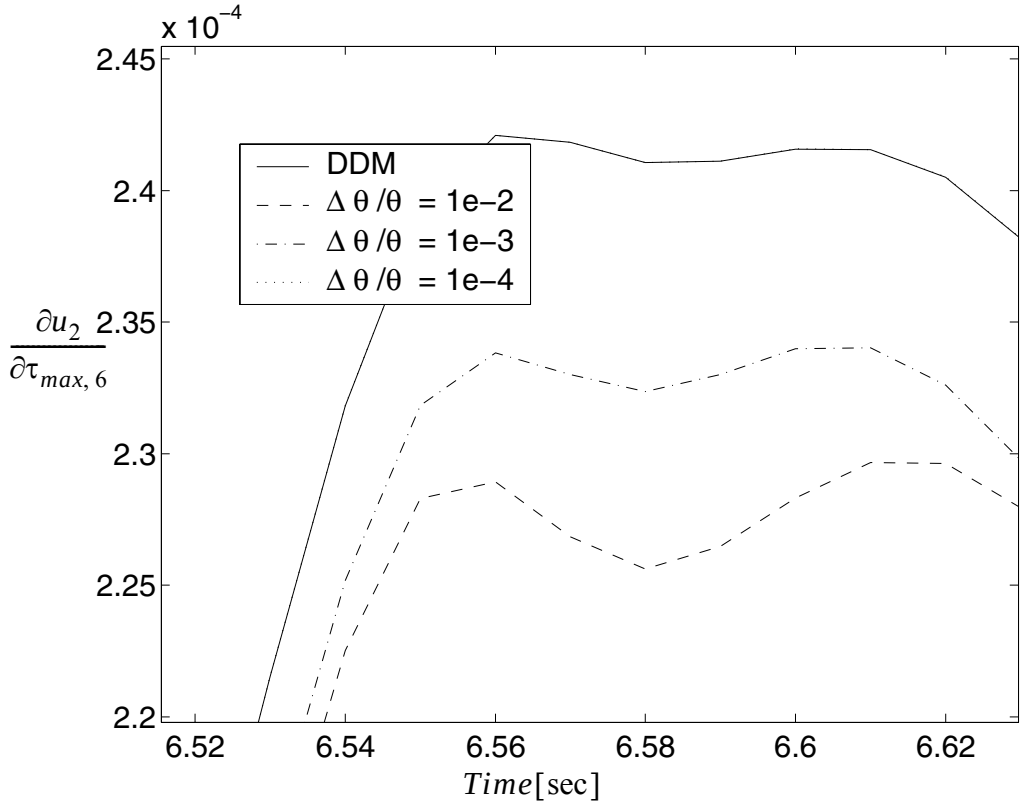


**Figure 4.46 Sensitivity of response $u_2$ with respect to $\tau_{max,6}$, detailed view (refer to Figure 4.18)**

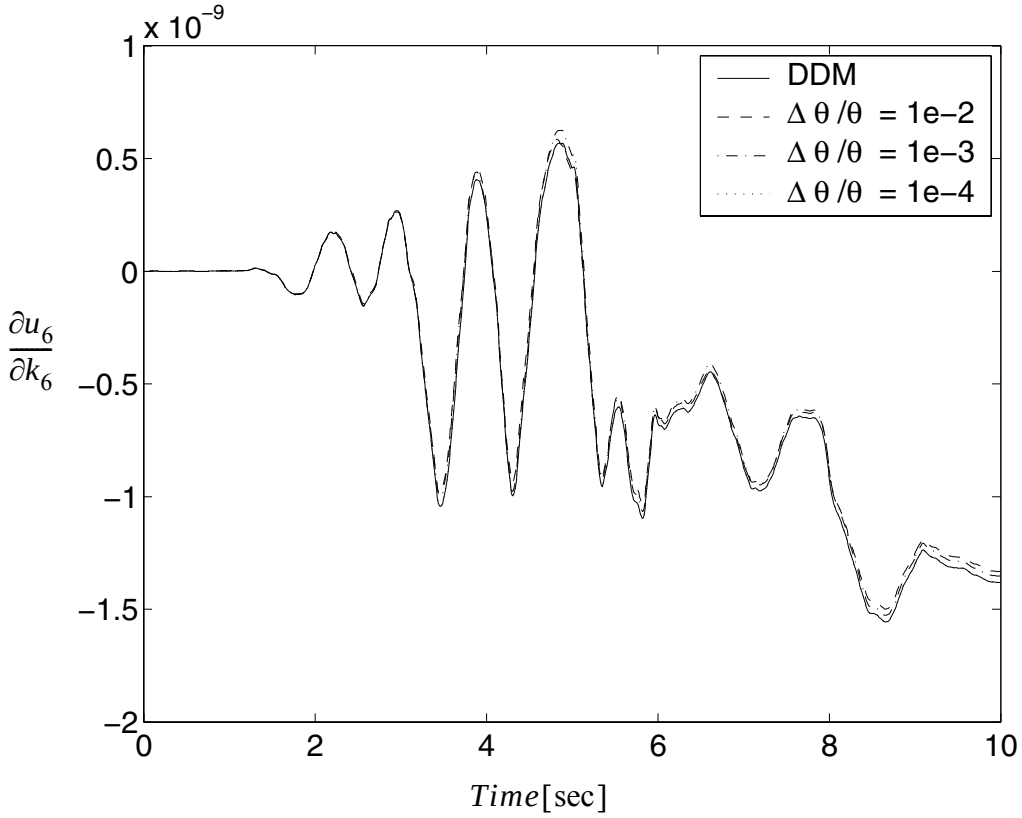


**Figure 4.47 Sensitivity of response $u_6$ with respect to bulk moduli $k_6$ (refer to Figure 4.18)**

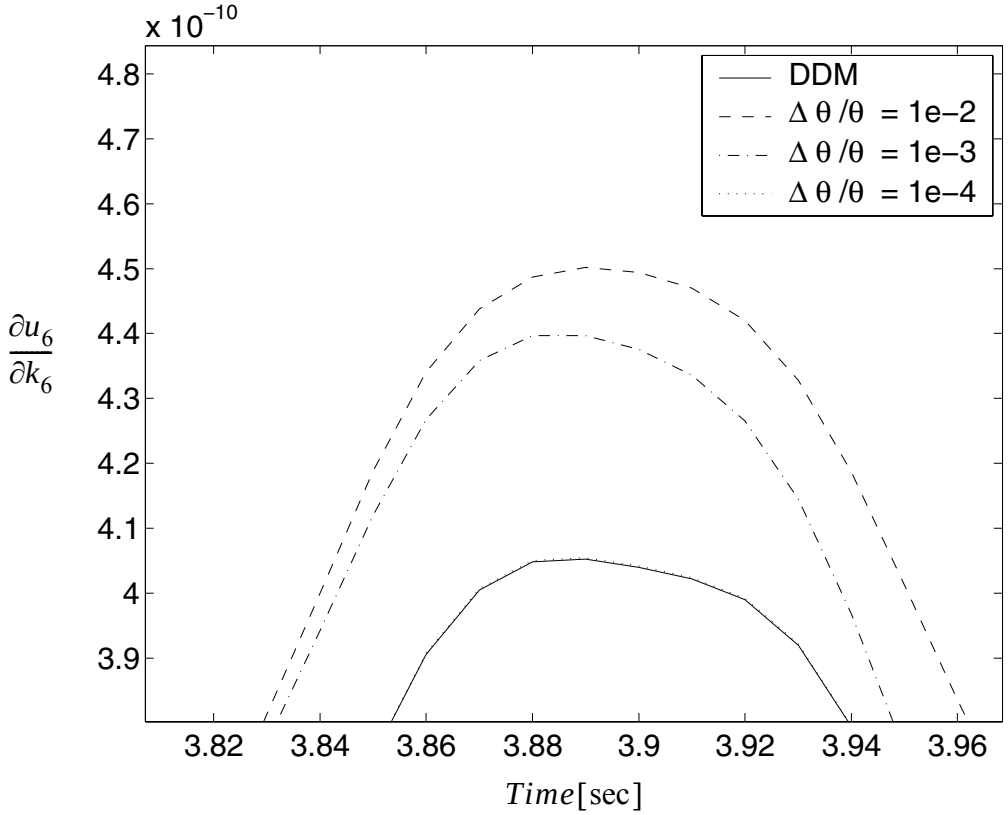


**Figure 4.48 Sensitivity of response $u_6$ with respect to bulk moduli $k_6$, detailed view (refer to Figure 4.18)**

From these results, it is obvious that the FFD results approach to the DDM results with the decreasing perturbation size within an acceptable range, proving that the DDM results are correct.

It is also noticed that the sensitivity results are very insightful when evaluating the relative importance of the parameters in affecting the responses. The sensitivity results are normalized by the nominal value of the variables to show the relative importance of the parameters in figures 4.49 through 4.56.

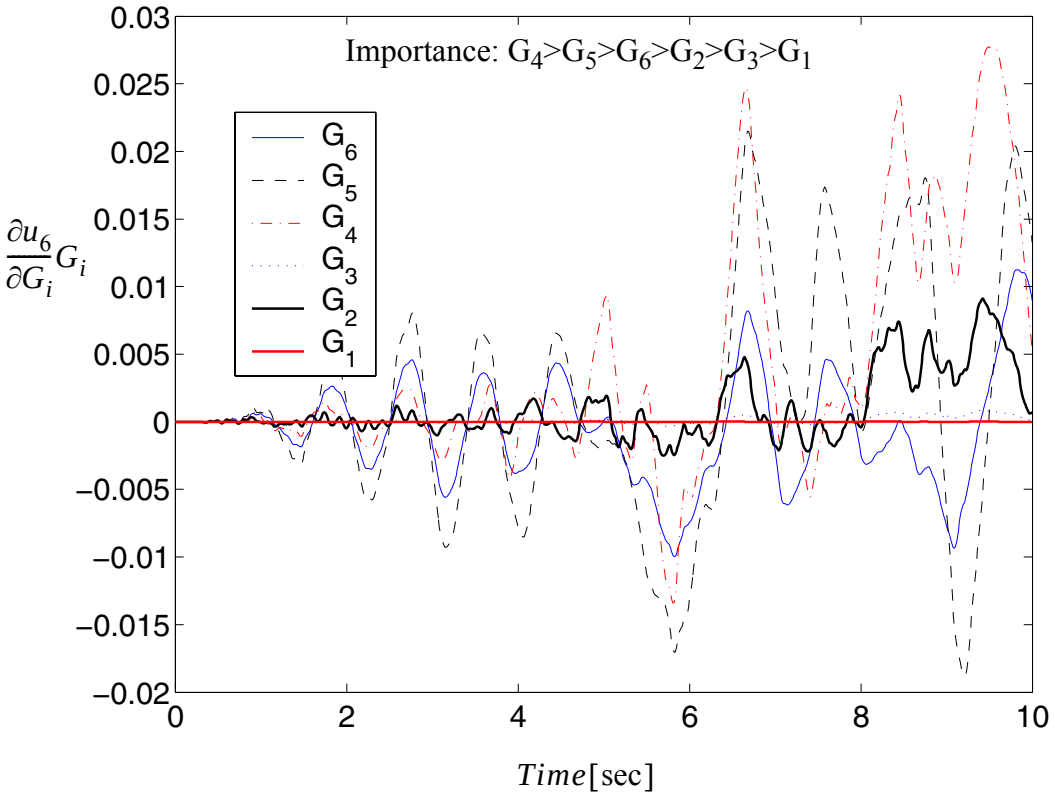


**Figure 4.49 Relative importance of shear modulis $G_i$'s on top horizontal displacement (refer to Figure 4.18)**

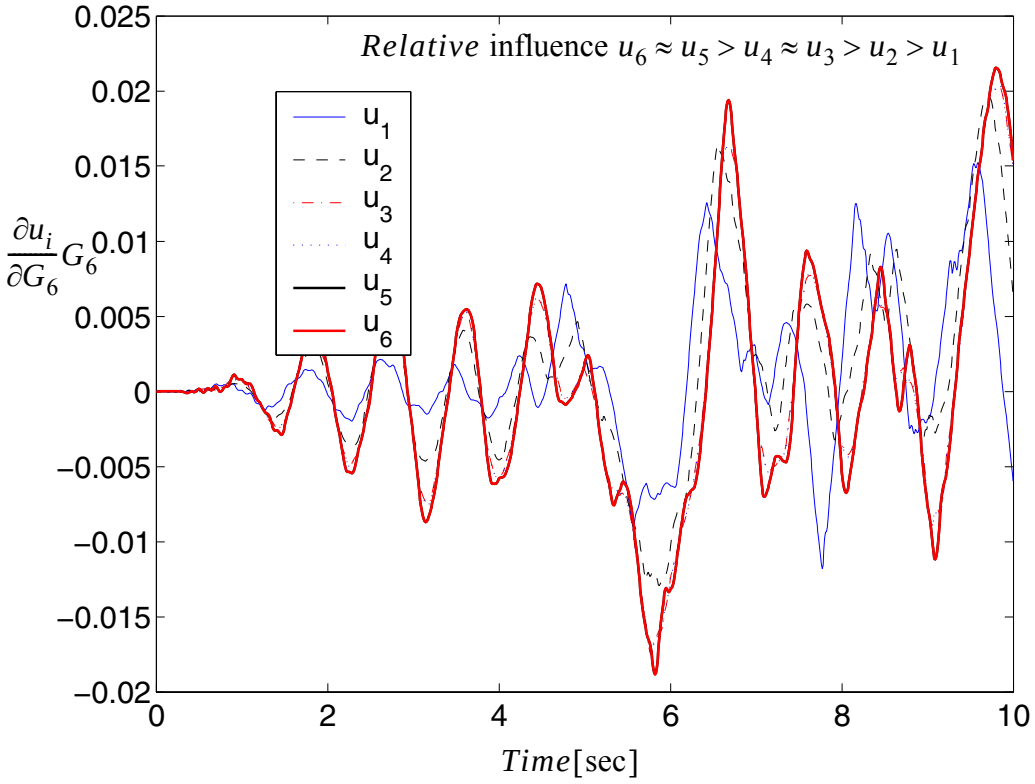


**Figure 4.50 Relative influence of shear moduli $G_6$ on the displacements (refer to Figure 4.18)**

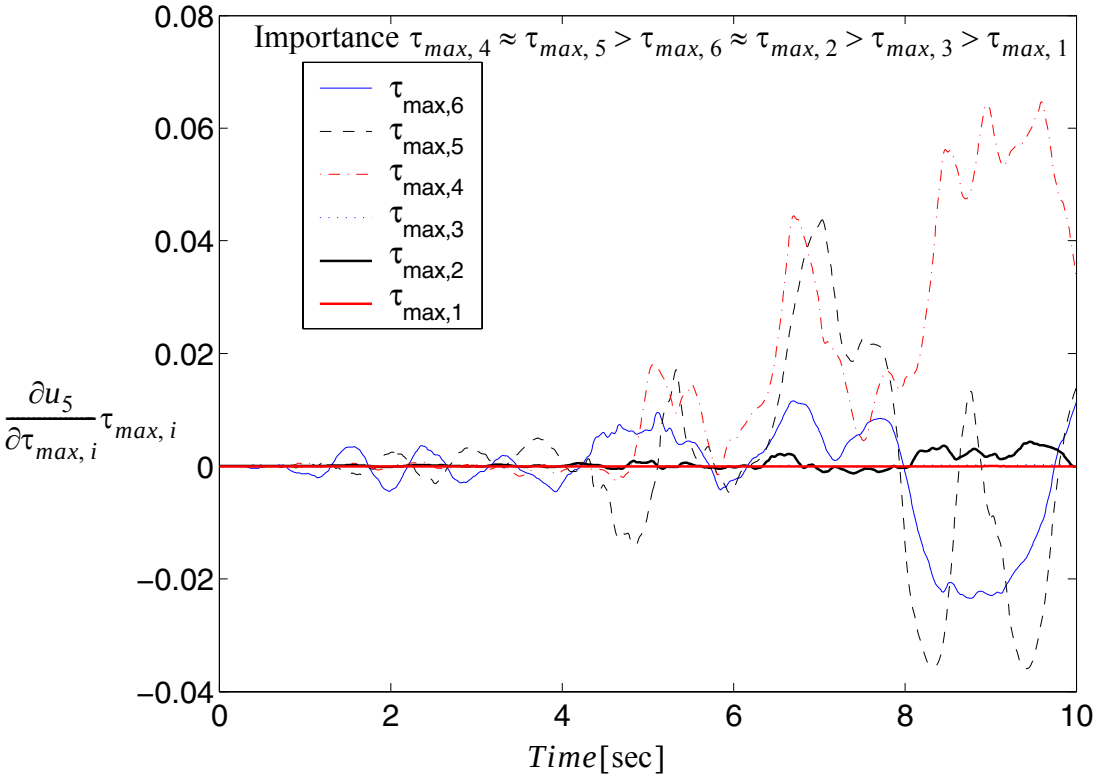


**Figure 4.51 Relative importance of shear moduli $\tau_{max,i}$ on second top horizontal displacement $u_5$ (refer to Figure 4.18)**

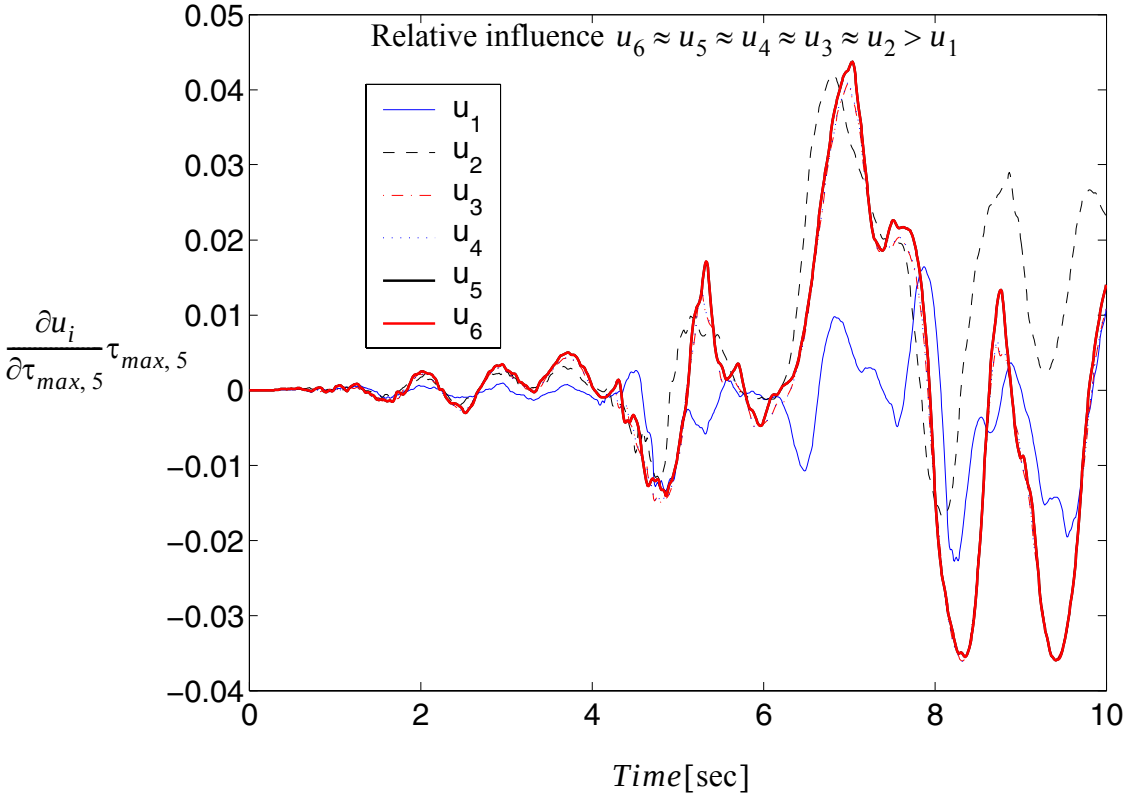


**Figure 4.52 Relative influence of shear strength $\tau_{max,5}$ on the displacements (refer to Figure 4.18)**

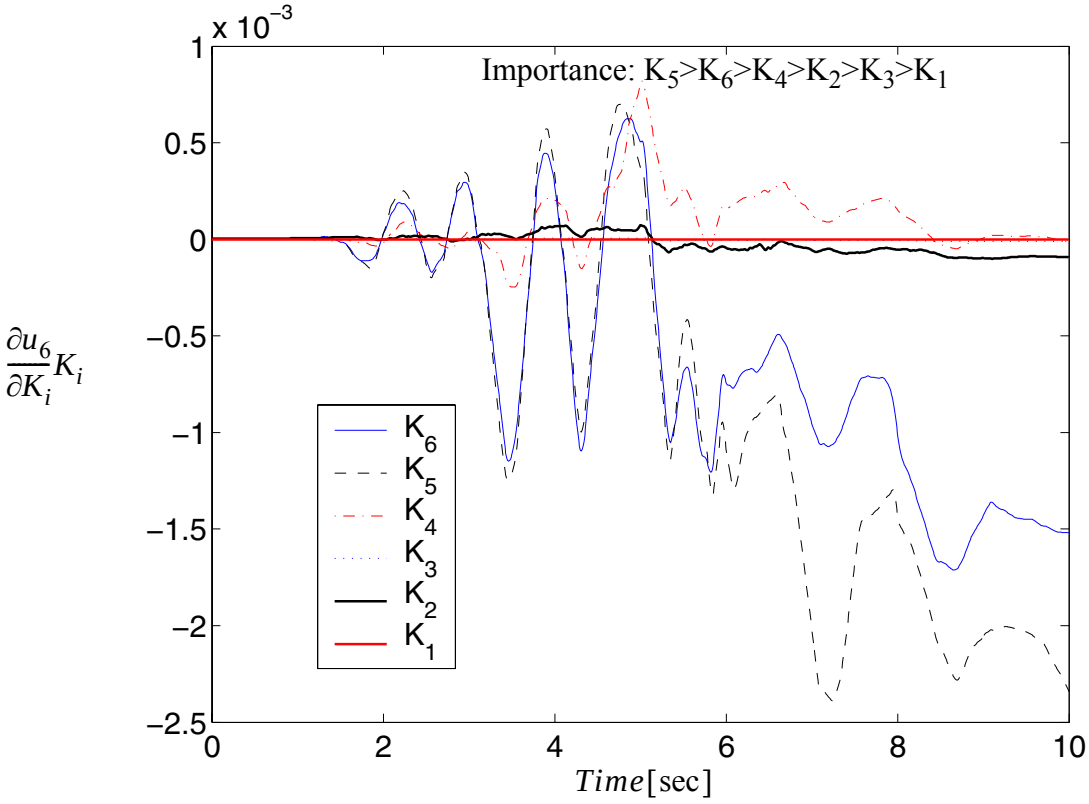


**Figure 4.53 Relative importance of bulk modulus $K_i$'s on top horizontal displacement (refer to Figure 4.18)**

Relative importance $\tau_{max,4} > \tau_{max,5} > \tau_{max,6} > G_4 > G_5 > G_6$

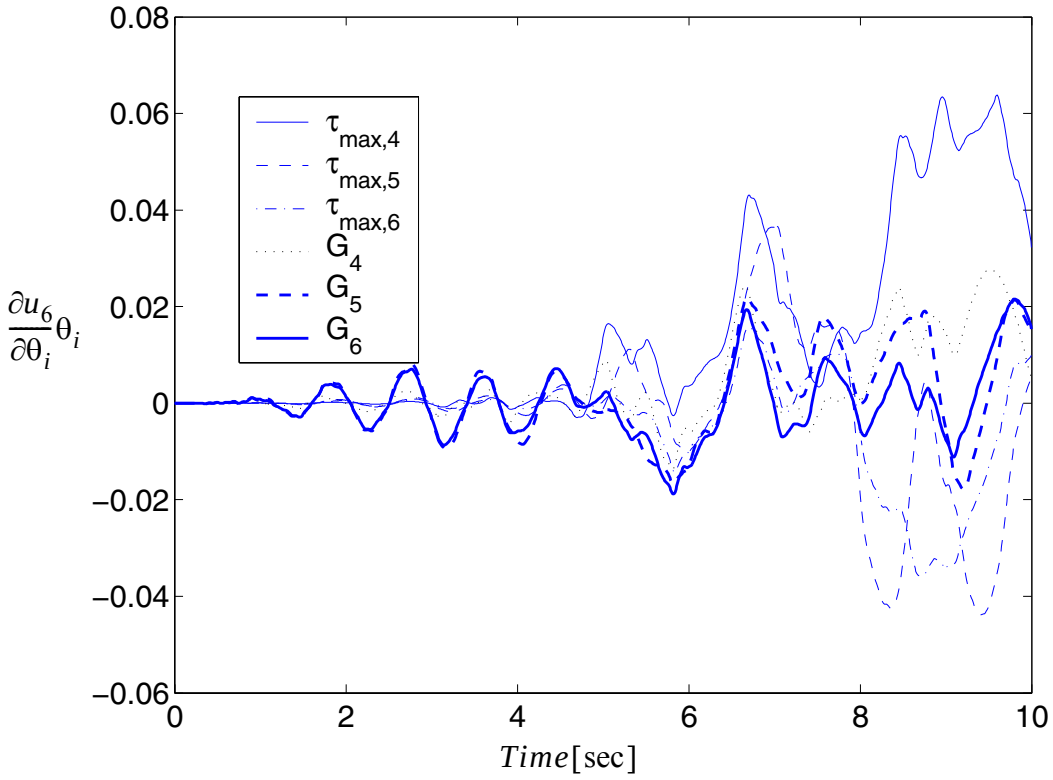


**Figure 4.54 Relative importance of θ's on top horizontal displacement (refer to Figure 4.18)**

*Relative* importance $G_2 > \tau_{max,2} > K_5 > K_6 > G_3 > K_4$

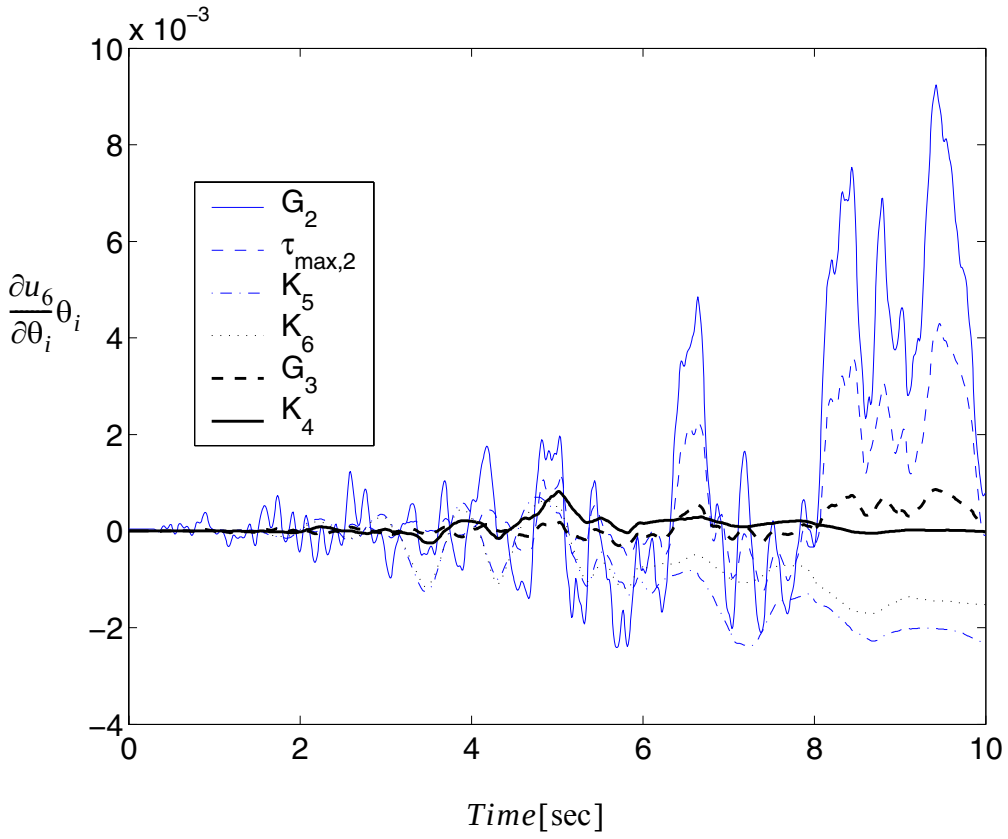


**Figure 4.55 Relative importance of θ's on top horizontal displacement (refer to Figure 4.18)**

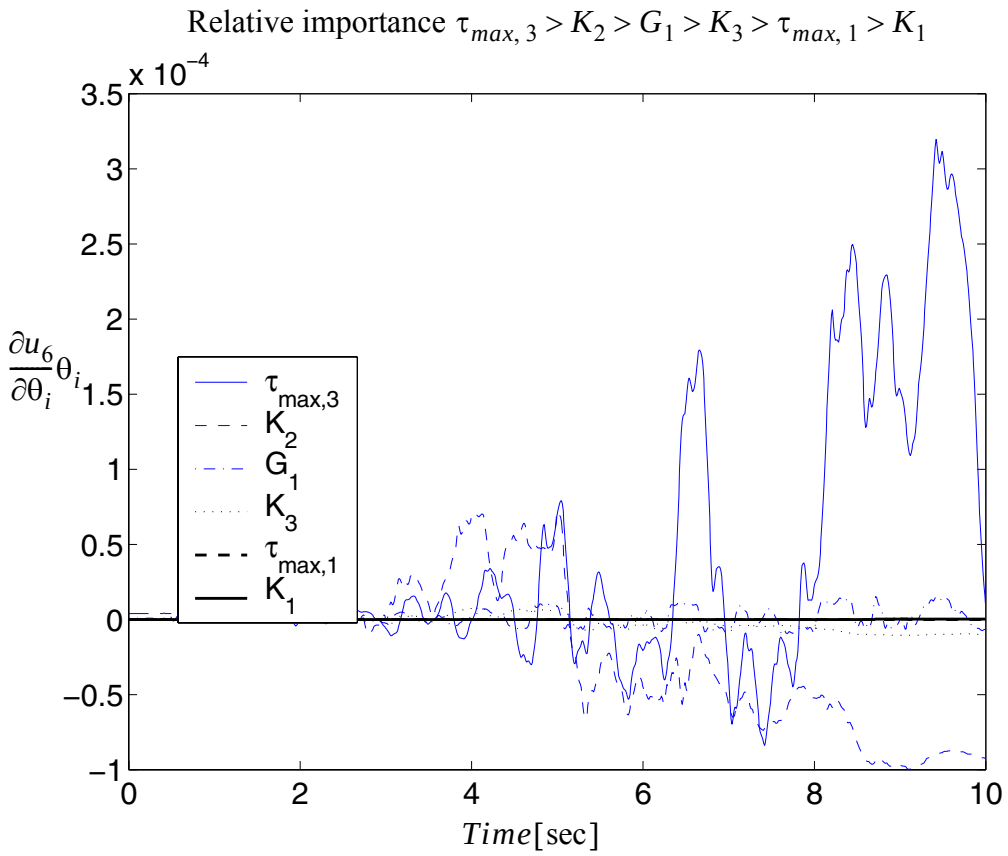


**Figure 4.56 Relative importance of θ's on top horizontal displacement (refer to Figure 4.18)**

From the normalized sensitivities of the top displacement, with respect to different parameters, as shown in Figures 4.54 to 4.56, it is observed that the relative importances of the random variables are:

$$\tau_{max,4} > \tau_{max,5} > \tau_{max,6} > G_4 > G_5 > G_6 > G_2 > \tau_{max,2} > K_5 > K_6 > G_3 > K_4 > \tau_{max,3} > K_2 > G_1 > K_3 > \tau_{max,1} > K_1$$

It is worth mentioning that the word 'importance' means 'sensitivity', or a parameter's influence on the response at the parameters' nominal values. This does not necessarily

mean it is important in resisting external forces. For example, in the R/C fiber section, the cover concrete is usually more sensitive (or more important) in determining the response than the core concrete, however this does not mean that the cover concrete is more important in resisting the external force. Furthermore, the assessment of relative importance described above is valid while parameters are allowed to vary within a very small region close to the nominal parameter values. While this relative importance is true locally, it is not guaranteed to be true globally when parameters vary beyond this local region.

#### 4.3.7.6 Summary

Based on the Direct Difference Method (DDM) in the context of FEM, this section provides a method to compute the response sensitivity for an existing multi-yield-surface $J_2$ plasticity model with respect to material parameters. Sensitivity analysis results are validated through the Forward Finite Difference (FFD) method. The computational results indicate that the FFD results converge to the DDM results as the perturbation decreases within an acceptable range determined by the computational round-off error.

The sensitivity computational method presented herein provides a way to evaluate the relative importance of the material parameters in terms of their relative influence on the structural/soil responses.

## 4.4 Extension of Sensitivity Framework to Multiple Point Constraint Handlers

This section studied the sensitivity derivative of the constraints enforce additional conditions on the degrees of freedom (DOFs) of a given system. The sensitivity derivation for

static case is shown in detail, while for dynamic case it is very similar and may be find in reference (Gu and Barbato, 2008).

A constraint either prescribes the value of a DOF, in which case it is called "single-point constraint" (e.g., support conditions), or prescribes a relation among two or more DOFs, in which case it is called "multi-point constraint" (e.g., rigid links, rigid elements). Handling of single-point constraints is an easy task and reduces to eliminating the constrained DOF from the equation of motion (dynamic case) or the equation of equilibrium (quasi-static case). Multi-point constraints can be expressed by introducing a set of equations that couple the DOFs affected by the constraints, called constraint equations, in the form,

$$\boldsymbol{C}\boldsymbol{u}_{n+1}(\theta) = \boldsymbol{Q} \tag{4.88}$$

Different techniques are available for handling of multi-point constraints, namely: (1) the transformation equations method, (2) the Lagrange multipliers method and (3) the penalty functions method.

The transformation equations method requires partitioning of the equation of motion (equilibrium) and of the constraint equations between retained DOFs (denoted by the subscript "r") and constrained DOFs (denoted by the subscript "c").

### 4.4.1 Sensitivity Computation

The computation of response sensitivities begins with the same set of equations for the three methods considered,

$$\begin{cases} \boldsymbol{R}(\boldsymbol{u}(\theta), \theta) - \boldsymbol{F}(\theta) = \boldsymbol{0} \\ \boldsymbol{C}\boldsymbol{u}(\theta) = \boldsymbol{Q} \end{cases} \tag{4.89}$$

#### 4.4.1.1 Transformation Equations Method

Let us consider the structure DOF displacement vector **u** and structure DOF resisting force vector **R** and let us partition them into d.o.f. to be retained (subscript 'r') and d.o.f. to be condensed out (subscript 'c') as

$$\boldsymbol{u} = \begin{bmatrix} \boldsymbol{u}_r \\ \boldsymbol{u}_c \end{bmatrix}, \quad \boldsymbol{R} = \begin{bmatrix} \boldsymbol{R}_r \\ \boldsymbol{R}_c \end{bmatrix}, \quad \boldsymbol{F} = \begin{bmatrix} \boldsymbol{F}_r \\ \boldsymbol{F}_c \end{bmatrix}, \quad \boldsymbol{C} = [\boldsymbol{T}_r \;\; \boldsymbol{T}_c], \quad \boldsymbol{K} = \begin{bmatrix} \boldsymbol{K}_{rr} & \boldsymbol{K}_{rc} \\ \boldsymbol{K}_{cr} & \boldsymbol{K}_{cc} \end{bmatrix}, \tag{4.90}$$

we obtain

$$\boldsymbol{u}_c(\theta) = \boldsymbol{T}_{rc}\boldsymbol{u}_r(\theta) + \boldsymbol{T}_c^{-1}\boldsymbol{Q} \tag{4.91}$$

where $\boldsymbol{T}_{rc} = -\boldsymbol{T}_c^{-1}\boldsymbol{T}_r$.

When the first Equation of the Equation (4.89) is multiplied by $\boldsymbol{C}$ on both side, it is obtained that,

$$\boldsymbol{R}_e(\boldsymbol{u}_r(\theta), \theta) - \boldsymbol{F}_e(\theta) = \boldsymbol{0} \tag{4.92}$$

in which

$$\begin{cases} \boldsymbol{R}_e = \boldsymbol{R}_r + \boldsymbol{T}_{rc}^T\boldsymbol{R}_c \\ \boldsymbol{F}_e = \boldsymbol{F}_r + \boldsymbol{T}_{rc}^T\boldsymbol{F}_c \end{cases} \tag{4.93}$$

(4.92) is wrote as incremental format,

$$[\boldsymbol{K}_{rr} + \boldsymbol{K}_{rc}\boldsymbol{T}_{rc} + \boldsymbol{T}_{rc}^T\boldsymbol{K}_{cr} + \boldsymbol{T}_{rc}^T\boldsymbol{K}_{cc}\boldsymbol{T}_{rc}] \cdot \delta\boldsymbol{u}_r = \delta\boldsymbol{F}_e(\theta) \tag{4.94}$$

or $\boldsymbol{K}_e \cdot \delta \boldsymbol{u}_r = \delta \boldsymbol{F}_e(\theta)$, where $\boldsymbol{K}_e = \boldsymbol{K}_{rr} + \boldsymbol{K}_{rc}\boldsymbol{T}_{rc} + \boldsymbol{T}_{rc}^T\boldsymbol{K}_{cr} + \boldsymbol{T}_{rc}^T\boldsymbol{K}_{cc}\boldsymbol{T}_{rc}$.

Differentiating (4.91) with respect to $\theta$, we have

$$\frac{d\boldsymbol{u}_c}{d\theta} = \boldsymbol{T}_{rc}\frac{d\boldsymbol{u}_r}{d\theta} \tag{4.95}$$

For computing sensitivities, the conditional and unconditional sensitivities of the equivalent structure d.o.f. forces $\left.\frac{\partial \boldsymbol{R}_e}{\partial \theta}\right|_{\boldsymbol{u}}$ and $\frac{d\boldsymbol{R}_e}{d\theta}$, respectively (subscript 'e' stands for 'equivalent') are obtained as,

$$\begin{aligned}
\frac{d\boldsymbol{R}_r}{d\theta} &= \left.\frac{\partial \boldsymbol{R}_r}{\partial \boldsymbol{u}_r}\right|_{\theta}\frac{d\boldsymbol{u}_r}{d\theta} + \left.\frac{\partial \boldsymbol{R}_r}{\partial \boldsymbol{u}_c}\right|_{\theta}\frac{d\boldsymbol{u}_c}{d\theta} + \left.\frac{\partial \boldsymbol{R}_r}{\partial \theta}\right|_{\boldsymbol{u}} = \boldsymbol{K}_{rr}\frac{d\boldsymbol{u}_r}{d\theta} + \boldsymbol{K}_{rc}\frac{d\boldsymbol{u}_c}{d\theta} + \left.\frac{\partial \boldsymbol{R}_r}{\partial \theta}\right|_{\boldsymbol{u}} \\
\frac{d\boldsymbol{R}_c}{d\theta} &= \left.\frac{\partial \boldsymbol{R}_c}{\partial \boldsymbol{u}_r}\right|_{\theta}\frac{d\boldsymbol{u}_r}{d\theta} + \left.\frac{\partial \boldsymbol{R}_c}{\partial \boldsymbol{u}_c}\right|_{\theta}\frac{d\boldsymbol{u}_c}{d\theta} + \left.\frac{\partial \boldsymbol{R}_c}{\partial \theta}\right|_{\boldsymbol{u}} = \boldsymbol{K}_{cr}\frac{d\boldsymbol{u}_r}{d\theta} + \boldsymbol{K}_{cc}\frac{d\boldsymbol{u}_c}{d\theta} + \left.\frac{\partial \boldsymbol{R}_c}{\partial \theta}\right|_{\boldsymbol{u}}
\end{aligned} \tag{4.96}$$

differentiating (4.92) and (4.93), we have

$$\frac{d\boldsymbol{F}_e}{d\theta} = \frac{d\boldsymbol{R}_e}{d\theta} = \frac{d\boldsymbol{R}_r}{d\theta} + \boldsymbol{T}_{rc}^T\frac{d\boldsymbol{R}_c}{d\theta} \tag{4.97}$$

Substituting (4.96) in (4.97), finally we obtain

$$\frac{d\boldsymbol{F}_e}{d\theta} = [\boldsymbol{K}_{rr} + \boldsymbol{K}_{rc}\boldsymbol{T}_{rc} + \boldsymbol{T}_{rc}^T\boldsymbol{K}_{cr} + \boldsymbol{T}_{rc}^T\boldsymbol{K}_{cc}\boldsymbol{T}_{rc}]\frac{d\boldsymbol{u}_r}{d\theta} + \left(\left.\frac{\partial \boldsymbol{R}_r}{\partial \theta}\right|_{\boldsymbol{u}} + \boldsymbol{T}_{rc}^T\left.\frac{\partial \boldsymbol{R}_c}{\partial \theta}\right|_{\boldsymbol{u}}\right) \tag{4.98}$$

Since

$$\left.\frac{\partial \boldsymbol{R}_e}{\partial \theta}\right|_{\boldsymbol{u}} = \left.\frac{\partial \boldsymbol{R}_r}{\partial \theta}\right|_{\boldsymbol{u}} + \boldsymbol{T}_{rc}^T\left.\frac{\partial \boldsymbol{R}_c}{\partial \theta}\right|_{\boldsymbol{u}} \tag{4.99}$$

The sensitivity equations become

$$\frac{d\boldsymbol{u}_r}{d\theta} = \boldsymbol{K}_e^{-1} \cdot \left( \frac{d\boldsymbol{F}_e}{d\theta} - \frac{\partial \boldsymbol{R}_e}{\partial \theta}\bigg|_{\boldsymbol{u}} \right)$$
$$\frac{d\boldsymbol{u}_c}{d\theta} = \boldsymbol{T}_{rc} \frac{d\boldsymbol{u}_r}{d\theta} \tag{4.100}$$

#### 4.4.1.2 Lagrange Multipliers Method

Equation (4.89) is rewritten as

$$\begin{cases} \boldsymbol{R}(\boldsymbol{u}_{n+1}(\theta), \theta) + \boldsymbol{C}^T \boldsymbol{\lambda}_{n+1}(\theta) - \boldsymbol{F}_{n+1}(\theta) = \boldsymbol{0} \\ \boldsymbol{C}\boldsymbol{u}_{n+1}(\theta) - \boldsymbol{Q} = \boldsymbol{0} \end{cases} \tag{4.101}$$

and (4.101) is differentiated wrt $\theta$ as

$$\begin{cases} (\boldsymbol{K}_T^{stat})_{n+1} \dfrac{d\boldsymbol{u}_{n+1}}{d\theta} + \boldsymbol{C}^T \dfrac{d\boldsymbol{\lambda}_{n+1}}{d\theta} = \dfrac{d\boldsymbol{F}_{n+1}}{d\theta} - \dfrac{\partial \boldsymbol{R}_{n+1}}{\partial \theta}\bigg|_{\boldsymbol{u}_{n+1}} \\ \boldsymbol{C} \dfrac{d\boldsymbol{u}_{n+1}}{d\theta} = \boldsymbol{0} \end{cases} \tag{4.102}$$

or in matrix form

$$\begin{bmatrix} (\boldsymbol{K}_T^{stat})_{n+1} & \boldsymbol{C}^T \\ \boldsymbol{C} & \boldsymbol{0} \end{bmatrix} \begin{Bmatrix} \dfrac{d\boldsymbol{u}_{n+1}}{d\theta} \\ \dfrac{d\boldsymbol{\lambda}_{n+1}}{d\theta} \end{Bmatrix} = \begin{Bmatrix} \dfrac{d\boldsymbol{F}_{n+1}}{d\theta} - \dfrac{\partial \boldsymbol{R}_{n+1}}{\partial \theta}\bigg|_{\boldsymbol{u}_{n+1}} \\ \boldsymbol{0} \end{Bmatrix} \tag{4.103}$$

#### 4.4.1.3 Penalty Functions Method

Equation (4.89) is rewritten as

$$\boldsymbol{R}(\boldsymbol{u}_{n+1}(\theta), \theta) + (\boldsymbol{C}^T \boldsymbol{\alpha} \boldsymbol{C})\boldsymbol{u}_{n+1}(\theta) - \boldsymbol{F}_{n+1}(\theta) - \boldsymbol{C}^T \boldsymbol{\alpha} \boldsymbol{Q} = \boldsymbol{0} \tag{4.104}$$

and (4.104) is differentiated wrt $\theta$ as

$$[(\boldsymbol{K}_T^{stat})_{n+1} + (\boldsymbol{C}^T \boldsymbol{\alpha} \boldsymbol{C})]\frac{d\boldsymbol{u}_{n+1}}{d\theta} = \frac{d\boldsymbol{F}_{n+1}}{d\theta} - \frac{\partial \boldsymbol{R}_{n+1}}{\partial \theta}\bigg|_{\boldsymbol{u}_{n+1}} \tag{4.105}$$

## 4.5 Extension of Sensitivity Framework to Variable Transient Integration Analysis

In the variable transient integration analysis case, the time step size is automatically adjusted (i.e., adaptive time step) according to the convergence conditions. It is required that the time step in the sensitivity computation be consistent with the integration time step.

It is worth mentioning that the FFD may not work in this case. In the FFD, the temporal discretization size must be the same between the perturbed and unperturbed cases. However, in the variable transient integration analysis, the perturbation may change the convergence state, and the adapted time step in the perturbed state may be inconsistent with that of the unperturbed case.

The DDM can deal with the adaptive time step well due to the fact that it analytically computes the sensitivity instead of using a perturbation.

## 4.6 Examples of Response Sensitivity Analysis of SFSI Systems

### 4.6.1 2D SFSI System

The first application example consists of a two-dimensional Soil-Foundation-Structure Interaction (SFSI) system, a model of which is shown in Figure 4.57. The structure is a two-story two-bay reinforced concrete frame with section properties given in Figure 4.57.

The foundations consist of reinforced concrete squat footings at the bottom of each column. The soil is a layered clay, with stiffness properties varying along the depth.

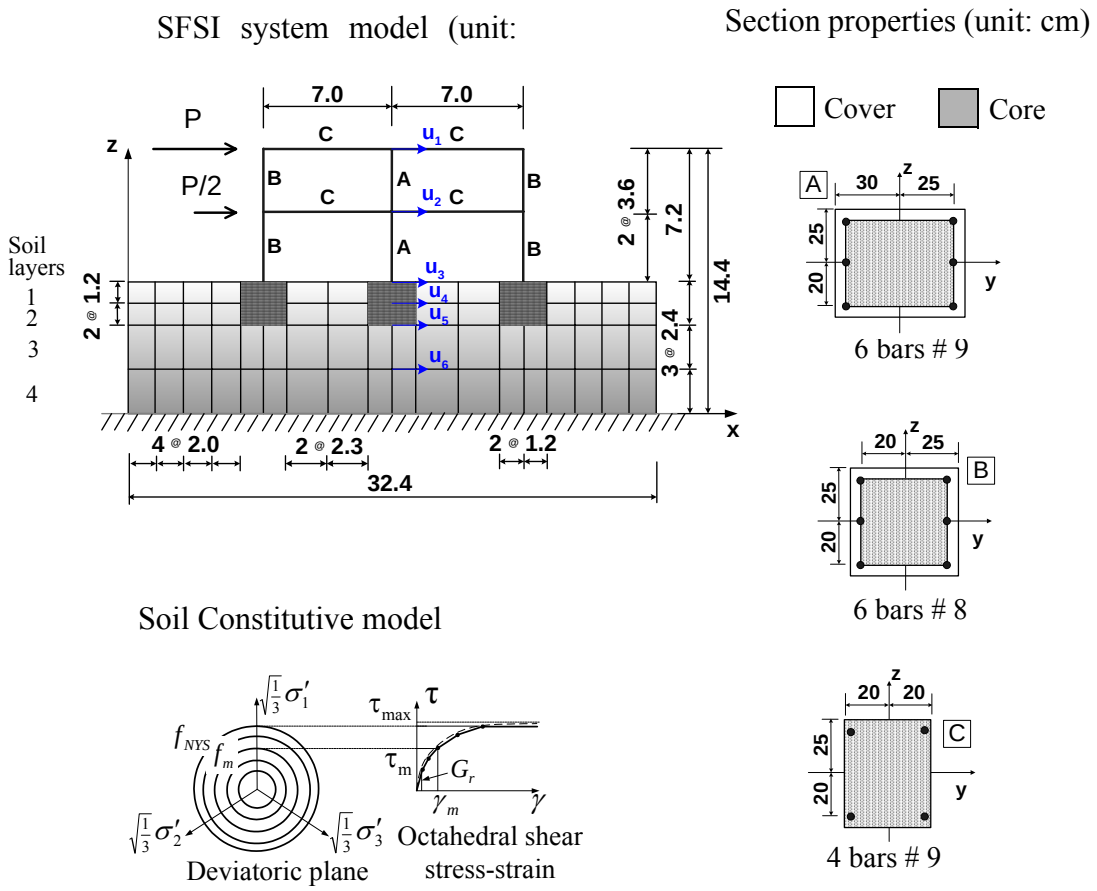


**Figure 4.57 2-D model of SFSI system: geometry, section properties and soil**

The frame structure of this SFSI system is modeled by using displacement-based Euler-Bernoulli frame elements with distributed plasticity, each with four Gauss-Legendre integration points. Section stress resultants at the integration points are computed by discretizing the frame sections by layers. Foundation footings and soil layers are modeled through isoparametric four-node quadrilateral finite elements with bilinear displacement

interpolation. The soil mesh is shown in Figure 4.57. The constitutive behavior of the steel reinforcement is modeled by using a one-dimensional $J_2$ plasticity model with both kinematic and isotropic linear hardening (Conte et al. 2003). The concrete is modeled by using a Kent-Scott-Park model with zero tension stiffening (Scott et al 1982). Different material parameters are used for confined (core) and unconfined (cover) concrete in the columns. The soil is modeled by using a pressure-independent multi-yield surface $J_2$ plasticity material model (Elgamal et al. 2003), specialized for plane strain analysis (Figure 4.57). Different material parameters are used for each of the four layers considered. The material parameters are shown in the Table 4.23. The material parameters are considered as random variables.

**Table 4.23 Material parameters**

| | Concrete | | Steel | | Soil | | | | Foundation |
|---|---|---|---|---|---|---|---|---|---|
| Mat | Core | Cover | Mat | | Mat | G | $\tau_{max}$ | K | E |
| $f_c$ | -3.449e4 | -2.759e4 | E | 2.0E8 | #1 | 54450 | 33 | 1.6e5 | 2.0e7 |
| $f_{cu}$ | -2.069e4 | 0 | s | 2.484e5 | #2 | 33800 | 26 | 1.0e5 | |
| $\varepsilon_c$ | -0.004 | -0.002 | $H_{kin}$ | 1.6129e6 | #3 | 61250 | 35 | 1.8e5 | |
| $e_{cu}$ | -0.014 | -0.008 | $H_{iso}$ | 0.0 | #4 | 96800 | 44 | 2.9e5 | |

The soil under a condition of simple shear has its bottom nodes fixed and the corresponding boundary nodes at same depth tied together (Figure 4.58). The node of the beam (3 DOF) and the corresponding node on the foundation concrete block (2 DOF), at the same location, are tied together in both the horizontal and vertical directions as shown in Figure 4.58.

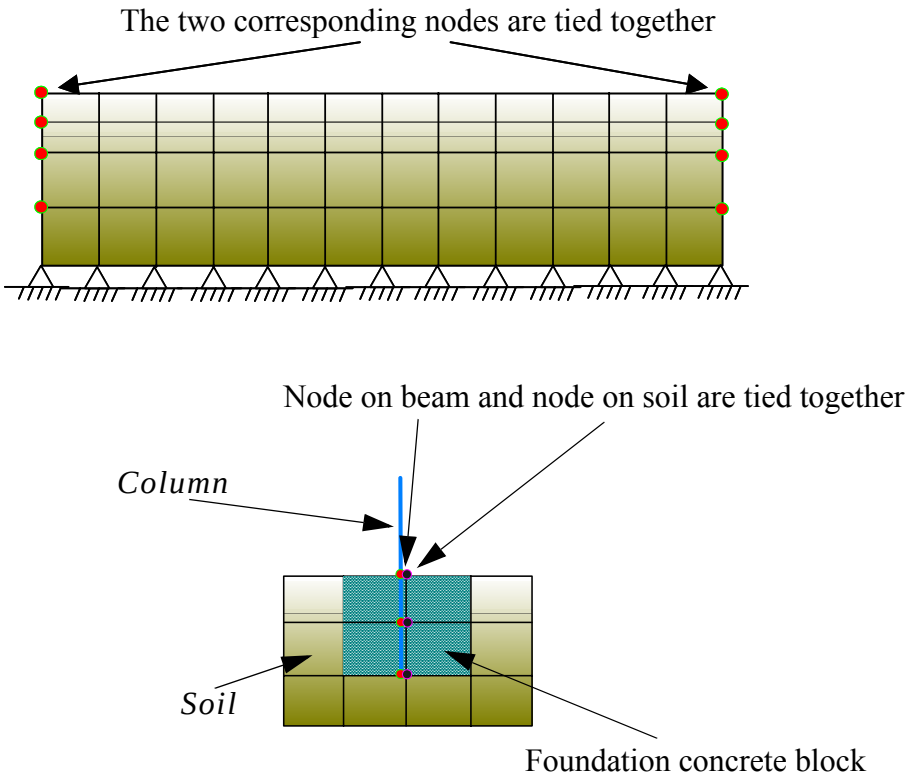


**Figure 4.58 Boundary conditions and multipoint constraints**

a, quasi-static pushover analysis

In this analysis, after static application of the gravity loads, the structure is subjected to a quasi-static pushover analysis, in which an upper triangular distribution of horizontal forces is applied at the floor levels (see Figure 4.57). The total base shear force, $P_{tot}$ =

1.5P, is considered as deterministic and is assumed to increase linearly during the analysis from 0kN to 750kN.

A response analysis and response sensitivity analysis based on DDM is performed. Interstory drift of each floor and interlayer drift of each soil layer are shown in Figure 4.59, Shear stress-strain relations of a girder A in second floor and in a Gauss point B of third soil layer are shown in Figure 4.60. It is clear that the systems yield significantly under the push over force.

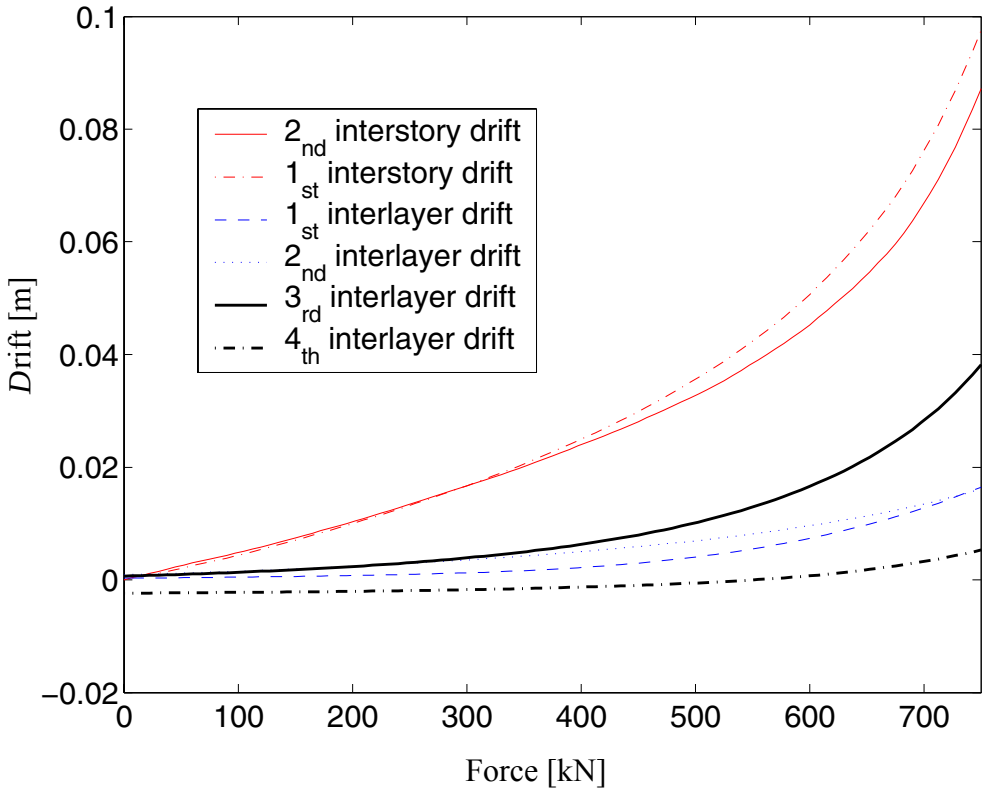


**Figure 4.59 Response histories at different floors and layers**

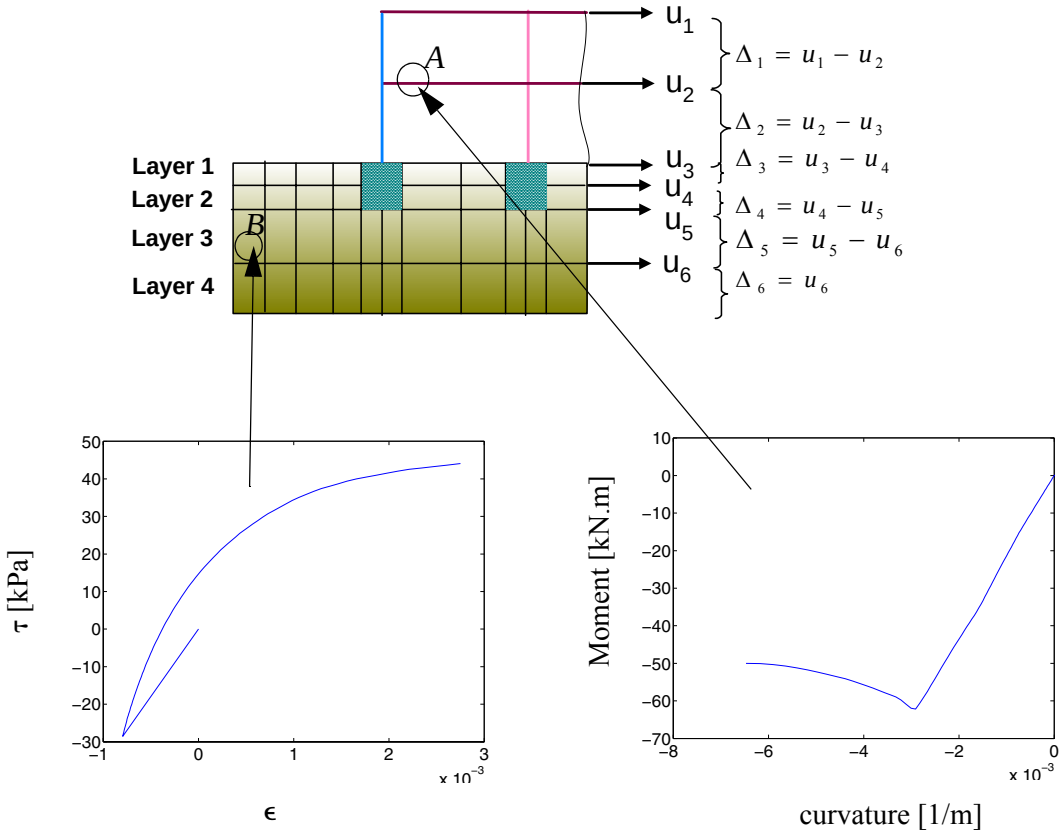


**Figure 4.60 Local response histories**

The DDM results are verified by using the forward finite difference (FFD) method. Part of results are shown in Figure 4.61 and Figure 4.62. From these figures, it is observed that the FFD results approach DDM results as the perturbation is reduced. While some time the FFD results can not convergence because the criterion (tolerance) of the response convergence is not small enough. (in this example, the displacement tolerance is 1.0e-8).

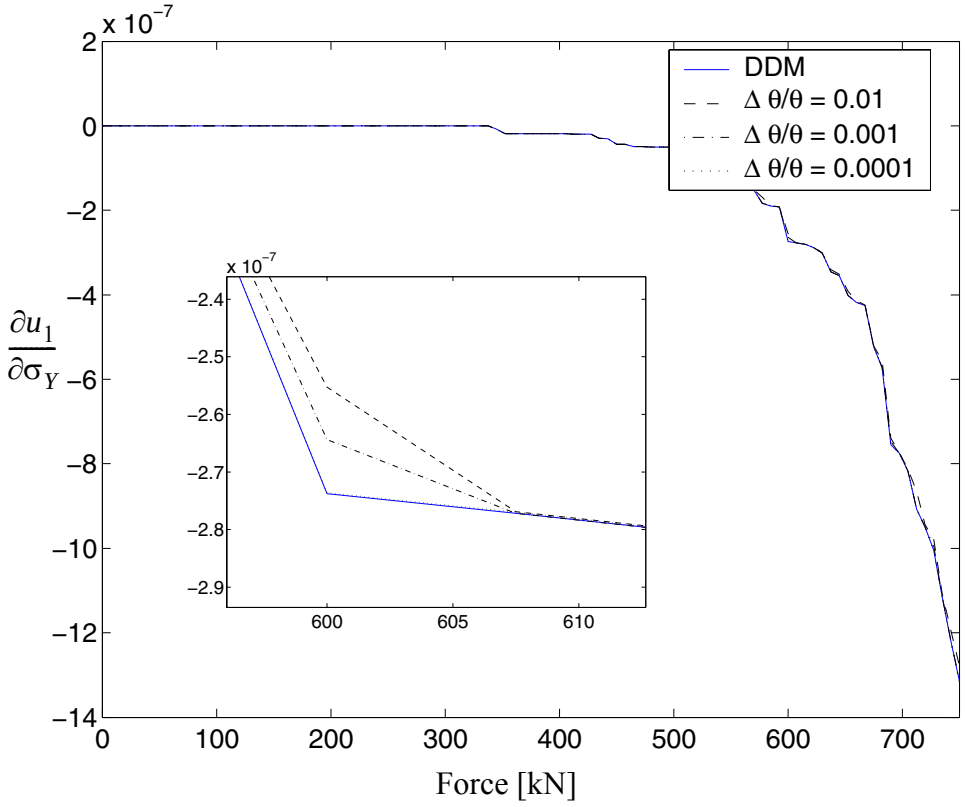


**Figure 4.61 Sensitivity of response $u_1$ with respect to steel $\sigma_Y$**

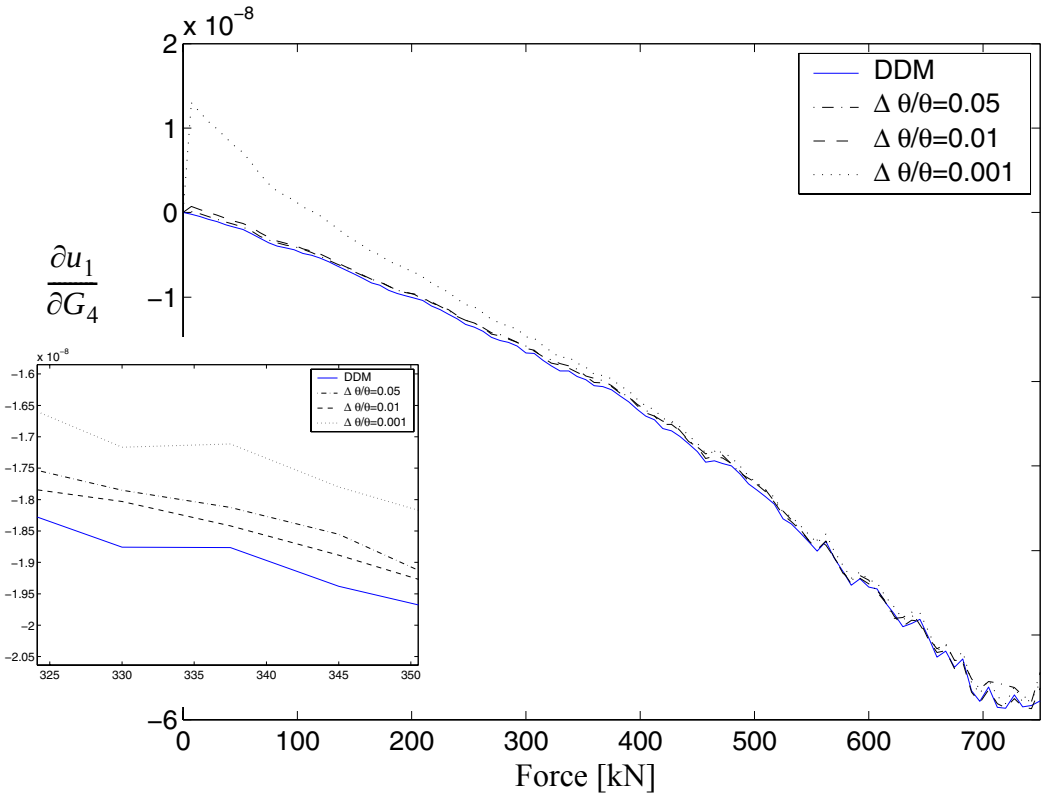


**Figure 4.62 Sensitivity of response $u_1$ with respect to the shear modulus $G_4$**

The normalized response sensitivity results are studied to compare the relative importance in determining the response of the first floor drift (except the $f_{cu}$ of the cover concrete and $H_{iso}$ of steel since their nominal values are zero and can not be normalized by the values). It is noticed that at different push over stage, (i.e., P=10% $P_{total}$, or P=50%$P_{total}$ and P=10% $P_{total}$), the importance of parameters are not same. The relative importance for these three cases are shown below:

1) P=10% $P_{total}$

$$E_{steel} > f_{c,\,cover} > \varepsilon_{c,\,cover} > \varepsilon_{c,\,core} > K_3 > \tau_{max,\,3} > \tau_{max,\,1} > f_{c,\,core} > G_3 > K_4 > \tau_{max,\,2} > G_1 > G_2 > \tau_{max,\,4} > K_1 > G_4 > E_{foundation} > K_2 > \sigma_{y,\,steel} = H_{kin} = 0$$

1) P=50% $P_{total}$

$$E_{steel} > f_{c,\,cover} > \varepsilon_{c,\,cover} > \tau_{max,\,3} > K_3 > \tau_{max,\,1} > \sigma_{y,\,steel} > \tau_{max,\,4} > K_4 > \tau_{max,\,2} > f_{c,\,core} > \varepsilon_{c,\,core} > G_3 > G_1 > G_2 > G_4 > K_1 > E_{foundation} > K_2 > H_{kin}$$

3) P=100% $P_{total}$

$$\sigma_{y,\,steel} > \tau_{max,\,3} > E_{steel} > f_{c,\,cover} > K_3 > K_4 > \tau_{max,\,4} > \tau_{max,\,1} > f_{c,\,core} > \tau_{max,\,2} > \varepsilon_{c,\,core} > \varepsilon_{c,\,cover} > K_1 > H_{kin} > K_2 > G_3 > G_4 > G_2 > G_1 > E_{foundation}$$

Based on the knowledge obtained, it is observed that,

The relative importance of the first floor drift to the steel yielding strength $\sigma_{y,\,steel}$ increases dramatically from zero ( $\frac{\partial u_{drift}}{\partial \sigma_{y,\,steel}} \sigma_{y,\,steel} = 0$ ) for 10% loading, to $\frac{\partial u_{drift}}{\partial \sigma_{y,\,steel}} \sigma_{y,\,steel} = -0.13$ for 100% loading case. And in full loading case $\sigma_{y,\,steel}$ becomes most important material parameters.

From 10% loading case to full loading case, the relative importance of concrete material parameters $\varepsilon_{c,\,core}, \varepsilon_{c,\,cover}$ and soil low strain shear strength $G_1$ to $G_4$ reduced, while the importance of the fourth layer soil parameters $K_4$ and $\tau_{max,\,4}$ , and the steel material parameter $H_{kin}$ increase.

The third soil layer material parameters $K_3$ and $\tau_{max,3}$, steel elastic modulus $E_{steel}$, cover concrete strength $f_{c,cover}$ are always very sensitive; The sensitivity of the first and second soil layer material parameters $\tau_{max,1}$ and $\tau_{max,2}$, core concrete strength $f_{c,core}$ are in the middle and not change; The sensitivity of the first and second soil layer material parameters $K_1$ and $K_2$ are low and not change; The foundation parameters $E_{foundation}$ are always not sensitive.

Part of the normalized sensitive results are shown in FIgures 4.63 to 4.65.

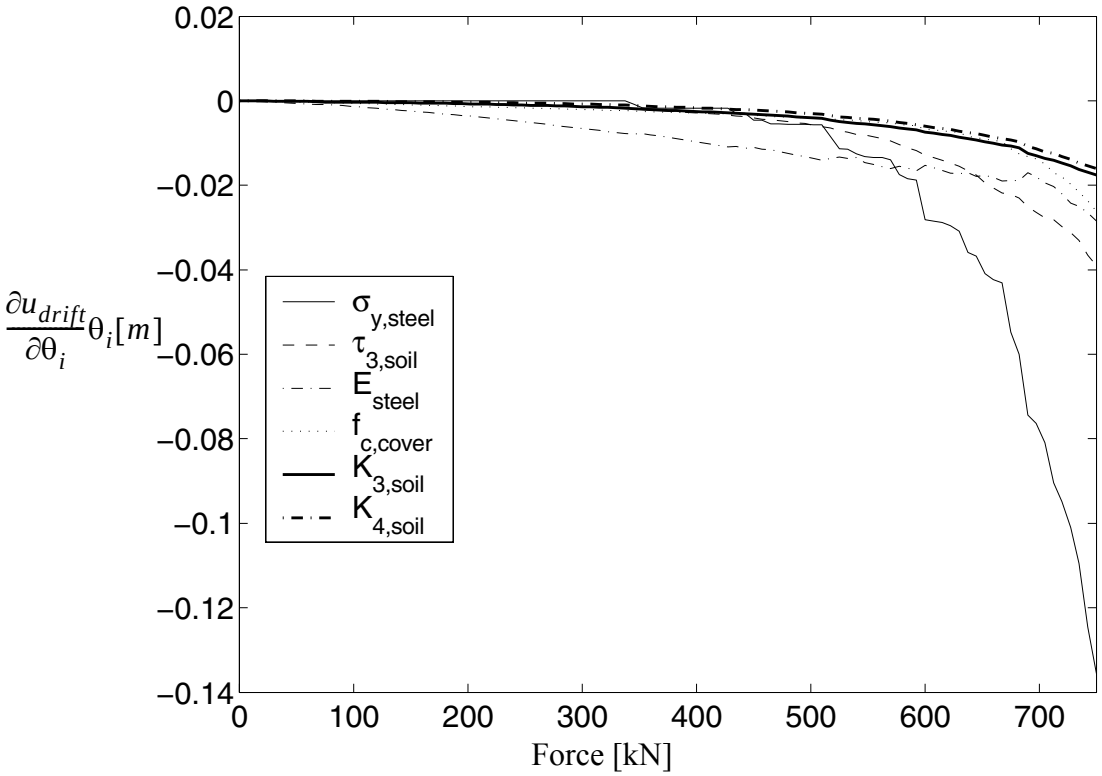


**Figure 4.63 Relative importance of θ's on the first floor drift**

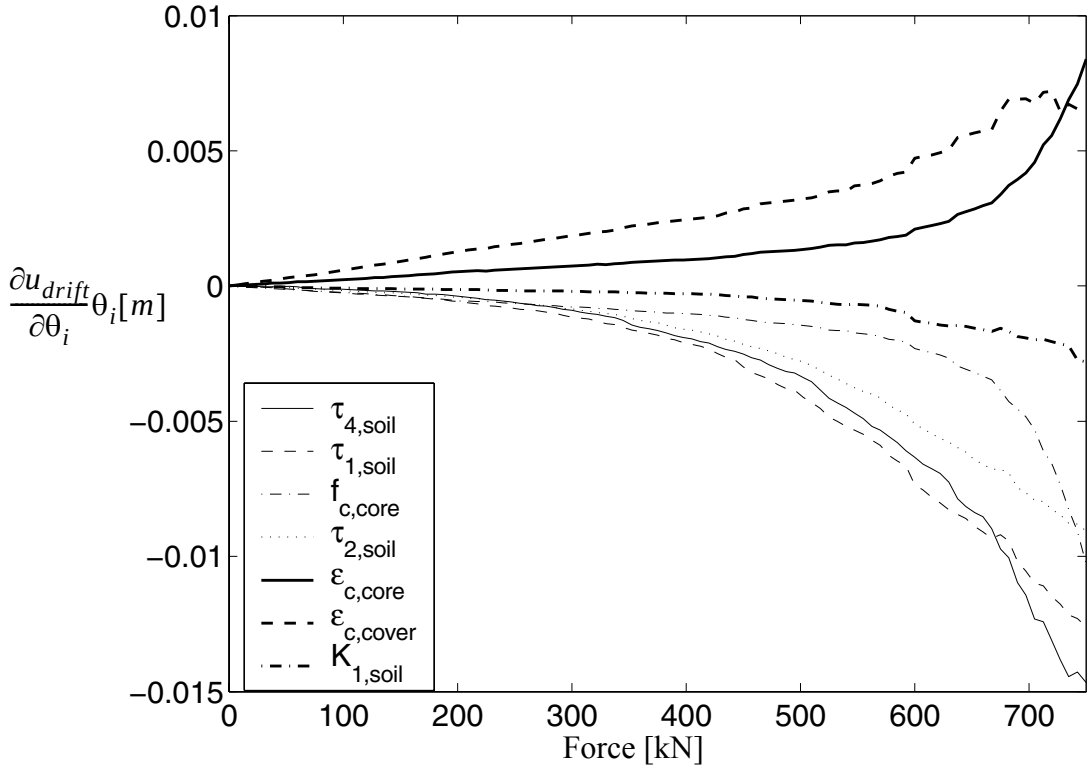


**Figure 4.64 Relative importance of θ's on the first floor drift**

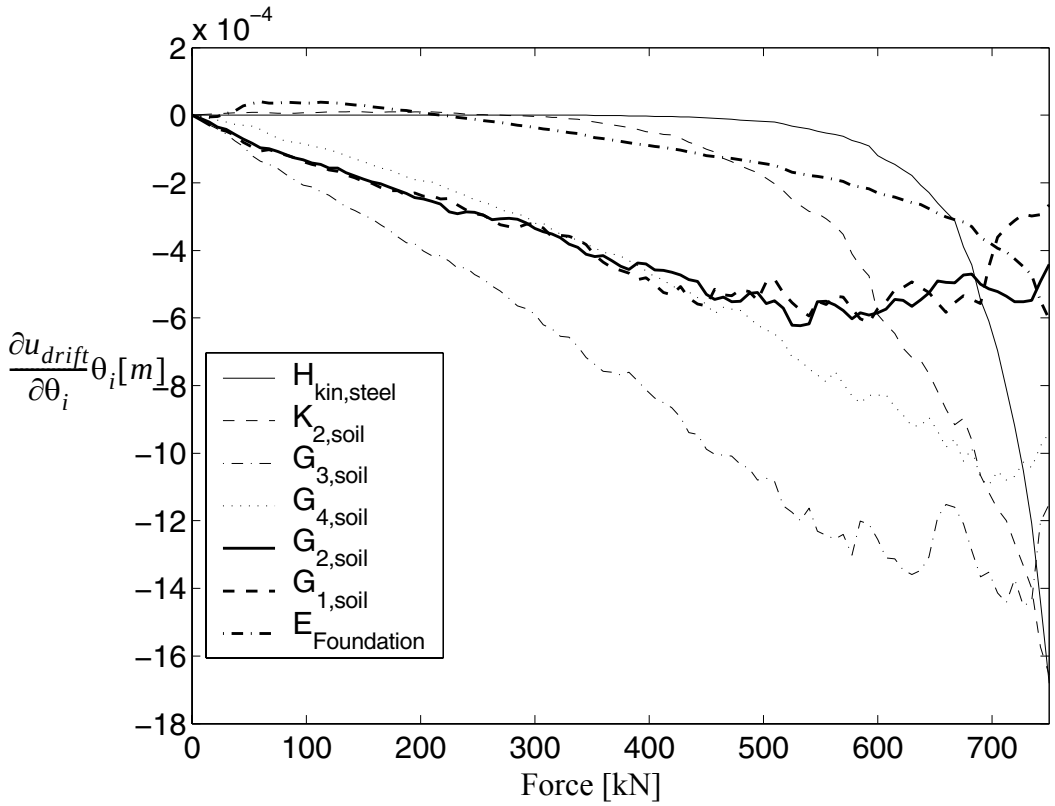


**Figure 4.65 Relative importance of θ's on the first floor drift**

b, base excitation

In this analysis, after static application of the gravity loads, the structure is subjected to a base excitation taken as three times of the earthquake recorder of Elcentro 1940 (N-S). A response analysis and response sensitivity analysis based on DDM is performed.

The interstory drifts of each floor and interlayer drifts of each soil layer are shown in Figure 4.66. The moment curvature relation of a girder at the second floor and the shear stress-strain relation of a Gauss point at the third layer of soil are shown in Figure 4.67.

From these figure, it is clear that the system yield significantly when subjected to the base excitation.

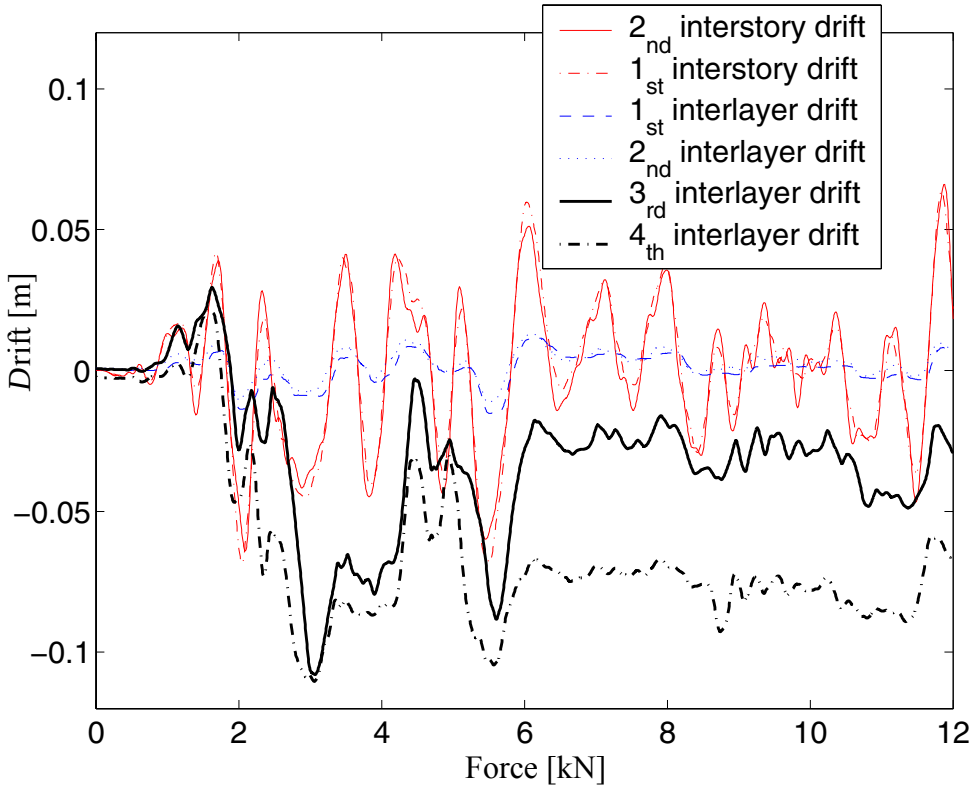


**Figure 4.66 Response histories at different floors and layers**

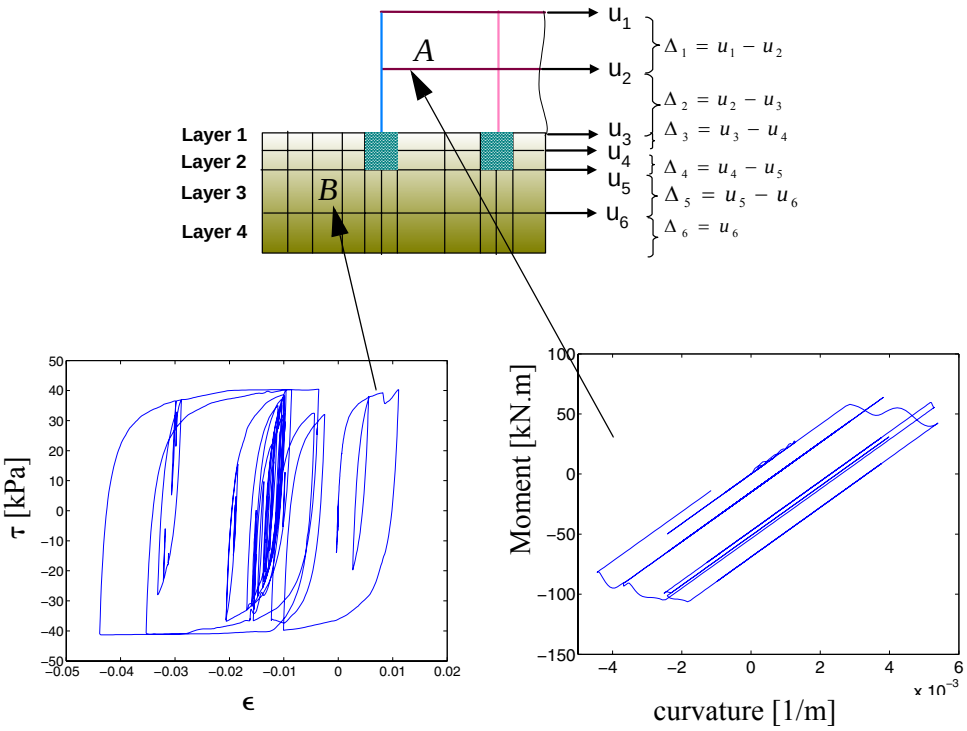


**Figure 4.67 Local response histories**

The DDM results are verified by using the forward finite difference (FFD) method. Part of results are shown in Figures 4.68 to 4.72.

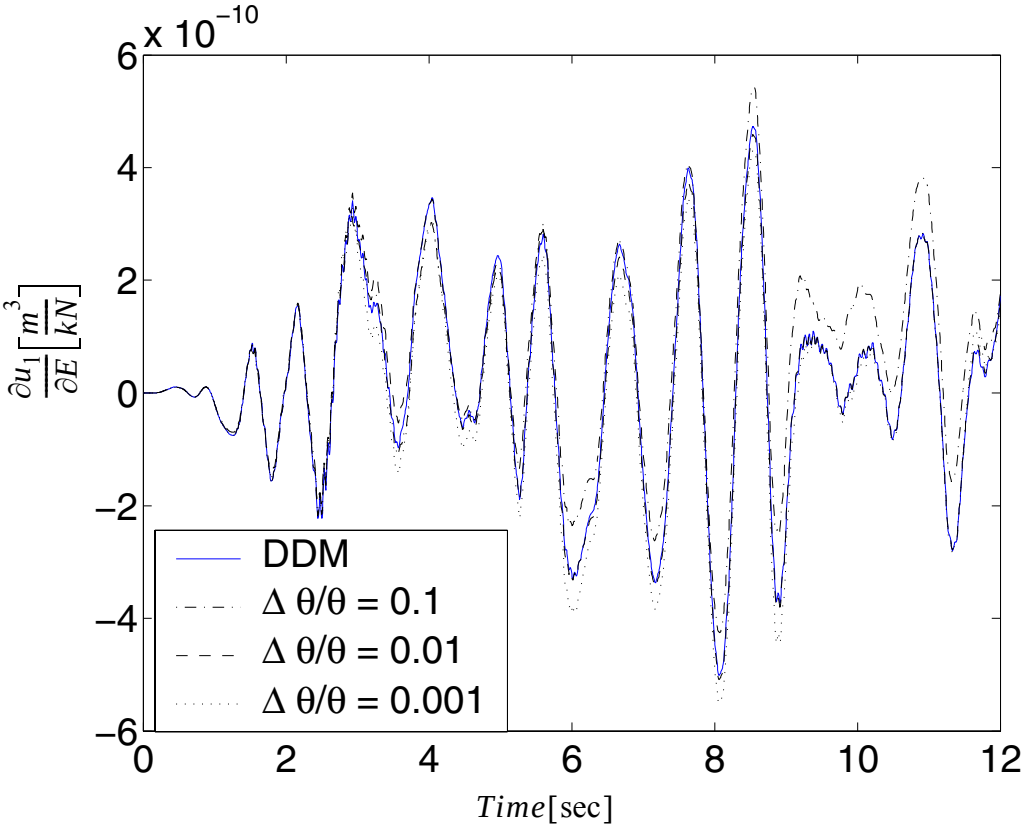


**Figure 4.68 Sensitivity of response $u_1$ with respect to steel elastic moduli E**

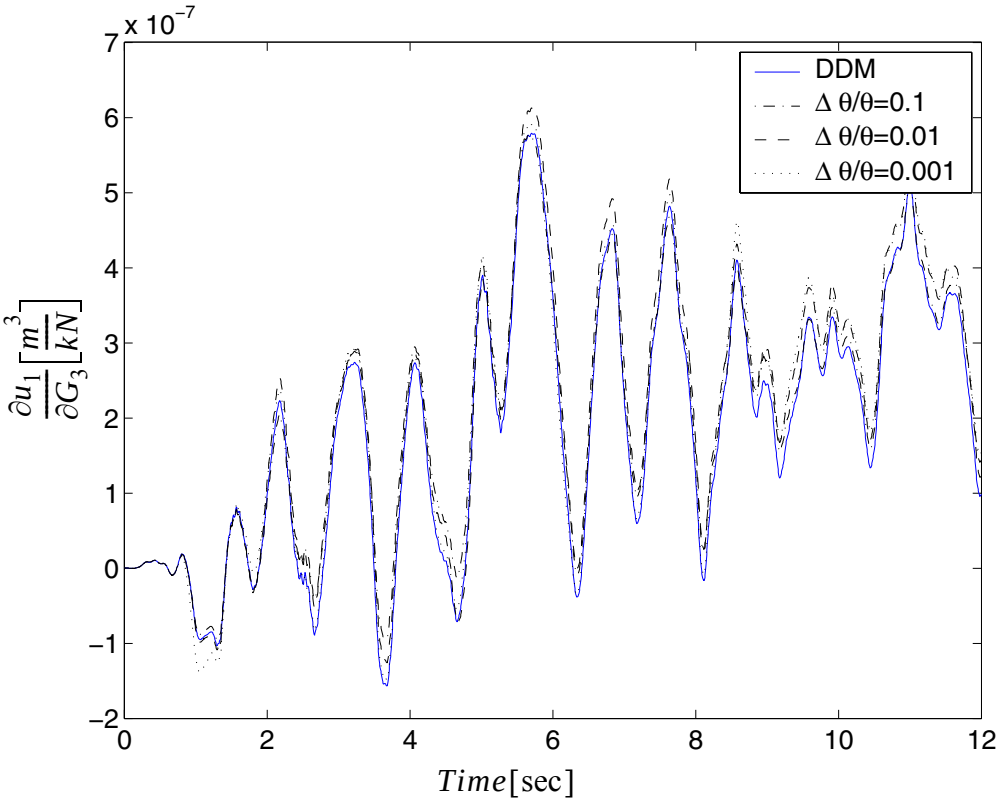


**Figure 4.69 Sensitivity of response $u_1$ with respect to the third layer low strain shear modulus $G_3$**

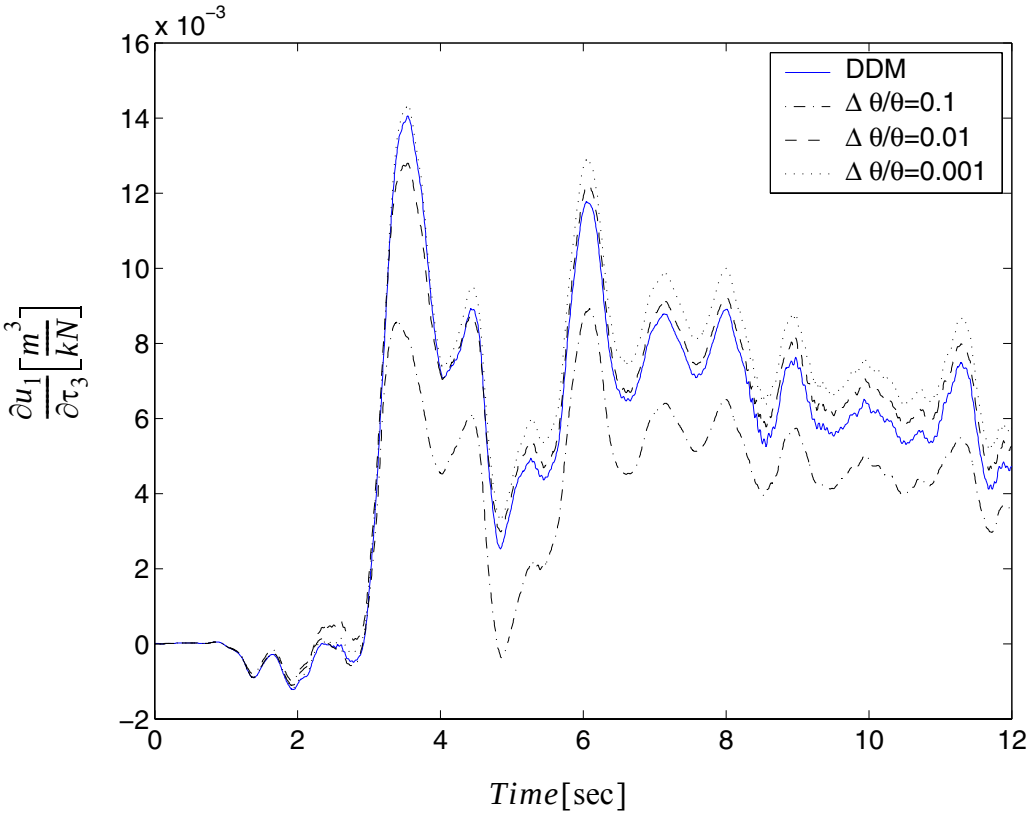


**Figure 4.70 Sensitivity of response $u_1$ with respect to the third layer maximum shear strength $\tau_3$**

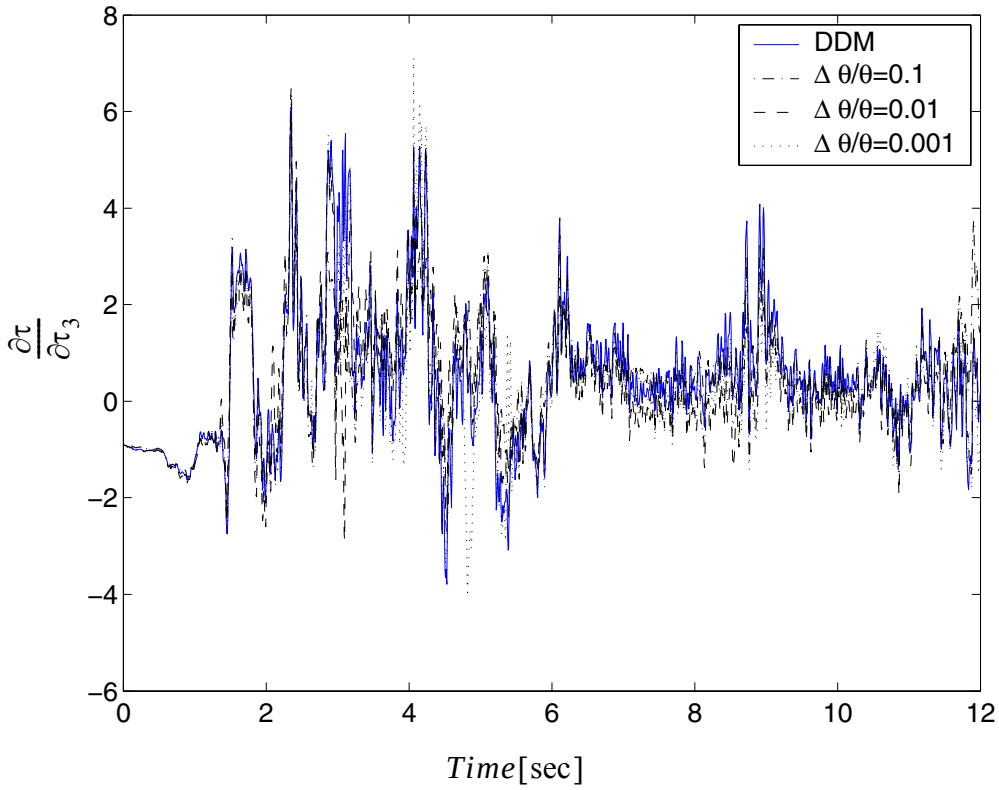


**Figure 4.71 Sensitivity of stress at point B with respect to the third layer maximum shear strength $\tau_3$**

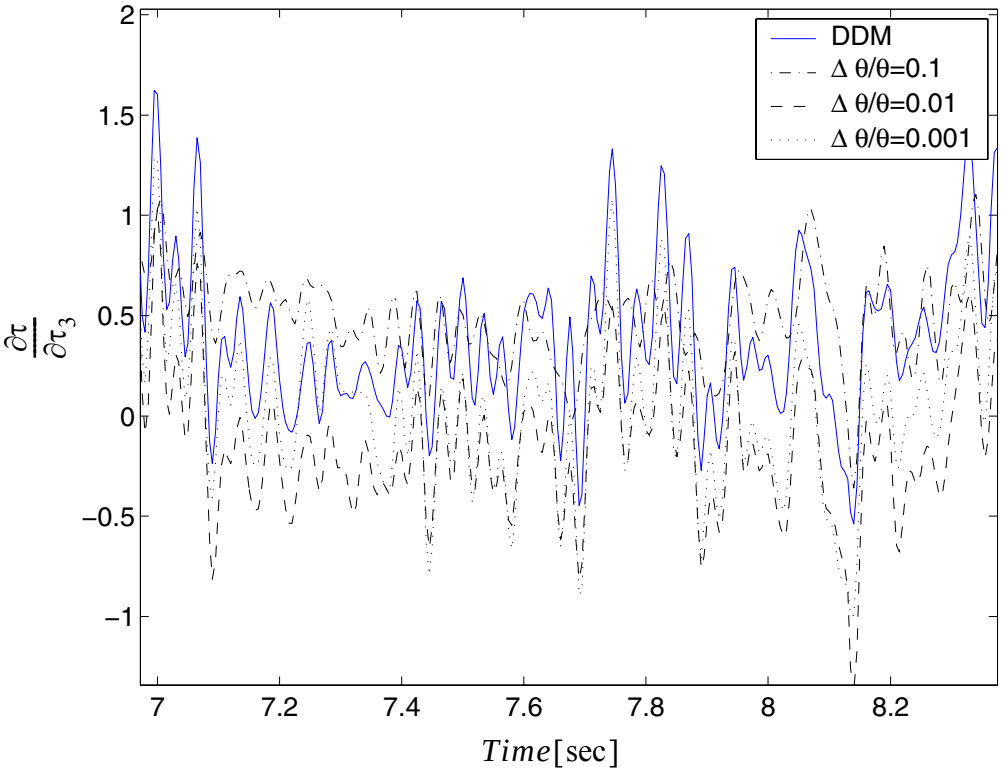


**Figure 4.72 Sensitivity of stress at point B with respect to the third layer maximum shear strength $\tau_3$ zoomed**

From these figures, it is observed that, the FFD results approach to DDM results with reduced perturbation $\frac{\Delta\theta}{\theta}$ in an acceptable range. There is alway a best perturbation $\frac{\Delta\theta}{\theta}$ that makes the FFD results closest to DDM results.

The sensitivity results are normalized to compare the relative importance in determining the response of the first floor drift (except the $f_{cu}$ of the cover concrete and $H_{iso}$ of steel since their nominal values are zero and can not be normalized by the values). The effect of the sensitive parameters in determining the first floor drift are shown in FIgures 4.73 to 4.76.

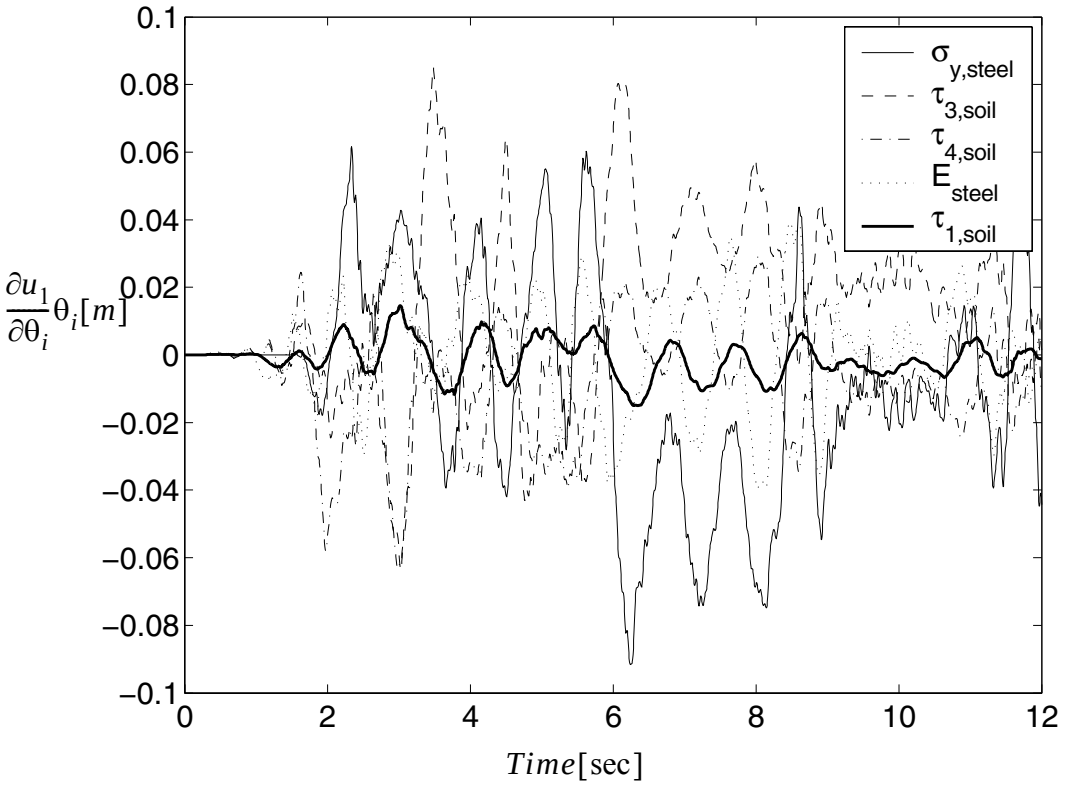


**Figure 4.73 Relative importance of θ's on the first floor drift**

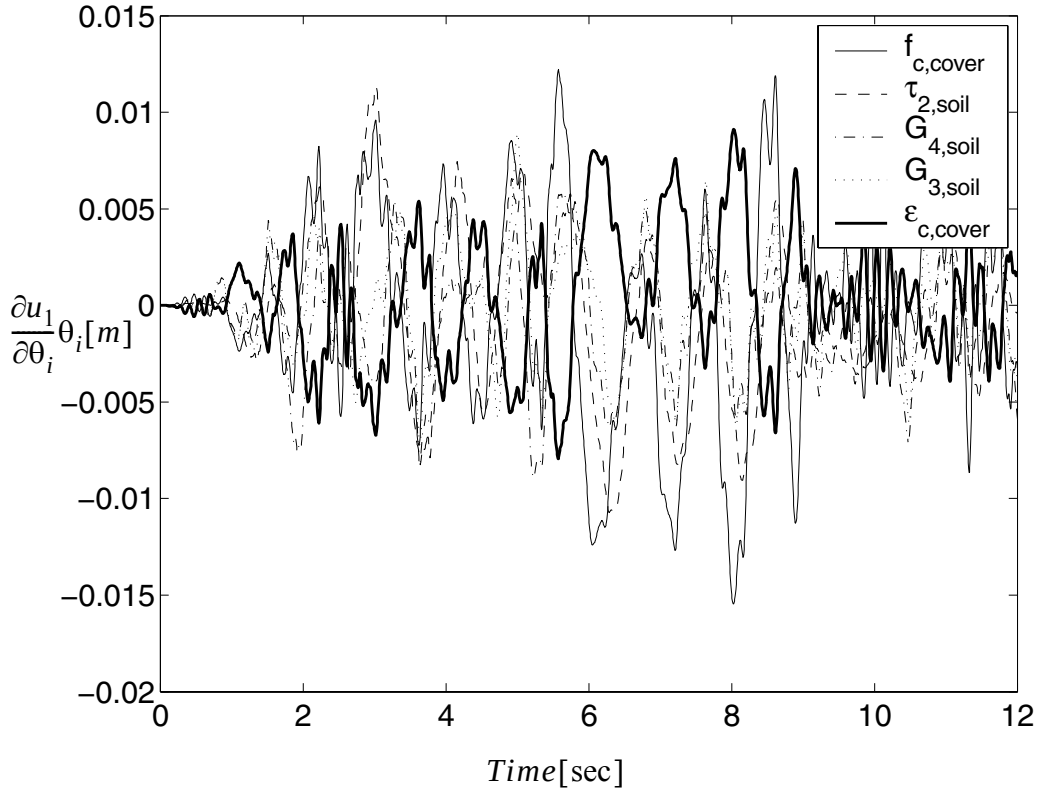


**Figure 4.74 Relative importance of θ's on the first floor drift**

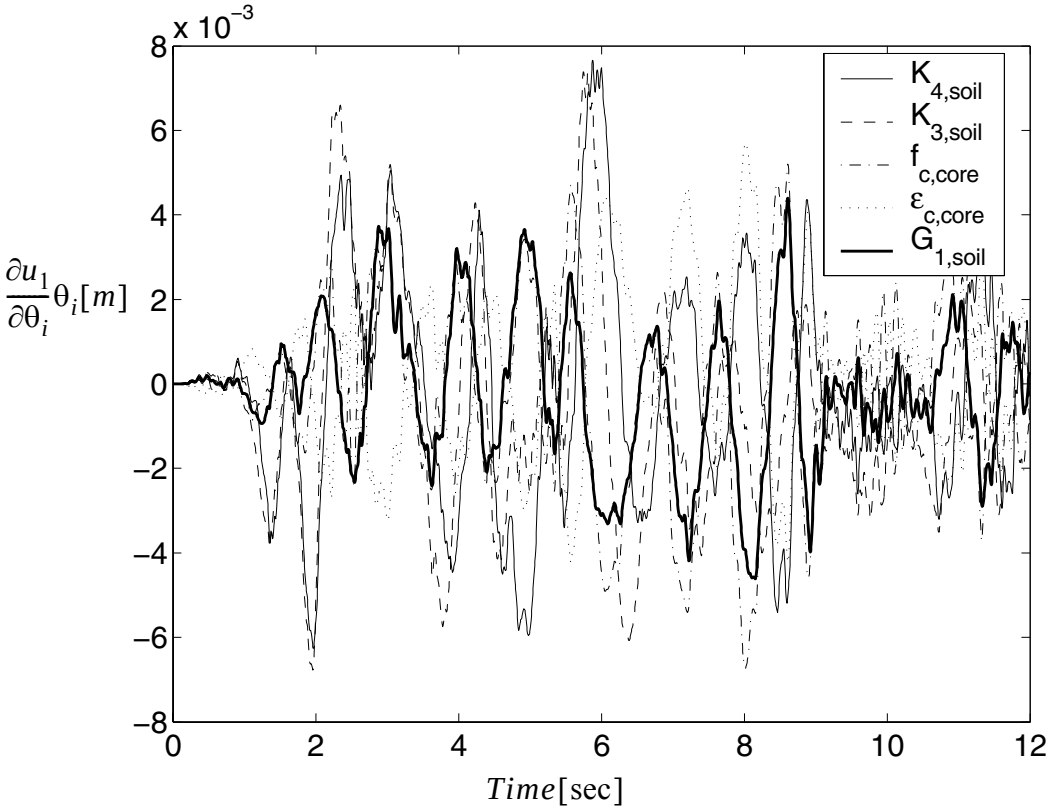


**Figure 4.75 Relative importance of θ's on the first floor drift**

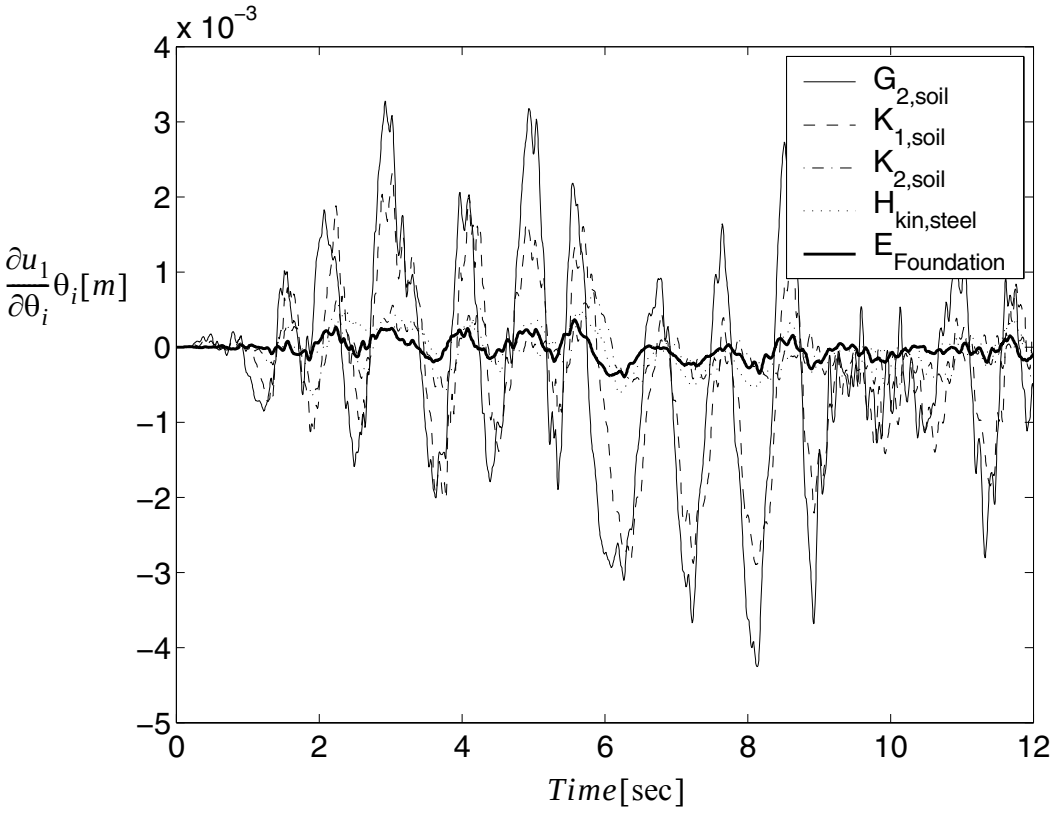


**Figure 4.76 Relative importance of θ's on the first floor drift**

From these results it is obvious that the relative importance of the material parameters in determining the first floor drift is:

$$\sigma_{y,\,steel} > \tau_{max,\,3} > \tau_{max,\,4} > E_{steel} > \tau_{max,\,1} > f_{c,\,cover} > \tau_{max,\,2} > G_4 > G_3 \approx \varepsilon_{c,\,cover}$$
$$> K_4 \approx K_3 > f_{c,\,core} > \varepsilon_{c,\,core} > G_1 > G_2 > K_1 > K_2 > H_{kin,\,steel} > E_{foundation} > \varepsilon_{cu,\,cover}$$

From these results, it is clear that the steel strength, elastic modulus, and the maximum shear strength of the soil are most important in determining the first floor drift; The cover concrete properties, and the low shear modulus of the third and fourth layer are second important; while the bulk modulus of the third and fourth layer, as well as the core con-

crete properties are third; the foundation concrete properties and bulk modulus of the first and second layers, as well as the post yielding properties $H_{kin}$, are last important. All other parameters are almost ignorable.

Comparing this case with static push over case, it is observed that the relative importance of most of the material parameters does not change, however the soil material parameters $\tau_{max,1}$, $\tau_{max,2}$, $\tau_{max,4}$, and $G_3$, $G_4$ increases, while that of $K_4$ decreases.

Similar study is also performed to a local variable shear stress at the Gauss point B (Figure 4.67). The most important variables in determining the shear stress is:

$$\tau_{max,4} > \tau_{max,3} > \sigma_{y,steel} > E_{steel} > K_4 > K_3 > \tau_{max,1} > f_{c,cover} > \tau_{max,2} > G_3 > G_4 > \varepsilon_{c,cover} > f_{c,core} > K_2 > \varepsilon_{c,core} > K_1 > G_2 > H_{kin} > E_{foundation}$$

Part of results are shown in Figures 4.77 to 4.80.

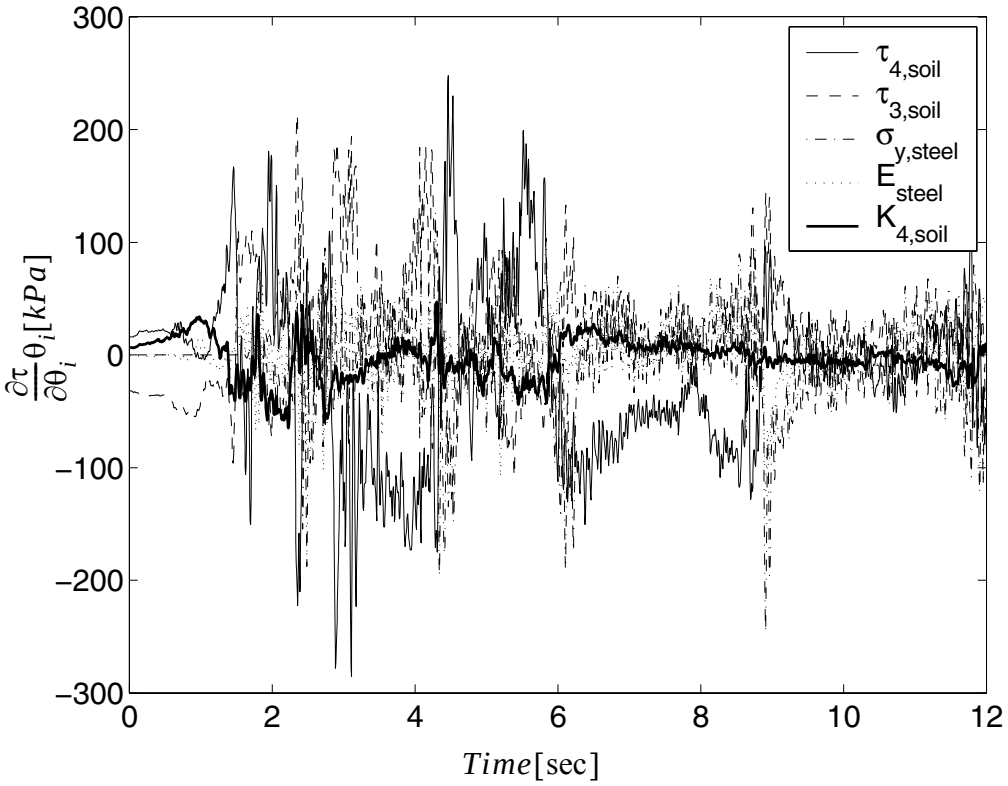


**Figure 4.77 Relative importance of θ's on the shear stress at Gauss point B (Figure 4.67)**

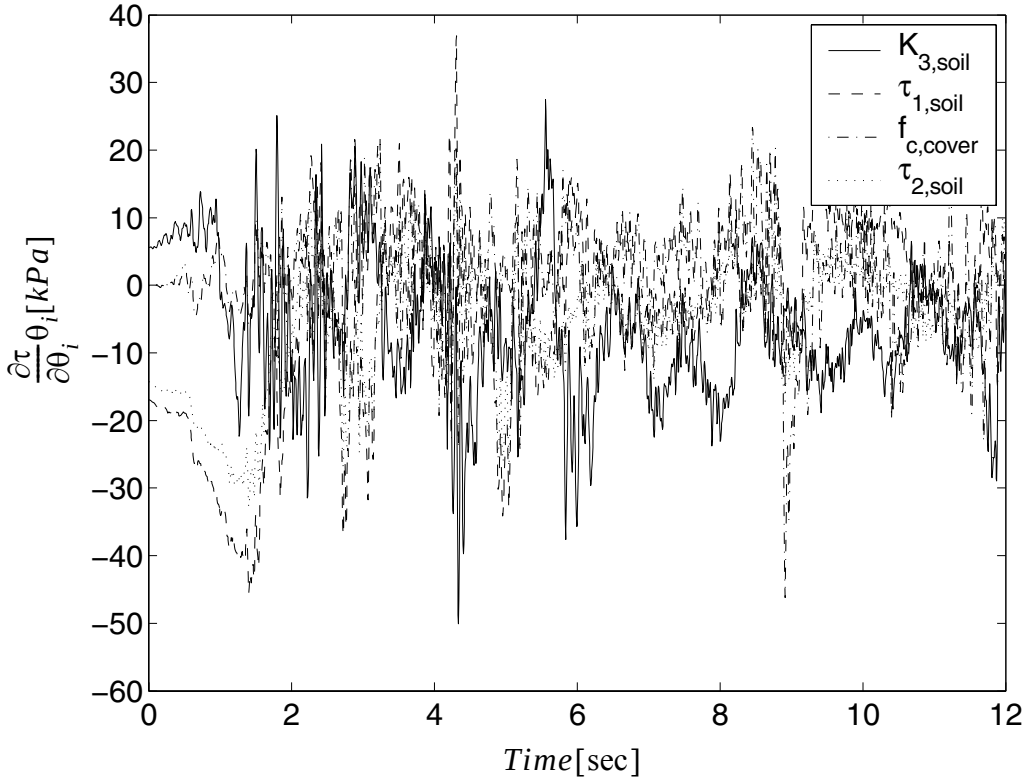


**Figure 4.78 Relative importance of θ's on the shear stress at Gauss point B (Figure 4.67)**

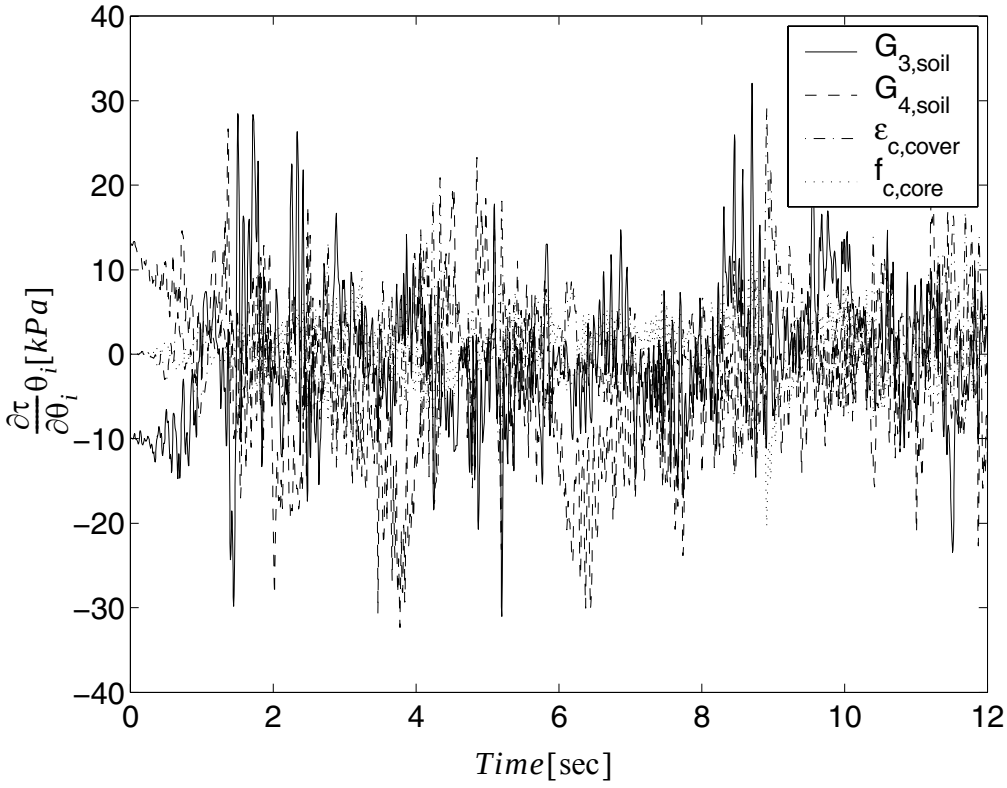


**Figure 4.79 Relative importance of θ's on the shear stress at Gauss point B (Figure 4.67)**

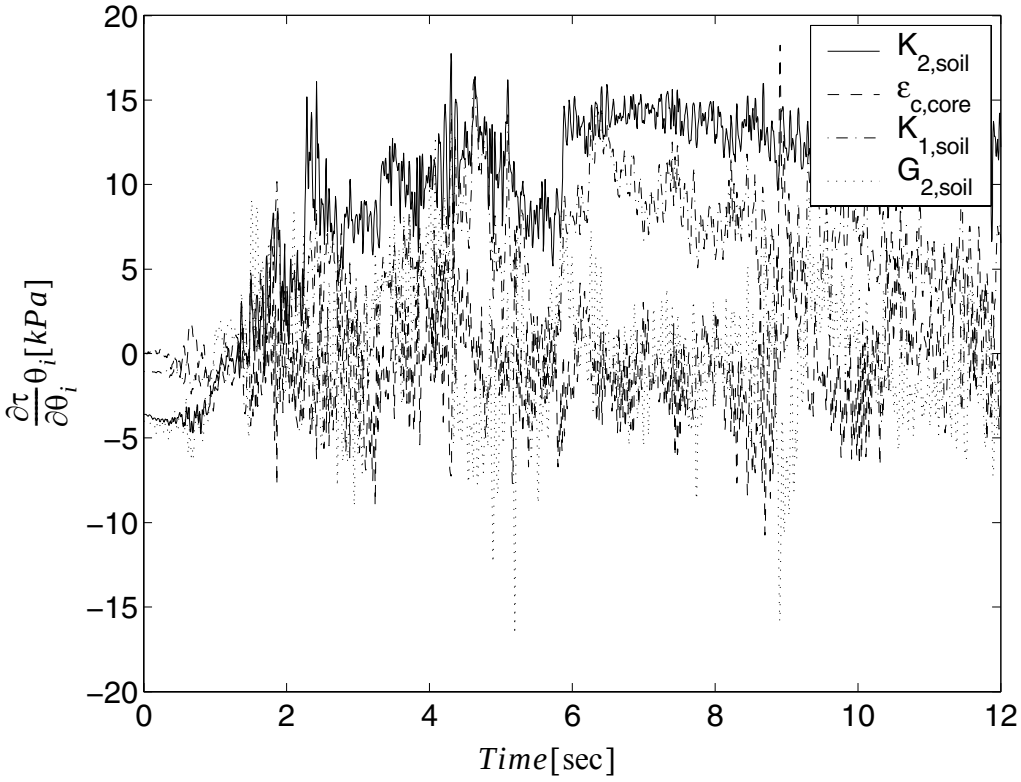


**Figure 4.80 Relative importance of θ's on the shear stress at Gauss point B (Figure 4.67)**

From these results, it is observed that the most important material parameters in determining the shear stress at point B are almost same as that in determining of the first floor drift, while the sequence of importance are not necessary same. For example, the bulk modulus of the third layer soil is important in determining the shear stress at point B, but is not sensitive in determining the first floor drift.

### 4.6.2 3D Pile Soil System

In this section a soil pile system subjected to a base excitation is studied as shown in Figure 4.81. The reinforced concrete pile has a 30cm diameter circular cross section. The pile is modeled using 3D displacement-based Euler-Bernoulli frame elements with distributed plasticity, each with four Gauss integration points. Section stress resultants at the integration points are computed by discretizing the frame sections by layers. Soil layers are modeled through isoparametric four-node quadrilateral finite elements with bilinear displacement interpolation. The constitutive behavior of the steel reinforcement is modeled by using a one-dimensional $J_2$ plasticity model with both kinematic and isotropic linear hardening (Conte et al. 2003). The concrete is modeled by using a Kent-Scott-Park model with zero tension stiffening (Scott et al 1982). Different material parameters are used for confined (core) and unconfined (cover) concrete in the columns.

The soil is modeled by using a pressure-independent multi-yield surface $J_2$ plasticity material model (Elgamal et al. 2003), specialized for plane strain analysis (Figure 4.81). Different material parameters are used for each of the five layers considered.

In order to model the behavior of the pile, the cross sectional area is taken into consideration by using a number of stiff beam elements to radially link the central node of the pile to corresponding soil nodes at the periphery of the pile as shown in the Figure 4.81. The material parameters are shown in the Table 4.24. The material parameters are taken to be random variables.

The base excitation in the horizontal direction is taken from the record of the El Centro 1940 (N) quake, amplified by 2. The time step is 0.01 seconds, while in the divergence

case, the time step is automatically adjusted from 0.001 to 0.01 seconds. The upper structure is modeled as a 10 ton lumped mass 1 meter above the ground.

**Table 4.24 Material parameters**

| | Concrete | | Steel | | Soil | | | |
|---|---|---|---|---|---|---|---|---|
| Mat | Core | Cover | Mat | | Mat | G | $\tau_{max}$ | K |
| $f_c$ | 3.4e4 | 2.8e4 | E | 2.10E8 | #1 | 54450 | 33 | 1.6e5 |
| $f_{cu}$ | 2.4e4 | 0 | s | 2.48e5 | #2 | 33800 | 26 | 1.0e5 |
| $\varepsilon_c$ | 0.005 | 0.002 | b | 0.02 | #3 | 61250 | 35 | 1.8e5 |
| $e_{cu}$ | 0.02 | 0.006 | | 0.0 | #4 | 96800 | 44 | 2.9e5 |
| | | | | | #5 | 180000 | 60 | 5.4e5 |

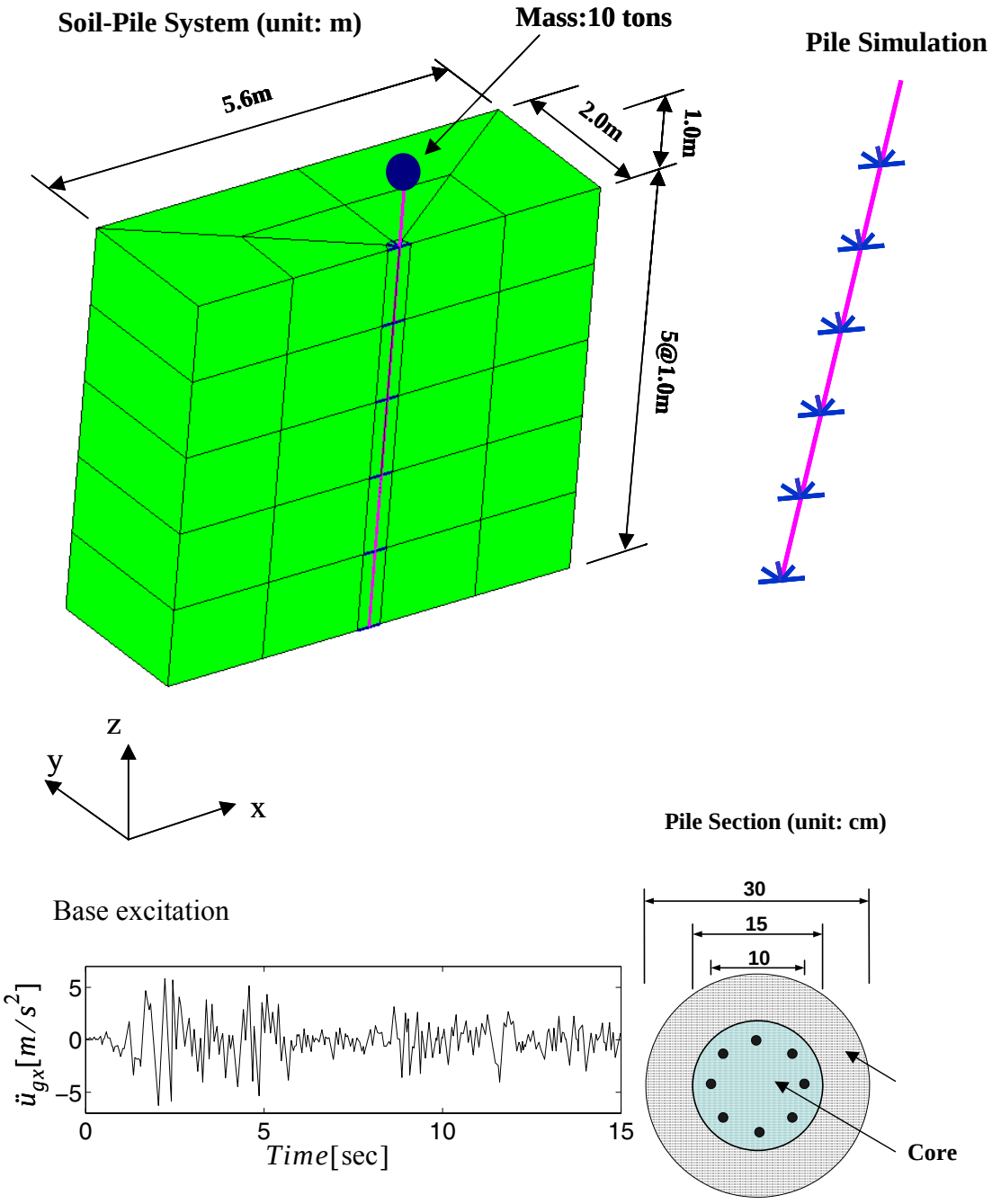


**Figure 4.81 Example of 3D pile soil system**

The response of the mass and the different soil layers are shown in Figure 4.82 below. Local moment curvature relations at point A and shear stress-strain relations at point B are shown in Figure 4.83. It is clear that the system yielded significantly under the base excitation.

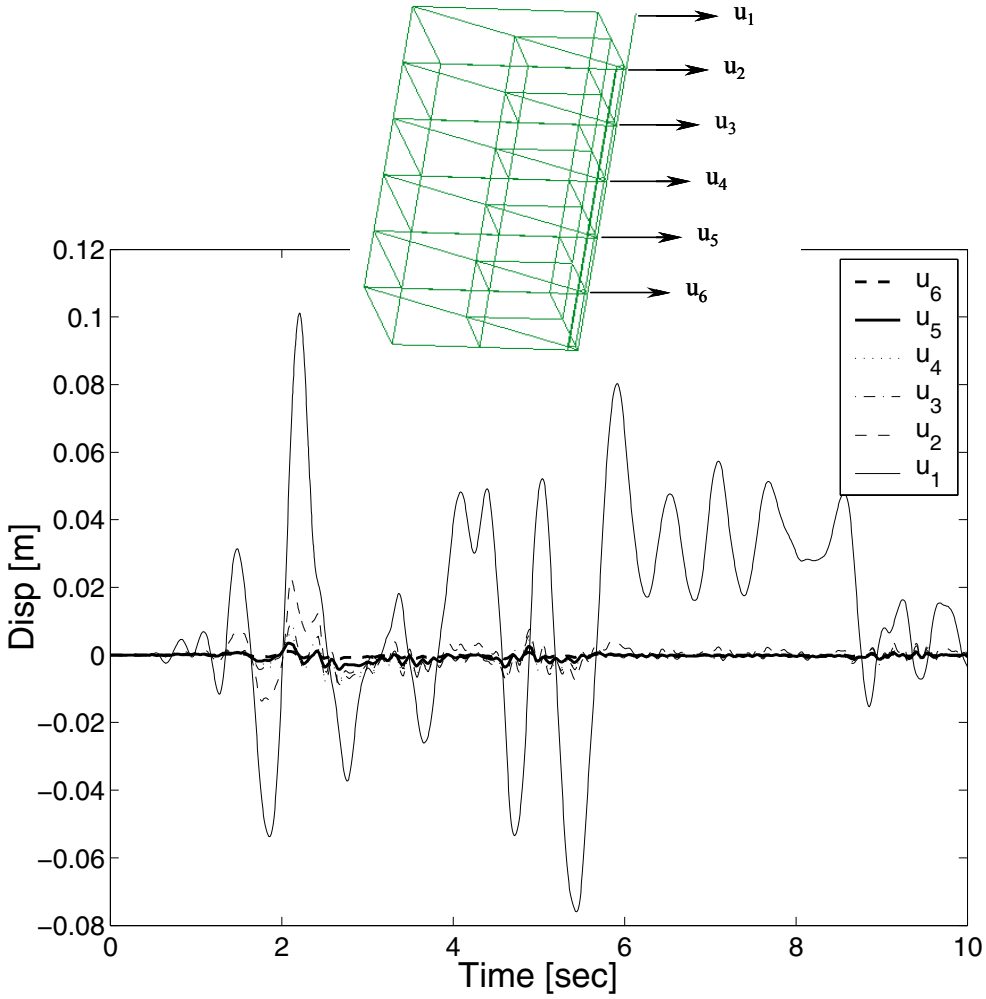


**Figure 4.82 Response of the 3D pile soil system**

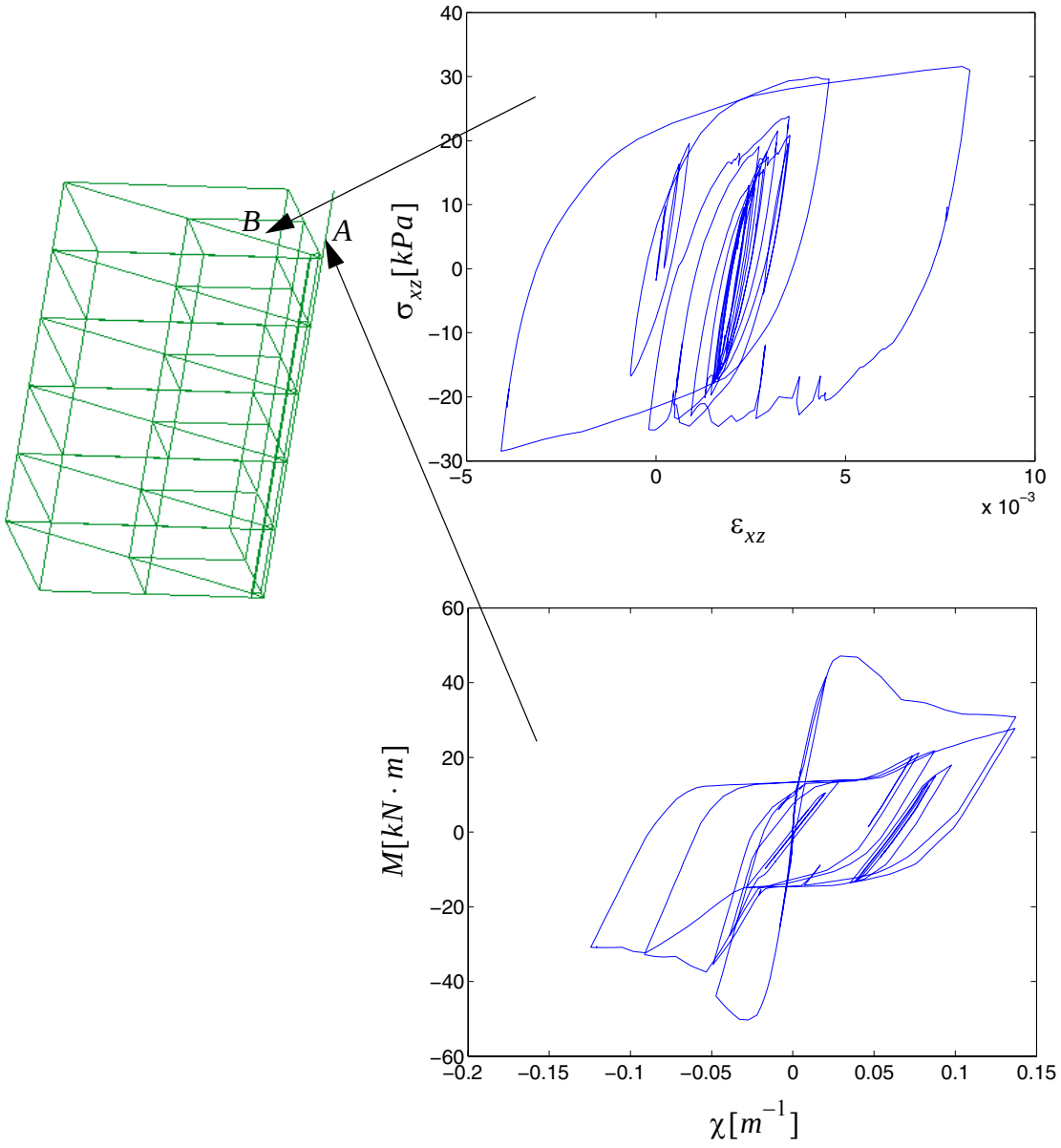


**Figure 4.83 Local responses**

Response sensitivity analysis is performed. The sensitivity obtained by DDM is verified by FFD as shown in Figures 4.84 and 4.85.

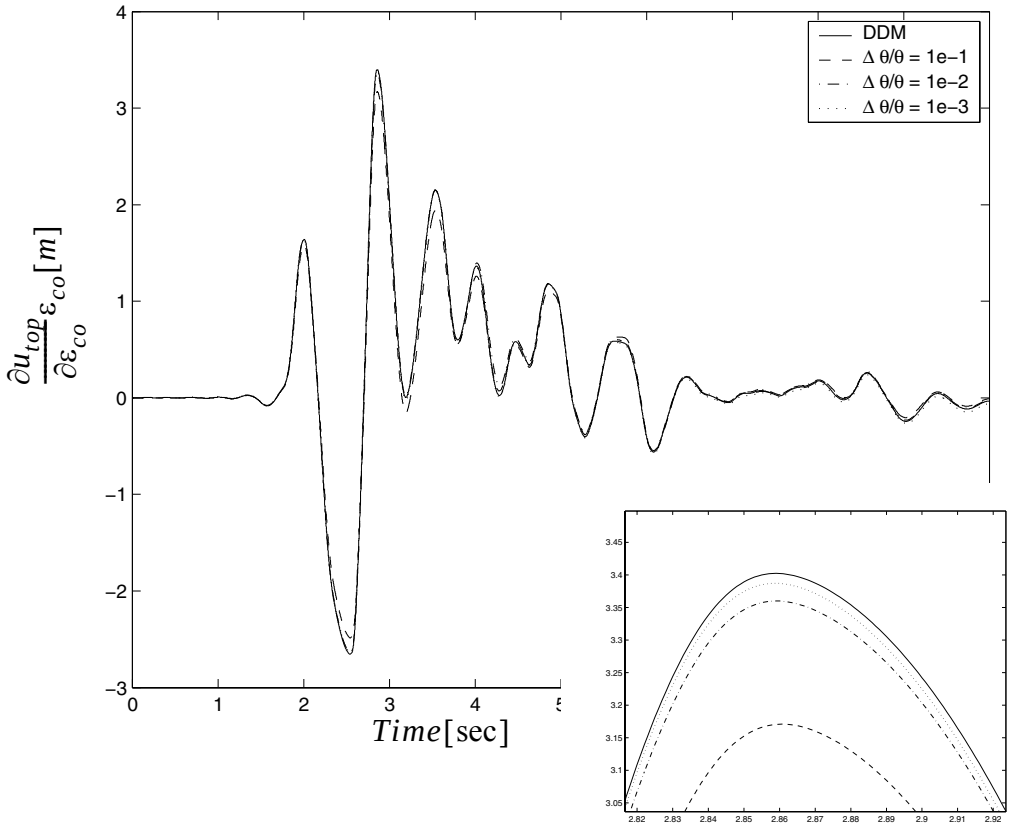


**Figure 4.84 Sensitivity of nodal displacement at top of beam with respect to core concrete $\varepsilon_{co}$**

The FFD results approach the DDM results as the perturbation is reduced. This shows that the DDM results are correct.

The normalized sensitivity results are analyzed and the relative importance of the material parameters are as follows

$$f_{c,\,cover} > \varepsilon_{cu,\,cover} > \sigma_{y,\,steel} > E_{steel} > \varepsilon_{c,\,cover} > \tau_{max,\,1} > G_1 > G_2 > \tau_{max,\,2}$$
$$G_3 > G_4 > f_{c,\,core} > G_5 > \varepsilon_{c,\,core} > \tau_{max,\,4} > \tau_{max,\,3} > b > \tau_{max,\,5} > f_{cu,\,core} > \varepsilon_{cu,\,core}$$

Part of the results are shown in Figures 4.85 to 4.88.

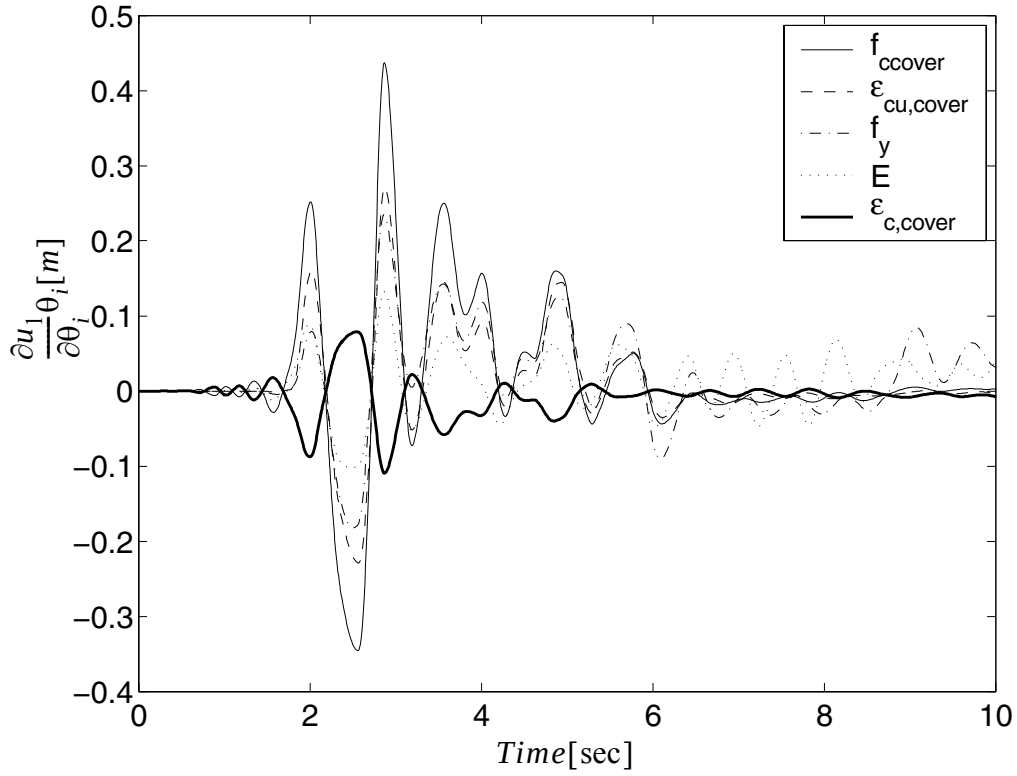


**Figure 4.85 Relative importance of θ's to the first floor drift**

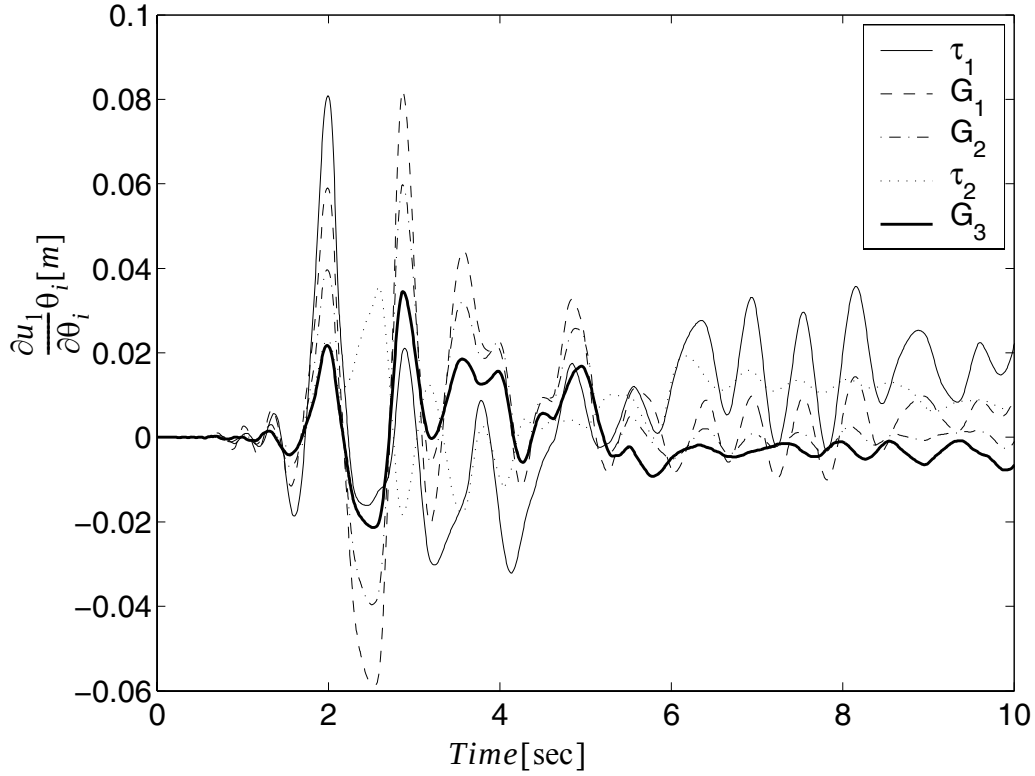


**Figure 4.86 Relative importance of θ's on the first floor drift**

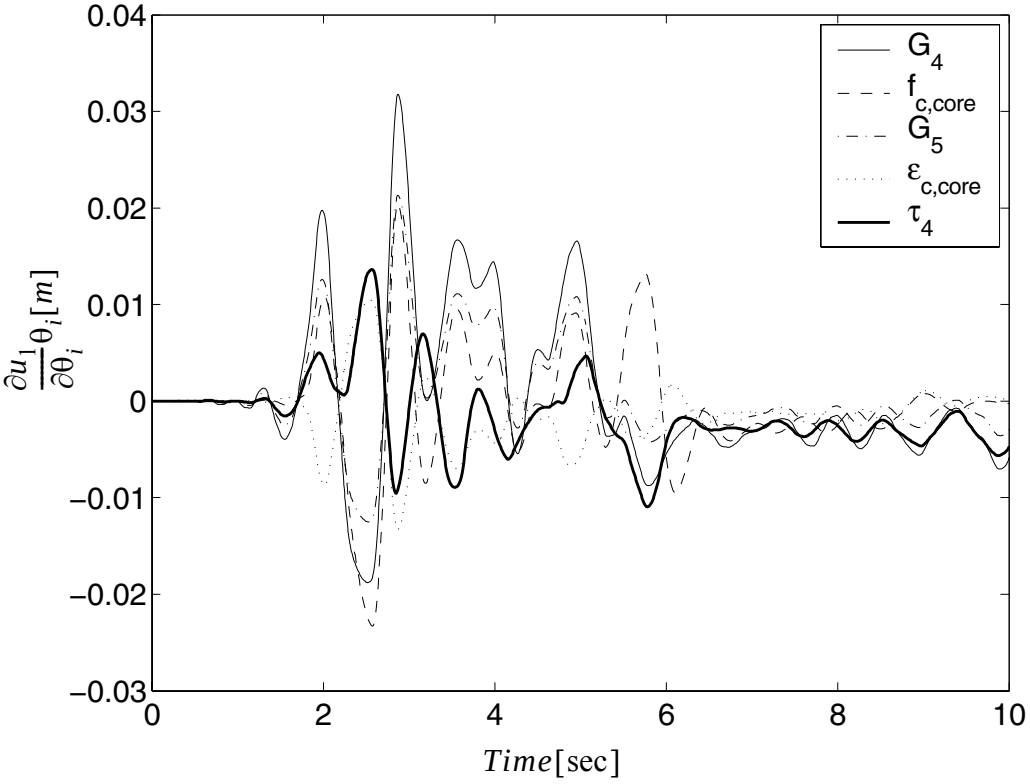


**Figure 4.87 Relative importance of θ's on the first floor drift**

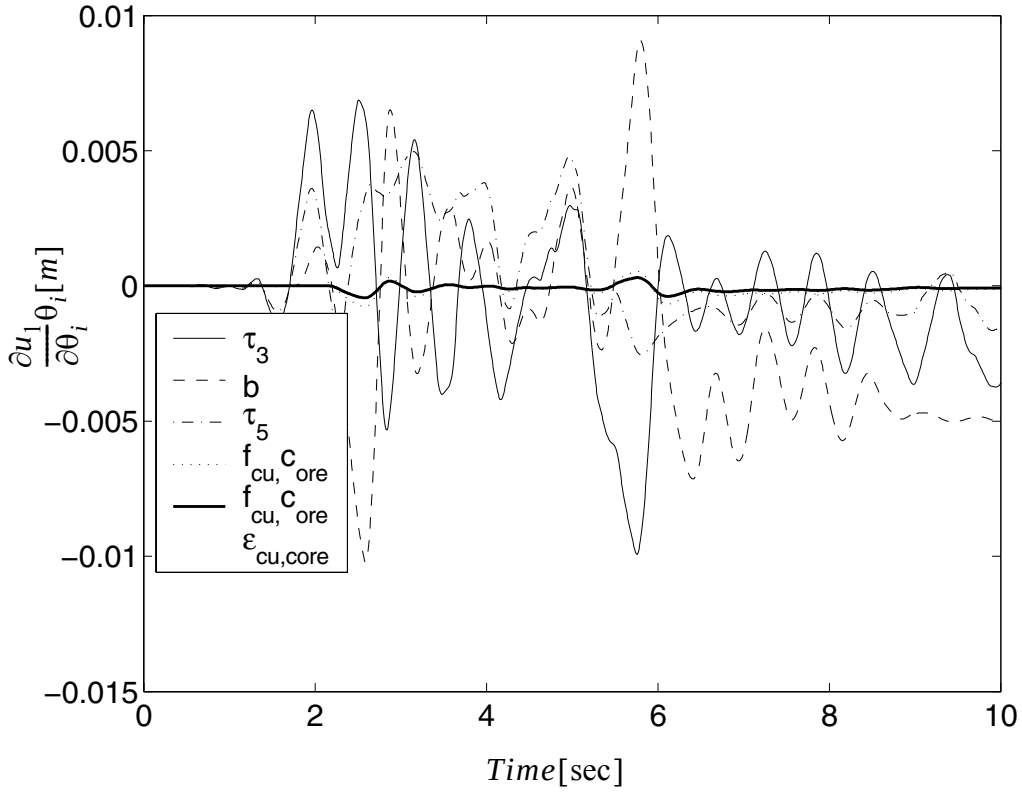


**Figure 4.88 Relative importance of θ's on the first floor drift**

From these results, it is clear that the cover concrete material parameters, as well as yield strength $\sigma_Y$ and elastic modulus of the steel E are most important. The first (top) soil layer properties are more important than that of the lower layers.

### 4.6.3 3D SFSI System

In this section a soil-structure system subjected to a base excitation is studied. The application example considered herein consists of a three-dimensional reinforced concrete (RC) frame with concrete slabs at each floor as shown in Figure 4.89. The frame consists of three stories of height h = 3.66m (12ft) each and one bay of span L = 6.10m (20ft) in each direction. Beam and column cross-sections are shown in Figure 4.90.

Beams and columns are modeled using displacement-based Euler-Bernoulli frame elements, each with four Gauss-Legendre integration points. Each column and beam is discretized into two and three finite elements, respectively. Beam and column cross-sections are discretized into fibers of confined concrete, unconfined concrete and steel reinforcement. The reinforcement steel is modeled through a bilinear hysteretic model, while the concrete is represented by the Kent-Scott-Park model with zero tension stiffening (Scott et al., 1982), as shown in Figure 4.90. Different material parameters are used for the confined (core) and unconfined (cover) concrete in the columns and beams. The concrete slabs are modeled through a diaphragm constraint at each floor to enforce rigid in-plane behavior.

In the foundation, the 4m RC piles are modeled in the same manner as the columns in the upper structure. The same beam\column elements, fiber sections, and material properties are used for both the piles and the columns. The soil is modeled using the multi-yield surface $J_2$ plasticity model (Elgamal et al. 2003) with four layers at different depths.

The connection of the soil and piles is achieved by tying the three translational dof of corresponding nodes of the piles (6DOF) and the nodes of the soil (3DOF) at the same

locations. A simple shear condition in the soil is modeled by tying the corresponding horizontal dof of the boundary nodes at same depth together in the x or y directions.

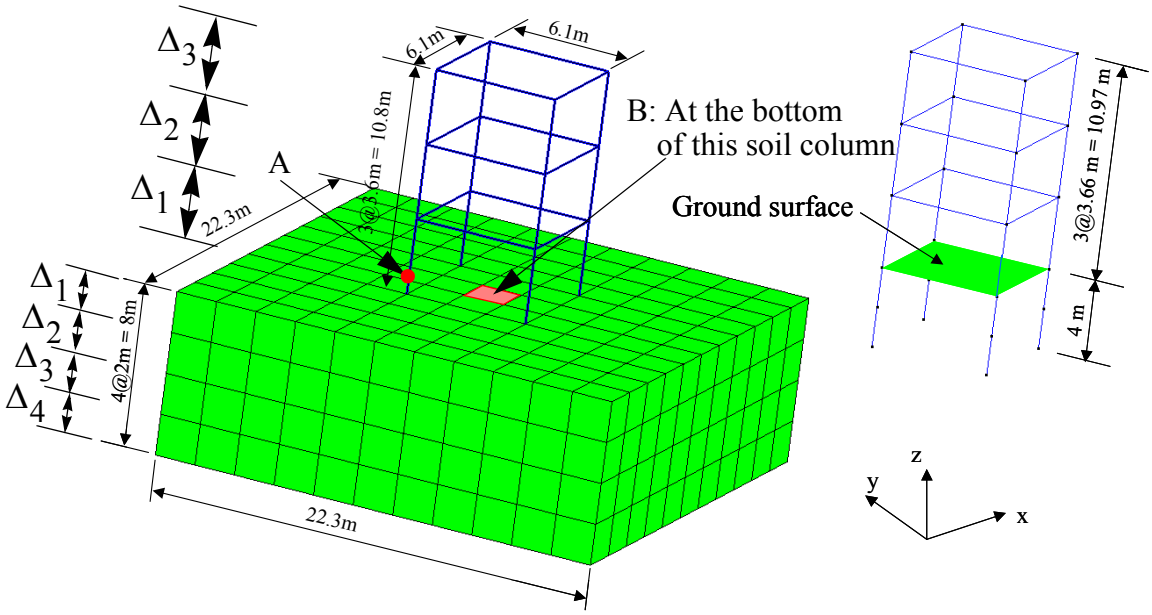


**Figure 4.89 Example of 3D SFSI system**

Twenty three random variables are studied, taken from the material parameters of the soil, foundation and frame. Their relative importance are shown later.

The parameters used to model the frame and soil materials are listed in Table 4.25.

**Table 4.25 Material parameters (unit:kPa)**

| | Frame and pile foundation | | | | Soil | | | |
|---|---|---|---|---|---|---|---|---|
| | Concrete | | Steel | | | | | |
| Mat | Core | Cover | Mat | | Mat | G | $\tau_{max}$ | K |
| $f_c$ | 34473.8 | 27579.04 | E | 2.1e8 | #1 | 54450 | 33. | 1.6e5 |
| $f_{cu}$ | 24131.66 | 0 | $s_Y$ | 248200 | #2 | 33800 | 26. | 1.0e5 |
| $\varepsilon_c$ | 0.005 | 0.002 | b | 0.02 | #3 | 61250 | 35. | 1.8e5 |
| $e_{cu}$ | 0.02 | 0.006 | | | #4 | 96800 | 44. | 2.9e5 |

The poission ration is computed by $\nu = \frac{3K-2G}{6K+2G}$. In this case it is about 0.35.

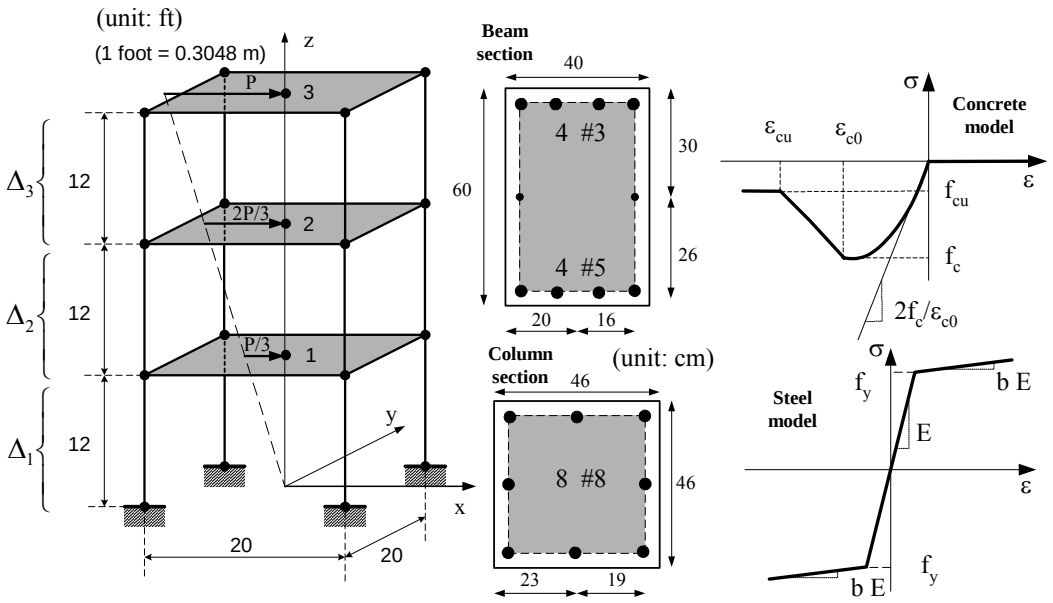


**Figure 4.90 Section properties of the column of 3D SFSI system**

After static application of the gravity loads, the structure is subjected to a bi-directional base excitation taken from the earthquake recorder of Tabas 1978 in both the normal and fault directions as shown in Figure 4.91. The maximum accelerations in both directions are approximately 1 g (9.81 m/s$^2$).

.

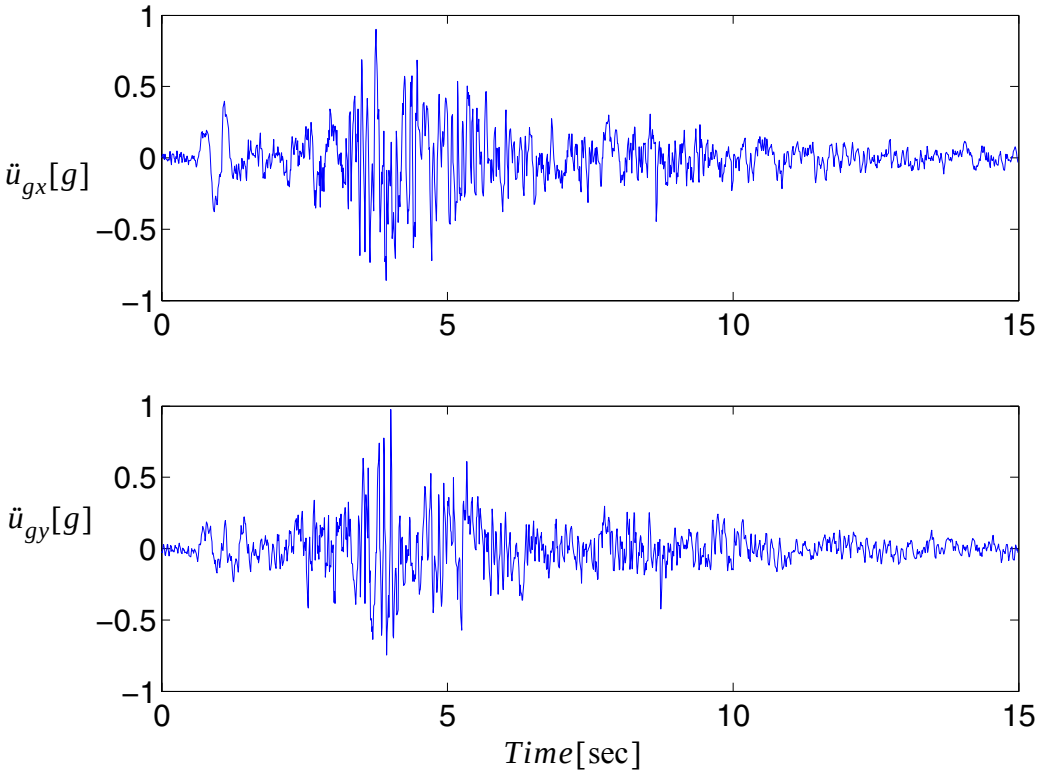


**Figure 4.91 Base excitation taken as the earthquake record of Tabas 1978**

A response analysis and response sensitivity analysis based on DDM is performed. An integration time step of 0.01 sec is used.

The response of the frame and different soil layers are shown in Figures 4.92 and 4.93 below. Local moment curvature relations at point A and shear stress-strain relations at point B are shown in Figure 4.94. It is clear that the system yields significantly under the base excitation loading case.

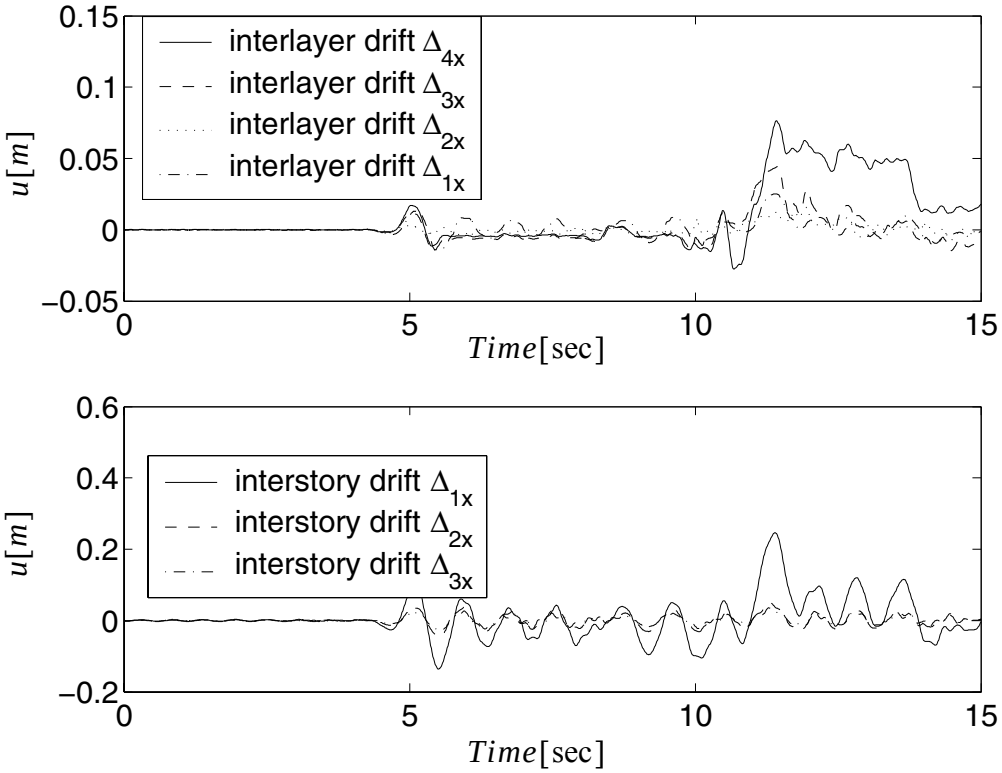


**Figure 4.92 Response in x direction of the 3D pile soil system (refer to Figure 4.89)**

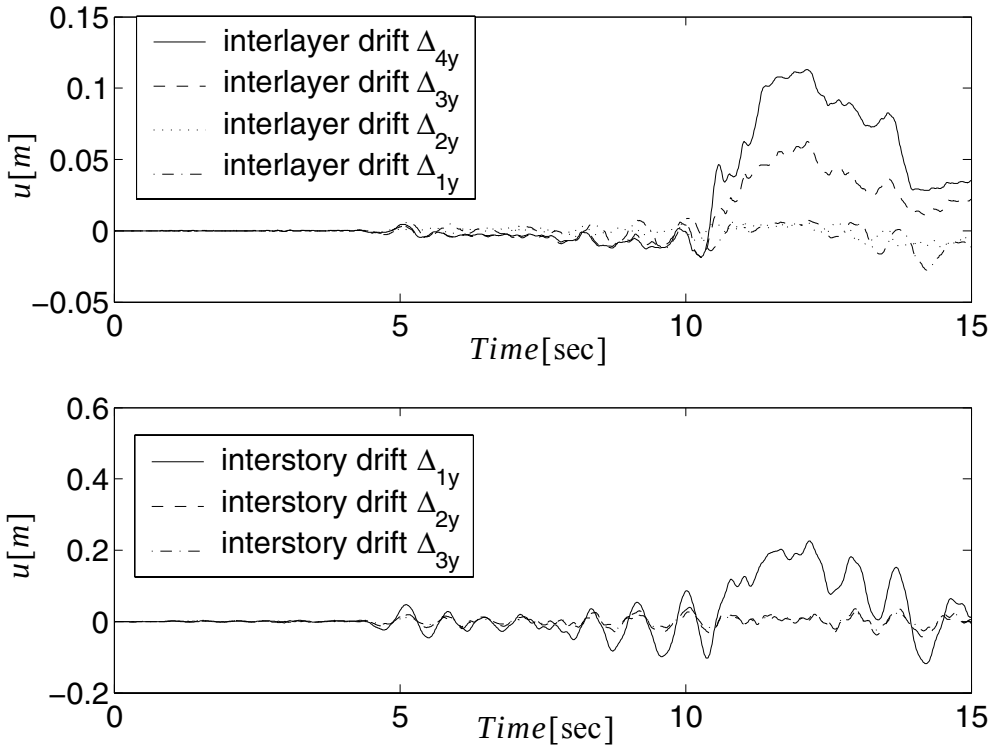


**Figure 4.93 Response in y direction of the 3D pile soil system (refer to Figure 4.89)**

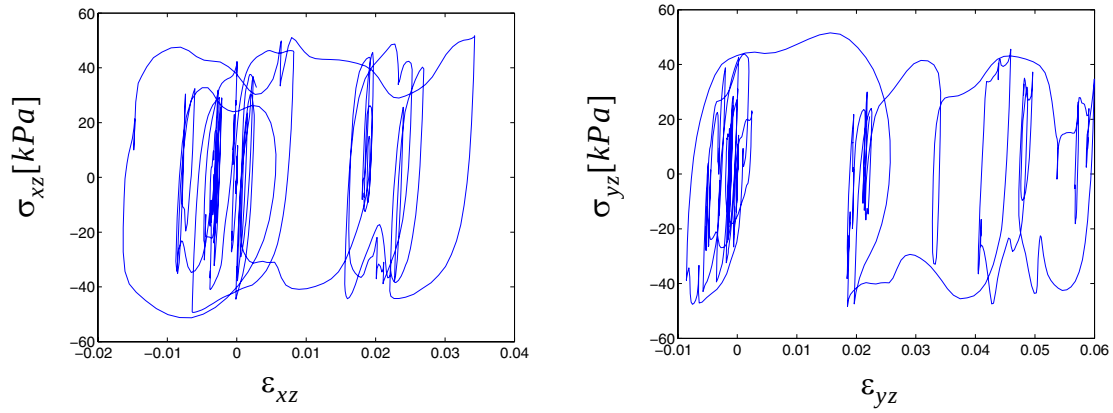


(a) local stress strain relation at point B

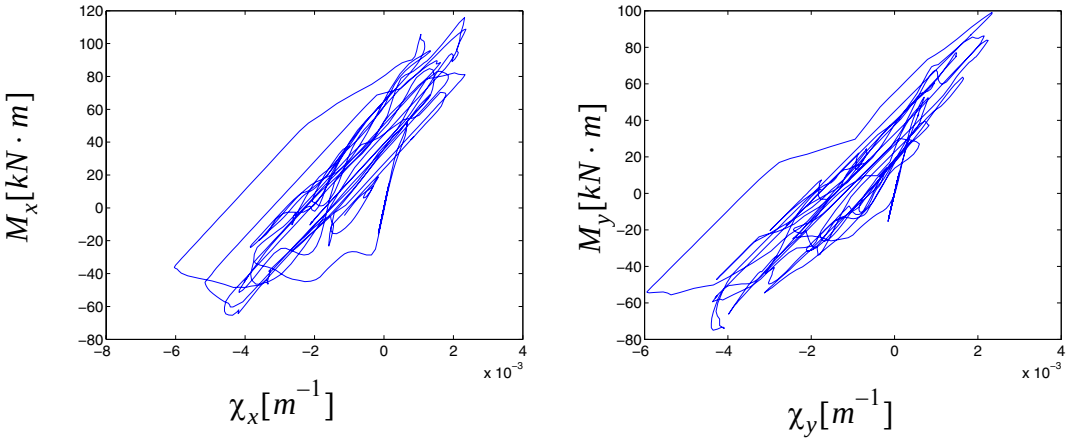


(b) local moment curvature relation at point A

**Figure 4.94 Local responses (refer to Figure 4.89 )**

Response sensitivity analysis is performed. Part of the sensitivity obtained by DDM is verified by FFD as shown in Figure 4.95.

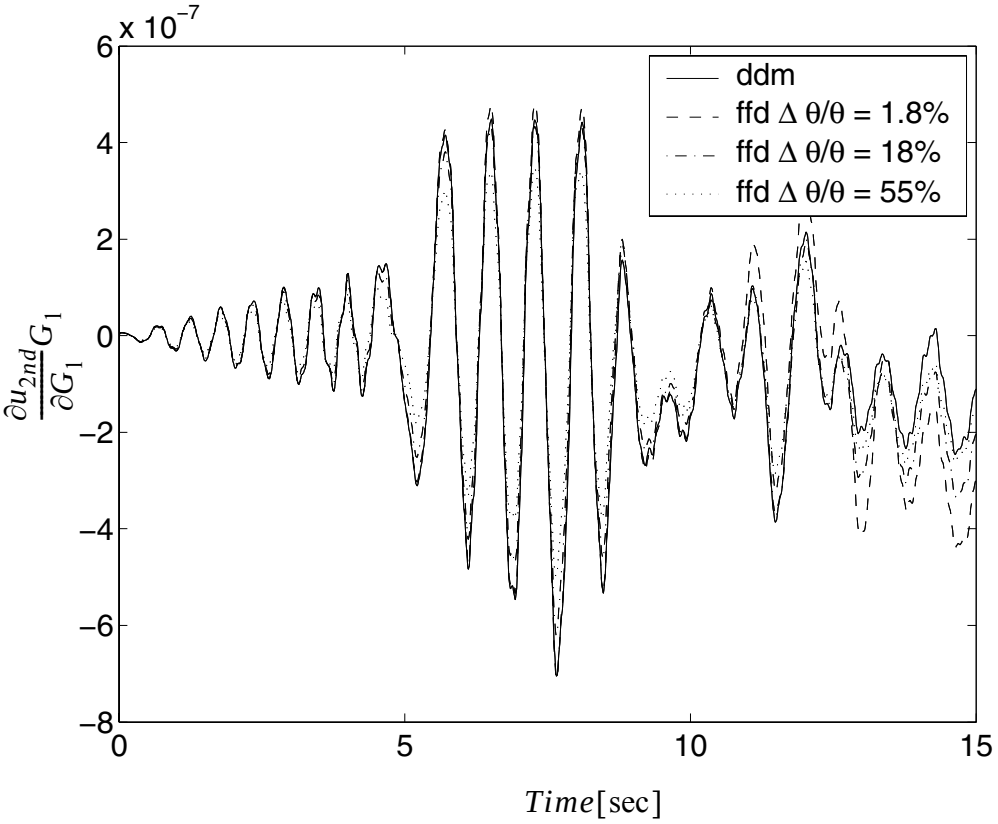


**Figure 4.95 Sensitivity of nodal displacement at the second floor with respect to the low strain shear modulus of the first layer soil $G_1$**

The FFD results approach the DDM results as the perturbation is increased. This is because the convergence criterion for the response is set very large (1.0e-3 [m]) such that too small a perturbation will cause the FFD to be inaccurate due to computational round off error.

The normalized sensitivity results are analyzed and the relative importance of the material parameters in determining the first floor drift in x direction are:

$$\tau_{max,\,4} > E_{steel} > \tau_{max,\,3} > \sigma_{y,\,steel} > f_{c,\,cover} > f_{c,\,core} > G_2 > \tau_{max,\,1} > G_1 > E_{foundation,\,steel} > \sigma_{y,\,foundation,\,steel} > \varepsilon_{c,\,core} > \varepsilon_{c,\,cover} > G_3 > \tau_{max,\,2} > G_4 > \varepsilon_{cu,\,cover} > b_{steel} > f_{c,\,core,\,foundation} > \varepsilon_{c,\,core,\,foundation} > b_{foundation,\,steel} > f_{cu,\,core} > \varepsilon_{cu,\,core}$$

in y direction are:

$$\sigma_{y,\,steel} > \tau_{max,\,4} > E_{steel} > \tau_{max,\,3} > f_{c,\,core} > f_{c,\,cover} > \tau_{max,\,1} > \sigma_{y,\,foundation,\,steel} > G_2 > \tau_{max,\,2} > G_3 > E_{foundation,\,steel} > G_4 > \varepsilon_{cu,\,cover} > \varepsilon_{c,\,core} > G_1 > \varepsilon_{c,\,cover} > b_{steel} > f_{c,\,core,\,foundation} > \varepsilon_{c,\,core,\,foundation} > b_{foundation,\,steel} > f_{cu,\,core} > \varepsilon_{cu,\,core}$$

Part of the results are shown in Figures 4.96 to 4.105.

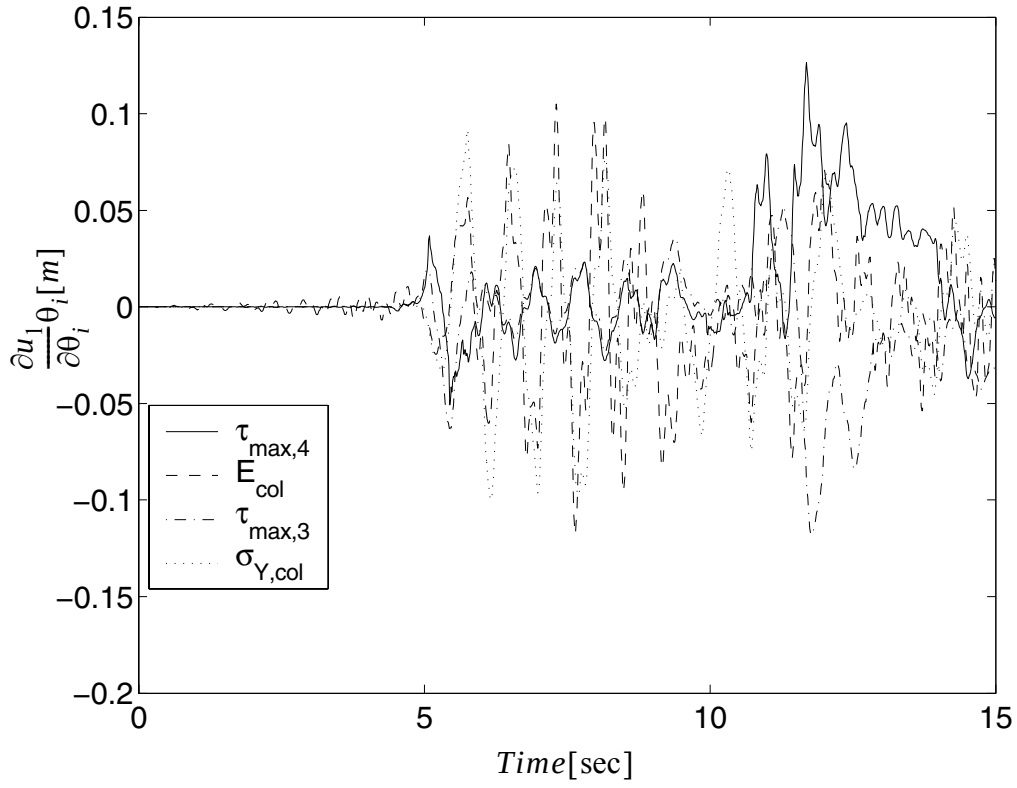


**Figure 4.96 Relative importance of θ's on the first floor drift in x direction**

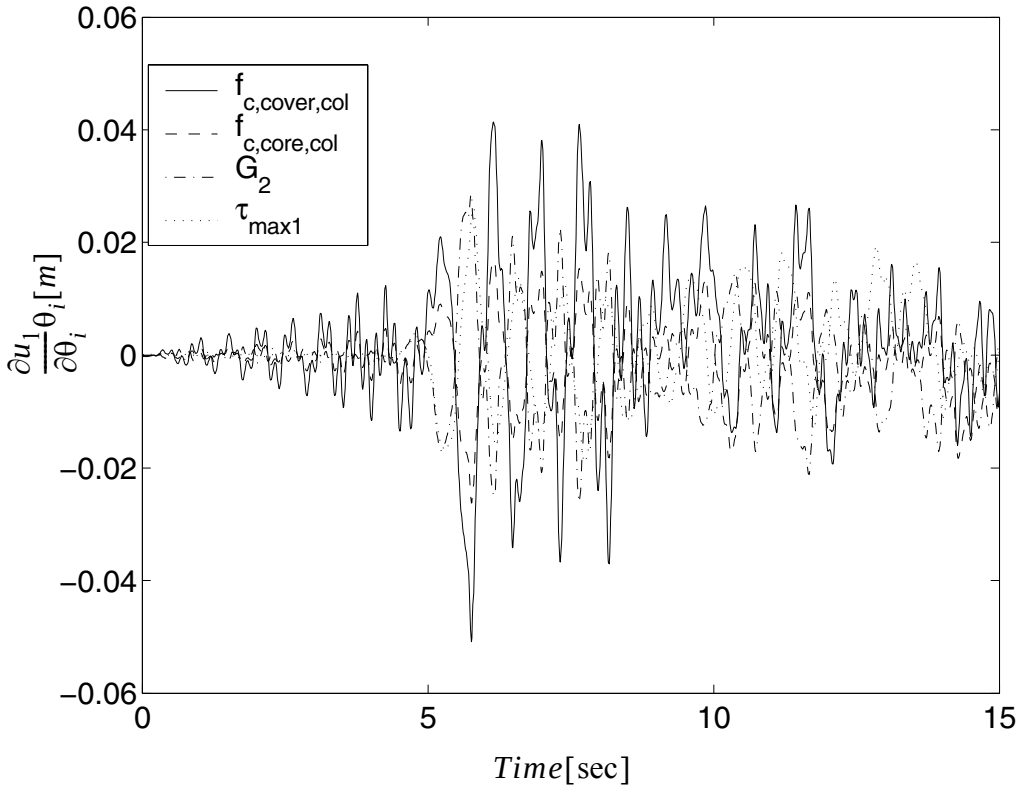


**Figure 4.97 Relative importance of θ's on the first floor drift in x direction**

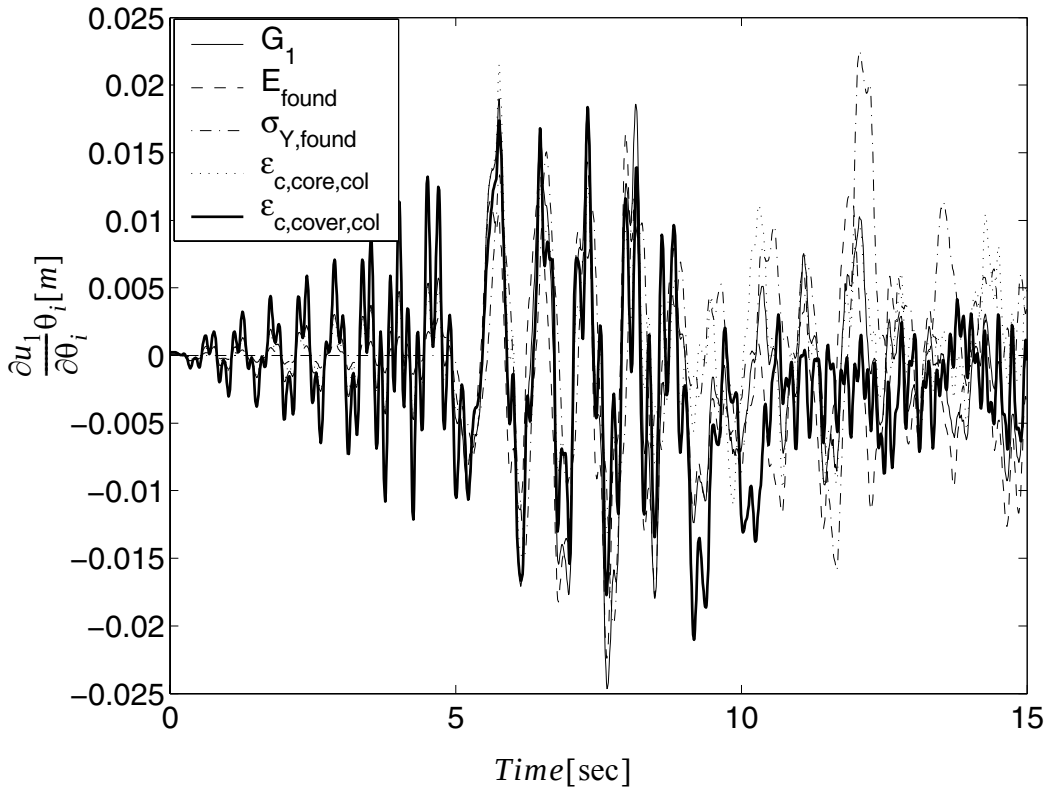


**Figure 4.98 Relative importance of θ's on the first floor drift in x direction**

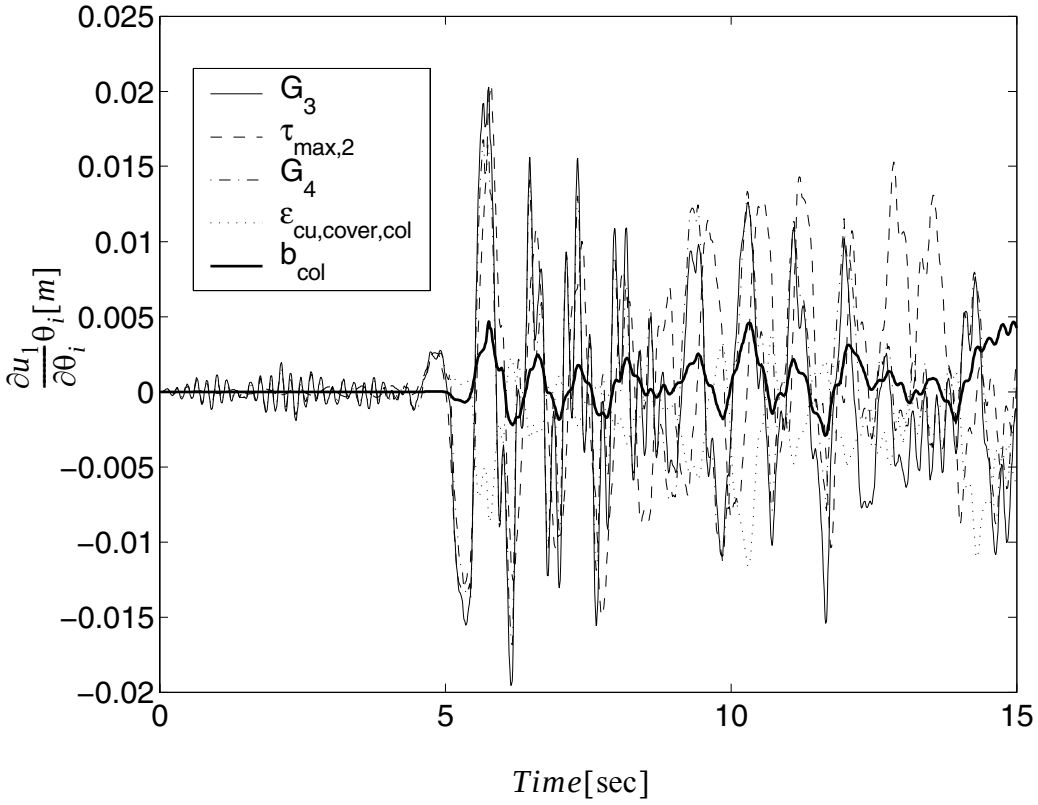


**Figure 4.99 Relative importance of θ's on the first floor drift in x direction**

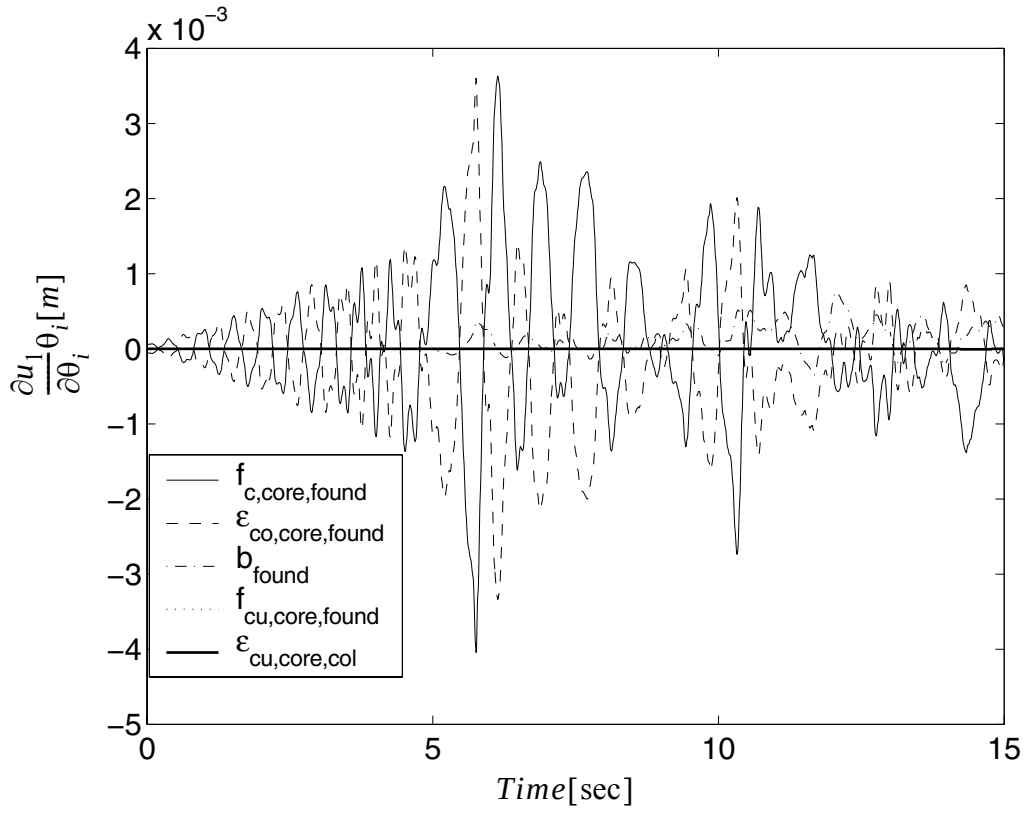


**Figure 4.100 Relative importance of θ's on the first floor drift in x direction**

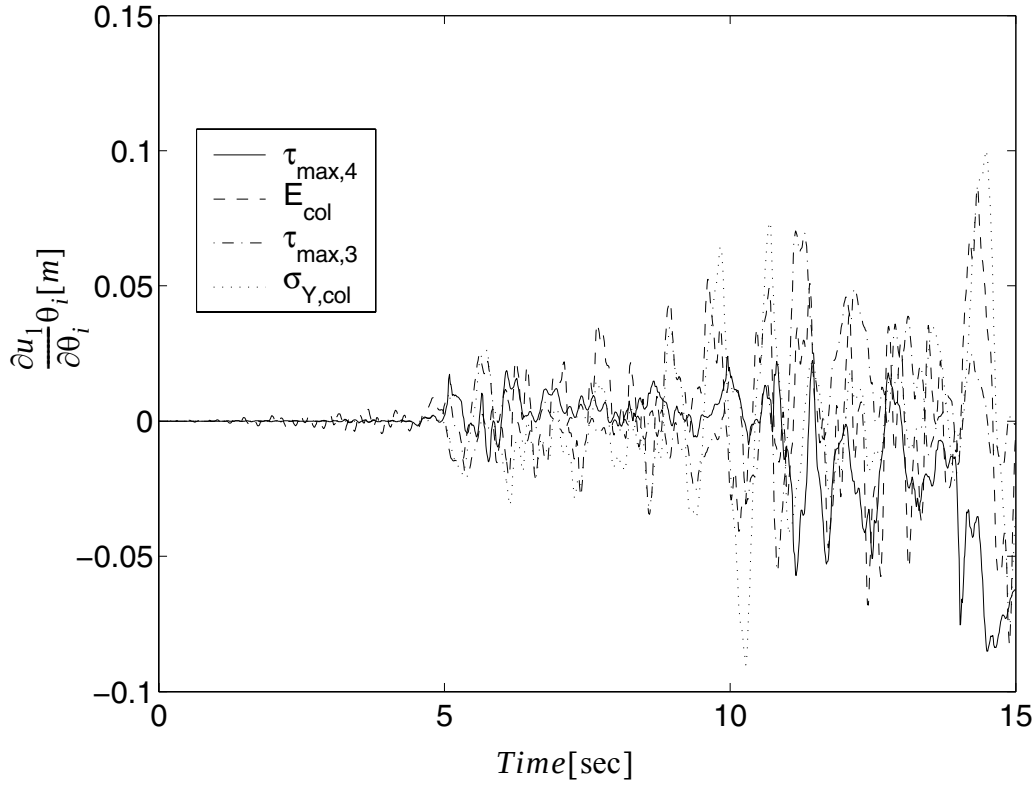


**Figure 4.101 Relative importance of θ's on the first floor drift in y direction**

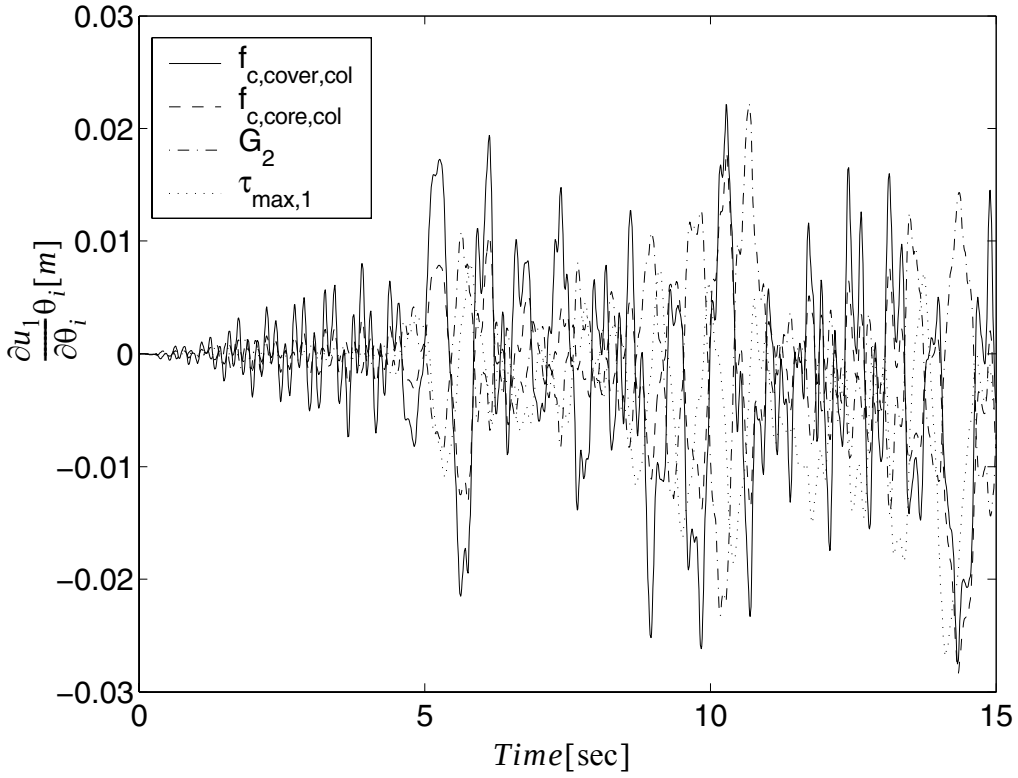


**Figure 4.102 Relative importance of θ's on the first floor drift in y direction**

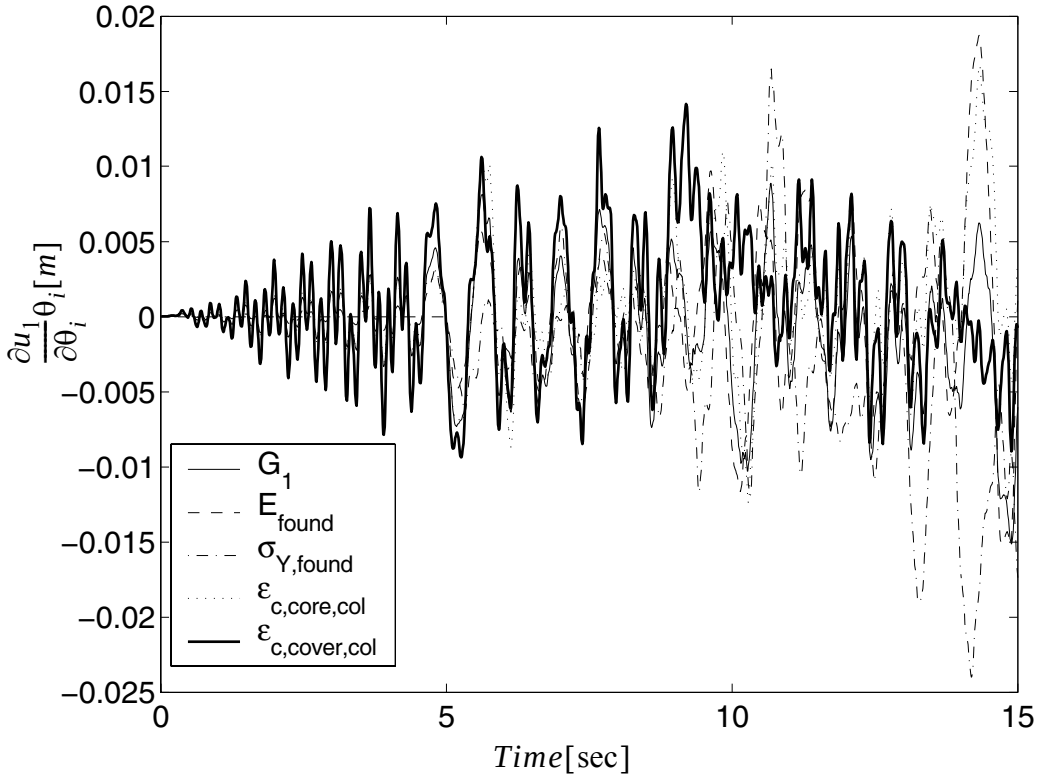


**Figure 4.103 Relative importance of θ's on the first floor drift in y direction**

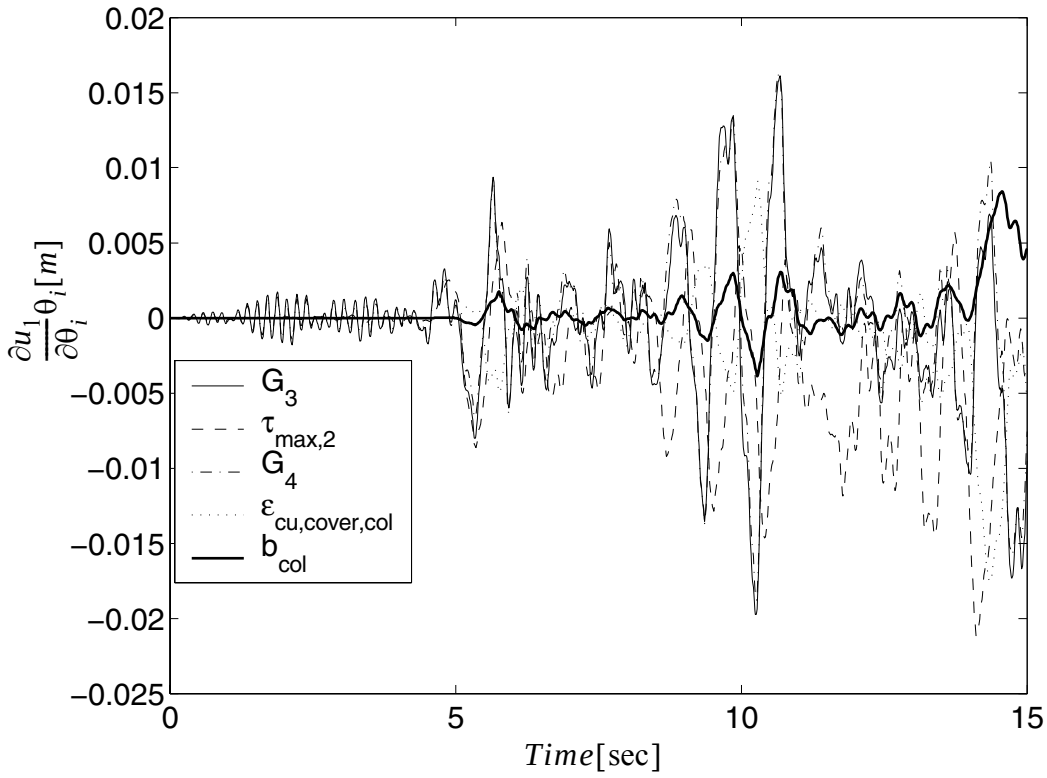


**Figure 4.104 Relative importance of θ's on the first floor drift in y direction**

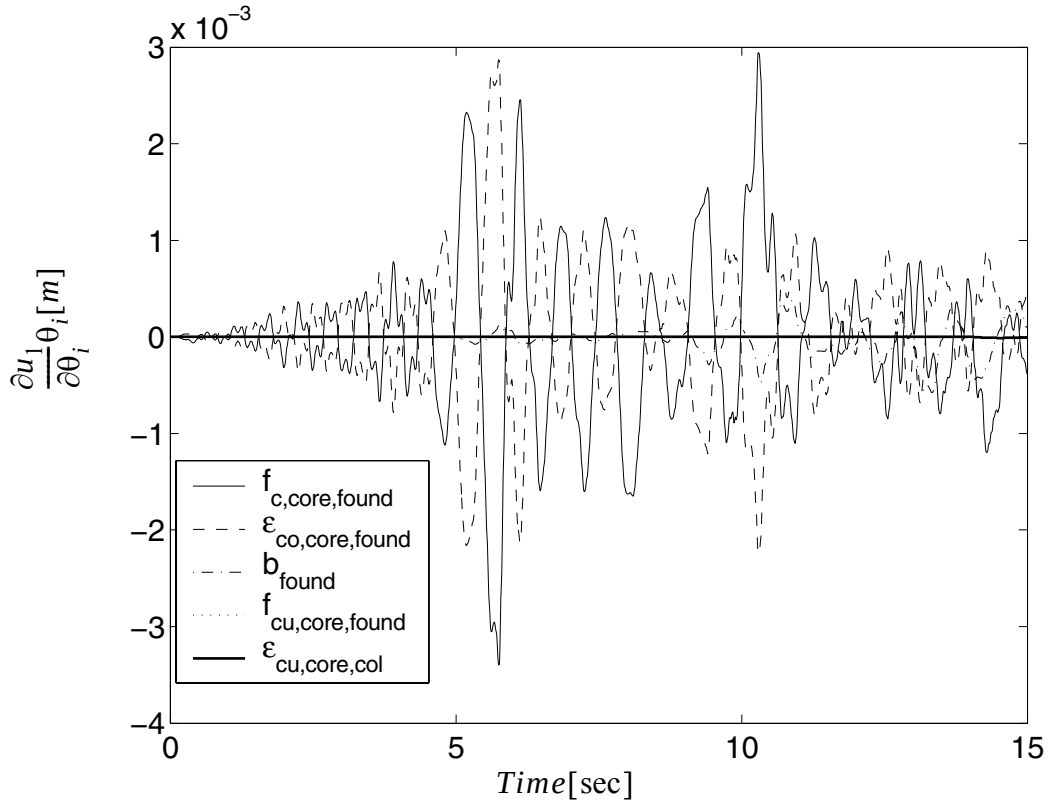


**Figure 4.105 Relative importance of θ's on the first floor drift in y direction**

From these results, it is observed that the importance sequence for x and y direction are almost same. $\sigma_{y,\,steel}$, $E_{steel}$, $\tau_{max,\,4}$, $\tau_{max,\,3}$, are always most important parameters; while $f_{c,\,core}$, $f_{c,\,cover}$, $\tau_{max,\,1}$, $\sigma_{y,\,steel}$, $G_2$, $G_3$, $E_{foundation,\,steel}$, $\sigma_{y,\,foundation,\,steel}$ are sensitive as well.

The normalized sensitivity results are analyzed and the relative importance of the material parameters in determining the second floor drift in x direction are:

$$\tau_{max,\,4} > \tau_{max,\,3} > E_{steel} > \sigma_{y,\,steel} > f_{c,\,cover} > G_2 > G_1 > G_3 > \tau_{max,\,1} > f_{c,\,core} > G_4 > E_{foundation,\,steel} > \sigma_{y,\,foundation,\,steel} > \varepsilon_{c,\,core} > \tau_{max,\,2} > \varepsilon_{cu,\,cover} > f_{c,\,core,\,foundation} > b_{steel} > \varepsilon_{c,\,core,\,foundation} > b_{foundation,\,steel} > f_{cu,\,core} > \varepsilon_{cu,\,core}$$

in y direction are:

$$\tau_{max,\,3} > E_{steel} > \sigma_{y,\,steel} > \tau_{max,\,4} > f_{c,\,cover} > \tau_{max,\,1} > G_2 > \varepsilon_{c,\,cover} > \tau_{max,\,2} > G_3 > E_{foundation,\,steel} > G_4 > f_{c,\,core} > \sigma_{y,\,foundation,\,steel} > G_1 > \varepsilon_{c,\,core} > \varepsilon_{cu,\,cover} > b_{steel} > f_{c,\,core,\,foundation} > \varepsilon_{c,\,core,\,foundation} > b_{foundation,\,steel} > f_{cu,\,core} > \varepsilon_{cu,\,core}$$

The relative importance to second floor drift is similar with that to the first drift. Part of the results are shown in Figures 4.106 to 4.109.

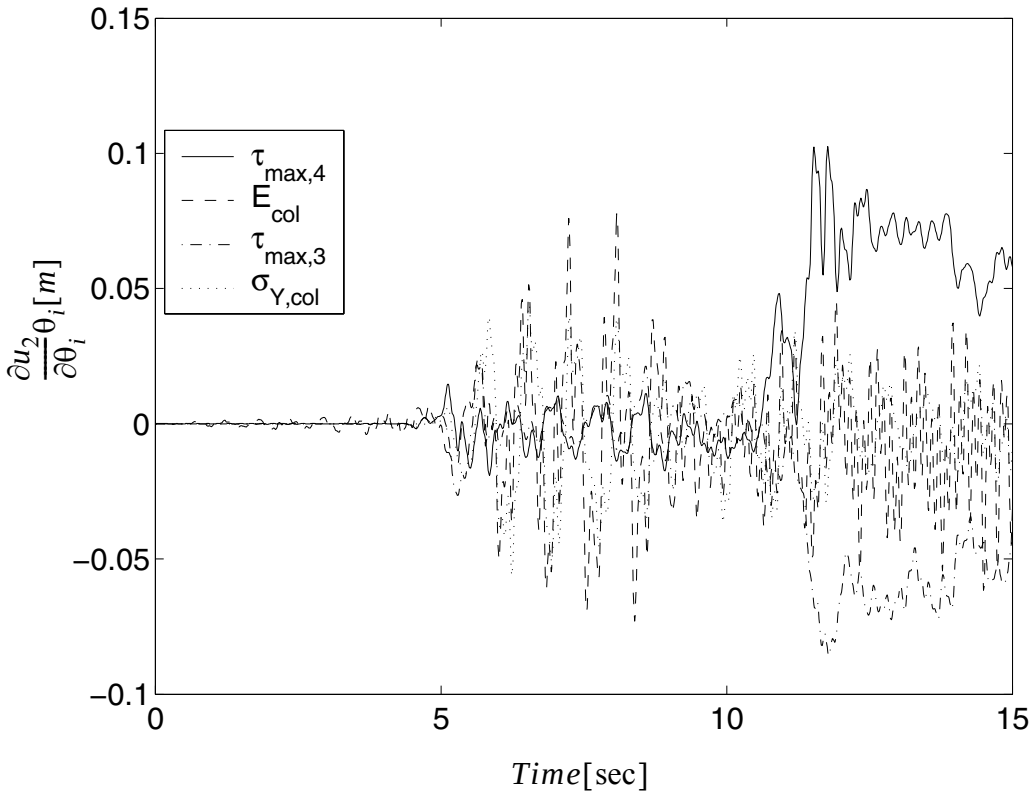


**Figure 4.106 Relative importance of θ's on the second floor drift in x direction**

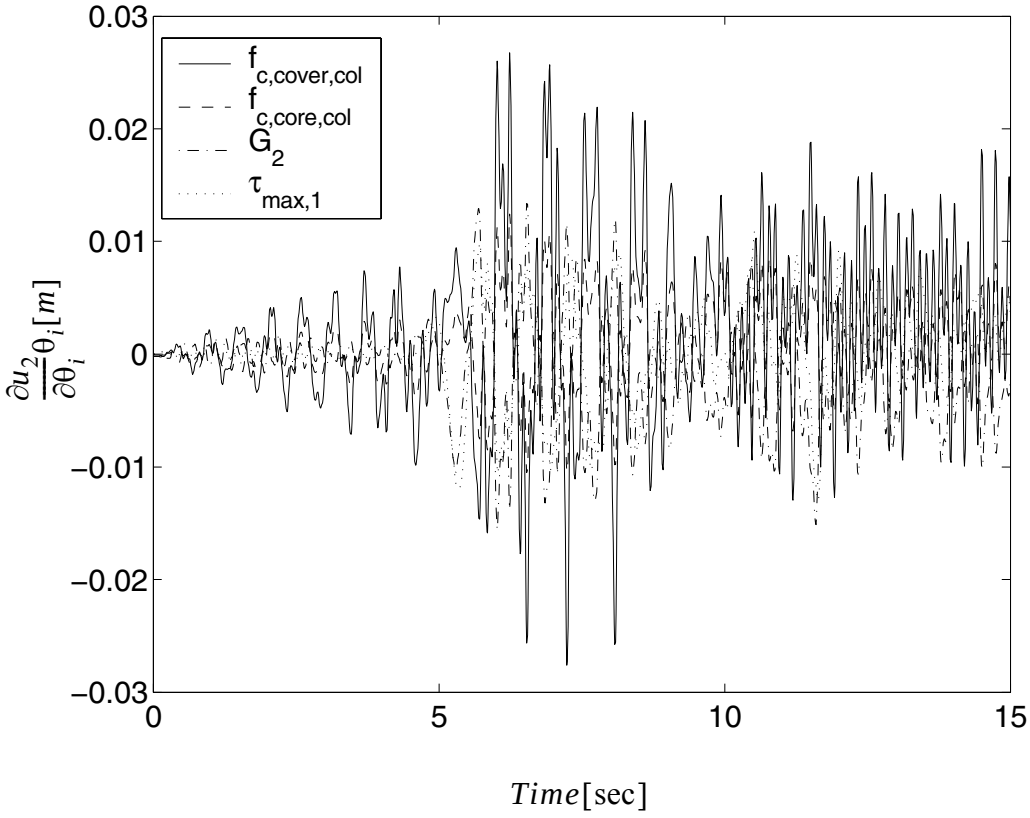


**Figure 4.107 Relative importance of θ's on the second floor drift in x direction**

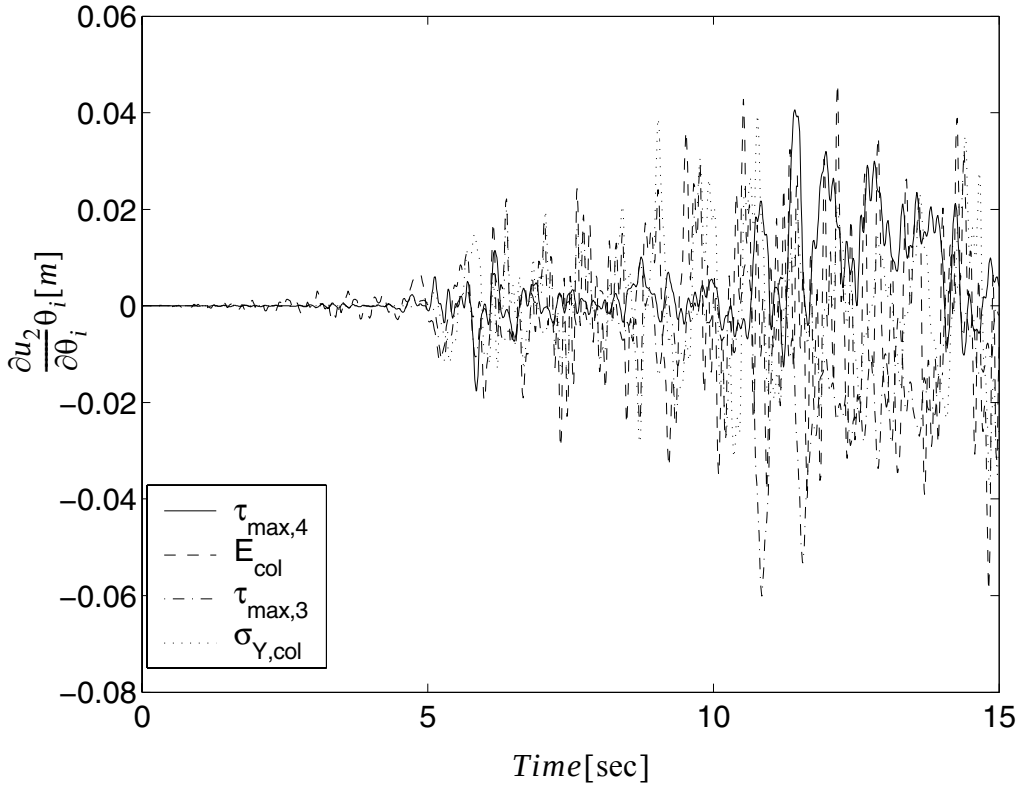


**Figure 4.108 Relative importance of θ's on the second floor drift in y direction**

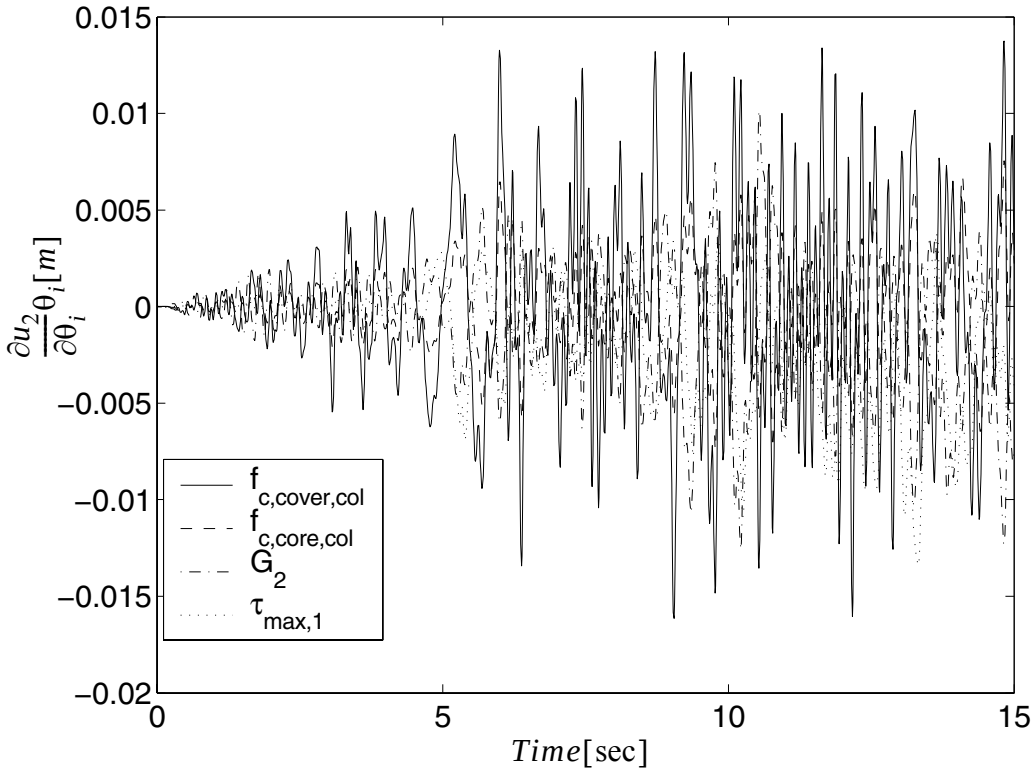


**Figure 4.109 Relative importance of θ's on the second floor drift in y direction**

Same sensitivity analysis is performed for local strain at point B and moment at point A. The normalized sensitivity results are used to obtain the relative importance of the material parameters in determining the strain at point B:

$$\tau_{max,1} > \tau_{max,4} > \tau_{max,2} > \sigma_{y,steel} > \tau_{max,3} > G_1 > f_{c,cover} > G_4 > E > G_2 > f_{c,core} > \varepsilon_{c,core} > G_3 > \varepsilon_{c,cover} > b$$

The relative importance to strain is similar with that to the first drift. Part of the results are shown in Figures 4.110 to 4.111.

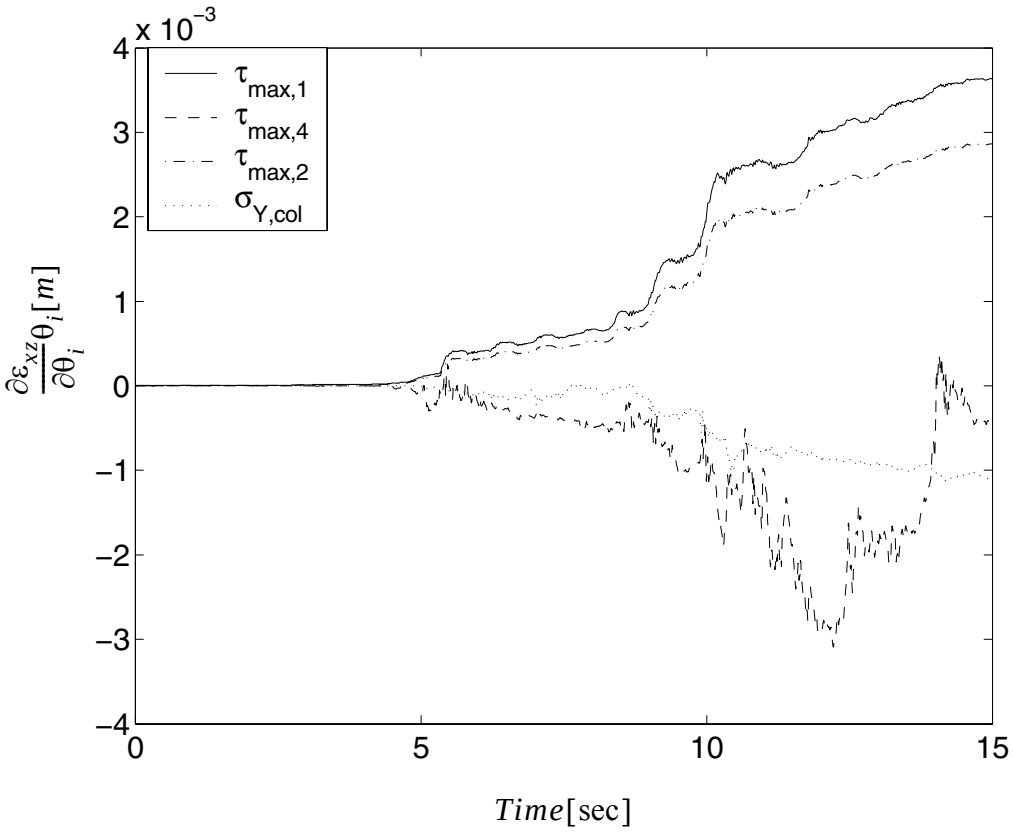


**Figure 4.110 Relative importance of θ's on the strain at point B**

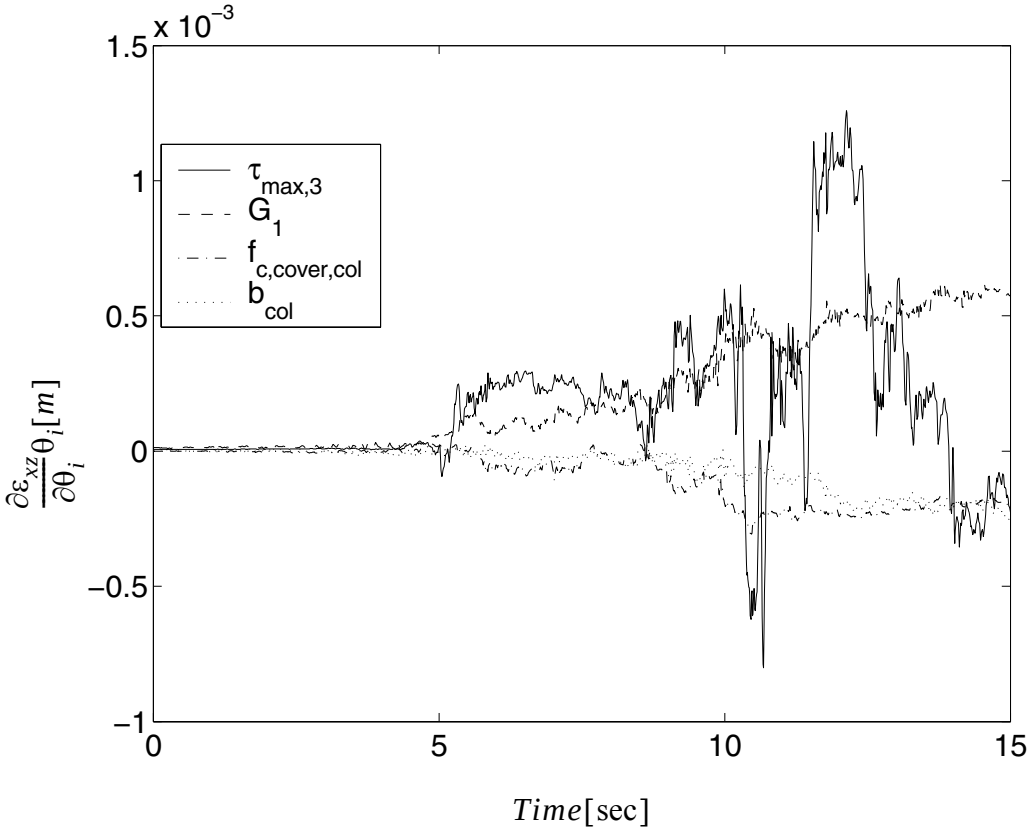


**Figure 4.111 Relative importance of θ's on the strain at point B**

The normalized sensitivity to the moment at point A is studied and the relative importance of the material parameters are:

$$G_3 > \tau_{max,4} > E > \tau_{max,3} > f_{c,cover} > \tau_{max,1} > \tau_{max,2} > f_{c,core} > \varepsilon_{c,core} > \varepsilon_{c,cover} > G_2 > G_1 > G_4 > G_3 > b$$

Part of the results are shown in Figures 4.112 to 4.113

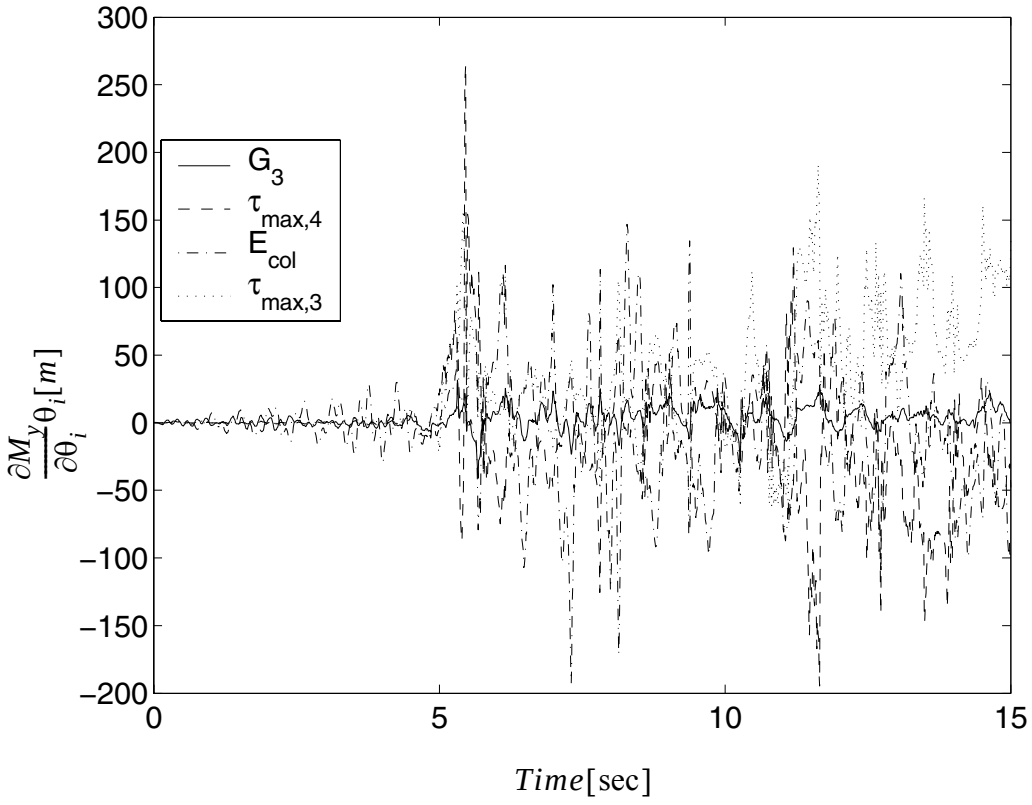


**Figure 4.112 Relative importance of θ's on the moment at point A**

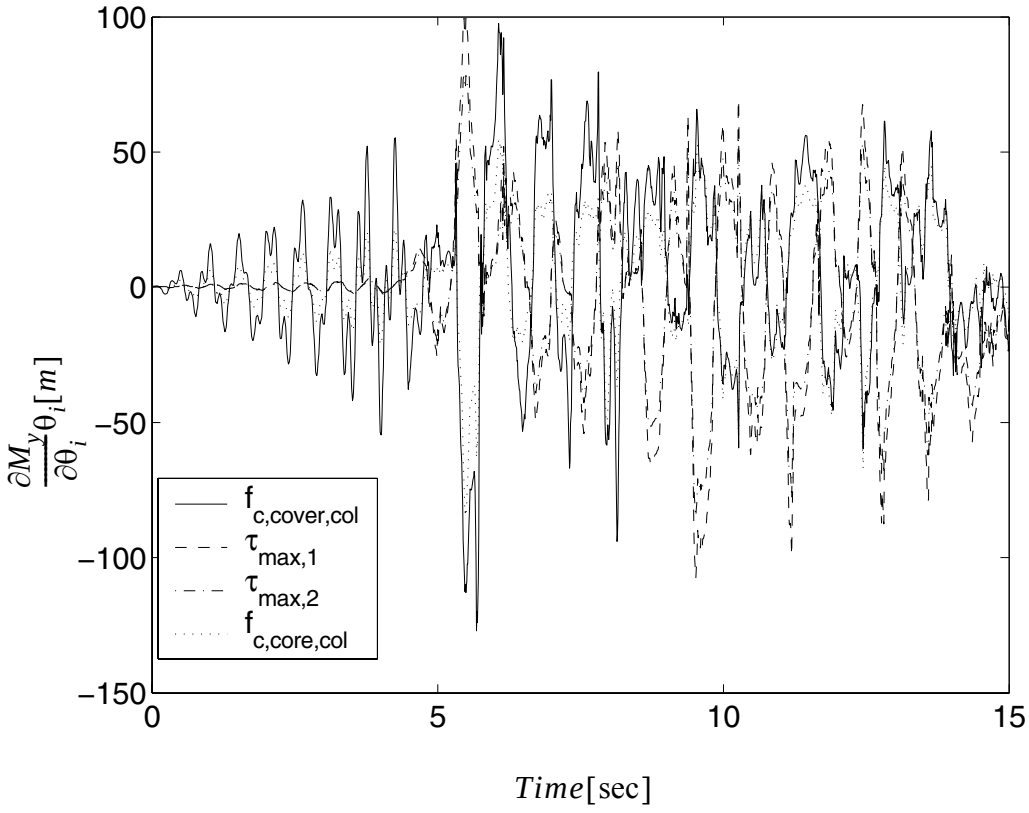


**Figure 4.113 Relative importance of θ's on the moment at point A**

## 4.7 Conclusion

The sensitivity computation framework based on DDM is extended to Soil Structure Interaction (SSI) systems. Various elements, sections, materials, as well as the multi-point constraint, and adaptive time step analyses are extended to adopt the sensitivity computation.

As a main contribution among these, an existing multi-surface yield $J_2$ plasticity model, a very versatile material model used extensively in geotechnical engineering, is studied and redeveloped in the following manner: (1) the consistent tangent moduli of this model is developed and implemented. (2) the response sensitivity algorithm is developed and implemented. Based on the studies between consistent tangent moduli and classic continuum tangent moduli, it is observed that when the tolerance is decreased, using consistent tangent moduli reduces both the number of iterations needed to achieve convergence per step and the computational time. The decreasing unbalanced forces show an asymptotically quadratic convergence of the Newton process when using consistent tangent moduli. In dynamic cases, when the time step increases, the use of the consistent tangent moduli reduces both the number of iterations needed to achieve convergence per step and computational time.

Response sensitivity analysis results based on the DDM algorithm are validated through the Forward Finite Difference (FFD) method. The computational results indicate that the FFD results converge to the DDM results as the perturbation decreases within an acceptable range determined by the computational round-off error, thus verifying the DDM results.

The response sensitivity computational method provides a way to evaluate the relative importance of the material parameters in terms of their relative influence on the structural or soil responses (both global and local). Various SSI examples are studied for the material sensitivity parameters and their importance ranking in regards to the response of interest.

# CHAPTER 5

# PROBABILISTIC PUSHOVER ANALYSIS OF STRUCTURAL AND GEOTECHNICAL SYSTEMS

In this chapter, the First-Order Second-Moment (FOSM) method is employed to perform a probabilistic pushover response analysis of structural and geothecnical systems. The research presented in this chapter is a collaborative work with another researcher (Barbato, M. and Gu Q. 2006). Approximations of the means and the standard deviations of response quantities of structural and soil-foundation-structure interaction (SFSI) system with random material parameters of prescribed probability distributions are computed by using quasi-static finite element response and response sensitivity analysis results. The finite element response sensitivity analysis is performed efficiently by using the Direct Differentiation Method (DDM). Response sensitivity analysis is also used to gain insight into the effects and relative importance of the various material parameters of the structural and geotechnical systems in influencing the variability of the system response. A three-dimensional symmetric three-story reinforced concrete (R/C) frame building and a two-dimensional SFSI system of a R/C frame structure on a layered soil, both subjected to non-linear quasi-static pushover analysis, are considered as application examples. First- and second-order statistical moments of response quantities computed through the Mean-Cen-

tered FOSM method are compared with the corresponding estimates obtained via Monte Carlo simulation (MCS). Comparisons are also made between results obtained using "exact" (computed by DDM) and "gross" (computed by finite difference using relatively large perturbation of the considered parameters) response sensitivities. The relative importance of the material parameters describing the system is studied in both the deterministic (response sensitivities scaled with the nominal/mean values of the considered parameters) and probabilistic (response sensitivities scaled with the standard deviations of the considered parameters) sense. These results are compared with the ones obtained by direct simulation and presented in the form of tornado diagrams. Effects of correlation between couples of material parameters are also considered and analyzed. A simple method for obtaining approximate information about the probability distributions of response quantities as functions of each random material parameter is introduced and presented in the form of javelin diagrams. Conclusions are drawn on both the appropriateness of using exact response sensitivities for simplified probabilistic response analysis and the limits of applicability of the FOSM by comparison with the corresponding MCS results. In particular, the Mean-Centered FOSM method provides sufficiently accurate estimates of the first and second statistical moments of response quantities for low-to-moderate non-linearities in the structural behavior and useful qualitative information on the importance ranking of the material parameters also for large non-linearities in the system response.

Evaluation of the uncertainty in the computed structural response of civil structures is of paramount importance in order to improve safety and optimize the use of economic resources. In the last two decades, significant research has been devoted to propagating

uncertainties from modeling parameters to structural response through the finite element method (Der Kiureghian, 1988). Probabilistic methodologies for describing the statistics of the random response of structures with uncertain properties or/and subjected to random loading have been developed and interfaced with the widely used and accepted finite element method. Some of these methods, used in particular for estimating the first- and second-moment statistics, are the Stochastic Equivalent Linearization Method (Crandall, 2006; Ghanem and Spanos, 1991) and the Stochastic Perturbation Method (Bolotin, 1968; Grigoriou, 2000)

This chapter presents a comparison of two different probabilistic response analysis methods based on non-linear finite element response simulation. A Mean-Centered First-Order Second-Moment (FOSM) approximation (Haukaas and Der Kiureghian, 2004) is used to estimate first- and second-moment statistics of finite element response quantities and these estimates are compared with results obtained using Monte Carlo simulation (MCS) (Liu, 2001). Finite element response sensitivities required by FOSM analysis are computed through the Direct Differentiation Method (DDM) (Kleiber et al., 1997) and through forward and backward finite difference analysis using relatively large perturbations of the uncertain parameters. Only material non-linearities and uncertainties in material parameters are considered in this study.

The FOSM is applied to advanced non-linear finite element models of realistic structures and Soil-Structure-Foundation-Interaction (SFSI) systems subjected to non-linear quasi-static pushover analysis. Non-linear quasi-static pushover analysis is a popular procedure in the earthquake engineering community, since it allows gaining insight into the

non-linear seismic response behavior of structures using simplified analysis techniques. Even though this procedure presents several shortcomings and is based more on intuition than on rigorous physical and mathematical modeling of the problem, it has been recognized by international codes (ATC, 1996; FEMA, 1997) as a possible substitute, under certain conditions, for non-linear dynamic analysis of structural systems.

## 5.1 First-Order Second-Moment Probabilistic Response Analysis

Probabilistic response analysis consists of computing the probabilistic characterization of the response of a specific structure, given as input the probabilistic characterization of material, geometric and loading parameters. An approximate method of probabilistic response analysis is the First-Order Second-Moment (FOSM) method, in which mean values (first-order statistical moments), variances and covariances (second-order statistical moments) of the response quantities of interest are estimated by using a first-order Taylor series expansion of the response quantities in terms of the random or uncertain modeling parameters (Haukaas and Der Kiureghian, 2004) about a given point in the space in which the modeling parameters are defined. Thus, this method requires only the knowledge of the first- and second-order statistical moments of the random parameters. It is noteworthy that often statistical information about the random parameters is limited to first and second moments and therefore probabilistic response analysis methods more advanced than FOSM analysis cannot be fully exploited.

Given the vector of n random parameters $\boldsymbol{\vartheta} \in \boldsymbol{\Theta}$, where $\boldsymbol{\Theta}$ the domain of variability of $\boldsymbol{\vartheta}$, the corresponding covariance matrix $\boldsymbol{\Sigma}_{\boldsymbol{\vartheta}}$ is

$$\boldsymbol{\Sigma}_{\boldsymbol{\vartheta}} = [\rho_{ij}\sigma_i\sigma_j]; \quad i, j = 1, 2, \ldots, n \tag{5.1}$$

where $\rho_{ij}$ is the correlation coefficient of random parameters $\theta_i$ and $\theta_j$ ($\rho_{ii} = 1$; i = 1, 2, …, n), and $\sigma_i$ denotes the standard deviation of random parameter $\theta_i$. FOSM analysis is based on a linearization of the vector **r** of the m response quantities of interest. In fact, the vector **r** is approximated by the following first-order truncation of its Taylor series expansion in the random parameters $\boldsymbol{\vartheta}$ about a given point $\boldsymbol{\vartheta}_0 \in \boldsymbol{\Theta}$

$$\boldsymbol{r}(\boldsymbol{\vartheta}) \approx \boldsymbol{r}_{lin}(\boldsymbol{\vartheta}) = \boldsymbol{r}(\boldsymbol{\vartheta}_0) + \nabla_{\boldsymbol{\vartheta}}\boldsymbol{r}\big|_{\boldsymbol{\vartheta} = \boldsymbol{\vartheta}_0}(\boldsymbol{\vartheta} - \boldsymbol{\vartheta}_0) \tag{5.2}$$

In general, the linearization point is chosen as the point $\boldsymbol{\mu}_{\boldsymbol{\vartheta}}$ of the mean values of the parameters. In fact, this is an optimal point (at least in a local sense) for estimating the mean of a scalar function (e.g., response quantity $r_k$, with $k = 1, 2, \ldots, m$) of the parameters by using a linear approximation, independently of the functional relation and of the joint probability distribution of the parameters (see Appendix). Using the Mean-Centered FOSM method, the vector **r** of m response quantities of interest is approximated by a first-order truncation of its Taylor series expansion in the random parameters $\boldsymbol{\vartheta}$ about their mean values $\boldsymbol{\mu}_{\boldsymbol{\vartheta}}$ as

$$\boldsymbol{r}(\boldsymbol{\vartheta}) \approx \boldsymbol{r}_{lin}(\boldsymbol{\vartheta}) = \boldsymbol{r}(\boldsymbol{\mu}_{\boldsymbol{\vartheta}}) + \nabla_{\boldsymbol{\vartheta}}\boldsymbol{r}\big|_{\boldsymbol{\vartheta} = \boldsymbol{\mu}_{\boldsymbol{\vartheta}}}(\boldsymbol{\vartheta} - \boldsymbol{\mu}_{\boldsymbol{\vartheta}}) \tag{5.3}$$

The first- and second-order statistical moments of the response quantities **r** are approximated by the corresponding moments of the linearized response quantities, i.e.,

$$\boldsymbol{\mu}_{\boldsymbol{r}} \approx \boldsymbol{\mu}_{\boldsymbol{r}_{lin}} = E[\boldsymbol{r}_{lin}(\boldsymbol{\vartheta})] = \boldsymbol{r}(\boldsymbol{\mu}_{\boldsymbol{\vartheta}}) + \nabla_{\boldsymbol{\vartheta}}\boldsymbol{r}\big|_{\boldsymbol{\vartheta} = \boldsymbol{\mu}_{\boldsymbol{\vartheta}}} E[\boldsymbol{\vartheta} - \boldsymbol{\mu}_{\boldsymbol{\vartheta}}] = \boldsymbol{r}(\boldsymbol{\mu}_{\boldsymbol{\vartheta}}) \tag{5.4}$$

$$\boldsymbol{\Sigma}_{\boldsymbol{r}} \approx \boldsymbol{\Sigma}_{\boldsymbol{r}_{lin}} = E[(\boldsymbol{r}_{lin}(\boldsymbol{\vartheta}) - \boldsymbol{\mu}_{\boldsymbol{r}_{lin}}) \cdot (\boldsymbol{r}_{lin}(\boldsymbol{\vartheta}) - \boldsymbol{\mu}_{\boldsymbol{r}_{lin}})^T] = \nabla_{\boldsymbol{\vartheta}} \boldsymbol{r}\big|_{\boldsymbol{\vartheta} = \boldsymbol{\mu}_{\boldsymbol{\vartheta}}} \cdot \boldsymbol{\Sigma}_{\boldsymbol{\vartheta}} \cdot (\nabla_{\boldsymbol{\vartheta}} \boldsymbol{r}\big|_{\boldsymbol{\vartheta} = \boldsymbol{\mu}_{\boldsymbol{\vartheta}}})^T \quad (5.5)$$

in which E[…] denotes the mathematical expectation operator. In particular, the explicit form for the variances of each of the response quantities considered is found from Eq. (5.5) as

$$\sigma_{r_k}^2 = \sum_{i=1}^{n} \left(\frac{\partial r_k}{\partial \theta_i}\right)^2 \sigma_{\theta_i}^2 + 2 \sum_{i=1}^{n} \sum_{j=1}^{i-1} \rho_{ij} \left(\frac{\partial r_k}{\partial \theta_i}\right)\left(\frac{\partial r_k}{\partial \theta_j}\right) \sigma_{\theta_i} \sigma_{\theta_j}; \quad k = 1, ..., m \quad (5.6)$$

The approximate response statistics computed through Equations (5.4) and (5.5) are extremely important in evaluating the variability of the response quantities of interest due to the intrinsic uncertainty of the modeling parameters and provide information on the statistical correlation between the different response quantities. It is noteworthy that these approximate first- and second-order response statistics can be readily obtained when response sensitivities evaluated at the mean values of the random parameters are available. Only a single finite element analysis is needed in order to perform a FOSM probabilistic response analysis, when the finite element response sensitivities are computed using the DDM. In the following, only Mean-Centered FOSM analyses will be considered and denoted as FOSM analyses, for sake of brevity.

## 5.2 Probabilistic Response Analysis Using Monte Carlo Simulation

Probabilistic response analysis can also be performed using Monte Carlo simulation (MCS) (Liu, 2001). In this study, MCS is used to assess the accuracy of the FOSM approximations in when applied to non-linear finite element response analysis of R/C

building structures characterized with random/uncertain material parameters and subjected to quasi-static pushover. The MCS procedure requires:

1. Generation of N realizations of the n-dimensional random parameter vector $\boldsymbol{\vartheta}$ according to a given n-dimensional joint probability density function (PDF).
2. Computation by finite element analysis of N pushover curves (i.e., force-response curves) for each component of the response vector **r**, corresponding to the N realizations of the random parameter vector $\boldsymbol{\vartheta}$.
3. Statistical estimation of specified marginal and joint moments of the components of response vector **r** at each load step of the finite element response analysis.

MCS is a general and robust methodology for probabilistic response analysis, but it suffers two significant limitations:

1. It requires knowledge of the joint PDF of the random parameters $\boldsymbol{\vartheta}$. In general, this joint PDF is only partially known and appropriate models, consistent with the incomplete statistical information available, must be used to generate realizations of the vector $\boldsymbol{\vartheta}$.
2. MCS requires performing N finite element response analyses. This number N can be very large for accurate estimates of marginal and joint moments of response quantities **r** and increases rapidly with the order of the moments. For real-world structures, complex non-linear finite element analyses are necessary for accurate prediction of the structural response and repeating such analyses a large number of times could be computationally prohibitive.

In this study, the Nataf model (Ditlevsen and Madsen, 1996) is used to generate realizations of the random parameters $\boldsymbol{\vartheta}$. It requires specification of the marginal PDFs of the random parameters $\boldsymbol{\vartheta}$ and their correlation coefficients. It is therefore able to reproduce the given first- and second-order statistical moments of the random parameters $\boldsymbol{\vartheta}$.

## 5.3 Estimation of Response probability distributions

The FOSM method used in this chapter allows to consider the effects of the variability of each random parameter on the variability of the response. Herein, two simplified procedures, based on the response and response sensitivities computed at the mean values of the parameters, are presented to obtain information on the dependency of the response quantities considered on each of the material random parameters.

The first procedure is used to find the relative importance of each material random parameter on the response quantities. Such relative importance is obtained using the response sensitivities computed at the mean values of the parameters and the variances of the parameters. The relative importance using FOSM results is validated against corresponding results obtained computing the response quantities changing the value of each parameter by $\pm 1$ standard deviation one at a time. Such validation is graphically represented through tornado diagrams (Howard, 1983; Porter et al., 2002). Another quantity commonly used to define a relative importance ranking of the uncertain/random parameters in influencing the variability of the response quantities considered is the so-called "swing" (Porter et al., 2002). The term swing denotes the variation in the response quantity of interest due to the variability of only one parameter when all the other parameters

are kept fixed at their corresponding mean values. The swing is computed in correspondence of the minimum and maximum values of the parameter considered when its probability distribution is defined over a finite interval (e.g., beta and uniform distributions) or of the 10% and 90% fractiles when the probability distribution of the parameter is defined over an infinite (e.g., normal distribution) or semi-infinite (e.g., lognormal or exponential distributions) interval. The swing is commonly represented by using tornado diagrams.

The second procedure is employed to find an approximation of the cumulative probability distributions (CDFs) and probability density functions (PDFs) of the response quantities of interest as functions of each random parameter considered one at a time. These approximations are obtained assuming that the response quantities of interest have the same distribution of the random parameter considered, with mean value and standard deviation given by the Mean-Centered FOSM estimates of mean and standard deviation, respectively. These approximate CDFs and PDFs are validated through the corresponding quantities obtained simulating repeatedly the response for several values of the material parameter considered and keeping all the other random parameters at their mean value. The results of this procedure are graphically represented using the so-called “javelin diagrams” (Felli and Hazen, 2004), which are used in the fields of Economics, Management and Decision Analysis but, to the authors knowledge, have not yet been employed by the Structural Engineering community.

## 5.4 Application Examples

### 5.4.1 Three-Dimensional R/C Frame Building

The first application example considered herein consists of a three-dimensional reinforced concrete frame building on rigid foundation with concrete slabs at each floor as shown in Figure 5.1. The frame consists of three stories of height $h = 3.66m$ (12ft) each and one bay of span $L = 6.10m$ (20ft) in each direction. Beam and column cross-sections are shown in Figure 5.1.

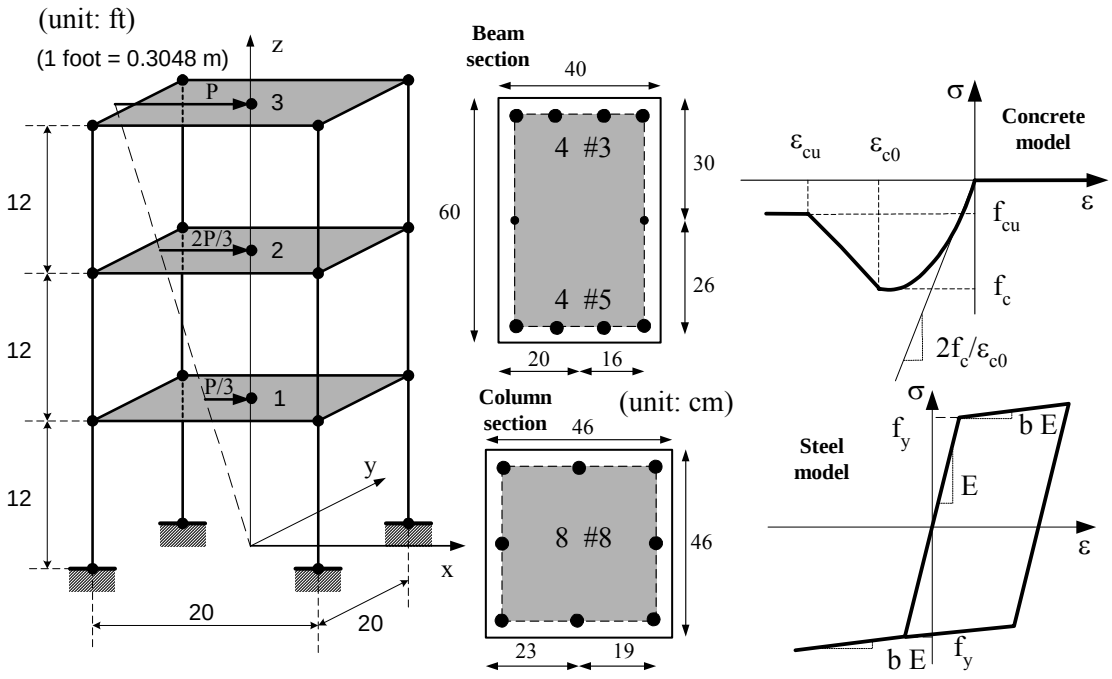


**Figure 5.1 Geometry, cross-sectional properties, applied horizontal loads and material constitutive models for the three-story R/C building**

Beams and columns are modeled using displacement-based Euler-Bernoulli frame elements with four Gauss-Legendre integration points each. Each column and beam is discretized in two and three finite elements, respectively. Beam and column cross-sections are discretized in fibers of confined concrete, unconfined concrete and steel reinforcement. The reinforcement steel is modeled through a bilinear hysteretic model, while the concrete is represented by the Kent-Scott-Park model with zero tension stiffening (Scott et al., 1982), as shown in Figure 5.1. Different material parameters are used for the confined (core) and unconfined (cover) concrete in the columns and beams. The concrete slabs are modeled through a diaphragm constraint at each floor to enforce rigid in-plane behavior.

Ten material constitutive parameters are used to characterize the various structural materials involved in the structure, namely four parameters for the confined concrete ($f_{c,\,core}$: peak strength, $\varepsilon_{c,\,core}$: strain at peak strength, $f_{cu,\,core}$: residual strength, $\varepsilon_{cu,\,core}$: strain at which the residual strength is reached), three parameters for the unconfined concrete ($f_{c,\,cover}$, $\varepsilon_{c,\,cover}$, $\varepsilon_{cu,\,cover}$) with the fourth parameter $f_{cu,\,cover} = 0MPa$, and three parameters for the reinforcement steel ($f_y$: yield strength, $E_0$: initial stiffness, b: post-yield to initial stiffness ratio). Figure 5.1 shows graphically the meaning of all the material parameters considered. These material parameters are modeled as random fields spatially fully correlated, i.e., each material parameter is modeled with a single random variable (RV). The marginal PDFs of these material parameters are given in table (5.1) and were obtained from studies reported in the literature (Mirza and MacGregor 1979, Mirza et al. 1979). The correlation coefficients between the various material parameters are assumed as follows: $\rho = 0.8$ for (1) $f_{c,\,core}$ and $f_{cu,\,core}$, (2) $\varepsilon_{c,\,core}$ and $\varepsilon_{cu,\,core}$, (3) $\varepsilon_{c,\,cover}$ and

$\varepsilon_{cu,\,cover}$, (4) $f_{c,\,core}$ and $f_{c,\,cover}$, (5) $\varepsilon_{c,\,core}$ and $\varepsilon_{c,\,cover}$, (6) $\varepsilon_{cu,\,core}$ and $\varepsilon_{cu,\,cover}$; $\rho = 0.64$ for (1) $f_{cu,\,core}$ and $f_{c,\,cover}$, (2) $\varepsilon_{c,\,core}$ and $\varepsilon_{cu,\,cover}$, (3) $\varepsilon_{cu,\,core}$ and $\varepsilon_{c,\,cover}$; and $\rho = 0.0$ for all other pairs of parameters. These correlation coefficients are chosen based on engineering judgement, since to the authors' knowledge, precise values of correlation coefficients are not available in the literature.

**Table 5.1 Marginal PDFs of material parameters for the three-story building (distribution parameters for lognormal distribution: (1) $\lambda = \mu_{\log(X)}$, (2) $\zeta = \sigma_{\log(X)}$; for beta distribution: (1) $x_{min}$, (2) $x_{max}$, (3) $\alpha_1$, (4) $\alpha_2$)**

| RV [unit] | Distribution | Par.#1 | Par.#2 | Par.#3 | Par.#4 | Mean | C.O.V. [%] |
|---|---|---|---|---|---|---|---|
| $f_{c,core}$ [MPa] | lognormal | 3.5205 | 0.1980 | - | - | 34.47 | 20 |
| $\varepsilon_{c,core}$ [-] | lognormal | -5.3179 | 0.1980 | - | - | 0.005 | 20 |
| $f_{cu,core}$ [MPa] | lognormal | 3.1638 | 0.1980 | - | - | 24.13 | 20 |
| $\varepsilon_{cu,core}$ [-] | lognormal | -3.9316 | 0.1980 | - | - | 0.020 | 20 |
| $f_{c,cover}$ [MPa] | lognormal | 3.2975 | 0.1980 | - | - | 27.58 | 20 |
| $\varepsilon_{c,cover}$ [-] | lognormal | -6.2342 | 0.1980 | - | - | 0.002 | 20 |
| $\varepsilon_{cu,cover}$ [-] | lognormal | -5.1356 | 0.1980 | - | - | 0.006 | 20 |
| $f_y$ [MPa] | beta | 227.53 | 427.48 | 3.21 | 4.28 | 307.46 | 10.6 |

**Table 5.1 Marginal PDFs of material parameters for the three-story building (distribution parameters for lognormal distribution: (1) $\lambda = \mu_{\log(X)}$, (2) $\zeta = \sigma_{\log(X)}$; for beta distribution: (1) $x_{min}$, (2) $x_{max}$, (3) $\alpha_1$, (4) $\alpha_2$)**

| RV [unit] | Distribution | Par.#1 | Par.#2 | Par.#3 | Par.#4 | Mean | C.O.V. [%] |
|---|---|---|---|---|---|---|---|
| $E_0$ [MPa] | lognormal | 12.1914 | 0.0330 | - | - | 201000 | 3.3 |
| b [-] | lognormal | -3.9316 | 0.1980 | - | - | 0.02 | 20 |

After static application of the gravity loads (assumed as uniformly distributed load per unit area $q = 8kN/m^2$ at each floor), the structure is subjected to a quasi-static pushover analysis, in which an upper triangular distribution of horizontal forces is applied on the master nodes of the floor diaphragm constraints in the x-direction (see Figure 5.1). The total base shear force, $P_{tot} = 2P$, is considered as deterministic and is assumed to increase linearly during the analysis from 0kN to 600kN. In this analysis, only material non-linearities are taken into account. A response analysis and response sensitivity analysis using the DDM are first performed at the mean values $\boldsymbol{\mu}_{\boldsymbol{\vartheta}}$ of the random parameters $\boldsymbol{\vartheta}$. A MCS analysis based on 1000 realizations is then carried out based on the Nataf model used as joint PDF of the random parameters $\boldsymbol{\vartheta}$. Gross sensitivities of the response quantities **r** are evaluated through FFD and BFD analysis, perturbing one material parameter at a time by plus and minus one standard deviation, respectively. Finally, the swing of the response quantities of interest is computed by performing two additional finite element analyses for each random material parameter at its upper and lower values (as previously defined in the above Section: "Estimation of response probability distributions"). Finite element

response, response sensitivity and probabilistic response computations are performed using the finite element analysis framework OpenSees (Mazzoni et al. 2005), in which new classes were added to perform MCS probabilistic response analysis, three-dimensional frame elements were augmented for response sensitivity analysis (Barbato et al., 2006b) and the response sensitivity algorithm for imposing multipoint constraints was implemented (Gu et al., 2006b).

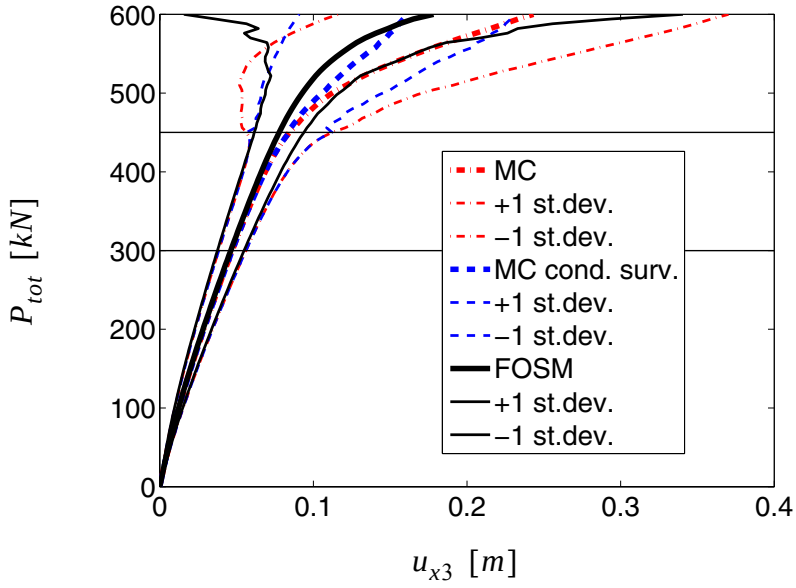


**Figure 5.2 Probabilistic response of the three-story R/C building**

Figure 5.2 shows a comparison of estimates of the mean and mean ± 1 standard deviation of the force - response curve for the roof displacement in the x-direction, $u_{x3}$, obtained through FOSM analysis using the DDM to compute the response sensitivities and MCS, respectively.

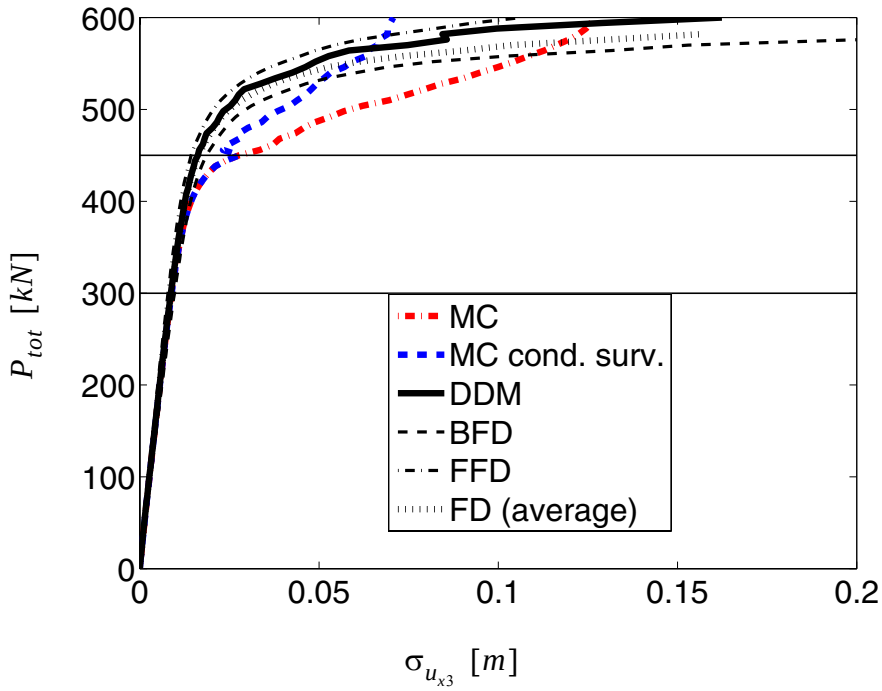


**Figure 5.3 ProStandard deviation of the three-story R/C building**

Figure 5.3 displays the standard deviation estimates of $u_{x3}$ obtained through MCS and FOSM analysis using different methods to compute the response sensitivities. For the given structure subjected to quasi-static pushover, the condition of failure is defined as (near) singularity of the structure stiffness matrix or roof displacement in the x-direction, $u_{x3}$, exceeding 0.4m (i.e., $u_{x3,fail}$ = 0.4m), whichever happens first. It is found that, until the load level $P_{tot} = 450kN$ is reached, no failure case is observed in the MCS performed, while nearly one third of the Monte Carlo realizations reach failure below load level $P_{tot} = 600kN$. In Figures 5.2 and 5.3, horizontal dashed lines mark the load levels $P_{tot} = 300kN$ and $P_{tot} = 450kN$, which denote the load levels below which the

response is almost linear and no failure occurs, respectively. In Figures 5.2 and 5.3, for load levels above $P_{tot} = 450kN$, both the unconditional (denoted as "MC") and conditional to survival ("MCS cond. surv.") MCS estimates of the mean value and standard deviation of $u_{x3}$ are plotted. The MCS mean response conditional to survival presents a stiffening behavior at high load levels, since it represents the mean response of only the realizations corresponding to structures with higher stiffness and/or strength. It is clear that MCS results conditional to survival cannot be directly compared with the FOSM approximations, because of the different meaning of the two sets of quantities. On the other hand, the presence of simulations with failure due to singularity of the structure stiffness matrix (i.e., non-convergence of the finite element pushover analysis) introduces some arbitrarity in the computation and interpretation of the unconditional MCS results. In fact, the value of the displacement $u_{x3}$ at the last converged step of the pushover analysis in these simulations is lower than the value assumed as failure threshold ($u_{x3,fail}$ = 0.4m) and thus the value to be used for the unconditional MCS estimates of mean and standard deviation is not clearly and uniquely defined for load levels higher than the one at which failure occurred (denoted here as $P_{tot,fail}$). In this work, for $P_{tot} \geq P_{tot,\,fail}$, $u_{x3} = u_{x3,\,fail} = 0.4m$ is assumed, which is consistent with the failure condition for the simulations reaching the failure threshold and provides unconditional MCS estimates comparable with FOSM results.

Figure 5.2 shows clearly that the FOSM approximation is in excellent agreement with the MCS results when the structural response is nearly linear (for load levels below

$P_{tot} = 300kN$), while the FOSM results slightly underestimate the MCS results when the structure undergoes low-to-moderate non-linear inelastic deformations (for load levels between $P_{tot} = 300kN$ and $P_{tot} = 450kN$). When MCS realizations start to reach failure as defined above (i.e., for load levels $P_{tot} \geq 450kN$), FOSM results significantly underestimate unconditional MCS results. It can be concluded that, for the first application example considered in this chapter, FOSM analysis provides, at very low computational cost, very good estimates of the mean of response quantities for low-to-moderate levels of material non-linearity in the structural response.

In Figure 5.3, the different techniques employed for computing response sensitivities used in FOSM are: (1) DDM; (2) BFD analysis with perturbations $\Delta\theta_i = -\sigma_i$ $(i = 1, 2, \ldots, 10)$; (3) FFD analysis with perturbations $\Delta\theta_i = \sigma_i$ $(i = 1, 2, \ldots, 10)$; and (4) FD average of gross sensitivities computed using BFD and FFD. It is observed that these four methods produce similar results and in particular the standard deviation estimate obtained using method (4) is very close to the one based on the DDM, except for very high load levels. However, it is important to note that, for each sensitivity parameter, the computational cost of response sensitivities using the DDM is only a fraction of the cost of an additional non-linear finite element analysis, which is required for BFD and FFD analyses. Thus, method (4) requires two additional non-linear finite element analyses for each sensitivity parameter, and is therefore significantly more expensive computationally than the DDM. In addition, the BFD analysis for parameter $f_{c,\,core}$ does not reach the load level $P_{tot} = 600kN$ and the corresponding structural model fails at $P_{tot} = 582kN$ and

$u_{x3} = 0.344m$. Therefore, it is not possible to compute the BFD and FD average estimates of the response standard deviation for $P_{tot} \geq 582kN$. As for the mean of the response, FOSM analysis using DDM provides, at very low computational cost, excellent estimates of the standard deviation of response quantities for low-to-moderate levels of material non-linearity in the structural response.

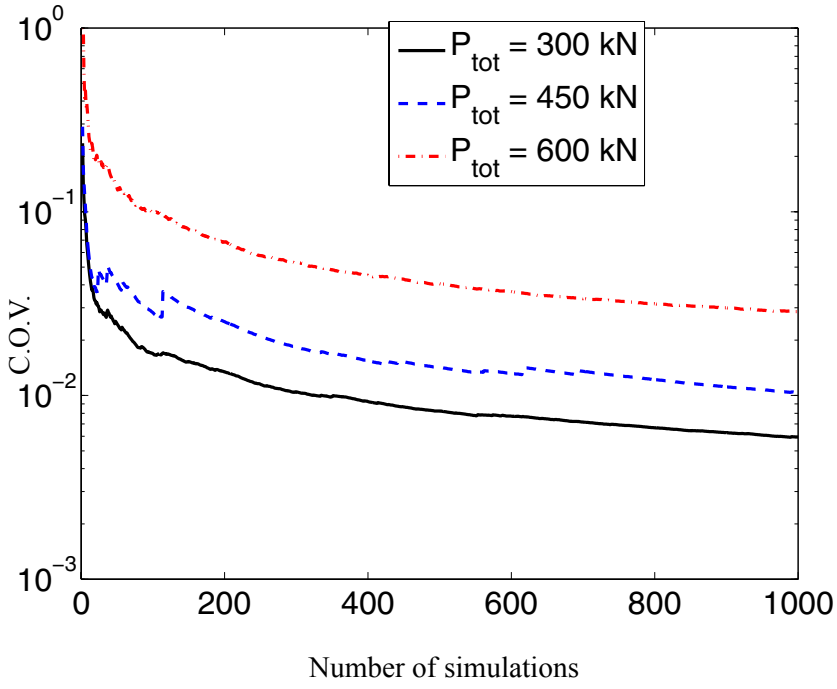


**Figure 5.4 Coefficient of variation of the mean response at different load levels computed using MCS for the three-story R/C building**

Figure 5.4 plots, on a semilogarithmic scale, the coefficient of variation (C.O.V.) of the mean of the response quantity $u_{x3}$ for different load levels as a function of the number of simulations performed. As expected, the C.O.V. is higher for higher load levels, for which the dispersion of the results is higher. At 1000 simulations, the C.O.V. for

$P_{tot} = 300kN, 450kN, 600kN$ are 0.59%, 1.04% and 2.85%, respectively, and thus the MCS results are very reliable. Notice also that the number of simulations required to obtain a C.O.V. lower than 10% are less than 10 for $P_{tot} = 300kN$ and $P_{tot} = 450kN$, but more than 100 for $P_{tot} = 600kN$.

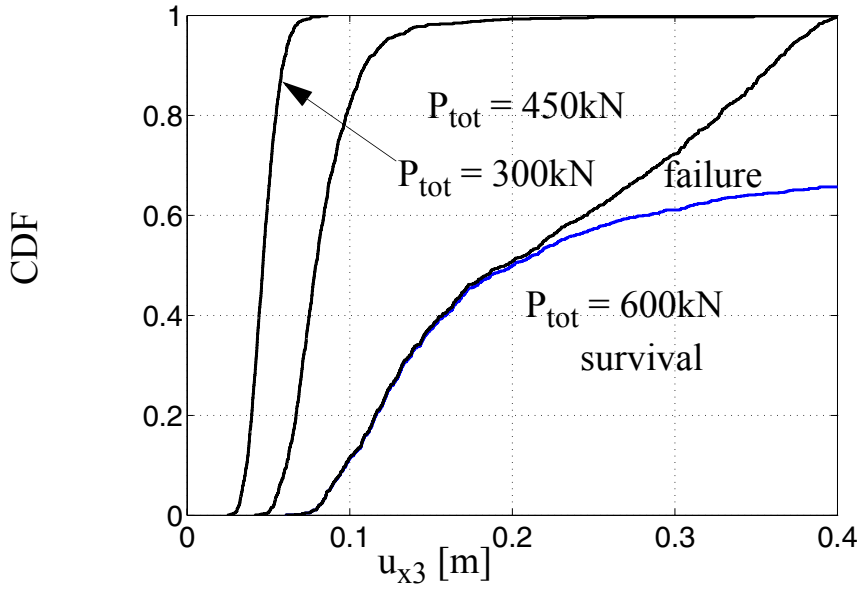


**Figure 5.5 CDFs of $u_{x3}$ for different load levels estimated using MCS for the three-story R/C building**

Figure 5.5 displays the cumulative density functions (CDFs) of $u_{x3}$ obtained by MCS for load levels $P_{tot} = 300kN$, 450kN and 600kN. For $P_{tot} = 600kN$, the CDF conditional to survival and scaled by the probability of survival is also shown, while the CDF condi-

tional to failure (and scaled by the probability of failure) corresponds to the difference between the unconditional CDF and the scaled CDF conditional to survival.

**Table 5.2 Normalized sensitivities computed by DDM of $u_{x3}$ to material parameters and their relative contribution to variance of $u_{x3}$ at different load levels (three-story building)**

| | Deterministic sense | | | Probabilistic sense | | | $\Delta(\sigma^2_{u_{x3}})/\sigma^2_{u_{x3}}$ [%] | | |
|---|---|---|---|---|---|---|---|---|---|
| $P_{tot}$ [kN] | 300 | 450 | 600 | 300 | 450 | 600 | 300 | 450 | 600 |
| $f_{c,core}$ | -0.2301 | -0.3126 | -2.7418 | -0.0460 | -0.0632 | -0.5484 | 6.01 | 9.22 | 36.21 |
| $\varepsilon_{c,core}$ | 0.2186 | 0.2841 | 1.5400 | 0.0437 | 0.0568 | 0.3080 | 5.42 | 7.44 | 11.42 |
| $f_{cu,core}$ | 0 | 0 | -0.0057 | 0 | 0 | -0.0011 | 0 | 0 | <0.01 |
| $\varepsilon_{cu,core}$ | 0 | 0 | -0.0033 | 0 | 0 | -0.0007 | 0 | 0 | <0.01 |
| $f_{c,cover}$ | -0.5207 | -0.6049 | -1.7370 | -0.1041 | -0.1210 | -0.3474 | 30.74 | 33.74 | 14.53 |
| $\varepsilon_{c,cover}$ | 0.4126 | 0.3047 | -0.1597 | 0.0825 | 0.0609 | -0.0319 | 19.30 | 8.56 | 0.12 |
| $\varepsilon_{cu,cover}$ | 0 | -0.0062 | -1.1417 | 0 | -0.0012 | -0.2283 | 0 | <0.01 | 6.28 |
| $f_y$ | 0 | -0.0626 | -2.0698 | 0 | -0.0066 | -0.2194 | 0 | 0.10 | 5.80 |

**Table 5.2 Normalized sensitivities computed by DDM of $u_{x3}$ to material parameters and their relative contribution to variance of $u_{x3}$ at different load levels (three-story building)**

| | Deterministic sense | | | Probabilistic sense | | | $\Delta(\sigma^2_{u_{x3}})/\sigma^2_{u_{x3}}$ [%] | | |
|---|---|---|---|---|---|---|---|---|---|
| $P_{tot}$ [kN] | 300 | 450 | 600 | 300 | 450 | 600 | 300 | 450 | 600 |
| E | -0.3689 | -0.4174 | -0.7647 | -0.0122 | -0.0138 | -0.0252 | 0.42 | 0.44 | 0.08 |
| b | 0 | -0.0001 | -0.0473 | 0 | ~0 | -0.0095 | 0 | <0.01 | 0.01 |

Table 5.2 provides the sensitivities of $u_{x3}$ to the random material parameters computed at the nominal/mean values of the latter and normalized in a deterministic sense, $(\partial u_{x3}/\partial\theta_i)(\theta_i/u_{x3})$, and probabilistic sense, $(\partial u_{x3}/\partial\theta_i)(\sigma_{\theta_i}/\mu_{u_{x3}})$, respectively (with the mean response $\mu_{u_{x3}}$ computed using FOSM). The sensitivities normalized in a deterministic sense can be interpreted as the percent change in the response due to one percent change in the sensitivity parameter considered. The sensitivities normalized in a probabilistic sense represent the percent change in the mean response due to a change in the mean of the random parameter taken as one percent of the standard deviation of this parameter, assuming this change to be equally likely for all random parameters. It is observed that these normalized sensitivities increase in absolute value for increasing load level $P_{tot}$, except the normalized sensitivity to $\varepsilon_{c,\,cover}$, which is first positive and relatively large for $P_{tot} = 300kN$, decreases in absolute value for $P_{tot} = 450kN$ and becomes negative for $P_{tot} = 600kN$. Table 5.2 gives also the specific relative contributions (or marginal contri-

butions) to the variance $\sigma^2_{u_{x3}}$ of $u_{x3}$ of each of the material random parameters, expressed as per cent of $\sigma^2_{u_{x3}}$ for different load levels. These relative contributions to the variance can be used as measures of relative importance in a probabilistic sense of the various parameters in regards to the response quantity of interest. In this case, it is noted that the most important parameter in the probabilistic sense is $f_{c,\,cover}$ for $P_{tot} = 300kN$ and $P_{tot} = 450kN$, while $f_{c,\,core}$ becomes predominant for $P_{tot} = 600kN$. The steel material parameters $f_y$ and E are found to be relatively less important in the probabilistic sense than in the deterministic sense (for which the relative importance is given by the absolute value of the sensitivities normalized in a deterministic sense), since their coefficients of variation are relatively small compared to other parameters. Note that for equal coefficients of variation of all random parameters, the order in terms of relative importance of these parameters in the deterministic and probabilistic sense are identical. Table 5.3 provides the contributions to the variance $\sigma^2_{u_{x3}}$ of $u_{x3}$ due to the cross-terms (for all pairs of correlated parameters) expressed as per cent of $\sigma^2_{u_{x3}}$ for different load levels. These normalized (dimensionless) cross-term contributions grow for increasing load level $P_{tot}$ and are of magnitude comparable or even larger than the marginal contributions of the random parameters to the variance of the response given in Table 5.2. In particular, the correlation between the parameters $f_{c,\,core}$ and $f_{c,\,cover}$ provides the highest contribution to the variance $\sigma^2_{u_{x3}}$ of $u_{x3}$ for the load level $P_{tot} = 600kN$.

**Table 5.3 Contribution (%) of the cross-correlation terms to the variance of the response quantity $u_{3x}$ (three-story building)**

| $P_{tot}$ [kN] | | 300 | 450 | 600 |
|---|---|---|---|---|
| $\varepsilon_{c,core}$ | $\varepsilon_{cu,core}$ | 0 | 0 | -0.04 |
| $\varepsilon_{c,core}$ | $\varepsilon_{c,cover}$ | 16.36 | 12.77 | -1.90 |
| $\varepsilon_{c,core}$ | $\varepsilon_{cu,cover}$ | 0 | -0.21 | -10.84 |
| $f_{c,core}$ | $f_{cu,core}$ | 0 | 0 | 0.12 |
| $f_{c,core}$ | $f_{c,cover}$ | 21.75 | 28.22 | 36.70 |
| $\varepsilon_{cu,core}$ | $\varepsilon_{c,cover}$ | 0 | 0 | <0.01 |
| $\varepsilon_{cu,core}$ | $\varepsilon_{cu,cover}$ | 0 | 0 | 0.03 |
| $f_{cu,core}$ | $f_{c,cover}$ | 0 | 0 | 0.06 |
| $\varepsilon_{c,cover}$ | $\varepsilon_{cu,cover}$ | 0 | -0.28 | 1.41 |

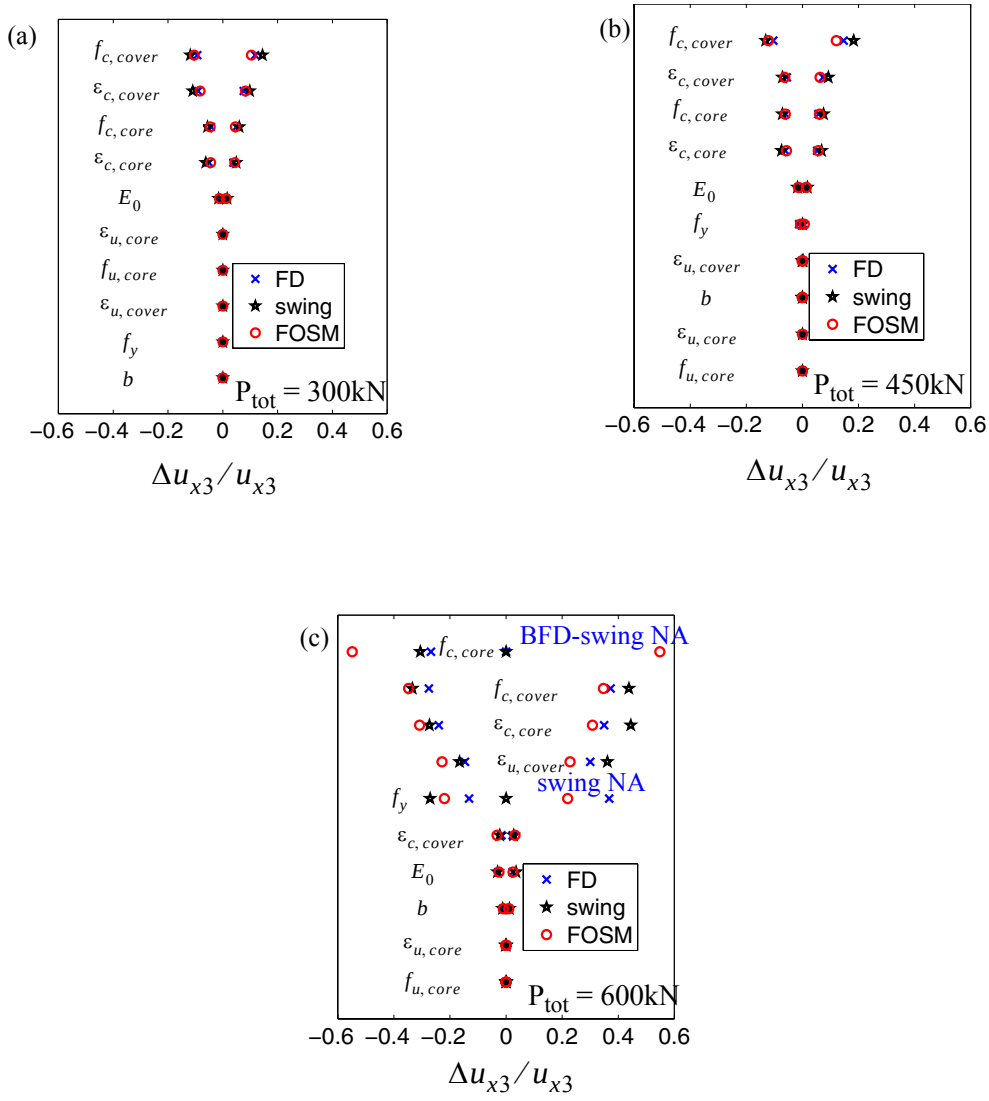


**Figure 5.6 Tornado diagrams for the three-story R/C building: (a)** $P_{tot} = 300kN$**, (b)** $P_{tot} = 450kN$**, and (c)** $P_{tot} = 600kN$

Figure 5.6 compares results for evaluating the relative importance and effects on the structural response $u_{x3}$ of the randomness of the material parameters for different load lev-

els by using the tornado diagrams. In particular, the estimate of the relative change in the response (taken as the change in the response normalized with the mean value of the response) due to a variation of ±1 standard deviation of each parameter considered one at the time is computed by FOSM and by FFD and BFD with changes in the parameters equal to ±1 standard deviation of the parameter considered, respectively. The response change are computed as follows

$$(\Delta u_{x3})_{DDM,\,i} = \pm \frac{\partial u_{x3}}{\partial \theta_i}\bigg|_{\boldsymbol{\vartheta} = \boldsymbol{\mu}_{\boldsymbol{\vartheta}}} \sigma_{\theta_i}; \quad \mathrm{i} = 1, ..., 10 \tag{5.7}$$

$$(\Delta u_{x3})_{FD,\,i} = u_{x3}(\boldsymbol{\mu}_{\boldsymbol{\vartheta}} \pm \boldsymbol{I}^{(i)} \boldsymbol{\sigma}_{\boldsymbol{\vartheta}}) - u_{x3}(\boldsymbol{\mu}_{\boldsymbol{\vartheta}}); \quad \mathrm{i} = 1, ..., 10 \tag{5.8}$$

where $\boldsymbol{I}^{(i)}$ is a Boolean vector of length equal to the number of parameters with 1 in the i-th position and 0's elsewhere and $\boldsymbol{\sigma}_{\boldsymbol{\vartheta}}$ is the vector collecting the standard deviation of the random parameters. The two tornado diagrams corresponding to $P_{tot} = 300kN$ and $P_{tot} = 450kN$, respectively, show that, for low-to-moderate non-linearities in the response, FOSM estimates of the response variability are in good agreement with the ones obtained through direct simulation using finite difference (FD). Furthermore, in the same range of non-linearities, the response variability due to the variation of ±1 standard deviation of each parameter is moderate. For large non-linearities ($P_{tot} = 600kN$), larger differences occur between FOSM and FD results, in particular for parameters to which the response is more sensitive, such as the core and cover concrete parameters. For these parameters, the FOSM estimate of the variation of the response due to the variation of ±1 standard deviation of each parameter is very large (more than 50% for $f_{c,\,core}$), while the

same estimate via FD provides lower values. For the parameter $f_{c,\,core}$, which is the parameter to which the response is more sensitive at load level $P_{tot} = 600kN$, the BFD analysis does not converge and the corresponding finite element models reaches failure due to near singularity of the structure stiffness matrix at the load level $P_{tot,\,fail} = 582kN$. This result is denoted in Figure 5.6 (c) as 'BFD NA'. In order to generate the tornado diagrams of Figure 5.6 using FD analysis, two additional non-linear finite element pushover analyses are required for each random parameter considered. On the other hand, the tornado diagrams using FOSM results are obtained at insignificant additional computational cost after performing the FOSM analysis. In addition, tornado diagrams using FD do not provide any information about the effects of correlation between couples of random parameters. In contrast with this, FOSM analysis provides information about the dependency of the response variance due to the correlation between parameters, as shown in Table 5.3. The tornado diagrams given in Figure 5.6 plot also the swing of the response quantity $u_{x3}$ due to the variability of each material parameter. The computed swings provide consistent information in terms of relative importance ranking of the material parameters to the results obtained through FOSM analysis. The only exception is at the load level $P_{tot} = 600kN$ for parameter $f_y$, which importance is underestimate by FOSM. In fact, for the lowest values of $f_y$, the structural system reaches failure at load levels lower than $P_{tot} = 600kN$ (represented in Fig. 6(c) with the note 'swing NA'), showing that the relation between the response quantity $u_{x3}$ and the parameter $f_y$ is strongly non-linear.

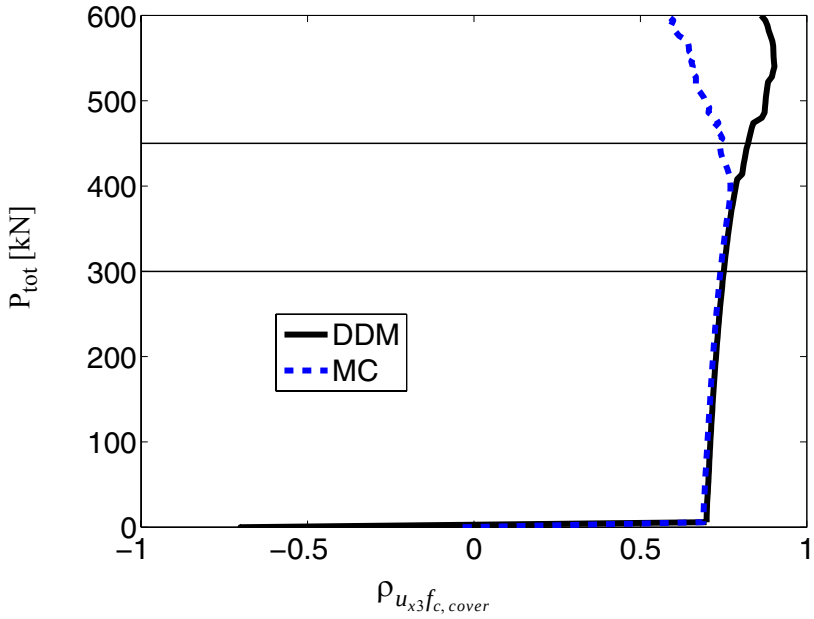


**Figure 5.7 Correlation of response quantity $u_{3x}$ with material parameter $f_{c,cover}$ for the three-story R/C building**

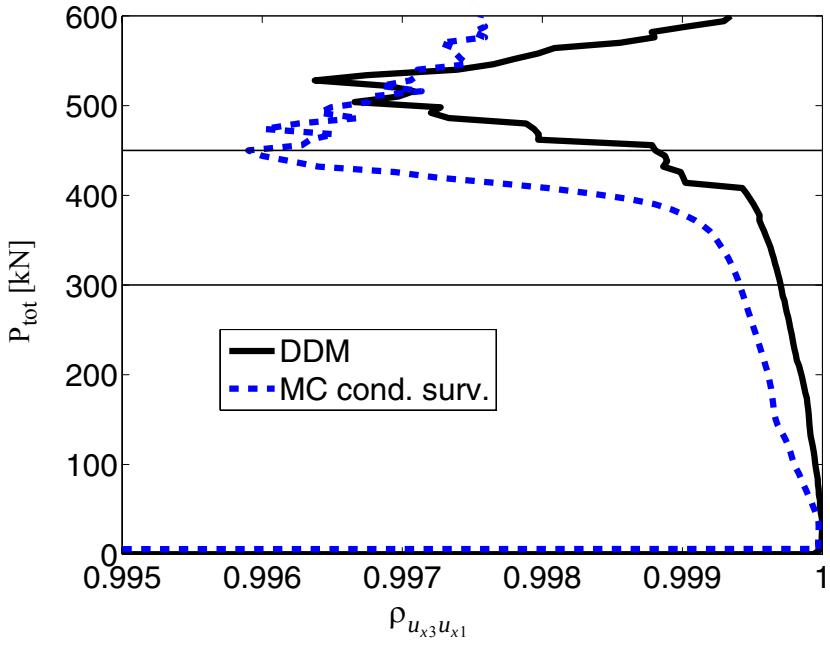


**Figure 5.8 Correlation of response quantities $u_{3x}$ and $u_{1x}$ for the three-story R/C building**

FOSM analysis provides additional information about correlation between different response quantities and between response quantities and random material parameters. As examples, Figures 5.7 and 5.8 compare the correlation coefficient between the response quantity $u_{x3}$ and the material parameter $f_{c,\,cover}$ and between the response quantities $u_{x3}$ and $u_{x1}$, respectively, computed by FOSM analysis and by MCS analysis. The results from the two different methods show good agreement for low-to-moderate non-linearities in the response behavior. Notice that for load levels above $P_{tot} = 450kN$, the MCS results used to compute the correlation coefficient between the response quantities $u_{x3}$ and $u_{x1}$ are conditional to the survival of the structure up to the corresponding load level and, thus, for

this specific case, the comparison between FOSM and MCS results is not very meaningful for $P_{tot} \geq 450kN$. On the other hand, computing the correlation coefficient from unconditional MCS results would give completely arbitrary results, since the value of the displacement $u_{x1}$ after failure is achieved is not uniquely defined.

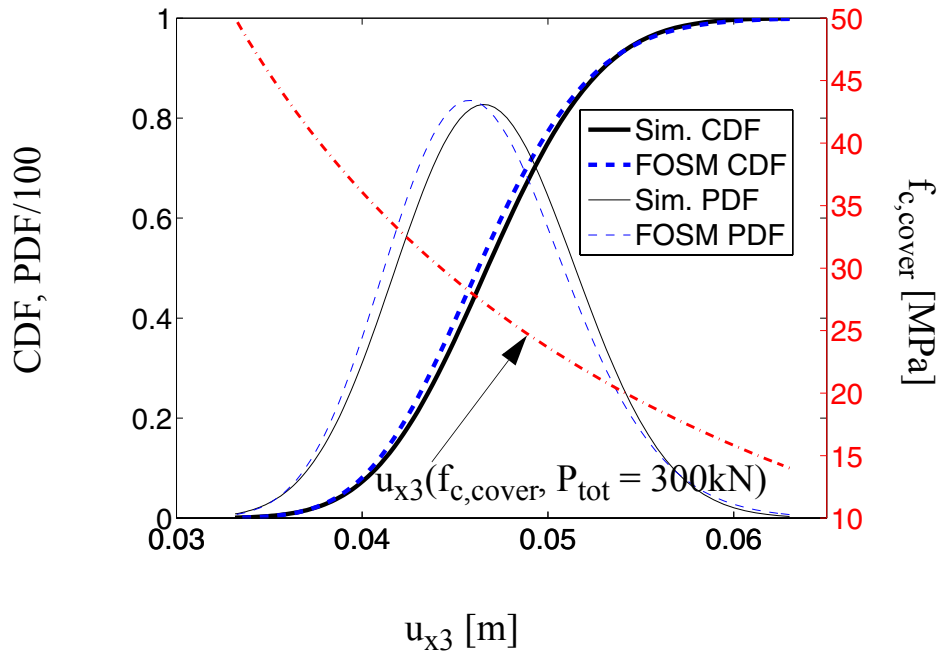


**Figure 5.9 CDF, PDF and relation of the response $u_{3x}$ of the three-story R/C building as function of fc,cover for $P_{tot}$ = 300kN**

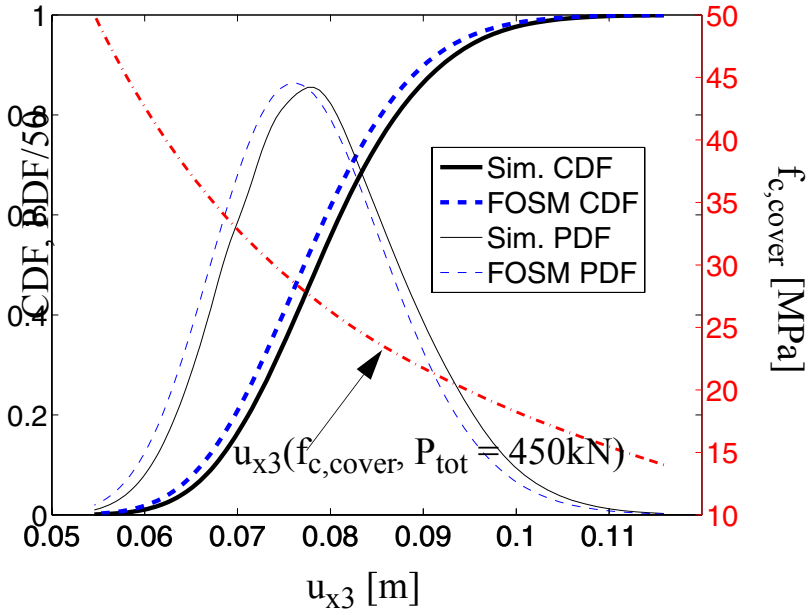


**Figure 5.10 CDF, PDF and relation of the response $u_{3x}$ of the three-story R/C building as function of fc,cover for $P_{tot}$ = 450kN**

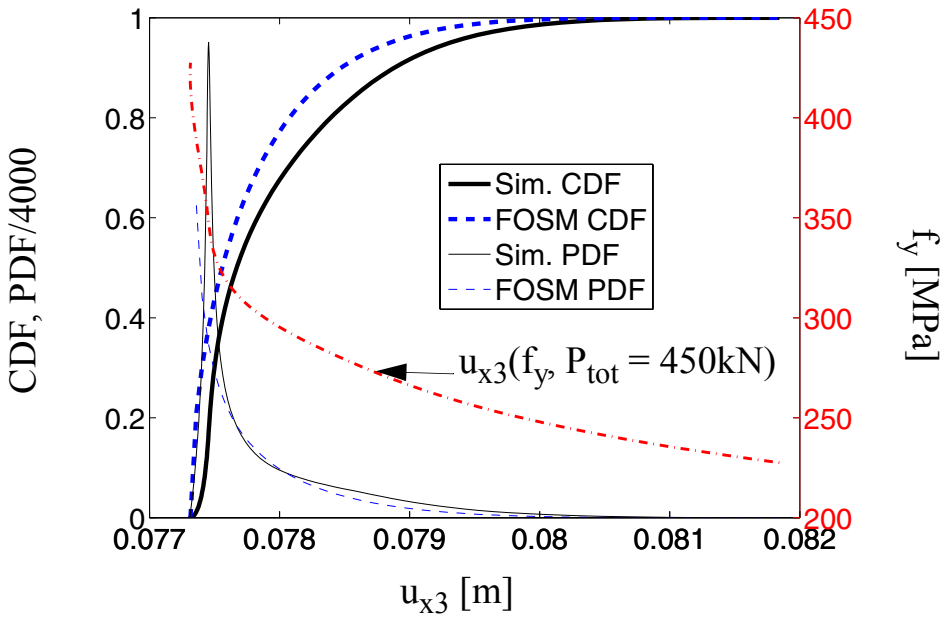


**Figure 5.11 CDF, PDF and relation of the response $u_{3x}$ of the three-story R/C building as function of $f_y$ for $P_{tot} = 450kN$**

Figures 5.9 through 5.11 show some results from the simplified procedure proposed to approximate the probability distributions of the response quantity considered as function of the modeling parameters considered as random one at the time. In Figures 5.9 and 5.10, the PDFs (scaled by a factor 100 and 50, respectively) and CDFs of the displacement $u_{x3}$ for $P_{tot} = 300kN$ and $P_{tot} = 450kN$, respectively, obtained by the proposed approximate procedure considering as variable the parameter $f_{c,\,cover}$, are compared with the corresponding quantities obtained by simulation. In the same Figures, the relations between $u_{x3}$ and $f_{c,\,cover}$ are also plotted. Figure 5.11 shows the PDFs (scaled by a factor 4000) and CDFs of the displacement $u_{x3}$ for $P_{tot} = 450kN$ obtained by the proposed approximate

procedure considering as variable the parameter $f_y$ are compared with the corresponding quantities obtained by simulation. In addition, the relation between $u_{x3}$ and $f_y$ is also plotted. The response probability distributions obtained by simulation are generated by repeating the non-linear finite element pushover analysis for 20 different values of the parameter considered. The response probability distributions obtained by the proposed simplified procedure are generated at a negligible additional computational cost for the parameter $f_{c,\,cover}$, which follows a lognormal distribution completely described by mean and standard deviation, while, for parameter $f_y$, two additional non-linear finite element analyses (corresponding to the minimum and maximum values of the parameter) are required to determine the corresponding beta distribution. From the results presented in Figures 5.9 through 5.11 and from results corresponding to other random material parameters not presented herein for space limitation, it is found that the proposed simplified procedure can provide approximate probability distributions which are in good agreement with the ones obtained through simulation for low-to-moderate non-linearities in the response at a very low computational cost. It is also found that, for large non-linearities as the ones encountered at the load level $P_{tot} = 600kN$, the approximate probability distributions could compare very poorly with the distributions obtained through direct simulation.

### 5.4.2 Two-Dimensional SFSI System

The first application example consists of a two-dimensional Soil-Foundation-Structure Interaction (SFSI) system, a model of which is shown in Figure 5.12. The structure is a two-storey two-bay reinforced concrete frame with section properties given in Figure

5.12. The foundations consist of reinforced concrete squat footings at the bottom of each column. The soil is a layered clay, with stiffness properties varying along the depth.

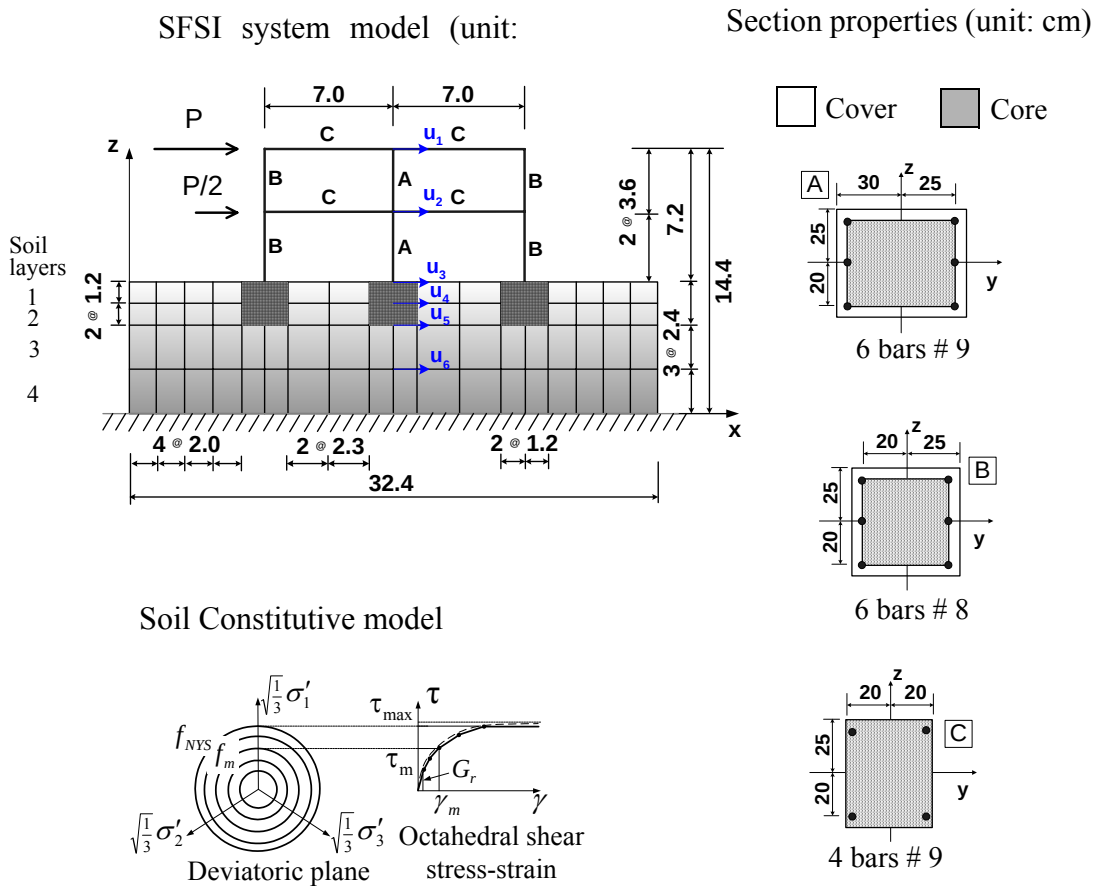


**Figure 5.12 2-D model of SFSI system: geometry, section properties and soil**

The frame structure of this SFSI system is modeled by using displacement-based Euler-Bernoulli frame elements with distributed plasticity, each with four Gauss-Legendre integration points. Section stress resultants at the integration points are computed by discretizing the frame sections by layers. Foundation footings and soil layers are modeled through isoparametric four-node quadrilateral finite elements with bilinear displacement

interpolation. The soil mesh is shown in Figure 5.12. The constitutive behavior of the steel reinforcement is modeled by using a one-dimensional $J_2$ plasticity model with both kinematic and isotropic linear hardening (Conte et al. 2003). The concrete is modeled by using a Kent-Scott-Park model with zero tension stiffening (Scott et al 1982). Different material parameters are used for confined (core) and unconfined (cover) concrete in the columns. The soil is modeled by using a pressure-independent multi-yield surface material model (Elgamal et al. 2003), specialized for plane strain analysis (Figure 5.12). Different material parameters are used for each of the four layers considered.

Similarly to the previous application example, ten material constitutive parameters are used to characterize the various structural materials involved in the structure, namely four parameters for the confined concrete ($f_{c,\,core}$, $\varepsilon_{c,\,core}$, $f_{cu,\,core}$, $\varepsilon_{cu,\,core}$), three parameters for the unconfined concrete ($f_{c,\,cover}$, $\varepsilon_{c,\,cover}$, $\varepsilon_{cu,\,cover}$) with the fourth parameter $f_{cu,\,cover} = 0MPa$, and three parameters for the reinforcement steel ($f_y$, $E_0$, $H_{kin}$: kinematic hardening modulus) with the fourth parameter $H_{iso}$ = 0MPa (isotropic hardening modulus). Notice that, assuming $H_{iso}$ = 0MPa, the one-dimensional $J_2$ plasticity model reduces to the bilinear inelastic model used in the first application example. These material parameters are assumed to follow lognormal distributions with parameters given in Table 5.4.

**Table 5.4 Material parameters (with lognormal distributions) for the two-dimensional SFSI system**

| Structural material parameters | | | Soil material parameters | | |
|---|---|---|---|---|---|
| RV [unit] | Mean | C.O.V. [%] | RV [unit] | Mean | C.O.V. [%] |
| $f_{c,core}$ [MPa] | 34.49 | 20 | $\tau_1$ [kPa] | 33 | 25 |
| $\varepsilon_{c,core}$ [-] | 0.004 | 20 | $G_1$ [kPa] | 54450 | 30 |
| $f_{cu,core}$ [MPa] | 20.69 | 20 | $\tau_2$ [kPa] | 50 | 25 |
| $\varepsilon_{cu,core}$ [-] | 0.014 | 20 | $G_2$ [kPa] | 77600 | 30 |
| $f_{c,cover}$ [MPa] | 27.59 | 20 | $\tau_3$ [kPa] | 75 | 25 |
| $\varepsilon_{c,cover}$ [-] | 0.002 | 20 | $G_3$ [kPa] | 121000 | 30 |
| $\varepsilon_{cu,cover}$ [-] | 0.008 | 20 | $\tau_4$ [kPa] | 100 | 25 |
| $f_y$ [MPa] | 248.20 | 10.6 | $G_4$ [kPa] | 150000 | 30 |
| $E_0$ [MPa] | 200000 | 3.3 | - | - | - |
| $H_{kin}$ [MPa] | 1612.9 | 20 | - | - | - |

The correlation coefficients between the couples of parameters are the same as in the first application example. In addition to the material parameters describing the structural materials, eight material parameters are used to model the four soil layers, i.e., the cohesion, $\tau_i$, and the initial shear modulus, $G_i$, with i = 1, 2, 3, 4. These material parameters are assumed to follow lognormal distributions with parameters given in Table 5.4. The correlation coefficients between the parameters are assumed as follows: $\rho = 0.4$ for (1) $\tau_1$ and $\tau_2$, (2) $\tau_1$ and $G_1$, (3) $\tau_2$ and $\tau_3$, (4) $\tau_2$ and $G_2$, (5) $\tau_3$ and $\tau_4$, (6) $\tau_3$ and $G_3$, (7) $\tau_4$

and $G_4$; and $\rho = 0.0$ for all other pairs of parameters. Also in this case, these correlation coefficients are chosen based on engineering judgement, since to the authors' knowledge, precise values of correlation coefficients are not available in the literature.

Similarly to the first application example, after static application of the gravity loads, the structure is subjected to a quasi-static pushover analysis, in which an upper triangular distribution of horizontal forces is applied at the floor levels (see Figure 5.12). The total base shear force, $P_{tot} = 1.5P$, is considered as deterministic and is assumed to increase linearly during the analysis from 0kN to 750kN. In this analysis, only material non-linearities are taken into account. A response analysis and response sensitivity analysis using the DDM are first performed at the mean values $\boldsymbol{\mu}_{\boldsymbol{\vartheta}}$ of the random parameters $\boldsymbol{\vartheta}$. A MCS analysis based on 1000 realizations is then carried out based on the Nataf model used as joint PDF of the random parameters $\boldsymbol{\vartheta}$. Finally, gross sensitivities of the response quantities **r** are evaluated through FFD and BFD analysis, perturbing one material parameter at a time by plus and minus one standard deviation, respectively. Finite element response, response sensitivity and probabilistic response computations are performed using the finite element analysis framework OpenSees (Mazzoni et al. 2005), in which the constitutive model for the soil was augmented for response sensitivity analysis (Gu et al., 2006a) and the response sensitivity algorithm for imposing multipoint constraints (in this case required for connecting the frame elements used to describe the structure with the quadrilateral elements employed to model the squat footings) was implemented (Gu et al., 2006b). The results of the analysis are presented in a similar way as for the first application example.

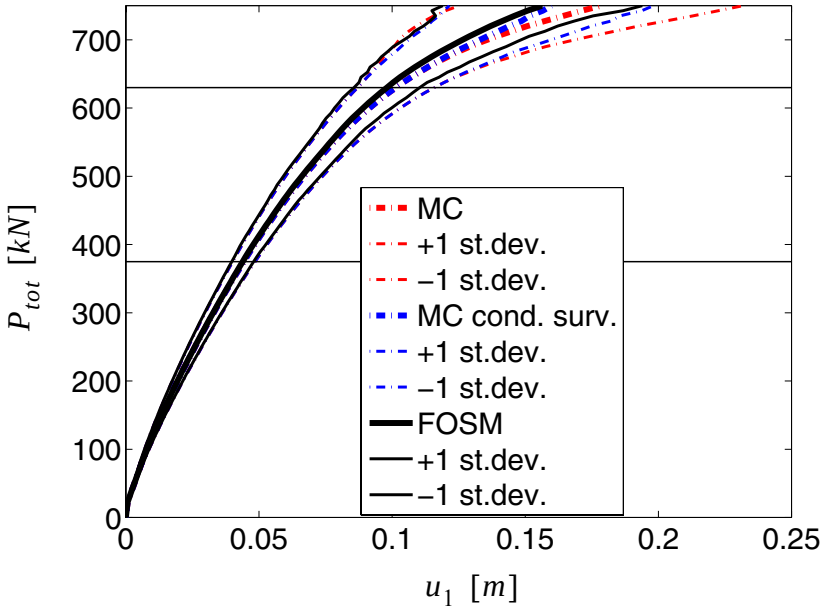


**Figure 5.13 Probabilistic response of the two-dimensional SFSI system**

Figure 5.13 shows a comparison of estimates of the mean and mean ±1 standard deviation of the force - response curve for the horizontal roof displacement at the top of the central column, $u_1$, obtained through FOSM analysis using the DDM to compute the response sensitivities and MCS, respectively. Figure 5.14 displays the standard deviation estimates of $u_1$ obtained through MCS and FOSM analysis using different methods to compute the response sensitivities. For the given structure subjected to quasi-static push-over, the condition of failure is defined as (near) singularity of the structure stiffness matrix or $u_{1,fail}$ = 0.28m (i.e., roof displacement over roof height ratio equal to 3.9%), whichever happens first. It is found that, until the load level $P_{tot} = 630kN$ is reached, no failure case is observed in the MCS performed, while nearly one quarter of the Monte

Carlo realizations reach failure below load level $P_{tot} = 750kN$. In Figs. 13 and 14, horizontal dashed lines mark the load levels $P_{tot} = 375kN$ and $P_{tot} = 630kN$, which denote the load levels below which the response is almost linear and no failure occurs, respectively. In Figure 5.13 and Figure 5.14, for load levels above $P_{tot} = 630kN$, both the unconditional (denoted as "MC") and conditional to survival ("MCS cond. surv.") MCS estimates of the mean value and standard deviation of $u_1$ are plotted. The results obtained using FOSM and MCS are qualitatively very similar to the ones presented for the first application example.

Figure 5.13 shows that the FOSM approximation is in excellent agreement with the MCS results when the structural response is nearly linear (for load levels below $P_{tot} = 375kN$), while the FOSM results slightly underestimate the MCS results when the structure undergoes low-to-moderate non-linear inelastic deformations (for load levels between $P_{tot} = 375kN$ and $P_{tot} = 630kN$), with differences increasing with increasing non-linearities. In this case, the maximum level of non-linearities reached in the analysis is less pronounced at the global level than in the previous example and the differences between FOSM analysis and MCS analysis are relatively small also for load levels ($P_{tot} \geq 630kN$) for which MCS realizations start to reach failure. It can be concluded that, also for the second application example considered in this chapter, FOSM analysis provides, at very low computational cost, very good estimates of the mean of response quantities for low-to-moderate levels of material non-linearity in the structural response.

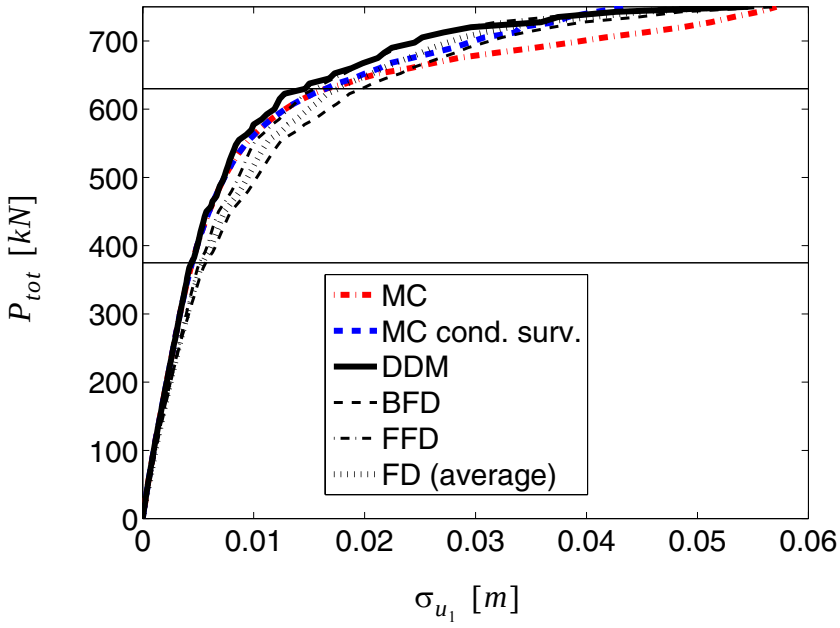


**Figure 5.14 Standard deviation of the two-dimensional SFSI system**

The different techniques employed for computing response sensitivities used in FOSM and shown in Figure 5.14 are: (1) DDM; (2) BFD analysis with perturbations $\Delta\theta_i = -\sigma_i$ $(i = 1, 2, \ldots, 18)$; (3) FFD analysis with perturbations $\Delta\theta_i = \sigma_i$ $(i = 1, 2, \ldots, 18)$; and (4) FD average of gross sensitivities computed using BFD and FFD. It is observed that these four methods produce similar results, but in this case the estimates of the standard deviation of $u_1$ obtained using BFD, FFD and FD average slightly overestimate the standard deviation computed through MCS for load levels below $P_{tot} \geq 665kN$, while the DDM estimate is extremely close to the MCS value for load levels up to $P_{tot} \geq 510kN$. For higher load levels, all the four sensitivity-based methods underestimate the MCS results.

As for the mean of the response, FOSM analysis using DDM provides, at very low computational cost, very good estimates of the standard deviation of response quantities for low-to-moderate levels of material non-linearity in the structural response also in the case of probabilistic pushover analysis of SFSI systems.

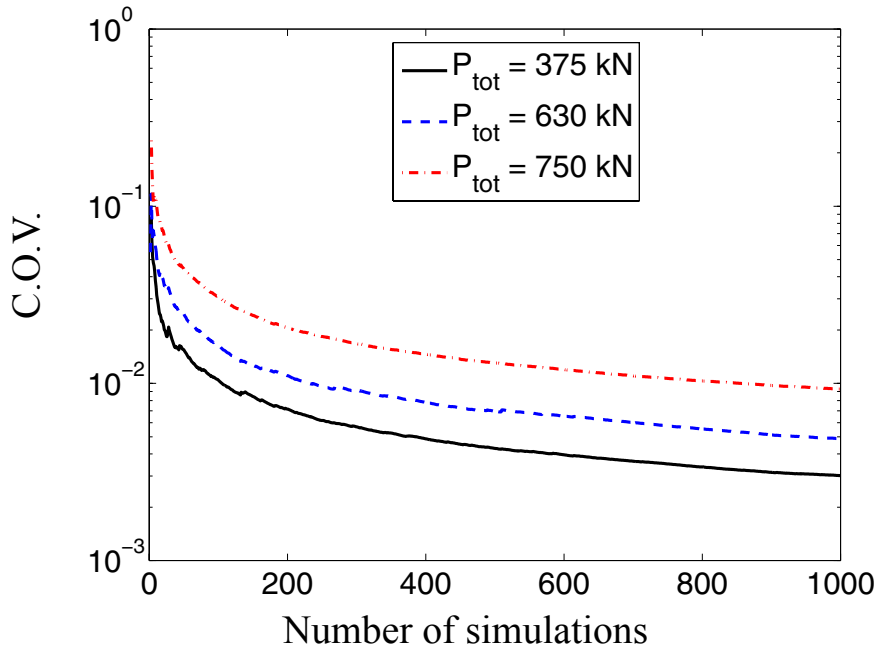


**Figure 5.15 Coefficient of variation of the mean response at different load levels computed using MCS for the two-dimensional SFSI system**

Figure 5.15 plots, on a semilogarithmic scale, the coefficient of variation (C.O.V.) of the mean of the response quantity $u_1$ for different load levels as a function of the number of simulations performed. At 1000 simulations, the C.O.V. for $P_{tot} = 375kN, 630kN, 750kN$ are 0.20%, 0.49% and 0.91%, respectively, and thus the MCS results are very reliable. In this case, the number of simulations required to obtain a

C.O.V. lower than 10% are less than 10 for $P_{tot} = 375kN$ and $P_{tot} = 630kN$, and about 50 for $P_{tot} = 750kN$, showing a faster convergence than in the previous application example.

**Table 5.5 Normalized sensitivities computed by DDM of $u_1$ to material parameters and their relative contribution to variance of $u_1$ at different load levels (two-dimensional SFSI system)**

| | Deterministic sense | | | Probabilistic sense | | | $\Delta(\sigma^2_{u_{x3}})/\sigma^2_{u_{x3}}$ [%] | | |
|---|---|---|---|---|---|---|---|---|---|
| $P_{tot}$ [kN] | 375 | 630 | 750 | 375 | 630 | 750 | 375 | 630 | 750 |
| $f_{c,core}$ | -0.0394 | -0.0542 | -0.1388 | -0.0079 | -0.0108 | -0.0278 | 0.67 | 0.56 | 0.69 |
| $\varepsilon_{c,core}$ | 0.0373 | 0.0478 | 0.1075 | 0.0075 | 0.0096 | 0.0215 | 0.60 | 0.43 | 0.41 |
| $f_{cu,core}$ | 0 | 0 | 0 | 0 | 0 | 0 | 0 | 0 | 0 |
| $\varepsilon_{cu,core}$ | 0 | 0 | 0 | 0 | 0 | 0 | 0 | 0 | 0 |
| $f_{c,cover}$ | -0.2801 | -0.3929 | -0.9425 | -0.0560 | -0.0786 | -0.1885 | 33.93 | 29.22 | 31.65 |
| $\varepsilon_{c,cover}$ | 0.2401 | 0.2492 | 0.2145 | 0.0480 | 0.0498 | 0.0429 | 24.93 | 11.76 | 1.64 |
| $\varepsilon_{cu,cover}$ | 0 | 0 | -0.0270 | 0 | 0 | -0.0054 | 0 | 0 | 0.03 |
| $f_y$ | -0.0428 | -0.6718 | -2.2599 | -0.0045 | -0.0712 | -0.2395 | 0.22 | 24.00 | 51.11 |
| $E_0$ | -0.4616 | -0.3918 | -0.3373 | -0.0152 | -0.0129 | -0.0111 | 2.51 | 0.79 | 0.11 |

**Table 5.5 Normalized sensitivities computed by DDM of $u_1$ to material parameters and their relative contribution to variance of $u_1$ at different load levels (two-dimensional SFSI system)**

| | Deterministic sense | | | Probabilistic sense | | | $\Delta(\sigma^2_{u_{x3}})/\sigma^2_{u_{x3}}$ [%] | | |
|---|---|---|---|---|---|---|---|---|---|
| $P_{tot}$ [kN] | 375 | 630 | 750 | 375 | 630 | 750 | 375 | 630 | 750 |
| $H_{kin}$ | 0 | -0.0026 | -0.0214 | 0 | -0.0005 | -0.0043 | 0 | <0.01 | 0.02 |
| $\tau_1$ | -0.0488 | -0.0765 | -0.0912 | -0.0122 | -0.0191 | -0.0228 | 1.61 | 1.73 | 0.46 |
| $G_1$ | -0.0173 | -0.0128 | -0.0067 | -0.0052 | -0.0038 | -0.0020 | 0.29 | 0.07 | <0.01 |
| $\tau_2$ | -0.0531 | -0.0845 | -0.1006 | -0.0133 | -0.0211 | -0.0252 | 1.90 | 2.11 | 0.56 |
| $G_2$ | -0.0235 | -0.0182 | -0.0120 | -0.0070 | -0.0055 | -0.0036 | 0.54 | 0.14 | 0.01 |
| $\tau_3$ | -0.0874 | -0.1462 | -0.1787 | -0.0218 | -0.0366 | -0.0447 | 5.16 | 6.32 | 1.77 |
| $G_3$ | -0.0490 | -0.0478 | -0.0449 | -0.0147 | -0.0143 | -0.0135 | 2.34 | 0.97 | 0.16 |
| $\tau_4$ | -0.0295 | -0.0645 | -0.0846 | -0.0074 | -0.0161 | -0.0211 | 0.59 | 1.23 | 0.40 |
| $G_4$ | -0.0300 | -0.0360 | -0.0344 | -0.0090 | -0.0108 | -0.0103 | 0.87 | 0.55 | 0.09 |

Table 5.5 provides the sensitivities of $u_1$ to the random material parameters computed at the nominal/mean values of the latter and normalized both in a deterministic sense and probabilistic sense respectively, together with the relative contributions (or marginal contributions) to the variance $\sigma_{u_1}^2$ of $u_1$ of each of the material random parameters, expressed as per cent of $\sigma_{u_1}^2$ for different load levels.

**Table 5.6 Contribution (%) of the cross-correlation terms to the variance of the response quantity $u_1$ (two-dimensional SFSI system)**

| $P_{tot}$ [kN] | | 375 | 630 | 750 |
|---|---|---|---|---|
| $\varepsilon_{c,core}$ | $\varepsilon_{cu,core}$ | 0 | 0 | -0.13 |
| $\varepsilon_{c,core}$ | $\varepsilon_{c,cover}$ | 6.19 | 3.61 | 1.32 |
| $\varepsilon_{c,core}$ | $\varepsilon_{cu,cover}$ | 0 | 0 | 0 |
| $f_{c,core}$ | $f_{cu,core}$ | 0 | 0 | 0 |
| $f_{c,core}$ | $f_{c,cover}$ | 7.63 | 6.45 | 7.46 |
| $\varepsilon_{cu,core}$ | $\varepsilon_{c,cover}$ | 0 | 0 | 0 |
| $\varepsilon_{cu,core}$ | $\varepsilon_{cu,cover}$ | 0 | 0 | 0 |
| $f_{cu,core}$ | $f_{c,cover}$ | 0 | 0 | 0 |
| $\varepsilon_{c,cover}$ | $\varepsilon_{cu,cover}$ | 0 | 0 | -0.33 |
| $\tau_1$ | $\tau_2$ | 1.40 | 0.28 | 0.03 |
| $\tau_1$ | $G_1$ | 0.55 | 1.53 | 0.41 |
| $\tau_2$ | $\tau_3$ | 2.51 | 2.92 | 0.80 |
| $\tau_2$ | $G_2$ | 0.81 | 0.44 | 0.06 |
| $\tau_3$ | $\tau_4$ | 1.40 | 2.23 | 0.67 |
| $\tau_3$ | $G_3$ | 2.78 | 1.98 | 0.42 |

**Table 5.6 Contribution (%) of the cross-correlation terms to the variance of the response quantity $u_1$ (two-dimensional SFSI system)**

| $P_{tot}$ [kN] | | 375 | 630 | 750 |
|---|---|---|---|---|
| $\tau_4$ | $G_4$ | 0.57 | 0.66 | 0.16 |

Table 5.6 shows the contributions to the variance $\sigma_{u_1}^2$ of $u_1$ due to the cross-terms (for all pairs of correlated parameters) expressed as per cent of $\sigma_{u_1}^2$ for different load levels. From Tables 5.5 and 5.6, the following pieces of information can be obtained:

1. The parameters $f_{cu,\,core}$ and $\varepsilon_{cu,\,core}$ do not influence the response, since the core concrete does not reach its peak strength at any load level and in any fiber in which the structure is discretized.
2. The parameter $f_{c,\,cover}$ is the most important for load levels $P_{tot} = 375kN$ and $P_{tot} = 630kN$ and is the second most important parameter for $P_{tot} = 750kN$. The parameter $\varepsilon_{c,\,cover}$ is very important at lower load levels and its importance decreases sensibly for increasing load levels. In fact, at lower load levels, the parameter $\varepsilon_{c,\,cover}$ influences the response mainly through its effects on the stiffness of the cover concrete (i.e., higher values of $\varepsilon_{c,\,cover}$ imply lower stiffness of the cover concrete for a fixed value of $f_{c,\,cover}$ and thus higher displacements), while at higher load levels, when the fibers of cover concrete start to reach their peak strength, higher values of $\varepsilon_{c,\,cover}$ have the effects also of reducing the number of fibers which reach the peak strength for a given load level, thus reducing the displacement. This shows that the structural

response behavior strongly depends on the cover concrete material parameters, in particular for low-to-moderate load levels.

3. The parameter $f_y$ increases its importance for increasing load levels. Its effects are almost negligible for $P_{tot} = 375kN$, when very few steel reinforcement fibers have reached yielding, while $f_y$ is the second and first most important parameter for load levels $P_{tot} = 630kN$ and $P_{tot} = 750kN$, respectively. In particular, for $P_{tot} = 750kN$, $f_y$ contributes with about 51% of the variance of the structural response $u_1$.
4. The variability of the soil properties has a small effect on the variability of the response $u_1$ and, in general, this effect decreases for increasing load levels. The only parameter which effect is significant at all load levels is the parameter $\tau_3$, which influences the sliding of the foundation over the soil layer on which they are posed.
5. The effects due to modeling parameter correlation are small and, in general, they decrease for increasing load levels. The only significant effects are due to the correlation between $\varepsilon_{c,\,core}$ and $\varepsilon_{c,\,cover}$ and between $f_{c,\,core}$ and $f_{c,\,cover}$.

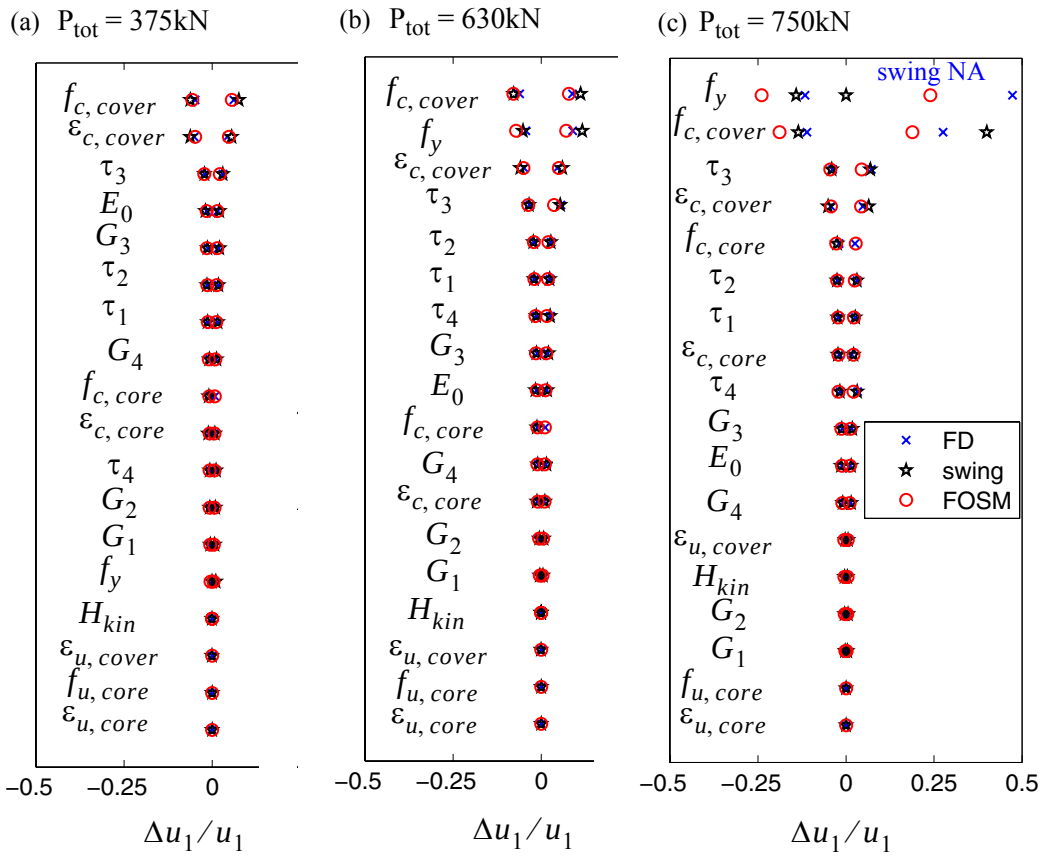


**Figure 5.16 Tornado diagrams for the two-dimensional SFSI system: (a)** $P_{tot} = 375kN$**, (b)** $P_{tot} = 630kN$**, and (c)** $P_{tot} = 750kN$**.**

Figure 5.16 provides the tornado diagrams referred to the structural response $u_1$ for different load levels. These tornado diagrams reproduce the information about the relative importance of the several random material parameters and also show that at higher load levels the variability of the response increases significantly. In fact, varying the most important parameters of ±1 standard deviation produce a variation in the response of less than 10%, about 10% and almost 50% for load levels $P_{tot} = 375kN$, 630kN and 750kN,

respectively. Results obtained through FOSM compare favorably with the one obtained by BFD and FFD for $P_{tot} = 375kN$ and $P_{tot} = 630kN$, while differences are evident for $P_{tot} = 750kN$, in particular because of the strong non-symmetry of the BFD and FFD responses with respect to the mean response which cannot be captured by FOSM. These tornado diagrams plot also the swings of the response quantity $u_1$ due to the variability of each parameter when all the others are kept constant at their mean values. The importance ranking of the parameters obtained considering the swings matches very well the one obtained by FOSM analysis at all the load levels considered.

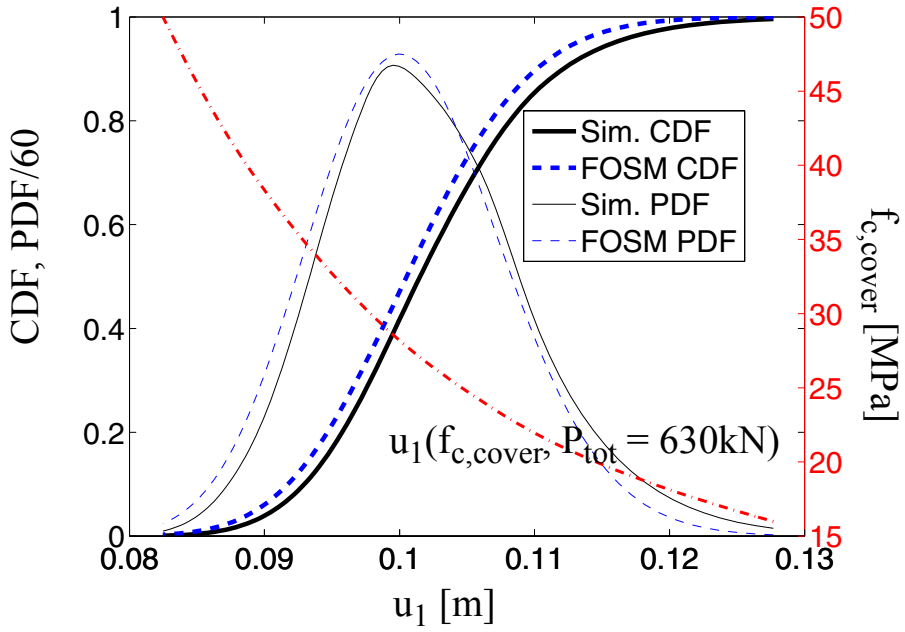


**Figure 5.17 CDF, PDF and relation of the response $u_1$ of the three-story R/C building as function of $f_{c,cover}$ for** $P_{tot} = 630kN$

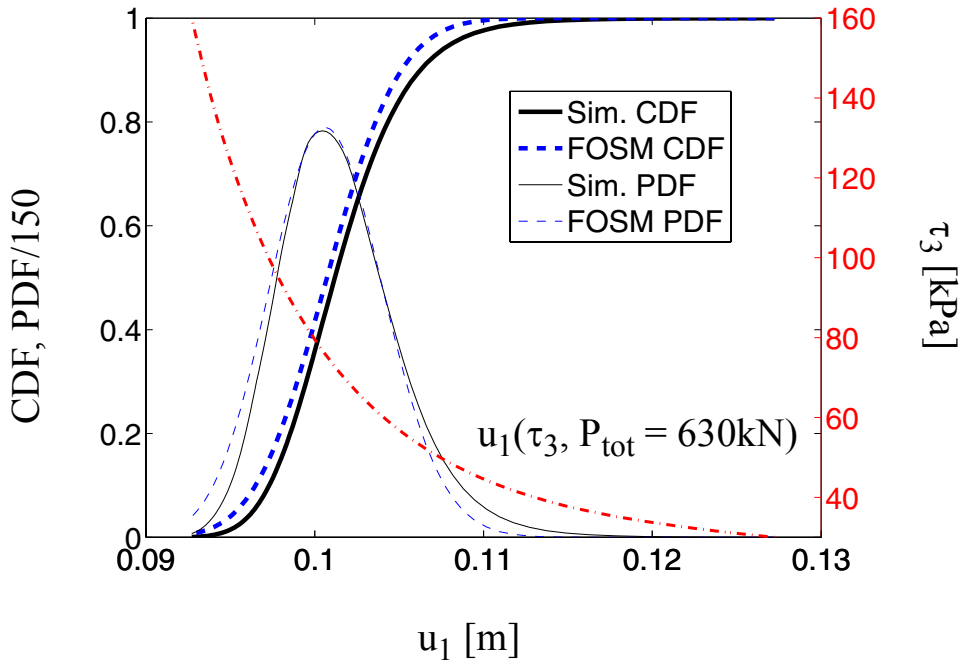


**Figure 5.18 CDF, PDF and relation of the response $u_1$ of the three-story R/C building as function of $\tau_3$ for $P_{tot} = 630kN$**

Figures 5.17 and 5.18 compare the approximate probability distributions of $u_1$ as function of $f_{c,\,cover}$ and $\tau_3$, respectively, for load level $P_{tot} = 630kN$ with the corresponding distributions obtained via direct simulation. In these figures, PDFs and CDFs are plotted together with the relation between the response and the parameter considered, when all the other parameters are kept fixed with values equal to the mean values. It is found that the proposed procedure can provide probability distributions in reasonable agreement with the ones computed by direct simulation at very small computational cost also for SFSI systems for low-to-moderate response non-linearities. For increasing non-linearities, the

agreement between probability distributions obtained through the proposed approximation and direct simulations degrades rapidly.

### 5.4.3 Conclusions

This chapter presents a comparison between probabilistic response analysis results obtained through Monte Carlo simulation and Mean Centered First-Order Second-Moment (FOSM) analysis using non-linear finite element response and response sensitivity analyses of a reinforced concrete building subjected to quasi-static pushover. The effects on FOSM analysis results of using different methods for computing response sensitivities are also investigated. It is found that FOSM approximation using the Direct Differentiation Method for computing response sensitivities provides, at very low computational cost, very good estimates of the mean and standard deviation of the response quantity considered herein for low-to-moderate levels of material non-linearity in the response of structural systems and SFSI systems subjected to quasi-static pushover analysis. Furthermore, the relative importance (in both the deterministic and probabilistic sense) of the material parameters on the structural response is obtained as by-product of a FOSM analysis at negligible additional computational cost. In addition, FOSM results can be used to obtain approximate probability distributions of response quantities of interest as function of a single random parameters which are in reasonable agreement (in the low-to-moderate range of non-linearities in the response) with the corresponding distributions obtained through direct simulation at a much higher computational cost. For high non-linearities in the structural system considered, agreement between FOSM and MCS results deteriorates but qualitative information, such as importance ranking of the material parameters in

influencing the response variability, can still be obtained. It is noteworthy that in cases where non-convergence of the simulations occur before the failure threshold of the response is reached, estimating of mean and variance of the response using MCS can lead to some difficulties and is not uniquely defined.

It can be concluded that FOSM analysis provides a large amount of probabilistic information at a very low computational cost and can provide satisfactory accuracy for probabilistic analysis of structural and SFSI systems subjected to quasi-static pushover analysis, provided that the level of non-linearities exhibited by the system considered are low-to-moderate. For large non-linearities, FOSM can be used effectively to obtain qualitative information on the importance ranking of modeling parameters on the system response.

## 5.5 APPENDIX A

The problem of finding the optimal point to which linearize the (scalar) response function r for obtaining the best estimate of the mean response can be formulated as follows

$$min\left|\int_{\boldsymbol{\Theta}}[r(\boldsymbol{\vartheta}_0)+\nabla_{\boldsymbol{\vartheta}}r\big|_{\boldsymbol{\vartheta}=\boldsymbol{\vartheta}_0}(\boldsymbol{\vartheta}-\boldsymbol{\vartheta}_0)-r(\boldsymbol{\vartheta})]p_{\boldsymbol{\Theta}}(\boldsymbol{\vartheta})d\boldsymbol{\vartheta}\right| \qquad \text{subject to: } \boldsymbol{\vartheta}_0\in\boldsymbol{\Theta};\ \int_{\boldsymbol{\Theta}}p_{\boldsymbol{\Theta}}(\boldsymbol{\vartheta})d\boldsymbol{\vartheta}=1 \tag{A 1}$$

The objective function $|f(\boldsymbol{\vartheta}_0)|$ can be written as follows

$$\begin{aligned}|f(\boldsymbol{\vartheta}_0)| &= \left|\int_{\boldsymbol{\Theta}}[r(\boldsymbol{\vartheta}_0)+\nabla_{\boldsymbol{\vartheta}}r\big|_{\boldsymbol{\vartheta}=\boldsymbol{\vartheta}_0}(\boldsymbol{\vartheta}-\boldsymbol{\vartheta}_0)-r(\boldsymbol{\vartheta})]p_{\boldsymbol{\Theta}}(\boldsymbol{\vartheta})d\boldsymbol{\vartheta}\right| \\ &= \left|r(\boldsymbol{\vartheta}_0)+\nabla_{\boldsymbol{\vartheta}}r\big|_{\boldsymbol{\vartheta}=\boldsymbol{\vartheta}_0}(\boldsymbol{\mu}_{\boldsymbol{\vartheta}}-\boldsymbol{\vartheta}_0)-\mu_r\right|\end{aligned} \tag{A 2}$$

Imposing the first order optimality conditions, we obtain

$$\begin{aligned} \nabla_{\boldsymbol{\vartheta}_0} f(\boldsymbol{\vartheta}_0) &= \nabla_{\boldsymbol{\vartheta}_0} r(\boldsymbol{\vartheta}_0) + \nabla_{\boldsymbol{\vartheta}_0}(\nabla_{\boldsymbol{\vartheta}} r\big|_{\boldsymbol{\vartheta}=\boldsymbol{\vartheta}_0})(\boldsymbol{\mu}_{\boldsymbol{\vartheta}} - \boldsymbol{\vartheta}_0) - \nabla_{\boldsymbol{\vartheta}} r\big|_{\boldsymbol{\vartheta}=\boldsymbol{\vartheta}_0} \\ &= \boldsymbol{H}_r\big|_{\boldsymbol{\vartheta}=\boldsymbol{\vartheta}_0}(\boldsymbol{\mu}_{\boldsymbol{\vartheta}} - \boldsymbol{\vartheta}_0) = \mathbf{0} \end{aligned} \tag{A 3}$$

which is always satisfied for $\boldsymbol{\vartheta}_0 = \boldsymbol{\mu}_{\boldsymbol{\vartheta}}$.

# CHAPTER 6

# RELIABILITY ANALYSIS FOR STRUCTURAL AND GEOTECHNICAL SYSTEMS

## 6.1 Introduction and Background

### 6.1.1 Classical Time Invariant Reliability Analysis in Performance Based Engineering

Recently, structural reliability methods have been employed in performance-based engineering (PBE) as a powerful tool to estimate the probability for various failure events. “Performance” herein in general denotes the structural response such as first floor drift, the maximum stress or strain in a column, due to design or earthquake loads.

During an earthquake, the structural system usually reaches the nonlinear state before the soil structure systems fails. Typically the nonlinear response can not be obtained as a closed-form solution. Furthermore it is not possible to predict the soil behavior without considering its strong nonlinear nature. The nonlinear FEM is a powerful tool to simulate these nonlinear responses. (Zienkiewicz and Taylor 2000, Hughes 1987, Bathe 1996, Cook et al. 1989). The merging of advanced reliability methods with the state of the art Finite Element Method leads to “Finite Element Reliability Methods“. (Haukaas and Der Kiureghian 2003).

Random variable distribution and correlation coefficient matrix.

In Finite Element Reliability Methods, one important task is to measure the uncertainties in the FE model by defining random variables. The vector of basic random variables (RVs) $\boldsymbol{\theta} = [\theta_1, \theta_2, ..., \theta_n]$ are defined to characterize the state of the computation, e.g., loads and environmental actions, material properties, geometric properties, boundary conditions, model uncertainty parameters.

Every random variable θ has a probability distribution function $f_\theta$ (or marginal pdf, e.g. normal, lognormal, beta distribution, etc.). The relationship between two random variables $\theta_i$ and $\theta_j$ is specified by the correlation coefficient $\rho_{ij,}$, with a value between -1 and 1. $\rho_{ij}$ is defined as

$$\rho_{ij} = \frac{cov[\theta_i, \theta_j]}{\sqrt{var[\theta_i]var[\theta_j]}} \tag{6.1}$$

where the covariance of $\theta_i$ and $\theta_j$ is defined as,

$$cov[\theta_i, \theta_j] = E[(\theta_i - \mu_i)(\theta_j - \mu_j)] \tag{6.2}$$

Here $E[\ ]$ is the expectation, $\mu_i$ is the mean of $\theta_i$.

The variance of $\theta_i$ is

$$var[\theta_i] = E[(\theta_i - \mu_i)^2] = (\sigma_{\theta_i})^2 \tag{6.3}$$

And $\sigma_{\theta_i}$ is the standard deviation of $\theta_i$. It is easy to shown that the covariance matrix $C_\theta = cov[\theta_i, \theta_j]$, correlation coeffcient matrix $R_\theta = [\rho_{ij}]$, and $D_\theta = \begin{bmatrix} \sigma_1 & & & \\ & \sigma_2 & & \\ & & . & \\ & & & \sigma_n \end{bmatrix}$ are related by,

$$C_\theta = D_\theta R_\theta D_\theta \tag{6.4}$$

Performance function g($\theta$) and failure probability

In reliability analysis in PBE, the performance criteria are very important in describing the failure of a structural or geotechnical system. Failure is generally defined as not meeting performance criteria. To define the failure, a *performance function* is defined in terms of engineering demand parameters, damage measures, or decision variables. The performance function is also called the Limit state function (LSF).

Performance functions (limit state functions) for structural components are commonly denoted $g(\boldsymbol{\theta})$, where $\boldsymbol{\theta}$ is the vector of basic random variables. The dependence of $g(\boldsymbol{\theta})$ on $\boldsymbol{\theta}$ is usually implicit through structural response quantities. The function g($\boldsymbol{\theta}$) must be a continuous and differentiable function of $\boldsymbol{\theta}$. The value of the performance function distinguishes the failure state from the safe state by:

$$\begin{aligned} g(\boldsymbol{\theta}) &> 0 \quad \text{safe domain} \\ g(\boldsymbol{\theta}) &= 0 \quad \text{limit state surface} \\ g(\boldsymbol{\theta}) &< 0 \quad \text{failure domain} \end{aligned} \tag{6.5}$$

A general form taken by performance functions is:

$$g(\boldsymbol{\theta}) = threshold - response\ quantity \tag{6.6}$$

where the response quantity is computed from a finite element solution, which may involve stresses, strains, displacements and accumulated damage, etc.

In dynamic problems, it may be not very meaningful to define the performance functions $g(\boldsymbol{\theta})$ in terms of response quantities at an individual time point during the process. Rather, the mean out-crossing rate may be of interest, or accumulated response/damage measures may be employed. This will be described in detail later.

In structural reliability analysis, a primary concern is to estimate the failure probability in order to achieve the pre-defined performance. In a component reliability problem, the failure probability is,

$$P_f = \int_{g(\boldsymbol{\theta}) \le 0} f(\boldsymbol{\theta}) d\boldsymbol{\theta} \tag{6.7}$$

where $g(\boldsymbol{\theta})$ is the performance function and $f(\boldsymbol{\theta})$ is the joint PDF of $\boldsymbol{\theta}$. As shown in Figure 6.1, the integration of the darker area is the failure probability.

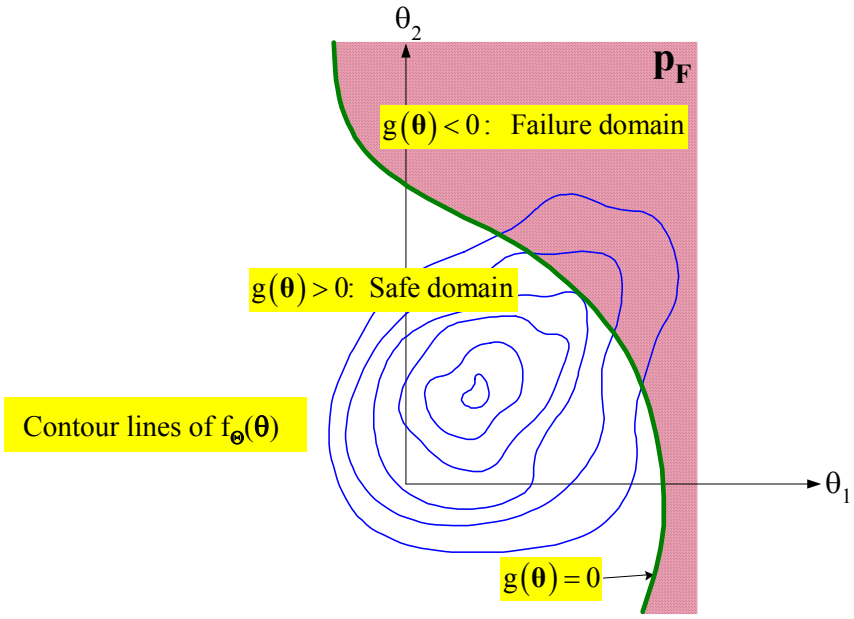


**Figure 6.1 Failure probability in 2 random variable case**

Estimation of the failure probability is a component reliability problem. However, failure according to one performance criterion may not constitute failure of an entire structural system. It is therefore of interest to define so called system reliability problems by sets of components and rules as to which combinations of component failures constitutes system failure. This is not the focus of this dissertation.

FORM, SORM and simulation techniques

The closed-form solution of Equation (6.7) is not available except for in a few special cases. To get the failure probability in Equation (6.7), several methods have been developed. These methods include the first order reliability method (FORM), second order reliability method (SORM), and sampling methods, including Monte Carlo simulation(MCS), Importance sampling (IS) method, Subset simulation method, etc.

In general, the number of random variables is large, at least a few dozen, and the crude MCS is not feasible due to the high computational cost of the limit state function evaluation. This makes methods such as FORM, SORM and IS attractive. While these methods are based on the so-called *design point*, which is defined as the closest point on the limit state surface to the origin in the *standard normal space*. The design point is denoted as **u***, while the unit vector in the direction from origin to **u*** is the *design point direction* as shown in Figure 6.2.

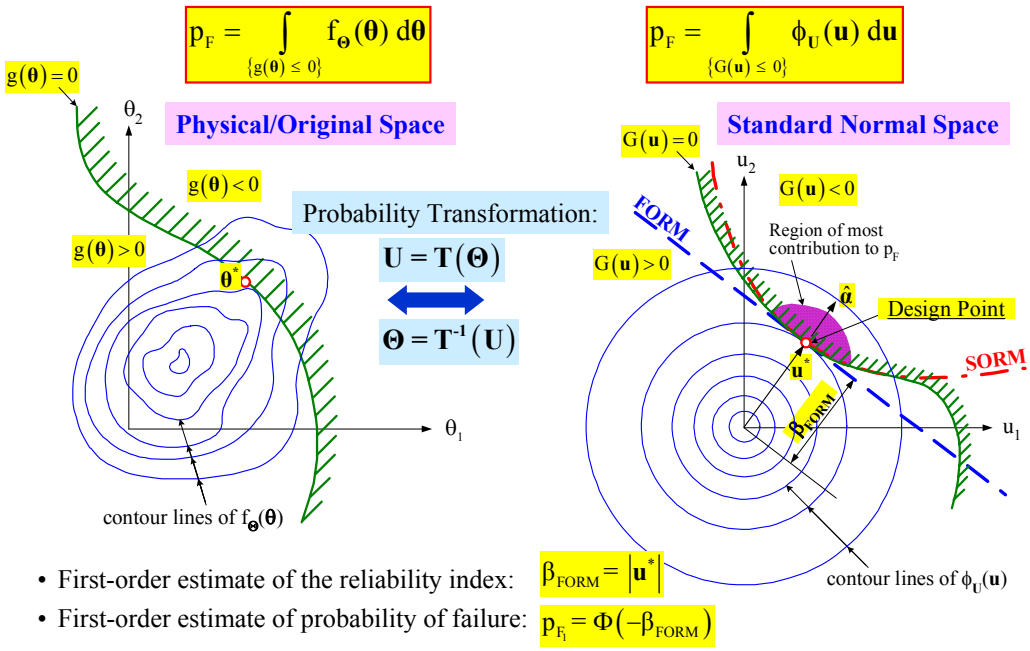


**Figure 6.2 FORM and SORM methods**

The standard normal space (**U** space) is used to simplify the integration of Equation (6.7). As shown in Figure 6.2, in the original physical space, the joint pdf $f_{\boldsymbol{\theta}}(\boldsymbol{\theta})$ is irregular as are the contour lines. Through a probability transformation, the irregular joint pdf is mapped into standard normal space, where the joint pdf $\phi_{\boldsymbol{U}}(\boldsymbol{u})$ decays exponentially in

the outward radial direction (Figure 6.3). The limit state function (LSF) in the standard normal space is expressed as,

$$G(\boldsymbol{u}) = g(\boldsymbol{\theta}(\boldsymbol{u})) \tag{6.8}$$

The integration Equation (6.7) then becomes,

$$P_f = \int_{G(\boldsymbol{u}) \le 0} \phi(\boldsymbol{u}) d\boldsymbol{u} \tag{6.9}$$

In the standard normal space, the closest point **u*** to the origin is extremely important because the greatest contribution to the failure probability is due to the dark region shown in Figure 6.2. If the limit state surface (LSS) in the standard normal space G(**u**)=0 is approximated by its linearized plane at point **u*** (the dashed blue line in Figure 6.2 represents the plane), then the *first order estimate of the failure probability* is computed by integration the Equation (6.9) along the plane as,

$$P_f = \Phi(-\beta) \tag{6.10}$$

where β is defined as the first order estimation of the *reliability index*:

$$\beta = |\boldsymbol{u}^*| \tag{6.11}$$

This method is also referred to as the first order reliability method (FORM).

If the limit state surface (LSS) in the standard normal space is highly nonlinear, FORM may be inaccurate. In this case the *second order estimate of the failure probability* may be employed, which considers two independent contributions from the LSS, one linear and the other quadratic, in the U-space (Fiessler et. al., 1979, Madsen et al., 1986.). The second order polynomial fit at point **u*** is represented by the dashed red line in Figure

6.2. The failure probability is computed by integration of Equation (6.9) along the surface. This method is referred to as the second order reliability method (SORM).

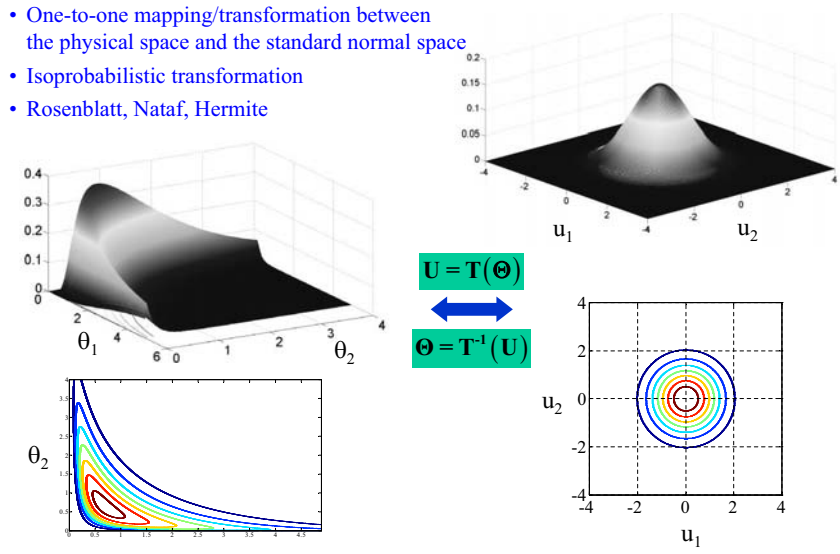


**Figure 6.3 Probability transformation**

Joint distribution model and probability transformation

Taking advantage of the information of the marginal distributions and the correlation structures of the random variables, several models can be used to obtain the joint pdf in standard normal space, including Rosenblatt, Nataf, Hermite, or Morgenstern etc. (see Liu and Der Kiureghian 1986, Haukaas 2001). The Nataf model allows a relatively wide range of correlation values, depending on the distribution type. The Nataf model is used in this dissertation.

In the Nataf model, the joint distributions are completely defined by specifying the marginal distributions and the correlation structures of the random variables. The joint normal distribution $f_{\boldsymbol{\theta}}(\boldsymbol{\theta})$ obtained by the marginal pdf $f_{\theta_i}(\theta_i)$ and correlation coefficient matrix $R$ is,

$$f_{\boldsymbol{\theta}}(\boldsymbol{\theta}) = f_{\theta_1}(\theta_1)...f_{\theta_n}(\theta_n)\frac{\varphi_n(Z, R')}{\varphi(z_1)...\varphi(z_n)} \tag{6.12}$$

where $\varphi_n(Z, R')$ is a n-dimensional joint pdf of variables with zero mean, unit variance and correlation coefficient matrix $R'$, $\varphi_{U_i}(u_i)$ is the standard normal pdf, and $z_i = \Phi^{-1}[F_{\theta_i}(\theta_i)]$ is the one-to-one mapping of RV $\theta_i$ with any pdf to RV $z_i$ with standard normal distribution. $F_{\theta_i}(\theta_i)$ and $\Phi_{U_i}(u_i)$ denote the cumulative distribution function (cdf) of variables with any distribution $f_{\theta_i}(\theta_i)$ and standard normal pdf $\varphi_{U_i}(u_i)$.

Here $R' = \rho'_{ij}$, while $\rho'_{ij}$ and $\rho_{ij}$ are related by,

$$\rho_{ij} = \int_{-\infty}^{\infty}\int_{-\infty}^{\infty}\left(\frac{x_i-\mu_i}{\sigma_i}\right)\left(\frac{x_j-\mu_j}{\sigma_j}\right)\varphi_2(z_i, z_j, \rho'_{ij})dz_i dz_j \tag{6.13}$$

$\varphi_2(z_i, z_j, \rho'_{ij})$ is a bi-variate normal pdf with zero means, unit variances, and correlation coefficient $\rho'_{ij}$. By iteration, $\rho'_{ij}$ can be solved for in terms of given values of $\rho_{ij}$. (Conte, reliability notes)

Design point search algorithm

In structural reliability analysis methods based on design point(s), like FORM, SORM, and IS, one crucial step is in finding the design point(s). An efficient and robust design point searching algorithm is very important. The design point searching process is also a minimum searching process, because the design point **u*** is the point on the limit state surface that has the closest distance from the origin in the standard normal space.

$$\boldsymbol{u}^{*}=\begin{pmatrix} min\ \ \frac{1}{2}\boldsymbol{u}^{T}\boldsymbol{u} \\ \text{s.t. } G(\boldsymbol{u})\ =\ 0 \end{pmatrix} \tag{6.14}$$

Several methods exist to obtain the design point(s). The so called HLRF algorithm originally developed by Hasofer and Lind (1974) and later extended to non-normal random variables by Rackwitz and Fiessler (1978) is a very popular method. In this method the design point is obtained by an iterative process. The updating rule for the $i^{th}$ iteration is,

$$\boldsymbol{u}_{i+1}\ =\ \left[\boldsymbol{\alpha}_i\cdot\boldsymbol{u}_i+\frac{G(\boldsymbol{u}_i)}{\left|\nabla_u G(\boldsymbol{u}_i)\right|}\right]\boldsymbol{\alpha}_i \tag{6.15}$$

where $\boldsymbol{\alpha}_i\ =\ -\dfrac{\nabla_u G(\boldsymbol{u}_i)}{\left|\nabla_u G(\boldsymbol{u}_i)\right|}$.

During each iteration, the LSF G(**u**) is computed by Equation (6.8). i.e.,

$$G(\boldsymbol{u})\ =\ g(\boldsymbol{\theta}(\boldsymbol{u}))\ =\ g(T^{-1}(\boldsymbol{u})) \tag{6.16}$$

where T is the probability transformation from original physical space to U space. Thus,

$$\nabla_u G(\boldsymbol{u})\ =\ \nabla_\theta g(\boldsymbol{\theta})\cdot\boldsymbol{J}^{-1}_{\boldsymbol{u},\,\boldsymbol{\theta}} \tag{6.17}$$

where $\boldsymbol{J}_{\boldsymbol{u},\boldsymbol{\theta}}^{-1}$ is the inverse of Jacobi matrix $\frac{d\boldsymbol{u}}{d\boldsymbol{\theta}}$. This gradient is obtained from the sensitivity algorithm mentioned in previous chapters. Accurate and efficient computation of the gradient by using DDM is essential.

The value of the LSF must be computed in the original physical space as in Equation (6.16), while the gradient $\nabla_u G(\boldsymbol{u})$ is obtained by Equation (6.17), which depends on values $\nabla_\theta g(\boldsymbol{\theta})$ in the physical space. Thus the new obtained $\boldsymbol{u}_i$ must be transformed back into the physical space by the probability transformation during each iteration. This back and forth transformation is shown in Figure 6.4.

Other methods to find the design point include Gradient Projection algorithm,, Sequential Quadratic Programming (SQP), Augmented Lagrangian Method, Gradient Projection Method. etc.

In this chapter, a general purpose optimization tool box SNOPT (Sparse Nonlinear Optimization) is implemented into OpenSees for design point searching purposes.

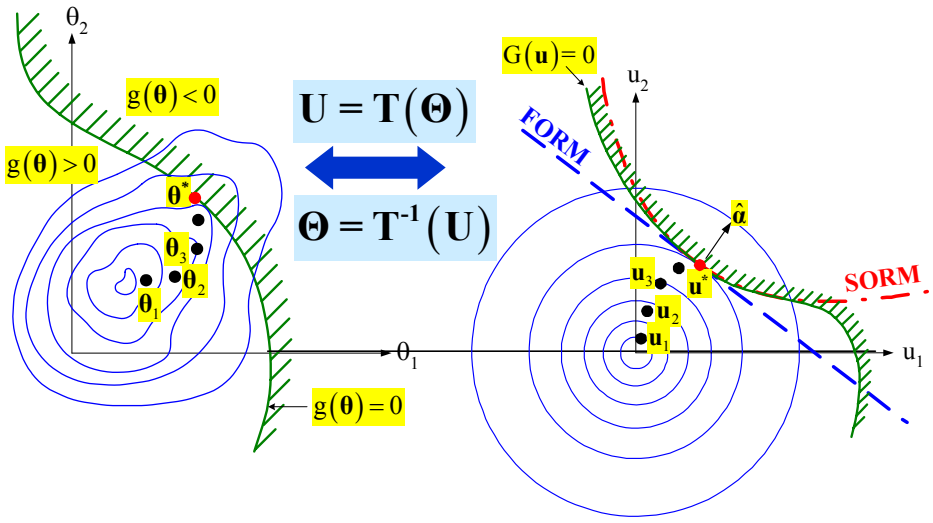


**Figure 6.4 Design point search algorithm**

## 6.2 SNOPT Based Design Point Search Algorithm

SNOPT is a software package developed by Philip Gill, Walter Murray and Michael Saunders (http://cam.ucsd.edu/~peg/; Gill 2005) for solving large-scale optimization problems (linear and nonlinear programs).

SNOPT is an efficient software toolbox for solving optimization problems with smooth nonlinear functions in the objective and constraints. Compared with other Sequential Quadratic Programming (SQP) algorithms, SNOPT provides a number of desirable features for civil engineering applications (e.g., structural reliability problems, optimization problems in model updating, etc.). These features include:

(1) Applicability for large scale problems.

In contrast to general SQP methods using a full transformed Hessian of the Lagrangian, SNOPT exploits sparsity in the constraint Jacobian and uses a limited memory quasi-Newton method. The QP subproblems are solved efficiently using an advanced 'inertia-controlling reduced-Hessian active-set method'(Gill 2005) that allows for variables appearing linearly in the objective and constraint functions. These are a few of the many features that make SNOPT suitable for solving large scale problems with many thousands of constraints and variables, and a moderate number of degrees of freedom (thousands of degree of freedom, dof = number of variables - number of constraints).

On large problems, SNOPT is most efficient if only some of the variables enter nonlinearly, or there are relatively few degrees of freedom at a solution (i.e., many constraints are active).

(2) Economical computation.

SNOPT uses techniques like early termination of the QP subproblems, and requires relatively few evaluations of the problem functions. Hence it is especially effective if the objective or constraint functions (and their gradients) are expensive to evaluate. In reliability problems, SNOPT requires relatively few evaluations of the limit state functions. Considering the high cost of evaluating the limit state function, SNOPT is especially effective and suitable for design point searching problems.

(3) Tolerance of discontinuities in the function gradients.

When computing the gradient of the LSF, discontinuities are inevitable when the material model is nonsmooth, or when the integration time step is large. For SNOPT, these dis-

continuities in the function gradients can often be tolerated if they are not too close to an optimum. This feature of SNOPT makes the design point searching algorithm very robust.

(4) Flexible options help customize SNOPT for design point searching problems.

SNOPT has many options that make the toolbox easily customizable for special problems like design point searching. These options include: whether sensitivity results need to be verified by Finite Difference Method (FDM), the perturbation size in FDM. The Basis file may be backed up as a safeguard against losing the results of a long run. Many tolerance selections such as the major feasibility tolerance setting for target nonlinear constraint violations, major optimality tolerance for target complementarity gap, the Minor feasibility tolerance for satisfying the QP bounds. These features are very useful for complicated problems like structural reliability problems.

### 6.2.1 Integration of SNOPT into OpenSees as Reliability Tool

OpenSees is an Object Oriented Finite Element software developed using the C++ language. In the existing reliability framework in OpenSees, several classes are defined for the purpose of finding design point(s) as shown in the red box in Figure 6.5.

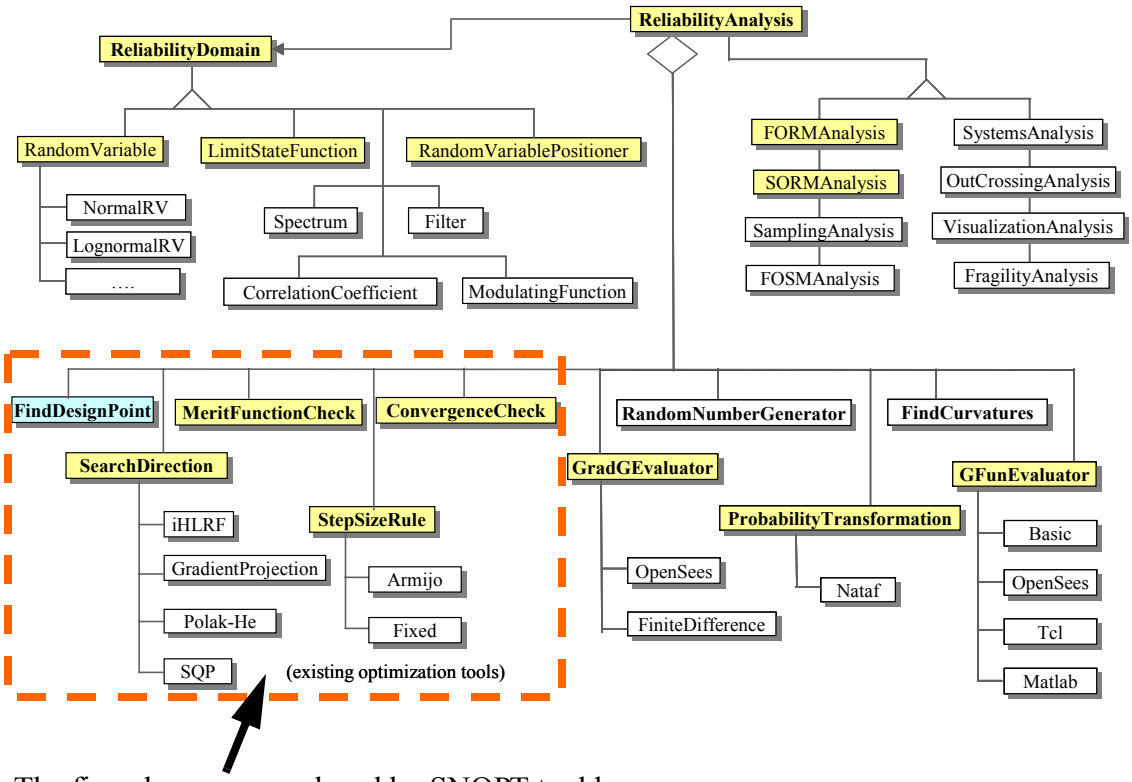


**Figure 6.5 Linking of SNOPT with OpenSees as Reliability Analysis Tool**

In Figure 6.5, there are several existing classes in OpenSees cooperating to perform the reliability analyses, such as FORM and SORM analysis (Haukaas 2001). In this chapter, a new class called SNOPT is created to wrap the SNOPT tool box as shown in Figure 6.6. This SNOPT class inherits the class FindDesignPoint, and implements the same interfaces of FindDesignPoint by calling the Fortran function inside the SNOPT tool box. SNOPT has its own sub-routines which have the same function as the four classes in OpenSees mentioned in Figure 6.5 (i.e., SearchDirection, MeritFunctionCheck, StepSizeRule, ConvergenceCheck). Thus it is unecessary for the user to create objects for these classes.

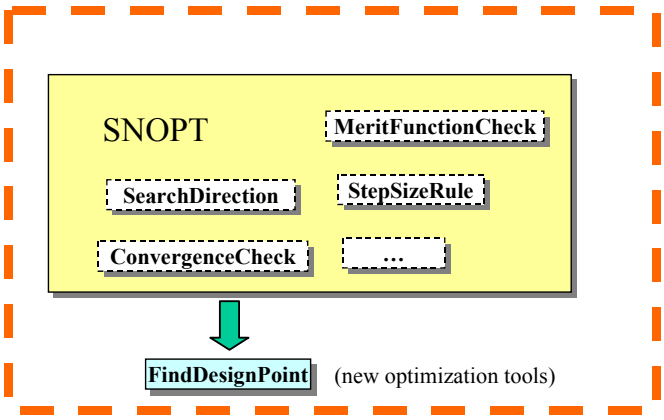


**Figure 6.6 Wrap of SNOPT tool box as a design point searching tool**

Following are the functions of these classes:

1, SearchDirection.

The SearchDirection class determines a direction that the searching process should take at each searching step.

In SNOPT, search directions are obtained from QP subproblems that minimize a quadratic model of the Lagrangian function subject to linearized constraints.

In SNOPT, an augmented Lagrangian function is taken as,

$$L(\boldsymbol{u}, \boldsymbol{\lambda}, \rho) = f(u) - \boldsymbol{\lambda}^T \boldsymbol{c}(\boldsymbol{u}) + \frac{\rho}{2}\boldsymbol{c}(\boldsymbol{u})^T \boldsymbol{c}(\boldsymbol{u}) \tag{6.18}$$

where $\boldsymbol{u}$ is the variable, $\lambda$ is a multiplier estimate and $\rho$ is a nonnegative penalty parameter, $f(\boldsymbol{u})$ is the objective function taken as $f(\boldsymbol{u}) = \frac{1}{2}\boldsymbol{u}^T\boldsymbol{u}$ in reliability problems, $\boldsymbol{c}(\boldsymbol{u})$ are

constraints here taken as the LSF $G(\boldsymbol{u})$. $\lambda$ and $\rho$ may be adjusted automatically by SNOPT.

An augmented Lagrangian merit function should be reduced at each step along directions that ensure convergence from the starting point.

2, MeritFunctionCheck

This class evaluates the augmented Lagrangian merit function at each searching step, then determines whether a selected step size is acceptable.

3, ConvergenceCheck

This class checks at each step whether the new point satisfies the minimum condition and constraint functions. If the answer is 'yes', it will terminate the searching process.

4, StepSizeRule

This class obtains a step size in the line search along a search direction. SNOPT has its own rule to control the steplength (Gill 2004). The user is allowed to select the limit of the change in $\boldsymbol{u}$ during a line search.

It is worthy mentioning that this interface is very flexible and user-friendly. The tcl commands used in OpenSees are the same as before except (1) the user does not need to create these four objects; (2) the user needs to specify the type of findDesignPoint to 'SNOPT'. SNOPT based design point(s) searching is very flexible due to the various choices offered to the user by SNOPT as mentioned above.

## 6.3 Sampling Analysis

As mentioned above, one major goal in structural reliability analysis is to estimate the failure probability for a given performance function. i.e.,

$$P_f = \int_{g(\boldsymbol{\theta}) \le 0} f(\boldsymbol{\theta}) d\boldsymbol{\theta} \tag{6.19}$$

where $P_f$ is the probability of failure, $\boldsymbol{\theta}$ is the random variable vector use to indicate the uncertainties of the structure, g($\boldsymbol{\theta}$) is the limit state function, f($\boldsymbol{\theta}$) is the joint pdf of $\boldsymbol{\theta}$.

This definition can be further expressed as,

$$P_f = \int_{g(\boldsymbol{\theta}) \le 0} f(\boldsymbol{\theta}) d\boldsymbol{\theta} = \int_{\boldsymbol{\theta}} I(\boldsymbol{\theta}) \cdot f(\boldsymbol{\theta}) d\boldsymbol{\theta} = E[I(\boldsymbol{\theta})] \tag{6.20}$$

where $I(\boldsymbol{\theta})$ is the indicator function, which is defined as,

$$I(\boldsymbol{\theta}) = \begin{cases} 0 \text{ The system is safe, or } g(\boldsymbol{\theta}) > 0 \\ 1 \text{ The systems fails, or } g(\boldsymbol{\theta}) \le 0 \end{cases} \tag{6.21}$$

The closed-form solution of (6.19) is not easy to obtain unless the format of g($\boldsymbol{\theta}$) is simple (e.g., linear elastic case). One solution to this problem is using Monte Carlo Simulation (MCS), a technique for sampling a probability density function based on computer generated random numbers.

### 6.3.1 Zero-One Indicator-Based Monte Carlo Simulation, or Crude Monte Carlo Method

In this method, the sampling distribution is centered at the mean point. By performing N-times simulations of the vector $\boldsymbol{\theta}$ with the pdf $f(\boldsymbol{\theta})$, and the failure probability is obtained by,

$$P_f = \frac{1}{N}\sum_{i=1}^{N} p_i \tag{6.22}$$

where $p_i = I(\boldsymbol{\theta})$

The variance of the $P_f$ can be computed by,

$$var[P_f] = E[(P_f - E[P_f])^2] = \frac{P_f \cdot (1 - P_f)}{N} \tag{6.23}$$

And so the coefficient of variation is,

$$c.o.v.[P_f] = \sqrt{\frac{P_f \cdot (1 - P_f)}{N}} / P_f = \sqrt{\frac{(1 - P_f)}{N \cdot P_f}} \tag{6.24}$$

In reliability problems, since failure events often occur in the tail regions of probability distributions, a large number of samples may be required in order to obtain good failure probability estimates. The number of MCS needed is computed as,

$$N = \frac{1 - P_f}{P_f} \cdot \frac{1}{(c.o.v.[P_f])^2} \approx \frac{1}{P_f} \cdot \frac{1}{(c.o.v.[P_f])^2} \tag{6.25}$$

According to this estimation, if *c.o.v.* = 0.10, N is about $100/P_f$. For example, if $P_f$ = 1.0e-4, then the MCS needed is about 1.0e6. The computational cost for the large number of evaluations of the performance function may be too high or even inacceptable, thus it is necessary to develop new techniques instead of the crude MCS.

### 6.3.2 Importance Sampling Method (IS)

One technique to improve the simulation efficiency is to bias the choice of the random vectors by using a designed sampling distribution $h(\boldsymbol{\theta})$, called the importance sampling

distribution, which has a greater portion of the pdf than the actual pdf $f(\boldsymbol{\theta})$ in the failure domain (i.e., the region $g(\boldsymbol{\theta}) \leq 0$ ). Then,

$$P_f = \int_{\boldsymbol{x}} I(\boldsymbol{\theta}) \frac{f(\boldsymbol{\theta})}{h(\boldsymbol{\theta})} h(\boldsymbol{\theta}) d\boldsymbol{\theta} \tag{6.26}$$

In this chapter, the $h(\boldsymbol{\theta})$ is selected to be a Gauss distribution centered at the design point, see Figure 6.7.

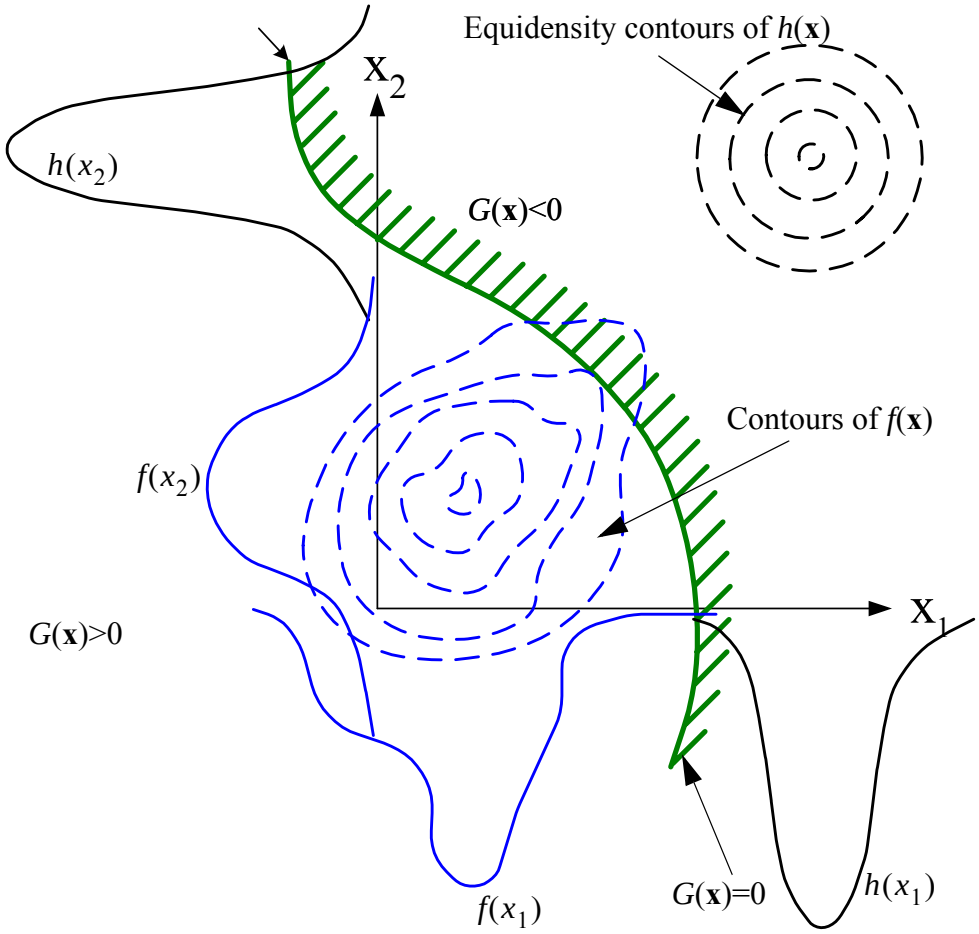


**Figure 6.7 The importance sampling distribution h(x) is such that it emphasises a sub-part of the failure region in which f(θ) is relatively small**

The failure probability is computed as,

$$P_f = \frac{1}{N}\sum_{i=1}^{N} p_i \tag{6.27}$$

where $p_i = I(\boldsymbol{\theta}_i)\dfrac{f(\boldsymbol{\theta}_i)}{g(\boldsymbol{\theta}_i)}$

The variance of the $P_f$ can be computed by,

$$\begin{aligned} var[P_f] &= \frac{1}{N}E_{h(\boldsymbol{x})}\left[\left(I(\boldsymbol{\theta})\frac{f(\boldsymbol{\theta})}{h(\boldsymbol{\theta})} - P_f\right)^2\right] \\ &\approx \frac{1}{N(N-1)}\sum_{i=1}^{N}\left(I(\boldsymbol{\theta}_i)\frac{f(\boldsymbol{\theta}_i)}{h(\boldsymbol{\theta}_i)} - P_f\right)^2 \end{aligned} \tag{6.28}$$

while the coefficient of variation is,

$$c.o.v.[P_f] = \frac{\sqrt{var[P_f]}}{P_f} \tag{6.29}$$

This method could be combined together with FORM or SORM by selecting the center of h(x) as the design point, which is the most likely failure point.

In this dissertation, the Importance Sampling process is combined with the design point to estimate the failure probability: (1) the sampling is performed in the standard normal space (U space) instead of the **θ** space. In this case, everything is the same as described in equations (6.26) to (6.29) except that the distribution of $f(\boldsymbol{u})$ is a standard normal distribution. (2) the center of **h(u)** is taken as the design point **u***. This is shown in Figure 6.8.

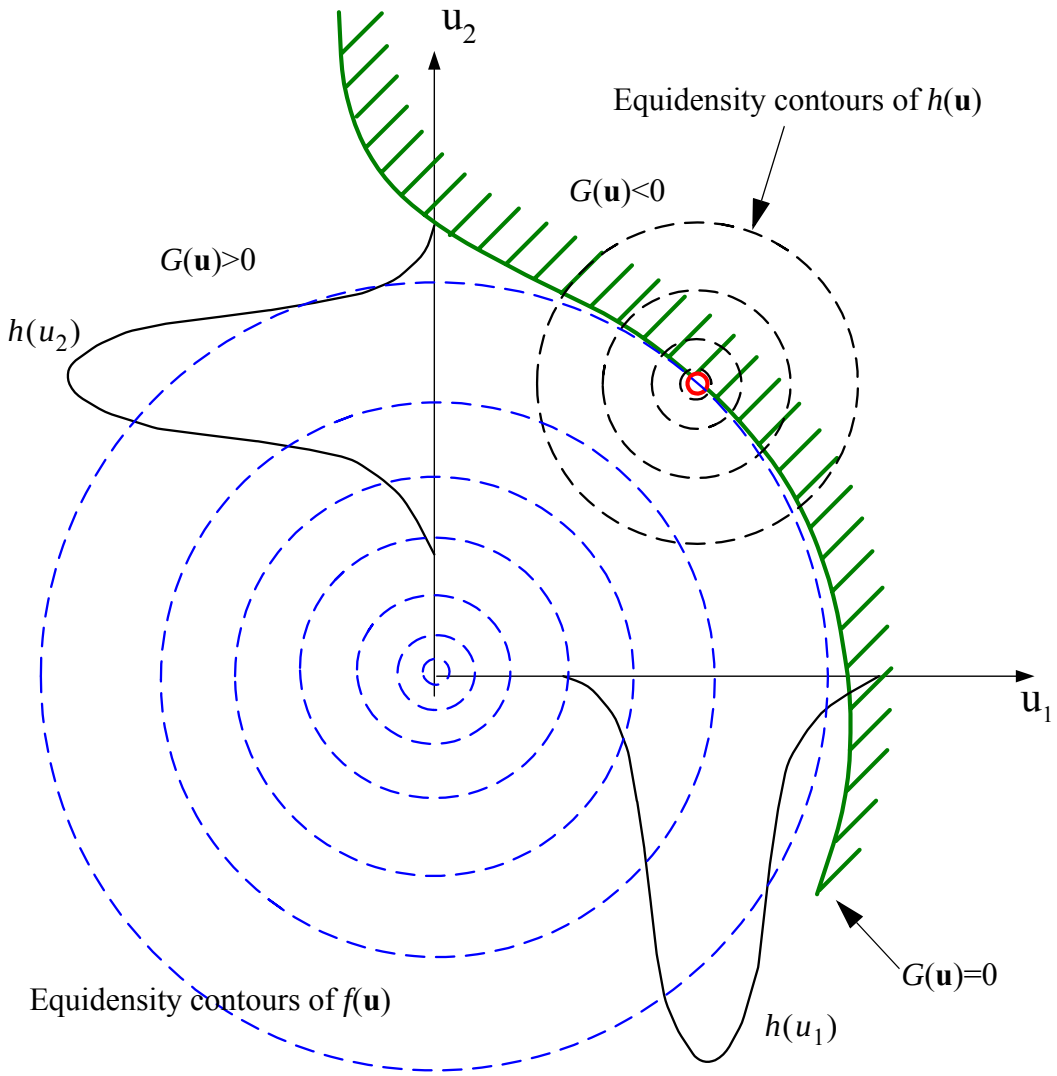


**Figure 6.8 Importance sampling combined with the design point in standard normal space**

### 6.3.3 Orthogonal Plane Sampling Method (OPS)

In this section, the direction of the design point is used as a guide for selecting the sampling direction.

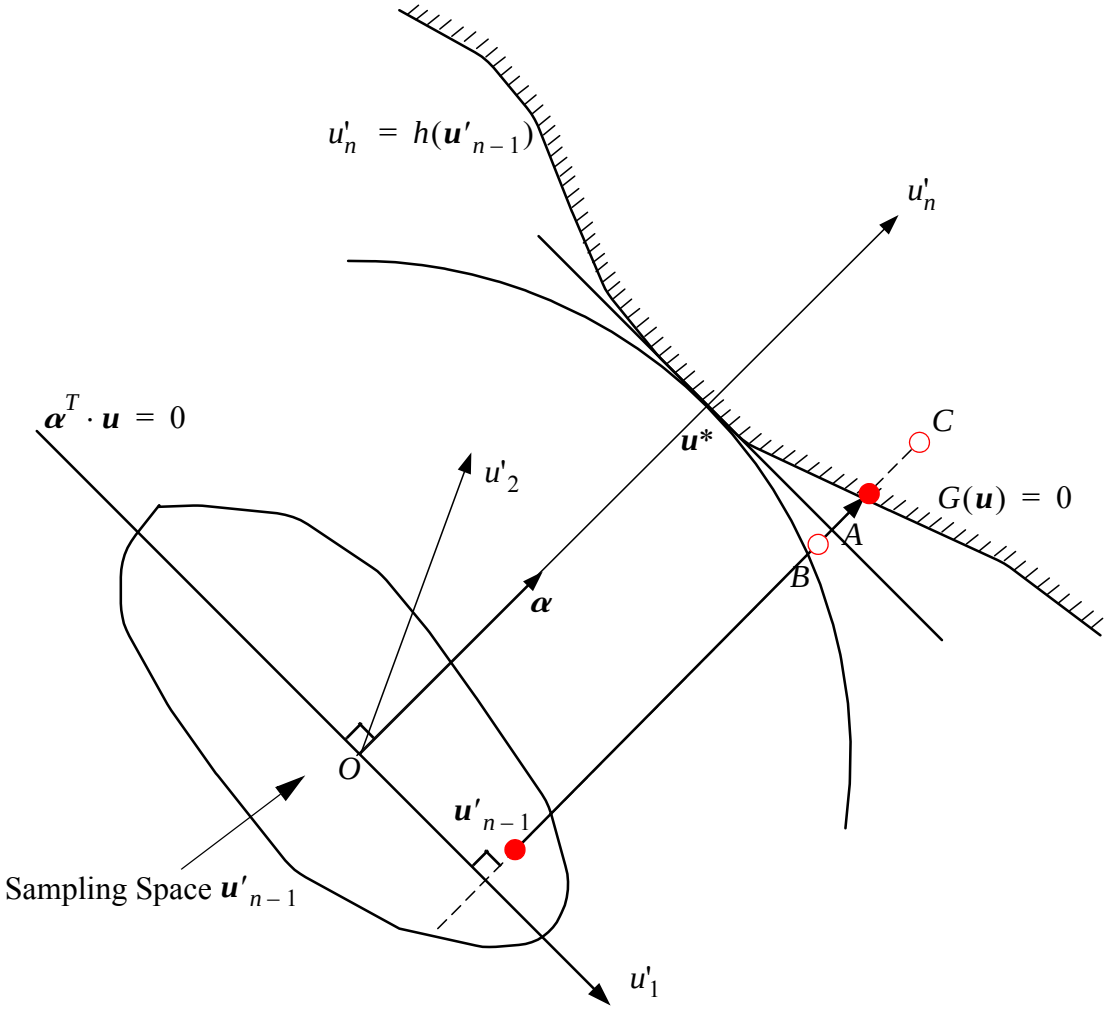


**Figure 6.9 Sampling in the orthogonal plane**

After the design point $\boldsymbol{u}^*$ and its corresponding negative normal vector $\boldsymbol{\alpha}$ is obtained (i.e., using FORM or SORM). The orthogonal plane is defined as the plane normal to $\boldsymbol{\alpha}$

$\boldsymbol{\alpha}^T \cdot \boldsymbol{u} = 0$ and passing through the origin O. Let $\boldsymbol{u}' = (u'_1, u'_2 \ldots u'_n)$ be an orthonormal transformation of a point **u** in the standard normal U space, such that the axis $u_n'$ coincides with **α**. Here an assumption is made that after this transformation, the limit-state surface G(**u**')=0 can be written in the form of a single-valued function $u'_n = h(\boldsymbol{u}'_{n-1})$, which is defined as the distance from the orthogonal plane to the limit state surface at the point **u**. This assumption sometimes does not hold( i.e., when the limit state surface is spherically shaped, there are two values satisfying $u'_n = h(\boldsymbol{u}'_{n-1})$). However this assumption may hold over a reasonable neighborhood of the design point (Koo 2003). For points far from the design point (if the distance of this point to the orthogonal plane is more than $\beta + 3$) in the failure domain, the contribution of this point to the failure probability is very small (less than $\Phi[-(\beta + 3)]$).

In the standard normal U space, for any sampling point $\boldsymbol{u}_n$, the first step is to project the point $\boldsymbol{u}_n$ onto the orthogonal plane $\boldsymbol{\alpha}^T \cdot \boldsymbol{u} = 0$ to obtain the projection point $\boldsymbol{u}'_{n-1}$. The resulting distance from the orthogonal plane to the limit state surface $u'_n$ is computed by solving G(**u**')=0 after which the failure probability can be computed as,

$$
\begin{aligned}
P[G(\boldsymbol{u}'_n) \le 0] &= \int_{G(\boldsymbol{u}'_n) \le 0} \varphi(\boldsymbol{u}'_n) d\boldsymbol{u}'_n \\
&= \int_{h(\boldsymbol{u}'_{n-1}) \le u'_n} \varphi(u'_n)\varphi(\boldsymbol{u}'_{n-1}) du'_n d\boldsymbol{u}'_{n-1} \\
&= \int_{\boldsymbol{u}'_{n-1}} \left[ \int_{h(\boldsymbol{u}'_{n-1})}^{\infty} \varphi(u'_n) du'_n \right] \varphi(\boldsymbol{u}'_{n-1}) d\boldsymbol{u}'_{n-1} \\
&= \int_{\boldsymbol{u}'_{n-1}} \Phi[-h(\boldsymbol{u}'_{n-1})]\varphi(\boldsymbol{u}'_{n-1}) d\boldsymbol{u}'_{n-1} \\
&= E_{\varphi(\boldsymbol{u}'_{n-1})}[\Phi[-h(\boldsymbol{u}'_{n-1})]]
\end{aligned}
\tag{6.30}
$$

Where $E_{\varphi(\boldsymbol{u}'_{n-1})}[\ ]$ denotes the expectation of the argument with respect to the distribution of $\varphi(\boldsymbol{u}'_{n-1})$. Define the random quantity $p$ as,

$$
p = \Phi[-h(\boldsymbol{u}'_{n-1})] \tag{6.31}
$$

In the orthogonal plane sampling method, the failure probability is computed as,

$$
P_f = \frac{1}{N} \sum_{i=1}^{N} p_i \tag{6.32}
$$

where $p_i$ is the i$^{th}$ sampling point as defined in Equation (6.31).

The variance of the $P_f$ can be computed by,

$$
var[P_f] = \frac{1}{N} E_{\varphi(\boldsymbol{u}'_{n-1})}[(p_i - P_f)^2] \tag{6.33}
$$

And so the coefficient of variation is,

$$
c.o.v.[P_f] = \frac{\sqrt{var[P_f]}}{P_f} \tag{6.34}
$$

In practice, the orthogonal plane sampling method has five steps as follows:

1, in U space, simulate n-D standard normal vector $\boldsymbol{u}_n$.

2, project this point $\boldsymbol{u}_n$ onto the orthogonal plane $\boldsymbol{\alpha}^T \cdot \boldsymbol{u} = 0$ to get $\boldsymbol{u}'_{n-1}$.

3, compute $h(\boldsymbol{u}'_{n-1})$ by solving $G(u'_n, \boldsymbol{u}'_{n-1}) = 0$ by zerofinding algorithm.

4, compute $p = \Phi[-h(\boldsymbol{u}'_{n-1})]$ as shown in Equation (6.31). compute mean and coefficient of variation of the failure probability as shown in Equation (6.32) and Equation (6.34).

5, repeat step 1-4 untill the maximum number of the simulation is reached or the designed coefficient of variation is satisfied.

The advantage of the orthogonal plane sampling method is that it is not necessary for the design point to be very accurate, which saves steps in the design point searching process. For each sampling point, the limit state function has to be evaluated repeatly in order to get the point on the limit state surface. Thus, it is necessary to figure out an efficient zero-finding algorithm for reducing the number of evaluations of the LSF.

Trust region zero finding method.

This algorithm is designed especially for orthogonal plane sampling method. i.e., to solve this problem:

$$G(\boldsymbol{u}'_n, \boldsymbol{u}'_{n-1}) = G(\boldsymbol{u}'_{n-1} + x\boldsymbol{u}'_n) = 0 \tag{6.35}$$

Where $x$ is a scalar value to be determined.

The properties of the orthogonal plane sampling analysis problem are:

1) the limit state function should be evaluated as few times as possible. For this purpose, the safeguarded zero-finding algorithm together with the secant method is employed (Gill E. 2004) . Assume the trust region is [a,b], where G(a)>0 G(b)<0. The starting point of the zerofinding algorithm is 'a'.

2) the starting trial point $\boldsymbol{u}'_{n-1} + xu'_n$ (or lower bound) should be chosen as close as possible to the (estimated) limit state surface. The starting point is selected as A in Figure 6.9; then if point A is already in the failure domain, point B is selected instead, which has the distance β to the origin. If B is still within the failure domain, it means the design point is a local minimum and is not the true design point, the design point should be re-evaluated.

3). If x is larger than $\beta + 2$, the random quantity $p$ in Equation (6.31) is extremely small and is negligible. No further zerofinding process is needed(e.g., if $\beta = 3$, $\Phi[-(\beta + 2)] = 2.87e-7$).

4.)If the trial point goes too far (i.e., $x$ too big) into the failure domain such that finite element code could diverge. The zerofinding algorithm will take this case same as the structural failure case (i.e.,$G(\boldsymbol{u}) \le 0$ ).

The FE divergence is checked for every evaluation of the limit state function. In case of FE divergence, the bisection method is used instead of the Newton method to continue the zero point searching process. The lower bound $a$ of the trust region is compared with $\beta + 2$ each time it is changed, to make sure it's 'contribution' to $P_f$ is not negligible. This could save a number of evaluations of the LSF as well as computational time.

## 6.4 Application Examples of Time Invariant Reliability Analysis of SFSI System

In this section, the methodology mentioned above is implemented in OpenSees. An example of a 2D SFSI application is presented to perform the time invariant reliability analysis.

### 6.4.1 2D SFSI Example

The first application example consists of a two-dimensional Soil-Foundation-Structure Interaction (SFSI) system, a model of which is shown in Figure 6.10. The structure is a two-story two-bay reinforced concrete frame with section properties given in Figure 6.10. The foundations consist of reinforced concrete squat footings at the bottom of each column. The soil is a layered clay, with stiffness properties varying along the depth.

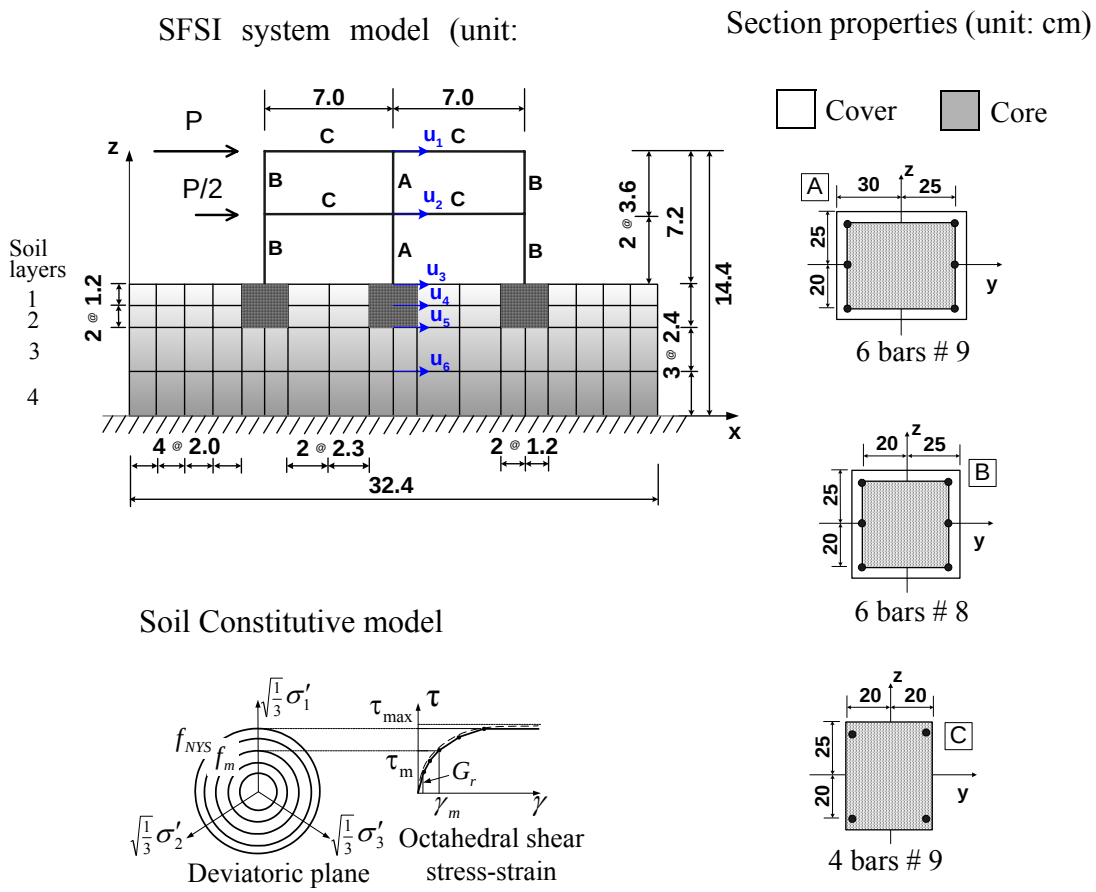


**Figure 6.10 2-D model of SFSI system: geometry, section properties and soil**

The frame structure of this SFSI system is modeled by using displacement-based Euler-Bernoulli frame elements with distributed plasticity, each with four Gauss-Legendre integration points. Section stress resultants at the integration points are computed by discretizing the frame sections by layers. Foundation footings and soil layers are modeled through isoparametric four-node quadrilateral finite elements with bilinear displacement interpolation. The soil mesh is shown in Figure 6.10. The constitutive behavior of the steel reinforcement is modeled by using a one-dimensional Menegotto-Pinto model (ref). The concrete is modeled by using a smoothed popovics-saenz model. Different material parameters are used for confined (core) and unconfined (cover) concrete in the columns. The soil is modeled by using a pressure-independent multi-yield surface $J_2$ plasticity material model (Elgamal et al. 2003), specialized for plane strain analysis (Figure 6.10). Different material parameters are used for each of the four layers considered. The material parameters are considered as random variables.

The soil under a condition of simple shear has its bottom nodes fixed and the corresponding boundary nodes at same depth tied together (Figure 6.11). The node of the beam (3 DOF) and the corresponding node on the foundation concrete block (2 DOF), at the same location, are tied together in both the horizontal and vertical directions as shown in Figure 6.11.

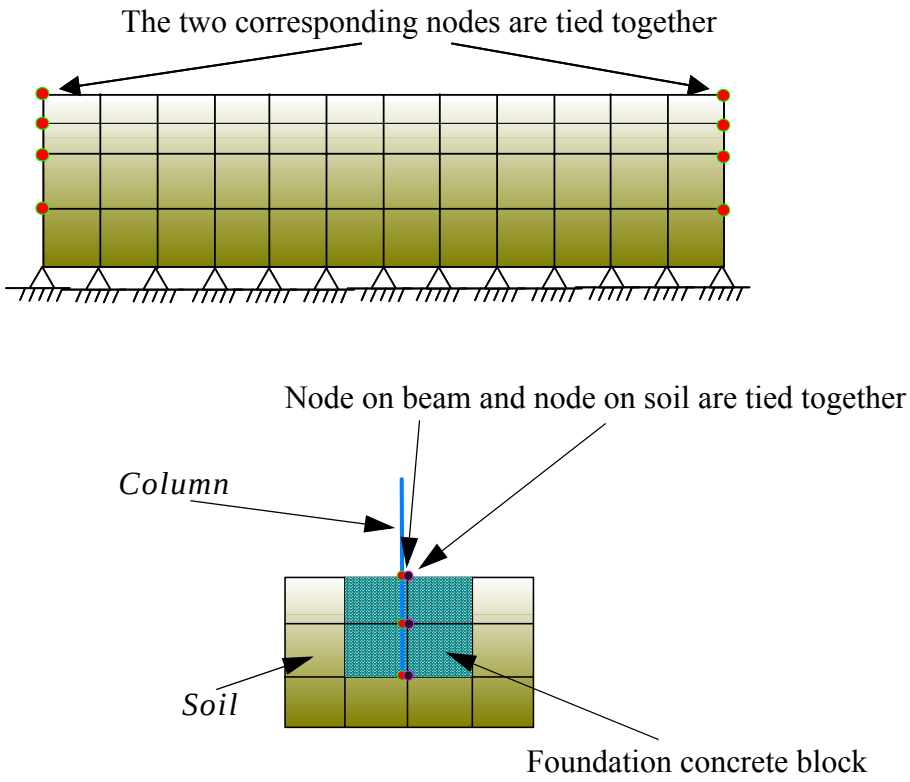


**Figure 6.11 Boundary conditions and multipoint constraints**

In this analysis, after static application of the gravity loads, the structure is subjected to a quasi-static pushover analysis, in which an upper triangular distribution of horizontal forces is applied at the floor levels (see Figure 6.10). The total base shear force, $P_{tot}$ = 1.5P. The maximum load P is considered a random variable.

All material and load RVs have lognormal distributions and the probabilistic properties are shown in Tables 6.1 through 6.3. The correlation between RVs are shown in Table 6.4.

**Table 6.1 Probabilistic properties of structure material (all has lognormal distribution except for the ones without c.o.v., unit: kPa)**

| Concrete | | | | | Steel | | |
|---|---|---|---|---|---|---|---|
| Mat | Core | | Cover | | Mat | mean | c.o.v. |
| | mean | c.o.v. | mean | c.o.v. | | | |
| $f_c$ | 3.447e4 | 0.2 | 2.758e4 | 0.2 | E | 2.1E8 | 0.033 |
| $f_{cu}$ | 2.572e4 | 0.2 | 1.0e3 | - | s | 2.482e5 | 0.106 |
| $\varepsilon_c$ | 0.005 | 0.2 | 0.002 | 0.2 | b | 0.02 | 0.2 |
| $e_{cu}$ | 0.02 | 0.2 | 0.012 | 0.2 | | | |
| $E_c$ | 2.785e7 | - | 2.491e7 | - | | | |

**Table 6.2 Probabilistic properties of soil material (all have lognormal distributions, unit: kPa )**

| layer | | mean | c.o.v. | layer | | mean | c.o.v. |
|---|---|---|---|---|---|---|---|
| #1 (top) | G | 54450 | 0.3 | #3 | G | 61250 | 0.3 |
| | $\tau_{max}$ | 99.0 | 0.25 | | $\tau_{max}$ | 105.0 | 0.25 |

**Table 6.2 Probabilistic properties of soil material (all have lognormal distributions, unit: kPa )**

| layer | | mean | c.o.v. | layer | | mean | c.o.v. |
|---|---|---|---|---|---|---|---|
| #2 | G | 33800 | 0.3 | #4 (bottom) | G | 96800 | 0.3 |
| | $\tau_{max}$ | 78.0 | 0.25 | | $\tau_{max}$ | 132.0 | 0.25 |

**Table 6.3 Probabilistic properties of load pattern ( lognormal distribution, unit: kN )**

| | mean | c.o.v. |
|---|---|---|
| $P_{max}$ | 250.0 | 0.2 |

**Table 6.4 Correlation between RVs)**

| RV | RV | correlation | RV | RV | correlation |
|---|---|---|---|---|---|
| $f_{c,core}$ | $f_{c,cover}$ | 0.8 | $f_{cu,core}$ | $f_{c,cover}$ | 0.64 |
| $\varepsilon_{c,core}$ | $\varepsilon_{c,cover}$ | 0.8 | $G_1$ | $t_{max,1}$ | 0.4 |
| $e_{cu,core}$ | $\varepsilon_{cu,cover}$ | 0.8 | $G_2$ | $t_{max,2}$ | 0.4 |
| $\varepsilon_{c,core}$ | $\varepsilon_{cu,core}$ | 0.8 | $G_3$ | $\tau_{max,3}$ | 0.4 |
| $f_{c,core}$ | $f_{cu,core}$ | 0.8 | $G_4$ | $\tau_{max,4}$ | 0.4 |
| $\varepsilon_{c,cover}$ | $\varepsilon_{cu,cover}$ | 0.8 | $\tau_{max,1}$ | $t_{max,2}$ | 0.4 |
| $\varepsilon_{c,core}$ | $\varepsilon_{cu,cover}$ | 0.64 | $\tau_{max,2}$ | $\tau_{max,3}$ | 0.4 |
| $\varepsilon_{cu,core}$ | $\varepsilon_{c,cover}$ | 0.64 | $\tau_{max,3}$ | $\tau_{max,4}$ | 0.4 |

Two kinds of limit state functions (LSF) are considered. One employs the criterion of the first floor drift,

$$g_1 = \Delta_{limit} - \Delta_1 = \Delta_{limit} - (u_2 - u_3) \tag{6.36}$$

The other considers the total structural displacement, where the $\Delta_{limit}$ is taken as 2.5cm, 5.0cm, and 7.5 cm or approximately 2% of the height of the first floor.

$$g_2 = u_{limit} - (u_1 - u_3) \tag{6.37}$$

where the $u_{limit}$ is taken as 5.0cm, 7.5 cm, 10 cm, and 14.4 cm or 2% of the height of the building. The design point obtained from a LSF is used as a 'warm' starting point' for the design point search of the subsequent LSF with higher criterion.

The design points, normalized by their means, of the two LSF are shown in Figures 6.12 and 6.13.

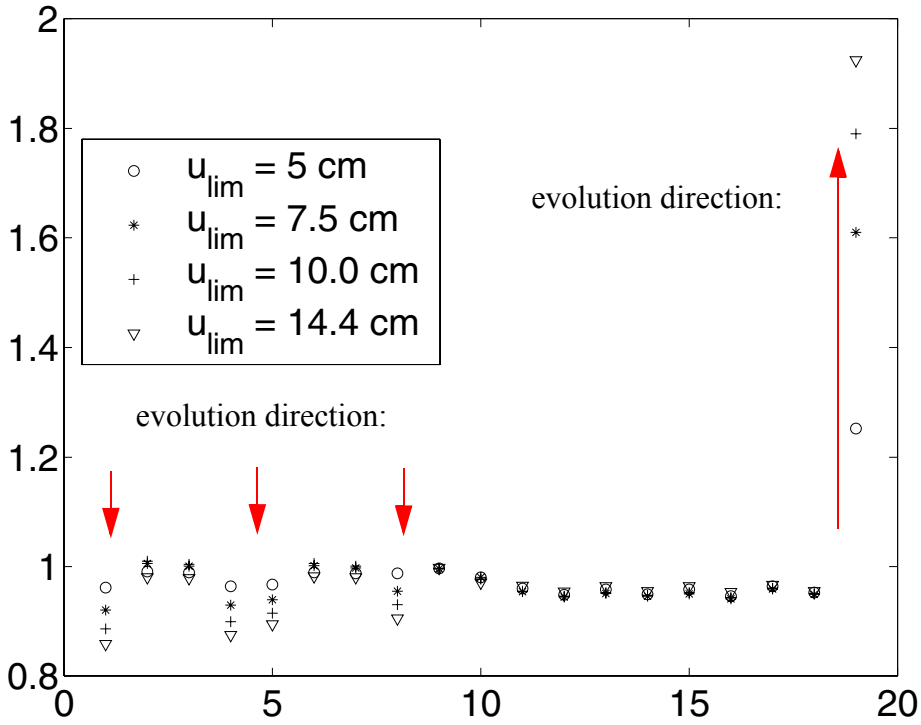


**Figure 6.12 Design points of $g_2 = u_{limit} - (u_1 - u_3)$ corresponding to different criterion levels**

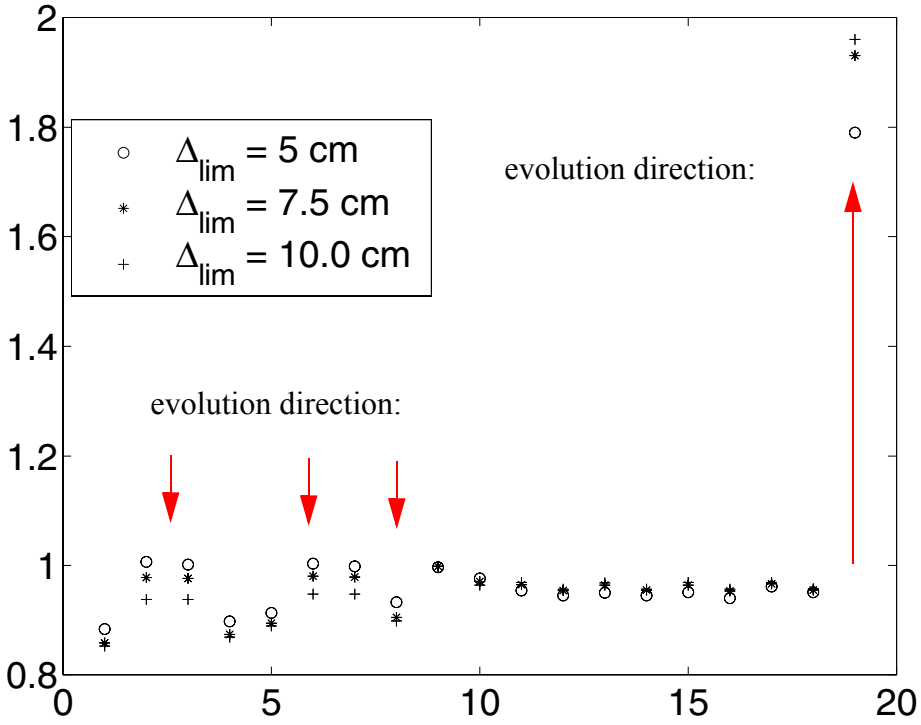


**Figure 6.13 Design points of $g_1 = \Delta_{limit} - \Delta_1$ corresponding to different criterion levels**

These figures show that as the limit criterion increase, the design points evolved along similar directions. (i.e., some RVs always increase while others always decrease). This path is also marked out by arrows denoted as 'evolution direction' in Figures 6.12 and 6.13. This shows that the design points from lower criterion are very meaningful for the design point search of higher criterion. A lower-criterion design point may serve as a 'warm' starting point for the design point search for a higher criterion. This searching method is also called the 'sequential design point searching method' by author.

The responses of the first floor drift at the design points for the LSF $g_1$ and $g_2$ at various $\Delta_{limit}$ and $u_{limit}$ are shown in Figure 6.14, and Figure 6.15 respectively. It is obvious that the system yields significantly at the design points.

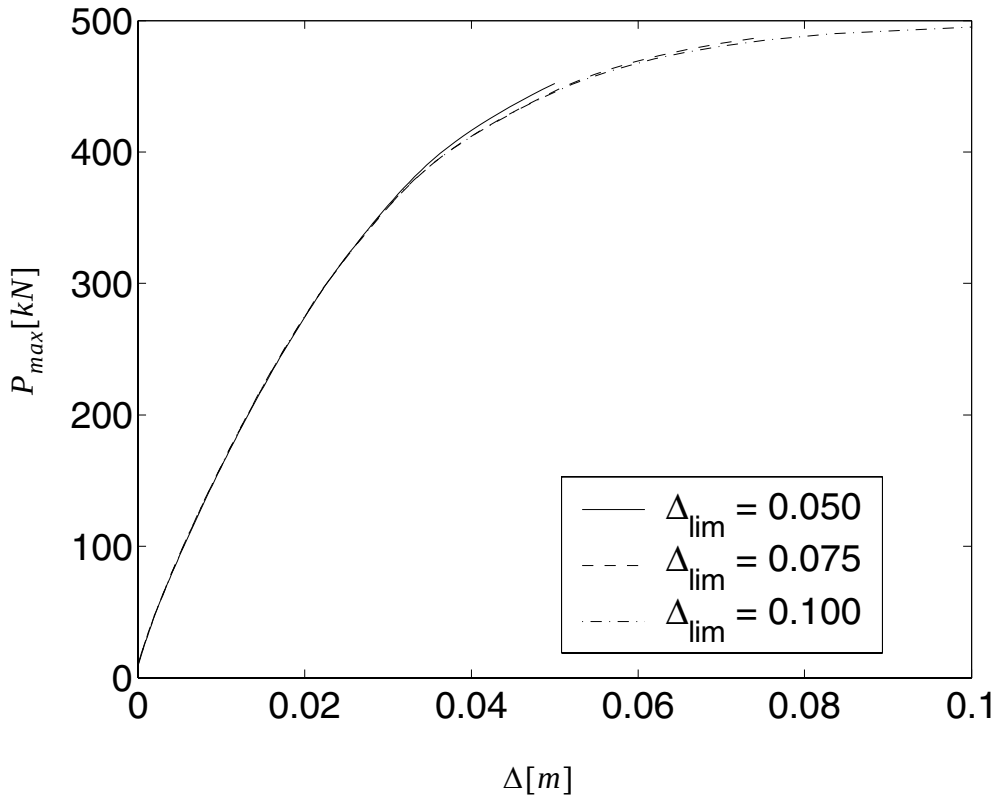


**Figure 6.14 Design points of $g_1 = \Delta_{limit} - \Delta_1$ corresponding to various criteria**

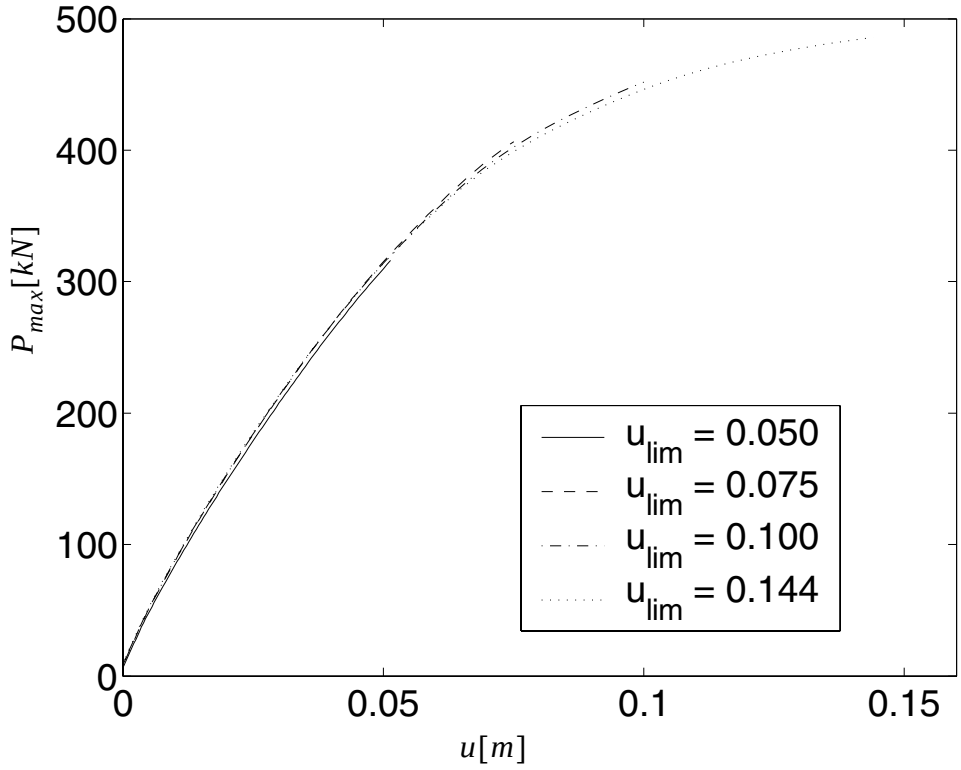


**Figure 6.15 Design points of $g_2 = u_{limit} - (u_1 - u_3)$ corresponding to various criteria**

After obtaining the design points, IS and OPS analysis is performed based on the design points. The results are reported in Tables 6.5 and 6.6 for the LLF defined by first floor drift and total structure displacement, respectively.

**Table 6.5 Comparison of various methods for computing the $P_f$ (LSF: $g_1 = \Delta_{limit} - \Delta_1$ )**

| | $\Delta_{limit}$ (cm) | 5.0 | 7.5 | 10.0 |
|---|---|---|---|---|
| FORM | $P_f$ | 8.94e-2 | 8.19e-4 | 1.59e-4 |
| | Number of evaluations | 19 | 18 | 18 |
| MCS | $P_f$ | 9.03e-2 | 5.00e-4 | 0 |
| | c.o.v. | 0.032 | 0.447 | - |
| | Number of evaluations | 10000 | 10000 | 10000 |
| IS | $P_f$ | 8.62e-2 | 8.27e-4 | 1.42e-4 |
| | c.o.v. | 0.1 | 0.1 | 0.1 |
| | Number of evaluations | 185 | 397 | 524 |
| OPS | $P_f$ | 8.85e-2 | 7.01e-4 | 1.05e-4 |
| | c.o.v. | 0.1 | 0.1 | 0.1 |
| | Number of samplings | 109 | 128 | 168 |
| | Number of evaluations | 586 | 860 | 1454 |

**Table 6.6 Comparison of various methods for computing the $P_f$ (**
**LSF:** $g_2 = u_{limit} - (u_1 - u_3)$ **)**

| | $u_{limit}$ (cm) | 5.0 | 7.5 | 10.0 | 14.4 |
|---|---|---|---|---|---|
| FORM | Pf | 1.07e-1 | 5.37e-3 | 8.10e-4 | 1.69e-4 |
| | Number of evaluations | 10 | 10 | 12 | 18 |
| MCS | $P_f$ | 1.08e-1 | 5.7e-3 | 5.0e-4 | 0 |
| | c.o.v. | 0.029 | 0.132 | 0.045 | - |
| | Number of evaluations | 10000 | 10000 | 10000 | 10000 |
| IS | $P_f$ | 1.14e-1 | 5.17e-3 | 7.65e-4 | 1.53e-4 |
| | c.o.v. | 0.1 | 0.1 | 0.1 | 0.1 |
| | Number of evaluations | 155 | 307 | 404 | 506 |
| OPS | $P_f$ | 9.13e-2 | 4.94e-3 | 7.39e-4 | 1.27e-4 |
| | c.o.v. | 0.1 | 0.1 | 0.1 | 0.1 |
| | Number of samplings | 123 | 119 | 120 | 150 |
| | Number of evaluations | 613 | 696 | 784 | 1270 |

From this data it is observed that:

1, the failure probability is consistent for FORM, IS, OPS, and MCS except when the MCS can not reach a small enough c.o.v. with acceptable computational cost.

2, Crude MCS is accurate but very expensive. When the failure criterion is set to be large enough such that the failure becomes an event with extremely small probability, MCS is not viable due to the computational cost.

3, FORM results are always reasonable and require a far less number of evaluations than IS and OPS. However it is not guaranteed to be accurate, especially when the LSS is highly nonlinear, as will be discussed in a later chapter.

4, IS is better than OPS in the sense that it requires fewer LSF evaluations. The results from IS and OPS are nearly consistent.

## 6.5 Time Variant Reliability Analysis

### 6.5.1 Background

There are two types of failure caused by random vibrations. (1) First excursion failures (or yield failures), which are defined as when the stochastic structural response 'x(t)' first reaches an upper level $\zeta^+$. (2) Fatigue failures, which occur when the accumulated damage due to several response cycles of small or moderate amplitudes reach a fixed total limit as shown in Figure 6.16. In this dissertation only the first type of failure is studied.

The failure probability can be defined as,

$$P_f(T) = P[min(g(\boldsymbol{x}(t), t)) \leq 0] \quad (0 < t < T) \tag{6.38}$$

One challenge is that the time and location of the maximum response itself is a random variable and can not be specified a priori by the user.

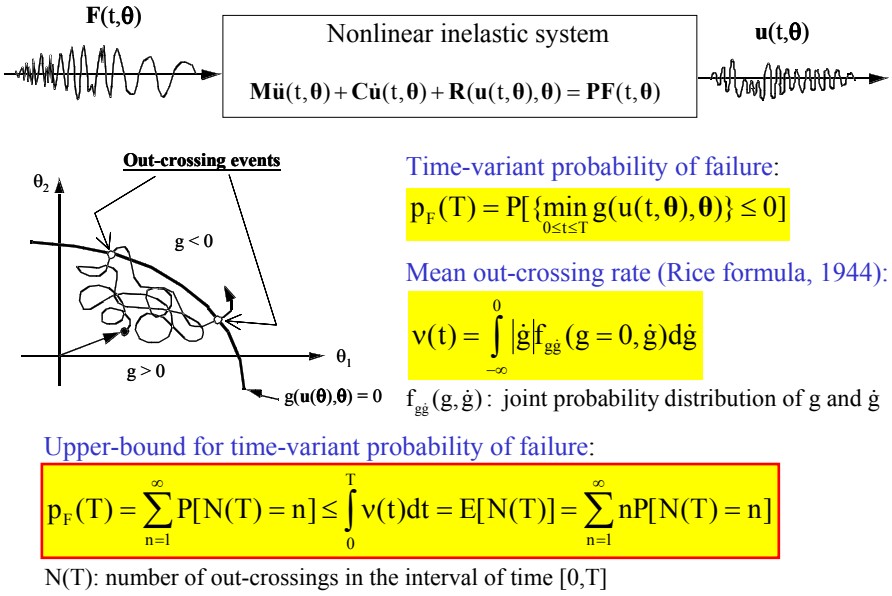


**Figure 6.16 Mean upcrossing rate analysis**

Later it will be demonstrated that in practice a solution to this problem is to define a limit state function at many time steps, and solve it as a series system reliability problem. At each time step, the problem becomes a time invariant reliability problem and may be solved by time invariant reliability methods such as FORM, SORM or sampling methods.

To compute the probability of failure at a specific time point $t$ (i.e., $g((\boldsymbol{x}(t)) < 0)$, or more generally, $y(t) > \zeta$, where *y(t)* is an uncertain quantity), Rice gives a formula to estimate the failure probability.

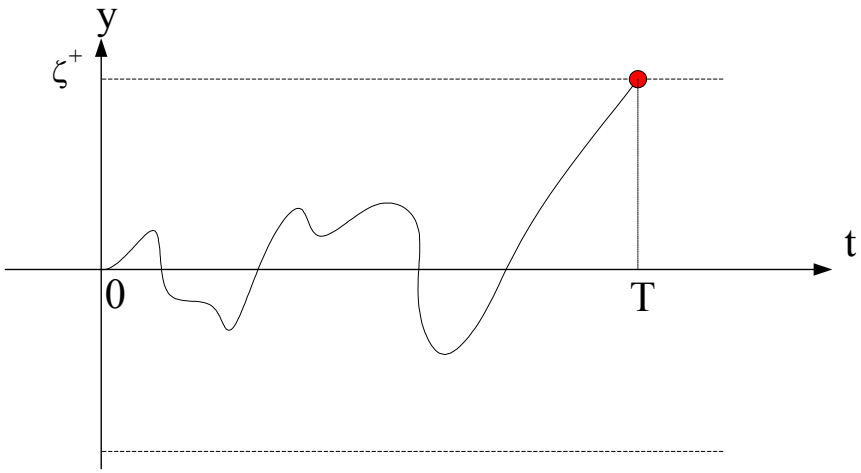


**Figure 6.17 The first excursion failure event**

### 6.5.2 Rice's Formula

Define $P[\zeta^+, t]$ as the probability corresponding to the out crossing level $\zeta^+$ in (*t*, *t*+*dt*). Then,

$$\begin{aligned} P[\zeta^+, t] &= P[(y(t) < \zeta) \cap (y(t) + \dot{y}(t)dt > \zeta) \cap (\dot{y}(t) > 0)] \\ &= P[\zeta - \dot{y}(t)dt < y(t) < \zeta] \end{aligned} \tag{6.39}$$

where $y(t)$ and $\dot{y}(t)$ are two random variables at a fixed time t.

As shown in Figure 6.18,

$$P[\zeta^+, t] = \int_0^\infty \int_{\zeta - \dot{y}(t)dt}^{\zeta} f_{x\dot{x}}(y, \dot{y}, t)dyd\dot{y} \tag{6.40}$$

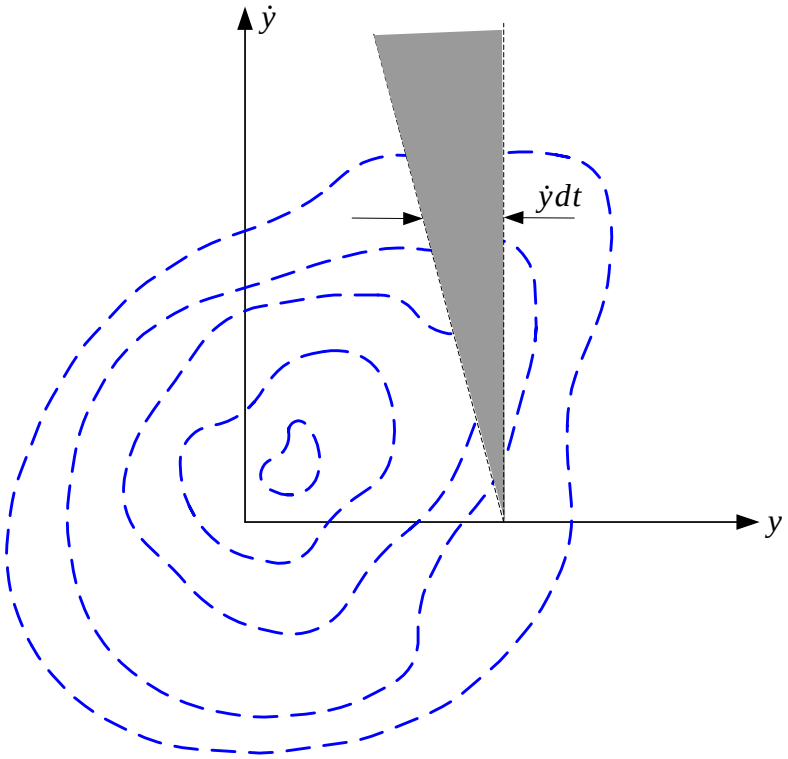


**Figure 6.18 The contour of** $f_{y\dot{y}}(y, \dot{y}, t)$

Using the mean value theorem, and considering the time $dt$ as infinitesimally small,

$$\int_{\zeta - \dot{y}(t)dt}^{\zeta} f_{y\dot{y}}(y, \dot{y}, t)dx = f_{y\dot{y}}(\zeta, \dot{y}, t)\dot{y}dt \tag{6.41}$$

From Equation (6.40) and (6.41),

$$P[\zeta^+, t] = dt\int_0^{\infty} f_{y\dot{y}}(\zeta, \dot{y}, t)\dot{y}d\dot{y} \tag{6.42}$$

Let $dN(\zeta^+, t, t+dt)$ be the number of outcrossings of level $\zeta^+$ in $(t, t+dt)$. Define the mean outcrossing rate of level $\zeta^+$ at time $t$ as,

$$\nu(\zeta^+, t) = E\left[\frac{dN}{dt}\right] \tag{6.43}$$

Then

$$\begin{aligned} '[dN] &= 0 \times P[0 \text{ outcrossing in } (t, t+dt)] \\ &\quad + 1 \times P[1 \text{ outcrossing in } (t, t+dt)] \\ &\quad + 2 \times P[2 \text{ outcrossing in } (t, t+dt)] + . \\ &\approx P[1 \text{ outcrossing in } (t, t+dt)] \end{aligned} \tag{6.44}$$

Since the higher order terms of the failure probability $P$[2 or more outcrossing in (t,t+dt)]can be ignored compared with the first order $P$[1 outcrossing in (t,t+dt)]. From Equations (6.42) to (6.44), consider the sign of *x(t)*, (Rice, 1945)

$$\nu(\zeta^+, t) = \int_0^\infty f_{y\dot{y}}(\zeta, \dot{y}, t)|\dot{y}|\,d\dot{y} \tag{6.45}$$

The mean outcrossing (upcrossing) rate can be a very good upper bound for the probability of failure as shown below:

$$\begin{aligned} P[\text{Failure in } (t_1, t_2)] &= P[1 \text{ crossing} \cup 2 \text{ crossings} \cup 3 \text{ crossings} \ldots] \\ &= \sum_{n=1}^{\infty} P[\text{n crossings}] \end{aligned} \tag{6.46}$$

since the events (n crossings) are mutually exclusive events.

And, from Equation (6.44),

$$
\begin{aligned}
E[N(\zeta^+, t_1, t_2)] &= \int_{t_1}^{t_2} \nu(\zeta^+, t)dt \\
&= 0 \times P[0 \text{ upcrossing in } (t_1, t_2)] \\
&+ 1 \times P[1 \text{ upcrossing in } (t_1, t_2)] \\
&+ 2 \times P[2 \text{ upcrossing in } (t_1, t_2)] + ...
\end{aligned} \tag{6.47}
$$

From Euqation (6.46) and (6.47)

$$
P[\text{ Failure in } (t_1, t_2)] \le \int_{t_1}^{t_2} \nu(\zeta^+, t)dt \tag{6.48}
$$

This is a very good upper bound when the failure probability is small. In this case, term n=1 dominates the whole failure probability. Reference (Bolotin, 1967)

### 6.5.3 Estimation of Mean Out Crossing Rate

The rate of out crossing of **x**(t) into a component domain of failure per unit time is $D = \{g[\boldsymbol{x}(t), \dot{\boldsymbol{x}}(t)] \le 0\}$. Based on the Rice equation (6.45), the mean value of the out-crossing rate is

$$
\nu(t) = -\int_{-\infty}^{0} |\dot{g}| f_{g\dot{g}}(0, \dot{g}, t)d\dot{g} \tag{6.49}
$$

where $f_{g\dot{g}}$ is the joint probability density function of the limit state function $g[\boldsymbol{x}(t), \dot{\boldsymbol{x}}(t)]$ at time t. This joint density function is extremely difficult or nearly impossible to obtain for a general nonlinear inelastic system. Alternatively, the mean out crossing rate can be computed from the limit formula (Hagen, O., 1991).

$$\nu(t) = \lim_{\delta t \to 0} \frac{P\left\{ g_1(\boldsymbol{x}) > 0 \cap g_2(\boldsymbol{x}) < 0 \right\}}{\delta t} \tag{6.50}$$

where $g_1(\boldsymbol{x}) = G[\boldsymbol{x}(\theta, t)]$ and $g_2(\boldsymbol{x}) = G[\boldsymbol{x}(\theta, t + \delta t)]$. This equation is understood as one or more outcrossing events having happened during the time $[t, t + \delta t]$. In practice, equation (6.50) is solved using a perturbation method, i.e.,

$$\nu(t) \approx \frac{P[g_1(\boldsymbol{x}) > 0 \cap g_2(\boldsymbol{x}) < 0]}{\delta t} \text{ for small } \delta t \tag{6.51}$$

To get an accurate result, the perturbation $\delta t$ must be small enough. However, the two events $g_1(\boldsymbol{x}) > 0$ and $g_2(\boldsymbol{x}) < 0$ are occur nearly at the same time (only $\delta t$ apart from each other) and with opposite inequality signs. If we use too small a $\delta t$, the correlation coefficient between the two linearized events approaches -1, causing a singularity in solving the $P[g_1(\boldsymbol{x}) > 0 \cap g_2(\boldsymbol{x}) < 0]$, and a loss in accuracy. In practice, $\delta t = \frac{\Delta t}{10} \sim \frac{\Delta t}{100}$ may be a good enough choice. where $\Delta t$ is the interval used to discretize the excitation. (Heonsang koo, 2003)

### 6.5.4 FORM Approximation of the Mean Upcrossing Rate and Failure Probability

To solve the $P[g_1(\boldsymbol{x}) > 0 \cap g_2(\boldsymbol{x}) < 0]$ in equation (6.51),the first order reliability method (FORM) is employed for computing the mean upcrossing rate. As shown in Figure 6.19, the mean up-crossing rate is represented by the shaded area. The two design

points at time $t$ and $t + \delta t$ are $u_1^*$ and $u_2^*$, with design point directions $\boldsymbol{\alpha}_1$ and $\boldsymbol{\alpha}_2$. In the FORM approximation, the two limit state surfaces linearized at design points $u_1^*$ and $u_2^*$, are $(h_1)_{Linearized} = 0$ and $(h_2)_{Linearized} = 0$. The real upcrossing rate is then approximated by the area between these two planes as shown in Figure 6.19.

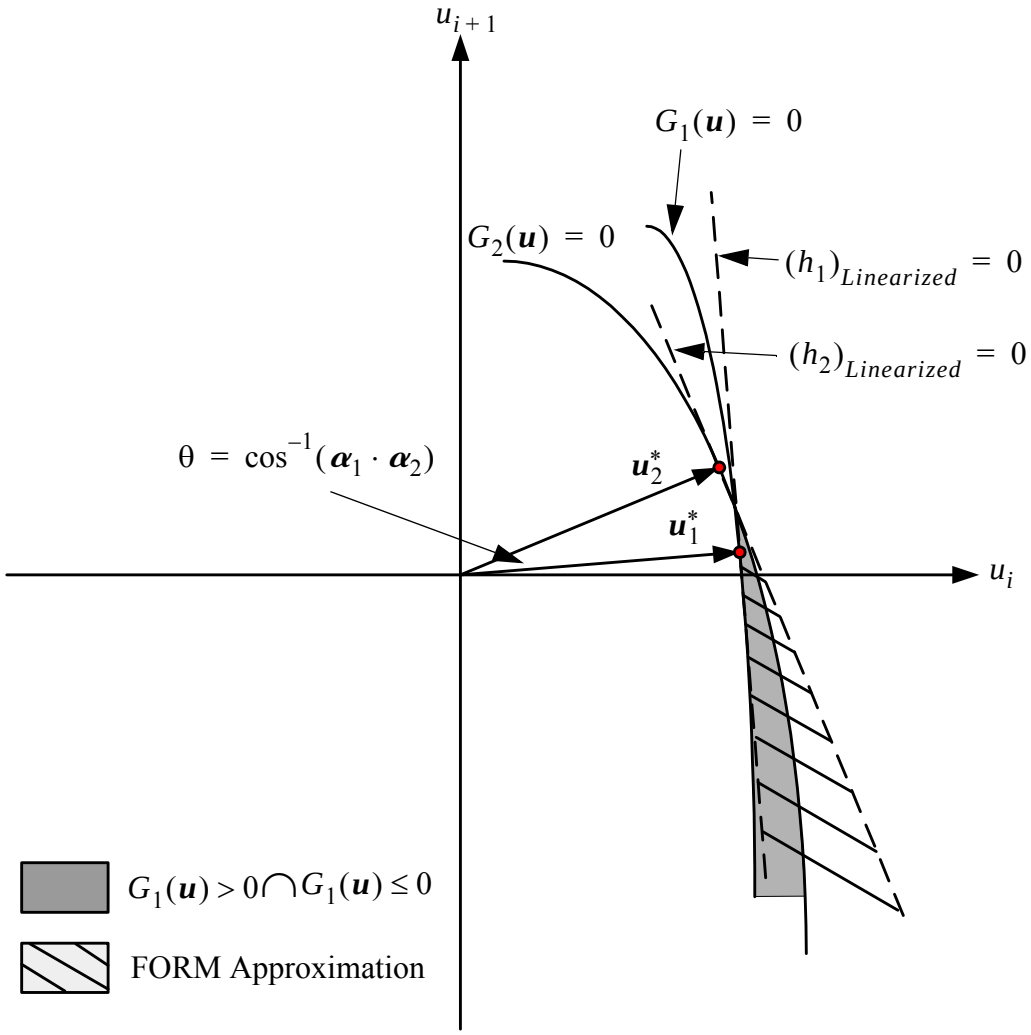


**Figure 6.19 Failure domain of the parallel system for computing the mean out-crossing rate**

The probability content in the failure domain defined by the intersection of the two linearized limit state surfaces is given by (Madsen, 1986)

$$P \approx \Phi(-\beta_1)\Phi(-\beta_2) + \int_0^{\rho_{12}} \phi_2(-\beta_1, -\beta_2, \rho) d\rho \tag{6.52}$$

where $\rho_{12} = \boldsymbol{\alpha}_1 \cdot \boldsymbol{\alpha}_2$ is the correlation coefficient between the two linearized failure modes, and $\phi_2(-\beta_1, -\beta_2, \rho)$ is the bi-variate normal joint PDF with zero means, unit variances and correlation coefficient $\rho$, i.e.,

$$\phi_2(-\beta_1, -\beta_2, \rho) = \frac{1}{2\pi(1-\rho^2)} \exp\left(-\frac{\beta_1^2 + \beta_2^2 - 2\rho\beta_1\beta_2}{2(1-\rho^2)}\right) \tag{6.53}$$

In practice, $g_1(\boldsymbol{x}) = G[\boldsymbol{x}(\theta, t)]$ and $g_2(\boldsymbol{x}) = G[\boldsymbol{x}(\theta, t+\delta t)]$. Writing a first order approximation for $g_2(\boldsymbol{x})$

$$g_2(\boldsymbol{x}) \approx G[\boldsymbol{x}(\theta, t)] + \nabla_{\boldsymbol{x}} G[\boldsymbol{x}(\theta, t)] \dot{\boldsymbol{x}}(\boldsymbol{x}, t)\delta t \tag{6.54}$$

In order to obtain the design points on these two limit state surfaces, the gradients $\frac{\partial g_1(\boldsymbol{x})}{\partial \theta}$ and $\frac{\partial g_2(\boldsymbol{x})}{\partial \theta}$ are required and are computed by using the chain rule:

$$\frac{\partial g_1(\boldsymbol{x})}{\partial \theta} = \frac{\partial G(\boldsymbol{x}(\theta, t))}{\partial \boldsymbol{x}} \cdot \frac{\partial \boldsymbol{x}}{\partial \theta} \tag{6.55}$$

$$\frac{\partial g_2(\boldsymbol{x})}{\partial \theta} = \frac{\partial G(\boldsymbol{x}(\theta, t))}{\partial \boldsymbol{x}} \cdot \frac{\partial \boldsymbol{x}}{\partial \theta} + \frac{\partial \nabla_{\boldsymbol{x}} G[\boldsymbol{x}(\theta, t)]}{\partial \theta} \dot{\boldsymbol{x}}(\boldsymbol{x}, t)\delta t + \nabla_{\boldsymbol{x}} G[\boldsymbol{x}(\theta, t)] \frac{\partial \dot{\boldsymbol{x}}(\boldsymbol{x}, t)}{\partial \theta} \delta t \tag{6.56}$$

For the simplest limit state function,

$G[\boldsymbol{x}(\theta, t)] = x_{limit} - x_i(\theta, t)$, $\dfrac{\partial \nabla_x G[\boldsymbol{x}(\theta, t)]}{\partial \theta} = 0$, then equation (6.56) becomes,

$$\frac{\partial g_2(\boldsymbol{x})}{\partial \theta} = \frac{\partial G(\boldsymbol{x}(\theta, t))}{\partial \boldsymbol{x}} \cdot \frac{\partial \boldsymbol{x}}{\partial \theta} + \nabla_x G[\boldsymbol{x}(\theta, t)] \frac{\partial \dot{\boldsymbol{x}}(\boldsymbol{x}, t)}{\partial \theta} \delta t \tag{6.57}$$

otherwise, the following equation is used to compute $\dfrac{\partial \nabla_x G[\boldsymbol{x}(\theta, t)]}{\partial \theta}$

$$\frac{\partial \nabla_x G[\boldsymbol{x}(\theta, t)]}{\partial \theta} = \frac{\partial \nabla_x G[\boldsymbol{x}(\theta, t)]}{\partial \boldsymbol{u}} \cdot \frac{\partial \boldsymbol{u}}{\partial \theta} \tag{6.58}$$

However, as mentioned before, the high correlation between $g_1$ and $g_2$ (or, $\rho_{12} = \boldsymbol{\alpha}_1 \cdot \boldsymbol{\alpha}_2 \approx 1.0$) and the fact $\beta_1 \approx \beta_2$ will cause the $\phi_2(-\beta_1, -\beta_2, \rho)$ in Equation (6.53) to be almost singular, thus the integration in Equation (6.52) requires the two design points to be very accurate. In the real SFSI problem, this requirement is very difficult to meet.

*Koo's Equation*

Considering the close relation of the two limit state functions $g_1(\boldsymbol{x}) = G[\boldsymbol{x}(\theta, t)]$ and $g_2(\boldsymbol{x}) = G[\boldsymbol{x}(\theta, t + \delta t)]$, the problem can be solved in a more simple alternative manner. The second limit state function (LSF) $g_2(\boldsymbol{x})$ is almost identical to the first one $g_1(\boldsymbol{x})$, however the second LSF has a very small time shift $\delta t$. After the design point excitation of the first component is found, $f_1(t)$, we can approximate the second design point excitation by shifting the first design point by the small time increment $\delta t$. i.e. $f_2(t) = f_1(t + \delta t)$. This is the case for the stationary excitation since the design point

excitations at different time points have the same shape but are shifted by the time interval $\delta t$ between these time points. For the non-stationary case, this equation also gives a good approximation when time interval $\delta t$ is much smaller than the time scale of changes of the probabilistic structure of the non stationary process. (Koo dissertation). Under this assumption, the second reliability index is $\beta_1 \approx \beta_2$, and the second designpoint direction $\boldsymbol{\alpha}_2$ is obtained by shifting $\boldsymbol{\alpha}_1$ in time by $\delta t$. Equation (6.53) can then be estimated directly by: (Koo, H. 2003).

$$\phi_2(-\beta, -\beta, \rho) \approx \frac{1}{2\pi}\exp\left(-\frac{\beta^2}{2}\right)[\sin^{-1}(\rho) - \sin^{-1}(-1)] \tag{6.59}$$

where $\rho = \boldsymbol{\alpha}_1 \cdot \boldsymbol{\alpha}_2$

Compared with the method of separately obtaining the two design points for $g_1(\boldsymbol{x})$ and $g_2(\boldsymbol{x})$, Koo's equation (6.59) has several advantages: the design point is computed only once cutting computational costs in half. Further more, the design point does not need to be extremely accurate as required by the "two design points method".

The Koo's equation are very useful in practical engineering problems, especially in large scale SFSI problems. In SFSI problems, in order to save computational time, the tolerance of the convergence of FEM is usually set to be large ( e.g., for norm of incremental displacement vector, the tolerance is usually set to be 1.0E-3 [m], for satisfying the engineer's requirement). Then the design point is not possible to be extremely accurate. Koo's equation is very powerful in these problems.

### 6.5.5 Discrete Representation of Stochastic Excitation

To solve structural random vibration problems, the input processes are represented in terms of a finite number of random variables. In current stochastic models, general nonstationary stochastic processes $Q(t)$ are typically expressed as,

$$Q(t) = \mu(t) + c_1 \sum_{k=1}^{K} q_k(t) \sum_{i=1}^{N} y_{ik} h_k(t - t_i) \tag{6.60}$$

where $\mu(t)$ is a deterministic time-varying mean function and parameter $c_2$ is a deterministic constant. The sequence $y_1\ y_2\ ...\ y_N$ is a train of pulses in which each $y_i$ is defined as a standard normal random variable at time point $t_i$, and $y_i$ are equally spaced along the time axis. This sequence $y_1\ y_2\ ...\ y_N$ represents the intermittent ruptures at the fault, and approaches a Gaussian white noise process as the number N approaches infinity. $q_k(t)$ is the $k^{th}$ deterministic modulating function, used to control the variance of the process along the time axis. The deterministic filter function $h(t-t_i)$, generally selected as the unit impulse response function with damping, can represent the ground medium through which the wave travels. (Der Kiureghian 2000, Koo, H., 2003. Koo, H. and Der Kiureghian, 2003) .

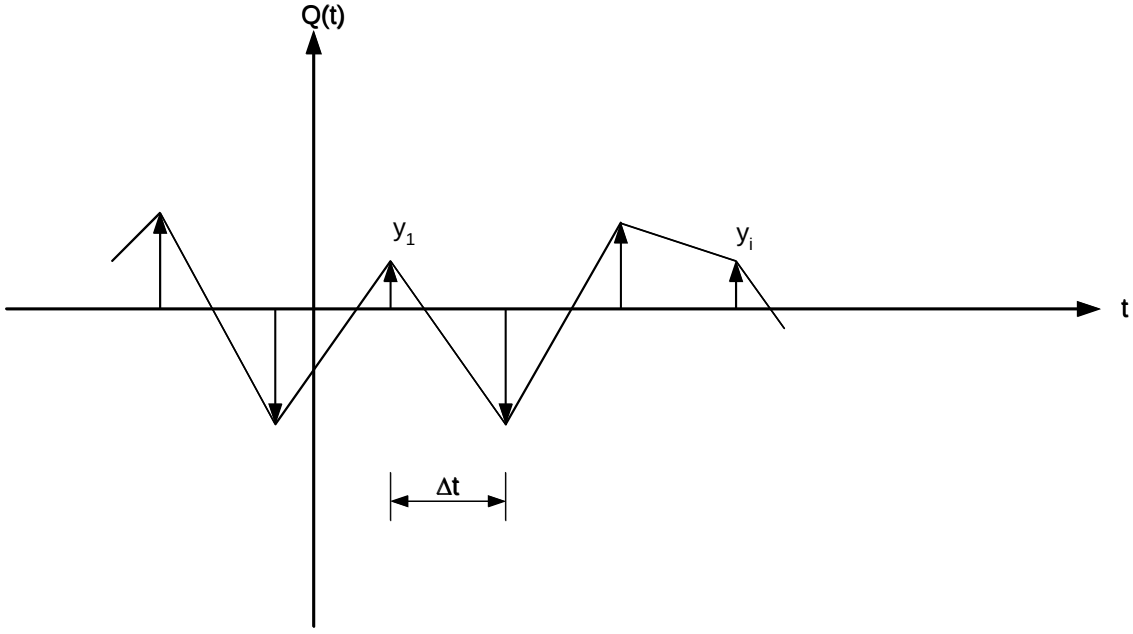


**Figure 6.20 Discrete representation of a white noise**

In this dissertation, the Gaussian white noise is employed to represent the earthquake input. By selecting $\mu(t) = 0$, $q_k(t) = 1.0$, $h_k(t - t_i) = 1.0$ in Equation (6.60), *Q(t)* is simplified to a Gaussian white noise with zero mean and standard deviation $c_1$.

In practice, the integration time step of the Finite Element analysis is often shorter than the time interval Δt between two neighboring impulses. In this case, the linear interpolation for discrete Gaussian white noise is employed. Assuming the random excitation process varies linearly between the values $y_i$ (i=1,2,...) as shown in the figure 6.20.

It can be shown that the standard deviation of the white noise, the time interval Δt, and the intensity $\phi_0$ are related by, (Conte P., 1998)

$$\frac{\sigma^2 \Delta t}{2\pi} = \phi_0 \tag{6.61}$$

## 6.6 Application Examples of Time variant Reliability Analysis of SFSI System

### 6.6.1 2D SFSI System

The example of a non-smooth model mentioned in section 4.6.1 is studied for the time variant case. The natural frequency is approximately f=5.5 Hz. The properties of the SSI system are considered to be determinant, while the only uncertainties are assumed in the earthquake input. This stochastic excitation takes the simple form of white noise, i.e., an impulse train $\sum_0^n f_i \delta(t - t_i)$ with constant time interval $\Delta t = t_i - t_{i-1} = 0.02 \text{ sec}$. The system is initially at rest. The integration time step is taken as $dt = 0.005 \text{ sec}$, and the time increment used to evaluate the mean out-crossing rate is taken as $\delta t = 0.0001 \text{ sec}$. The intensity of the white noise is $\phi_0 = 0.0275$. The system does not have Rayleigh damping, however equivalent damping is observed by the strongly nonlinear plastic behavior or the soil and structure systems. If assuming the damping ratio $\zeta$ of the SSI system is between 10% and 20%, using Mile's equation, the root mean square acceleration in g's is:

$$\ddot{u}_g = \sqrt{\frac{\pi}{4\zeta} \cdot f \cdot \phi_0} = 0.7\sim1.1[g] \tag{6.62}$$

The performance function is defined as,

$$g_1 = \Delta_{limit} - \Delta_1 \tag{6.63}$$

where $\Delta_1$ is the first floor drift. $\Delta_{limit}$ is taken as 3.6 cm, which is 1% of the height of the first floor.

The mean upcrossing rate analysis is performed from a time t=0.5sec, to t = 3.0sec, at $\Delta t = 0.5\text{sec}$ time increments. The design point at a time t is shifted along the time axis to $t + \Delta t$ and filled with zeros between $(0, \Delta t)$. This shifted point is used as the 'warm' starting point of the design point searching algorithm at $t + \Delta t$. As will be shown later, the shape of the design points at two sequential times are very similar except the values are shifted along the time axis. This provides a proof that the shifted design point may serve as a good 'warm' starting point for the design-point-searching at the next time point.

The FORM and OPS results are shown in Figure 6.21. From this figure, it is clear that after 2.0 sec, the mean upcrossing rate obtained by both methods tend to be stable, while FORM and OPS give significantly different mean upcrossing rates. This difference is due to the fact that the LSS, close to the design point is highly non-linear, the FORM results consider only the first order contribution of the mean upcrossing rate and thus are potentially very inaccurate.

The mean upcrossing rate obtained by FORM at point t=2.5 sec is higher than its neighbors because at this point, the design point can not be obtained with the same accuracy (1.0e-5) as at other points, instead a relaxed criterion (1.0e-4) is used to obtain an

approximate design point. As previously mentioned the OPS does not require a highly accurate design point. As a result the design point at t=2.5 sec, while inaccurate, is still acceptable.

A Crude MCS method is used to check the mean of the upcrossing events and the failure probability. The comparison results for the mean of the upcrossing events and the failure probability by different methods are shown in Figure 6.22. From these results, it is clear that the OPS gives a much better approximation of the mean upcrossing events than that obtained by FORM.

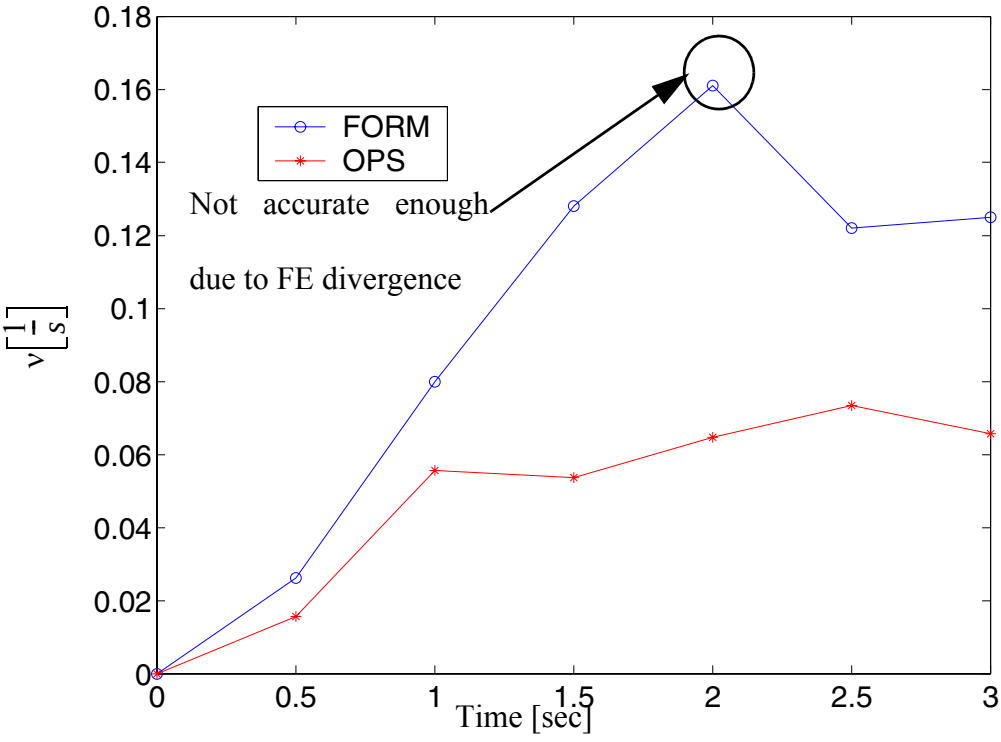


**Figure 6.21 Comparison of the FORM approximation of the mean upcrossing rate and OPS results**

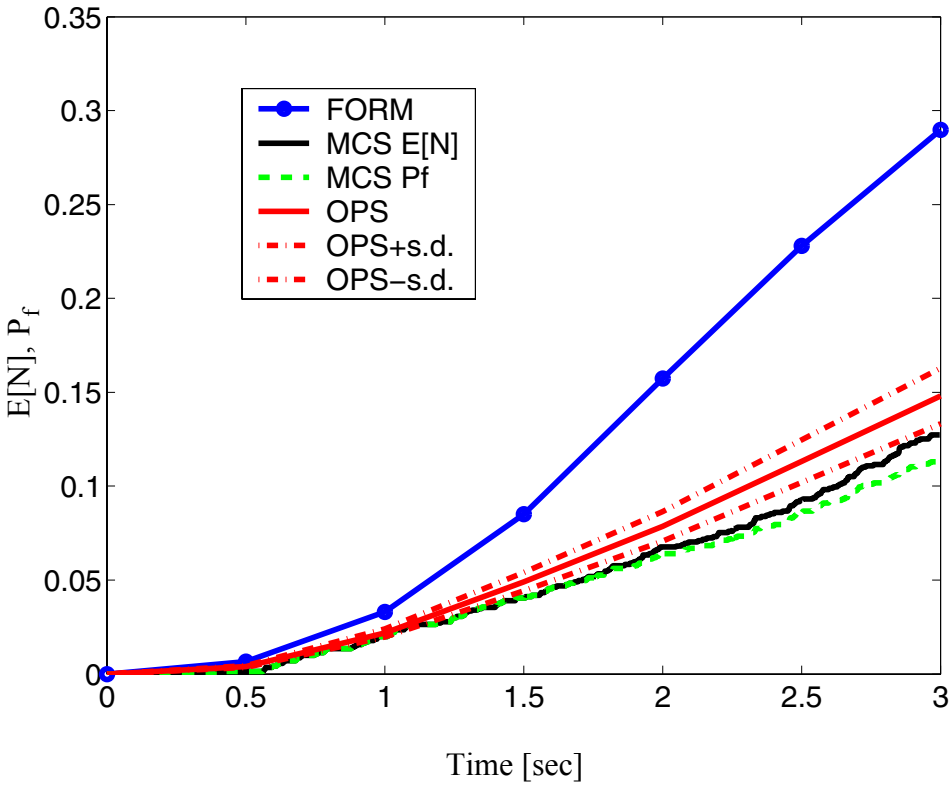


**Figure 6.22 Mean upcrossing events and failure probability estimates**

The estimate of the mean upcrossing events and failure probability are reported in Table 6.7. The OPS greatly improved the accuracy of the mean upcrossing events obtained by FROM. For example, at time t=3.0 sec, the tolerance of OPS is 19.64%, while FORM is 208%.

**Table 6.7 Comparison of mean upcrossing rate and mean upcrossing events obtained by using FORM, OPS and MCS**

| Time [sec] | Mean upcrossing rate | | Failure probability (%) | | | Number of simulations | |
|---|---|---|---|---|---|---|---|
| | FORM | OPS | FORM | OPS | MCS | OPS | MCS |
| 0.5 | 2.62e-2 | 1.57e-2 | 0.66 | 0.39 | 0.14 | 1631 | 2800 |
| 1.0 | 7.99e-2 | 5.56e-2 | 3.31 | 2.17 | 1.99 | 1809 | 2800 |
| 1.5 | 1.28e-1 | 5.37e-2 | 8.51 | 4.91 | 4.05 | 2398 | 2800 |
| 2.0 | 1.61e-1 | 6.47e-2 | 15.73 | 7.87 | 6.75 | 2300 | 2800 |
| 2.5 | 1.22e-1 | 7.34e-2 | 22.81 | 11.32 | 9.24 | 3058 | 2800 |
| 3.0 | 1.25e-1 | 6.57e-2 | 28.98 | 14.80 | 12.37 | | 2800 |

The design points at different times are shown in Figure 6.23. It is observed that the shape of the design points at two sequential times are very similar except the values are shifted along the time axis. This provides a proof that the shifted design point may serve as a ‘warm’ starting point for the design-point-searching at the next time point.

The responses of the first floor drift at design points are shown in Figure 6.24.

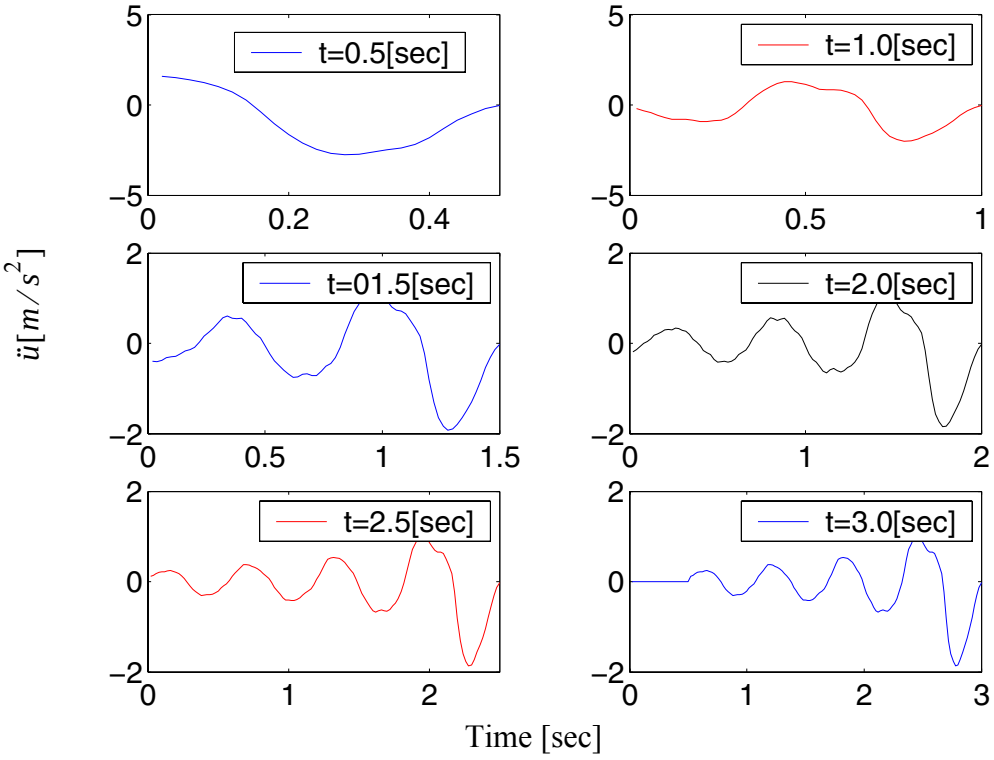


**Figure 6.23 Design points**

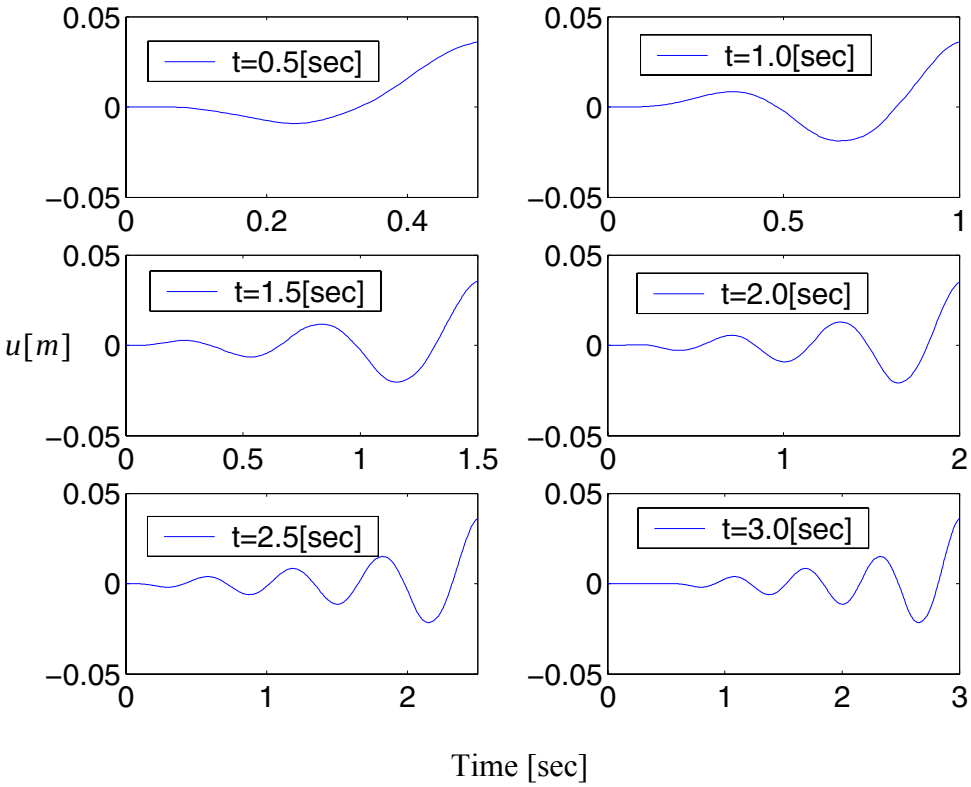


**Figure 6.24 The first interstory drift response histories at design points**

The local moment-curvature and stress-strain responses at Gauss points A and B (Figures 6.25) are shown in Figures 6.26 and 6.27. It is obvious that the system yields significantly at the design points.

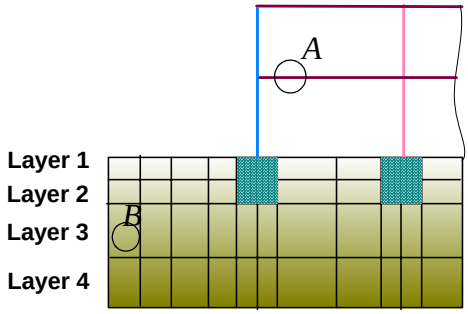


**Figure 6.25 Points where the local responses are recorded**

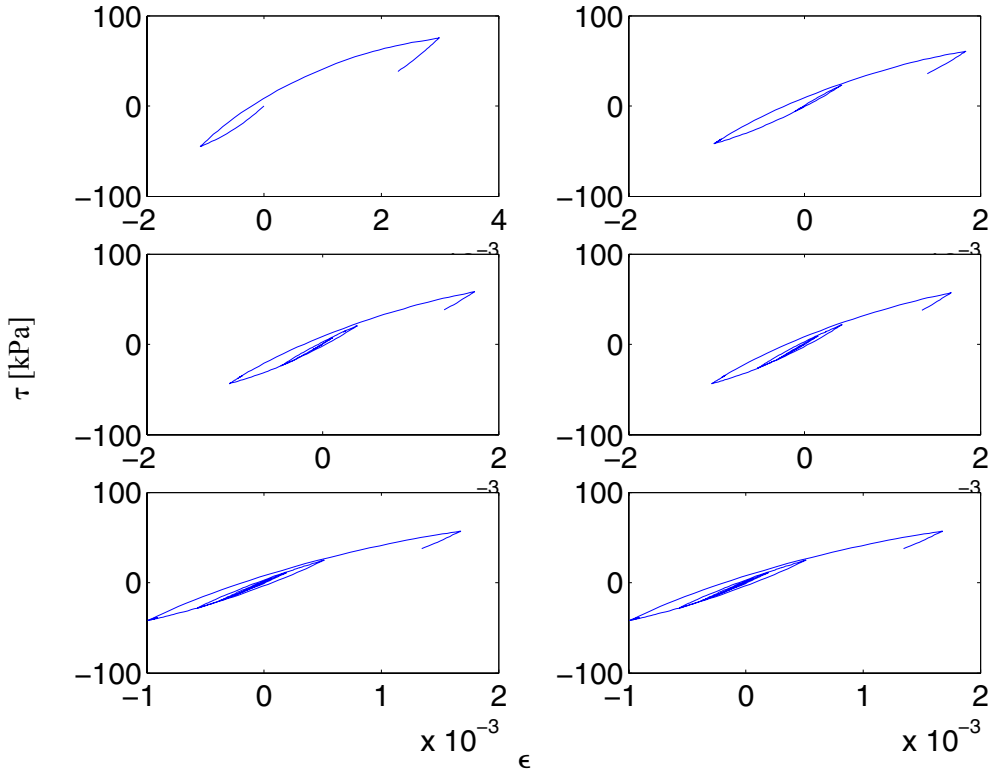


**Figure 6.26 Stress strain responses at point B of the third soil layer**

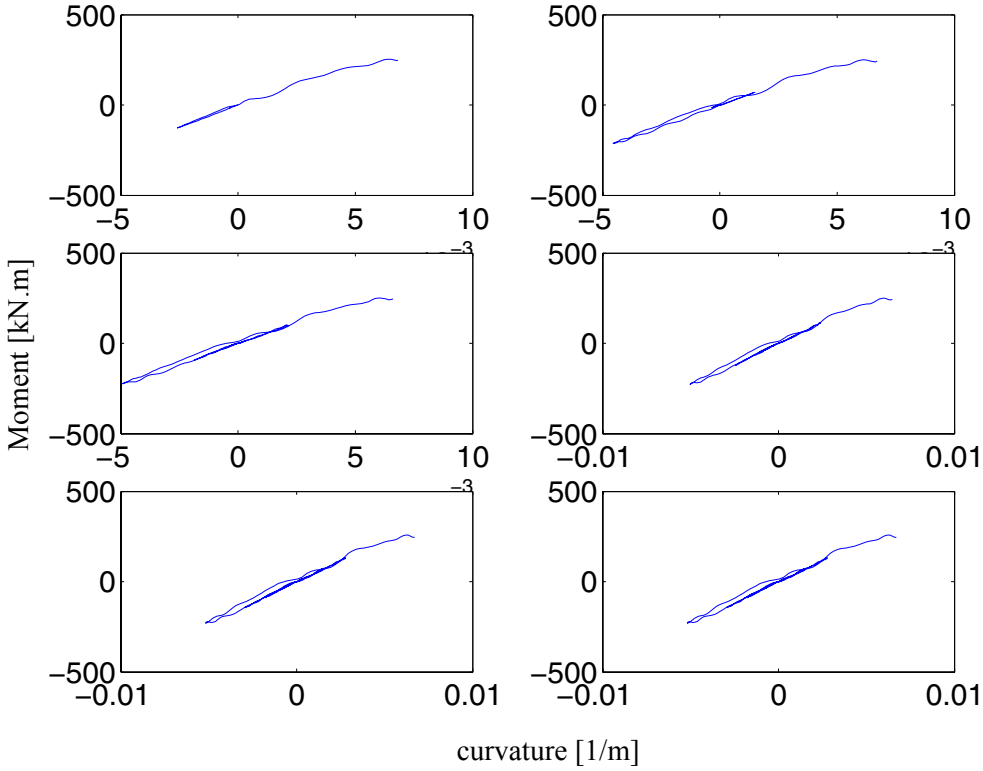


**Figure 6.27 Moment curvature responses at point A**

In nonlinear SSI systems time variant reliability analyses, the OPS combined with design points provides a good estimate of the upper bound of the failure probability, which is much more accurate than the FORM estimate.

## 6.7 Multi-Dimensional Visualization in Principle Planes (MVPP)

In this chapter, a new visualization technique is provided to study the limit state surface in standard normal space. One motivation for a new visualization technique comes from the results that in the nonlinear case, the FORM approximation of the mean upcross-

ing rate analysis is hardly accurate as previously mentioned. This suggests that the LSS at the design point is highly nonlinear and cannnot be approximated by a plane. The LSS is usually a surface in a multi-dimensional space. The dimension depends on the number of random variables which could range from a few to several thousands. Knowledge of the topology of the LSS is valuable in the following sense: (1) it aids in understanding the reasons for potential divergence in the design point search process, and thus may suggest ways to develop more robust and efficient design point search algorithms; (2) it may explain the inaccuracies of the FORM/SORM approximations for time-invariant probability of failure probability and mean out-crossing rate computations, leading to the development of more efficient and accurate algorithms for these computations.

However, only limited studies may be found in the literature (Der Kiureghian 2000, Haukaas and Der Kiureghian 2004), probably because of the difficulties encountered in the study of the topology of the LSS in high-dimensional spaces. In this dissertation, a new method is developed for the visualization of LSF or LSS in high-dimensional spaces, denoted here as Multi-Dimentional Visualization in Principle Planes (MVPP), for both time-invariant and time-variant finite element reliability analysis.

The basic idea of MVPP is to visualize the LSF (LSS is one contour of the LSF) at the design point in each principal plane, which is defined by the DP direction **u*** and one of the eigenvectors (or Principal Direction) of the normalized and reduced Hessian matrix **A** defined as (see MB dissertation Chapter 11, Section 11.4):

$$\boldsymbol{A} = \frac{\boldsymbol{H}_{reduced}}{\left\| \nabla_{\boldsymbol{u}} G \big|_{\boldsymbol{u}^*} \right\|} \tag{6.64}$$

in which $\boldsymbol{H}_{reduced}$ is the reduced Hessian with dimension $(n-1)\times(n-1)$, defined as $[\boldsymbol{H}_{reduced}]_{ij} = [\boldsymbol{R}\cdot\boldsymbol{H}\cdot\boldsymbol{R}]_{ij}$ with i, j = 1, 2, ..., n-1; The rotation matrix **R** is such that the DP direction is coincident with the last axis of the rotated coordinate system. **H** is the $n\times n$ Hessian matrix of the LSF at the DP in the standard normal space, and $\left\|\nabla_{\boldsymbol{u}}G\big|_{\boldsymbol{u}^*}\right\|$ denotes the Euclidean norm of the gradient of the LSF at the DP. It is worth noting that the hessian matrix **H** exists only if the LSF is twice differentiable, which is the case when the constitutive material models are smooth such that they are differentiable with respect to the sensitivity parameters.

In each Principal plane, a grid is created and on each grid point the value of the LSF is computed by FE simulations. The LSF is then visualized in the principal plane by using the grid values.

Obtaining the principal directions of the LSF is a crucial task in this MVPP method or the new DP-RS-Sim method mentioned later. It is possible to compute these directions by applying an existing algorithm (Der Kiureghian and De Stefano 1991) without computing the Hessian matrix. However, these methods are not yet available for the SNOPT based design point search algorithm. In this dissertation, the Hessian matrix **H** is computed by combining the FFD with the DDM based sensitivity results. That is,

$$H_{i,j} \approx \frac{\Delta\dfrac{\partial G}{\partial u_i}}{\Delta u_j} \tag{6.65}$$

where the sensitivity of the LSF to $\boldsymbol{u}$, $\frac{\partial G}{\partial u_i}$, is obtained by DDM. Determining the principal directions by using this method as shown in Equation 6.656.65 is expensive and considered only as a temporarily solution. More advanced algorithms need to be developed to compute the principal directions.

## 6.8 Design Point-Response Surface Method-Simulation (DP-RS-Sim) Technique

Knowledge obtained by MVPP about the the topology of the LSS near the DP(s) is valuable for improving FORM's approximation of the failure probability or mean upcrossing rate when accounting for nonlinearities in the LSF. It is observed that the LSS is highly nonlinear and cannot be approximated by a plane in nonlinear FE reliability problems. In this case the FORM/SORM approximations of nonlinear LSS(s) can be very inaccurate and may be a major source of error in estimating time-invariant and time-variant failure probabilities for structural systems exhibiting nonlinear behavior.

A new hybrid reliability method, referred to as Design Point-Response Surface-Simulation (DP-RS-Sim) method, is developed and implemented into OpenSees to solve the general reliability problems. The DP-RS-Sim method combines three steps ( and thus combines the strength of these three component/method):

(1) the design point(s) search,

(2) the RS method to approximate the LSF in a neighborhood around the DP, by an analytical or polynomial form,

(3) a simulation technique (Sim) used to evaluate the failure probability based on the RS representation of the actual LSF.

Steps (1) and (3) have previously been described while step (2) is developed in the following section.

### 6.8.1 Response Surface Method

In structural reliability analysis, the dimension of the LSS is usually between a few dozen to many thousands. It is therefore difficult to fit the LSF in the original high dimensional space. From the knowledge of the topology of the LSF obtained by MVPP, it is observed that only a few (5-7 at most) of the principal curvatures of the LSF at the DP are non-negligible, while the others are small enough that their nonlinear contributions may be ignored. Thus, the response surface method developed herein considers the nonlinearity only along the first several principal directions. Along all other directions the LSF is approximated by a linear function. Therefore, it is assumed that the contributions to the LSF along the first several principal directions of the LSF can be decoupled from those of the remaining principal directions, along which the LSF can be linearized with little or negligible loss of accuracy in representing the LSF.

Decomposition of the hyperdimensional space

For any point $\boldsymbol{u}$ in the standard normal space, we may rewrite $\boldsymbol{u}$ as

$$\boldsymbol{u} = u_1'\hat{\boldsymbol{e}}_{\mathbf{1}} + u_2'\hat{\boldsymbol{e}}_2 + \ldots u_N'\hat{\boldsymbol{e}}_N + u_{N+1}'\hat{\boldsymbol{e}}_{N+1} + \ldots + u_M'\hat{\boldsymbol{e}}_M \tag{6.66}$$

where M is the total number of the RVs, N is the number of principal axes along which the LSS is considered nonlinear. $\hat{\hat{\boldsymbol{e}}}_i$ is the direction of the i[th] principal direction of the LSS at the DP. Note that the DP direction is considered to be the first principal direction, while other directions are defined according to the decreasing magnitude of the principal curvatures of the LSS at DP. M is usually much larger than N. $u_i'$ is the projection of $\boldsymbol{u}$ on $\hat{\hat{\boldsymbol{e}}}_i$ and may be expressed as

$$u_i' = \boldsymbol{u} \cdot \hat{\boldsymbol{e}}_i . \tag{6.67}$$

If a new local coordinate system **Y**' is set up such that the new origin is at the DP $\boldsymbol{u}^*$, and each local axis $Y_i$ coincident with $\hat{\boldsymbol{e}}_i$, then in the new system **Y**', $\boldsymbol{u}$ may be expressed as a vector consisting of nonlinear and linear parts in vector format:

$$\boldsymbol{u} = \begin{bmatrix} \boldsymbol{u}_{non}' \\ \boldsymbol{u}_{lin}' \end{bmatrix} = \begin{bmatrix} u_1' \\ \vdots \\ u_N' \\ \text{----} \\ u_{N+1}' \\ \vdots \\ u_M' \end{bmatrix}_{M \times 1} \tag{6.68}$$

where,

$$\boldsymbol{u}_{non}' = \begin{bmatrix} u_1' \\ \vdots \\ u_N' \end{bmatrix}_{N \times 1} \quad \text{and } \boldsymbol{u}_{lin}' = \begin{bmatrix} u_{N+1}' \\ \vdots \\ u_M' \end{bmatrix}_{(M-N) \times 1} \tag{6.69}$$

are vectors in the subspace. In practice, these vectores are related to the corresponding vectors in the original space as,

$$\boldsymbol{u} = \begin{bmatrix} \boldsymbol{u}_{non}' \\ \boldsymbol{u}_{lin}' \end{bmatrix} = \boldsymbol{u}_{non} + \boldsymbol{u}_{lin} \tag{6.70}$$

where

$$\boldsymbol{u}_{non} = \begin{bmatrix} \boldsymbol{u}_{non}' \\ \boldsymbol{0}' \end{bmatrix} = \boldsymbol{u} - \boldsymbol{u}_{lin} = \boldsymbol{u} - \sum_{i=N+1}^{M} u_1' \hat{\boldsymbol{e}}_i = \boldsymbol{u} - \sum_{i=N+1}^{M} (\boldsymbol{u} \cdot \hat{\boldsymbol{e}}_i)\hat{\boldsymbol{e}}_i \tag{6.71}$$

and

$$\boldsymbol{u}_{lin} = \begin{bmatrix} \boldsymbol{0}' \\ \boldsymbol{u}_{lin}' \end{bmatrix} = \sum_{i=N+1}^{M} u_1' \hat{\boldsymbol{e}}_i = \sum_{i=N+1}^{M} (\boldsymbol{u} \cdot \hat{\boldsymbol{e}}_i)\hat{\boldsymbol{e}}_i \tag{6.72}$$

are vectors with dimension $M \times 1$. N is the total number of RV, M is the number of non-linear axes. The LSF G($\boldsymbol{u}$) is assumed to be expressed as,

$$G(\boldsymbol{u}) = G_{non}(\boldsymbol{u}_{non}') + G_{lin}(\boldsymbol{u}_{lin}') \tag{6.73}$$

in other words, the nonlinear part $G_{non}(\boldsymbol{u}_{non}')$ and the linear part $G_{lin}(\boldsymbol{u}_{lin}')$ are assumed decoupled and thus are evaluated separately.

### 6.8.2 Nonlinear Surface Fitting

To fit the nonlinear part of the LSF $G_{non}(\boldsymbol{u}_{non}')$, two general methods are used, i.e., Univariate Decomposition Method (UDM) and Bivariate Decomposition Method (BDM).

Considering a nonlinear function G(**y**) of the N-dimensional vector **y** = [$y_1$ ... $y_N$]$^T$, the UDM assumes the approximation $G(\boldsymbol{y}) \cong \tilde{G}_1(\boldsymbol{y})$ , in which $\tilde{G}_1(\boldsymbol{y})$ is given by

$$\tilde{G}_1(\boldsymbol{y}) = \sum_{i=1}^{N} G_i(y_i) - (N-1)G(\bar{\boldsymbol{y}}) \tag{6.74}$$

where $\bar{\boldsymbol{y}} = [\bar{y}_1 \ \ldots \ \bar{y}_N]^T$ is the DP, while the univariate component function is $G_i(y_i) = G(\bar{y}_1, \ldots, \bar{y}_{i-1}, y_i, \bar{y}_{i+1}, \ldots, \bar{y}_N)$ .

The BDM assumes the following approximation $G(\boldsymbol{y}) \cong \tilde{G}_2(\boldsymbol{y})$ , in which $\tilde{G}(\boldsymbol{y})$ is given by

$$\begin{aligned} \tilde{G}(\boldsymbol{y}) &= \sum_{i_1 < i_2 \le N} G_{i_1, i_2}(y_{i_1}, y_{i_2}) - (N-2)\sum_{i=1}^{N} G_i(y_i) + \frac{(N-1)(N-2)}{2} \cdot G(\bar{\boldsymbol{y}}) \\ &= \sum_{i_1 < i_2 \le N} G_{i_1, i_2}(y_{i_1}, y_{i_2}) - (N-2)\tilde{G}_1(\boldsymbol{y}) - \frac{(N-1)(N-2)}{2} \cdot G(\bar{\boldsymbol{y}}) \end{aligned} \tag{6.75}$$

where $G_{i_1, i_2}(y_{i_1}, y_{i_2}) = G(\bar{y}_1, \ldots, \bar{y}_{i_1-1}, y_{i_1}, \bar{y}_{i_1+1}, \ldots, \bar{y}_{i_2-1}, y_{i_2}, \bar{y}_{i_2+1}, \ldots, \bar{y}_N)$ is the bivariate component function.

It is assumed that the function evaluations $G_i^{(j)}$ are available from FE simulations. Using Lagrangian interpolation, each univariate component function is given by

$$G_i(y_i) = \sum_{j=1}^{n_P} [G_i^{(j)} \cdot \varphi_j(y_i)] \tag{6.76}$$

where $n_P$ is the number of function evaluations, $\varphi_j(y_i)$ denotes the following shape function

$$\varphi_j(y_i) = \frac{\prod_{k=1,\,k\neq j}^{n_P} (y_i - y_i^{(k)})}{\prod_{k=1,\,k\neq j}^{n_P} (y_i^{(j)} - y_i^{(k)})} \tag{6.77}$$

In a similar way, the bivariate components is

$$G_{i_1,\,i_2}(y_{i_1}, y_{i_2}) \approx \sum_{j_1=1}^{n_P} \sum_{j_2=1}^{n_P} [G_{i_1,\,i_2}^{(j_1,\,j_2)} \cdot \varphi_{j_1}(y_{i_1}) \cdot \varphi_{j_2}(y_{i_2})] \tag{6.78}$$

where the coefficients $G_{i_1,\,i_2}^{(j_1,\,j_2)}$ are given by

$$\begin{aligned} G_{i_1,\,i_2}^{(j_1,\,j_2)} &= G(\bar{y}_1, \ldots, \bar{y}_{i_1-1}, y_{i_1}^{(j_1)}, \bar{y}_{i_1+1}, \ldots, \bar{y}_{i_2-1}, y_{i_2}^{(j_2)}, \bar{y}_{i_2+1}, \ldots, \bar{y}_N) \\ &= G_{i_1,\,i_2}(y_{i_1}^{(j_1)}, y_{i_2}^{(j_2)}) \end{aligned} \tag{6.79}$$

It is clear that a bivariate approximation first requires the development of the univariate approximation.

### 6.8.3 Linear Part Estimate

The linear part of the LSF $G_{lin}(\boldsymbol{u}_{lin}')$ is:

$$G_{lin}(\boldsymbol{u}_{lin}') = [\nabla_{\boldsymbol{u}} G|_{\boldsymbol{u}^*}]'_{1\times(M-N)} \cdot (\boldsymbol{u}_{lin}' - \boldsymbol{u}^{*\prime})_{(M-N)\times 1} \tag{6.80}$$

The contribution from the linear part $G_{lin}(\boldsymbol{u}_{lin}') = 0$ for the time invariant reliability case, because the gradient of the LSS at design point $\boldsymbol{u}_1^*$ $([\nabla_{\boldsymbol{u}} G|_{\boldsymbol{u}^*}]'_{1\times(M-N)})$ is opposite to the DP direction, while the vector $(\boldsymbol{u}_{lin}' - \boldsymbol{u}^{*\prime})_{(M-N)\times 1}$ does not have any component in the DP direction (because the component in DP direction is counted in the nonlinear part). However this does not hold for the second LSF in time variant reliability analysis case. This will be explained later.

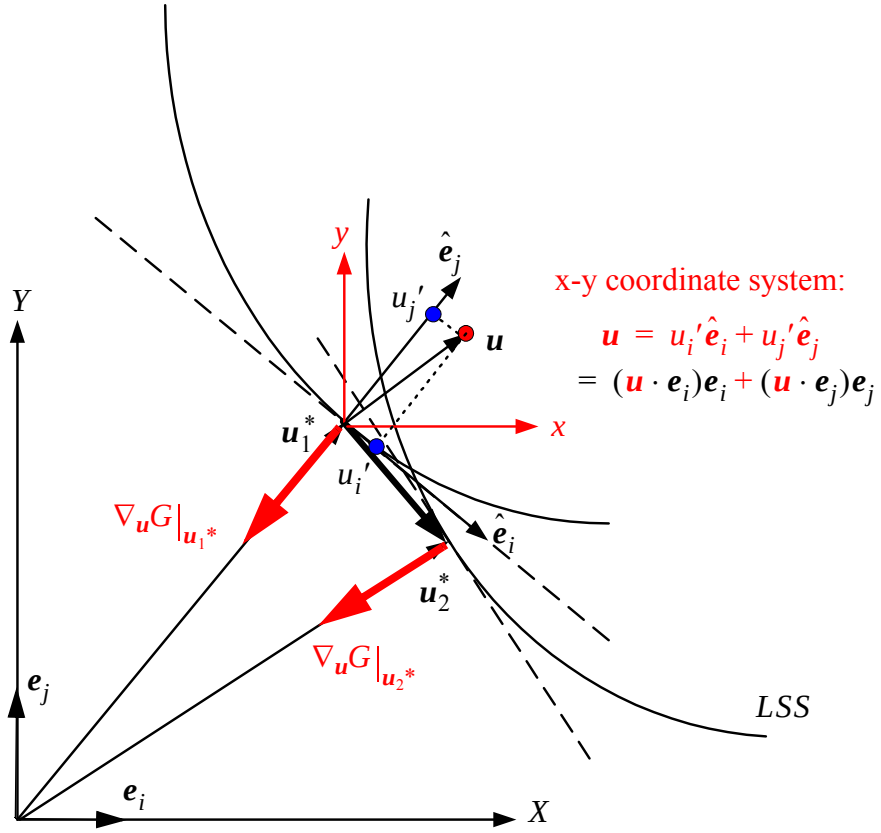


**Figure 6.28 Response surface fitting method**

### 6.8.4 Estimation of Values on the Second LSF

For the time variant reliability analysis, the second LSS is approximated by the response surface method. The DP is obtained by shifting a very small time shift $\delta t$ of the first DP as mentioned in Koo's equation in section 6.5.4. The value of $G_2$ is computed by Eq. (6.54), while the gradient $\nabla_{\boldsymbol{u}} G\big|_{\boldsymbol{u}_2^*}$ is assumed to have the same magnitude as $\nabla_{\boldsymbol{u}} G\big|_{\boldsymbol{u}_1^*}$ yet with opposite direction as the second DP. The nonlinear contribution to the second LSF is the same as that when evaluating the first LSF. For the linear part, the contribution is finite and can not be ignored. To get the contribution of the linear part to $G_2$, following equation is used,

$$\begin{aligned} G_{2,\,lin}(\boldsymbol{u}_{lin}{}') &= \nabla_{\boldsymbol{u}} G_2\big|_{\boldsymbol{u}_2^*} \cdot \begin{bmatrix} \boldsymbol{0}' \\ \boldsymbol{u}_{lin}{}' - \boldsymbol{u}_2^{*\prime} \end{bmatrix} \\ &= \nabla_{\boldsymbol{u}} G_2\big|_{\boldsymbol{u}_2^*} \cdot \sum_{i=N+1}^{M} ((\boldsymbol{u} - \boldsymbol{u}_2^{*\prime}) \cdot \hat{\boldsymbol{e}}_i)\hat{\boldsymbol{e}}_i \end{aligned} \tag{6.81}$$

The contribution from the linear part $G_{2,\,lin}(\boldsymbol{u}_{lin}{}')$ is nonzero because the gradient of the LSS at design point $\boldsymbol{u}_2^*$ $([\nabla_{\boldsymbol{u}} G|_{\boldsymbol{u}^*}]'_{1\times(M-N)})$ is not normal to the vector $(\boldsymbol{u}_{lin}{}' - \boldsymbol{u}_2^{*\prime})_{(M-N)\times 1}$.

### 6.8.5 The Fitting Process in OpenSees

As shown in Figure 6.28, the global coordinates are X-Y. On each grid plane, defined by the vectors ($\hat{\boldsymbol{e}}_i$, $\hat{\boldsymbol{e}}_j$), a local coordinate system x-y is set up by setting DP as the new

origin and translating the X-Y axes. In the local coordinate system x-y, every point on the grid in the local coordinate system ($u_i'$ , $u_j'$ ) is translated back into the global system as:

$$\boldsymbol{u} = u_i'\hat{\boldsymbol{e}}_i + u_j'\hat{\boldsymbol{e}}_j \tag{6.82}$$

where $\hat{\boldsymbol{e}}_i$ and $\hat{\boldsymbol{e}}_j$ are the two axes expressed in the global system. Eq. (6.82) may be further understood in the local coordinate system **Y**', as described in Eq. (6.68) as,

$$\boldsymbol{u} = \begin{bmatrix} \boldsymbol{u}_{non}' \\ \boldsymbol{u}_{lin}' = \boldsymbol{0} \end{bmatrix} = \begin{bmatrix} u_1' = 0 \\ \vdots \\ u_i' \neq 0 \\ \vdots \\ u_j' \neq 0 \\ \vdots \\ u_N' = 0 \\ \text{----} \\ u_{N+1}' = 0 \\ \vdots \\ u_M' = 0 \end{bmatrix} \tag{6.83}$$

Thus, From Eq. (6.73)

$$G_{non}^{fit}(\boldsymbol{u}_{non}') = G^{OpenSees}(\boldsymbol{u}) = G_{non}(\boldsymbol{u}_{non}') + G_{lin}(\boldsymbol{0}_{lin}') \tag{6.84}$$

Thus,

$$G_{non}(\boldsymbol{u}_{non}') = G_{non}^{fit}(\boldsymbol{u}_{non}') - G_{lin}(\boldsymbol{0}_{lin}') \tag{6.85}$$

And so,

$$G(\boldsymbol{u}) = G_{non}^{fit}(\boldsymbol{u}_{non}') + G_{lin}^{fit}(\boldsymbol{u}_{lin}') - G_{lin}(\boldsymbol{0}_{lin}') \tag{6.86}$$

The prime here has the same meaning as in Eq. (6.69), i.e., with reduced dimension. For the time invariant case, $G_{lin}(\mathbf{0}') = 0$.

### 6.8.6 FE Divergence Case

In practice, FE divergence is inevitable when the simulation point is far from a realistic value. In this case a linear extrapolation algorithm is used to obtain the value of the LSF by taking advantage of values at previous neighboring grid points (pre-values). In other words,

$$G(x_i, y_i) = \frac{[f(G(x_{i-2}), G(x_{i-1})) + f(G(y_{i-2}), G(y_{i-1}))]}{2.0} \tag{6.87}$$

where $f$ is a linear extrapolation function. In some cases only one set of pre-values on either the x or y axes are available.

In this case the value of the LSF is extrapolated by only one set of values. If no pre-values on the two axes are available, the user is requested to reset the region of the grid plane. Because of the possibility of FE divergence and extrapolation, the LSF is evaluated in a special sequence. The points on the axes are evaluated first, while the other points are evaluated in a sequence such that those closer to the origin are evaluated first. This approach ensures that the extrapolation is possible.

### 6.8.7 Application Example

In this section, the 2D two story frame used as the superstructure in section 6.4 is studied to verify the newly developed MVPP and DP-RS-Sim methods. The structures are

shown again in Figure 6.29. The material parameters are set as random variables and their distribution properties are shown in Table 6.8. The LSF is set the same as before as,

$$g = 0.144 - \{\text{roof displacement}\} \tag{6.88}$$

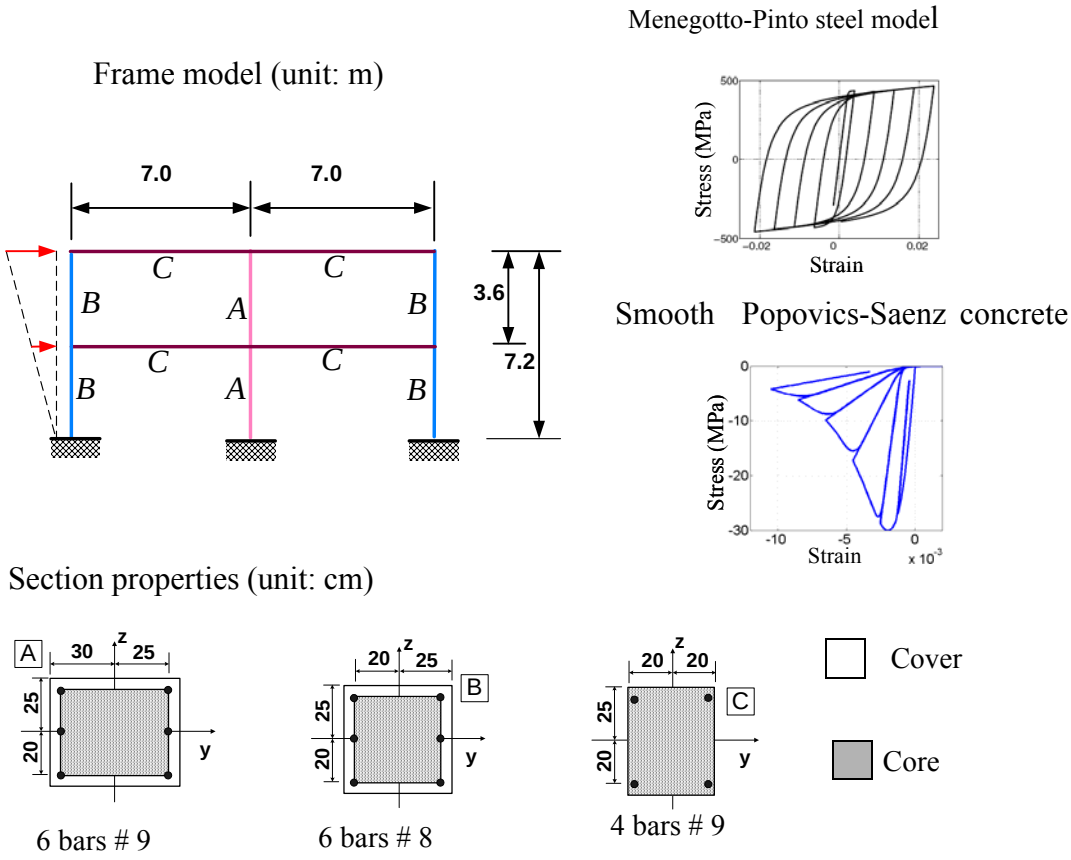


**Figure 6.29 2-D Frame model: geometry, section properties and material model**

**Table 6.8 Material properties**

| parameters | | distribution | mean | | c.o.v. |
|---|---|---|---|---|---|
| | | | core | cover | |
| concrete | $f_c$ [kPa] | lognormal | 27579.0 | 34473.8 | 0.2 |
| | $f_{cu}$ [kPa] | lognormal | 1000.0 | 25723.0 | 0.2 |
| | $E_c$ [kPa] | lognormal | 2.491e7 | 2.785e7 | 0.2 |
| | $\varepsilon_c$ | lognormal | 0.002 | 0.005 | 0.2 |
| | $\varepsilon_{cu}$ | lognormal | 0.012 | 0.02 | 0.2 |
| steel | $E$ [kPa] | lognormal | 2.1e8 | | 0.033 |
| | $\sigma_y$ [kPa] | beta | 248200.0 | | 0.106 |
| | $b$ | lognormal | 0.02 | | 0.2 |
| maximum distributed-force | $P$ [kN] | lognormal | 250 | | 0.2 |

After the DP is found, the hessian matrix is computed by using the forward finite difference (FFD) perturbation method combined with the DDM based sensitivities results. The principal curvatures are then computed as shown in Table 6.9.

**Table 6.9 Principal curvatures**

| Index of principal curvature | curvature |
|---|---|
| 1st | -0.0414268 |
| 2nd | -0.0239904 |

**Table 6.9 Principal curvatures**

| Index of principal curvature | curvature |
|---|---|
| 3rd | -0.0122722 |
| 4th | -0.0022057 |
| 5th and more | absolute value < 0.001 |

The visualization of the LSS at the DP in the first to fourth principal planes are shown in Figures 6.30 through 6.37.

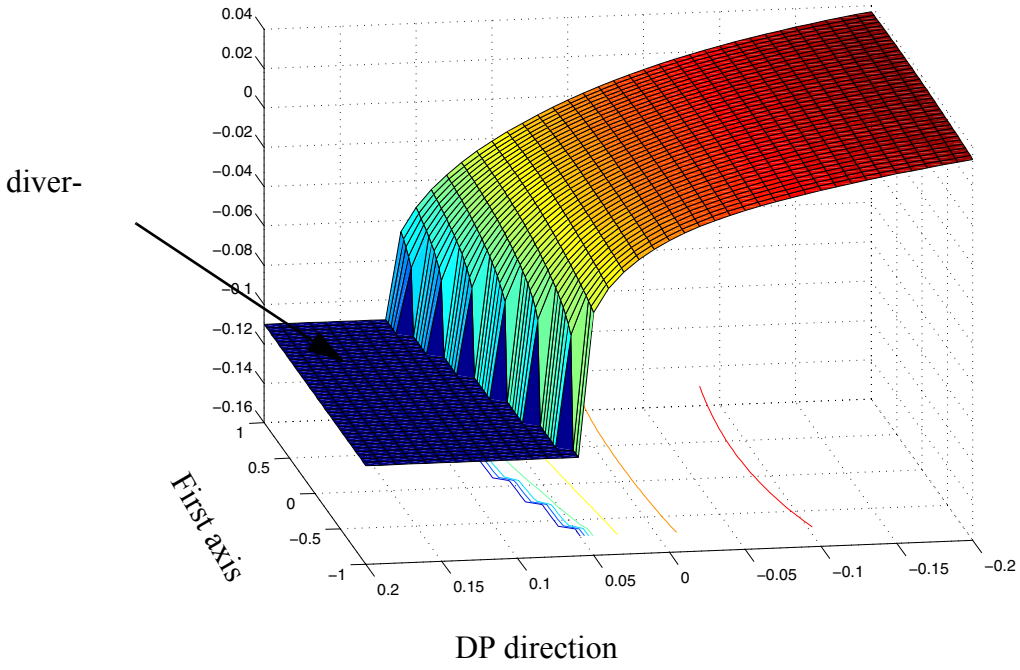


**Figure 6.30 Response surface at DP on the first principal plane**

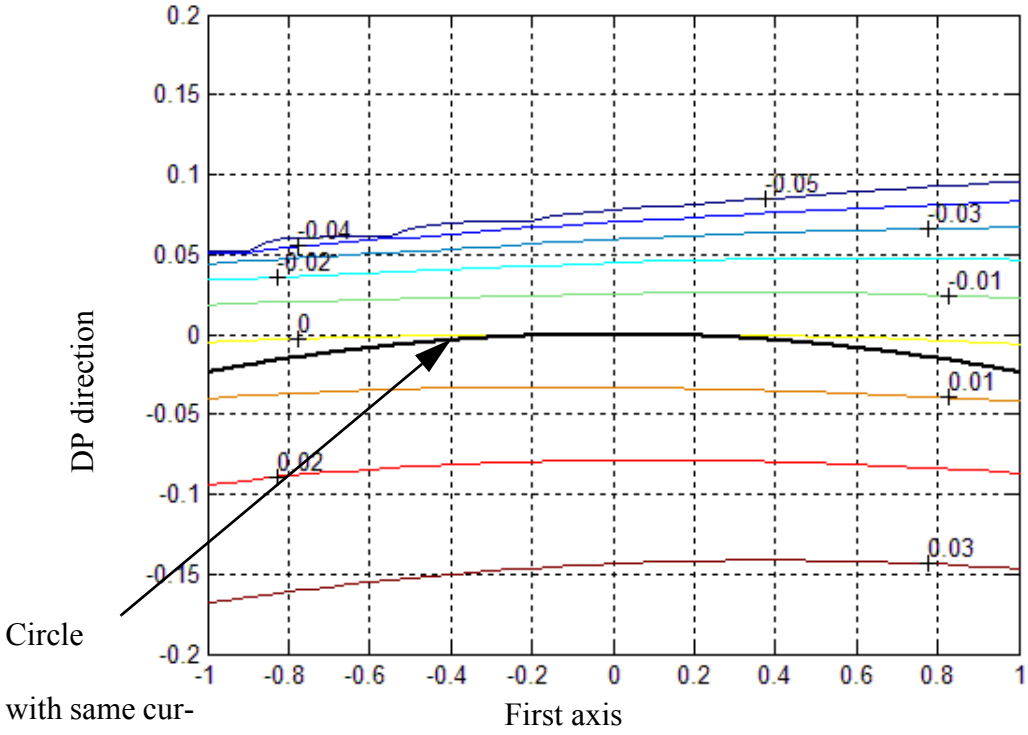


**Figure 6.31 Contour of response surface at DP on the first principal plane**

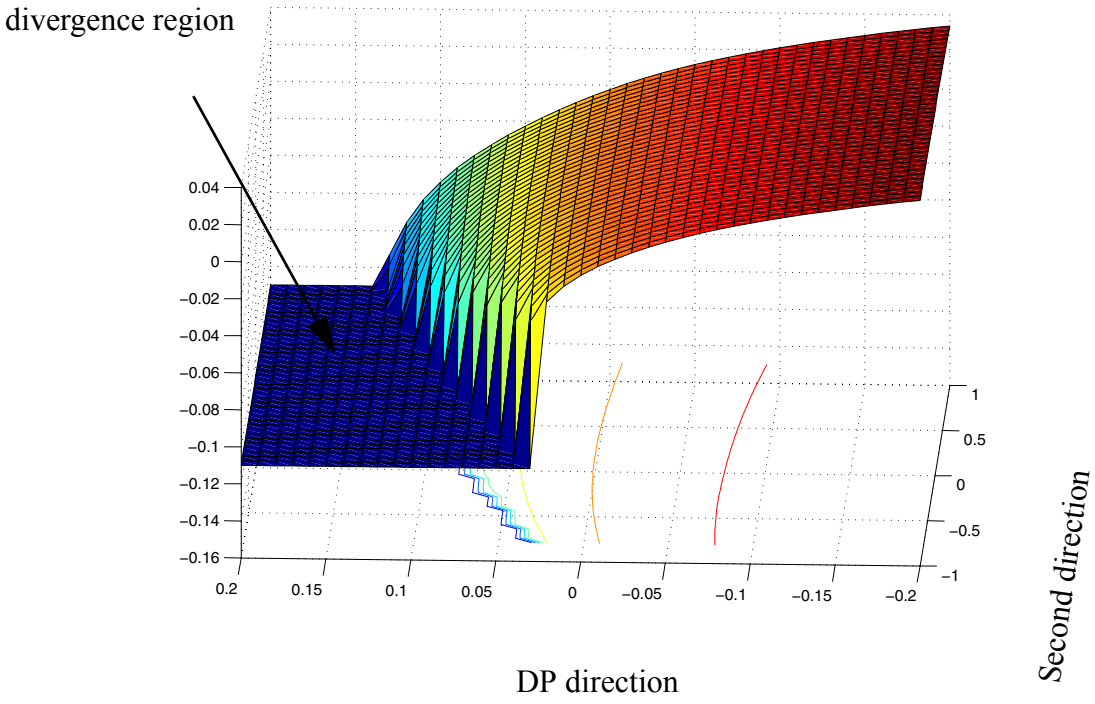


**Figure 6.32 Response surface at DP on the second principal plane**

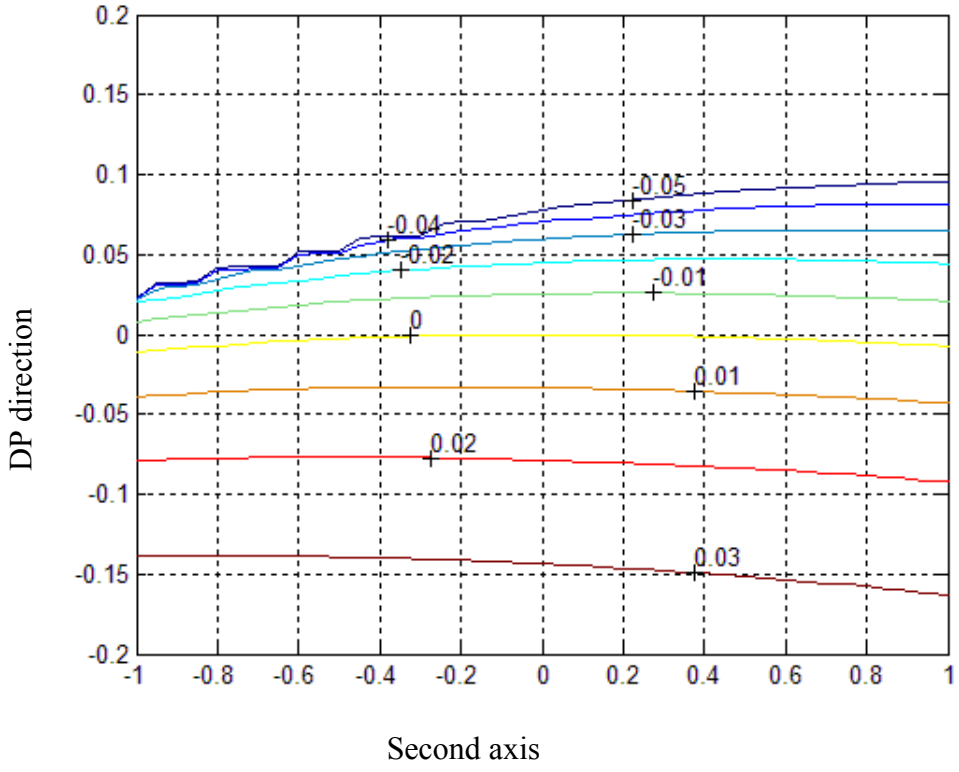


**Figure 6.33 Contour of response surface at DP on the second principal plane**

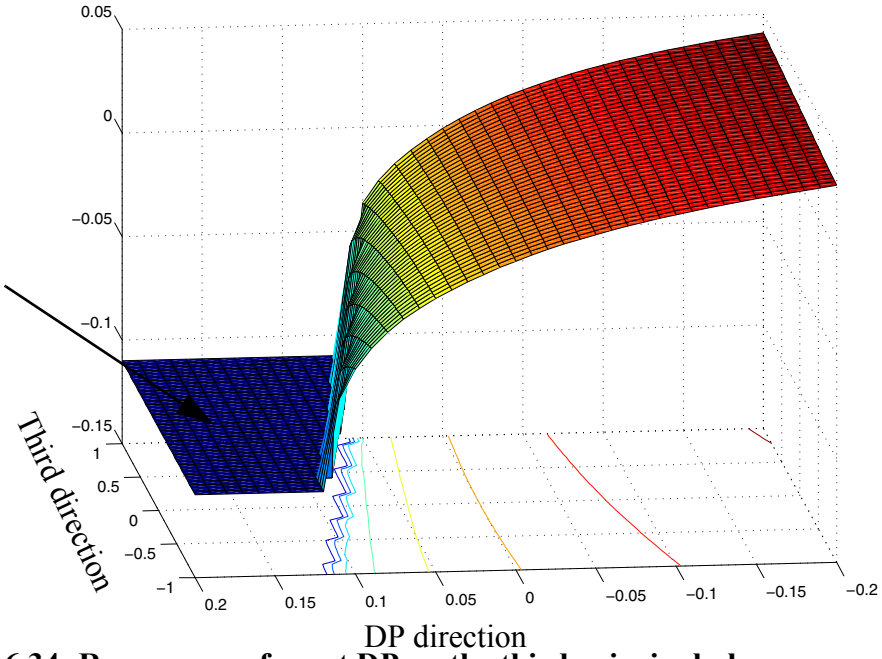


**Figure 6.34 Response surface at DP on the third principal plane**

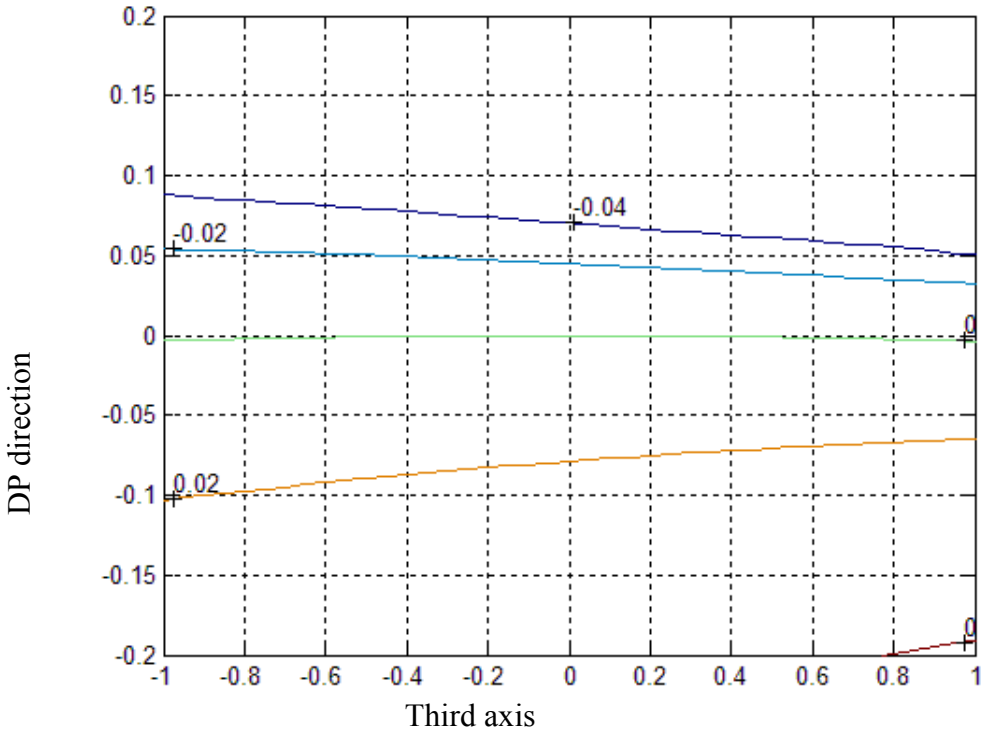


**Figure 6.35 Contour of response surface at DP on the third principal plane**

diver-

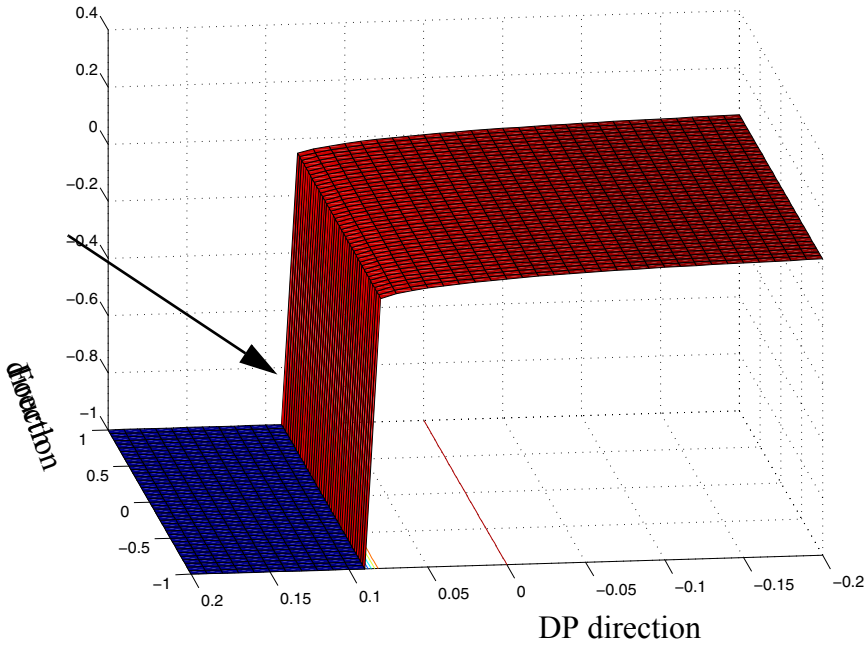


**Figure 6.36 Response surface at DP on the fourth principal plane**

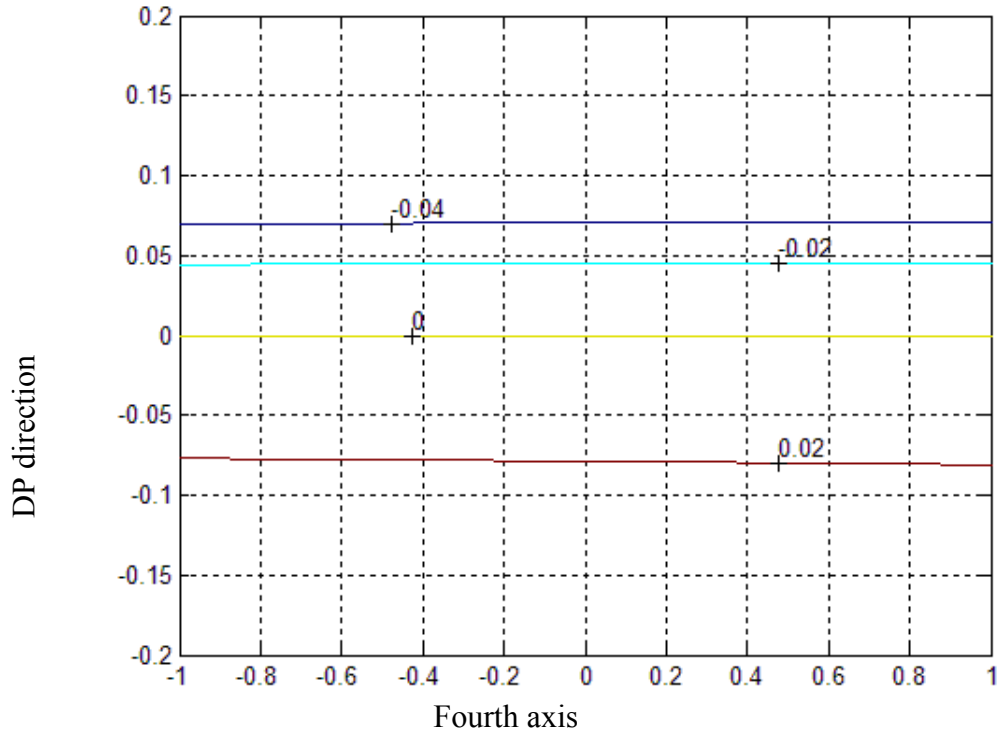


**Figure 6.37 Contour of response surface at DP on the fourth principal plane**

DP-RS-Sim time invariant reliability analysis

After obtaining the design points, DP-RS-Sim time invariant analysis is performed by using one to four principal directions as the nonlinear directions, and the failure probability obtained is compared with those from FORM, SORM and IS analysis. The results are reported in Tables 6.10.

**Table 6.10 Comparison of various methods for computing the $P_f$**

| Methodologies | | $P_f$ | c.o.v. | number of simulations | number of simulations based on the fitted response surface |
|---|---|---|---|---|---|
| FORM | | 0.020305 | - | - | - |
| SORM (1 curv.) | | 0.021574 | - | - | - |
| SORM (all curv.) | | 0.022114 | - | - | - |
| IS | | 0.022927 | - | 40830 | - |
| DP-RS-Sim Univariate Decomposition method | one nonlinear direction | 0.023507 | 0.01 | 16 | 22345 |
| | two nonlinear directions | 0.023865 | 0.01 | 24 | 21451 |
| | three nonlinear directions | 0.023956 | 0.01 | 32 | 19185 |
| | four nonlinear directions | 0.023963 | 0.01 | 40 | 20915 |
| DP-RS-Sim Bivariate Decomposition method | one nonlinear direction | 0.0253316 | 0.005 | 80 | 70189 |
| | two nonlinear directions | 0.0220717 | 0.005 | 240 | 84248 |
| | three nonlinear directions | 0.0211082 | 0.005 | 480 | 91471 |
| | four nonlinear directions | 0.022472 | 0.005 | 800 | 92019 |

From this data it is observed that:

1, the failure probability obtained by FORM is 10% smaller than the real failure probability obtained by IS. This may be undersood by the visualization results as shown in Figure 6.31. The curvature at the DP is negative, i.e., the LSS is concave with respect to the failure domain at DP. Thus the FORM estimation, that uses a plane tangent to the LSS at the DP to approximate the failure probability, underestimates the failure probability.

2, DP-RS-Sim is accurate and efficient in the sense that it obtains good resuls with much fewer simulations in comparison to IS. Although it requires many simulations based on the fitted response surface LSF, the computations are so cheap that the simulations may be done in almost no time.

3, In DP-RS-Sim Univariate decompositon analysis, as the number of principal directions is increased (the LSF is considered nonlinear along these directions), the failure probability increases, which is consistent with the fact that the first four principal curvatures are all negative. While these are not observed in Bivariate decomposition analysis.

### 6.8.8 Conclusion of DP-RS-Sim Method

In this section, a new visualization method MVPP is developed and used to understand the sources of inaccuracy in FORM. Based on the insight obtained, a new method DP-RS-Sim reliability analysis is developed and applied to a real structural system. The method is accurate and efficient, and greatly improves the failure probability obtained by FORM.

## 6.9 Conclusions

In this chapter, several advanced reliability analysis methods are further developed and applied to SFSI systems for both time invariant and time variant reliability analysis. Except for crude Monte Carlo simulation, these methods are based on the knowledge of the design point(s). In order to obtain a robust design point(s) search algorithm, the general-purpose optimization toolbox SNOPT is adopted, customized to reliability analysis problems and interfaced with the finite element analysis software framework OpenSees used in this research. SNOPT offers significant advantages for solving large-scale design point search problems, such as robustness, efficiency, and flexibility. In order to estimate the failure probability accurately, several sampling methods have been implemented in the reliability framework of OpenSees. These methods include crude Monte Carlo Simulation (MCS), Importance Sampling (IS), and Orthogonal Plane Sampling (OPS) combined with a robust line search root finding algorithm.

Based on the newly developed/modified/extended reliability analysis methods and the FE response sensitivity analysis framework, a realistic nonlinear SFSI application example is studied for time invariant reliability analysis. The failure probability estimates obtained using different methods (FORM, IS, OPS, and MCS) are consistent, thus validating the software implementation of these methods. For cases in which the failure probability is very small (e.g., pF < 10-3), or when a small coefficient of variation (e.g., < 5%) of the failure probability estimate is required, the use of MCS is not feasible due to its unacceptable computational cost. In the present work, it was found that FORM results for time-invariant reliability analysis are of acceptable accuracy and require far fewer evaluations

than IS and OPS. However, in general, FORM is not guaranteed to be accurate. In time-invariant reliability analysis, IS is more efficient than OPS in the sense that it requires significantly fewer evaluations of the performance function.

An existing algorithm for computing the mean upcrossing rate in time variant reliability analysis, already implemented in the reliability framework of OpenSees, was further refined and improved for example to deal with non-converging cases in limit-state function evaluation. This algorithm was then used to solve SFSI time variant reliability analysis problems. In time variant reliability analysis of nonlinear SFSI systems, it was found that the FORM approximation for mean upcrossing rate is significantly inaccurate, especially in the case of highly nonlinear response behavior of the system. In this case, the OPS based on the design point(s) provides a good estimate of the mean up-crossing rate time history and, therefore, of an upper bound of the failure probability. It provides significant improvement on the FORM results.

In order to study the topology of limit state surfaces (LSS) for both time invariant and time variant structural reliability problems, a new visualization method called Multi-dimensional Visualization in Principal Plane (MVPP) is developed and implemented in OpenSees. It was found that LSSs for typical nonlinear structural and SFSI systems are significantly nonlinear along only a few principal directions (i.e., 3-5 directions) and the nonlinearity along the remaining directions is small and can be ignored without significant loss of accuracy in estimating the failure probability. The geometrical insight gained from the MVPP has led to the development and implementation of a new hybrid computational reliability method, called the DP-RS-Sim method, which combines the design point (DP)

search, the response surface methodology (RS), and simulation techniques (Sim). This method is applied for the time invariant reliability analysis of a nonlinear structural system subjected to quasi-static pushover. Based on the experience gained so far, it is observed that the DP-RS-Sim method is accurate and efficient in the sense that it yields very good results with significantly less simulations compared to IS or OPS. The efficiency of the DP-RS-Sim method is still hindered by the expensive computation of the Hessian matrix of the limit-state function at the design point.

# CHAPTER 7

# NONLINEAR MODEL UPDATING AND PARAMETER CALIBRATION FOR STRUCTURAL AND GEOTECHNICAL SYSTEMS

## 7.1 Overview of Finite Element Model Updating

The Finite Element (FE) method is commonly used in design and analysis of structural and geotechnical systems. Due to incomplete knowledge of structural and/or geotechnical systems and simplifying modelling assumptions based on engineering judgment, an initial FE model can be unable to represent the actual system behaviour with a required level of accuracy. This inaccuracy could be particularly significant for dynamic cases, when comparing actual vibration data, obtained from dynamic tests or from earthquake records, with numerical simulations. The objective of FE model updating is to correct the initial FE model in order to tune it to the experimental vibration data, obtaining an updated FE able to better predict the response of the considered structural/geotechnical system. ("Inverse modelling of civil engineering structures based on operational model data", Anne Teughels, dissertation 2003, Katholieke University Leuven).

Two general methods used in FE model updating, i.e. direct methods and sensitivity based methods. Direct methods update the global stiffness or mass matrices based on the

structural equations of motion as well the orthogonality equations (Baruch M. 1982, Wei F.S. 1990). This method is straightforward but has drawbacks. The updated matrices reproduce the measured structural modal properties exactly but do not generally maintain structural connectivity. The corrections suggested may not have any physical meaning since all the elements in the stiffness or mass matrices are changed separately. The resulting matrix is not guaranteed to be positive difinite.

Sensitivity based methods can overcome these problems since they adjust only a set of physical parameters, keeping the connectivity of the original model(Link M. 1999). A major problem in sensitivity based model updating is the relatively low information content of the measured data, which may cause the model updating procedure to converge to local solutions. To solve this problem, either the information content of the data is increased by further testing the system in different configurations(Nalitolela et al. 1992), or the number of uncertain parameters must be reduced(Fritzen and Bohle 1999).

The proper selection of these parameters (parameterization) is a key issue in FE model updating. It is important that the chosen parameters be able to clarify the ambiguity of the model, and the model output should be sensitive to these parameters.(Mottershead 1995, Link 1999 and Shi et al. 2000).)

A general optimization framework based on the integration of the SNOPT(Sparse Nonlinear Optimization) optimization tool box into OpenSees, is developed and applied for nonlinear FE model updating purpose in this chapter. This framework is refered as SNOPT-OpenSees framework, has very flexible user interface and can therefore be used

for multiple purposes: such as model updating by either direct or sensitivity based methods.

The following two sensitivity based model updating studies have been performed utilizing this framework: (1) The response data generated from a FE model was used as the 'experimental' data in calibrating a FE model with different initial parameters. Two methods for computing gradients, DDM and FFD, were used. A comparison of the convergence rate of the model updating procedure is made between the use of DDM and FFD. It is found that the convergence rate of the updating procedure when using DDM is significantly faster than when using FFD. (2) By using the downhole acceleration records obtained during the Lotung Taiwan earthquake of 1986, an example of the actual application of soil model updating is provided.

## 7.2 SNOPT as a General Optimization Tool Box for Structural and Geotechnical Model Updating

As mentioned in chapter 6.1, the SNOPT optimization toolbox has several features that make it suitable for strucutral and geotechnical systems model updating: (1) It is applicable to large scale problems such as geotechnical models which may easily include over a million degrees of freedom. The capacity of SNOPT to deal with such problems makes it especially suitable for solving optimization problems in civil engineering. (2) SNOPT needs relatively few evaluations of the objective function. In FE soil and structural model updating problems, one of the most time consuming steps is the evaluation of the objective function. This is particularly true when the entire response history is desired. This feature makes the optimization process when using SNOPT very efficient. (3)

SNOPT can tolerate the discontinuity of gradients close to the optimization point. In non-smooth plastic FE models, the discontinuity of the gradients is inevitable due to the state transition of the material point (i.e., between elastic to plastic). This feature makes SNOPT a robust algorithm for model updating. (4) SNOPT has many flexible selections allowing for its customization for special problems.

As described in chapter 6.1, SNOPT has its own rules for determining the search direction, performing the merit-function and convergence checks, and deciding on the step size.

In the following section, the method by which SNOPT is integrated into OpenSees as a general optimization tool is explained.

## 7.3 Integration of SNOPT into OpenSees as a General Optimization Tool

The SNOPT interface is very simple as seen below:

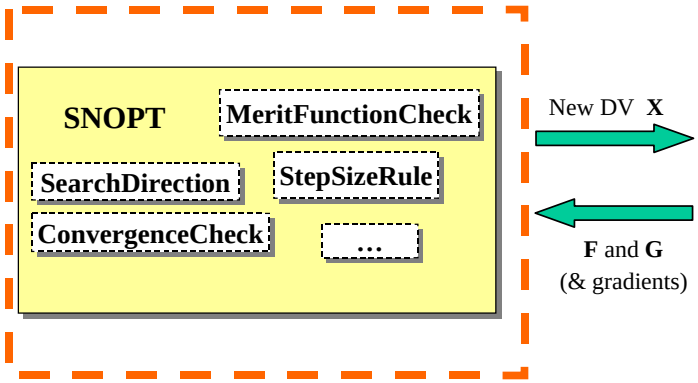


**Figure 7.1 Interface of SNOPT tool box as a general optimization tool**

In the optimization process, following SNOPT's output of a Design Variable vector (DV) **x**, values of the objective function F(**x**) and the constraint function(s) G(**x**) are

required. If the gradients of F(**x**) and G(**x**) are provided, SNOPT takes advantage of them directly, otherwise SNOPT will perform the Finite Difference (FD) method to get the approximate gradients. i.e., by perturbing the DV **x** by $\Delta\mathbf{x}$, to get the gradients as:

$$\frac{\partial F(\boldsymbol{x})}{\partial \boldsymbol{x}} \approx \frac{\Delta F(\boldsymbol{x})}{\Delta \boldsymbol{x}} \text{ and } \frac{\partial G(\boldsymbol{x})}{\partial \boldsymbol{x}} \approx \frac{\Delta G(\boldsymbol{x})}{\Delta \boldsymbol{x}} \tag{7.1}$$

By default the pertubation $\Delta\mathbf{x}/\mathbf{x}$ is $5.5e-7$, a value which can be specified by the user.

In order to integrate SNOPT into OpenSees, a main C++ class 'SNOPTAnalysis' is created while four other classes (e.g., 'DesignVariable', 'DesignVariablepositioner', 'ObjectiveFunction' and 'ConstraintFunction') are created to achieve the communication between SNOPT and OpenSees as shown below in Figure 7.2.

The role of 'SNOPTAnalysis' is:

(1) when the command is received from SNOPT to obtain new values of the objective and constraint functions using the new DV **x**, it will call the domain components 'Design-Variable' and 'DesignVariablePositioner' to update the DV **x**. In structural or geotechnical systems, DV **x** can generaly be material, geometric or loading properties, etc. The 'DesignVariablePositioner' is responsible for finding all corresponding components in the FE model with the DV **x**, and update them.

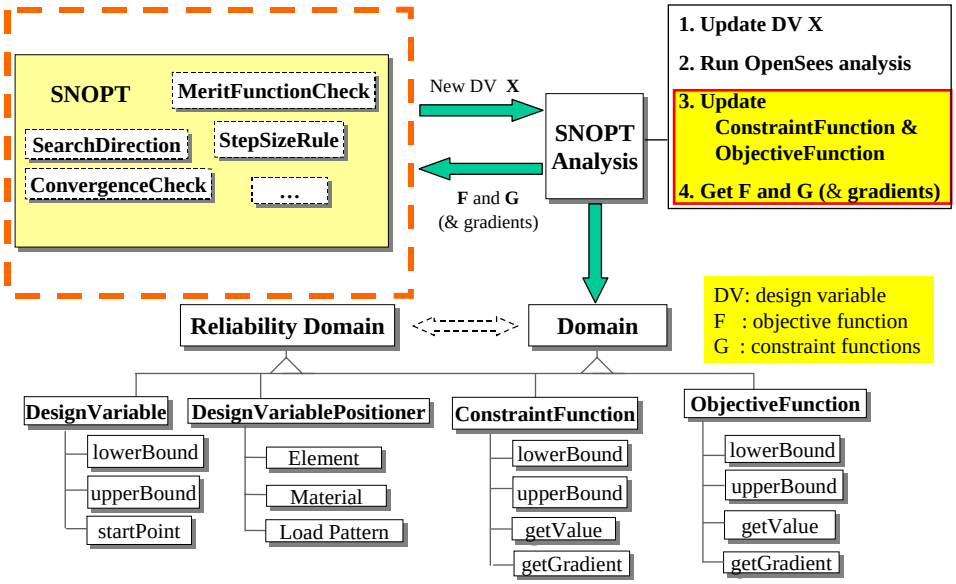


**Figure 7.2 Integration of SNOPT tool box into OpenSees as a general optimization tool box**

(2) After updating the parameters to the new DV **x**, 'SNOPTAnalysis' will rerun the OpenSees analysis using the updated parameters. The analysis' requirements such as the analysis type or the number of steps, are specified in user defined tcl files and saved in 'SNOPTAnalysis', which allow user to customize the analysis. According to the user's requirements, 'SNOPTAnalysis' can perform the sensitivity analysis in order to obtain the gradients of the constraint and objective functions in step (3).

(3) After performing the analysis in OpenSees, 'SNOPTAnalysis' calls functions of classes 'ConstriantFunction' and 'ObjectiveFunction', to update the values of the objective and constraint functions. These values are stored in the objects of the 'Constriant-Function' and 'ObjectiveFunction' classes.

(4) ‘SNOPTAnalysis’ gets the values and possibly the gradients of the objective and constraint functions from the objects of ‘ConstriantFunction’ and ‘ObjectiveFunction’. These values and gradients are then returned to SNOPT.

In order to make the optimization as flexible as possible, a ‘Do It Yourself’ (DIY) concept is used to allow users to match whichever quantities that OpenSees can output (i.e. natural frequencies, response histories, force-displacement curves). In steps (3) and (4), users are capable of freely defining the objective and constraint functions, F and G, in the TCL input file. The C++ based classes ‘ConstraintFunction’ and ‘ObjectiveFunction’ will run the TCL file and obtain values from the TCL memory as shown in Figure 7.3. These functions F and G (and their gradients) are computed by using the responses (and response sensitivities) recorded from the OpenSees analysis results. This implementation takes advantage of the flexibility of the TCL language in order to allow a general-purpose optimization using SNOPT.

A simple example of how to write this TCL file is shown in Figure 7.3.

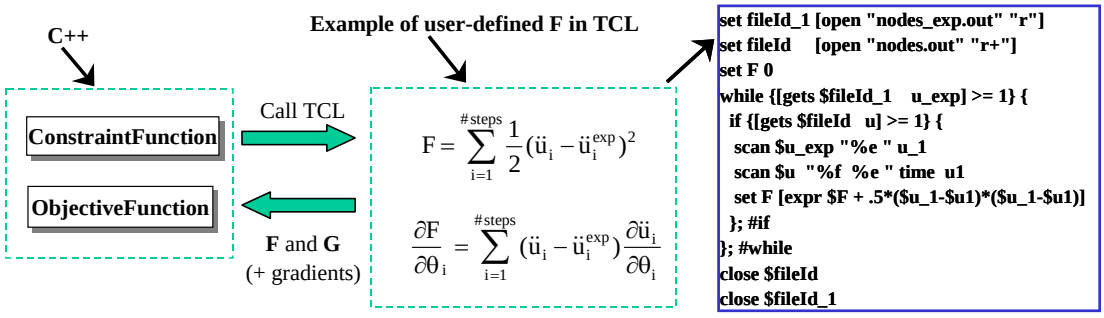


**Figure 7.3 Communication between C++ class and user defined funciton in TCL**

The user tries to match empirical valuse of the entire acceleration process $\ddot{u}^{\exp}$ . The quantity $\ddot{u}$ is recorded by OpenSees. The objective function is defined as,

$$F(\boldsymbol{x}) = \sum_{i=1}^{\#steps} \frac{1}{2}(\ddot{u}_i(\boldsymbol{x}) - \ddot{u}_i^{\exp})^2 \tag{7.2}$$

If the gradients are provided by the user, they are done so in the following form,

$$\frac{\partial F(\boldsymbol{x})}{\partial \boldsymbol{x}} = \sum_{i=1}^{\#steps} (\ddot{u}_i(\boldsymbol{x}) - \ddot{u}_i^{\exp}) \frac{\partial \ddot{u}_i(\boldsymbol{x})}{\partial \boldsymbol{x}} \tag{7.3}$$

where $\frac{\partial \ddot{u}_i(\boldsymbol{x})}{\partial \boldsymbol{x}}$ is obtained from the sensitivity algorithm.

The TCL implementation when the gradients are not provided by the user is shown in Figure 7.3 as,

```
set fileId_1 [open "nodes_exp.out" "r"]; # file containing experimental recorder
set fileId     [open "nodes.out" "r+"]; # file containing OpenSees simulation recorder
set F 0.0 ;# objective function initialized to 0
while {[gets $fileId_1     u_exp] >= 1} {;# read line ‘u_exp’ from experimental data file
  if {[gets $fileId   u] >= 1} { ; # read line ‘u’ from OpenSees recorded data file
   scan $u_exp "%e " u_1 ; # split line ‘u_exp’ and save acceleration into u_1
   scan $u  "%f  %e " time  u1; # split line ‘u’ and save acceleration into u1
   set F [expr $F + .5*($u_1-$u1)*($u_1-$u1)]; compute the objective function
```

```
  }; #if
}; #while
close $fileId
close $fileId_1
```

This interface is flexible for the following reasons:

(1) it allows users to match various quantities such as frequency, modeshape, stress-strain relationship, or force-displacemnt relationship, etc. (2) it allows the design variable to be any input quantity such as node coordinates, material parameters, loads, and damping paramenters etc. (3) It can easily take advantage of the existing sensitivity results to obtain the gradients of F and G by performing the chain rule as shown in Equation (7.3).

## 7.4 Nonlinear Model Updating for Soil Column

### 7.4.1 Numerical Example 1. Nonlinear Model Updating of a Soil Column Subjected to Weak Ground Motions

In this section, taking advantage of the new developed optimization system, a numerical example is studied by using the gradients obtained from both DDM and FFD. The ‘experimental’ data herein are generated by using OpenSees. In this example, a 3D clay soil column beginning at the ground surface and extending below ground to a depth of 17 m, is studied. The column, under simple shear, is fixed along its lower boundary while corresponding nodes at the same elevation on the two lateral boundaries are tied together (i.e., their horizontal and verticle displacements are forced to be the same). Three investigation points at the surface, and at depths of 6m and 11m are ‘monitored’ while their acce-

lation histories are ‘recorded’(simulated by OpenSees). In simulating the base excitation, the downhole acceleration records at the depth of 17m below ground surface, at a site near Lotung, China, with station code FA1-5, no.6 oriented in N-S direction, during the earthquake of February 8th 1986, are used. (A. Elgamal. Identification and Modeling of Earthquake Ground Response I: Site Amplification, Soil Dynamics and Earthquake Engineering, Volume 15, Number 8, December 1996, pp. 499-522(24) ).

The model and acceleration are shown in Figure 7.4 below. The maximum acceleration is 0.14 $[m/s^2]$. The FFT of the acceleration is shown in Figure 7.5. No signal filter process is used for this acceleration input. No Rayleigh damping is considered.

The soil column is modeled using a 3D pressure independent multi-yield surface clay model (A. Elgamal and Yang, 2002) with three sets of material properites as shown in Table 7.1. Nine 2D four-node quadratic elements are used.

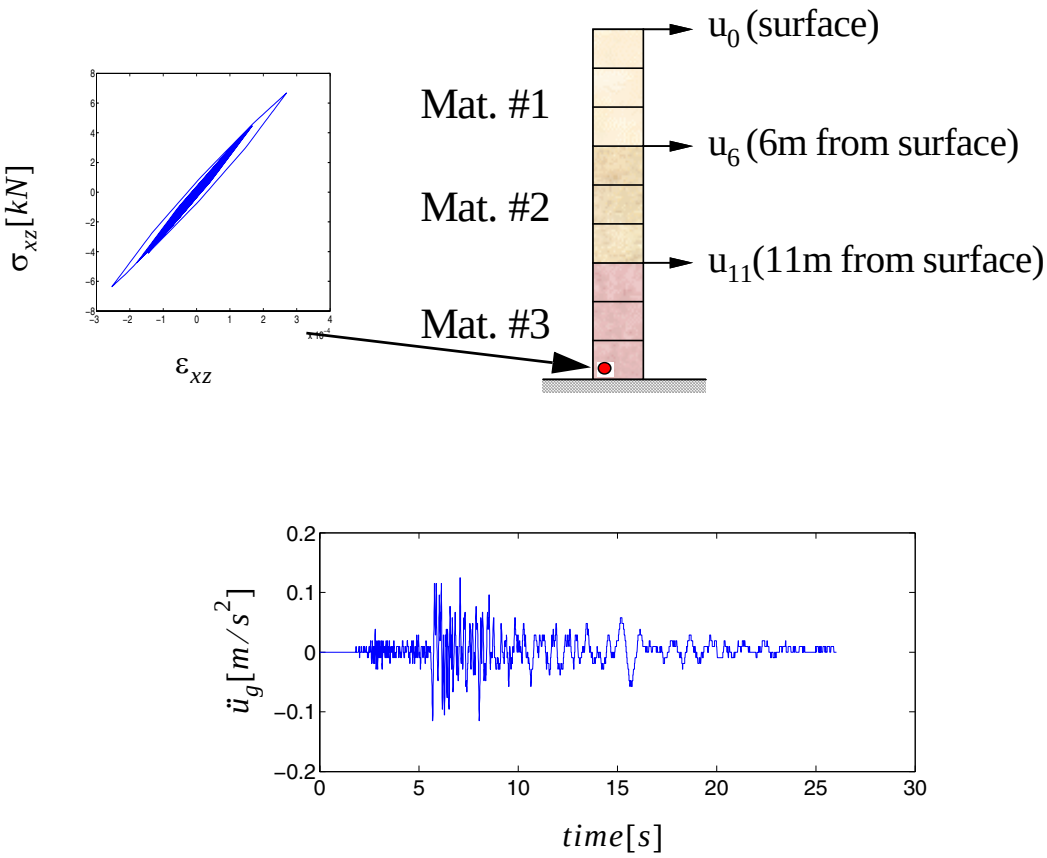


**Max accel: 0.14** $[m/s^2]$

**Figure 7.4 Soil column subject to base excitation**

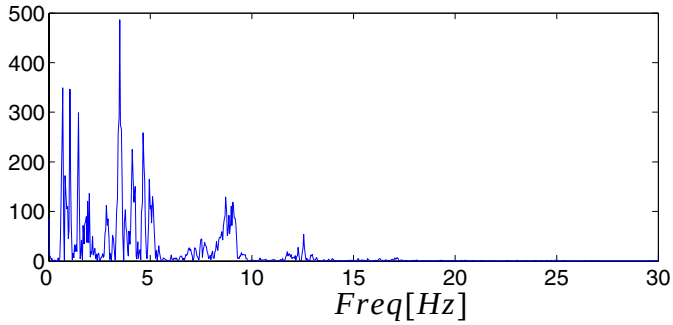


**Figure 7.5 FFT of the acceleration**

As shown in Table 7.1, the parameters to be updated are the low strain shear moduli and the max shear strength of the soil. The actual values of the parameters used to generate the experimental responses in Figure 7.6 are refered as ‘real’ values. The initial values of these parameters, used by SNOPT, are shown in Table 7.1.

**Table 7.1 Real parameters and initial parameters used in model updating**

| Parameter [kPa] | $G_1$ | $G_2$ | $G_2$ | $\tau_1$ | $\tau_2$ | $\tau_3$ |
|---|---|---|---|---|---|---|
| ‘real’ values | 28800 | 39200 | 57800 | 31 | 33 | 34 |
| initial values | 30000 | 30000 | 30000 | 30 | 30 | 30 |

The ‘experimental’ structural responses are shown in Figure 7.6. The stress-strain relations at a Gauss point at the bottom of the column is shown in Figure 7.4. From this figure, it is clear that the bottom of the soil is in the plastic state.

The comparison between the ‘experimental’ acceleration response and the acceleration response obtained by using the initial values in Table 7.1 is shown in Figure 7.7. From

these curves, it is clear that before model updating, the FE responses are very different from the experimental ones.

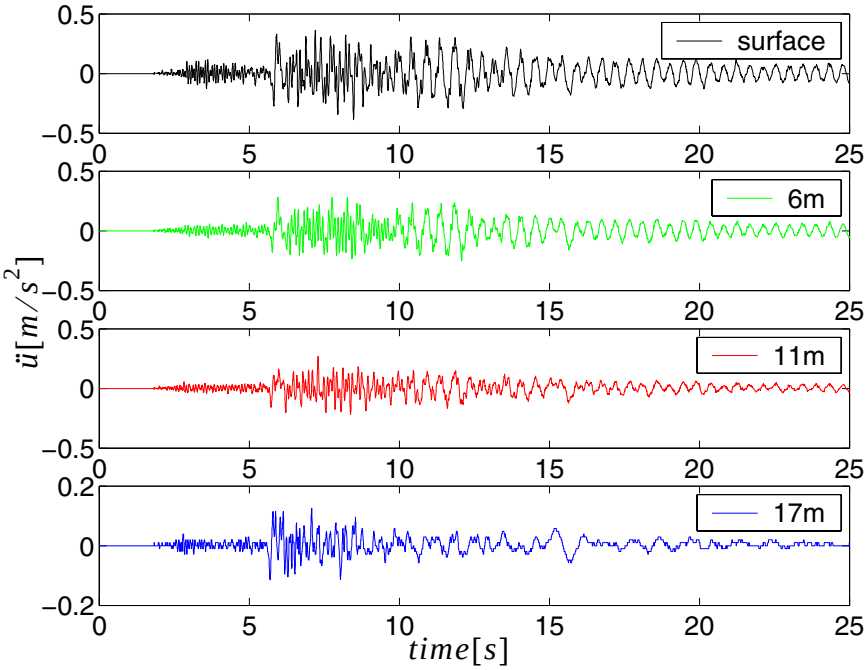


**Figure 7.6 'Experimental' soil responses at different height of the soil**

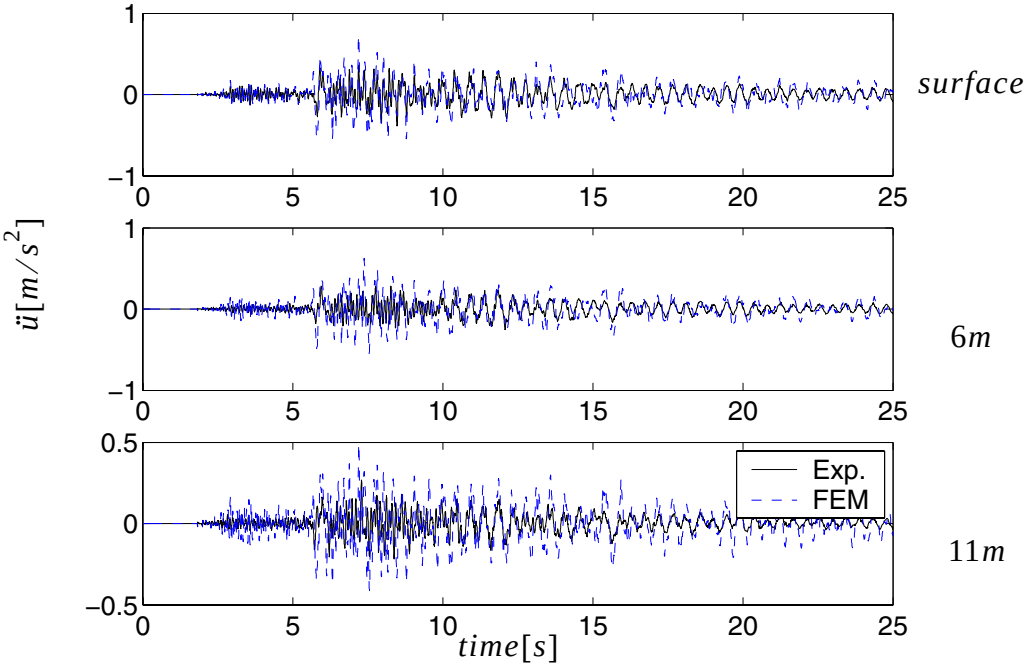


**Figure 7.7 Comparison of 'experimental' soil responses with those obtained by using 'initial' parameter values**

Objective and constraint functions

Among the various possible approaches for solving FE model updating problems, the least squares approach is a commonly used and efficient way. (Link 1999) The objective function in an ordinary least squares problem is then defined as,

$$F = \frac{1}{2} \sum_{j=1}^{\#\,\text{stations}} \left( \sum_{n=1}^{timeStep} (\ddot{u}_j(t_n) - \ddot{u}_{j,n}^{\exp})^2 \right) \tag{7.4}$$

where $\ddot{u}_j(t_n)$ and $\ddot{u}_{j,n}^{\exp}$ are simulated and experimental accelerations respectively at time step $t_n$, at the j$^{th}$ station. F is defined as the square of the difference between the sim-

ulated and experimental accelerations, summed over all time steps n and all downhole stations j.

In this example, the ranges of the parameters are,

$$20000 < G_i < \infty \text{ and } 20 < \tau_i < \infty \tag{7.5}$$

The major feasibility tolerance is set to $5.0 \times 10^{-2}$.

Gradients of the objective function

In this example the Direct Differetiation Method (DDM) and the Finite Difference Method (FDM) are used to compute the gradients. A comparison of the convergence rates when using the two methods is performed. When using FDM, the gradients of the objective function are computed as,

$$\frac{\partial F}{\partial \theta} \approx \frac{\Delta F}{\Delta \theta} \tag{7.6}$$

The perturbation $\frac{\Delta\theta}{\theta}$ is taken as $5.5 \times 10^{-7}$, which is equal to square root of the full function precision (User's Guide for SNOPT Version 7, A Fortran Package for Large-Scale Nonlinear Programming. Philip E. GILL, Department of Mathematics, UCSD, November 24, 2004).

When using the DDM algorithm, the gradients of the objective function are,

$$\frac{\partial F}{\partial \theta} = \sum_{j=1}^{\#\text{ stations}} \left( \sum_{n=1}^{timeStep} (\ddot{u}_j(t_n) - \ddot{u}_{j,n}^{\exp}) \frac{\partial \ddot{u}_j(t_n)}{\partial \theta} \right) \tag{7.7}$$

where $\frac{\partial \ddot{u}_j(t_n)}{\partial \theta}$ is computed by the DDM algorithm which is efficient and gives 'exact' gradients (Gu, Conte, 2001). It can be shown that when using Forward Finite Difference (FFD) method with a decreasing perturbation $\Delta\theta$, the gradients $\frac{\partial \ddot{u}_j(t_n)}{\partial \theta}$ approach the DDM results. However, too small a perturbation $\Delta\theta$ will lead to erroneous results due to round off error.(Gu, Conte, 2001)

Comparison of the results obtained by FFD with DDM when using noise-free 'experimental' date.

In contrast to data including numerical noise, to be shown in a later section, in this example, the 'experimental' data is noise-free as shown in Figure 7.6. Both FFD and DDM give good results as shown in Table 7.2.

**Table 7.2 Parameters obtained by updating procedure when using DDM and FFD**

| Parameter [kPa] | $G_1$ | $G_2$ | $G_2$ | $\tau_1$ | $\tau_2$ | $\tau_3$ |
|---|---|---|---|---|---|---|
| 'real' values | 28800 | 39200 | 57800 | 31 | 33 | 34 |
| DDM | 28800 | 39200 | 57800 | 31 | 33 | 34 |
| FFD | 28800.02 | 39200.02 | 57799.93 | 30.99999 | 33.00020 | 34.00028 |

The convergence rates are compared in terms of the objective function values at each major iteration of the updating procedure as shown in Table 7.3.

**Table 7.3 Comparison of objective function values when using DDM or FFD**

| iteration # | DDM | FFD | iteration # | FFD |
|---|---|---|---|---|
| 1 | 8.8E01 | 8.8E01 | 16 | 2.42E00 |
| 2 | 7.87E01 | 7.69E01 | 17 | 2.40E00 |
| 3 | 1.67E01 | 4.36E01 | 18 | 2.39E00 |
| 4 | 8.53E00 | 4.30E01 | 19 | 2.35E00 |
| 5 | 8.42E00 | 2.00E01 | 20 | 2.35E00 |
| 6 | 6.06E00 | 1.99E01 | 21 | 2.29E00 |
| 7 | 5.25E00 | 1.89E01 | 22 | 2.12E00 |
| 8 | 4.93E00 | 1.71E01 | 23 | 2.03E00 |
| 9 | 3.54E00 | 1.69E01 | 24 | 1.72E00 |
| 10 | 2.50E00 | 1.46E01 | 25 | 1.14E00 |
| 11 | 1.08E00 | 1.46E01 | 26 | 1.14E00 |
| 12 | 6.18E-1 | 1.46E01 | 27 | 3.80E-1 |
| 13 | 1.52E-1 | 1.31E01 | 28 | 1.06E-1 |
| 14 | 3.62E-2 | 3.12E00 | 29 | 7.02E-2 |
| 15 | 7.07E-3 | 2.96E00 | 30 | 5.60E-2 |

From the values of the objective function listed in Table 7.3, it is obvious that the convergence rate of the model updating procedure is faster when using DDM than FFD. In order to reach the criterion F=1.0E-2, DDM requires 15 iterations while FFD requires at least 30. The efficiency of DDM over FFD is clear from Figure 7.8 below where the results in Table 7.3 are plotted.

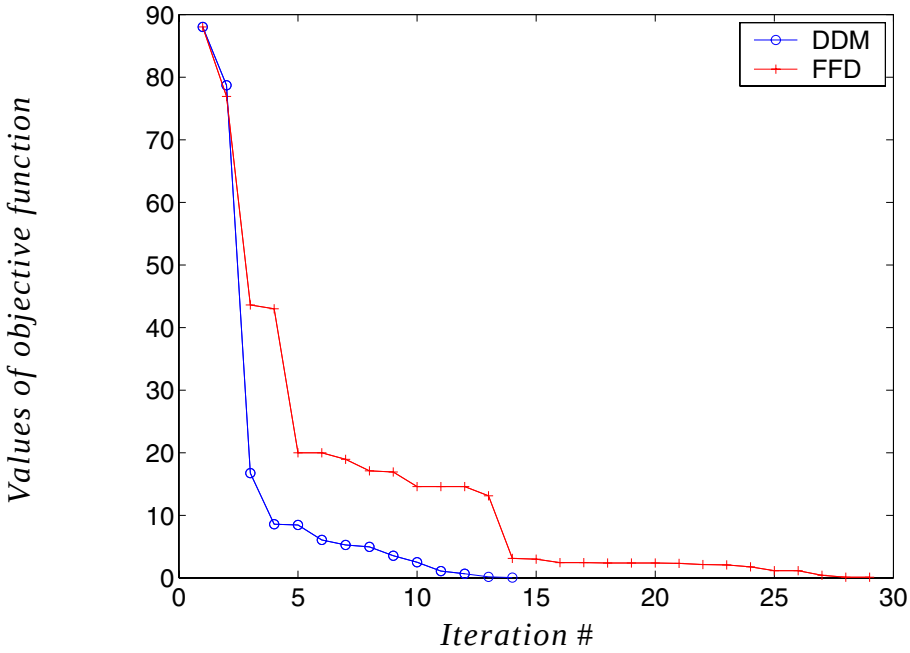


**Figure 7.8 Comparison of objective function values resulting from the use of DDM and FFD**

Comparison of the results obtained by FFD and DDM when the 'experimental' data includes artificial white noise

In order to better simulate the 'real' experimental data, 2% noise was included in the 'experimental data' (i.e., white noise with a PSD = 2% of the standard deviation of the original noise-free response signal during the whole process) while all other conditions were kept the same.

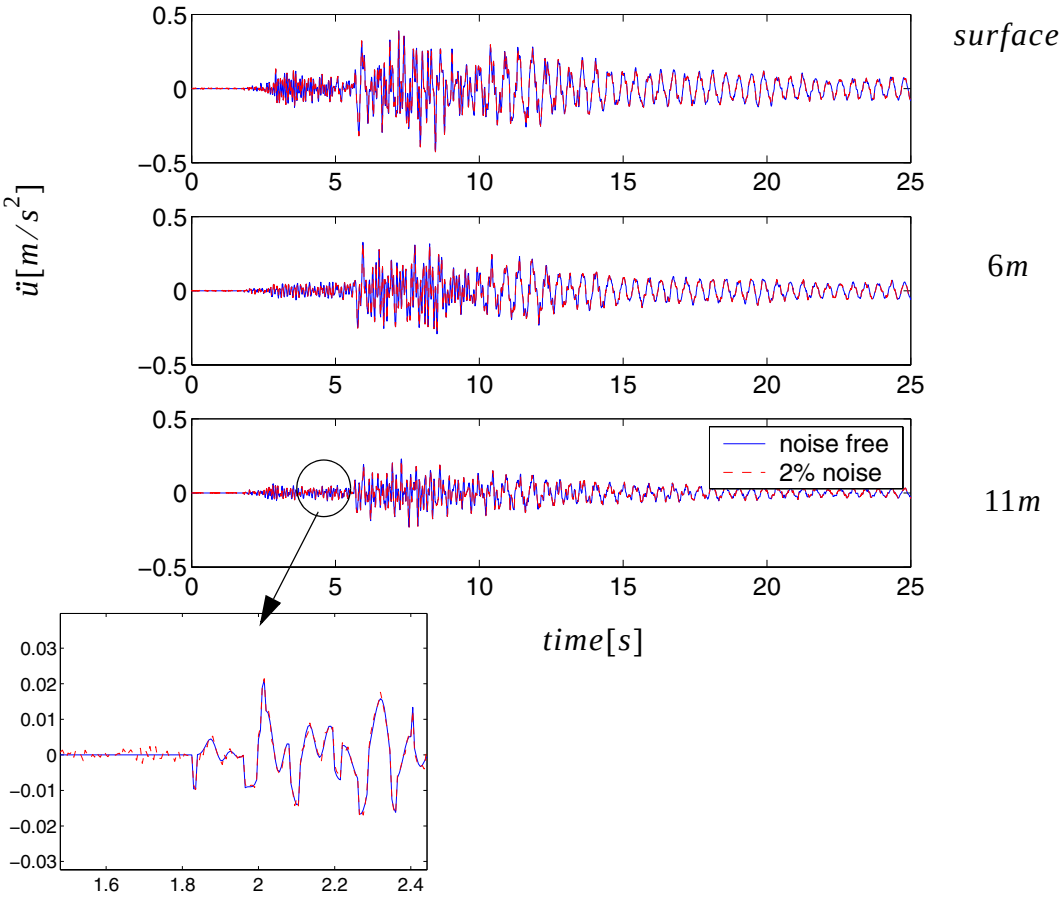


**Figure 7.9 'Experimental' responses with 2% noise**

A comparison of the 'experimental' data between the noise-free and 2% noise cases are shown in Figure 7.9.

The model updating procedure (SNOPT) obtains the values of the parameters by using DDM or FFD methods as shown in Table 7.4.

**Table 7.4 Parameters obtained by updating procedure when using DDM and FFD**

| Parameter [kPa] | $G_1$ | $G_2$ | $G_2$ | $\tau_1$ | $\tau_2$ | $\tau_3$ |
|---|---|---|---|---|---|---|
| 'real' values | 28800 | 39200 | 57800 | 31 | 33 | 34 |
| DDM | 28799.58 | 39199.93 | 57799.58 | 30.98898 | 33.00695 | 34.00770 |
| FFD | 28799.57 | 39199.92 | 57799.60 | 30.98897 | 33.00695 | 34.00773 |

A comparison of the convergence rate in terms of the objective function values, when using FFD and DDM, are shown in Table 7.5.

**Table 7.5 Comparison of objective function values by using DDM or FFD**

| iteration # | DDM | FFD | iteration # | FFD |
|---|---|---|---|---|
| 1 | 8.81E01 | 8.81E01 | 16 | 8.77E-01 |
| 2 | 7.87E01 | 7.70E01 | 17 | 7.56E-01 |
| 3 | 1.68E01 | 4.35E01 | 18 | 6.27E-01 |
| 4 | 8.54E00 | 9.32E00 | 19 | 5.75E-01 |
| 5 | 8.42E00 | 8.67E00 | 20 | 5.31E-01 |
| 6 | 6.06E00 | 8.35E00 | 21 | 4.85E-01 |
| 7 | 5.26E00 | 7.33E00 | 22 | 4.85E-01 |
| 8 | 4.94E00 | 3.87E00 | 23 | 4.82E-01 |

**Table 7.5 Comparison of objective function values by using DDM or FFD**

| iteration # | DDM | FFD | iteration # | FFD |
|---|---|---|---|---|
| 9 | 3.55E00 | 3.73E00 | 24 | 4.69E-01 |
| 10 | 2.51E00 | 3.52E00 | 25 | 4.52E-01 |
| 11 | 1.09E00 | 3.39E00 | 26 | 4.09E-01 |
| 12 | 6.18E-1 | 2.76E00 | 27 | 3.97E-01 |
| 13 | 1.52E-1 | 2.32E+00 | 28 | 3.84E-01 |
| 14 | 3.63E-2 | 1.55E+00 | 29 | 3.67E-01 |
| 15 | 7.07E-3 | 1.26E+00 | 30 | 3.42E-01 |

From the values of the objective function listed in Table 7.5, it is observed that the convergence rate of the model updating procedure (SNOPT) when using DDM is faster than with FFD when 2% white noise is added to the ‘experimental’ data.

Studies of various initial values

Here the problem is reevaluated by using different initial values while other conditions are kept the same, as in the noise free case. The computational results are shown in Table 7.6.

**Table 7.6 Parameters obtained by updating procedure when using DDM and FFD**

| Parameter [kPa] | $G_1$ | $G_2$ | $G_2$ | $\tau_1$ | $\tau_2$ | $\tau_3$ |
|---|---|---|---|---|---|---|
| ‘real’ values | 28800 | 39200 | 57800 | 31 | 33 | 34 |
| Initial values | 40000 | 40000 | 40000 | 40 | 40 | 40 |
| SNOPT results | 32468.05 | 30319.71 | 72127.28 | 39.92503 | 27.66459 | 33.35095 |

**Table 7.6 Parameters obtained by updating procedure when using DDM and FFD**

| Parameter [kPa] | $G_1$ | $G_2$ | $G_2$ | $\tau_1$ | $\tau_2$ | $\tau_3$ |
|---|---|---|---|---|---|---|
| Initial values | 20000 | 20000 | 20000 | 20 | 20 | 20 |
| SNOPT results | 131554.8 | 30332.77 | 24814.41 | 20.87335 | 20.00000 | 20.00000 |

In the above cases, the model updating procedure converges to local minimums when the initial values are far from the ‘real’ values. One way to alleviate this problem is to add more constraints.

**Table 7.7 Parameters obtained by updating procedure when using DDM and FFD**

| Parameter [kPa] | $G_1$ | $G_2$ | $G_2$ | $\tau_1$ | $\tau_2$ | $\tau_3$ |
|---|---|---|---|---|---|---|
| ‘real’ values | 28800 | 39200 | 57800 | 31 | 33 | 34 |
| Initial values | 40000 | 40000 | 40000 | 40 | 40 | 40 |
| Con-straints | $G_1 < G_2 < G_3$<br>$\lvert G_1 - G_2 \rvert < 100000$<br>$\lvert G_2 - G_3 \rvert < 100000$ | | | $\tau_1 < \tau_2 < \tau_3$<br>$\lvert \tau_1 - \tau_2 \rvert < 10$<br>$\lvert \tau_2 - \tau_3 \rvert < 10$ | | |
| SNOPT results | 28800.00 | 39200.00 | 57800.00 | 31.00 | 33.00 | 34.00 |

As shown in Table 7.7, when the bounds of the parameters are restricted, SNOPT can find the global minimum. There are global optimization methods, such as the method of coupled local minimizers (CLM) by Suykens et al.(2001, 2002), however this is beyond the scope of this chapter.

### 7.4.2 Numerical Example 2. Nonlinear Model Updating for a Soil Column Subjected to Strong Ground Motions

The model considered in section 7.4.1 is reevaluated however it is now subjected to a strong ground excitation taken as the real downhole acceleration records at the depth of 17m below the ground surface, at a site near Lotung, China during the earthquake of July $30^{th}$, 1986. (station code DHB17, no.12 oriented in N-S direction). (A. Elgamal. Identification and Modeling of Earthquake Ground Response I: Site Amplification, Soil Dynamics and Earthquake Engineering, Volume 15, Number 8, December 1996, pp. 499-522(24) ). The maximum acceleration was 1.86 $[m/s^2]$ as shown in Figure 7.10.

As in section 7.4.1, the parameters to be calibrated are the low strain shear moduli and the max shear strength of the soil. The ‘real’ values and the initial values of these parameters are the same as in Table 7.1.

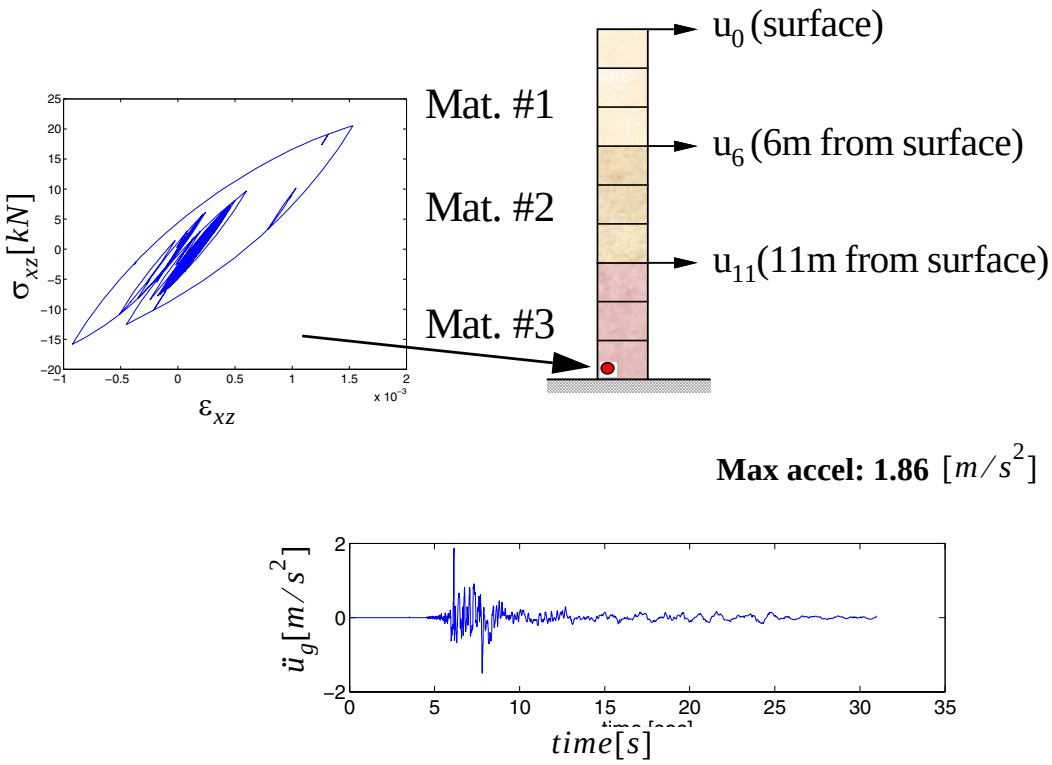


**Figure 7.10 Soil column subjected to strong base excitation**

The 'experimental' structural responses are shown in Figure 7.11. The stress-strain relations at a Gauss point at the bottom of the column is shown in Figure 7.10. From the stress-strain relations at the bottom of the soil, it is clear that the soil yields significantly duing the earthquake.

The comparison between the 'experimental' acceleration response and the acceleration response obtained by using the initial values in Table 7.1 is shown in Figure 7.12.

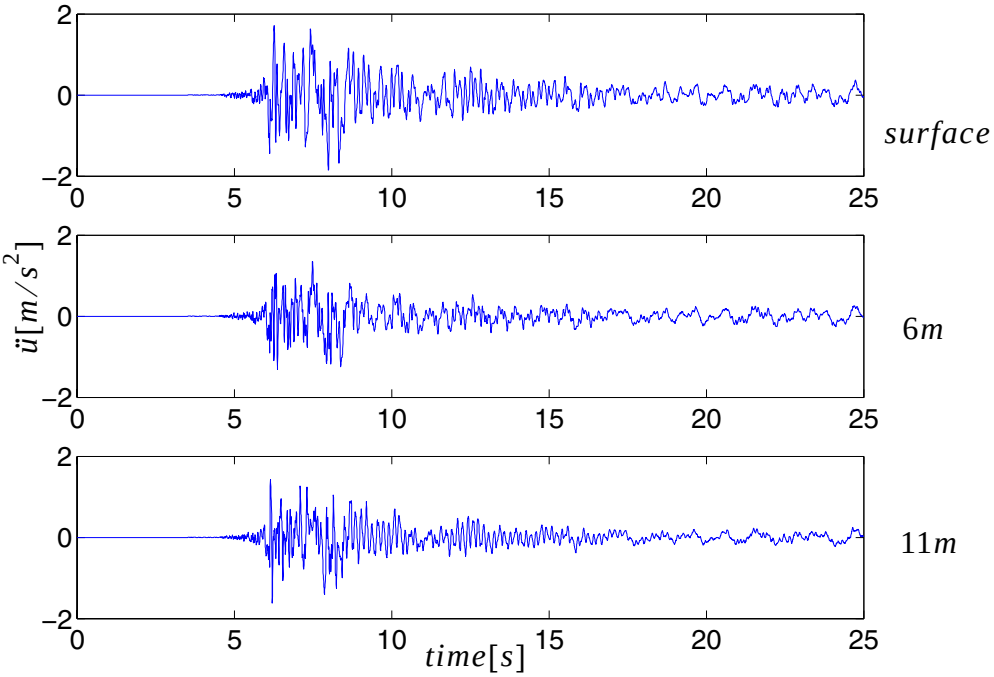


**Figure 7.11 'Experimental' soil responses at different heights of the soil column**

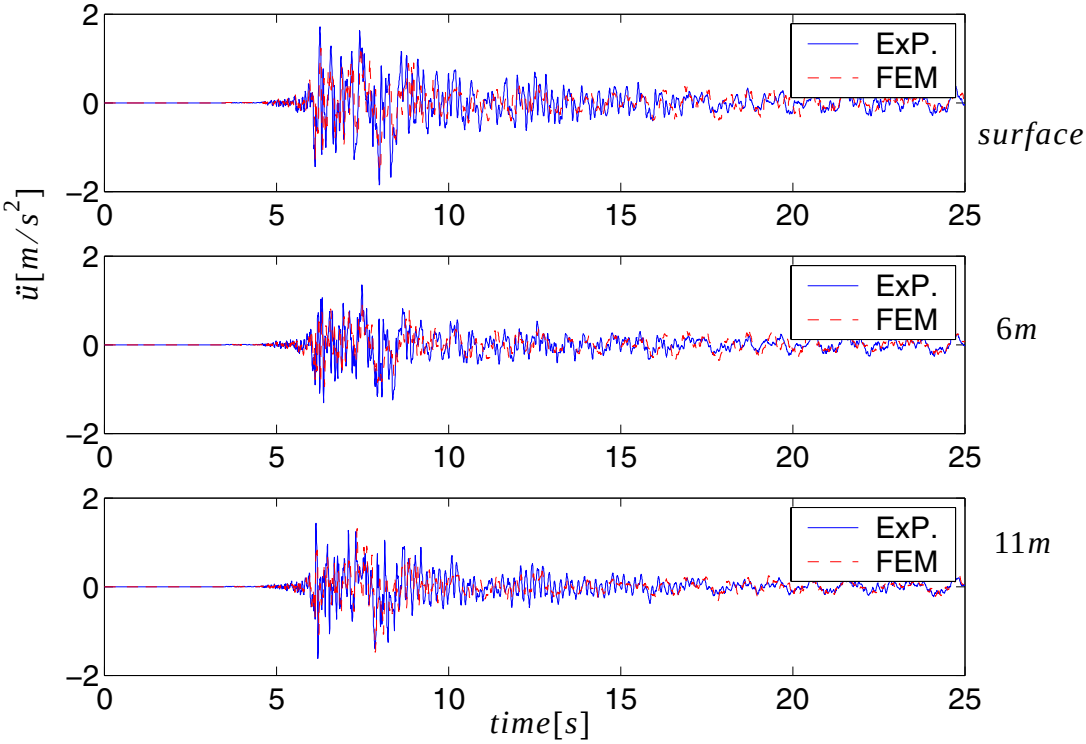


**Figure 7.12 Comparison of 'Experimental' soil responses with responses obtained by using initial values of parameters**

The objective and constraint functions are the same as in Equations (7.4) and (7.5), while the gradients using FFD and DDM are the same as in Equations (7.6) and (7.7) respectively.

Comparison of the results obtained by FFD and DDM when using noise-free 'experimental' data.

In this example, the 'experimental' data is noise free as shown in Figure 7.11. Both FFD and DDM give good results as shown in Table 7.8.

**Table 7.8 Parameters obtained by updating procedure when using DDM and FFD**

| Parameter [kPa] | $G_1$ | $G_2$ | $G_2$ | $\tau_1$ | $\tau_2$ | $\tau_3$ |
|---|---|---|---|---|---|---|
| 'real' values | 28800 | 39200 | 57800 | 31 | 33 | 34 |
| initial values | 30000 | 30000 | 30000 | 30 | 30 | 30 |
| DDM | 28800.03 | 39199.89 | 57800.08 | 31.0 | 33.0 | 34.0 |
| FFD | 28797.40 | 38941.76 | 57977.04 | 31.145 | 33.660 | 34.156 |

The convergence rate is compared in terms of the values of the objective function at each major iteration of the updating procedure as shown in Table 7.3.

**Table 7.9 Objective function values comparison between using DDM and FFD**

| iteration # | DDM | iteration # | FFD |
|---|---|---|---|
| 1 | 3.981E+02 | 1 | 3.981E2 |
| 2 | 1.687E+02 | 5 | 1.017E2 |
| 3 | 1.321E+02 | 10 | 7.482E1 |
| 4 | 4.429E+01 | 15 | 6.993E1 |
| 5 | 2.644E+01 | 20 | 5.210E1 |
| 6 | 2.253E+01 | 25 | 2.066E1 |
| 7 | 1.221E+01 | 30 | 1.944E1 |
| 8 | 8.829E+00 | 40 | 1.887E1 |
| 9 | 5.909E+00 | 50 | 1.789E1 |
| 10 | 8.577E-01 | 60 | 1.779E1 |
| 11 | 3.924E-01 | 70 | 4.043E0 |

**Table 7.9 Objective function values comparison between using DDM and FFD**

| iteration # | DDM | iteration # | FFD |
|---|---|---|---|
| 12 | 1.225E-01 | 80 | 2.676E-1 |
| 13 | 1.239E-02 | 90 | 1.546E-1 |
| 14 | 2.778E-04 | 100 | 1.253E-1 |

From the values of the objective function listed in Table 7.9, it is observed that the convergence rate of the model updating procedure when using DDM is tremendously faster than when using FFD. In order to reach the criterion of F=1.0E-2, DDM requires 14 iterations while FFD requries over 100. The efficiency of DDM over FFD is clear from Figure 7.13 below where the results in Table 7.9 are plotted.

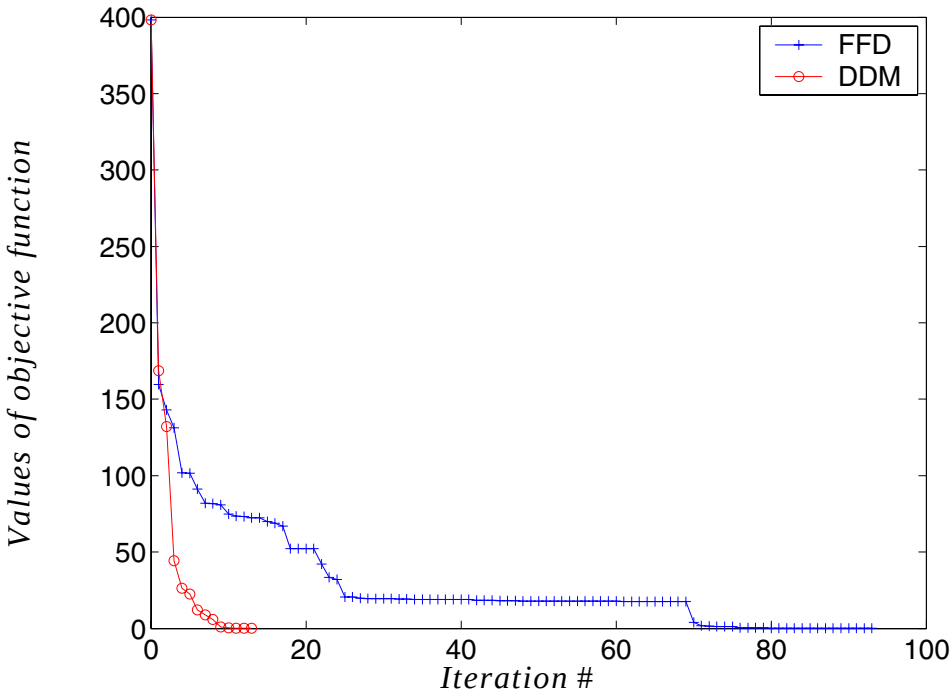


**Figure 7.13 Comparison of objective function values resulting from the use of DDM and FFD**

Comparison of the results obtained by FFD and DDM when the ‘experimental’ data includes artificial white noise

In order to better simulate the ‘real’ experimental data, 2% noise was included in the ‘experimental data’ (i.e., white noise with a PSD = 2% of the standard deviation of the original noise-free response signal during the whole process) while all other conditions were kept the same.

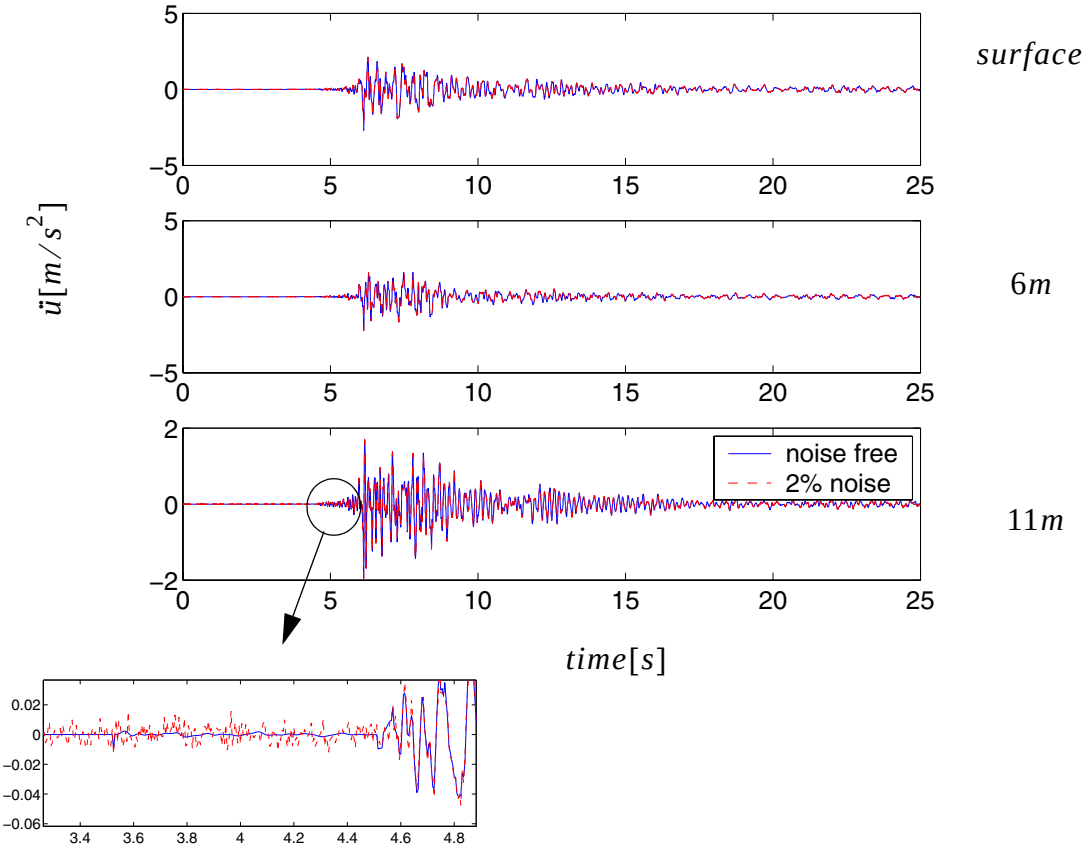


**Figure 7.14 ‘Experimental’ responses with 2% noise**

A comparison of the ‘experimental’ data between the noise-free and 2% noise cases are shown in Figure 7.14.

The model updating procedure (SNOPT) obtains the values of the parameters by using DDM or FFD methods as shown in Table 7.11.

**Table 7.10 Parameters obtained by updating procedure when using DDM and FFD**

| Parameter [kPa] | $G_1$ | $G_2$ | $G_2$ | $\tau_1$ | $\tau_2$ | $\tau_3$ |
|---|---|---|---|---|---|---|
| ‘real’ values | 28800 | 39200 | 57800 | 31 | 33 | 34 |
| initial values | 30000 | 30000 | 30000 | 30 | 30 | 30 |
| DDM | 28794.41 | 39208.08 | 57796.08 | 31.012 | 32.992 | 33.997 |
| FFD | 28751.71 | 39365.45 | 57781.26 | 30.662 | 32.662 | 33.970 |

A comparison of the convergence rate in terms of the objective function values, when using FFD and DDM, are shown in Table 7.11 and are plotted in Figure 7.15.

**Table 7.11 Objective function values comparison between using DDM and FFD**

| iteration # | DDM | iteration # | FFD |
|---|---|---|---|
| 1 | 3.981E+02 | 1 | 3.981E2 |
| 2 | 1.682E+02 | 10 | 2.262E2 |
| 3 | 1.423E+02 | 20 | 2.108E2 |
| 4 | 3.118E+01 | 30 | 1.281E2 |
| 5 | 1.875E+01 | 40 | 5.460E1 |
| 6 | 7.964E+00 | 50 | 4.770E1 |

**Table 7.11 Objective function values comparison between using DDM and FFD**

| iteration # | DDM | iteration # | FFD |
|---|---|---|---|
| 7 | 3.314E+00 | 60 | 4.758E1 |
| 8 | 1.655E+00 | 70 | 3.895E1 |
| 9 | 1.035E+00 | 80 | 3.110E1 |
| 10 | 4.236E-01 | 90 | 3.103E1 |
| 11 | 3.108E-01 | 100 | 2.050E1 |
| 12 | 2.698E-01 | 120 | 7.691E0 |
| 13 | 2.579E-01 | 140 | 2.658E0 |
| 14 | 2.548E-01 | 160 | 1.325E0 |
| | | 180 | 6.664E-1 |
| | | 200 | 5.777E-1 |

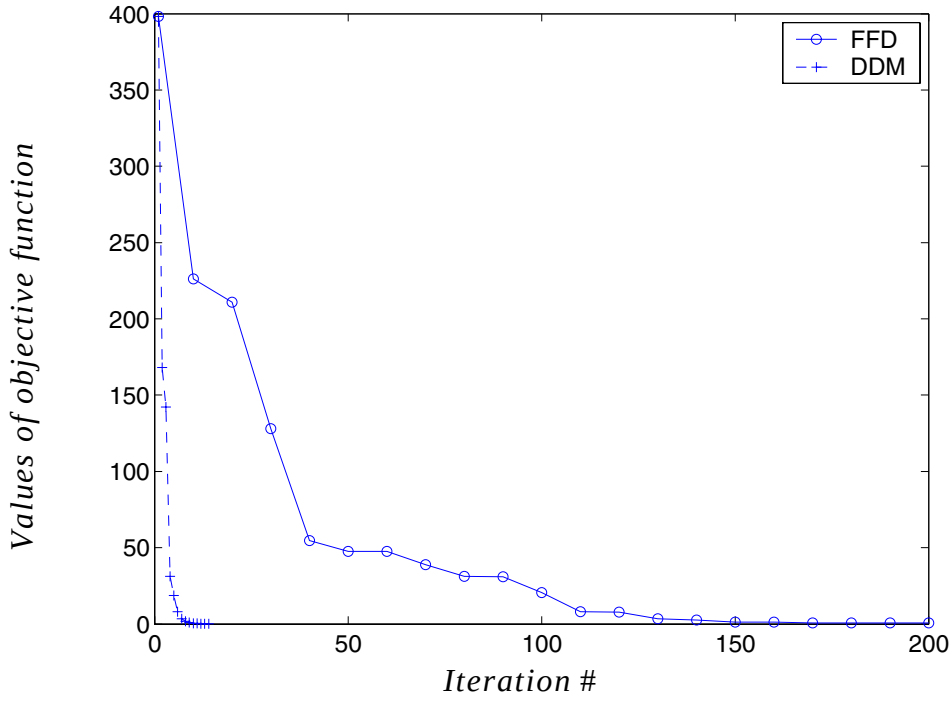


**Figure 7.15 Comparison of objective function values resulting from the use of DDM and FFD**

From the values of the objective function listed in Table 7.11 and Figure 7.15, it is observed that the convergence rate of model updating procedure (SNOPT) when using DDM is significantly faster than FFD. To reach the same accuracy (i.e., value of objective function less than 5.0e-1), the model updating procedure using FFD needs about 20 times more iterations than when using DDM!

### 7.4.3 Real Example 1, Linear Model Updating

In this example, the soil at a site near Lotung, China (Tang 1987) was studied. The Electric Power Research Institute (EPRI) in cooperation with the Taiwan Power Company (TPC) conducted a Large-Scale Seismic Test (LSST) at this site. Field exploration showed that the upper layer (30-40m thick) consists predominantly of interlayered silty-sand and sandy-silt with some gravel (Lotung downhole array. I: Evaluation of site dynamic properites. A. Elgamal et al. Journal of Geotechnical Engineering vol 121, no.4, Apr. 1995.). Taking advantage of the data obtained by downhole triaxial accelerometers at ground surface and at depths of 6m, 11m and 17m, model updating was performed to dertemine the soil properties in this example.

The FE model used in this example consists of twenty 3D-brick elements containing lateral nodes fixed in the E-W direction to simulate a plane strain case. The soil behavior is simulated using a pressure dependent multi-yield surface model (Elgamal et al, 2002), the acceleration is considered the same as in section 7.4.1. The model is described below in Figure 7.16.

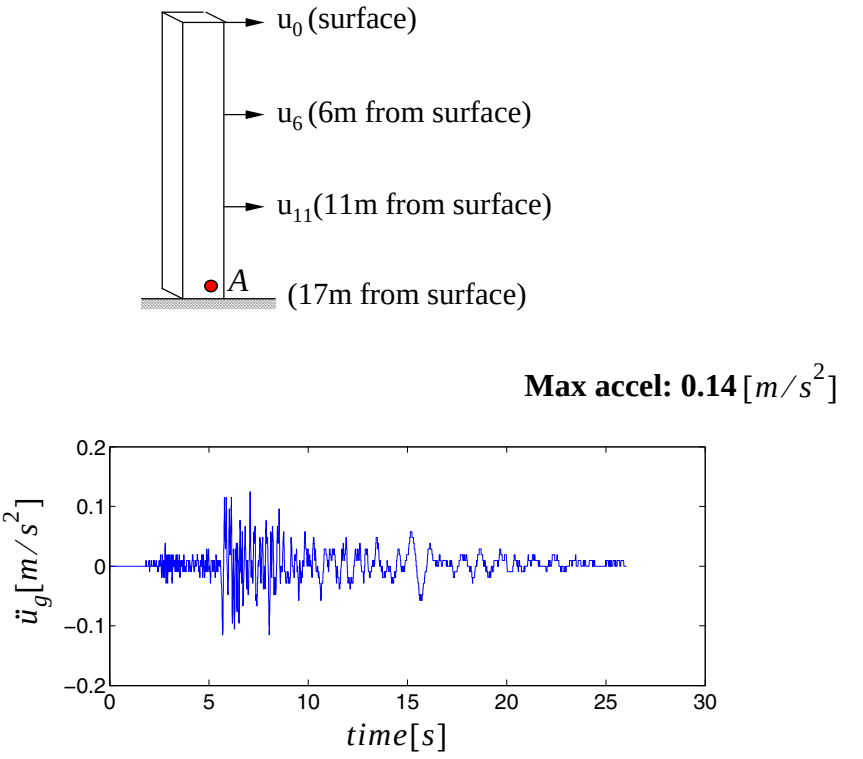


**Figure 7.16 Soil column subject to base excitation**

The parameters (Design Variables, or DVs) to be updated are chosen as

(1) the shear wave velocity *v* at a reference mean effective confining pressure (Frank, OpenSees manual). For the linear elastic case, the shear wave velocity is related to the low strain shear modulus G as $G = \rho v^2$, where $\rho$ is the mass density.

(2) the Rayleigh damping parameter $\beta_{k,\,init}$. The damping used in this model is stiffness proportional Rayleigh damping.

(3) pressure dependent coefficient d, a positive constant defining variations of G and B as a function of instantaneous effective confinement p' as, $G = G_r\left(\frac{p'}{p_r'}\right)^d$ and $B = B_r\left(\frac{p'}{p_r'}\right)^d$, where the subscript r denotes the reference value. (http://opensees.berkeley.edu/OpenSees/manuals/usermanual/index.html).

These three parameters are most sensitive for determing the response. The recorded response of the soil at different depths is shown in Figure 7.17.

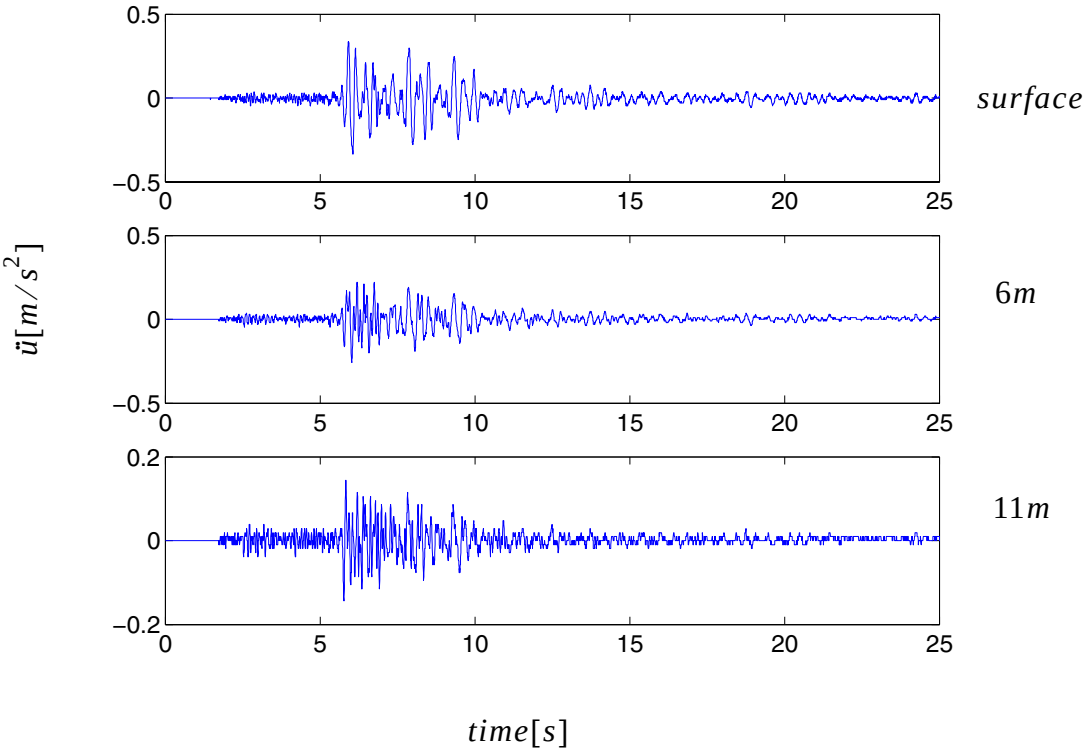


**Figure 7.17 Recorded soil responses at different depths**

Here the objective function is taken to be the same as in Equation (7.4). The objective function, defining an ordinary least squares problem, minimizes the difference between the recorded and FE simulated acceleration histories at different stations.

Field exploration results suggest that the bounds of the DVs may be defined as,

$$150 < v < 250 \tag{7.8}$$

and

$$0 < \beta_{k,\,init} < 0.0067 \tag{7.9}$$

corresponding to a damping ratio $0 < \zeta_1 < 5\%$. The natural frequency of the simulated soil column is 2.367 Hz. and

$$0 < d < 1.0 \tag{7.10}$$

Parameter values obtained by SNOPT and the values of the objective function are listed in Table 7.12.

**Table 7.12 SNOPT optimization results**

| DVs and Objective function | initial value | lower bound | upper bound | SNOPT results |
|---|---|---|---|---|
| $v[m/s]$ | 210 | 150 | 250 | 176.2 |
| $\beta_{k,\,init}$ | 0 | 0 | 0.0067 | 0.0067 |
| d | 0.5 | 0 | 1.0 | 0.383 |
| F $[m/s^2]$ | 360.23 | 0 | None | 5.34 |

The value of the objective function decreased from an initial value of 360.2 to 5.34. The damping ratio corresponding to $\beta_{k,\,init} = 0.0067$ is about 5%.

Before model updating, the reponses between recorded responses and FE simulations using initial values at different soil depths(stations) are compared as shown in Figure 7.18. It can be observed that the two responses are totally different.

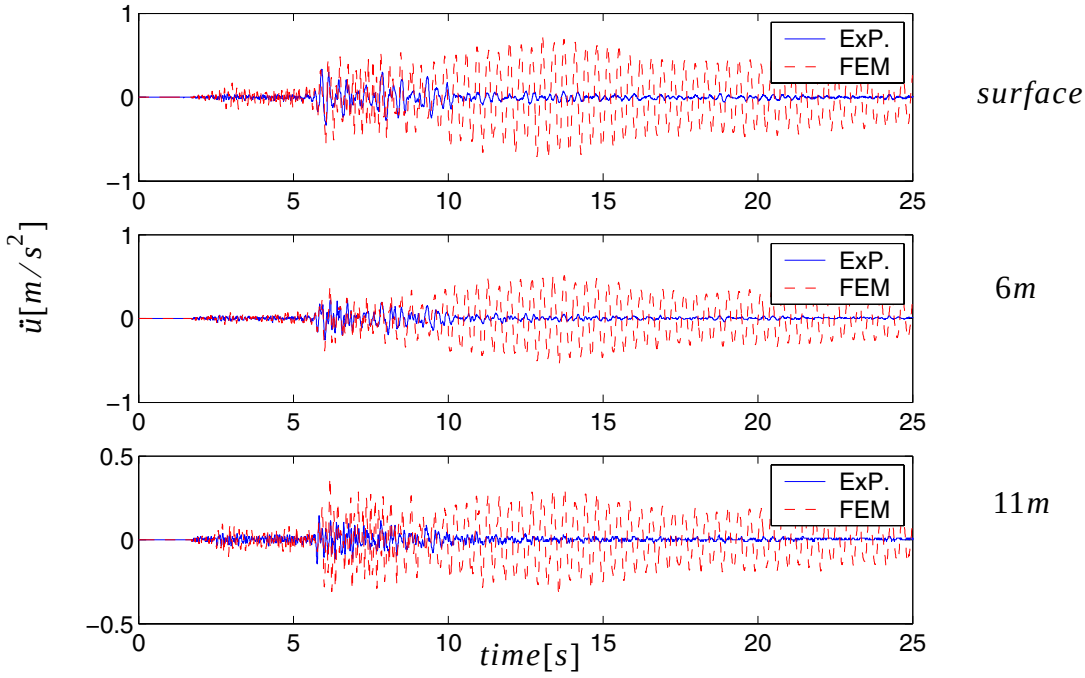


**Figure 7.18 Comparison of real soil responses with responses obtained by using initial values of parameters**

After model updating, using the values obtained by SNOPT, the comparison between actual and simulated responses are shown in Figure 7.19 below. The comparison of acceleration histories between seconds 4 and 10 in Figure 7.19 are zoomed in and shown in Figure 7.20.

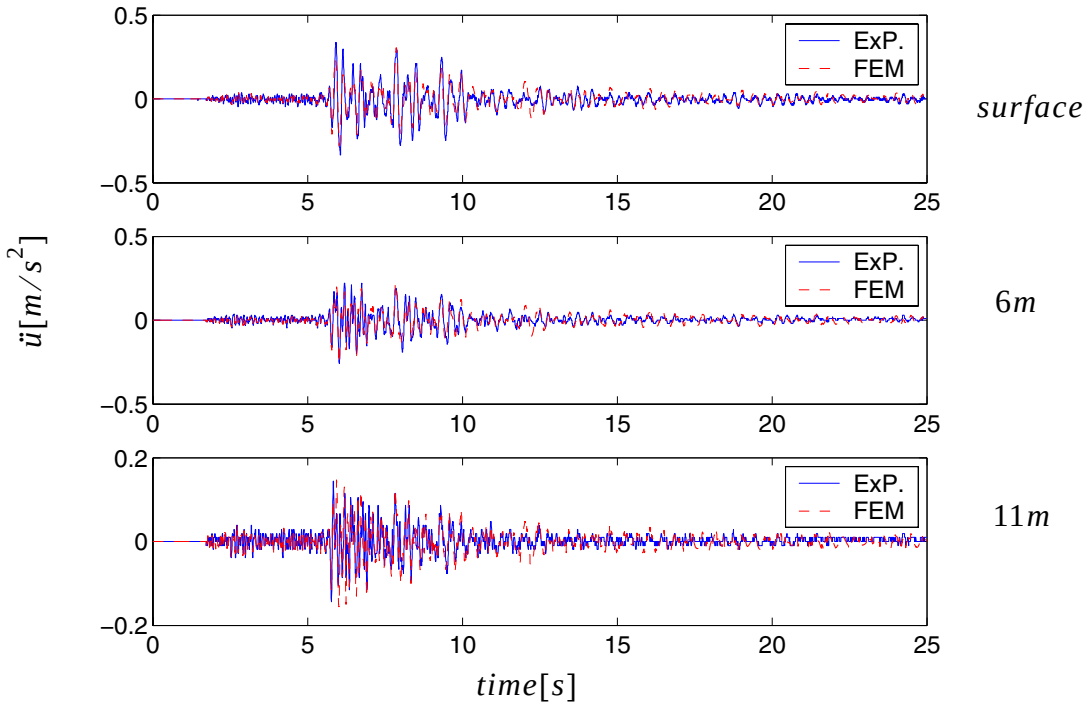


**Figure 7.19 Comparison of actual soil responses with FE simulated responses after model updating**

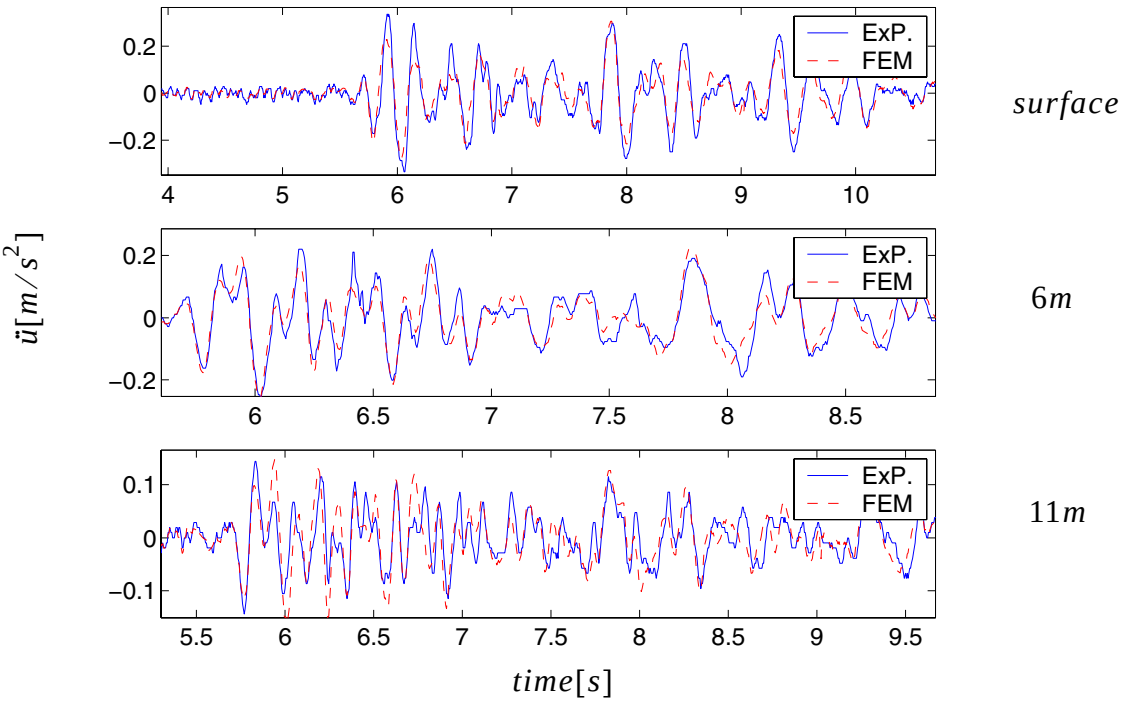


**Figure 7.20 Comparison of actual soil responses with FE simulated responses after model updating (zoomed)**

A comparson is also made in the frequency domain as shown in Figure 7.21. Unlike the generaly applied linear model updating method, which matches the first several frequencies, this model updating method tries to match all frequencies as shown in Figure 7.21. This is due to the fact that it tries to match the entire response history, including contribution from all frequencies.

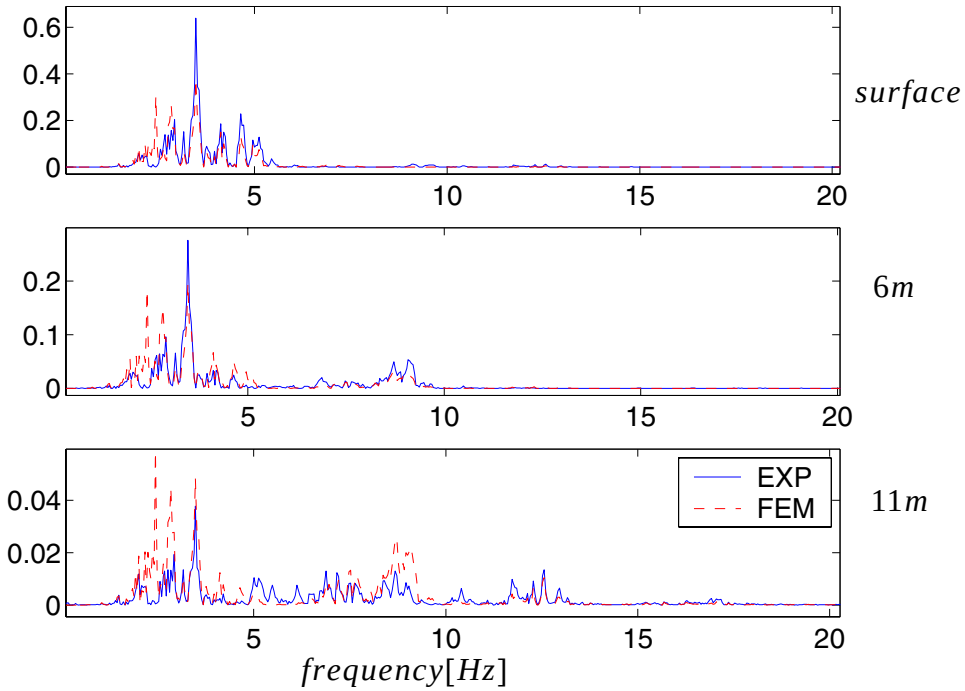


**Figure 7.21 Comparison of actual soil responses with FE simulated responses in the frequency domain**

In order to check whether the parameters obtained in Table 7.13 are physicaly acceptable, the set of parameters are used to check another earthquake response at the same site, Site no. 8 oriented in N-S direction, during the earthquake of May 20 1986, is used in this case. The maximum acceleration was recorded as 0.13 $m/s^2$. The comparison is shown in Figure 7.22. From this figure, it can be seen that the parameters obtained by SNOPT are an excellent estimation of the physical values.

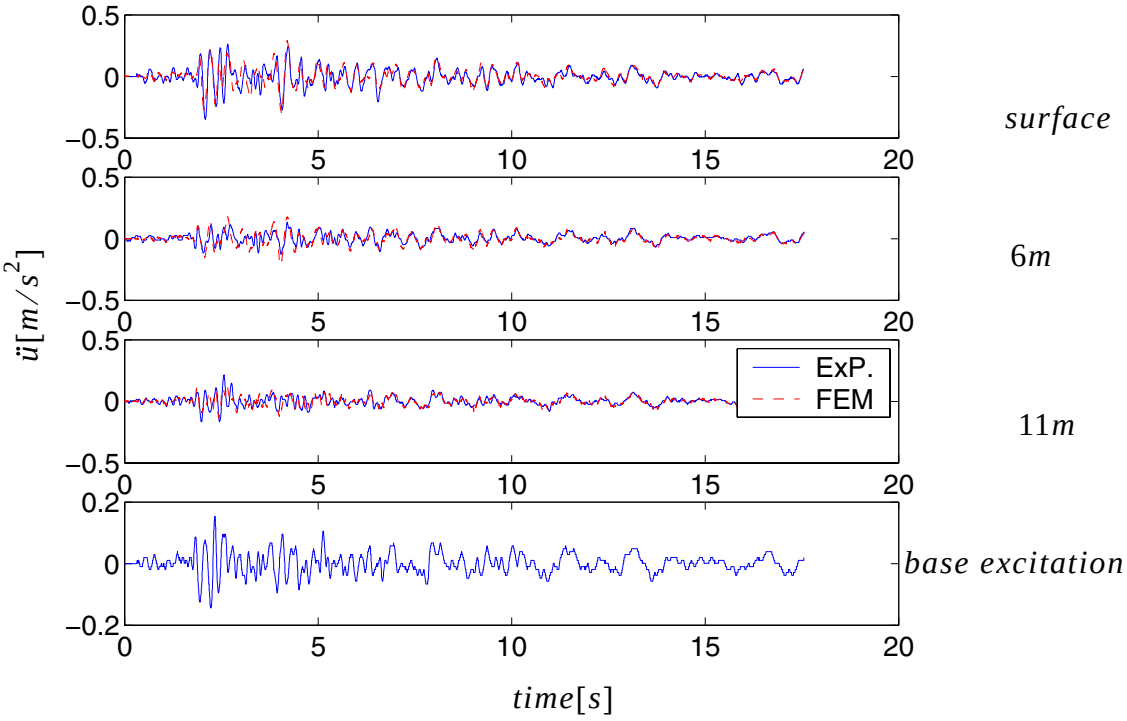


**Figure 7.22 Comparison of actual soil responses with FE responses computed with parameters in** Table 7.13 **for May 20 1986 earthquake**

### 7.4.4 Real Example 2, Nonlinear Model Updating

In this section, the same soil model is reconsidered for strong earthquake inputs (max base excitation close to or large than 0.1g). The model parameters are re-evaluated by SNOPT during the earthquake of Nov. 14, 1986 at site 16N. The maximum acceleration was 0.84 $m/s^2$.

The recorded soil responses at different depths are shown in Figure 7.23.

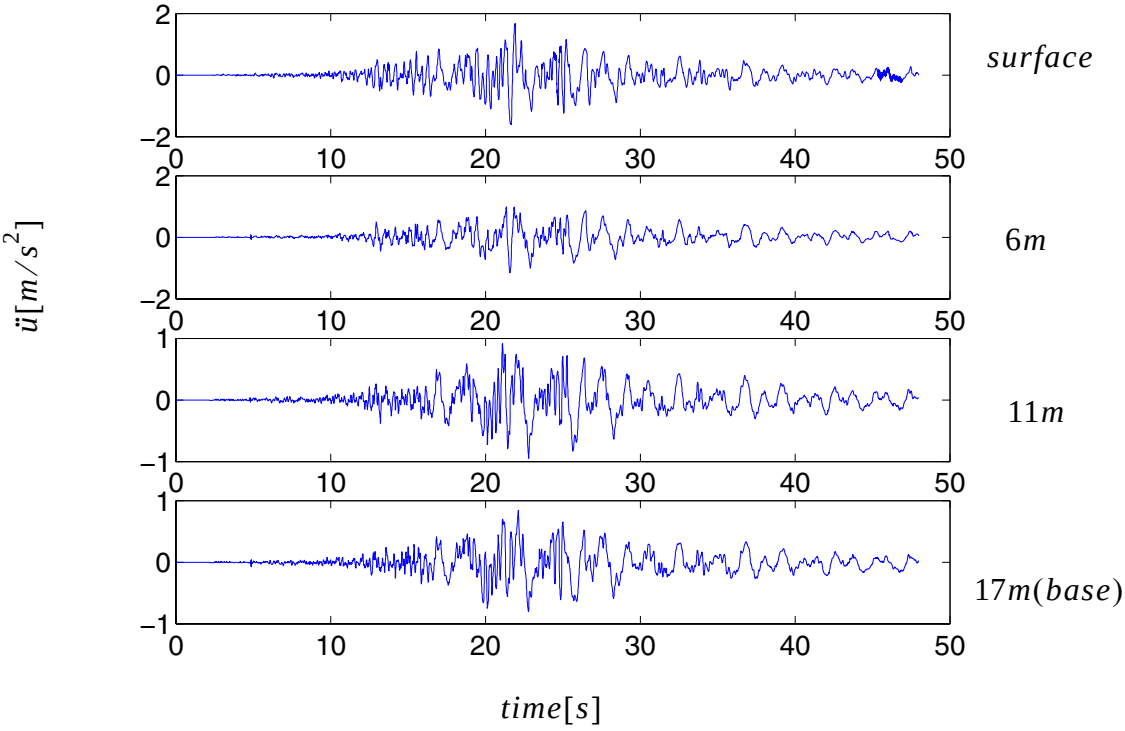


**Figure 7.23 Recorded soil responses at different depths**

It was discovered that the most sensitive parameters in the nonlinear model updating case were the same as those in the linear case in section 7.4.3. The data obtained from the linear model updating case, shown in Table 7.12, was used as the initial values of the parameters in the nonlinear case. Responses at different soil depths are compared between actual ground motion records and FE simulations as shown in Figure 7.24. Comparisons of the responses in the frequency domain are shown in Figure 7.25. It is observed that the responses close to 5 Hz are not modeled well. The high frequency(5Hz) predicted by the FE model is not observed in the actual response history. These high frequencies are not

observed due to the liquefaction caused by the intense ground motion. This suggests that

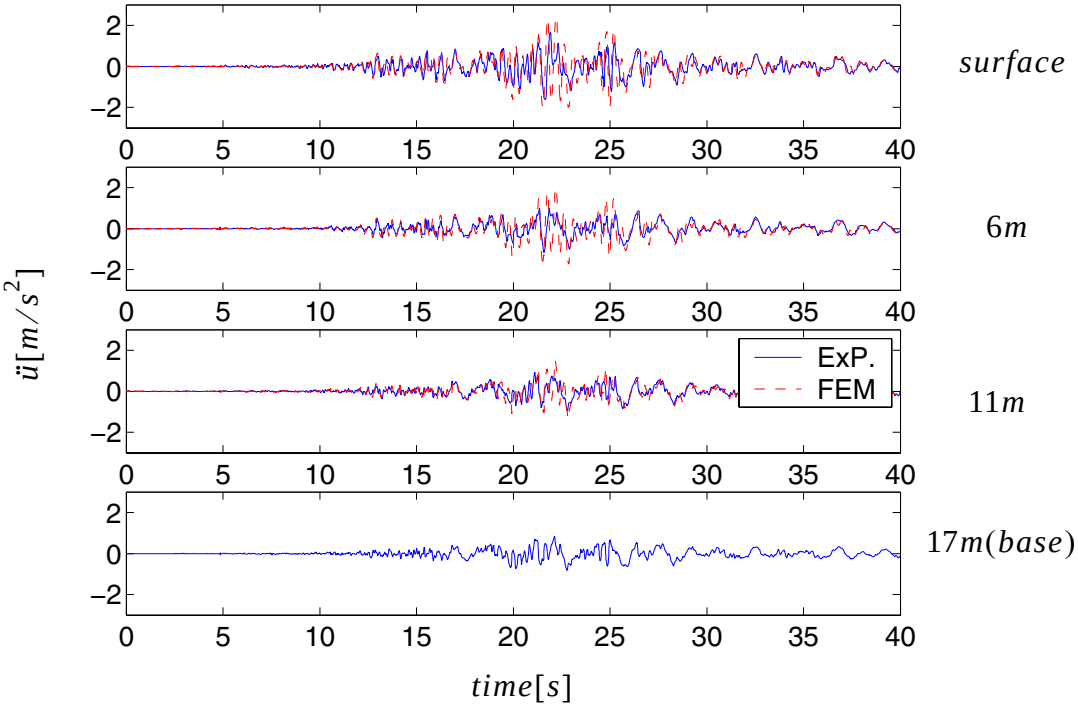


**Figure 7.24 Comparison of actual soil responses with responses obtained by using SNOPT results in Table 7.12 as initial parameter values**

either the effect of soil-fluid interaction should be considered or the soil parameters should be re-calibrated to fit the case of strong earthquakes. In the current model, no soil-fluid coupling is considered. Liquefaction effects were simulated by adjusting the soil properties and damping parameter.

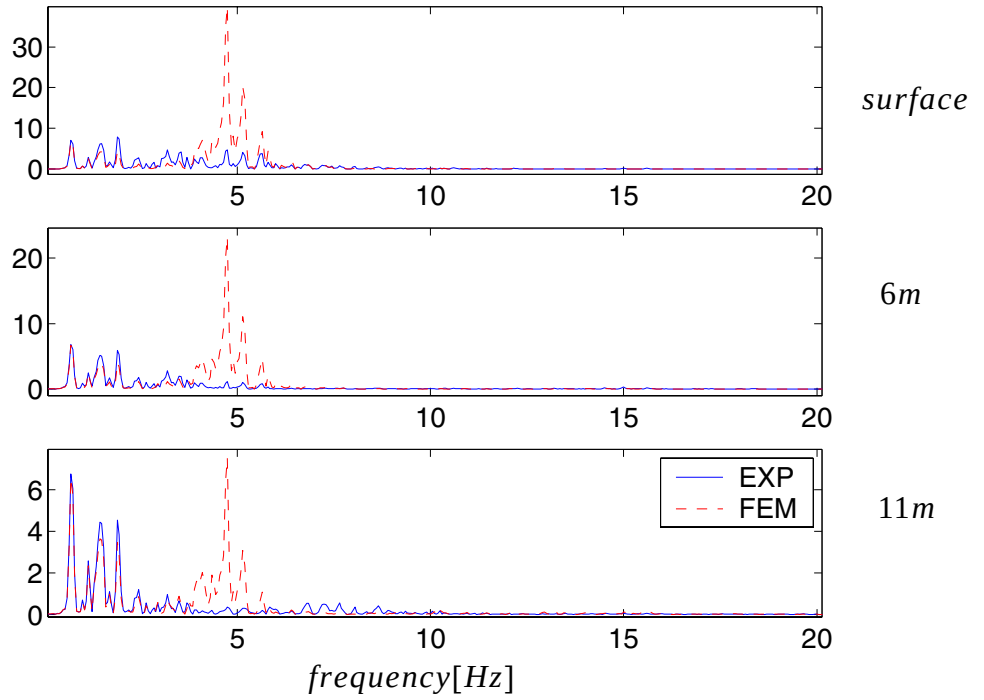


**Figure 7.25 Comparison of actual soil responses with responses obtained by using SNOPT results in Table 7.12 as initial parameter values in the frequency domain**

The objective function is same as section 7.4.1 as shown in Equations (7.4). The bounds are defined similarly as before with,

$$120 < v < 220 \tag{7.11}$$

and

$$0 < \beta_{k,\,init} < 0.0067 \tag{7.12}$$

corresponding to damping ratio $0 < \zeta_1 < 5\%$.

and,

$$0 < d < 1.0 \tag{7.13}$$

The parameter results obtained by SNOPT are shown in Table 7.13. The objective function F changes from 660.05 to 165.74, and can not be further reduced. This is due to the fact that the model is not accurate enough to simulate the sand behavior during liquifaction.

**Table 7.13 Parameters obtained by SNOPT**

| DVs and Objective function | initial value | lower bound | upper bound | results by SNOPT |
|---|---|---|---|---|
| $v[m/s]$ | 176.2 | 120 | 220 | 133.729 |
| $\beta_{k,\,init}$ | 0.0067 | 0.001 | 0.0067 | 0.0067 |
| d | 0.383 | 0 | 1.0 | 0.6316 |
| F | 660.05 | 0 | None | 165.74 |

The damping ratio corresponding to $\beta_{k,\,init} = 0.0067$ is about 5%.

After model updating, using the values obtained by SNOPT, the comparison between real records and simulated responses are shown in Figure 7.26 below. Figure 7.27 focuses on the time interval between seconds 15 through 25 in Figure 7.26. The comparison in the frequency domain is shown in Figure 7.28. The shear-stress shear-strain relations at point A (Figure 7.16) are shown in Figure 7.29 where the nonlinear behavior of the soil is observed.

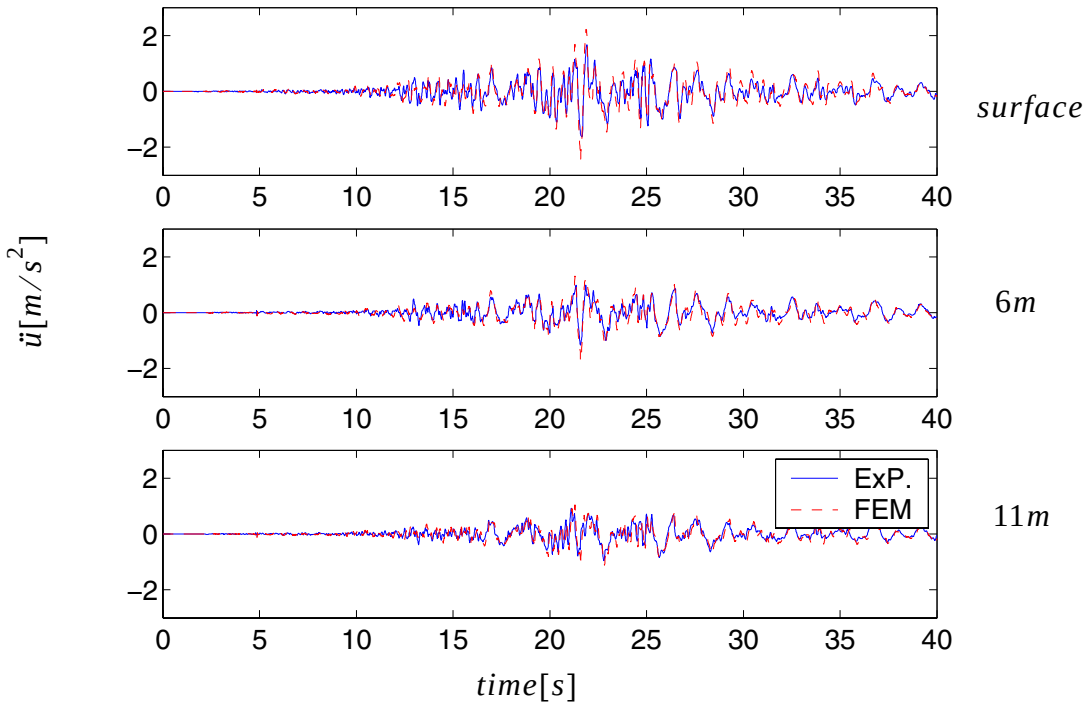


**Figure 7.26 Comparison of actual soil responses with FE simulation responses**

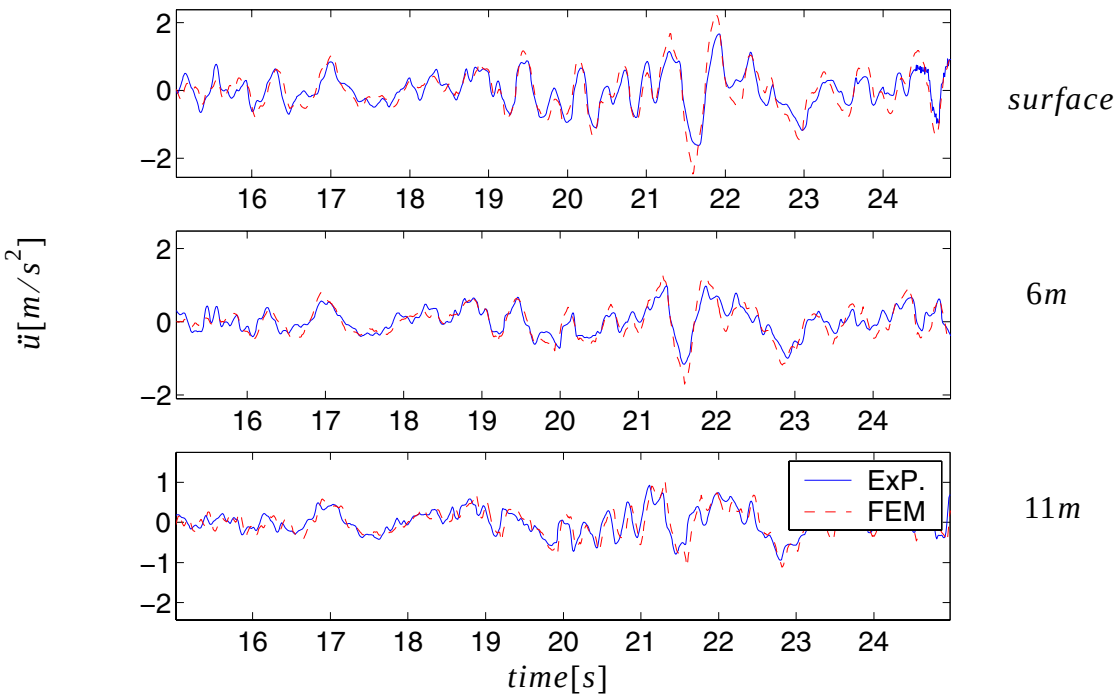


**Figure 7.27 Comparison of actual soil responses with FE simulation responses during time interval 15-25 sec.**

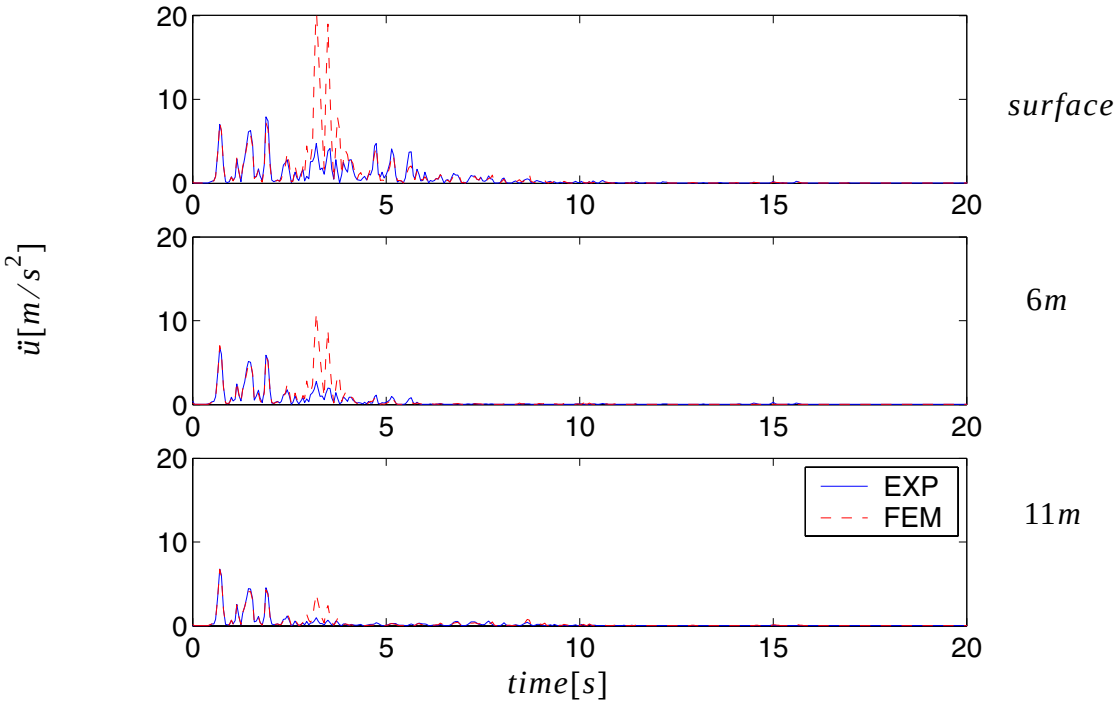


**Figure 7.28 Comparison of actual soil responses with FE simulation responses in the frequency domain**

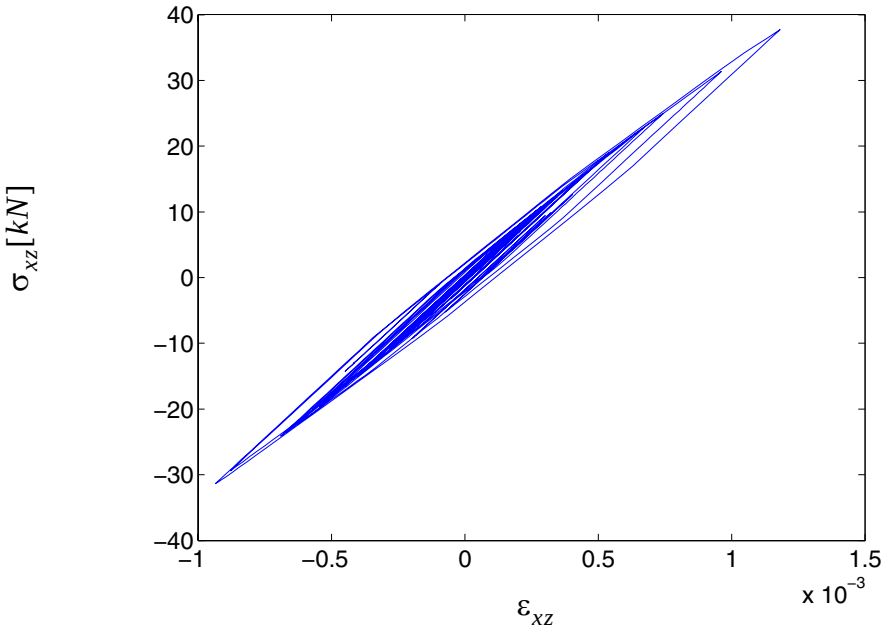


**Figure 7.29 Shear stress-strain responses at point A in Figure 7.16**

From these results, it is observed that the parameters obtained by SNOPT in Table 7.13 are excellent when simulating the actual soil behavior during strong earthquakes.

In order to verify the parameters obtained in Table 7.13, records during another strong earthquake (No. 7, May 20, 1986, Lotung, the maximum acceleration was 0.89 $m/s^2$) is compared with the FE simulations. The comparison is shown in Figure 7.30. It is seen that the parameters are very good when modeling the soil during strong earthquakes. The shear stress-strain relations at point A (see Figure 7.16) are shown in Figure 7.31.

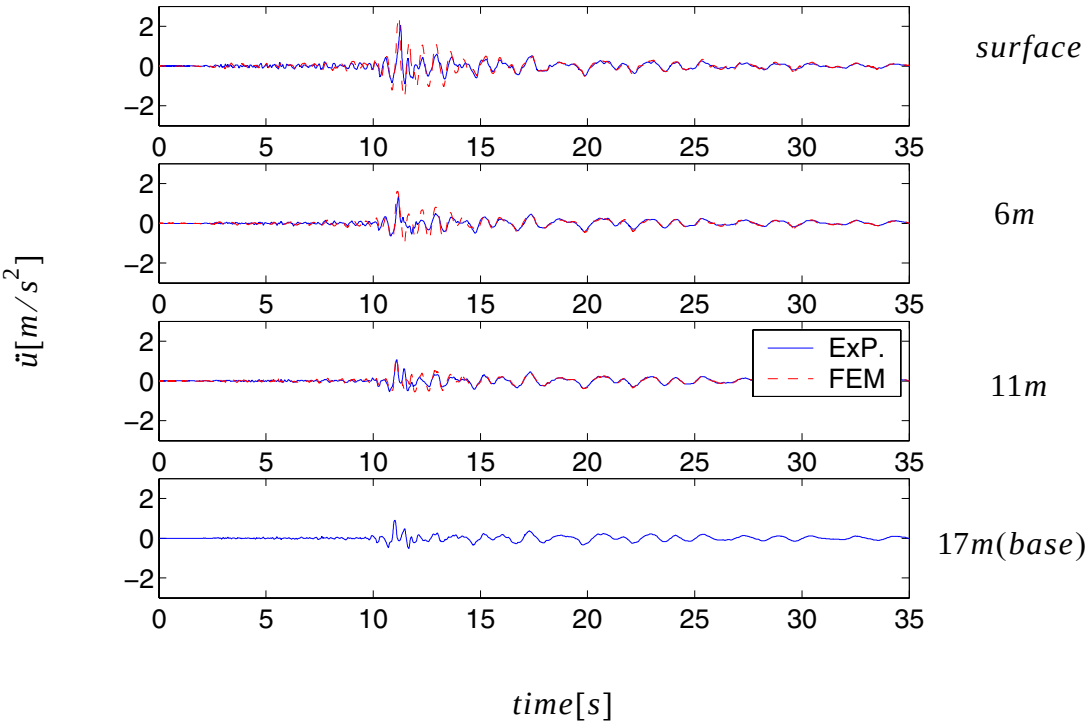


**Figure 7.30 Comparison of actual soil responses with FE simulated responses**

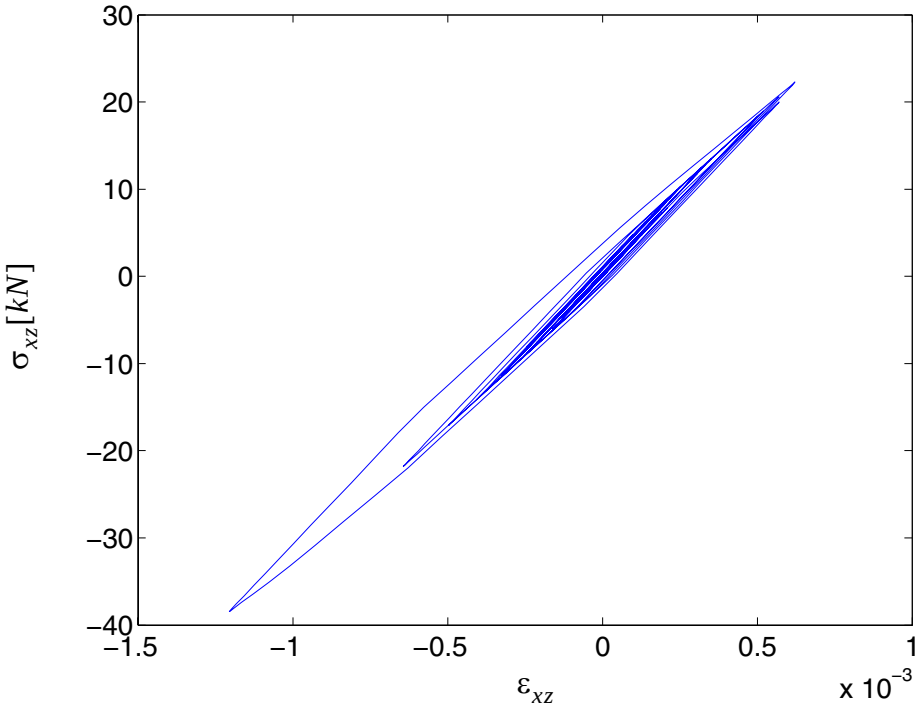


**Figure 7.31 Shear stress-strain responses at point A in Figure 7.16**

## 7.5 Conclusion

In this chapter, a general-purpose OpenSees-SNOPT framework for solving optimization problems in nonlinear structural and/or geotechnical systems is developed and presented. Several application examples in nonlinear soil FE model updating are studied using this framework and presented.

Based on the numerical examples considered, the OpenSees-SNOPT framework allows to obtain the global minimum of the objective function provided the initial parameter values are not far from their actual (“true”) values, or when appropriate constraints are added. The convergence rates obtained using OpenSees-SNOPT combined with FE

response sensitivities computed using the DDM and FFD methods, respectively, were compared. It was found that the DDM-based computation of the gradients of the objective and constraint functions increased drastically the rate of convergence (as measured by the number of iterations to achieve convergence) of the nonlinear finite element model updating process as compared to when using FFD-based gradient computation. This advantage of the DDM-based over FFD-based gradient computation increases with the nonlinearity in the system response behavior. Furthermore, it was observed that this advantage is even more significant when artificial numerical noise is added to the simulated 'experimental' response data so as to model measurement noise.

The OpenSees-SNOPT based nonlinear FE model updating strategy was then applied to a real world example consisting of a multi-layered nonlinear soil column at the Lotung downhole array in Taiwan. A linear soil FE model was calibrated (through FE model updating) to best represent the Lotung soil behavior during a low intensity earthquake, while a nonlinear FE model was calibrated to capture the actual nonlinear soil behavior during a strong earthquake. The calibrated linear and nonlinear soil FE models with parameters obtained from OpenSees-SNOPT were then used to simulate the response of the Lotung soil to other recorded earthquakes. In both the linear and nonlinear cases, the simulated soil response is very close to the recorded response. This demonstrates that the calibrated/optimum soil FE models obtained using the OpenSees-SNOPT framework are physically meaningful.

# CHAPTER 8

# USER'S GUIDE TO RESPONSE SENSITIVITY AND RELIABILILY ANALYSES OF SSI SYSTEM IN OPENSEES

In this chapter, a complete set of commands for performing sensitivity and reliability analyses for SSI systems are described. Performing the analyses in OpenSees requires creating and running a set of TCL commands. Fundamental reliability commands can be found in Haukaas disertation (2001). New TCL commands are integrated into the TCL library, allowing for the use of new models, methodologies and algorithms in OpenSees.

## 8.1 SSI Model Development

### 8.1.1 Basic Requirements

The modeling of SSI systems may include structure, foundation, and soil components and considers their interaction. The focus of this chapter is to show how to apply the sensitivity and reliability commands. While the vast number of options in Opensees allow for the development of highly complex models, simple examples are offered here for pedagogical purposes. The structure consists of simple beam/column elements with various sections and materials. The foundation described bellow is modeled with beam/column elements when considering pile foundations, and brick elements when considering shal-

low foundations. The soil here is modeled as a multi-yield surface $J_2$ plasticity model. A complete model may be found at http://opensees.berkeley.edu/ or may be available from the author.

In this chapter, commands are specified in *italic* format, while new or updated commands are denoted in ***bold*** format.

The first command the user must apply is

*reliability*

which creates the reliability domain in which the sensitivity, reliability, and optimization components, are kept (e.g. random variables, FORMAnalysis, etc.)

The model is then created as with response-only analyses. For details regarding model creation, please refer to the OpenSees manual at http://opensees.berkeley.edu. From this point on only new or updated commands are explained in detail.

### 8.1.2 Structure Model

Both 2D and 3D RC concrete material models are described herein to simulate structural behavior. The sensitivity framework is extended to the following elements, sections, and materials.

1. Elements

Sensitivity framework is extended to the following elements in order to model SSI systems:

Quad Element: 2D four-node quadrilateral bilinear isoparametric element.

***zeroLength Element***: used to construct a 1D zeroLength element object.

***DispBeamColumn2d & DispBeamColumn3d element***: displacement based beam column element.

***bbarBrick Element***: an 3D eight-node mixed volume/pressure brick element object, using a trilinear isoparametric formulation

The commands to create these elements are available online in the OpenSees manual (http://opensees.berkeley.edu/OpenSees/manuals/usermanual/index.html).

2. Sections

The sensitivity framework has recently been extended to the following existing sections in OpenSees:

*ElasticSection3d, FiberSection2d, FiberSection3d, sectionAggregator.*

To specify the random variables for these sections, the user must create the ***randomVariablePositioner*** object, which specifies the location of a previously defined random variable. For example:

***randomVariablePositioner $pos -rvNum $gradNumber -element $ele -sectionAggregator $secAgg -section $section -material $mat $h***

*$pos:* This argument indicates the identification number or tag, of a random variable positioner.

NOTE: Within the reliability model, *$pos* should begin with 1 and increase sequentially by 1.

*$gradNumber:* The tag of a random variable, previously created by the ‘randomvariable’ command created in the reliability model.

*$ele:* The element tag, previously created by the ‘element’ command in the FE model.

$secAgg: The tag of a section aggregator previously created by the ‘section Aggregator’ command in the FE model.

$section: *The tag of a section within the aggregator, previously created by the ‘section’ command in the FE model.*

*$mat:* The tag of a material previously created by the ‘material’ command in the FE model.

*$h:* The material parameter defined as the random variable.

*$h* is a string variable in TCL, representing different parameters of various uniaxial materials that can be used in the fiber sections. The available materials and their material parameters are shown in Table 8.1. For example, if the user wished to compute the response sensitivity w.r.t. the elastic modulus of material ‘steel01,’ following command should be performed before the *randomVariablePositioner* command.

*set h E*

*randomVariablePositioner.....*

**Table 8.1 Sensitivity parameters available in uniaxial materials**

| concrete01 | steel01 | Elastic | Hardening | steelMP | smoothPSC oncrete |
|---|---|---|---|---|---|
| fc | sigmaY | E | sigmaY | sigmaY | fc |

**Table 8.1 Sensitivity parameters available in uniaxial materials**

| concrete01 | steel01 | Elastic | Hardening | steelMP | smoothPSConcrete |
|---|---|---|---|---|---|
| epsco | E | eta | E | E | epsco |
| fcu | b | | H_kin | b | epsu |
| epscu | a1 | | H_iso | | fcu |
| | a2 | | | | Ec |
| | a3 | | | | eta |
| | a4 | | | | |

In which the *steelMP* and *smoothPSConcrete* build the Menegotto-Pinto model and the smoothed Popovics-Saenz model (refer to Michele dissertation). The sensitivities of these two models are developed and implemented into OpenSees by the author and co-workers. For more information regarding other material models, please refer to the OpenSees manual at http://opensees.berkeley.edu.

3. 1D uniaxial materials

From the materials available for sensitivity analysis in Table 8.1, the ‘steelMP’ and ‘smoothPSConcrete’ models have recently been implemented into OpenSees. To create these material models, the following commands are required:

***uniaxialMaterial SmoothPSConcrete $tag $fc $fu $Ec $eps0 $epsu $eta***

***uniaxialMaterial SteelMP $tag $fy $E $b <r=20.0 coeffR1 =18.5 coeffR2 =0.15 a1=0 a2=0>***

....

### 8.1.3 Soil Model

In this dissertation, a pressure independent multi-yield surface J2 plasticity model is used to simulate soil behavior:

***2D & 3D pressureIndependMultiYield material***

After this material is created, user needs to run '*updateMaterialStage -material $mat -stage 101'* to change the material model to an elastoplastic model before the loading begins. The sensitivity parameters may then be set as,

*randomVariablePositioner $pos -rvNum $gradNumber -element $ele -material $h*

'h' is a string variable in TCL, representing different parameters. (e.g., set h equal to '*G*', '*cohesion*', or '*K*' to specify the random variables as the low strain shear modulus, maximum shear strength, and bulk modulus, respectively. For example:

*set h G*

*randomVariablePositioner ....*

### 8.1.4 Connection between Structure and Soil

The nodes in shallow or pile foundations may have different dof as the soil nodes at the same location. The corresponding nodes may be tied together either by using the ***zero-length*** elements, or the *equalDOF* command. When using the ***zerolength*** element, each pair of nodes (e.g., pile node and soil node) must be tied at corresponding dof by a single zerolength element. When using the *equalDOF* command, two kinds of constraints, whose sensitivites have been implemented, may be available:

***constraint transformation***

***constraint penalty***

In the reliability analysis for SSI, not only may random variables be material parameters, but also forces within a load pattern. This is explained in the next section.

### 8.1.5 Load Pattern

The random variable may be a point load (terje's dissertation), or the maximum load of a load pattern. In the latter case, the random variable is defined as,

***randomVariablePositioner $pos -rvNum $gradNumber -loadPattern $numPattern -maxLoad $p_max***

where $pos and $gradNumber are defined as above, while $numPattern is the load pattern tag, and $p_max is the value of the maximum load in the loadpattern.

For large scale SSI problems, FE divergence may happen occasionally. In this case, an adaptive time step may be used to achieve the convergence of this step.

### 8.1.6 Adaptive Integration Time Step

In OpenSees, the following command is used to construct a VariableTimeStepDirectIntegrationAnalysis object, which may manage the adaptive time step.

***analysis VariableTransient***

The sensitivity framework is extended to accomodate this case.

In OpenSees, several sensitivity recorders are added for global response and local variable sensitivities as described in the next section.

### 8.1.7 Response Sensitivity Recorder

The global response sensitivities include the sensitivities of the node displacement, velocity, and acceleration. To record these quantities, the following commands may be used:

***recorder Node -file $filename -time -node 4 5 6 -dof 1 2 "sensitivity 1 2"***

***recorder Node -file $filename -time -node 4 5 6 -dof 1 2 "velSensitivity 1 2"***

***recorder Node -file $filename -time -node 4 5 6 -dof 1 2 "accSensitivity 1 2"***

which record the displacement, velocity, and acceleration sensitivities for nodes 4 through 6, along dof 1 and 2, w.r.t. random variables 1 and 2. The sensitivities are recorded in file $filename. In the same manner, the local responses, such as stress and strain sensitivities, at a single Gauss point, may be recorded as:

***recorder Element 23 -time -file stressS23G3.out material 2 stressSensitivity 1***

***recorder Element 23 -time -file strainS23G3.out material 2 strainSensitivity 1***

Here the stress and strain sensitivities at the second Gauss point of element 23 w.r.t. the random variable 1 are saved into files 'stressS23G3.out' and 'strain23G3.out.'

## 8.2 Response Sensitivity Analysis

In OpenSees, a two stage analysis (e.g., gravity and seismic stages) is commonly performed for the response analysis. In the next section, an example of a two stage analysis for both response and response sensitivities are described.

### 8.2.1 Two Stage Analysis

The following is an example of a two stage analysis (e.g., first static, then dynamic):

*integrator LoadControl 1 1 1 1*

*sensitivityIntegrator -static*

*sensitivityAlgorithm -computeAtEachStep*

*analysis Static*

*analyze 1*

*wipeAnalysis*

*integrator NewmarkWithSensitivity  0.55 0.275625  0. 0. 0. 0.*

*sensitivityIntegrator -definedAbove*

*sensitivityAlgorithm -computeAtEachStep*

*analysis Transient*

*analyze $nsteps $dt*

It is worth mentioning that the dynamic analysis follows the static one, without reset the time for the entire analysis. Thus the commands to reset time such as "*setTime 0.0*" or "*loadConst*", do not work for sensitivity analysis.

In some cases, the user needs to modify the values of the RVs (model updating case), or check the values of the RVs in either the physical or standard normal spaces. The following section will address these commands.

### 8.2.2 Random Variable Updating

The following command is used to update RV values by the starting point, which must be previously defined by the command '*startPoint'* (Terje's dissertation).

***updateParameter -startPoint***

If the user wants to update a single RV, the following command is used:

***updateParameter -rv $rv -value $v***

where $rv is the tag-number of RV, and $v is the new value given to the RV.

The command transformXtoU transforms a point in the physical space (saved in pointX.out) into the standard normal space (output to the file pointu.out).

***transformXtoU -fileX PointX.out -fileU pointu.out***

A 'probabilityTransformation' must be previously defined before this command is used.

The command *transformUtoX* transforms a point in the standard normal space (saved in the file pointu.out) to the physical space (output to pointX.out).

***transformUtoX -fileX PointX.out -fileU pointu.out***

## 8.3 Reliability Analysis

In reliability analysis, an important task is searching for the design point(s). For this purpose, SNOPT is integrated into OpenSees as an optimization tool.

### 8.3.1 Design Point Search

When using SNOPT as the optimization tool to seek out a design point, the tcl commands are the same as when using other optimization algorithms (e.g., HLRF, SQL, etc.). However in the SNOPT based design point search (1) users do not need to create the following four objects: *convergence check, search direction, meritFunctionCheck,* and *stepSizeRule*. (2) Users do need to specify the type of *findDesignPoint* to 'SNOPT'. A simple example of FORM analysis using SNOPT as the design point search algorithm is shown in Figure 8.1. The strikethrough commands used by other existing findDesignPoint algorithms in OpenSees are unnecessary.

```
performanceFunction 1 "0.15-{u_55_1}"
randomNumberGenerator       CStdLib
probabilityTransformation   Nataf          -print 0
reliabilityConvergenceCheck  Standard        e1 5.0e-3    e2  5.0e-3   print 1
gFunEvaluator               OpenSees        -file tclFileToRun450.tcl
gradGEvaluator              OpenSees
searchDirection             iHLRF
meritFunctionCheck          AdkZhang        multi 2.0    add 0.1    factor 0.5
stepSizeRule                Armijo          maxNum 10    base 0.5   initial 0.5 2  print 0
startPoint                  Mean
findDesignPoint             SNOPT   -maxNumIter 100 -printDesignPointX designPoint.out
runFORMAnalysis             FORMresults450.out  -relSens 1
```

**Figure 8.1 SNOPT based design point search algorithm**

The text file ‘sntoya.spc’, used with SNOPT, allows users to customize optimization parameters (e.g., set tolerances, whether the sensitivity results are verified). The details of the file ‘sntoya.spc’ can be found in reference of Professor Philip Gill (Gill 2004). SNOPT may be used for any existing reliability analysis, like first order and second order reliability analysis (FORM and SORM), for design point search purposes.

### 8.3.2 FORM, SORM and Mean Upcrossing Rate Analyses

The format of commands *runFORMAnalysis, runSORMAnalysis* is the same as that in the OpenSees Manual. If SNOPT is specified as the optimization algorithm, SNOPT will be called implicitly.

If the HLRF algorithm is used to find the design point, then after the design point is found, the first principal curvature of the LSS at the design point may be obtained with the command:

***findCurvatures firstPrincipal -exe***

With this command the first principal curvature is saved into a file with the name "principalAxes_.out".

In time variant reliability analysis, the FORM approximation of the mean upcrossing rate is computed by using the following command:

***runOutCrossingAnalysis $filename -results $stepsToStart $stepsToEnd $freq $sampleFreq -littleDt $little_dt -Koo***

The use of this command is shown in Figure 8.2. Three integers *$stepsToStart*, *$stepsToEnd*, and *$freq*, corresponding to the $n_{start}$, $n_{end}$ and freq in the Figure 8.2, specify the points at which the mean upcrossing rate is performed.

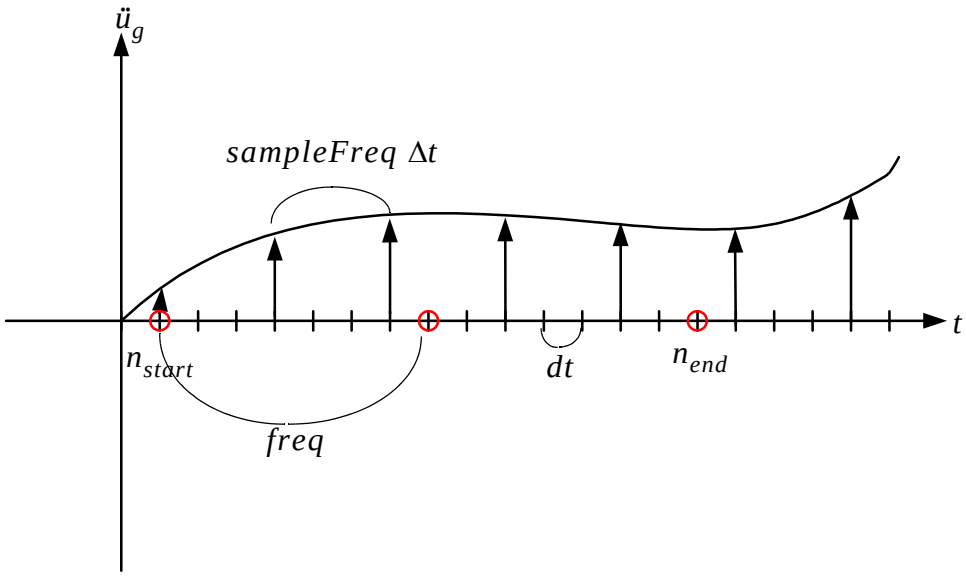


**Figure 8.2 Mean upcrossing rate analysis command**

where $stepsToStart, $stepsToEnd, and $freq are parameters (i.e., $n_{start}$, $n_{end}$, $freq$ in terms of the integration time step $dt$, in Figure 6.20) determining at which time point the mean upcrossing rate is evaluated. These time points are:

$stepsToStart, $stepsToStart+$freq, $stepsToStart+2*$freq, ... until $stepsToEnd

*$sampleFreq* is the time interval Δt (refer to Figure 6.20) between two neighboring impulses. The $little_dt ($\delta t$) is the small time increment by which the the second design point excitation $f_2(t)$ is obtained through shifting the first design point $f_1(t)$, i.e. $f_2(t) = f_1(t + \delta t)$.

For the design point search at time $t_n$, a “warm” initial point may be used by shifting the previous design point at time $t_{n-1}$ to the current time point as follows:

***startPoint -file designPointX.out -shiftStartPt***

in which the file designPointX.out should have the previous design point stored. Since the dimensions of the previous design point and current design point are not same, zeroes are added at the beginning of the previous design point.

To specify white noise input, which is a special case of the general nonstationary stochastic processes expressed as Equation (6.60), the following two commands are used together:

***filter $filterTag delta***

***modulatingFunction $functionTag constant $filterTag 1***

Where the *$filterTag* and *$functionTag* values must begin with 1. In the *modulating-Function*, the ‘constant’ is the type, and the ‘1’ is the number of filters (Haukaas dissertation, 2001). For white noise only 1 filter is necessary.

### 8.3.3 Sampling Analysis

Several sampling methods are developed, including Importance Samplint (IS), Orthogonal Plane Sampling (OPS), and crude Monte Carlo Sampling (MCS), and the corresponding commands are:

***runImportanceSamplingAnalysis $filename -type failureProbability -variance $var -maxNum $maxNum -targetCOV $cov -print $printflag***

where *$maxNum* denotes the maximum number of simulations, *$cov* denotes the target coefficient of variation of the estimate (default = 0.05), *$var* denotes the standard deviation of the sampling distribution (default = 1.0) and *$printflag* is a print flag with the following meaning: 0, the status of the sampling analysis is not printed to the screen or file; 1, the status after each sample is printed only to the screen; 2, the status after each sample is printed only to the screen, while necessary information is printed into a file as well such that the sampling analysis may be restarted (i.e., analysis will continue from current point at the next run). The selection 2 is very useful for computational cases that need a large number of FE simulations.

***runOrthogonalPlaneSamplingAnalysis -fileName $fileName -maxNum $maxNum -type $type -targetCOV $cov -print $printFlag < -funcTol $funTol -varTol $varTol -maxIter $NumIter -littleDt $little_dt>***

where $type may be ‘failureProbability’ or ‘outCrossing’, corresponding to the time invariant (failure probability computation) and time variant reliability (upcrossing rate computation) reliability analysis, respectively. The parameters $fileName, $maxNum, $cov, $printFlag are the same as those in the ‘*runImportanceSamplingAnalysis*’ command. $funTol is the tolerance of LSF (G), such that the zerofinding algorithm stops when |G|< $funTol. $varTol is the tolerance criterion between two neighboring x in Equation (6.35): when $|x_{i+1}-x_i|<$*$varTol*, the zerofinding algorithm will also stop. $NumIter is the maximum number of iterations in the zerofinding algorithm. The default values for $funTol, $varTol, and $NumIter are 1e-5, 1e-3, and 20 respectively. The $little_dt ($\delta t$) is the small time increment between the two LSF as shown in Equation (6.50).

***runMonteCarloResponseAnalysis -outPutFile $fileName -maxNum $maxNum -print $printFlag -tclFileToRun $tclfile***

The $fileName, $maxNum, $printFlag are the same as before, while the $tclfile is the name of a tcl file that specifies the analysis. An example of such a tcl file is:

*test EnergyIncr 1.0e-16 20 2*

*algorithm Newton*

*system BandSPD*

*constraints Transformation*

*numberer RCM*

*integrator Newmark 0.55 0.275625 0. 0. 0. 0.*

*analysis Transient*

*analyze 20 0.01*

In the context of reliability analysis, a new visualization method called multidimensional visualization in principal plane (MVPP) is developed, which visualizes the LSF and thus the LSS in each principal plane defined by the design point direction and the principal direction of the LSS as mentioned in Chapter 6. From the results obtained from MVPP method, a new reliability analysis method named 'DP-RS-Sim' is developed, which combining the design point, and approximation of the LSF by response surface method, and simulation techniques. The necessary commands are described in next section.

### 8.3.4 Response Surface Method

It is first necessary to compute the Hessian matrix at the design point. The Hessian is computed by perturbation of the sensitivity results. i.e., $H_{i,j} \approx \frac{\Delta \frac{\partial G}{\partial u_i}}{\Delta u_j}$ (refer to chapter 6). The Tcl command is:

***computeHessian -FDM -file $fileName -designPoint $designPtFile -perturbation $perturbSize***

where $fileName is the name of the file in which the hessian matrix will be stored. $designPtFile is provided by the user and contains the previously computed design point in a single column(i.e., each value of RVs saved in one line). $perturbSize is the size of the perturbation $\Delta u_j$, default value is 1e-5.

The visualization command may be performed by the ‘runMultiDimVisualPrinPlane’ command, which may take advantage of the hessian matrix obtained by ‘computeHessian’ command. In case that hessian matrix is not available, it will call the ‘computeHessian’ command implicitly to obtain the hessian matrix. An example of using the ‘computeHessian’ command is:

***runMultiDimVisualPrinPlane -funSurf function -designPt designPointX.out -ndir 2 -output vis.out -gridInfo {0 -0.1 0.1 21 1 -0.2 0.2 11 2 -2.0 2.0 5}***

where the previously computed design point is stored in the file designpointx.out. The LSF will be visualized in the first two principal planes, the visualization results will be saved in the file vis.out. Along the design point axis, there are 21 points between [-0.1, 0.1]; Along the first principal axis, there are 11 points between [-0.2, 0.2]; Along the second principal axis, there are 5 points between [-2.0 2.0]. The output data format inside vis.out is: ‘ x y G(x,y) ’ for each point in each line.

The format of the newly developed ‘*runDP_RSM_SimTimeInvariantAnalysis*’ command will work only after the following commands are used:

*performanceFunction*

*probabilityTransformation*

*gFunEvaluator*

*randomNumberGenerator*

An example of the use of ‘*runDP_RSM_SimTimeInvariantAnalysis*’ is:

***runDP_RSM_SimTimeInVariantAnalysis -designPt designPointX.out -output results.out -ndir 2 -experimentalPointRule Uniform -gridInfo { -1 -2.0 2.0 9 0 -1.0 1.0 9 } -saveHessian hessian.out -surfaceDesign $type -simulation $SamplingMethod -tarCOV $cov -numSimulation $maxNum***

where designPointX.out contains the previously computed design point; results.out saves the output; 'ndir =2' indicates that the first 2 principal axes and the design point direction are used to fit the response surface (i.e., along these three directions, LSF is nonlinear, while along all other axes, the LSF is considered as linear plane), thus the number of grid planes is computed by $\frac{ndir \times (ndir+1)}{2} = 3$ (refer to chapter 6). Note that the design point direction is an extra direction used to fit the response surface; 'Uniform' means that the grid point is uniformly distributed along each axis; gridInfo is the same as in the *run-MultiDimVisualPrinPlane* command; hessian.out saves the hessian matrix, in case the Hessian matrix is not provided by the user, the command *compupteHessian* is called; $type specifies how to fit the response surface, currently 'UnivariateDecomposition' and 'BivariateDecomposition' are available; $samplingMethod describes which sampling method is used to get the failure probability after the response surface is obtained, currently only 'ImportanceSampling' is available; $cov, $maxNum are the same as those in the *runOrthogonalPlaneSamplingAnalysis* command.

The runDP_RSM_SimTimeVariantAnalysis command is used to compute the mean upcrossing rate for time variant reliability analysis. An example is:

***runDP_RSM_SimTimeVariantAnalysis -designPt designPointX.out -output results.out -ndir 2 -experimentalPointRule Uniform -gridInfo { -1 -2.0 2.0 9 0 -1.0 1.0 9 } -saveHessian hessian.out -surfaceDesign $type -simulation $SamplingMethod -tarCOV $cov -numSimulation $maxNum -littleDt $little_dt -ImpulseInterval $delt_t***

Most of the parameters in this command are the same as for the command *runDP_RSM_SimTimeVariantAnalysis*, while two more parameters are necessary: $little_dt is the same as that in *runOrthogonalPlaneSamplingAnalysis*. $delt_t is the time interval between two sequential random variables (or impulse in white noise excitation case).

## 8.4 General SNOPT Based Optimization

The framework of the general SNOPT based optimization is described in chapter seven. In order to take advantage of the framework, the user may need to use the following commands: *designVariable, designVariablePositioner, constraintFunction, objectiveFunction,* and *runSNOPTAnalysis*. The format of *designVariable* is:

***designVariable $gradNumber -name $nameDV -startPt $startPoint -lowerBound $lBound -upperBound $upperBound***

where $gradNumber is the design variable (DV) tag; $nameDV is the unique TCL variable name given to this DV by the user, $startPoint is the initial point from which the optimization begins; $lBound and $uBound are lower and upper bounds of this DV.

For the command *designVariablePositioner*, most parameters are the same as for the command *randomVariablePositioner*, except that the $gradNumber is the tag of the DV instead of a RV. An example of *designVariablePositioner* is as follows:

***designVariablePositioner $pos -dvNum $gradNumber -element 1 -sectionAggregator 2 -section 1 -material 1 $h***

The user has to define the objectiveFunction as follows:

***objectiveFunction $tag -name $nameF -tclFile $tclFile -lowerBound $lBound -upperBound $uBound < -gradientName $gradF >***

where $tag is the tag of the objectiveFunction begining from 1 (in the current version of SNOPT only one objective function), $nameF is the unique name of the objective function, $tclFile is the TCL file provided by the user in which the values of the objective function (and its gradient if available) are computed, and saved in the TCL variables $nameF (and $gradF). $lBound, $uBound are the same as in the designVariable command. $gradF is the unique name that user gives to gradients of the F.

In case that the constraint function is used, the following command may be performed:

***constraintFunction $tag -name $nameG <-gradientName $gradG> -tclFile $fileG -upperBound $uBound -lowerBound $lBound***

where $tag is the tag of the constraint function begining with 1 (in the current version of OpenSees there is only one constraint function). $nameG and/or $gradG are unique names of the constraint function and its gradient. $fileG is the file including TCL script that computes values of $nameG and/or $gradG. $uBound and $lBound are upper and

lower bounds of the constraint function. It is worth mentioning that the TCL variables $uBound and $lBound are arrays of the same size as the number of constraints in the *constraintFunction*. A typical way to set these two arrays for the case number of constraints=2 are (refer to TCL user manual):

***array set uBound {1 4.0 2 5.0}***

***array set lBound {1 -1e20 2 -1e20}***

After *designVariable, designVariablePositioner, constraintFunction, objectiveFunction, runSNOPTAnalysis* are defined, the command *runSNOPTAnalysis* may be performed to find the optimum as:

***runSNOPTAnalysis -maxNumIter $maxNumber -printOptPointX $resultFile -printFlag $printFlag < -tclFileToRun $tclFile>***

where $maxNumber is the limit of the number of iterations of the optimization process; $resultFile is the file to save the optimization results. $printFlag is the same as that in the command *runOrthogonalPlaneSamplingAnalysis*; $tclFile is the file containing the analysis information such as: static or dynamic analysis, how many steps to run, etc, the same as that in the command *runMonteCarloResponseAnalysis*.

In order to adopt SNOPT based optimization to various realistic problems, more commands are developed such that users may have greater control over the software. These command are described below:

***updateParameter -dv $numDV -value $newValue***

where $numDV is the tag of the DV whose value needs to be updated, while $newValue is the new value assigned to this DV.

***tryOneStep <$dt>***

This command will run one integration time step in OpenSees without commit state. That is: The global equilibrium of the current step is achieved with the converged state variables (e.g. node displacement, element trial stress, etc.) stored in the trial variables; while the commited-variables are not updated to trial variables. This allows users to revert to the last step if necessary. The optional parameter <$dt> is the size of the time step in the dynamic case.

***revertToLastCommit***

This command reverts the whole system to the last committed state and cancels the operation from '*tryOneStep*'. That is, the trial state variables are updated by the last converged state variables, and the system time reverts to the last committed time.

***commitOneStep***

This command will perform the operation that updates the committed variables with the trial variables, and updates the system time to the current time. The combined commands *trialOneStep* and *commitOneStep* in succesion are equivalent to the command *analyze 1 <$dt>*.

# CHAPTER 9

# CONCLUSIONS

## 9.1 Summary of Findings and Contributions

The research work described in this thesis makes significant contributions in the following areas: (1) extension of the finite element response sensitivity framework based on the direct differentiation method (DDM) to Soil-Foundation-Structure Interaction (SFSI) systems. (2) Computational probabilistic and reliability analysis of structural and/or geotechnical systems. (3) Nonlinear finite element model updating for structural and/or geotechnical systems.

The specific contributions and major findings of this research work are summarized below:

1. A general DDM-based FE response sensitivity computation algorithm is studied in detail and extended to SFSI systems. This sensitivity algorithm consists of differentiating exactly the FE algorithm for response-only computation with respect to material, geometric, and loading parameters. The algorithm involves the various hierarchical layers of FE response analysis, namely: structure level, element level, Gauss point level (or section level), and material level. A number of finite element types, section and material models, the multi-point constraint model, and the adaptive time stepping scheme are all extended for response sensitivity computation. Based on several appli-

cation examples, many issues related to DDM based response sensitivity analysis are studied. The subjects of these studies include: (1) The effect and acceptable range of the perturbation size when using forward finite difference (FFD) analysis to approach and thus validate the DDM results; (2) The convergence of DDM-based response sensitivity results with respect to the temporal and spatial resolutions; and (3) the effect of damping and strain-hardening (i.e., post-yield material stiffness) on response sensitivity results.

2. As one of the main contributions to sensitivity and reliability analysis for SFSI systems, an existing multi-yield surface $J_2$ plasticity model, a very versatile material model used extensively in geotechnical engineering, is studied and further developed as follows: (1) The consistent (or algorithmic) tangent moduli of this plasticity model are developed and software implemented. (2) A DDM-based response sensitivity algorithm is developed for this model and software implemented. When using consistent tangent moduli, the decreasing norm of the unbalanced force vector follows the asymptotic rate of quadratic convergence characteristic of Newton's process.

   Based on the comparative studies performed between the use of consistent and continuum tangent moduli, it is observed that in some computational cases (i.e., when the convergence tolerance is relatively small, or for large time step size in dynamic analysis), the use of the consistent tangent moduli reduces significantly both the number of iterations needed per load/time step to achieve convergence and the computational time.

The algorithm developed for response sensitivity analysis based on the DDM and the material consistent tangent moduli is validated through the Forward Finite Difference (FFD) method. The computational results indicate that the FFD results converge to the DDM results as the perturbation of the sensitivity parameter decreases within an acceptable range which depends on the computational round-off error, thus verifying the DDM results.

The DDM-based response sensitivity algorithm provides quantitative measures to evaluate the relative importance of the material parameters in terms of their relative influence on the structural and/or soil response (both global and local) of interest. It is found that stiffness related material parameters in both the structure and the soil are dominant when the system is subjected to low intensity earthquake excitation, while strength related material parameters are the most important ones when the system is subjected to strong earthquake excitation.

(3) A simplified probabilistic response analysis method based on the mean centered First-Order Second-Moment (FOSM) analysis using non-linear finite element response and response sensitivity analyses, is applied to structural and/or geotechnical systems subjected to quasi-static pushover loads. The effects on FOSM analysis results of using different methods for computing response sensitivities are also investigated. It is found that the FOSM approximation using the DDM for computing response sensitivities provides, at very low computational cost, very good estimates of the mean and standard deviation of the response for low-to-moderate levels of material non-linearity in the response of structural and/or geotechnical systems subjected to quasi-static pushover load.

Furthermore, the relative importance (in both the deterministic and probabilistic sense) of the material parameters on the structural response is obtained as by-product of an FOSM analysis at small additional computational cost.

It can be concluded that FOSM analysis provides a large amount of probabilistic information at low computational cost and can provide satisfactory accuracy for probabilistic analysis of structural and/or geotechnical systems subjected to quasi-static pushover load, provided that the level of material non-linearity exhibited by the system is low to moderate. For high level of material non-linearity, FOSM can still be used effectively to obtain qualitative information on the importance ranking of material model parameters on the system response.

4. Several advanced reliability analysis methods are further developed and applied to SFSI systems for both time invariant and time variant reliability analysis. Except for crude Monte Carlo simulation, these methods are based on the knowledge of the design point(s). In order to obtain a robust design point(s) search algorithm, the general-purpose optimization toolbox SNOPT is adopted, customized to reliability analysis problems and interfaced with the finite element analysis software framework OpenSees used in this research. SNOPT offers significant advantages for solving large-scale design point search problems, such as robustness, efficiency, and flexibility. In order to estimate the failure probability accurately, several sampling methods have been implemented in the reliability framework of OpenSees. These methods include crude Monte Carlo Simulation (MCS), Importance Sampling (IS), and Orthogonal Plane Sampling (OPS) combined with a robust line search root finding algorithm.

Based on the newly developed/modified/extended reliability analysis methods and the FE response sensitivity analysis framework, a realistic nonlinear SFSI application example is studied for time invariant reliability analysis. The failure probability estimates obtained using different methods (FORM, IS, OPS, and MCS) are consistent, thus validating the software implementation of these methods. For cases in which the failure probability is very small (e.g., $p_F < 10^{-3}$), or when a small coefficient of variation (e.g., < 5%) of the failure probability estimate is required, the use of MCS is not feasible due to its unacceptable computational cost. In the present work, it was found that FORM results for time-invariant reliability analysis are of acceptable accuracy and require far fewer evaluations than IS and OPS. However, in general, FORM is not guaranteed to be accurate. In time-invariant reliability analysis, IS is more efficient than OPS in the sense that it requires significantly fewer evaluations of the performance function.

An existing algorithm for computing the mean upcrossing rate in time variant reliability analysis, already implemented in the reliability framework of OpenSees, was further refined and improved for example to deal with non-converging cases in limit-state function evaluation. This algorithm was then used to solve SFSI time variant reliability analysis problems. In time variant reliability analysis of nonlinear SFSI systems, it was found that the FORM approximation for mean upcrossing rate is significantly inaccurate, especially in the case of highly nonlinear response behavior of the system. In this case, the OPS based on the design point(s) provides a good esti-

mate of the mean up-crossing rate time history and, therefore, of an upper bound of the failure probability. It provides significant improvement on the FORM results.

In order to study the topology of limit state surfaces (LSS) for both time invariant and time variant structural reliability problems, a new visualization method called Multi-dimensional Visualization in Principal Plane (MVPP) is developed and implemented in OpenSees. It was found that LSSs for typical nonlinear structural and SFSI systems are significantly nonlinear along only a few principal directions (i.e., 3-5 directions) and the nonlinearity along the remaining directions is small and can be ignored without significant loss of accuracy in estimating the failure probability. The geometrical insight gained from the MVPP has led to the development and implementation of a new hybrid computational reliability method, called the DP-RS-Sim method, which combines the design point (DP) search, the response surface methodology (RS), and simulation techniques (Sim). This method is applied for the time invariant reliability analysis of a nonlinear structural system subjected to quasi-static pushover. Based on the experience gained so far, it is observed that the DP-RS-Sim method is accurate and efficient in the sense that it yields very good results with significantly less simulations compared to IS or OPS. The efficiency of the DP-RS-Sim method is still hindered by the expensive computation of the Hessian matrix of the limit-state function at the design point.

5. A general-purpose OpenSees-SNOPT framework for solving optimization problems in nonlinear structural and/or geotechnical systems is developed and presented. Several application examples in nonlinear soil FE model updating are solved using this framework and presented.

Based on the numerical examples considered, the OpenSees-SNOPT framework allows to obtain the global minimum of the objective function provided the initial parameter values are not far from their actual (“true”) values, or when appropriate constraints are added. The convergence rates obtained using OpenSees-SNOPT combined with FE response sensitivities computed using the DDM and FFD methods, respectively, were compared. It was found that the DDM-based computation of the gradients of the objective and constraint functions increased drastically the rate of convergence (as measured by the number of iterations to achieve convergence) of the nonlinear finite element model updating process as compared to when using FFD-based gradient computation. This advantage of the DDM-based over FFD-based gradient computation increases with the nonlinearity in the system response behavior. Furthermore, it was observed that this advantage is even more significant when artificial numerical noise is added to the simulated ‘experimental’ response data so as to model measurement noise.

The OpenSees-SNOPT based nonlinear FE model updating strategy was then applied to a real world example consisting of a multi-layered nonlinear soil column at the Lotung downhole array in Taiwan. A linear soil FE model was calibrated (through FE model updating) to best represent the Lotung soil behavior during a low intensity earthquake, while a nonlinear FE model was calibrated to capture the actual nonlinear soil behavior during a strong earthquake. The calibrated linear and nonlinear soil FE models with parameters obtained from OpenSees-SNOPT were then used to simulate the response of the Lotung soil to other recorded earthquakes. In both the linear and nonlinear cases, the simulated soil response is very close to the recorded response.

This demonstrates that the calibrated/optimum soil FE models obtained using the OpenSees-SNOPT framework are physically meaningful.

## 9.2 Recommendations for Future Work

Based on the research work performed and presented herein, several research areas have been identified as open to and in need of future work. Most of these can be investigated based on the analysis framework for SFSI systems presented in this dissertation with little if any new software development.

(6) In order to fully exploit the advantages of the state-of-the-art finite element technology, DDM-based response sensitivity analysis needs to follow the advances of FE response-only methods. Derivation and implementation of the response sensitivity algorithms are required for new elements, new integration points (e.g., frame section models), new material constitutive models (such as sand), two-phase soil models, and various analysis options (e.g., displacement-control and arc-length solution strategies).

(7) The role and effect of the soil in SSI problems needs to be further studied in the context of probabilistic and reliability analysis (e.g., difference in results of response sensitivity analysis, probabilistic response analysis, and reliability analysis between SSI systems with or without soil, which may affect the analysis of such systems in the new performance-based earthquake engineering methodology). This is particularly necessary for structures made of new materials or structures with extremely high safety requirements such as nuclear power plants, or when considering very innovative designs.

(8) The source of discontinuities (along the parameter(s) axis) in FE dynamic response sensitivity analysis due to time discretization needs to be investigated.

(9) The proposed DP-RS-Sim reliability analysis method is still in its infancy stage of development. Further testing and extensions of this method are needed. To compute the first few principal directions of the limit-state surface without computing the whole Hessian matrix would lead to a crucial improvement of this method in terms of computational cost. Application of this newly developed method to SFSI systems will be very valuable. This DP-RS-Sim method should be extended/adapted to the case of multiple design points.

(10) The sensitivity-based nonlinear FE model upating strategy must be applied to SFSI systems, for which experimental and/or field data is available. Such applications will allow to evaluate the nonlinear prediction capabilities of state-of-the-art modeling and analysis tools of structural and geotechnical systems combined.

(11) Parallel/distributed computing is a promising approach to alleviate the computational demand in conducting large-scale FE analysis of structural and/or geotechnical systems. Considering the advantage of OpenSees as a C++ based software, parallel/distributed computing methods for response-only analysis is already functional. These high performance computing capabilities should be extended to support response sensitivity, probabilistic response, and reliability analyses of large-scale structural and/or geotechnical systems.

(12) Other methods of analysis for SFSI systems besides the direct approach using FE analysis should be considered. A hybrid method consisting of combining theoretical closed form solutions for the soil domain (assumed to be linear elastic) and a nonlin-

ear FE model of the structure has been developed by the author and co-workers, which does not appear in this dissertation. The response sensitivity and reliability analysis methods presented herein could be extended to this hybrid method of analysis of SFSI systems.

(13) The topic of Reliability Based Optimum Design (RBOD) of SFSI systems should be investigated based on the response sensitivity and reliability analysis framework developed in this reserch.

(14) The optimization software package SNOPT is a powerful computational tool for local optimization, but it cannot guarantee finding of the global minimum. Advanced global optimization algorithms, such as the coupled local minimizer, may be adopted and combined with SNOPT for finding the global optimum in structural reliability analysis and FE model updating.

(15) The numerical difficulties (e.g., numerical divergence) encountered in nonlinear static and dynamic response analysis of SFSI systems suggest that the soil plasticity models used need to be further investigated. Furthermore, more refined/realistic modeling of the interface between soil and (deep) foundations should be considered.

# REFERENCES

AASHTO, AASHTO LRFD Bridge Design Specification, American Association of State Highway and Transportation Officials, 2nd ed., 1998.

Arora, J. S., and Cardoso, J. B. . “A design Sensitivity Analysis Principle and its Implementation into ADINA.” Comp. & Structures, 32, 691-705. 1989.

Anandarajah, A. and Dafalias, Y.F. "Bounding Surface Plasticity. III: Application to Anisotropic Cohesive Soils,” Journal of Engineering Mechanics, ASCE, 112, pp. 1292-1318, 1986.

ATC-55: Evaluation and Improvement of Inelastic Seismic Analysis Procedures, Advanced Technology Council, Redwood City, California, 2005.

ATC-58: Development of Next-Generation Performance-Based Seismic Design Procedures for New and Existing Buildings, Applied Technology Council, California, 2005.

Atkinson, G. M., and Silva, W., “Stochastic Modeling of California Ground Motions,” Bulletin of the Seismological Society of America, 90(2), pp. 255-274, 2000.

Au, S. K., Papadimitriou, C., and Beck, J. L., “Reliability of Uncertain Dynamical Systems with Multiple Design Points,” Structural Safety, 21, 113-133, 1999.

Au, S. K., and Beck, J. L., “Important Sampling in High Dimension”, Structural Safety, 25, pp. 139-163, 2003.

Au, S. K., and Beck, J. L., “Subset Simulation and its Application to Seismic Risk Based

on Dynamic Analysis", J. of Engineering Mechanics, ASCE, 129(8), pp. 901-917, 2003.

Baecher, G. B., and Christian, J. T., Reliability and Statistics in Geotechnical Engineering, Wiley, 2003.

Barbato, M., and Conte, J. P., "Finite Element Response Sensitivity Analysis: A Comparison between Force-Based and Displacement-Based Frame Element Models, Comput. Methods Appl. Mech. Engrg. 194, pp. 1479–1512, 2005a.

Barbato, M., Zona, A., and Conte, J. P., "Finite Element Response Sensitivity Analysis using Three-Field Mixed Formulation: General Theory and Application to Frame Structures," under preparation, 2005b.

Barbato, M., and Conte, J. P., "Smooth versus Non-Smooth Material Constitutive Models in Gradient-Based Optimization for Structural Reliability Analysis," Proc. 9th International Conference on Structural Safety and Reliability, Rome, Italy, June 19-23, 2005c.

Barbato, M., Gu, Q., and Conte, J.P., "Response Sensitivity and Probabilistic Response Analyses of Reinforced Concrete Frame Structures", Proceeding of 8th National Conference on Earthquake Engineering, San Francisco, CA, USA, 2006.

Barbato, M., Gu, Q., and Conte, J.P., "Framework for Finite Element Response Sensitivity and Reliability analyses of Structural and Geotechnical Systems", First European Conference on Earthquake Engineering and Seismology (a joint event of the 13th ECEE & 30th General Assembly of the ESC), Geneva, Switzerland. 2006.

Baruch,M., "Methods of reference basis for identification of linear dynamic structures". In 23rd Structures, structural dynamics and materials conference, pages 557–563, New

Orleans, Louisiana, 1982.

Bathe, K. J., Finite Element Procedures. Prentice Hall, 1996.

Betti, R., Abdel-Ghaffar, A. M., and Niazy, A. S., “Kinematic Soil-Structure Interaction for Long-Span Cable-Supported Bridges,” Earthquake Engineering and Structural Dynamics, 22, pp. 415-430, 1993.

Bielak, J., “Dynamic Response of Non-Linear Building-Foundation Systems,” Earthquake Engineering and Structural Dynamics, Vol. 6, pp. 17-30, 1978.

Borja, R. I., Smith, H. A., Wu, W.-H., and Amies, A. P., “A Methodology for Nonlinear Soil-Structure Interaction Effects Using Time-Domain Analysis Techniques,” Rep. No. 101, Blume Earthquake Engineering Center, Stanford Univ., Stanford, California, 1992.

Borja, R. I., Chao, H. Y., Montans, F. J., and Lin, C. H., “Nonlinear Ground Response at Lotung LSST Site,” Journal of Geotechnical and Geoenvironmental Engineering, ASCE, 125(3), pp. 187-197, 1999.

Borja, R. I., Lin, C. H., Sama, K. M., and Masada, G. M., “Modelling Non-Linear Ground Response of Non-Liquefiable Soils,” Earthquake Engineering and Structural Dynamics, 29(1), pp. 63-83, 2000.

Bolotin, v.v., Statistical Methods in Structural Mechanics, Holden Day, 1967

Breitung, K., “Asymptotic Approximations for Multinormal Integrals,” Journal of the Engineering Mechanics Division, ASCE, 110(3), pp. 357-366, 1984.

BSSC, The 2003 NEHRP Recommended Provisions for New Buildings And Other Struc-

tures.

Part 1: Provisions (FEMA 450), Building Seismic Science Council, http://www.bsscon-line.org/, 2004.

Celebi, M., “Turkish Earthquakes: Two Reports. Lessons from the Adana-Ceyhan Quake and the Dinar Aftershock,” EERI Newsletter, 32(9), 8 pp, 1998.

Chiasson, P., Lafleur, J., Soulie, M., and Lay, K. T., “Characterizing Spatial Variability of a Clay by Geostatistics,” Canadian Geotechnical Journal, Vol. 32, pp. 1-10, 1995.

Ching, J., Au, S.K., and Beck, J. L., “Reliability Estimation for Dynamical Systems Subject to Stochastic Excitation Using Subset Simulation with Splitting,” Comput. Methods Appl. Mech. Engrg. 194, pp. 1557–1579, 2005.

Christian, J. T.,”Geotechnical Engineering Reliability: How Well Do We Know What We Are Doing?,” Journal of Geotechnical and Geoenvironmental Engineering, ASCE, 130(10), pp. 985-1003, 2004.

Choi, K. K., and Santos, J. L. T. “Design Sensitivity Analysis of Non-linear Structural Systems, Part 1: Theory.” Internat. J. Numer. Methods Engrg., 24, 2039-2055, 1987.

Chopra, A. K., Dynamics of Structures: Theory and Applications to Earthquake Engineering, Second Edition, Prentice Hall, 2001.

Conte, J. P., and Jagannath, M. K. “Seismic Reliability Analysis of Concrete Gravity Dams.” A Report on Research Sponsored by the Main Italian Electricity Company (ENEL), Department of Civil Engineering, Rice University, Houston, Texas, April 1995a.

Conte, J. P., Jagannath, M. K., and Meghella, M. “Earthquake Response Sensitivity Analysis of Concrete Gravity Dams.” Proc. Seventh International Conference on Applications of Statistics and Probability, 395-402, Paris, France, July 10-13, 1995b.

Conte, J. P., and Vijalapura, P. K. “Seismic Safety Analysis of Concrete Gravity Dams Accounting for Both System Uncertainty and Excitation Stochasticity.” A Report on Research Sponsored by the Italian National Power Board (ENEL-CRIS), Department of Civil Engineering, Rice University, Houston, Texas, June 1998.

Conte, J. P., and Peng, B.-F., “Fully Nonstationary Analytical Earthquake Ground Motion Model,” Journal of Engineering Mechanics, ASCE, 123(1), 15-24, 1997.

Conte, J. P., “Finite Element Response Sensitivity Analysis in Earthquake Engineering,” Earthquake Engineering Frontiers in the New Millennium. Spencer and Hu, Swets and Zeitlinger, pp. 395-401, 2001.

Conte, J. P., Elgamal, A., Yang, Z., Zhang, Y., Acero, G., and Seible, F., “Nonlinear Seismic Analysis of a Bridge Ground System,” 15-th ASCE Engineering Mechanics Conference, Columbia University, New York, NY, June 2-5, 2002.

Conte, J. P., Vijalapura, P. K., and Meghella, M., “Consistent Finite-Element Response Sensitivity Analysis,” Journal of Engineering Mechanics, ASCE, 129(12), pp. 1380-1393, 2003.

Conte, J.P., Barbato, M., and Spacone, E., “Finite element response sensitivity analysis using force-based frame models,” International Journal of Numerical Methods in Engineering 59(13) 1781-1820, 2004.

Cornell, C. A., and Krawinkler, H., “Progress and Challenges in Seismic Performance Assessment, PEER Center News, Spring 2000.

Courant, R. Differential and Integral Calculus, Vol. II, Wiley, 1988.

Crouse, C. B., and Jennings, P. C., “Soil-Structure Interaction during the San Fernando Earthquake,” Bull. Seism. Soc. Amer., 65(1), pp. 13-36, 1975.

Crouse, C. B., Hushmand, B., and Martin, G. R., “Dynamic Soil-Structure interaction of a Single-Span Bridge,” Earthquake Engineering and Structural Dynamics, Vol. 15, pp. 711-729, 1987.

Crouse, C. B., and Hushmand, B., “Soil-Structure Interaction and Non-Linear Site Response at the Differential Array Accelerograph Station,” Proc. 4th U.S. National Conf. on Earthquake Eng., Vol. 3, pp. 815-823, 1990.

Cutter, S. L., Ed., American Hazardscapes: The Regionalization of Hazards and Disasters, Washington, D. C.: Joseph Henry Press, 2001.

Dafalias, Y. F., “Bounding surface plasticity. I: Mathematical Foundation and Hypoplasticity,” Journal of Eng. Mech. Div., ASCE, 112(9), 966-987, 1986a.

Dafalias, Y. F., and Herrmann, L.R., "Bounding Surface Plasticity. II: Application to Isotropic Cohesive Soils," Journal of Engineering Mechanics, ASCE, 112(9), 1263-1291, 1986b.

Davis, J. C., Geostatistics and Data Analysis in Geology, Wiley & Sons, 1986.

DeGroot, D. J., “Analyzing Spatial Variability of Insitu Soil Properties (invited paper),” Uncertainty in the Geologic Environment, From Theory to Practice, Proc. of Uncertainty ’96, Geotechnical Special Publication No. 58, 1996.

Deodatis, G., Saxena, V. and Shinozuka, M. “Effect of Spatial Variability of Ground

Motion on Bridge Fragility Curves," Proceedings (CD-ROM) of the 8th ASCE Specialty Conference on Probabilistic Mechanics and Structural Reliability, University of Notre Dame, 2000.

Der Kiureghian, A., and Liu, P.-L., "Structural Reliability under Incomplete Probability Information", J. of the Engineering Mechanics Division, ASCE, 111(EM1), pp. 85-104, 1986.

Der Kiureghian, A., Lin, H.-Z., and Hwang, S.-J., "Second-Order Reliability Approximations," Journal of the Engineering Mechanics Division, ASCE, 113, No EM8, pp. 1208-1225, 1987.

Der Kiureghian, A., and Ke, J. B., "The Stochastic Finite Element Method in Structural Reliability," Probabilistic Engineering Mechanics, 3(2), 83-91, 1988.

Der Kiureghian, A., and Neuenhofer, A., "Response Spectrum Method for Multi-Support Seismic Excitations," Earthquake Engineering and Structural Dynamics, 21(8), pp. 713-714, 1992.

Der Kiureghian, A., 'The Geometry of Random Vibrations and Solutions by FORM and SORM," Probabilistic Engineering Mechanics, 15, pp. 81-90, 2000.

Der Kiureghian, A., and Li, C. C., "Nonlinear Random Vibration Analysis through Optimization," Proc. 7th IFIP WG7.5 Conference on Reliability and Optimization of Structural Systems, pp. 197-206, Boulder, Colorado, U.S.A., 1996.

Der Kiureghian, A., and Dakessian, T., "Multiple Design Points in First and Second-Order Reliability, Structural Safety, 20(1), pp. 37-49, 1998.

De Souza, Remo Magalhães, "Force-Based Finite Element for Large Displacement Inelas-

tic Analysis of Frames," Ph.D. dissertation, Department of Civil and Environmental Engineering, University of California, Berkeley, 2000.

DiPasquale, E., and Cakmak, A. S., "Detection and Assessment of Seismic Structural Damage," Report NCEER-87-0015, Nat. Ctr. For Earthquake Engrg. Res., State Univ. of New York at Buffalo, Buffalo, N. Y., 1987.

Ditlevsen, O., and Madsen, H. O., Structural Reliability Methods, Wiley, 1996.

Duncan, J. M., "Factors of Safety and Reliability in Geotechnical Engineering," Journal of Geotechnical and Geoenvironmental Engineering, ASCE, 126(4), pp. 307-316, 2000.

Elgamal, A., Yang, Z., and Parra, E., "Computational Modeling of Cyclic Mobility and Post-Liquefaction Site Response," Soil Dynamics and Earthquake Engineering, 22(4), 259-271, 2002.

Elgamal, A., Yang, Z., Parra, E., and Ragheb, A., "Modeling of Cyclic Mobility in Saturated Cohesionless Soils," International Journal of Plasticity, 19(6), pp. 883-905, 2003.

Elgamal, A., Yan, L., and Conte, J. P., "Computational Simulation of Bridge-Foundation-Ground System," in preparation, 2005.

FEMA, Federal Emergency Management Agency "NEHRP Guidelines for the Seismic Rehabilitation of Buildings." FEMA 273, Washington, DC, 1997.

Fenton, G. A., and Vanmarcke, E., "Simulation of Random Fields via Local Average Subdivision," Journal of Engineering Mechanics, ASCE, 116(8), 1733-1749, 1990.

Fenton, G. A., "Estimation for Stochastic Soil Models," Journal of Geotechnical and

Geoenvironmental Engineering, ASCE, 125(6), pp. 470-485, 1999.

Fenton, G. A., “Probabilistic Foundation Settlement on Spatially Random Soil,” Journal of Geotechnical and Geoenvironmental Engineering, ASCE, 128(5), pp. 381-390, 2002.

Fenves, G. L., McKenna, F., Scott, M. H., and Takahashi, Y., “An Object-Oriented Software Environment for Collaborative Network Simulation,” Proc. (CD-ROM) 13-th World Conf. on Earthquake Eng., Vancouver, Canada, August 1-6, 2004.

Filippou, F. C., and Constantinides, M., “FEDEASLab Getting Started Guide and Simulation Examples,” Technical Report NEESgrid-2004-22, August 31, 2004.

Franchin, P., “Reliability of uncertain inelastic structures under earthquake excitation,” Journal of Engineering Mechanics, ASCE, 130, pp. 180-191, 2004.

Fritzen C.P. and Bohle K., Identification of damage in large scale structures by means of measured FRFs - Procedure and application to the I40 highway bridge. In Proceedings of DAMAS 99, pages 310–319, Dublin, Ireland, 1999.

Friswell M. I. and Mottershead J. E. Finite Element Model Updating in Structural Dynamics. Kluwer Academic Publishers, Dordrecht, The Netherlands, 1995.

Gill, P.E., Murray, W., and Wright, M.H., Practical Optimization, Academic Press, New York, 1981.

Gill, P.E., Numerical Nonlinear Optimization. classnotes, June 2004

Gill P. E., Murray W. and Saunders M. A., “SNOPT: An SQP algorithm for large-scale constrained optimization”. SIAM Review 47, 2005, 99-131

Grama, A., Gupta, A., Karypis, G., and Kumar, V., Introduction to Parallel Computing, Addison Wesley, 2nd edition, 2003.

Griffiths, D. V., and Fenton, G. A., "Three-Dimensional Seepage through Spatially Random Soil," Journal of Geotechnical and Geoenvironmental Engineering, ASCE, 12392), pp. 153-160, 1997.

Gu, Q., Barbato, M., Conte, J. P., and McKenna, F., "Handling of Constraints in Finite Element Response Sensitivity Analysis," under preparation, 2008a.

Gu, Q., Conte J.P., "Convergence Studies in Nonlinear Finite Element Response Sensitivity Analysis". The 9th International Conference on Applications of Statistics and Probability in Civil Engineering, Berkeley, California, USA, 2003

Gu, Q., Conte, J. P., Yang, Z., and Elgamal A., 2008. Response Sensitivity Analysis of A Multi-Yield-Surface $J_2$ Plasticity Model by Direct Differentiation Method, under preparation, 2008b.

Gu, Q., Barbato, M., and Conte, J.P., Handling of Constraints in Finite Element Response Sensitivity Analysis, to be submitted to *Journal of Engineering Mechanics*, ASCE, 2008.

Hagen, O., and Tvedt, L. "Vector Process Out-Crossing as Parallel System Sensitivity Measure," J. of Engrg. Mech., ASCE, 121(10), pp. 2201-2220, 1991.

Harichandran, R. S., and Vanmarcke, E. H., "Stochastic Variation of Earthquake Ground Motion in Space and Time," Journal of Engineering Mechanics, ASCE, 112(2), pp. 154-174, 1986.

Harichandran, R. S., "Estimating the Spatial Variation of Earthquake ground Motion from

Dense Array Recordings, Structural Safety, 10(1-3), pp. 219-233, 1991.

Harichandran, R. S., Hawwari, A., and Sweidan, B., “Response of Long-Span Bridges to Spatially Varying Ground Motion,” Journal of Structural Engineering, ASCE, 122(5), 1996.

Hasofer, A. M., and Lind, N. C., “Exact and Invariant Second-Moment Code Format”, Journal of the Engineering Mechanics Division, ASCE, 118 (EM10), pp. 2148-2155, 1992.

Hasofer, A. M., “Simulation of Random Fields,” Probabilistic Methods in Geotechnical Engineering, Li & Lo (eds.), Balkema, Rotterdam, 1993.

Haukaas, T., and Der Kiureghian, A. User’s Guide for Reliability and Sensitivity Analysis in OpenSees, Pacific Earthquake Engineering Research Center, University of California, Berkeley, CA, 2003. (http://www.ce.berkeley.edu/~haukaas/OpenSees-Reliability/opensees-reliability.html)

Haukaas, T., and Der Kiureghian, A., Finite element reliability and sensitivity methods for performance-based engineering. Report PEER 2003/14, Pacific Earthquake Engineering Research Center, University of California, Berkeley, 2004.

Heinkenschloss, M. Optimization Methods for Optimal Control Problems. Lecture Notes, Summer School in Continuous Optimization, Technical University Hamburg-Harburg, Germany, September, 1997.

Heonsang koo, FORM, SORM and simulation techniques for nonlinear random vibrations. PhD Dissertation. UC Berkeley. 2003

Hudson, D. E., “Dynamic Tests of Full Scale Structures,” Earthquake Engineering, R. L.

Wiegel, ed., Prentice-Hall, Englewood Cliffs, N.J., pp. 127-149, 1970.

ICC, International Building Code 2003, International Code Council, CD-ROM, 2003.

Jennings, P. C., and Bielak, J., “Dynamics of Building-Soil Interaction,” Bulletin of the Seismological Society of America, 63, pp. 9-48, 1973.

Jin, S., Lutes, L. D., and Sarkani, S., “Response Variability for a Structure with Soil-Structure Interactions and Uncertain Soil Properties,” Probabilistic Engineering Mechanics, 15, pp. 175-183, 2000.

Jones, A. L., Kramer, S. L., and Arduino, P., Estimation of Uncertainty in Geotechnical Properties for Performance-Based Earthquake Engineering, Report PEER 2002/16, Pacific Earthquake Engineering Research Center, University of California, Berkeley, December 2002.

Jordan, H. F., and Sawyer, P. L., "A Multi-Microprocessor System for Finite Element Structural Analysis", Computers & Structures, 10, 21-29, 1979.

Kamal, R., and Conte, J. P., “Nonlinear Geometric and Material Analysis of Shell Structures with Particular Emphasis on Tubular Joints,” A Report on Research Sponsored by the Advanced Technology Program (ATP) of the State of Texas, Dept. of Civil Engineering, Rice University, Houston, Texas, October, 1997, 401 pages.

Kleiber, M., Antunez H., Hien T. D., and Kowalczyk, P., Parameter Sensitivity in Nonlinear Mechanics: Theory and Finite Element Computations, Wiley, New York, 1997.

Koo, H-S., and A. Der Kiureghian. “Design point excitation for stationary random vibrations,” Proc. 8th Int. Conf. On Structural Safety and Reliability, Newport Beach, CA, June 2001.

Koo, H., A. Der Kiureghian. “FORM, SORM and simulation techniques for nonlinear random vibrations. Report No. UCB/SEMM-2003/01”, Department of Civil & Environmental Engineering, University of California, Berkeley, CA, February, 2003.

Koutsourelakis, S., Prevost, J. H., and Deodatis, G., “Risk Assessment of an Interacting Structure-Soil System due to Liquefaction,” Earthquake Engineering and Structural Dynamics, 31(4), pp. 851-879, 2002.

Kuschel, N., Pieracci, A., Rackwitz, R., “Multiple b-points in Structural Reliability,” 3rd Int. Conference on Computational Stochastic Mechanics, Santorini, 14-17 June, 1998.

Lacasse, S., and Nadim, F., “Uncertainties in Characterizing Soil Properties (Plenary), Uncertainty in the Geologic Environment, From Theory to Practice,” Proceeding of Uncertainty’96, Geotechnical Special Publication No. 58, 1996.

Lade, P. V., and Duncan, J. M., “Cubical Triaxial Tests on Cohesionless Soil,” J. Soil Mech. Found. Division, ASCE, 99(SM10), pp. 793-812, 1973.

Lade, P. V., and Duncan, J M., “Elastoplastic Stress-Strain Theory for Cohesionless Soil,” J. Geotechnical Engineering Division, ASCE, 101(GT10), pp. 1037-1053, 1975.

Lade, P. V., “Elasto-Plastic Stress-Strain Theory for Cohesionless Soil with Curved Yield Surfaces,” Intl. J. Solids Structures, 13, pp. 1014-1035, 1977.

Lawrence, M. “Basic Random Variables in Finite Element Analysis”, Int. J. of Numerical Methods in Engrg., 24(10), 1849-1863, 1987.

Li, C.-C., and Der Kiureghian, A., “Optimal Discretization of Random Fields,” J. Engrg. Mech., ASCE, 119(6), 1136-1154, 1993.

Li, C. C., and Der Kiureghian, A., “Mean Out-Crossing Rate of Nonlinear Response to Stochastic Input,” Proc. . 7th Int. Conf. on Applic. of Statistics and Probability, 295-302, Paris, France, July 10-13, 1995.

Limkatanyu, S., and Spacone, “R/C Frame Element with Bond Interfaces. Part 1: Displacement-Based, Force-Based and Mixed Formulations,” Journal of Structural Engineering, ASCE, 128(3), pp. 346-355, 2002.

Link, M. Updating of analytical models - Review of numerical procedures and application aspects. In Proceedings of the Structural Dynamics Forum, SD2000, Los Alamos, 1999.

Liu, W. K., Belytschko, T. and Mani, A., “Random Field Finite Elements.” Int. J. of Numerical Methods in Engrg., 23(10), 1831-1845, 1986.

Liu, P.-L., and Der Kiureghian, A., Optimization Algorithms for Structural Reliability,” Structural Safety, 9(3), pp. 161-177, 1991.

Lu, R., Luo, Y., and Conte, J. P., “Reliability Evaluation of Reinforced Concrete Beams,” Structural Safety, 14, pp. 277-298, 1994.

Lu, J., Yang, Z., He, L., Peng, J., Elgamal, A., and Law, K. H., “Computational modeling of Nonlinear Soil-Structure Interactio on Parallel Computers,” Proc. (CD-ROM) 13-th World Conf. on Earthquake Eng., Vancouver, Canada, August 1-6, 2004.

Lu, J., Peng, J., Elgamal, A., Yang, Z. and Law, K. H., “Parallel Finite Element Modeling of Earthquake Ground Response and Liquefaction,” Journal of Earthquake Engineering and Engineering Vibration, 3(1), June 2004.

Lubliner, J. Plasticity Theory. Macmillan Pub. Co., 1990.

Luco, J. E., “Linear Soil-Structure Interaction,” Soil Structure Interaction: The Status of Current Analysis Methods and Research, J. J. Johnson, ed., Rep. No. NUREG/CR-1780 and UCRL-53011, U.S. Nuclear Regulatory Commission, Washington, D. C. and Lawrence Livermore Laboratory, Livermore, California, 1980.

Luco, J. E., and Wong, H. L., “Response of a Rigid Foundation to a Spatially Random Ground Motion,” Earthquake Engineering & Structural Dynamics, 14(6), pp. 891-908, 1986.

Luco, J. E., and Mita, A., “Response of Circular Foundation to Spatially Random Ground Motion,” Journal of Engineering Mechanics, ASCE, 113(1), pp. 1-15, 1987.

Luco, J. E., Trifunac, M. D., and Wong, H. L., “On the Apparent Change in Dynamic Behavior of a Nine Story Reinforced Concrete Building,” Bull. Seismological Soc. of America, 77(6), pp. 1961-1873, 1987.

Luco, J. E., Trifunac, M. D., and Wong, H. L., “Isolation of Soil-Structure Interaction Effects by Full-Scale Forced Vibration Tests,” Earthquake Engineering and Structural Dynamics, Vol. 16, pp. 1-21, 1988.

Lumb, P., “The Variability of Natural Soils,” Canadian Geotechnical Journal, 3(2), pp. 74-97, 1966.

Lutes, L. D., Sarkani, S., and Jin, S., “Response Variability of an SSI System with Uncertain Structural and Soil Properties,” Engineering Structures, 22, pp. 605-620, 2000.

Lysmer, J., and Kuhlemeyer, R. L., “Finite Dynamic Model for Infinite Media,” J. Eng. Mech. Div., ASCE, 95(EM4), pp. 859-877, 1969.

MacGregor, J. G., Mirza, S. A., and Ellingwood, B. R., “Statistical Analysis of Resistance

of Reinforced and Prestressed Concrete Members," ACI J., 80(3), pp. 167-176, 1983.

Madsen, H.O., Krenk, S., and Lind, N.C., Methods of structural safety. Prentice-Hall Inc., Englewood Cliffs, New Jersey, 1986.

Makris, N., Badoni, D., Delis, E., and Gazetas, G., "Prediction of observed Bridge Response with Soil-Pile-Structure Interaction," Journal of Structural Engineering, ASCE, 120(10), pp. 2992-3011, 1994.

Malone, J.G., "Parallel Nonlinear Dynamic Finite Element Analysis of Three-Dimensional Shell Structures", Computers & Structures, 35, 523-539, 1990.

Marini, A., and Spacone, E., "Analysis of R/C Elements Including Shear Effects," ACI Structures Journal, under review, 2005.

McKenna, F., and Fenves, G. L. An Object-Oriented Software Design for Parallel Structural Analysis. Proc. of the SEI/ASCE Structures Congress, Philadelphia, PA, 2000.

McKenna, F., Fenves, G. L., et al. OpenSees (Open System for Earthquake Engineering Simulation) Users Manual, Version 1.6.0, 2004.

Matlab - High Performance Numeric Computation and Visualization Software, User's Guide, The MathWorks Inc., Natick, Massachusetts, 1997.

Merritt, G. H., and Housner, G. W., "Effects of Foundation Compliance on Earthquake Stresses in Multistory Buildings," Bull. Seism. Soc. Amer., 44(4), pp. 551-569, 1954.

Miller, A. K. (editor). Unified Constitutive Equations for Creep and Plasticity. Elsevier Applied Science, Pub., London, 1987.

Mirza, S. A., and MacGregor, J. G., “Variations of Dimensions of Reinforced Concrete Members,” J. Struct. Div., ASCE, 105(4), pp. 751-765, 1979a.

Mirza, S. A., and MacGregor, J. G., “Variability of Mechanical Properties of Reinforcing Bars,” J. Struct. Div., ASCE, 105(5), pp. 921-937, 1979b.

Mirza, S. A., Hatzinikolas, M., and MacGregor, J. G., “Statistical Descriptions of Strength of Concrete,” J. Struct. Div., ASCE, 105(6), pp. 1021-1035, 1979c.

National Research Council, Preventing Earthquake Disasters – The Grand Challenge in Earthquake Engineering, The National Academies Press, 2003.

Moehle, J., and Deierlein, G. G., "A Framework Methodology for Performance-Based Earthquake Engineering,“ Proc. (CD-ROM) 13-th World Conf. on Earthquake Eng., Vancouver, Canada, August 1-6, 2004.

Muraleetharan, K. K., Mish, K. D., Yogachandran, C., Arulanandan, K., “DYSAC2: Dynamic Soil Analysis Code for 2-Dimensional Problems,” Computer Code, Department of Civil Engineering, University of California, 1988.

Mylonakis, G., and Gazetas, G., “Seismic Soil-Structure Interaction Beneficial or Detrimental?”, Journal of Earthquake Engineering, 4(3), pp. 277-301, 2000.

Nalitolela N. G. , Penny J. E. T., and Friswell M. I. . A mass or stiffness addition technique for structural parameter updating. International Journal of Analytical and Experimental Modal Analysis, 7:157–168, 1992.

Nazmy, A. S., and Abdel-Ghaffar, A. M., “Effects of Ground Motion Spatial Variability on the Response of Cable-Stayed Bridges,” Earthquake Engineering and Structural Dynamics, 21(1), pp. 1-20, 1992.

Neuenhofer, A., and Filippou, F.C. "Evaluation of Nonlinear Frame Finite-Element Models." Journal of Structural Engineering, ASCE, 123(7), pp. 958-966., 1997.

Park, Y. J., and Ang, A. H.-S., “Mechanistic Seismic Damage Model for Reinforced Concrete,” Journal of Structural Engineering, ASCE, Vol. 111, No. 4, 1985, pp. 722-739.

PEER (Pacific Earthquake Engineering Research Center), OpenSees – Open System for Earthquake Engineering Simulation. Available online at http://opensees.berkeley.edu/, 2004.

Peng, J., Lu, J., Law, K. H., and Elgamal, A., “ParCYCLIC: Finite Element Modelling of Earthquake Liquefaction Response on Parallel Computers”, International Journal for Numerical and Analytical Methods in Geomechanics, 28, pp. 1207-1232, 2004.

Peng, J., Lu, J., Law, K. H., and Elgamal A., “Simulation of Earthquake Liquefaction Response on Parallel Computers,” Proc. of ASCE Structural Congress and Expositions, Nashville, TN, May 2004.

Phoon, K., and Kulhawy, F. H., “Characterization of Geotechnical Variability,” Canadian Geotechnical Journal, Vol. 36, pp. 625-639, 1999.

Phoon, K., and Kulhawy, F. H., “Evaluation of Geotechnical Property Variability,” Canadian Geotechnical Journal, Vol. 36, pp. 612-624, 1999.

Popescu, R., Deodatis, G., and Prevost, J. H., “Simulation of Homogeneous Non-Gaussian Stochastic Vector Fields,” Probabilistic Engineering Mechanics, 13(1), pp. 1-13, 1998.

Porter, K. A., “An Overview of PEER’s performance-based earthquake engineering methodology,” Proc. 9-th Int. Conf. on Applic. Of Statistics and Probability (ICASP9) in

Civil Eng., San Francisco, CA, July 2003, A. Der Kiureghian et al., Eds., 2:973-980.

Powell, G. H., and Allahabadi, R., “Seismic Damage Prediction by Deterministic Methods: Concepts and Procedures,” Earthquake Engineering and Structural Dynamics, Vol. 16, 1988, pp. 719-734.

Prevost, J-H., “Anistropic Undrained Stress-Strain Behavior of Clays,” Journal of the Geotechnical Engineering Division, ASCE, 104(GT8), pp. 1075-1090, 1978.

Prevost, J. H., “DYNAFLOW: A Nonlinear Transient Finite Element Analysis Program,” Technical Report, Department of Civil Engineering and Operational Research, Princeton University, Princeton, N.J., 1995.

Prevost, J., and Popescu, R., “Constitutive Relations for Soil Materials,” The Electronic Journal of Geotechnical Engineering, Vol. 1, 1996 (http://www.ejge.com/index_ejge.htm).

Priestley, M. J. N., and Park, R., “Strength and Ductility of Concrete Bridge Columns Under Seismic Loading,” ACI Structural Journal, 84(1), pp. 61-76, 1987.

Rackwitz, R., and Fiessler, B. “Structural Reliability under Combined Random Load Sequences,” Journal of Computers and Structures, 9, pp. 489-499, 1978.

Rackwitz, R., “Reviewing Probabilistic Soils Modelings,” Computers and Geotechnics, 26(3-4), pp. 199-223, 2000.

Resendiz, D., and Roesset, J. M., “Soil-Structure Interaction in Mexico City during the 1985 Earthquake,” The Mexico Earthquake – 1985 ASCE, eds. M. A. Cassaro and E. M. Romero, pp. 193-203, 1985.

Rice, O. S. “Mathematical analysis of random noise“, Bell system technical Journal, Vol. 23, pp. 282-332, 1944, vol. 24, pp. 46-156, 1945.

Romero, M. L., Miguel, P. F., and Cano, J. J., “A Parallel Procedure for Nonlinear Analysis of Reinforced Concrete Three-dimensional Frames” Computers & Structures, 80, pp. 1337-1350, 2002.

Saxena, V., Deodatis, G., Shinozuka, M. and Feng, M.Q. “Development of Fragility Curves for Multi-Span Reinforced Concrete Bridges,” Proceedings of the International Conference on Monte Carlo Simulation, Principality of Monaco, Balkema Publishers, pp. 499-504, 2000.

Schulz, M., and Filippou, F. C., “Nonlinear Spatial Timoshenko Beam Element with Curvature Interpolation,” International Journal of Numerical Methods in Engineering, 50(4), pp. 761-785, 2001.

Scott, R. F., “Plasticity and Constitutive Relations in Soil Mechanics,” Journal of Geotechnical Engineering, ASCE, 111(5), pp. 563-605, 1985.

Simo, J. C., and Hughes, T. J. R. Computational Inelasticity. Springer-Verlag, 1998.

Shi Z. Y. , Law S. S. , and Zhang L. M. Structural damage detection from modal strain energy change. Journal of Engineering Mechanics, 126(12):1216–1223, 2000.

Shinozuka, M., and Deodatis, G., “Simulation of Stochastic Processes by Spectral Representation,” Applied Mechanics Reviews, ASME, 44(4), pp. 191-204, 1991.

Shrikhande, M., and Gupta, V. K., “Dynamic Soil-Structure Interaction Effects on the Seismic Response of Suspension Bridges,” Earthquake Engineering and Structural Dynamics, 28, pp. 1383-1403, 1999.

Sivaselvan, M.V. and Reinhorn, A.M., “Collapse Analysis: Large Inelastic Deformations Analysis of Planar Frames,” Journal of Structural Engineering, ASCE, 128(12), 1575-1583, 2002.

Sotelino, E. D., and Dere, Y., “Parallel and distributed finite element analysis of structures,” in Engineering computational technology, pp. 221-250, Topping, B. H. V., and Bittnar, Z. eds., Civil-Comp press, Edinburgh, UK, 2002.

Spacone, E., Ciampi, V., and Filippou, F.C. "Mixed Formulation of Nonlinear Beam Finite Element." Computers and Structures, Vol. 58, No. 1, 71-83, 1996a.

Spacone, E., Filippou, F.C., and Taucer, F.F. "Fiber Beam-Column Model for Nonlinear Analysis of R/C Frames. I: Formulation." Earthquake Engineering and Structural Dynamics 25 (7), 711-725, 1996b.

Spacone, E., Filippou, F.C., and Taucer, F.F. "Fiber Beam-Column Model for Nonlinear Analysis of R/C Frames. II: Applications." Earthquake Engineering and Structural Dynamics 25 (7), 726-742, 1996c.

Spacone, E., and El-Tawil, “Nonlinear Analysis of Steel-Concrete Composite Structures: State-of-the-Art,” Journal of Structural Engineering, ASCE, 130(2), pp. 159-168, 2004.

SEAOC, Structural Engineers Association of California. "Performance Based Seismic Engineering of Buildings." April 3, 1995.

Stewart, J. P., Fenves, G. L., and Seed, R. B., “Seismic Soil-Structure Interaction in Buildings. I: Analytical Methods,” Journal of Geotechnical and Geoenvironmental Engineering, 125(1), pp. 26-37, 1999a.

Stewart, J. P., Fenves, G. L., and Seed, R. B., “Seismic Soil-Structure Interaction in Buildings. II: Empirical Findings,” Journal of Geotechnical and Geoenvironmental Engineering, 125(1), pp. 38-48, 1999b.

Stewart, J. P., Fenves, G. L., and Seed, R. B., Closure of Discussion of “Seismic Soil-Structure Interaction in Buildings. I: Analytical Methods; II: Empirical Findings,” by M. Trifunac, Journal of Geotechnical and Geoenvironmental Engineering, 126(7), pp. 668-670, 2000.

Stewart, J. P., Kim, S., Bielak, J., Dobry, R., and Power, M. S., “Revision to Soil-Structure Interaction Procedures in NEHRP Design Provisions,” Earthquake Spectra, 19(3), pp. 677-696, 2003.

Suykens J. A. K. and Vandewalle J. . Coupled Local Minimizers: Alternative formulations and extensions. In 2002 World Congress on Computational Intelligence - International Joint Conference on Neural Networks IJCNN 2002, pages 2039–2043, Honolulu, USA, May 2002.

Suykens J. A. K., Vandewalle J., and De Moor B. Intelligence and cooperative search by Coupled Local Minimizers. International Journal of Bifurcation and Chaos, 11(8):2133–2144, August 2001.

Taylor, R. L., “FEAP - A Finite Element Analysis Program - Version 7.1 User Manual,” Department of Civil and Environmental Engrg., Univ. of California at Berkeley, Berkeley, CA, 94720-1710, November, 1998. (http://www.ce.berkeley.edu/~rlt/feap/)

Tsay, J. J., and Arora, J. S. (1990). “Nonlinear Structural Design Sensitivity Analysis for Path Dependent Problems. Part 1: General Theory.” Comput. Methods Appl. Mech. Engrg., 81, 183-208.

Tsay, J. J., Cardoso, J. E. B., and Arora, J. S. (1990). Nonlinear Structural Design Sensitivity Analysis for Path Dependent Problems. Part 2: Analytical Examples." Comp. Methods Appl. Mech. Engrg., 81, 209-228.

Tan, C. P., Donald, I. B., and Melchers, R. E., "Probabilistic Slope Stability Analysis – State-of-Play," Proc. of the Conf. On Probabilistic Methods in Geotechnical Engineering, Canberra, Australia, pp. 89-110, 1993.

Tantalla, J., Prevost, J-H. and Deodatis, G., "Spatial Variability of Soil Properties in Slope Stability Analysis: Fragility Curve Generation," Proceedings (CD-ROM) of the 8th International Conference on Structural Safety and Reliability (ICOSSAR), Newport Beach, California, June 17-21, 2001.

Toubalem, F., Zeldin, B., Thouverez, F., and Labbe, P., "Vertical Excitation of Stochastic Soil-Structure Interaction Systems," Journal of Geotechnical and Geoenvironmental Engineering, ASCE, 125(5), 1999.

Trifunac, M. D., and Todorovska, M. I., "Reduction of Structural Damage by Nonlinear Soil Response," Journal of Structural Engineering, ASCE, 125(1), pp. 89-97, 1999.

Trifunac, M. D. Discussion of "Seismic Soil-Structure Interaction in Buildings. I: Analytical Methods; II: Empirical Findings," Journal of Geotechnical and Geoenvironmental Engineering, 126(7), pp. 668-670, 2000.

Udwadia, F. E., and Trifunac, M. D., "Time and Amplitude Dependent Response of Structures," Earthquake Engineering and Structural Dynamics, 2, pp. 359-378, 1974.

Uscinski, B. J., The Elements of Wave Propagation in Random Media, McGraw Hill, 1977.

Vanmarcke, E. H., “Probabilistic Modeling of Soil Profiles,” Journal of the Geotechnical Engineering Division, ASCE, 103(11), pp. 1227-1246, 1977.

Vanmarcke, E. H., Simulation of Random Fields, The MIT Press, Cambridge, Massachusetts, 1983.

Vanmarcke, E. H., and Grigoriu, M., “Stochastic Finite Element Analysis of Simple Beams” J. of Engrg. Mech., ASCE, 109 (5), 1203-1214, 1983.

Veletsos, A. S., and Verbic, B., “Dynamics of Elastic and Yielding Structure-Foundation Systems,” Proc. 5th world Conf. on Earthquake Eng., Rome, Italy, pp. 2610-2613, 1973.

Veletsos, A. S., and Meek, J. W., “Dynamic Behavior of Building-Foundation Systems,” Journal of Earthquake Engineering and Structural Dynamics, 3(2), pp. 121-138, 1974.

Vijalapura, P. K., Conte, J. P., and Meghella, M., “Time-Variant Reliability Analysis of Hysteretic SDOF Systems with Uncertain Parameters and Subjected to Stochastic Loading,” Proc. Eighth Int. Nat. Conf. on Applic. of Statistics and Probability, pp. 827-834, Sydney, Australia, Dec. 12-15, 1999.

Wei F.S., Structural dynamic model improvement using vibration test data. AIAA Journal, 28:175–177, 1990.

Wong, H. L., Trifunac, M.D., and Luco, J. E., “A Comparison of Soil Structure Interaction Calculations with results of a Full-Scale Forced Vibration Test,” Soil Dynamics and Earthquake Engineering, 7(1), pp. 22-31, 1988.

Yamada, Y., Takemiya, H., and Kawano, K., “Random Response Analysis of Non-Linear

Soil-Suspension Bridge Pier," Earthquake Engineering and Structural Dynamics, 7, pp. 31-47, 1979.

Yamazaki, F., and Shinozuka, M., "Digital Generation of Non-Gaussian Stochastic Fields," Journal of Engineering Mechanics, ASCE, 114(7), pp. 1183-1197, 1988.

Yang, Z. and Elgamal, E., "Influence of Permeability on Liquefaction-Induced Shear Deformation", Journal of Engineering Mechanics, ASCE, Vol. 128, No. 7, July 1, 2002.

Yang, Z., Elgamal, A., and Parra, E., "Computational Model for Cyclic Mobility and Associated Shear Deformation," Journal of Geotechnical and Geoenvironmental Engineering, ASCE, 129(12), pp. 1119-1127, 2003.

Zerva, A., "Response of Multi-Span Beams to Spatially Incoherent Seismic Ground Motions," Earthquake Engineering and Structural Dynamics, pp. 819-832, 1990.

Zhang, J., and Makris, N., "Seismic Response Analysis of Highway Overcrossings Including Soil-Structure Interaction," Earthquake Engineering and Structural Dynamics, 31, pp. 1967-1991, 2002.

Zhang, J., Makris, N., and Delis, T., "Structural Characterization of Modern Highway Overcrossings – Case Study," Journal of Structural Engineering, ASCE, 130(6), pp. 846-860, 2004.

Zhang, Y., and Der Kiureghian, A., "Dynamic Response Sensitivity of Inelastic Structures," Computer Methods in Applied Mechanics and Engineering, 108, pp. 23-36, 1993.

Zhang, Y., and Der Kiureghian, A., "First-Excursion Probability of Uncertain Structures,"

Probabilistic Engineering Mechanics, 9, pp. 135-143, 1994.

Zhang, Y., Yang, Z., Bielak, J., Conte, J. P., and Elgamal, A., “Treatment of Seismic Input and Boundary Conditions in Nonlinear Seismic Analysis of a Bridge Ground System,” Proc. of 16-th ASCE Engineering Mechanics Conference, University of Washington, Seattle, WA, July 16-18, 2003.

Zhang, Y., Acero, G., Conte, J., Yang, Z., and Elgamal, A., “Seismic Reliability Assessment of a Bridge Ground Syste,” Proc. (CD-ROM) 13-th World Conf. on Earthquake Eng., Vancouver, Canada, August 1-6, 2004.

Zhang Y, Conte JP, Yang Z, Elgamal A, Bielak J, Acero G. Two-dimensional nonlinear earthquake response analysis of a bridge-foundation-ground system. *Earthquake Spectra*. Accepted for publication, 2008.

Zienkiewicz, O. C., Chan, A. H. C., Pastor, M., Paul, D. K., and Shiomi, T., “Static and Dynamic Behavior of Soils: A Rational Approach to Quantitative Solutions: I. Fully Saturated Problems,” Roy. Soc. London, A429, pp. 285-309, 1990.

Zienkiewicz, O. C., Chan, A. H. C., Pastor, M., Schrefler, B. A., and Shiomi, T., Computational Geomechanics with Special Reference to Earthquake Engineeering, Wiley, 1999.

Zienkiewicz, O. C., and Taylor, R. L. The Finite Element Method, Vol. 2 - Solid Mechanics. 5-th Ed., Butterworth Heinemann, 2000.

Zona, A., Barbato, M., and Conte, J. P., “Finite Element Response Sensitivity Analysis of Steel-Concrete Composite Beams with Deformable Shear Connection,” Journal of Engineering Mechanics, ASCE, in press, 2005.